



The  
University  
Of  
Sheffield.

***High energy density positive insertion  
electrodes for next generation lithium-ion  
batteries***

**Beth Ilse Joyce Johnston**

**Submitted in fulfilment of the requirements for the  
degree of Doctor of Philosophy**

**Department of Chemical and Biological Engineering  
Faculty of Engineering  
The University of Sheffield**

**Supervisor: Professor Serena A. Corr**

**March 2021**

## Abstract

This thesis focuses on the synthesis and characterization of high energy density materials for cathode applications in lithium ion batteries with a strong emphasis on the application of microwave-assisted synthetic strategies which can be utilised in order to reduce processing times. The structural and transport properties arising from modifications to the materials aimed at suppressing material degradation, have also been investigated here. Synthesised materials presented here have been characterised and analysed using laboratory based techniques such as powder X-ray diffraction, scanning electron microscopy and electrochemical cycling studies, with more advanced central facility based experiments conducted on some materials including neutron diffraction, pair distribution function analysis and X-ray absorption spectroscopy measurements to provide detailed structural properties and muon-spin spectroscopy studies which probe ion transport properties. Such analysis is conducted to more fully understand the structure-property relationships that ultimately underpin the functionality of these battery materials.

**Chapter 1** presents a general introduction to lithium ion batteries, detailing the working principles behind lithium ion battery operation. The material properties that can induce high energy densities within cathode materials are also presented, before discussing several well-known cathode materials. Included in these discussions are the high-nickel content layered oxides, the processes that can lead to their rapid degradation and some strategies commonly used to suppress this degradation. Some basics on current anode technologies and sodium ion batteries are then discussed. Finally, different synthetic strategies to obtain such materials are introduced including discussion into the benefits arising from sol-gel and microwave-assisted type methods. This is followed by a brief outline of the aims of the thesis.

**Chapter 2** provides information on the chemicals used and the experimental procedures undertaken to synthesise the materials presented and used throughout the thesis. Furthermore, each of the techniques used throughout this thesis for the characterisation and analysis are introduced and explained to make the reader familiar with the basic scientific principles behind each technique.

In **Chapter 3** the local-scale cationic diffusion in three different polyanionic materials is investigated using muon spin relaxation ( $\mu^+$ -SR) measurements. An adapted microwave-assisted synthesis of the fluorinated, high voltage cathode material  $\text{LiFeSO}_4\text{F}$  in the tavorite phase is first investigated, showing the successful conversion to the higher voltage triplite phase using a short heat treatment.  $\mu^+$ -SR measurements conducted on

the favorite phase are presented alongside the data analysis and the structural considerations required for the calculation of the activation energies and diffusion coefficients, which are representative of the behaviour of the microscopic  $\text{Li}^+$  diffusion throughout the structure. The  $\text{Na}^+$  diffusion in fluorinated sodium-ion battery cathode  $\text{Na}_2\text{FePO}_4\text{F}$  is also investigated using  $\mu^+$ -SR and values of the activation energy and diffusion coefficients are presented. Finally, the maricite phase of  $\text{NaFePO}_4$  which is expected to be an ionic insulator is studied using  $\mu^+$ -SR to investigate whether any local-scale diffusion can be detected.

The microwave-assisted sol-gel synthesis of well-known layered oxides  $\text{LiNi}_x\text{Mn}_y\text{Co}_{1-x-y}\text{O}_2$  (NMCs) is presented in **Chapter 4** focusing initially on the synthesis and characterisation of NMC-111 and comparing the material properties and electrochemical performance to those obtained using a conventionally synthesised sample using PXRD, SEM and galvanostatic cycling techniques. The progression to higher nickel content NMC-622 and NMC-811 is then introduced, presenting the PXRD, SEM and galvanostatic cycling analysis conducted on samples of these compositions synthesised by the microwave-assisted sol-gel method. The local  $\text{Li}^+$  diffusion properties between these samples and commercially supplied samples of NMC-622 and NMC-811 are investigated using  $\mu^+$ -SR and comparisons between samples of differing nickel contents and between laboratory and commercial samples are made. Finally, the optimisation of reaction parameters involved in the microwave-assisted sol-gel synthesis of NMC-811 is presented where samples have been examined by PXRD, SEM, EDX and galvanostatic cycling techniques to ascertain sample quality.

Keeping a focus on NMC-811, **Chapter 5** presents a simple and cheap method to apply an amorphous protective  $\text{Al}_2\text{O}_3$  coating to NMC-811 in an attempt to mitigate electrode degradation. PXRD and SEM are used to investigate whether any structural or morphological changes are brought on by the coating method and galvanostatic cycling is performed to investigate any changes in the cycling stability afforded by the protective coating. *Operando* X-ray absorption spectroscopy measurements are conducted to examine changes in the Ni environment and local structure during cycling in order to compare between commercial NMC-811 and uncoated and coated microwave-synthesised NMC-811. Neutron diffraction and PDF analysis is also used to examine and compare the bulk and local structure between these three samples. Finally, the microwave-assisted sol-gel method has been used to synthesise samples of NMC-811 containing  $\text{Al}^{3+}$  and  $\text{Mg}^{2+}$  dopant cations where PXRD is used to investigate the change in lattice parameters as a result of the introduction of these dopants. Any changes to the local  $\text{Li}^+$  diffusion resulting from the introduction of these dopants is also investigated with  $\mu^+$ -SR measurements.

Finally, **Chapter 6** concludes the main findings from the research presented in this thesis and outlines possible avenues of future work that builds upon this research.

## Acknowledgements

I would first like to offer my deepest gratitude to my supervisor Prof. Serena Corr for allowing me the opportunity to carry out this PhD in your research group. It has been a truly exciting and life-changing experience. Your knowledge, expertise and passion for the research has kept me motivated throughout this entire process. I would also like to thank you for allowing me the experience of travelling for numerous conferences and research related activities that has been wholly appreciated. I am so grateful to have had you as my supervisor.

My sincere gratitude is also extended to The Carnegie Trust for the Universities of Scotland for funding my PhD. The opportunity to be a Carnegie PhD Scholar has been an honour and I am proud to belong to such a prestigious organisation.

I would also like to thank the past and present members of the Corr group and the Cussen group who I have come to know. It has been so much fun to be part of such a dynamic and interesting group and all your help has not gone unnoticed. I also can't forget all the laughs we have had during long lunchtimes and mandatory Friday Pub o'clock sessions. A special mention goes to Mr Michael Beglan for all your help in the lab and for making me feel so welcome when I first joined the group.

Furthermore, I would like to thank all other people who have helped me in my research: Dr Peter Baker at the ISIS Pulsed Neutron and Muon source for all your help pertaining to all things muon related. I would like to thank Dr Helen Playford at ISIS for all the help on Polaris for the neutron diffraction and PDF analysis of some of my materials and Dr Fred Mosselmans on the I20 beamline at the Diamond Light Source for all the help during XAS experiments. My thanks are also extended to Mr Peter Chung in the School of Geographical and Earth Sciences at The University of Glasgow for getting me some really nice HR-SEM images from my materials and the Sorby Centre at The University of Sheffield for use of the SEM facilities.

I would also like to extend my gratitude to the Department of Chemical and Biological Engineering at The University of Sheffield and the School of Chemistry at The University of Glasgow for hosting me and for allowing me the use of facilities throughout my research. I would also like to thank The Faraday Institution and the EPSRC for funding contributions and the STFC for beamtime allocation on the EMU and Polaris beamlines at the ISIS Pulsed Neutron and Muon Source and the I20 beamline at Diamond Light Source.

Finally, I would like to extend my warmest thanks to my family for supporting me through my journey through higher education and especially the PhD process, including most

importantly my Dad and Mum who have never wavered in their support. Without you, I could not have achieved all that I have. I would also like to thank my brother Paul who has never failed in making me laugh, and Isabel and Bill who have also shown me great support over the years. I love and appreciate you all.

# Table of Contents

Abstract .....	I
Acknowledgements .....	IV
Table of Contents .....	VI
List of Tables .....	X
List of Figures .....	XIII
Abbreviations .....	XXVII
<b>1 Introduction.....</b>	<b>1</b>
<b>1.1 Introduction to lithium ion batteries.....</b>	<b>1</b>
<b>1.2 Working principles behind LIBs.....</b>	<b>3</b>
<b>1.3 Routes to high energy density batteries.....</b>	<b>7</b>
<b>1.4 Cathode Materials for LIBs.....</b>	<b>9</b>
1.4.1 Layered oxide materials $\text{LiMO}_2$ ( $M = \text{Co, Ni, Mn}$ ).....	9
1.4.2 Properties of nickel rich layered oxides for higher energy density cathodes and their degradation under cycling.....	15
1.4.3 Mitigating Degradation in nickel rich layered oxides.....	22
1.4.4 Polyanionic Frameworks .....	26
<b>1.5 Anode materials for lithium ion batteries.....</b>	<b>32</b>
1.5.1 Lithium metal .....	32
1.5.2 Carbon based anodes.....	32
<b>1.6 Sodium ion batteries.....</b>	<b>33</b>
<b>1.7 Synthesis of electrode materials .....</b>	<b>34</b>
1.7.1 Sol-gel synthesis.....	35
1.7.2 Microwave-assisted synthesis methods .....	37
<b>1.8 Aims .....</b>	<b>41</b>
<b>2 Materials and experimental methods.....</b>	<b>43</b>
<b>2.1 Materials.....</b>	<b>43</b>
<b>2.2 Synthetic methodologies.....</b>	<b>43</b>
2.2.1 Dehydration of $\text{FeSO}_4 \cdot 7\text{H}_2\text{O}$ to $\text{FeSO}_4 \cdot \text{H}_2\text{O}$ .....	43

2.2.2	Microwave assisted synthesis of tavorite $\text{LiFeSO}_4\text{F}$ .....	43
2.2.3	Conversion of tavorite $\text{LiFeSO}_4\text{F}$ to triplite $\text{LiFeSO}_4\text{F}$ .....	44
2.2.4	Solid state synthesis of $\text{Na}_2\text{FePO}_4\text{F}$ .....	44
2.2.5	Sol-gel synthesis of layered oxides $\text{LiNi}_x\text{Mn}_y\text{Co}_{1-x-y}\text{O}_2$ .....	44
2.2.6	Dispersion based $\text{Al}_2\text{O}_3$ coating of $\text{LiNi}_{0.8}\text{Mn}_{0.1}\text{Co}_{0.1}\text{O}_2$ .....	45
2.2.7	Microwave assisted co-precipitation synthesis of $\text{LiNi}_{0.8}\text{Mn}_{0.1}\text{Co}_{0.1}\text{O}_2$ .....	46
2.2.8	Sol-gel microwave-assisted synthesis of $\text{Al}^{3+}$ and $\text{Mg}^{2+}$ doped $\text{LiNi}_{0.8}\text{Mn}_{0.1}\text{Co}_{0.1}\text{O}_2$ .....	46
<b>2.3</b>	<b>Characterisation Techniques.....</b>	<b>47</b>
2.3.1	Powder x-ray diffraction (PXRD).....	47
2.3.2	Neutron Powder Diffraction (NPD) .....	50
2.3.3	Rietveld Method.....	52
2.3.4	Neutron Pair Distribution Function analysis (PDF).....	54
2.3.5	X-ray Absorption Spectroscopy (XANES and EXAFS) .....	55
2.3.6	Scanning Electron Microscopy (SEM) .....	58
2.3.7	Energy Dispersive X-ray spectroscopy (EDX).....	59
2.3.8	Muon spin relaxation spectroscopy ( $\mu^+$ -SR) .....	59
2.3.9	Galvanostatic cycling.....	62
<b>3</b>	<b>Muon spin relaxation studies of polyanionic cathodes .....</b>	<b>65</b>
<b>3.1</b>	<b>Introduction .....</b>	<b>65</b>
<b>3.2</b>	<b>Local <math>\text{Li}^+</math> diffusion in fluorosulphate <math>\text{LiFeSO}_4\text{F}</math> measured using <math>\mu^+</math>-SR .....</b>	<b>66</b>
3.2.1	Microwave-assisted synthesis of tavorite phase $\text{LiFeSO}_4\text{F}$ .....	67
3.2.2	Muon spin spectroscopy measurements on tavorite $\text{LiFeSO}_4\text{F}$ .....	74
<b>3.3</b>	<b>Local <math>\text{Na}^+</math> diffusion in <math>\text{Na}_2\text{FePO}_4\text{F}</math> measured using <math>\mu^+</math>-SR .....</b>	<b>82</b>
3.3.1	Synthesis and structural characterisation of $\text{Na}_2\text{FePO}_4\text{F}$ .....	83
3.3.2	Muon spin spectroscopy measurements on $\text{Na}_2\text{FePO}_4\text{F}$ .....	86
<b>3.4</b>	<b>Local <math>\text{Na}^+</math> diffusion in maricite <math>\text{NaFePO}_4</math> measured using <math>\mu^+</math>-SR.....</b>	<b>90</b>
<b>3.5</b>	<b>Conclusions .....</b>	<b>93</b>
<b>4</b>	<b>Microwave assisted sol-gel synthesis of layered <math>\text{LiNi}_x\text{Mn}_y\text{Co}_{1-x-y}\text{O}_2</math> cathodes.....</b>	<b>96</b>

4.1	Introduction .....	96
4.2	Results and Discussion.....	97
4.2.1	Synthesis and structural characterisation of $\text{LiNi}_{1/3}\text{Mn}_{1/3}\text{Co}_{1/3}\text{O}_2$ prepared from a microwave assisted sol-gel process .....	97
4.2.2	Scanning electron microscopy of $\text{LiNi}_{1/3}\text{Mn}_{1/3}\text{Co}_{1/3}\text{O}_2$ prepared using a microwave assisted sol-gel synthesis .....	101
4.2.3	Electrochemical performances of $\text{LiNi}_{1/3}\text{Mn}_{1/3}\text{Co}_{1/3}\text{O}_2$ prepared using a microwave assisted sol-gel synthesis .....	103
4.2.4	Post-cycling structural and morphological analysis of $\text{LiNi}_{1/3}\text{Mn}_{1/3}\text{Co}_{1/3}\text{O}_2$ .....	109
4.2.5	Structural and Electrochemical characterisation of $\text{LiNi}_{0.8}\text{Mn}_{0.1}\text{Co}_{0.1}\text{O}_2$ and $\text{LiNi}_{0.6}\text{Mn}_{0.2}\text{Co}_{0.2}\text{O}_2$ synthesised by a microwave-assisted sol-gel method.....	114
4.2.6	Muon spin spectroscopy measurements on high nickel content layered oxides $\text{LiNi}_{0.8}\text{Mn}_{0.1}\text{Co}_{0.1}\text{O}_2$ and $\text{LiNi}_{0.6}\text{Mn}_{0.2}\text{Co}_{0.2}\text{O}_2$ .....	120
4.2.7	Optimisation of the microwave assisted sol-gel synthesis of $\text{LiNi}_{0.8}\text{Mn}_{0.1}\text{Co}_{0.1}\text{O}_2$ .....	129
4.2.8	Electrochemical performance of $\text{LiNi}_{0.8}\text{Mn}_{0.1}\text{Co}_{0.1}\text{O}_2$ synthesised by a microwave-assisted sol-gel method.....	138
4.2.9	Scanning electron microscopy of $\text{LiNi}_{0.8}\text{Mn}_{0.1}\text{Co}_{0.1}\text{O}_2$ prepared using a microwave assisted sol-gel synthesis .....	146
4.3	Conclusions .....	148
5	Degradation mitigation in nickel rich layered oxide $\text{LiNi}_{0.8}\text{Mn}_{0.1}\text{Co}_{0.1}\text{O}_2$ via coating and doping strategies.....	151
5.1	Introduction .....	151
5.2	Results and discussion.....	153
5.2.1	Degradation mitigation in $\text{LiNi}_{0.8}\text{Mn}_{0.1}\text{Co}_{0.1}\text{O}_2$ via the application of an $\text{Al}_2\text{O}_3$ coating by a liquid phase dispersive technique .....	153
5.2.2	<i>Operando</i> X-ray absorption spectroscopy analysis of $\text{Al}_2\text{O}_3$ coated $\text{LiNi}_{0.8}\text{Mn}_{0.1}\text{Co}_{0.1}\text{O}_2$ .....	168
5.2.3	Neutron powder diffraction and total scattering studies of $\text{Al}_2\text{O}_3$ coated $\text{LiNi}_{0.8}\text{Mn}_{0.1}\text{Co}_{0.1}\text{O}_2$ .....	179
5.2.4	Local-scale diffusional studies on $\text{Al}^{3+}$ and $\text{Mg}^{2+}$ doped $\text{LiNi}_{0.8}\text{Mn}_{0.1}\text{Co}_{0.1}\text{O}_2$ .....	195

5.3	Conclusions .....	203
6	Overall conclusions and future work .....	206
6.1	Overall conclusions .....	206
6.2	Future work .....	208
	References.....	212
7	Appendix.....	230

## List of Tables

<b>Table 2.1</b> Quantities of precursors used for the sol-gel microwave-assisted synthesis of $\text{LiNi}_x\text{Mn}_y\text{Co}_{1-x-y}\text{O}_2$ materials. ....	45
<b>Table 2.2</b> Quantities of reactants used in the alumina coating of NMC-811. ....	46
<b>Table 2.3</b> Quantities of metal sulphate reactants and deionised $\text{H}_2\text{O}$ used to make up solutions of the appropriate concentration for the co-precipitation synthesis of NMC-811. ....	46
<b>Table 2.4</b> Quantities of $\text{Ni}(\text{Ac})_2 \cdot 4\text{H}_2\text{O}$ , $\text{Al}(\text{NO}_3)_3 \cdot 9\text{H}_2\text{O}$ $\text{Mg}(\text{Ac})_2 \cdot 4\text{H}_2\text{O}$ $\text{Li}(\text{Ac})$ precursors used for the sol-gel microwave-assisted synthesis of $\text{Al}^{3+}$ and $\text{Mg}^{2+}$ doped NMC-811 materials. ....	47
<b>Table 2.5</b> Signal types produced during scanning electron microscopy and the information provided. ....	58
<b>Table 3.1</b> Calculated lattice parameters for microwave synthesised tavorite $\text{LiFeSO}_4\text{F}$ and atomic parameters obtained from the Rietveld refinement using a model containing $P1$ $\text{LiFeSO}_4\text{F}$ and $Fm\bar{3}m$ $\text{LiF}$ crystalline phases.....	73
<b>Table 3.2</b> Calculated lattice parameters for triplite $\text{LiFeSO}_4\text{F}$ and atomic parameters obtained from the Rietveld refinement using a model containing the $C2/c$ $\text{LiFeSO}_4\text{F}$ phase. ....	74
<b>Table 3.3</b> Diffusion directions for lithium ion transport in tavorite $\text{LiFeSO}_4\text{F}$ and the distinct hops that describe the ionic diffusion. Adapted from Tripathi <i>et al.</i> <sup>117</sup> .....	80
<b>Table 3.4</b> Calculated lattice parameters, atomic parameters and goodness of fit parameters $R_{\text{wp}}$ and $\chi^2$ , for $\text{Na}_2\text{FePO}_4\text{F}$ obtained from the Rietveld refinement using a model containing $Pbcn$ $\text{Na}_2\text{FePO}_4\text{F}$ . ....	86
<b>Table 3.5</b> Calculated $D_{\text{Na}}$ values for $\text{Na}_2\text{FePO}_4\text{F}$ at 300 K and 400 K, showing individual [100] and [001] diffusion coefficients and the combined diffusion coefficient obtained from the sum of the two pathways according to equation 3.3. ....	90
<b>Table 4.1</b> Calculated lattice parameters and Ni site occupancies for three samples of NMC-111 synthesised by a sol-gel method using a conventional heating step for 8 hours and microwave-assisted ( $\mu\lambda$ ) heating steps of 3 hours and 1 hour. ....	101
<b>Table 4.2</b> Calculated lattice parameters and Ni site occupancies for three samples of cycled NMC-111.....	112
<b>Table 4.3</b> Calculated lattice parameter and Li/Ni mixing from Rietveld refinements and calculated $I_{(003)}/I_{(104)}$ ratios obtained for NMC-811 and NMC-622 synthesised by a microwave-assisted sol-gel method with a reaction time of 2 hours at 850 °C.....	117

<b>Table 4.4</b> Calculated lattice parameter and Li/Ni mixing from Rietveld refinements and calculated $I_{(003)}/I_{(104)}$ ratios obtained for samples of NMC-811 and NMC-622 obtained from a commercial supplier. ....	128
<b>Table 4.5</b> Activation energies and room temperature (300 K) diffusion coefficients calculated from $\mu^+$ -SR measurements for microwave synthesised sol-gel samples of NMC-811 and NMC-622 (850 °C, 2 h) and samples of both obtained from a commercial supplier. ....	128
<b>Table 4.6</b> Calculated lattice parameter and Li/Ni mixing from Rietveld refinements and calculated $I_{(003)}/I_{(104)}$ ratios obtained for NMC-811 samples synthesised by a microwave-assisted sol-gel method with a reaction time of 1 hour and reaction temperatures of 750 °C, 800 °C, 850 °C and 900 °C. ....	133
<b>Table 4.7</b> Calculated lattice parameter and Li/Ni mixing from Rietveld refinements and calculated $I_{(003)}/I_{(104)}$ ratios obtained for NMC-811 samples synthesised by a microwave-assisted sol-gel method with a reaction time of 3 hours and reaction temperatures of 750 °C and 775 °C. ....	137
<b>Table 5.1</b> Structural parameters of the commercial NMC-811 sample from Rietveld analysis of NPD data at 60 K. ....	182
<b>Table 5.2</b> Structural parameters of the uncoated microwave-synthesised NMC-811 sample from Rietveld analysis of NPD data at 60 K. ....	183
<b>Table 5.3</b> Structural parameters of the microwave-synthesised, 0.2 wt% Al <sub>2</sub> O <sub>3</sub> coated NMC-811 sample from Rietveld analysis of NPD data at 60 K. ....	183
<b>Table 5.4</b> Structural parameters of the commercial NMC-811 sample from Rietveld analysis of NPD data at room temperature. ....	184
<b>Table 5.5</b> Structural parameters of the uncoated microwave-synthesised NMC-811 sample from Rietveld analysis of NPD data at room temperature. ....	185
<b>Table 5.6</b> Structural parameters of the microwave-synthesised, 0.2 wt% Al <sub>2</sub> O <sub>3</sub> coated NMC-811 sample from Rietveld analysis of NPD data at room temperature. ....	185
<b>Table 5.7</b> Lattice parameters obtained from the Rietveld refinements of PXRD data at room temperature. ....	186
<b>Table 5.8</b> Lattice parameters and $R_w$ values obtained from neutron PDF fits of commercial, uncoated and coated NMC-811 between 1 Å - 30 Å at 60 K. ....	194
<b>Table 5.9</b> Lattice parameters and $R_w$ values obtained from neutron PDF fits of commercial, uncoated and coated NMC-811 between 1 Å - 30 Å at room temperature. ....	194
<b>Table 5.10</b> Lattice parameters and $\chi^2$ values calculated from the Rietveld refinements on 1 % and 2 % Al <sup>3+</sup> -doped NMC-811 and 1 % Mg <sup>2+</sup> -doped NMC-811. ....	196

<b>Table 5.11</b> Activation energies and room temperature (300 K) diffusion coefficients calculated from $\mu^+$ -SR measurements for microwave synthesised sol-gel samples of NMC-811, 1 % Al-doped NMC-811 and 1 % Mg-doped NMC-811.....	203
<b>Table 7.1</b> The discharge capacity retentions after the first 5 cycles calculated for microwave-synthesised NMC-811, showing that the best retention was exhibited by the 775 °C 3 hour sample. ....	236

## List of Figures

<b>Figure 1.1</b> Comparison of the volumetric and gravimetric energy densities for a range of common battery technologies, including lead-acid, Ni-Cd, Ni-MH and lithium ion. <sup>3</sup> .....	2
<b>Figure 1.2</b> The present and predicted future market share of LIB technologies, including consumer electronics, EVs, industry & stationary energy (large scale storage) and miscellaneous others. <sup>5</sup> .....	3
<b>Figure 1.3</b> Visualisation of a LIB during discharge operation. A flow of electrons ( $e^-$ ) through the external circuit is concomitant with movement of the positive charge carrier, $Li^+$ (pink spheres), across the cell. $Li^+$ and $e^-$ are extracted from a lithiated graphite. ..	4
<b>Figure 1.4</b> Schematic of the relative electrode potentials and the electrolyte stability window, $E_g$ within a lithium ion electrochemical system. Adapted from Goodenough and Kim. <sup>7</sup> .....	6
<b>Figure 1.5</b> Spider diagram for common cathode materials LCO, LMO, LFP, NCA and NMC comparing various different physical and electrochemical properties. <sup>22</sup> .....	9
<b>Figure 1.6</b> Crystal structures of (a) fully lithiated $LiCoO_2$ with an O3 structure and (b) fully delithiated $CoO_2$ possessing the O1 structure. ....	10
<b>Figure 1.7</b> Density of states diagrams for $Li_{1-x}CoO_2$ at increasing states of charge, highlighting the overlapping of the $Co^{4+/3+}:t_{2g}$ and $O^{2-}:2p$ bands leading to eventual $O^{2-}$ oxidation on removal of $> 0.5 Li^+$ ions. <sup>27</sup> .....	12
<b>Figure 1.8</b> Density of states diagrams for layered oxides $LiCoO_2$ , $LiNiO_2$ and $LiMnO_2$ showing very little or no overlap between the redox active bands in $LiNiO_2$ and $LiMnO_2$ . <sup>29</sup> .....	13
<b>Figure 1.9</b> Visual representation of the degradation of NMC-532 cathodes precipitated by surface phase transformations occurring when implementing higher voltage cut-offs. <sup>51</sup> .....	16
<b>Figure 1.10</b> General visual overview of the many processes that lead to cathode degradation. <sup>57</sup> .....	18
<b>Figure 1.11</b> Cause and effect of degradation mechanisms in cathodes. <sup>58</sup> .....	18
<b>Figure 1.12</b> Comparison of thermal stabilities and discharge capacities achieved for a range of $LiNi_xMn_yCo_{1-x-y}O_2$ materials. NMC-811 is circled. <sup>63</sup> .....	20
<b>Figure 1.13</b> Energy level diagrams depicting the difference in energy levels between the $\sigma$ bonding and anti-bonding orbitals (formed between 3d orbitals on transition metals $M^{n+}$ and oxygen 2p orbitals). The effect of the nature of the M-O bond <i>i.e.</i> covalent or ionic, on the open circuit voltage, $V_{oc}$ , is evident. ....	27
<b>Figure 1.14</b> Crystal structure of the olivine phase of $LiFePO_4$ , showing the channels of lithium along [010]......	28

<b>Figure 1.15</b> Crystal structures for (a) tavorite phase $\text{LiFeSO}_4\text{F}$ looking along the $a$ direction and (b) triplite phase $\text{LiFeSO}_4\text{F}$ looking along the $b$ direction. In tavorite, Li (blue) and Fe (brown) sit on distinctly separate sites whereas in triplite they are evenly distributed over two crystallographic sites M1 and M2. Oxygen (red), fluorine (green) and $(\text{SO}_4)^{2-}$ groups (yellow tetrahedra) are shown also. ....	31
<b>Figure 1.16</b> Schematic of the sol-gel process for materials synthesis. The flexibility of both the sol and the gel is highlighted by the different possible processing techniques that can be applied in order to yield desired material properties. <sup>143</sup> .....	36
<b>Figure 1.17</b> Temperature profiles of a liquid reaction medium after 60 s facilitated by microwave irradiation (left) and conventional heating in an oil bath (right) highlighting the entire volume undergoes uniform and rapid heating, whereas the medium is heated from the outside inwards in the conventional heating. The vertical scale zero corresponds to the meniscus. <sup>151</sup> .....	39
<b>Figure 2.1</b> Illustration of the geometry used for the derivation of the $n\lambda = 2d\sin\theta$ form of Bragg's law. Adapted from Dinnebier and Billinge. <sup>161</sup> .....	49
<b>Figure 2.2</b> The Polaris diffractometer at ISIS. Detectors are grouped into different banks, differentiated here by colour. The neutron beam enters in the top right hand corner and exits in the middle section of Bank 1. <sup>165</sup> .....	51
<b>Figure 2.3</b> XAS data highlighting the XANES and EXAFS regions with respect to the absorption edge. Data shown here was collected at the Ni K-edge for NMC-811. ....	57
<b>Figure 2.4</b> Schematic of a typical $\mu^+$ -SR experiment where decay positrons are detected in the forwards and backwards detectors. Adapted from S. J. Blundell. <sup>177</sup> .....	61
<b>Figure 2.5</b> Set-ups of the three different types of battery cells used in this thesis showing (a) Swagelok type cells, (b) CR2032 coin cells and (c) the AMPIX cell. The AMPIX cell diagram reproduced from Borkiewicz <i>et al.</i> <sup>173</sup> .....	64
<b>Figure 3.1</b> PXRD pattern of the product formed during microwave solvothermal heating of $\text{FeSO}_4\cdot\text{H}_2\text{O}$ and LiF precursors for 30 minutes at 220 °C in a TEG medium (red), alongside reference patterns for tavorite phase $\text{LiFeSO}_4\text{F}$ (black) and $\text{FeSO}_4\cdot\text{H}_2\text{O}$ (green) obtained from the ICSD (collection code 182944). <sup>189</sup> Peaks indicating the presence of LiF are also annotated (*). ....	68
<b>Figure 3.2</b> PXRD pattern of the product formed during the short, solid state heat treatment of the tavorite-like precursor at 350 °C for 3.5 hours under Ar (blue), alongside reference patterns for triplite phase $\text{LiFeSO}_4\text{F}$ (black) and $\text{Fe}_3\text{O}_4$ (green) obtained from the ICSD (collection codes 187799 and 26410). Also annotated are small amounts of $\text{Li}_2\text{Fe}(\text{SO}_4)_2$ impurity (*) and an unidentified phase (+). ....	69

**Figure 3.3** PXRD patterns for two different dehydration strategies applied to  $\text{FeSO}_4 \cdot 7\text{H}_2\text{O}$ . The product after heating in a vacuum oven for 45 minutes at  $60^\circ\text{C}$  (red) is clearly the tetrahydrate form whereas the monohydrate can be formed in a tube furnace reaction at  $100^\circ\text{C}$  under a flow of  $\text{Ar}/\text{H}_2$  (5 %) for 3 hours (orange). Reference ICSD diffraction patterns are also displayed for  $\text{FeSO}_4 \cdot 4\text{H}_2\text{O}$  (black) and  $\text{FeSO}_4 \cdot \text{H}_2\text{O}$  (green). ..... 71

**Figure 3.4** Rietveld refinement for the microwave synthesised tavorite  $\text{LiFeSO}_4\text{F}$  PXRD data using a model consisting of two phases,  $P1$   $\text{LiFeSO}_4\text{F}$  and  $Fm3m$   $\text{LiF}$ , with  $R_{wp} = 2.26\%$  and  $\chi^2 = 1.18$ . ..... 72

**Figure 3.5** Rietveld refinement for the PXRD data collected for triplite  $\text{LiFeSO}_4\text{F}$  synthesised by heating 0.15 g of the microwave assisted tavorite  $\text{LiFeSO}_4\text{F}$  for 4.5 hours at  $350^\circ\text{C}$  under  $\text{Ar}$ . Fit using a model of  $C2/c$  phase  $\text{LiFeSO}_4\text{F}$  with  $R_{wp} = 3.05\%$  and  $\chi^2 = 1.18$ . ..... 73

**Figure 3.6** Raw  $\mu^+$ -SR data obtained for tavorite phase  $\text{LiFeSO}_4\text{F}$  at 100 K (upper plot) and 300 K (lower plot) at zero field (black circles) and applied longitudinal fields of 10 G (blue squares) and 20 G (orange triangles) alongside the fit to the data using a dynamic Kubo-Toyabe function (solid lines). ..... 77

**Figure 3.7** Temperature dependence of the field fluctuation rate ( $\nu$ ) and the field distribution width at the muon stopping site ( $\Delta$ ) for  $\mu^+$ -SR data obtained for tavorite phase  $\text{LiFeSO}_4\text{F}$  between 100 - 400 K at ZF and LFs of 10, 20 G, fit using an exponentially relaxing Kubo-Toyabe function. ..... 78

**Figure 3.8** Arrhenius plot of the field fluctuation rate over the thermally activated region calculated from  $\mu^+$ -SR measurements for tavorite phase  $\text{LiFeSO}_4\text{F}$ . The calculated activation energy,  $E_a = 48$  meV. .... 79

**Figure 3.9** Visualisation of the lithium diffusion pathway along the (a) [100] and (b) directions in tavorite phase  $\text{LiFeSO}_4\text{F}$ . Each pathways consists of two distinct hops, each with unique activation energies, designated coloured arrows, which build-up the zig-zag hopping pattern along the diffusion channel. .... 80

**Figure 3.10** Visualisation of the crystallographic structure of  $Pbcn$   $\text{Na}_2\text{FePO}_4\text{F}$  showing (a) the unit cell and the positions of the two unique sodium sites and (b) expansion of the structure to highlight the its layered nature allowing for  $\text{Na}^+$  diffusion along the [100] and [001] directions. Sodium ions are presented by blue spheres and  $(\text{PO}_4)^{3-}$  and  $\text{FeO}_4\text{F}_2$  units are represented by purple and brown polyhedral respectively. Oxygen and fluorine ions are represented by red and yellow spheres respectively. .... 83

**Figure 3.11** PXRD data obtained for  $\text{Na}_2\text{FePO}_4\text{F}$  synthesised by a solid state method. The reference pattern was obtained from the ICSD (collection code 167044). The presence of an unidentified impurity phase is highlighted by asterisks. .... 84

**Figure 3.12** Rietveld refinement between (a) 10 to 70 degrees for the solid-state synthesised tavorite  $\text{Na}_2\text{FePO}_4\text{F}$  PXRD data using a model consisting of *Pbcn*  $\text{Na}_2\text{FePO}_4\text{F}$ , with  $R_{wp} = 3.97\%$  and  $\chi^2 = 1.42$ . Impurities mainly in the region between 30 to 40 degrees are shown shaded in blue and magnified for clarity in (b). .....85

**Figure 3.13** Visualisation of some possible stopping sites for muons implanted into  $\text{Na}_2\text{FePO}_4\text{F}$  powder. Muons (orange spheres) implanted close to electronegative sites such as  $\text{O}^{2-}$  (red spheres) and  $\text{F}^-$  (yellow spheres) are in good positions to “see” the  $\text{Na}^+$  (blue spheres) diffusion. ....87

**Figure 3.14** Raw  $\mu^+$ -SR data obtained for  $\text{Na}_2\text{FePO}_4\text{F}$  measured at 300 K at zero field (black circles) and applied longitudinal fields of 10 G (blue squares) and 20 G (orange triangles) alongside the fit to the data using a dynamic Kubo-Toyabe function (solid lines). .....87

**Figure 3.15** Temperature dependence of the field fluctuation rate ( $\nu$ ) and the field distribution width at the muon stopping site ( $\Delta$ ) for  $\mu^+$ -SR data obtained for tavorite phase  $\text{Na}_2\text{FePO}_4\text{F}$  between 200 - 600 K at ZF and LFs of 10 and 20 G, fit using an exponentially relaxing Kubo-Toyabe function. ....88

**Figure 3.16** Arrhenius plot of the field fluctuation rate over the thermally activated region calculated from  $\mu^+$ -SR measurements for  $\text{Na}_2\text{FePO}_4\text{F}$ . The calculated activation energy,  $E_a$ , is calculated as 102 meV.....89

**Figure 3.17** Structure of the maricite phase of  $\text{NaFePO}_4$  where  $\text{Fe}^{2+}$  and  $\text{Na}^+$  essentially swap crystallographic sites compared to the olivine phase, forming chains of  $\text{FeO}_6$  (brown octahedra) along the [010] direction and immobile  $\text{Na}^+$  cations (blue spheres). Purple octahedra represent  $\text{PO}_4$  groups. ....91

**Figure 3.18** Raw  $\mu^+$ -SR data obtained for maricite phase  $\text{NaFePO}_4$  measured at 300 K at zero field (black circles) and applied longitudinal fields of 10 G (blue squares) and 20 G (orange triangles) alongside the fit to the data using the Keren function (solid lines)..92

**Figure 3.19** Temperature dependence of the field fluctuation rate ( $\nu$ ) and the field distribution width at the muon stopping site ( $\Delta$ ) for  $\mu^+$ -SR data obtained for maricite phase  $\text{NaFePO}_4$  between 200 - 600 K at ZF and LFs of 10 and 20 G, fit using the Keren function. ....93

**Figure 4.1** PXRD patterns obtained from NMC-111 synthesised by a sol-gel method utilising both conventional and microwave-assisted heating alongside a standard PXRD pattern for NMC-111 obtained from the ICSD (collection code 171750).....99

**Figure 4.2** Rietveld refinements on PXRD data obtained from three samples of NMC-111 synthesised by a sol-gel method using a conventional heating step for 8 hours and microwave-assisted heating steps of 3 hours and 1 hour. A model consisting of *R3m* phase  $\text{LiNi}_{1/3}\text{Mn}_{1/3}\text{Co}_{1/3}\text{O}_2$  was fit to the collected PXRD data. .... 100

**Figure 4.3** SEM images of NMC-111 prepared using (a,b) a conventional sol-gel method and microwave-assisted sol-gel methods with a final heating step of (c-e) 3 hours and (f-h) 1 hour. .... 102

**Figure 4.4** Electrochemical data obtained for NMC-111 synthesised *via* a conventional sol-gel method at 850 °C for 12 hours and cycled between 2.5 - 4.6 V vs. Li/Li<sup>+</sup> at a rate of C/10 in a Swagelok type cell. Including (a) charge-discharge profiles, (b) voltage-composition plot for cycles 1 and 10, (c) charge and discharge capacity stability and coulombic efficiencies over 10 cycles and (d) differential capacity dQ/dV plots for cycles 1, 2 and 10. .... 107

**Figure 4.5** Electrochemical data obtained for NMC-111 synthesised *via* a microwave-assisted sol-gel method at 850 °C for 3 hours and cycled between 2.5 - 4.6 V vs. Li/Li<sup>+</sup> at a rate of C/10 in a Swagelok type cell. Including (a) charge-discharge profiles, (b) voltage-composition plot for cycles 1 and 10, (c) charge and discharge capacity stability and coulombic efficiencies over 10 cycles and (d) differential capacity dQ/dV plots for cycles 1, 2 and 10. .... 108

**Figure 4.6** Electrochemical data obtained for NMC-111 synthesised *via* a microwave-assisted sol-gel method at 850 °C for 1 hour and cycled between 2.5 - 4.6 V vs. Li/Li<sup>+</sup> at a rate of C/10 in a Swagelok type cell. Including (a) charge-discharge profiles, (b) voltage-composition plot for cycles 1 and 10, (c) charge and discharge capacity stability and coulombic efficiencies over 10 cycles and (d) differential capacity dQ/dV plots for cycles 1, 2 and 10. .... 109

**Figure 4.7** PXRD patterns collected after cycling for the three NMC-111 materials. A peak corresponding to PTFE (from the cathode mix) at  $2\theta \approx 18^\circ$  is highlighted in a grey box and a possible NiO impurity in the 1 h sample is labelled by (\*). .... 111

**Figure 4.8** Rietveld refinements on PXRD data collected from three samples of NMC-111 after cycling in a Swagelok cell between 2.5 - 4.6 V vs. Li/Li<sup>+</sup> at a rate of C/10 for 10 cycles. A model consisting of *R3m* phase  $\text{LiNi}_{1/3}\text{Mn}_{1/3}\text{Co}_{1/3}\text{O}_2$  was fit to the collected PXRD data..... 112

**Figure 4.9** SEM images obtained for NMC-111 (a) 12C, (b) 3MW and (c) 1MW samples after cycling. Very small observed particles are most likely carbon black particles..... 113

**Figure 4.10** Rietveld refinements on PXRD data obtained from (a) NMC-811 and (b) NMC-622 synthesised by a microwave-assisted sol-gel method with a reaction time of 2 hours at 850 °C. A model of *R3m* phase  $\text{LiNi}_{0.8}\text{Mn}_{0.1}\text{Co}_{0.1}\text{O}_2$  or  $\text{LiNi}_{0.6}\text{Mn}_{0.2}\text{Co}_{0.2}\text{O}_2$  was fit to the collected PXRD data respectively..... 117

**Figure 4.11** SEM images at magnifications of (a,b) NMC-811 and (c,d) NMC-622 prepared by a microwave-assisted sol-gel method at 850 °C for 2 hours..... 119

**Figure 4.12** Charge discharge profiles obtained from galvanostatic cycling at room temperature of (a) NMC-811 and (b) NMC-622 cathode pellets (NMC: carbon black: PVDF in a 90:5:5 wt% ratio) synthesised by a microwave-assisted sol-gel method with a reaction time of 2 hours at 850 °C. Coin cells were cycled between 3.0 - 4.2 V vs. Li/Li<sup>+</sup> at a rate of C/10. .... 119

**Figure 4.13** Raw  $\mu^+$ -SR data collected at (a) 300 K for layered oxide NMC-811 synthesised by the microwave-assisted sol-gel method and (b) NMC-811 obtained from a commercial supplier and at (c) 400 K for layered oxide NMC-811 synthesised by the microwave-assisted sol-gel method and (d) NMC-811 obtained from a commercial supplier. Data at zero field (black circles) and applied longitudinal fields of 5 G (blue squares) and 10 G (orange triangles) is shown alongside the fit to the data using a dynamic Kubo-Toyabe function (solid lines). .... 122

**Figure 4.14** Raw  $\mu^+$ -SR data collected at (a) 300 K for layered oxide NMC-622 synthesised by the microwave-assisted sol-gel method and (b) NMC-622 obtained from a commercial supplier and at (c) 400 K for layered oxide NMC-622 synthesised by the microwave-assisted sol-gel method and (d) NMC-622 obtained from a commercial supplier. Data at zero field (black circles) and applied longitudinal fields of 5 G (blue squares) and 10 G (orange triangles) is shown, alongside the fit to the data using a dynamic Kubo-Toyabe function (solid lines). .... 123

**Figure 4.15** Temperature dependence of the field fluctuation rate ( $\nu$ ) and the field distribution width at the muon stopping site ( $\Delta$ ) for  $\mu^+$ -SR data obtained for (a) and (c) NMC-811 sol-gel and commercial samples and (b) and (d) NMC-622 sol-gel and commercial between 100 K to 400 K at ZF and LFs of 5 and 10 G, fit using an exponentially relaxing Kubo-Toyabe function. .... 124

**Figure 4.16** Arrhenius plot of the field fluctuation rate over the thermally activated region calculated from  $\mu^+$ -SR measurements for NMC-811 sol-gel (circles), NMC811 commercial (diamonds), NMC-622 sol-gel (triangles) and NMC-622 commercial (squares). Activation energies were estimated as 44 meV, 48 meV, 54 meV and 53 meV respectively. .... 125

**Figure 4.17** Projection onto the lithium containing *ab* plane for *R3m* LiMO<sub>2</sub> (*M* = Ni, Mn, Co) showing the two different jump-paths available for Li<sup>+</sup> diffusion. One path involves a jump to an adjacent Li site with a distance of *a* and the other path involves a jump to an interstitial site with distance *a*/ $\sqrt{3}$ . .... 127

**Figure 4.18** Rietveld refinements on PXRD data obtained from NMC-811 and NMC-622 obtained from a commercial supplier. Models of *R3m* phase LiNi<sub>0.8</sub>Mn<sub>0.1</sub>Co<sub>0.1</sub>O<sub>2</sub> and LiNi<sub>0.6</sub>Mn<sub>0.2</sub>Co<sub>0.2</sub>O<sub>2</sub> were fit to the corresponding collected PXRD data. .... 127

**Figure 4.19** PXRD patterns collected between  $2\theta$  angles of (a)  $10 - 70^\circ$  for NMC-811 synthesised by a microwave-assisted sol-gel method with a reaction time of 1 hour and reaction temperatures of  $650^\circ\text{C}$ ,  $750^\circ\text{C}$ ,  $800^\circ\text{C}$ ,  $850^\circ\text{C}$  and  $900^\circ\text{C}$ . A standard pattern for NMC-811 obtained from the ICSD is shown also. Portions of the data between (b)  $20 - 25^\circ$  and (c)  $63 - 66^\circ$  are also shown to highlight any present impurity phases and the peak splitting of the (108) and (110) reflections indicating the “layered-ness” of the structure. .... 131

**Figure 4.20** Rietveld refinements on PXRD data obtained from NMC-811 samples synthesised by a microwave-assisted sol-gel method with a reaction time of 1 hour and reaction temperatures of  $750^\circ\text{C}$ ,  $800^\circ\text{C}$ ,  $850^\circ\text{C}$  and  $900^\circ\text{C}$ . A model consisting of  $R3m$  phase  $\text{LiNi}_{0.8}\text{Mn}_{0.1}\text{Co}_{0.1}\text{O}_2$  was fit to the collected PXRD data. .... 132

**Figure 4.21** PXRD patterns collected between  $2\theta$  angles of (a)  $10 - 70^\circ$  for NMC-811 synthesised by a microwave-assisted sol-gel method with a reaction time of 3 hours and reaction temperatures of  $650^\circ\text{C}$ ,  $750^\circ\text{C}$  and  $775^\circ\text{C}$ . A standard pattern for NMC-811 obtained from the ICSD is shown also. Portions of the data between (b)  $20 - 25^\circ$  and (c)  $63 - 66^\circ$  are also shown to highlight any present impurity phases and the peak splitting of the (108) and (110) reflections indicating the “layered-ness” of the structure. .... 136

**Figure 4.22** Rietveld refinements on PXRD data obtained from NMC-811 samples synthesised by a microwave-assisted sol-gel method with a reaction time of 3 hours and reaction temperatures of  $775^\circ\text{C}$  and  $750^\circ\text{C}$ . A model consisting of  $R3m$  phase  $\text{LiNi}_{0.8}\text{Mn}_{0.1}\text{Co}_{0.1}\text{O}_2$  was fit to the collected PXRD data. .... 137

**Figure 4.23** Charge discharge profiles obtained from galvanostatic cycling at room temperature of  $\text{LiNi}_{0.8}\text{Mn}_{0.1}\text{Co}_{0.1}\text{O}_2$  cathode pellets (NMC-811: carbon black: PTFE in a 60:30:10 wt% ratio) synthesised by a microwave-assisted sol-gel method with a reaction time of 1 hour and reaction temperatures of (a)  $750^\circ\text{C}$ , (b)  $800^\circ\text{C}$ , (c)  $850^\circ\text{C}$  and (d)  $900^\circ\text{C}$ . Swagelok type cells were cycled between 2.5 - 4.2 V vs.  $\text{Li}/\text{Li}^+$  at a rate of C/10. .... 139

**Figure 4.24** Charge discharge capacity retention and calculated coulombic efficiencies obtained from galvanostatic cycling at room temperature of  $\text{LiNi}_{0.8}\text{Mn}_{0.1}\text{Co}_{0.1}\text{O}_2$  cathode pellets (NMC-811: carbon black: PTFE in a 60:30:10 wt% ratio) synthesised by a microwave-assisted sol-gel method with a reaction time of 1 hour and reaction temperatures of (a)  $750^\circ\text{C}$ , (b)  $800^\circ\text{C}$ , (c)  $850^\circ\text{C}$  and (d)  $900^\circ\text{C}$ . Swagelok type cells were cycled between 2.5 - 4.2 V vs.  $\text{Li}/\text{Li}^+$  at a rate of C/10. .... 141

**Figure 4.25** Differential capacity ( $dQ/dV$ ) profiles obtained from galvanostatic cycling at room temperature of  $\text{LiNi}_{0.8}\text{Mn}_{0.1}\text{Co}_{0.1}\text{O}_2$  cathode pellets (NMC-811: carbon black: PTFE in

a 60:30:10 wt% ratio) synthesised by a microwave-assisted sol-gel method with a reaction time of 1 hour and reaction temperatures of (a) 750 °C, (b) 800 °C, (c) 850 °C and (d) 900 °C. Swagelok type cells were cycled between 2.5 - 4.2 V vs. Li/Li<sup>+</sup> at a rate of C/10. .... 143

**Figure 4.26** Charge discharge profiles obtained from galvanostatic cycling at room temperature of LiNi<sub>0.8</sub>Mn<sub>0.1</sub>Co<sub>0.1</sub>O<sub>2</sub> cathode pellets (NMC-811: carbon black: PTFE in a 60:30:10 wt% ratio) synthesised by a microwave-assisted sol-gel method with a reaction time of 3 hours and reaction temperatures of (a) 750 °C and (b) 775 °C. Swagelok type cells were cycled between 2.5 - 4.2 V vs. Li/Li<sup>+</sup> at a rate of C/10. .... 144

**Figure 4.27** Charge and discharge capacity retention and calculated coulombic efficiencies obtained from galvanostatic cycling at room temperature of LiNi<sub>0.8</sub>Mn<sub>0.1</sub>Co<sub>0.1</sub>O<sub>2</sub> cathodes synthesised by a microwave-assisted sol-gel method with a reaction time of 3 hours and reaction temperatures of (a) 750 °C and (b) 775 °C. Swagelok type cells were cycled between 2.5 - 4.2 V vs. Li/Li<sup>+</sup> at a rate of C/10. .... 144

**Figure 4.28** Differential capacity (dQ/dV) profiles obtained from galvanostatic cycling at room temperature of LiNi<sub>0.8</sub>Mn<sub>0.1</sub>Co<sub>0.1</sub>O<sub>2</sub> cathode pellets (NMC-811: carbon black: PTFE in a 60:30:10 wt% ratio) synthesised by a microwave-assisted sol-gel method with a reaction time of 3 hours and reaction temperatures of (a) 750 °C and (b) 775 °C. Swagelok type cells were cycled between 2.5 - 4.2 V vs. Li/Li<sup>+</sup> at a rate of C/10. .... 145

**Figure 4.29** Rate capabilities for the specific charge and discharge capacities obtained from galvanostatic cycling at room temperature of NMC-811 750 °C 3h sample synthesised by a microwave-assisted sol-gel method. Swagelok type cells were cycled between 2.5 - 4.2 V vs. Li/Li<sup>+</sup>. .... 145

**Figure 4.30** SEM images of NMC-811 synthesised by a microwave-assisted sol-gel synthesis with a reaction temperature of 750 °C and reaction times of (a,b) 1 hour and (c,d) 3 hours. .... 147

**Figure 4.31** (a) SEM image of NMC-811 and elemental mapping results obtained for (b) Ni, (c) Mn and (d) Co from SEM-EDX analysis of the NMC-811 sample synthesised at 750 °C for 3 hours using a microwave-assisted sol-gel method. .... 147

**Figure 4.32** SEM images of NMC-811 synthesised by a microwave-assisted sol-gel synthesis with a reaction temperature of 775 °C for 3 hours at different magnifications of (a) × 10000, (b) × 25000 and (c) × 50000. .... 148

**Figure 5.1** PXRD data collected for microwave-synthesised pristine NMC-811 (850 °C, 1 hour) and NMC-811 samples coated with 0.2, 0.5 and 1.0 wt.% Al<sub>2</sub>O<sub>3</sub> using the dispersion method coating process. A standard pattern obtained from the ICSD for NMC is also shown. .... 155

**Figure 5.2** Charge-discharge profiles obtained from galvanostatic cycling of coated NMC-811 materials with (a) 0.2 wt.%, (b) 0.5 wt.% and (c) 1.0 wt% Al<sub>2</sub>O<sub>3</sub> coatings cycled in Swagelok-type half-cells between 2.5 V - 4.2 V vs. Li/Li<sup>+</sup> at a rate of C/10..... 157

**Figure 5.3** Discharge capacity retentions and Coulombic efficiencies for pristine NMC-811 and the 0.2, 0.5 and 1.0 wt.% coated samples of NMC-811 across the first 10 - 18 cycles for materials cycled in Swagelok-type half-cells between 2.5 V - 4.2 V vs. Li/Li<sup>+</sup> at a rate of C/10..... 158

**Figure 5.4** Differential capacity (dQ/dV) profiles obtained from galvanostatic cycling at room temperature of (a) 0.2 wt.%, (b) 0.5 wt.% and (c) 1.0 wt.% Al<sub>2</sub>O<sub>3</sub> coated NMC-811. Swagelok-type half-cells were cycled between 2.5 V - 4.2 V vs. Li/Li<sup>+</sup> at a rate of C/10. .... 160

**Figure 5.5** PXRD patterns collected after cycling for the 0.2 wt.%, 0.5 wt.% and the 1.0 wt.% Al<sub>2</sub>O<sub>3</sub> coated NMC-811 for cathodes cycled in Swagelok-type half-cells between 2.5 V - 4.2 V vs. Li/Li<sup>+</sup> at a rate of C/10. A peak corresponding to PTFE (from the binder) at 2θ ≈ 18 ° is highlighted in a grey box. Due to cell failure the pattern collected for the 0.2 wt.% coated sample corresponds to the material obtained in charged state whereas the data were collected for the 0.5 wt.% and 1.0 wt.% samples in the discharged state. .... 162

**Figure 5.6** SEM images of 0.2 wt.% Al<sub>2</sub>O<sub>3</sub> coated NMC-811 at increasing levels of magnification. .... 162

**Figure 5.7** Charge-discharge profiles obtained from galvanostatic cycling of (a) uncoated NMC-811 and (b) NMC-811 coated with 0.2 wt.% Al<sub>2</sub>O<sub>3</sub> cycled in Swagelok-type half-cells between 3.0 V - 4.2 V vs. Li/Li<sup>+</sup> at a rate of C/20 for 2 cycles and then C/2 up to 500 cycles..... 164

**Figure 5.8** Discharge capacity retentions obtained (filled symbols) and Coulombic efficiencies (unfilled symbols) calculated from galvanostatic cycling of uncoated NMC-811 (black circles) and NMC-811 (orange squares) coated with 0.2 wt.% Al<sub>2</sub>O<sub>3</sub> cycled in Swagelok-type half-cells between 3.0 V - 4.2 V vs. Li/Li<sup>+</sup> at a rate of C/20 for 2 cycles and then C/2 up to 500 cycles. .... 166

**Figure 5.9** Differential capacity (dQ/dV) profiles obtained from galvanostatic cycling of (a) uncoated NMC-811 and (b) NMC-811 coated with 0.2 wt.% Al<sub>2</sub>O<sub>3</sub> cycled in Swagelok-type half-cells between 3.0 V - 4.2 V vs. Li/Li<sup>+</sup> at a rate of C/20 for 2 cycles and then C/2 up to 500 cycles. .... 167

**Figure 5.10** (a) XANES region and (b) the pre-edge region from the XAS data collected on the Ni K-edge for commercial NMC-811, uncoated NMC-811 and 0.2 wt.% Al<sub>2</sub>O<sub>3</sub> coated

NMC-811 synthesised by a microwave assisted sol-gel method. Standard for NiO and $\text{LiNi}_{1/3}\text{Mn}_{1/3}\text{Co}_{1/3}\text{O}_2$ are also included. ....	170
<b>Figure 5.11</b> XANES region for the <i>in-situ</i> XAS data collected on the Ni K-edge for AMPIX cells containing (a,b) NMC-811 obtained from a commercial supplier, (c,d) uncoated and (e,f) 0.2 wt.% coated NMC-811 synthesised by a microwave-assisted sol-gel method. AMPIX cells were cycled between 3.0 V - 4.5 V vs. Li/Li <sup>+</sup> at a rate of C/5. Left and right panels show charging and discharging data respectively. ....	171
<b>Figure 5.12</b> The edge region of the XANES data collected on the Ni K-edge for the <i>in-situ</i> XAS measurements for AMPIX cells containing (a,b) NMC-811 obtained from a commercial supplier, (c,d) uncoated and (e,f) 0.2 wt.% coated NMC-811 synthesised by a microwave-assisted sol-gel method. Left and right panels show charging and discharging data respectively. ....	175
<b>Figure 5.13</b> Pre-edge XANES region for the <i>in-situ</i> XAS data collected on the Ni K-edge for AMPIX cells containing (a,b) NMC-811 obtained from a commercial supplier, (c,d) uncoated and (e,f) 0.2 wt.% coated NMC-811 synthesised by a microwave-assisted sol-gel method. Left and right panels show charging and discharging data respectively. ....	176
<b>Figure 5.14</b> Magnitude of the Fourier transformed EXAFS spectra for the <i>in-situ</i> XAS data collected on the Ni K-edge for (a,b) NMC-811 obtained from a commercial supplier, (c,d) uncoated and (e,f) 0.2 wt.% coated NMC-811 synthesised by a microwave-assisted sol-gel method. Left and right panels show charging and discharging data respectively. ....	178
<b>Figure 5.15</b> Laboratory PXRD data collected for uncoated and 0.2 wt.% $\text{Al}_2\text{O}_3$ coated NMC-811 synthesised by a microwave-assisted co-precipitation method at 850 °C for 1 hour. A reference pattern of NMC obtained from the ICSD is also included with the reflections labelled. ....	181
<b>Figure 5.16</b> Rietveld refinements of neutron powder diffraction data collected on Polaris at ISIS (detector bank 5) at 60 K for commercial NMC-811, uncoated microwave co-precipitation synthesised NMC-811 and 0.2 wt.% $\text{Al}_2\text{O}_3$ coated microwave co-precipitation NMC-811. ....	182
<b>Figure 5.17</b> Rietveld refinements of neutron powder diffraction data collected on Polaris at ISIS (detector bank 5) at room temperature for commercial NMC-811, uncoated microwave co-precipitation synthesised NMC-811 and 0.2 wt.% $\text{Al}_2\text{O}_3$ coated microwave co-precipitation NMC-811. ....	184
<b>Figure 5.18</b> Rietveld refinements of laboratory PXRD data collected at room temperature for, uncoated microwave co-precipitation synthesised NMC-811 and 0.2 wt.% $\text{Al}_2\text{O}_3$ coated microwave co-precipitation NMC-811. ....	186

<b>Figure 5.19</b> Raw neutron PDF data obtained at 60 K for commercial NMC-811, microwave synthesised uncoated NMC-811 and 0.2 wt.% coated NMC-811 in the range from 1 Å - 100 Å. The scattering data was terminated at $Q_{\max} = 52 \text{ \AA}^{-1}$ .....	189
<b>Figure 5.20</b> Raw neutron PDF data obtained at room temperature for commercial NMC-811, microwave synthesised uncoated NMC-811 and 0.2 wt.% coated NMC-811 in the range from 1 Å - 100 Å. The scattering data was terminated at $Q_{\max} = 52 \text{ \AA}^{-1}$ . ....	189
<b>Figure 5.21</b> Superimposed raw neutron PDF data 1 Å - 5 Å for (a) commercial, (b) uncoated and (c) coated samples of NMC-811 obtained at 60 K and room temperature. ....	190
<b>Figure 5.22</b> Superimposed raw neutron PDF data between 1 Å - 5 Å for commercial, uncoated and coated samples of NMC-811 obtained at (a) 60 K and (b) room temperature. ....	191
<b>Figure 5.23</b> Fits of the neutron PDF data for commercial NMC-811 and uncoated and 0.2 wt.% $\text{Al}_2\text{O}_3$ coated microwave-synthesised NMC-811 between 1 Å - 30 Å at 60 K. .	193
<b>Figure 5.24</b> Fits of the neutron PDF data for commercial NMC-811 and uncoated and 0.2 wt.% $\text{Al}_2\text{O}_3$ coated microwave-synthesised NMC-811 between 1 Å - 30 Å at room temperature.....	194
<b>Figure 5.25</b> Rietveld refinements of laboratory PXRD data collected at room temperature for NMC-811 synthesised by a microwave-assisted sol-gel method with 1 %, 2 % $\text{Al}^{3+}$ -doping on the Ni site and 1 % $\text{Mg}^{2+}$ -doping on the Li site. ....	196
<b>Figure 5.26</b> Raw $\mu^+$ -SR data collected at (a) 300 K for 1 % Al-doped NMC-811 synthesised by the microwave-assisted sol-gel method and (b) 400 K 1 % Al-doped NMC-811 prepared by a microwave assisted sol-gel method. Data at zero field (black circles) and applied longitudinal fields of 5 G (blue squares) and 10 G (orange triangles) is shown alongside the fit to the data using a dynamic Kubo-Toyabe function (solid lines).....	199
<b>Figure 5.27</b> Raw $\mu^+$ -SR data collected at (a) 300 K for 1 % Mg-doped NMC-811 synthesised by the microwave-assisted sol-gel method and (b) 400 K 1 % Mg-doped NMC-811 prepared by a microwave assisted sol-gel method. Data at zero field (black circles) and applied longitudinal fields of 5 G (blue squares) and 10 G (orange triangles) is shown alongside the fit to the data using a dynamic Kubo-Toyabe function (solid lines).....	199
<b>Figure 5.28</b> Temperature dependence of the field fluctuation rate ( $\nu$ ) and the field distribution width at the muon stopping site ( $\Delta$ ) for $\mu^+$ -SR data obtained for sol-gel and microwave-synthesised pristine NMC-811 (circles), 1 % Mg-doped NMC-811 (diamonds) and 1 % Al-doped NMC-811 (triangles) between 100 K to 400 K at ZF and LFs of 5 and 10 G, fit using an exponentially relaxing Kubo-Toyabe function. ....	200

**Figure 5.29** Arrhenius plot of the field fluctuation rate over the thermally activated region calculated from  $\mu^+$ -SR measurements for NMC-811 sol-gel (circles), 1 % Mg-doped NMC-811 (diamonds) and 1 % Al-doped NMC-811 (triangles). Activation energies were estimated as 48, 64, and 70 meV respectively. .... 202

**Figure 6.1** Structure of the bis-flavin BF-Me<sub>2</sub> with the 1,4-diazabuta-1,3-diene groups shaded in red. .... 211

**Figure 6.2** Results obtained from galvanostatic cycling of the bis-flavin molecule in a Swagelok type cell between (a) 1.2 V - 4.0 V and (b) 1.5 V - 3.2 V vs. Li/Li<sup>+</sup> and (c) discharge capacity retentions and Coulombic efficiencies. The cyclic voltammogram obtained when the material was cycled vs. a sodium metal anode is shown in (d). ... 211

**Figure 7.1** ICSD reference patterns for tavorite LiFeSO<sub>4</sub>F (collection code 182944) and FeSO<sub>4</sub>·H<sub>2</sub>O (collection code 71345) showing the similarities between both patterns that can be attributed to the similar structures exhibited by both materials. .... 230

**Figure 7.2** PXRD patterns collected for the product formed following the microwave assisted solvothermal synthesis of FeSO<sub>4</sub>·H<sub>2</sub>O and LiF (1:1.1 molar ratio) for 10 mins at 230 °C showing how ball milling time of the precursors affects the phase of the final product. Reactions were carried out in 5 mL of TEG in a 10 mL quartz vessel. Longer ball milling times of 30 minutes seem to form a product more like tavorite LiFeSO<sub>4</sub>F but with a much weaker intensity (PXRD data was collected on samples of similar mass and set-up) indicating a degree of amorphous product as a result of the ball milling procedure. .... 230

**Figure 7.3** PXRD patterns obtained for tavorite LiFeSO<sub>4</sub>F obtained from a 10 minute, 230 °C microwave reactant with 0.4 mmol and 0.5 mmol of precursors used in the ball milling step and the final reaction. Larger amounts of reactants in the ball mill failed to mix together and would result in no reaction taking place under microwave heating. The ability to scale a successful reaction to 0.5 mmol helped with the preparation of 1 g for muon measurements. .... 231

**Figure 7.4** PXRD patterns obtained from tavorite LiFeSO<sub>4</sub>F obtained from a 10 minute, 230 °C microwave reactant with 0.5 mmol of precursors but different atmospheres during the dehydration step of FeSO<sub>4</sub>·7H<sub>2</sub>O. Similar masses of powder were used in the PXRD data collection and so peak intensities correlate to the crystallinity of the final material. .... 231

**Figure 7.5** PXRD patterns obtained for microwave synthesised tavorite LiFeSO<sub>4</sub>F showing that an improved product can be formed with ball milling times of 30 mins and a reaction time of 1 hour at 230 °C. .... 232

**Figure 7.6** PXRD patterns for favorite phase  $\text{LiFePO}_4\text{F}$  using Ar in the initial dehydration of  $\text{FeSO}_4 \cdot 7\text{H}_2\text{O}$ , 0.5 mmol of reactants ball milled for 1 hour and then subject to microwave solvothermal heating in 5 ml of TEG in a 10 ml quartz vessel for reaction times of 1 hour and 2 hours. The peak intensities for  $2\theta$  values between  $25 - 30^\circ$  match better with those of the reference pattern for the sample reacted for 1 hour. Therefore, the 1-hour sample was carried forward for batch synthesis for muon measurements. .... 232

**Figure 7.7** Particle size distributions of NMC-111 prepared by (a) a conventional heating method (12 hours at  $850^\circ\text{C}$ ) and a microwave assisted method at  $850^\circ\text{C}$  for (b) 3 hours and (c) 1 hour. Particle sizes were calculated for 100 particles. .... 233

**Figure 7.8** Expanded plot of the charge and discharge profiles for NMC-111 synthesised by microwave-assisted method with reaction times of (a) 3 hours and (b) 1 hour showing the low open circuit voltages of 1.59 V and 1.62 V respectively obtained when the cell was initially connected to the potentiostat..... 234

**Figure 7.9** Particle size distributions of NMC-111 after cycling, prepared by (a) a conventional heating method (12 hours at  $850^\circ\text{C}$ ) and a microwave assisted method at  $850^\circ\text{C}$  for (b) 3 hours and (c) 1 hour. Particle sizes were calculated for 100 particles. .... 235

**Figure 7.10** Particle size distributions of (a) NMC-811 and (b) NMC-622 prepared by a microwave-assisted sol-gel method at  $850^\circ\text{C}$  for 2 hours. Particle sizes were calculated for 100 particles. .... 235

**Figure 7.11** Differential capacity ( $dQ/dV$ ) profiles for microwave synthesised NMC-811 at  $900^\circ\text{C}$  over the first two cycles showing the intense charging peak obtained during the first cycle. .... 236

**Figure 7.12** Charge and discharge profiles obtained for the galvanostatic cycling of NMC-811 synthesised by a microwave-assisted sol-gel method at  $775^\circ\text{C}$  for 3 hours. Excellent capacity retention is achieved over  $\approx 5$  cycles for repeat cells, however, evidence of cell failure is observed after this. .... 237

**Figure 7.13** Particle size distributions of NMC-811 prepared by a microwave-assisted sol-gel method at  $750^\circ\text{C}$  for (a) 1 and (b) 3 hours. Particle sizes were calculated for 100 particles. .... 238

**Figure 7.14** Full elemental mapping data obtained from EDX analysis of the NMC-811  $750^\circ\text{C}$  3 h sample showing the EDS layered image of the analysed region alongside separate elemental maps for oxygen, cobalt, manganese, nickel and oxygen..... 238

**Figure 7.15** Particle size distribution of NMC-811 prepared by a microwave-assisted sol-gel method at  $775^\circ\text{C}$  for 3 hours. Particle sizes were calculated for 100 particles. .. 239

**Figure 7.16** Charge and discharge profiles of the 0.2 wt.% Al<sub>2</sub>O<sub>3</sub> coated NMC-811 showing the behaviour beyond the 10<sup>th</sup> cycle. Upon the end of the 11<sup>th</sup> charge process some malfunction happens rendering the cell inoperable. .... 239

**Figure 7.17** Particle size distribution of 0.2 wt% Al<sub>2</sub>O<sub>3</sub> coated NMC-811. Particle sizes were calculated for 100 particles. .... 240

## Abbreviations

(HR)SEM	(High resolution) scanning electron microscopy
$\mu^+$ -SR	Muon spin relaxation
$\mu\lambda$	Microwave
ASSB	All solid-state battery
CEI	Cathode electrolyte interface/phase
DMC	Dimethyl carbonate
EC	Ethylene carbonate
EDX	Energy dispersive X-ray spectroscopy
EMC	Ethylmethyl carbonate
EVs	Electric vehicles
GCPL	Galvanostatic cycling with potential limitation
ICSD	Inorganic Crystal Structure Database
LCO	Lithium cobalt oxide
LF	Longitudinal field
LFP	Lithium iron phosphate
LIB	Lithium ion battery
NCA	Lithium nickel cobalt aluminium oxide
NMC	Lithium nickel manganese cobalt oxide
NMR	Nuclear magnetic resonance
NPD	Neutron powder diffraction
PDF	Pair distribution function
PTFE	Polytetrafluoroethylene
PVDF	Polyvinylidene fluoride
PXRD	Powder X-ray diffraction
RT	Room temperature
SEI	Solid-electrolyte interface/phase
TEG	Tetraethylene glycol
TF	Transverse field
THF	Tetrahydrofuran
TOF	Time of flight
XANES	X-ray absorption near-edge spectroscopy
XAS	X-ray absorption spectroscopy
ZF	Zero field

# 1 Introduction

*“Lithium-ion batteries have revolutionized our lives since they first entered the market in 1991. They have laid the foundation of a wireless, fossil fuel-free society, and are of the greatest benefit to humankind” - Royal Swedish Academy of Sciences upon awarding the 2019 Nobel Prize in Chemistry to John B. Goodenough, M. Stanley Whittingham and Akira Yoshino*

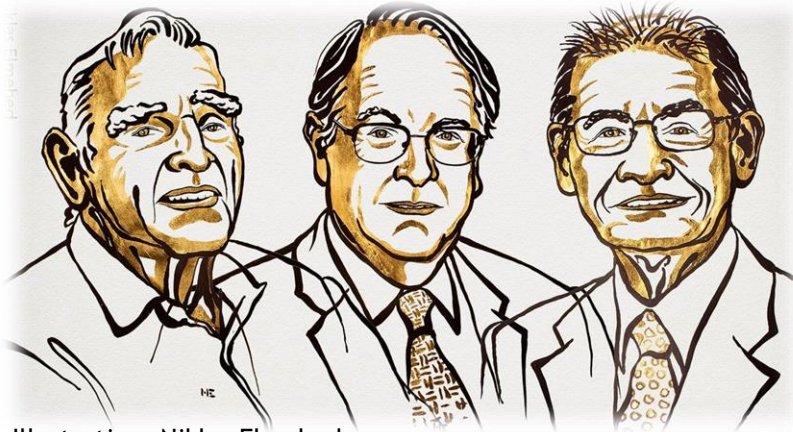


Illustration: Niklas Elmehed

## 1.1 Introduction to lithium ion batteries

Due to the widespread concern in the global usage of fossil-fuel based energy production means, there has been a shift in the energy paradigm with major progress in more renewable and environmentally conscious ways to both produce and store energy. One of the most well-known advances has been the development of the lithium ion battery (LIB) as an energy storage device. Research into lithium ion based reversible energy storage systems started with work done in 1976 by M. Whittingham (then at Exxon), who demonstrated the reversible intercalation of  $\text{Li}^+$  into a layered  $\text{TiS}_2$  framework.<sup>1</sup> This was followed by John Goodenough at Oxford University in 1980, who recognised the potential for voltage increases in oxides and demonstrated this same intercalation process for layered type  $\text{LiMO}_2$  ( $M = \text{Co}, \text{Mn}, \text{Ni}$ ) compounds.<sup>2</sup> Following further research on the use of carbonaceous species as a safe anode materials, the LIB was eventually commercialised by Sony in 1991.

As an energy storage device, LIBs convert chemical energy to electrical energy with the initial chemical energy stored within the materials that make up the cell's electrodes. These usually consist of some crystalline material, with the chemical energy converted to electrical energy *via* redox reactions occurring at these electrodes. These working principles, involving the conversion of chemical energy to electrical energy through redox reactions, are common to battery technologies, such as lead-acid (used mainly for stationary applications and starting automobiles), Ni-MH and Ni-cadmium (most suitable for high power applications e.g. power tools). However, LIBs present a storage medium

with much increased energy densities compared to earlier battery technologies, as shown in Figure 1.1.<sup>3</sup> Higher volumetric (with units  $\text{Wh l}^{-1}$ ) and gravimetric energy densities (with units of  $\text{Wh kg}^{-1}$ ) result in smaller and lighter batteries respectively; an essential property of more advanced energy storage technologies and the driving force behind the rapid rise in utilisation and popularity of the LIB. These increased energy densities arise as a consequence of the lithium ions from which these batteries derive their name. The lithium ion is small, light and electropositive with a low  $\text{Li}^0/\text{Li}^+$  redox potential of  $-3.04\text{ V}$  vs. the standard hydrogen electrode. These three factors unite in imparting both higher specific capacities and higher operating voltages when compared to older battery technologies, and it is the product of the specific capacity and operating voltage which yield the high energy density storage capabilities of LIBs.

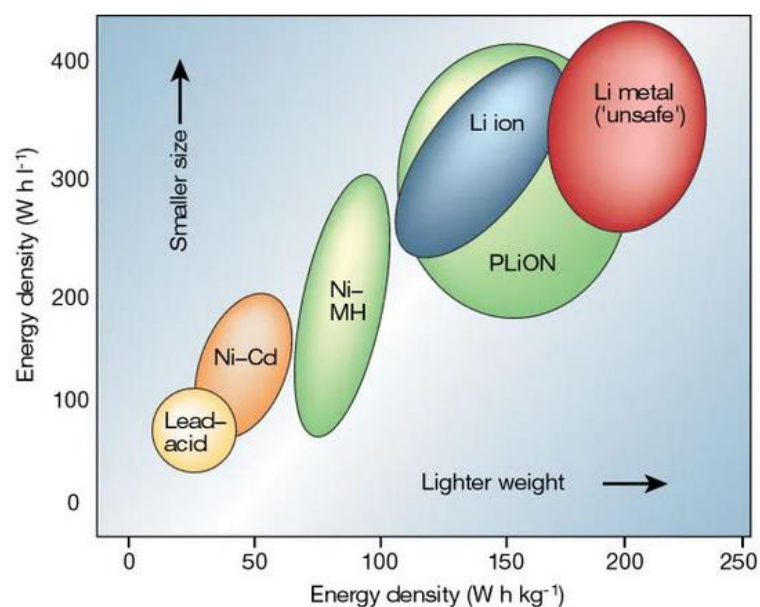


**Figure 1.1** Comparison of the volumetric and gravimetric energy densities for a range of common battery technologies, including lead-acid, Ni-Cd, Ni-MH and lithium ion.<sup>3</sup>

Since its commercialisation, the LIB has become ubiquitous to life in the modern world, where they have been traditionally used to power mobile phones and laptops amongst various other rechargeable portable devices. More recently, with the signing of the Paris Agreement in 2016 by 195 United Nations members, worldwide policy is now more focused than ever on mitigating greenhouse gas emissions, alongside the adaptations and financial aspects which accompany such efforts.<sup>4</sup> While consumer electronics is a relatively stagnant market for LIBs regarding the growth capacity (as opposed to the market for next generation battery applications), larger scale applications such as electric vehicles (EVs) and stationary energy storage (e.g. grid storage) have presented themselves as a prime opportunity for technological advancement of LIBs. This is

evidenced in the rapid growth of the LIB market in the decade between 2006 and 2016 from 11 GWh to 78 GWh (doubling approximately every 5 years), with new market growth arising from the needs of EVs and stationary energy uses, highlighted in Figure 1.2.<sup>5</sup> These larger scale applications, particularly in the field of EVs, provides a major push to the development of higher energy density systems. For EVs to become desirable to the majority of consumers, they must be able to provide equal (if not superior) characteristics to conventional vehicles which rely on the internal combustion engine. For example, current LIB technology for EVs suffers presently from issues relating to cost, range, charging rates, lifetime, reliability, and limited charging infrastructure. Many of these properties can be tackled with increased research and development, inevitably bringing costs down, with materials development providing safe and reliable batteries with higher energy and power densities with longer lifetimes.

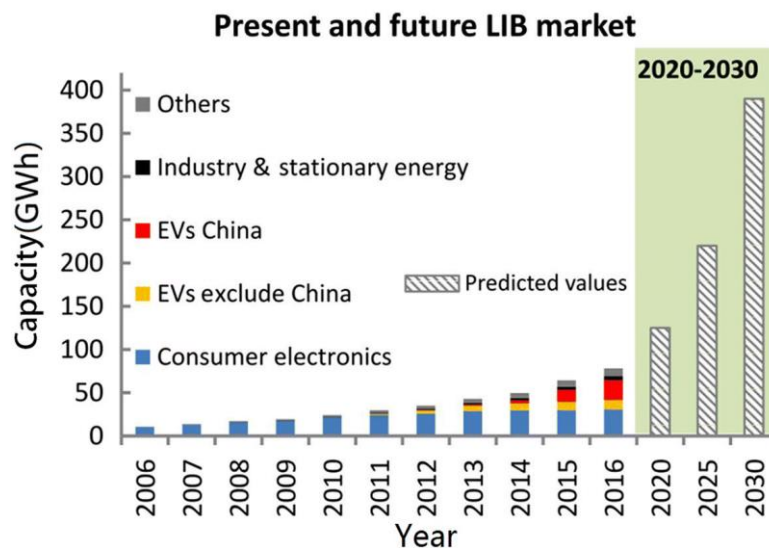


**Figure 1.2** The present and predicted future market share of LIB technologies, including consumer electronics, EVs, industry & stationary energy (large scale storage) and miscellaneous others.<sup>5</sup>

## 1.2 Working principles behind LIBs

The main components of a LIB are the cathode and anode (known collectively as the electrodes), separator, electrolyte, current collectors and casing. LIBs are considered as a type of secondary battery technology, meaning that reversibility of the redox reactions occurring allows for the battery to be both discharged during use and then charged again, allowing the battery multiple cycles of use and subsequently long lifetimes. The operation of the LIB specifically depends on the reversible intercalation and de-intercalation of  $\text{Li}^+$  ions into and from host electrode materials. Ideally, the intercalation process should impart minimal structural change to these host electrodes

in order to prevent lattice strain and destabilisations which could result in irreversible lattice damage.

During the discharge operation, when connected to some external circuit,  $\text{Li}^+$  ions are extracted from a high energy configuration (the anode) and diffuse across the cell through a  $\text{Li}^+$  conducting electrolyte (usually a  $\text{LiPF}_6$  salt dissolved in carbonate liquids). The  $\text{Li}^+$  ions are then intercalated into the lower energy state within the cathode. In order to preserve charge balance, the extraction of  $\text{Li}^+$  from the anode is accompanied by removal of an electron from the anode also. This negative charge carrier is allowed to flow through the external circuit where it reaches the cathode, providing the current needed to operate the connected device while flowing. Once the store of  $\text{Li}^+$  in the anode has been consumed, the reverse process is allowed to happen when an external current is applied and the cell is able to recharge. The discharge process can be visualised in Figure 1.3, which shows a cell consisting of a lithiated graphite anode and an  $\text{LiCoO}_2$  cathode, the configuration most commonly utilised in mobile phone batteries.

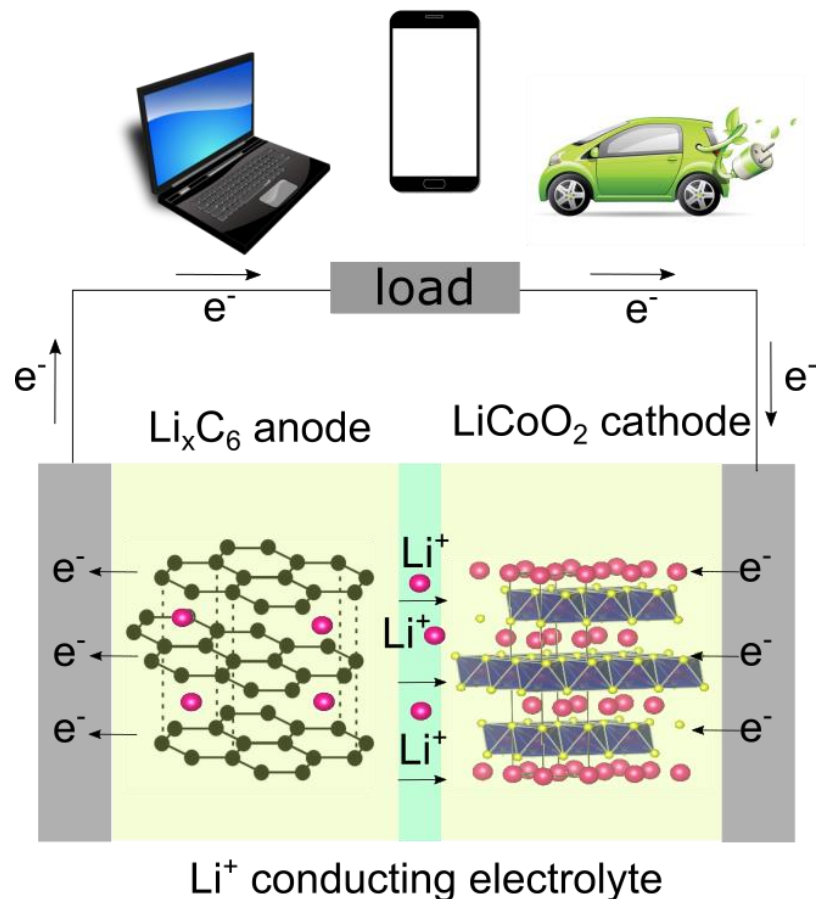


**Figure 1.3** Visualisation of a LIB during discharge operation. A flow of electrons ( $e^-$ ) through the external circuit is concomitant with movement of the positive charge carrier,  $\text{Li}^+$  (pink spheres), across the cell.  $\text{Li}^+$  and  $e^-$  are extracted from a lithiated graphite.

As previously mentioned, the two properties of the cell which determine the energy density are the specific capacity and the cell voltage. The specific capacity of an electrode material is determined by the mass of the material and the number of Li<sup>+</sup> able to be extracted/inserted per formula unit (thus determining the number of e<sup>-</sup> that are free to flow through the external circuit). The theoretical specific capacity,  $Q_{\text{theoretical}}$  (in units of mAh g<sup>-1</sup>) of an electrode material can be calculated from Equation 1.1, where  $n$  is the number of electrons released (equal to the number of Li<sup>+</sup>) per formula unit during discharge,  $F$  is the Faraday constant (96485 C mol<sup>-1</sup>),  $M_w$  is the molecular mass of the electrode material and 3.6 is a factor to convert from sA g<sup>-1</sup> to mAh g<sup>-1</sup>:

$$Q_{\text{theoretical}} = \frac{nF}{M_w \times 3.6} \quad (1.1)$$

From the above equation, in order to increase the theoretical capacity, either the molecular weight of the electrode must decrease, or the number of Li<sup>+</sup> per formula unit must increase. There is also an interest in replacing Li<sup>+</sup> with multivalent cations such as Mg<sup>2+</sup> where one cation can promote the release of two electrons in order to preserve charge neutrality.

The cell voltage is determined from the difference in electrochemical potential across the cell, and is calculated according to Equation 1.2, where  $V_{OC}$  is the open circuit potential,  $\mu_A$  and  $\mu_C$  are the chemical potentials of lithium in the anode and cathode respectively and  $e$  is the charge on the electron, a fundamental constant with a magnitude of  $1.6 \times 10^{-19}$  C. <sup>6</sup>

$$V_{OC} = \frac{\mu_A - \mu_C}{e} \quad (1.2)$$

It can therefore be seen that the cell voltage is directly proportional to the difference in the chemical potentials of the electrodes. By inspection of equation 1.2, to obtain a high cell voltage,  $\mu_C$  must be small, and hence, a low energy state, and  $\mu_A$  must be large, and therefore a high energy state. However, it is not as simple as choosing two electrode materials to obtain the largest energy gap possible - the stability window of the electrolyte (Figure 1.4) at certain voltages plays an important role and must not be overlooked.

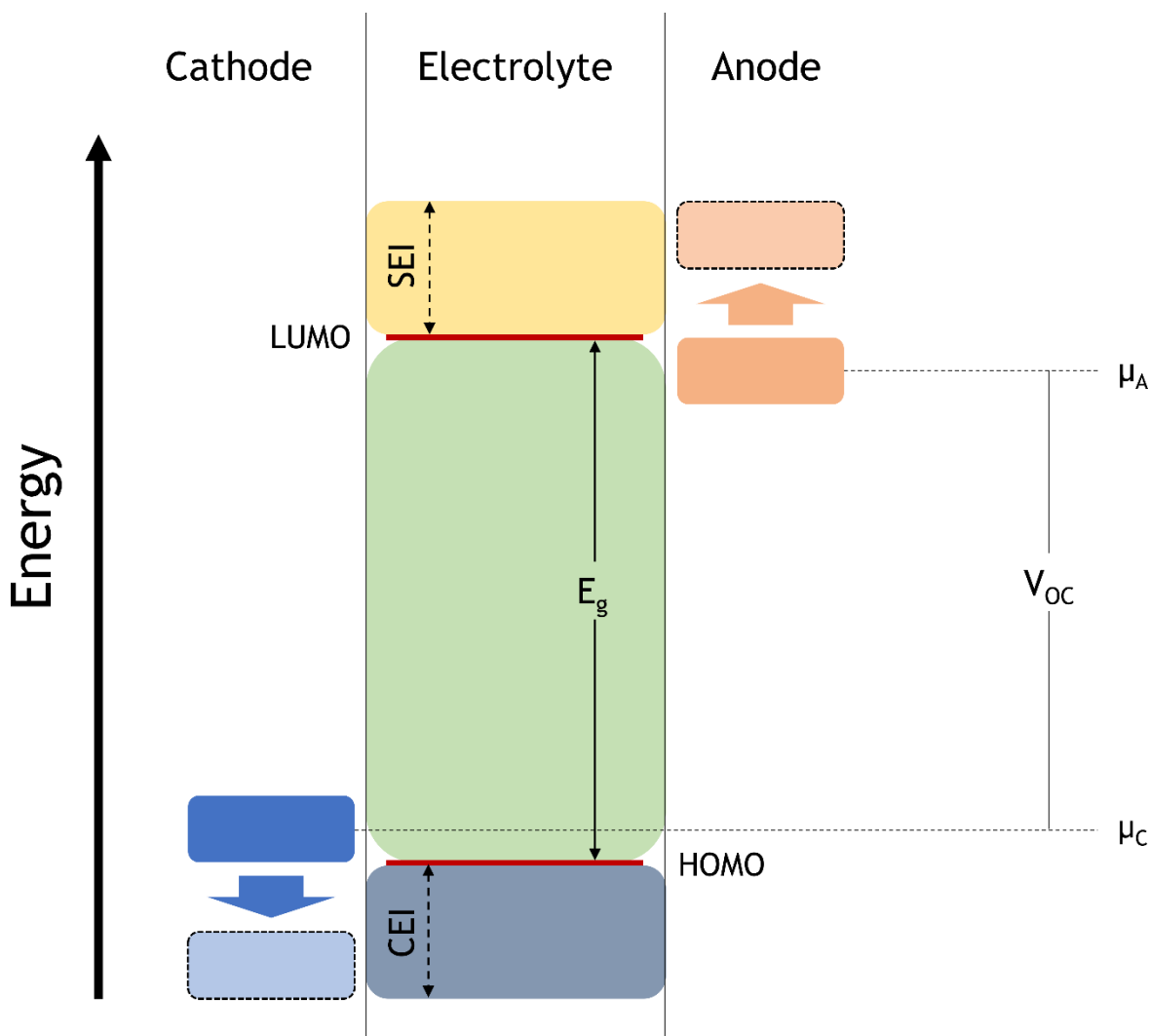


**Figure 1.4** Schematic of the relative electrode potentials and the electrolyte stability window,  $E_g$  within a lithium ion electrochemical system. Adapted from Goodenough and Kim.<sup>7</sup>

The electrolyte stability window,  $E_g$ , defines the stability limits providing the voltage is within a specific range. If  $\mu_A$  lies above the LUMO of the electrolyte, reduction of the electrolyte will occur, and if  $\mu_C$  lies below the HOMO, the electrolyte will be oxidised. Upon electrolyte reduction and oxidation, a passivating solid electrolyte interphase (SEI) and cathode-electrolyte interphase (CEI) are formed on the anode and cathode surfaces respectively. On one hand this can aid in particle aggregation, maintaining a uniform chemical composition at the electrodes and preventing exfoliation of the graphite, but on the other hand can increase the internal cell resistance and consume lithium ions from the electrochemical system, leading to a reduction in achievable capacities and power.<sup>6</sup> To circumvent these issues, development of new electrolytes with wider electrochemical stability windows is paramount to realising high voltage electrode configurations. Traditional electrolytes used in LIBs consist of a lithium salt (usually  $\text{LiPF}_6$ ) dissolved in organic carbonates (*e.g.* ethylene carbonate and dimethyl carbonate) and start to readily

decompose above 4.5 V. Advanced formulation of electrolyte solutions, including replacing  $\text{LiPF}_6$  with more stable lithium salts, the introduction of electrolyte additives to commercial electrolytes and the replacement of common flammable organic solvents with non-flammable solvents has been shown to greatly improve cell safety and allow high voltage cathodes to be used.<sup>8</sup> For example, the utilisation of fluorinated electrolyte systems has shown enhanced cycling performances up to 5.0 V when used in conjunction with high voltage cathodes such as  $\text{LiNi}_{0.5}\text{Mn}_{1.5}\text{O}_4$ .<sup>9,10</sup> However, completely replacing the liquid component with a lithium conducting ceramic material has garnered much interest also, with garnet, perovskite, LISICON and sulphide-type materials showing potential application in solid-state cells.<sup>11-13</sup> The development of the all-solid state LIB (ASSB) presents many advantages over conventional liquid electrolytes and will be discussed further in section 1.3.

### 1.3 Routes to high energy density batteries

As previously mentioned, the energy density of a system is defined as the amount of energy stored in a system per unit mass or per unit volume and is usually quoted in units of  $\text{Wh kg}^{-1}$  or  $\text{Wh l}^{-1}$  respectively when referring to lithium ion batteries. The energy density is simply a product of the specific capacity and the working voltage of the cell. Thus it is logical that in order to obtain high energy density cell configurations the cell must be able to deliver high specific capacities at high voltages while remaining light and compact. Currently, achievable discharge capacities of up to  $200 \text{ mAh g}^{-1}$  have been observed for new cathode technologies such as high nickel content  $\text{LiNi}_{0.8}\text{Mn}_{0.1}\text{Co}_{0.1}\text{O}_2$  and common anode material  $\text{Li}_x\text{C}_6$ , exhibits a comparatively high specific capacity of  $\approx 372 \text{ mAh g}^{-1}$ . Furthermore, a pure Li metal anode, which is currently not used due to safety reasons, has a theoretical capacity of  $3860 \text{ mAh g}^{-1}$ , one of the highest capacity amongst anode materials.<sup>14</sup> Other anode technologies actively researched include alloys based on Sn, Sb and Si which have been shown to deliver up to  $500 - 700 \text{ mAh g}^{-1}$  over 300 cycles, and nanostructured MnO which exhibits a reversible capacity of  $2014 \text{ mAh g}^{-1}$  after 150 cycles.<sup>15,16</sup>

From observation of specific capacities of common anode and cathode materials, it is the cathode which limits the overall energy density of the cell, and therefore designing and tailoring new cathode technologies to exhibit higher energy densities is a logical choice in materials development. Strategies to affect an increase in electrode energy density include design of new materials or careful manipulation of current chemistries to increase the cathode's deliverable capacities. For example, by replacing cobalt in layered oxide material  $\text{LiCoO}_2$  with nickel, the specific capacities achieved increase from

$\approx 140 \text{ mAh g}^{-1}$  to  $> 200 \text{ mAh g}^{-1}$ . This capacity increase arises from increased reversible extraction of  $\text{Li}^+$  during charge and discharge - in  $\text{LiCoO}_2$  only  $\approx 0.5$  Li can be reversibly intercalated due to safety issues and this will be discussed further in section 1.4.1. Following this thread, it is therefore evident that systems where more than one  $\text{Li}^+$  per formula unit can be reversibly intercalated would also be capable of achieving higher energy densities. This type of behaviour has been observed in high-valent oxides of vanadium such as  $\text{Li}_x\text{V}_2\text{O}_5$  where up to 3  $\text{Li}^+$  can be intercalated per formula unit accompanied by several phase changes.<sup>17</sup> Similar behaviour is seen for other vanadium oxides such as  $\text{LiV}_3\text{O}_8$  which was shown to intercalate between three and four  $\text{Li}^+$  ions per unit.<sup>18</sup> Moving away from inorganic materials, as will be discussed in Chapter 6, organic-based cathode materials also have been shown to react with  $> 1$   $\text{Li}^+$  per formula unit to achieve higher capacities.

The cell voltage of the battery is associated with transition metal redox reactions and corresponding redox couples. It is possible to tailor the redox potential by careful materials manipulation and substitution of certain moieties within well-known structures. This will be discussed in much greater detail in section 1.4.4.

The development of new electrolyte technologies to enable the use of high voltage cathodes is not limited to advances in liquid electrolytes. By replacing the flammable liquid electrolyte with a solid ceramic that allows facile  $\text{Li}^+$  transport throughout its structure, safety concerns relating to the thermal runaway problem may be alleviated. Furthermore, utilisation of solid state electrolytes may help to address the issues associated with Li metal anodes which acts to further accelerate the practical applications of high energy density systems.<sup>19</sup> There are many candidate systems of inorganic solid-state electrolytes currently under intensive research within the battery community such as garnets, perovskites and LISICON- and NASICON-like structures.<sup>12,20</sup> The structural stability of some of these proposed solid state electrolytes allow them to be stable well above 6 V vs.  $\text{Li}/\text{Li}^+$  opening up the opportunity to be used in conjunction with high voltage cathodes. Solid state batteries furthermore have the ability to be fabricated with thin film type architectures, with footprint areas of a few square millimetres and typical thicknesses of approximately  $1 \mu\text{m}$ , whereas liquid containing cells are restricted in size and design due to the available separators and electrolytes.<sup>21</sup> These solid state micro-batteries offer high energy systems with inherent safety features and are thus an extremely attractive option for next generation lithium ion technologies when combined with a pure lithium anode and a high energy density cathode material.

## 1.4 Cathode Materials for LIBs

One major advantage of LIBs compared to other well-known battery technologies, is the versatility in compatible electrode materials and the relative ease of tailoring known materials to enhance existing or impart new properties. Five of the most common cathode materials are  $\text{LiCoO}_2$  (LCO),  $\text{LiNi}_{1/3}\text{Mn}_{1/3}\text{Co}_{1/3}\text{O}_2$  (NMC),  $\text{LiNi}_{0.8}\text{Co}_{0.15}\text{Al}_{0.05}\text{O}_2$  (NCA),  $\text{LiFePO}_4$  (LFP) and  $\text{LiMn}_2\text{O}_4$  (LMO), whose characteristics are shown in Figure 1.5.<sup>22</sup> These structures all operate on the intercalation principles, where  $\text{Li}^+$  ions can be reversibly extracted and inserted into a host lattice during charge and discharge respectively. To allow this intercalation mechanism, some change in valence state within the electrode must occur and the host lattice must also provide space to accommodate  $\text{Li}^+$  ions which can take the form of tunnels, layers and complex 3-dimensional pathways.

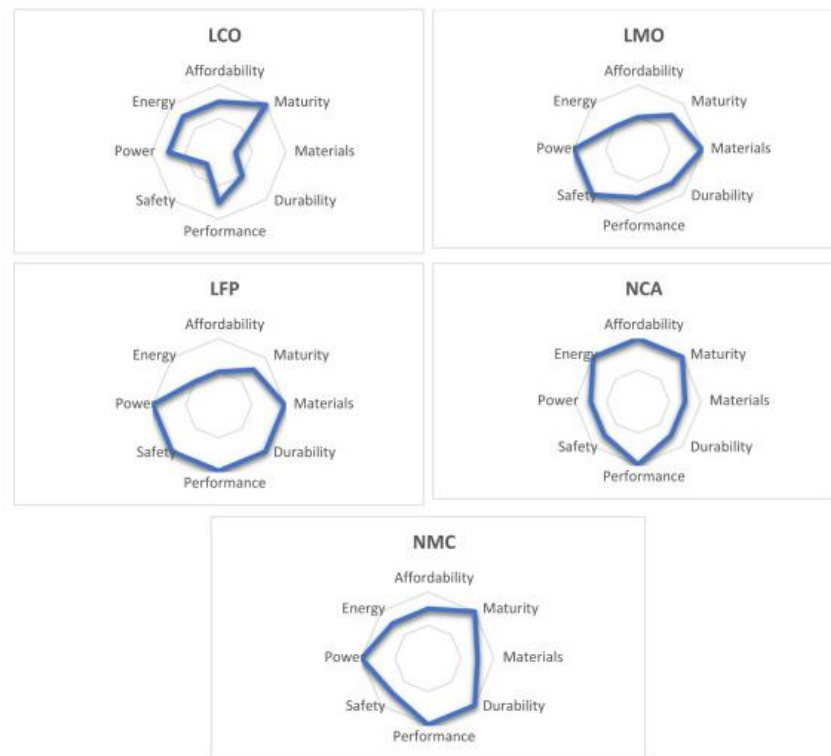
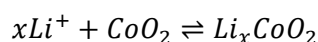


**Figure 1.5** Spider diagram for common cathode materials LCO, LMO, LFP, NCA and NMC comparing various different physical and electrochemical properties.<sup>22</sup>

### 1.4.1 Layered oxide materials $\text{LiMO}_2$ ( $M = \text{Co}, \text{Ni}, \text{Mn}$ )

Layered transition metal oxides currently form one of the practical classes of commercialised materials for LIBs.<sup>23</sup> For example, the  $\text{LiCoO}_2$  cathode discovered by Goodenough *et al.* is the archetypal cathode material for LIBs and is still utilised in the present day.<sup>2</sup> This material benefits from a large theoretical capacity, low self-discharge and good cycling performance. The layered structure of  $\text{LiCoO}_2$  possesses rhombohedral

symmetry and adopts the  $R\bar{3}m$  space group, isostructural with  $\alpha\text{-NaFeO}_2$ . The structure consists of planes of oxygen with an ABCABC stacking pattern where  $\text{Li}^+$  and  $\text{Co}^{3+}$  ions reside in octahedral sites in alternating planes between the oxygen sheets.<sup>24</sup> The planes of  $\text{Li}^+$  ions effectively screen and stabilize the negatively charged  $\text{CoO}_2$  sheets within the lattice.<sup>25</sup> This arrangement is known as the O3-type lattice. During battery operation,  $\text{Li}^+$  ions can be reversibly extracted from and inserted into layered host  $\text{CoO}_2$  lattice, operating on the  $\text{Co}^{3+/4+}$  redox couple with a cell voltage of  $\approx 4\text{ V vs. Li/Li}^+$ . During the insertion/extraction process the half-reaction proceeds as:



for  $0 \leq x \leq 1$ . Increased  $\text{Li}^+$  extraction from  $\text{LiCoO}_2$  increases the electrostatic repulsions between  $\text{CoO}_2$  sheets which results in an increase in the  $c$  parameter, as reported separately by Ohzuku and Ueda and Amatucci *et al.*<sup>26,25</sup> Upon full delithiation to the  $\text{CoO}_2$  end structure, the oxygen slabs rearrange into an ABAB stacking pattern - named the O1-type phase. This fully delithiated end member was first isolated by Amatucci *et al.* The transformation from the O3 to the O1 phase during delithiation is shown in Figure 1.6.

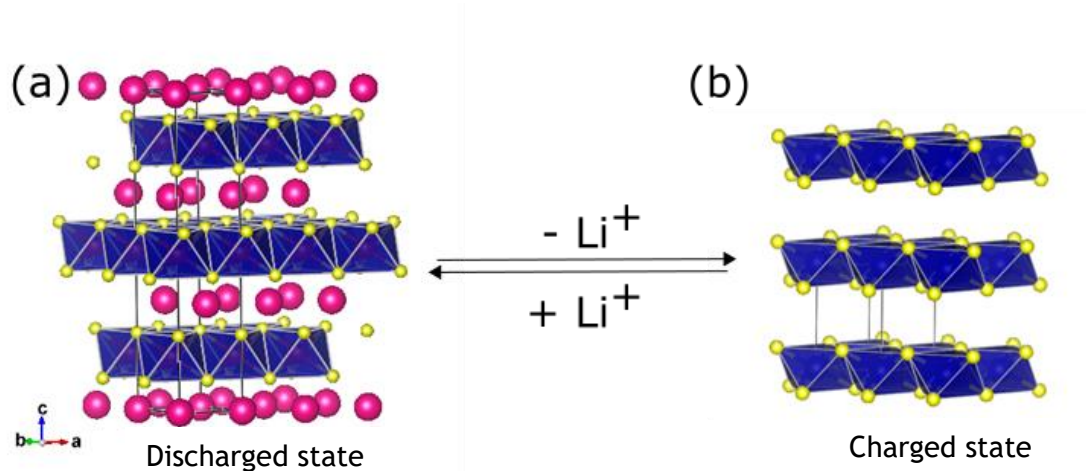


**Figure 1.6** Crystal structures of (a) fully lithiated  $\text{LiCoO}_2$  with an O3 structure and (b) fully delithiated  $\text{CoO}_2$  possessing the O1 structure.

The layered nature of  $\text{LiCoO}_2$  makes the material receptive to changes in Li concentration within a certain range without large structural changes and so provides an ideal environment for  $\text{Li}^+$  intercalation. Upon removal of  $> 0.5$   $\text{Li}^+$  per formula unit, the exact nature of phase transformations is poorly understood and there remains controversy in the literature over the material's behaviour upon cycling. Indeed, the fully delithiated end member  $\text{CoO}_2$  is difficult to isolate and could only be isolated upon charging the

material to 5.2 V vs. Li/Li<sup>+</sup>, a voltage that is too high for safe operation in commercial electrolytes. Considering the extraction/insertion of 1 Li<sup>+</sup> per formula unit, LiCoO<sub>2</sub> theoretically can provide large specific capacities of 274 mAh g<sup>-1</sup>. However, commercially, LIBs containing a LiCoO<sub>2</sub> cathode are charged to allow the removal of ≈ 0.5 Li<sup>+</sup> per formula unit, delivering specific capacities of approximately 140 mAh g<sup>-1</sup>. The reasons for this encompass both structural and chemical changes occurring upon increased delithiation. Upon deep charging above 4 V vs. Li/Li<sup>+</sup>, a rhombohedral to monoclinic phase transition is observed, where repeated structural changes over continued cycling can cause physical deformities in the crystal structure and can lead to cracking, dislocations and general physical instabilities. Chemically, the issues caused by deep delithiation are more dangerous. This issue lies in the overlapping of the bottom of the Co<sup>3+/4+</sup> and the top of the O:2p bands as shown in the density of states diagrams for Li<sub>x</sub>CoO<sub>2</sub> (x = 1, 0.5, 0) in Figure 1.7.<sup>27</sup> As the Li content in the cathode decreases upon charging, this is accompanied by a removal of electrons from the Co<sup>4+/3+;t<sub>2g</sub></sup> band. However, there is band overlap between the filled O<sub>2</sub> and half-filled Co bands and further removal beyond 0.5 Li<sup>+</sup> per formula unit corresponds to a removal of electrons from the overlapping region - a removal of electrons from the O:2p band and thus, oxidation of the bound O species occurs, resulting in the evolution of O<sub>2</sub> gas.

The evolved O<sub>2</sub> gas is free to react with the organic liquid electrolyte (often containing compounds such as EC, EMC and DMC), generating heat in the process. If heat dissipation cannot keep up with heat generation, the temperature continues to rise which then increases the reaction rates and the process proceeds at ever increasing rates. This situation is known as thermal runaway and can result in ignition of the organic liquid electrolyte when the cell temperature reaches the liquid's flash point and can even cause the cell to catch on fire, presenting a major safety issue.<sup>28</sup> Alongside this potentially dangerous process, the loss of O<sup>2-</sup> anions from the structure, and parasitic electrode-electrolyte reactions that also occur lead to loss of active electrode material over time too, which, while not posing a safety hazard, manifests itself as gradual capacity fade upon extended cycling. Due to this instability, LiCoO<sub>2</sub> is only electrochemically viable and safe when cycled so as to ensure removal of only ≈ 0.5 Li<sup>+</sup> per formula unit, and, as a result specific capacities delivered by the cell are limited to ≈ 140 mAh g<sup>-1</sup>. Although it is unquestionable that LiCoO<sub>2</sub> revolutionised the portable electronics industry, indeed it is LiCoO<sub>2</sub> that is still used in today's mobile phones and laptops, the use of this type of cell in larger applications such as EVs is impractical due to the safety issues and resulting lower deliverable specific capacities. LiCoO<sub>2</sub> has reached its potential and new, improved

cathodes are required which can deliver capacities close to the theoretical capacity of these layered oxides.

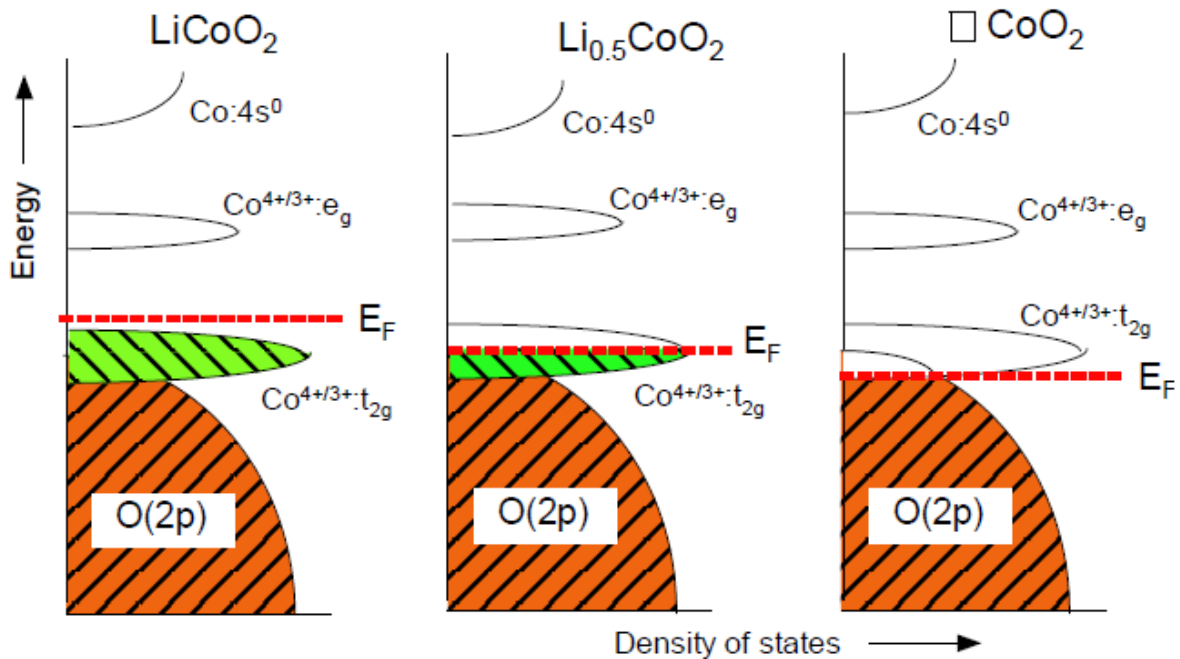


**Figure 1.7** Density of states diagrams for  $\text{Li}_{1-x}\text{CoO}_2$  at increasing states of charge, highlighting the overlapping of the  $\text{Co}^{4+/3+}:t_{2g}$  and  $\text{O}^{2-}:2p$  bands leading to eventual  $\text{O}^{2-}$  oxidation on removal of  $> 0.5 \text{ Li}^+$  ions.<sup>27</sup>

By comparing the density of states diagrams for the Ni and Mn analogues, it can be seen that less band overlap occurs, indicating that  $\text{LiNiO}_2$  and  $\text{LiMnO}_2$  could be viable alternatives. Nickel and manganese are also cheaper and less toxic than Co which presents further economical and safety benefits. In Figure 1.8, it can be seen that the bottom of the redox active  $\text{Ni}^{3+/4+}:e_g$  band only overlaps a very small amount with the top of the  $\text{O}^{2-}:2p$  band and in the case of the Mn analogue there is no overlap at all between these two bands, indicating that the  $\text{Ni}^{3+/4+}$  and  $\text{Mn}^{3+/4+}$  redox couples exhibit improved chemical stability in terms of  $\text{O}_2$  loss compared with that of  $\text{Co}^{3+/4+}$ .<sup>29</sup> The filled  $\text{Ni}^{3+/4+}:t_{2g}$  and  $\text{Mn}^{3+/4+}:t_{2g}$  will not undergo any change during electrochemical extraction of  $\text{Li}^+$  therefore their overlap with the  $\text{O}^{2-}:2p$  band is of no consequence when considering chemical stability during charging.<sup>29</sup>

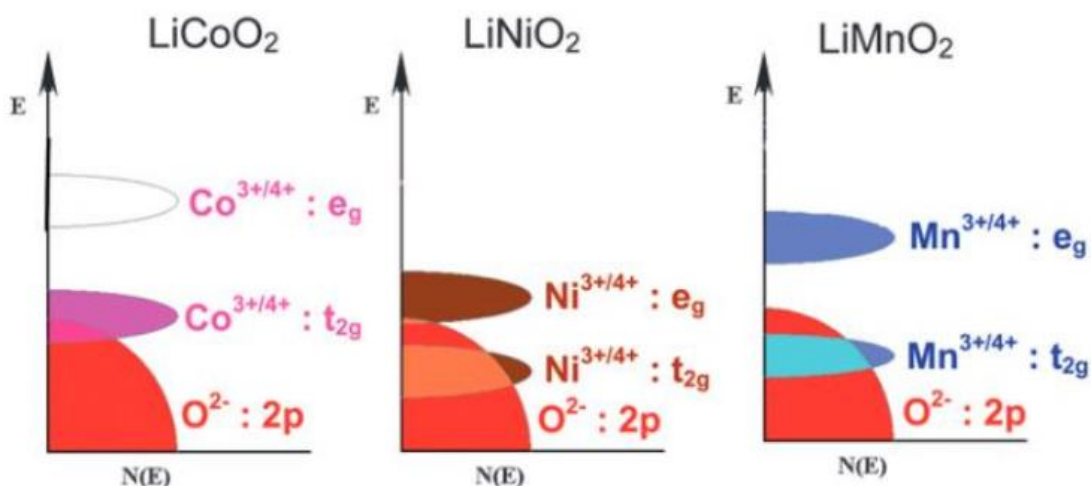


**Figure 1.8** Density of states diagrams for layered oxides  $\text{LiCoO}_2$ ,  $\text{LiNiO}_2$  and  $\text{LiMnO}_2$  showing very little or no overlap between the redox active bands in  $\text{LiNiO}_2$  and  $\text{LiMnO}_2$ .<sup>29</sup>

However, it is known that  $\text{LiNiO}_2$  is difficult to synthesise as an ordered layered material, instead yielding materials with compositions  $\text{Li}_{1-z}\text{Ni}_{1+z}\text{O}_2$  where the Li deficiencies are not caused by  $\text{Li}^+$  ion vacancies in the lithium layers, but rather excess  $\text{Ni}^{2+}$  cations occupying  $\text{Li}^+$  sites. Thus these disordered structures are more accurately represented as  $(\text{Li}^{+1-z}\text{Ni}^{2+z}) (\text{Ni}^{3+1-z}\text{Ni}^{2+z})\text{O}_2$ .<sup>30,31</sup> This disorder and the presence of divalent Ni cations has consequences on the cycling behaviour, as oxidation of the  $\text{Ni}^{2+}$  to  $\text{Ni}^{3+}$  on charging can cause local collapse of the interslab space. Structural instability arising from multiple phase transitions during cycling and thermal instability due to exothermic reactions between the organic electrolyte and the highly delithiated  $\text{Li}_{1-\delta}\text{NiO}_2$  further place limitations on the practical use of  $\text{LiNiO}_2$  in lithium ion batteries.<sup>32,33</sup> Structural transitions are also present in  $\text{LiMnO}_2$ , where a layered to spinel transition is observed.<sup>34</sup>

This has led researchers into the field of mixed transition metal oxides adopting the layered  $\alpha\text{-NaFeO}_2$  structure (space group  $R\bar{3}m$ ). These types of materials have very similar theoretical capacities of  $\approx 275 \text{ mAh g}^{-1}$  owing to the similar masses of the transition metals commonly used (Co, Ni and Mn) and all operate at voltages close to 4 V. Mixed oxides containing Ni and Co were studied where it was proposed that the presence of a small amount of  $\text{Co}^{3+}$  cations would stabilise the overall structure and prevent some of the cationic site mixing between  $\text{Ni}^{2+}$  and  $\text{Li}^+$ . The good reversibility of the  $\text{LiCoO}_2$  system and the large capacities observed for the  $\text{LiNiO}_2$  system led researchers to investigate solid solutions for optimization of structural and electrochemical properties. For  $\text{LiNi}_{1-y}\text{Co}_y\text{O}_2$  a solid solution was found for the entire range  $0 \leq y \leq 1$ , where  $\text{Ni}^{3+}$  and  $\text{Co}^{3+}$  homogeneously reside in 3a sites.<sup>35,36</sup> Good electrochemical properties have been observed for  $\text{Li}_{1-x}\text{Ni}_{0.85}\text{Co}_{0.15}\text{O}_2$  as observed by Li *et al.* where an initial discharge capacities

of 180 mAh g<sup>-1</sup> and 200 mAh g<sup>-1</sup> were obtained for Li<sub>1-x</sub>Ni<sub>0.85</sub>Co<sub>0.15</sub>O<sub>2</sub> when cycled between 3.0 and 4.25 V at 25 °C and 40 °C respectively, also showing excellent capacity retention over 30 to 50 cycles.<sup>37</sup> The reasons for these high capacities compared to LiCoO<sub>2</sub> were pointed out by Manthiram *et al.* who highlighted that the onset of oxygen loss under deep delithiation occurs at > 0.7 extraction of Li<sup>+</sup> compared to ≈ 0.5 for LiCoO<sub>2</sub>. This allows the structure to retain the O3 stacking arrangement over a longer extent of charge whereas changes to P3 and O1 oxygen stacking is observed for LiCoO<sub>2</sub> due to sliding of the oxygen layers. By measuring oxygen loss (using iodometric titration to ascertain transition metal oxidation state) over a full chemical delithiation for both Li<sub>1-x</sub>Ni<sub>0.85</sub>Co<sub>0.15</sub>O<sub>2</sub> and LiCoO<sub>2</sub>, it was observed that the Ni containing compound retained an oxygen content close to 2 between 0 to 0.7 Li<sup>+</sup> extracted and only a small loss upon further extraction. For LiCoO<sub>2</sub> the oxygen loss was found to be three times larger over the same delithiation.<sup>38</sup> Despite these excellent advantages, Li<sub>1-x</sub>Ni<sub>0.85</sub>Co<sub>0.15</sub>O<sub>2</sub> suffers from gradual capacity fade on long term cycling or holding in the delithiated state which can be explained by the migration of Ni<sup>2+</sup> cations from the transition metal layers into the Li<sup>+</sup> layers which can block migration pathways and impede Li<sup>+</sup> diffusion. Low thermal stability, especially in the charged state furthermore causes safety issues with liquid electrolytes and prevent the use of these materials in commercial cells.

The ternary transition metal oxide LiNi<sub>1/3</sub>Mn<sub>1/3</sub>Co<sub>1/3</sub>O<sub>2</sub> (NMC-111) offers attractive properties, where the combination of Ni, Mn and Co have a synergistic effect on the electrochemical properties and structural stability. The mixture of transition metals combines the good rate capability of LiCoO<sub>2</sub>, the high deliverable discharge capacities of LiNiO<sub>2</sub> and a structural stabilization imparted by the presence of Mn<sup>4+</sup> cations.<sup>39</sup> Many synthesis methods can be used in order to produce NMC-111 (also called NMC-333 in some conventions) including solid state, sol-gel and co-precipitation, with co-precipitation remaining the most common synthesis technique.<sup>40-45</sup> Many methods comprise a final calcination temperature of 750 to 1000 °C and similar electrochemical behaviour characterised by average and stable discharge capacities of 150 to 160 mAh g<sup>-1</sup> when charged to ≈ 4.3 V vs. Li/Li<sup>+</sup> and initial discharge capacities of 200 mAh g<sup>-1</sup> when charged to higher voltages which is often subject to gradual fading upon extended cycling. NMC-111 adopts the same layered  $R\bar{3}m$  structure as LiCoO<sub>2</sub> with the transition metals distributed across the same crystallographic site with octahedral symmetry. A first principles approach to the electronic structure of NMC-111 sheds interesting information about the oxidation states of the transition metals in NMC-111 compared to those in LiMO<sub>2</sub> structures. It is reported by Koyama *et al.* that the electronic structure of Co in NMC-111 is the same in the formal sense as that for in LiCoO<sub>2</sub> (a half filled Co t<sub>2g</sub> band), whereas

the Ni  $e_g$  band in NMC-111 is fully filled compared to half-filled for  $\text{LiNiO}_2$  and the Mn  $e_g$  band is empty for NMC-111 compared to half-filled for  $\text{LiMnO}_2$ . This means that the oxidation states adopted by these cations are not the same as what is seen in the parent  $\text{LiMO}_2$  structures: Ni, Co and Mn have oxidation states of 2+, 3+ and 4+ respectively in NMC-111.<sup>46</sup> This has also been shown by Hwang *et al.* in the transition metal K edge XANES spectra for NMC-111. By comparing with reference materials NiO ( $\text{Ni}^{2+}$ ) and  $\text{LiNiO}_2$  ( $\text{Ni}^{3+}$ ) it could be seen that the Ni-K edge spectrum obtained for NMC-111 overlapped with that obtained for NiO. The Co-K edge spectrum overlapped with that obtained for  $\text{LiCoO}_2$  and the Mn K edge spectra showed overlap with the  $\text{MnO}_2$  reference spectrum, confirming the nominal oxidation states of +2, +3 and +4 for Ni, Co and Mn respectively in NMC-111.<sup>42</sup> Electrochemically therefore,  $\text{Mn}^{4+}$  is inactive and the cell mainly operates on the  $\text{Ni}^{2+/4+}$  redox couple. The contribution of the  $\text{Co}^{3+/4+}$  redox couple is under debate. Koyama *et al.* suggest that initial  $\text{Li}^+$  extraction for  $\text{Li}_{1-x}\text{Ni}_{1/3}\text{Mn}_{1/3}\text{Co}_{1/3}\text{O}_2$  where  $0 \leq x \leq 1/3$  operates on the  $\text{Ni}^{2+/3+}$  redox couple which lies highest in energy. Further  $\text{Li}^+$  extraction in the region  $1/3 \leq x \leq 2/3$  involves the  $\text{Ni}^{3+/4+}$  redox couple, and showing a similar potential compared to  $\text{Li}_{1-x}\text{NiO}_2$  (ca. 3.30 V compared to 3.35 V vs.  $\text{Li}/\text{Li}^+$ ). The next segment of oxidation,  $2/3 \leq x \leq 1$ , finally involves the  $\text{Co}^{3+/4+}$ . In experiments undertaken by Clare Grey's group,  $^6\text{Li}$  MAS NMR and neutron pair distribution (PDF) techniques were combined in order to investigate the transition metal cation ordering in NMC-111.<sup>47</sup> According to the neutron pair distribution analysis, it was found that local distribution of cations involved  $\text{Ni}^{2+}$  cations prefer to be close to  $\text{Mn}^{4+}$  within the first coordination shell, with a more random ordering of  $\text{Co}^{3+}$ . This is backed up by the NMR studies where intensities of the resonance associated with  $\text{Co}^{3+}$  rich regions matched with the idea of a non-random distribution of transition metals.

#### 1.4.2 Properties of nickel rich layered oxides for higher energy density cathodes and their degradation under cycling

As mentioned before, the electrochemical activity of NMC-111 is primarily attributed to the  $\text{Ni}^{2+/4+}$  redox process. Therefore, there is interest in developing higher nickel content materials isostructural with NMC-111 which still maintain small amounts of  $\text{Co}^{3+}$  and  $\text{Mn}^{4+}$  to impart increased rate capabilities and stability associated with both of these cations respectively. Such compounds containing at least 50 % Ni in the transition metal layer are known as nickel rich structures. Amongst nickel rich layered oxides,  $\text{LiNi}_{0.5}\text{Mn}_{0.3}\text{Co}_{0.2}\text{O}_2$  (NMC-532),  $\text{LiNi}_{0.6}\text{Mn}_{0.2}\text{Co}_{0.2}\text{O}_2$  (NMC-622) and  $\text{LiNi}_{0.8}\text{Mn}_{0.1}\text{Co}_{0.1}\text{O}_2$  (NMC-811) are promising. For NMC-111 where the average oxidation state of the total transition metal content could be kept at 3+ to preserve neutrality by having equal numbers of  $\text{Ni}^{2+}$  and  $\text{Mn}^{4+}$  and  $\text{Co}^{3+}$ , the uneven proportions present in NMC-532, -622 and -811 evidently cannot balance

these charges. Instead, the charge is compensated *via* partial oxidation of Ni<sup>2+</sup> to Ni<sup>3+</sup> in these structures (while the Mn<sup>4+</sup> and Co<sup>3+</sup> retain their original oxidation states).<sup>48,49</sup> These nickel rich layered oxide materials benefit from higher capacities - NMC-532 has been shown to deliver discharge capacities of 214 mAh g<sup>-1</sup> and 175 mAh g<sup>-1</sup> when upper cut-off voltages of 4.6 V and 4.3 V are used respectively.<sup>50</sup> It is clear from the evidence that higher cut-off voltages are essential in delivering high capacities during cycling, however rapid capacity fade under these high charge conditions indicate that severe degradation processes are occurring on the cathode which reduce the amount of electrochemically active material over prolonged cycling.

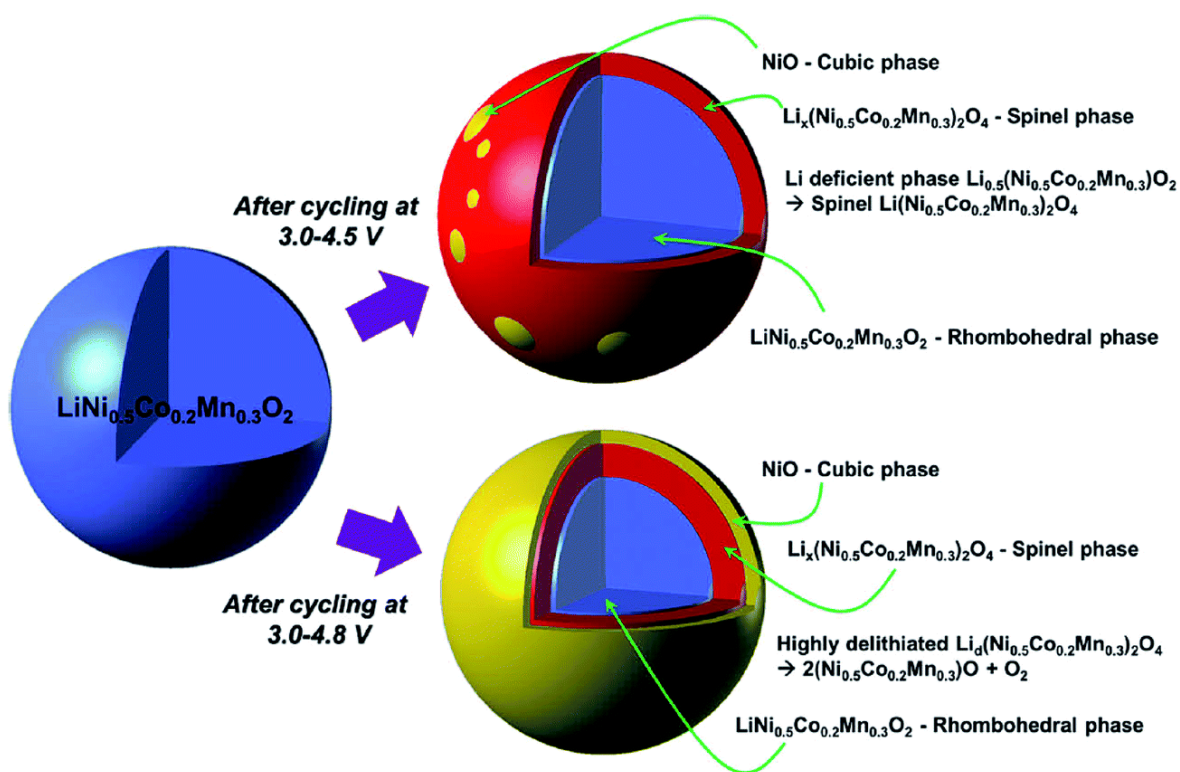


**Figure 1.9** Visual representation of the degradation of NMC-532 cathodes precipitated by surface phase transformations occurring when implementing higher voltage cut-offs.<sup>51</sup>

A paper by Jung *et al.* attempted to pin down these degradation processes in NMC-532 and it was found that the processes occurring in nickel rich layered cathodes are different to those observed in NMC-111, indicating that degradation pathways are different for differing ratios of Ni, Co and Mn and therefore should be considered for individual compositions. The research involved the structural and electrochemical analysis of NMC-532 with upper cut-off voltages of 4.3, 4.5 and 4.8 V. Initial discharge capacities of 150, 180 and 200 mAh g<sup>-1</sup> were observed respectively with capacity retentions of 95, 72 and 61 % over 50 cycles. It was found that surface phase transformations from rhombohedral to spinel and rock-salt NiO occurred upon cycling to 4.5 and 4.8 V leading

to loss of active rhombohedral phase (resulting in capacity fade) and an increase in the charge transfer resistance, with a greater extent of NiO phase formed at high states of charge. The presence of these surface phases is visualised in Figure 1.9. Unlike for NMC-111 where O3 to O1 phase transitions are pivotal in structural material degradation, an O3 to O1 phase transition was not observed for NMC-532, where it is believed that site mixing between  $\text{Li}^+$  and  $\text{Ni}^{2+}$  acts to prevent the layer sliding.<sup>51</sup> The presence of  $\text{Ni}^{2+}$  on the surface has also been observed using soft X-ray absorption spectroscopy (sXAS) during a study into the valence state evolution in NMC-532 during charging, further corroborating that some form of surface reconstruction occurs at higher levels of charge.<sup>52</sup> These irreversible phase transitions from layered to spinel and rock salt occur during cycling when  $\text{Li}^+$  removed from the lithium layer can be replaced by  $\text{Ni}^{2+}$  cations which are able to migrate from the transition metal layer due to the similar ionic radii of  $\text{Li}^+$  (0.076 nm) and  $\text{Ni}^{2+}$  (0.069 nm).<sup>53</sup> Another factor in cathode degradation at high charge states (high voltages) is the oxidative decomposition of the traditional  $\text{LiPF}_6$ /carbonate electrolyte. Under high charge voltages the decomposition products such as polyethylene carbonate species and lithium alkyl carbonates can form an undesirable surface film on the cathode. Besides consuming quantities of active  $\text{Li}^+$  from the electrolyte, if these surface films are thick and ionically insulating, the further insertion/extraction of  $\text{Li}^+$  from the cathode structure can be severely affected. Where the solid-electrolyte interphase (SEI) is a feature commonly associated with carbonaceous anode species during electrolyte decomposition, this surface film on the cathode is named the cathode-electrolyte interphase (CEI). Accumulation of these decomposition products causes continual film growth and eventually leads to increased impedances and poor cyclabilities over increased cycling.<sup>54,55</sup> Mechanical issues can furthermore precipitate cathode degradation in the form of particle cracking, whereby repulsive interactions between transition metal layers, accompanied by the formation of new phases with larger lattice parameters induces an anisotropic stress in the particles, eventually leading to cracking.<sup>56</sup> As new surface area is exposed during cracking, the CEI is disrupted and rebuilt to form on these new surfaces, further hastening active  $\text{Li}^+$  consumption and hindering access to the active cathode material. Further processes that may influence cathode degradation include migration of soluble species (such as transition metals), binder decomposition, corrosion of the current collector and the oxidation of conductive particles which are shown alongside major contributing factors in Figures 1.10 and 1.11. It is clear that there is a complex interplay between all of these processes where they interact and mutually aggravate each other and making delineation intractable.<sup>57,58</sup>

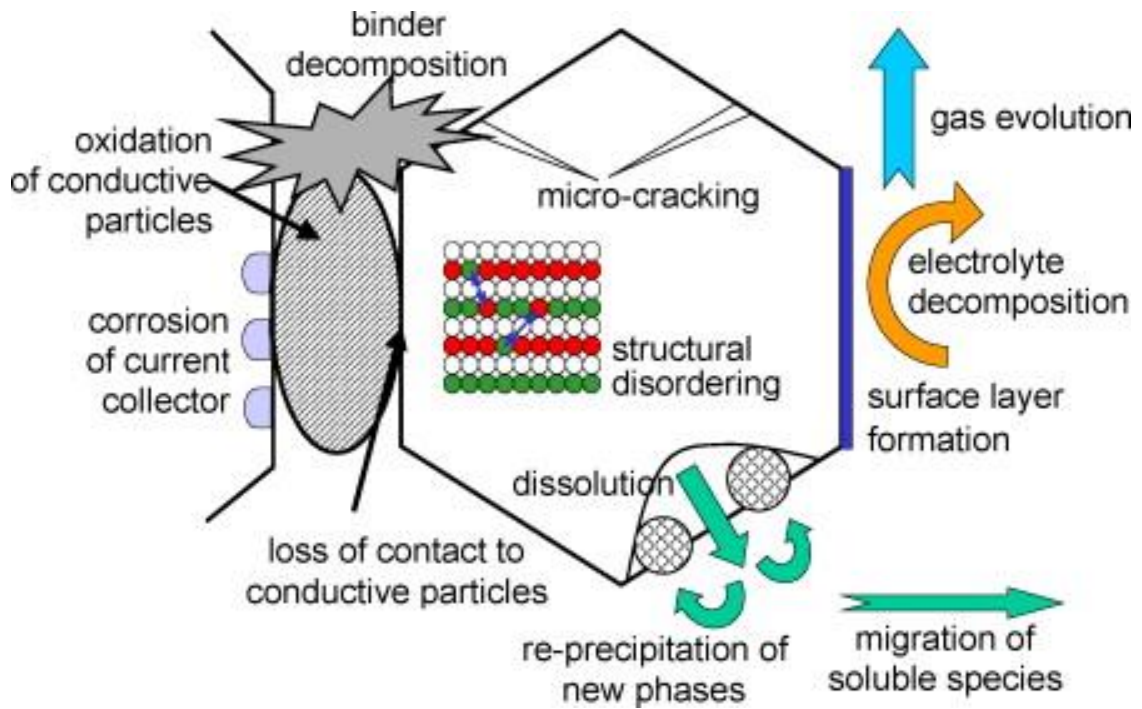


Figure 1.10 General visual overview of the many processes that lead to cathode degradation.<sup>57</sup>

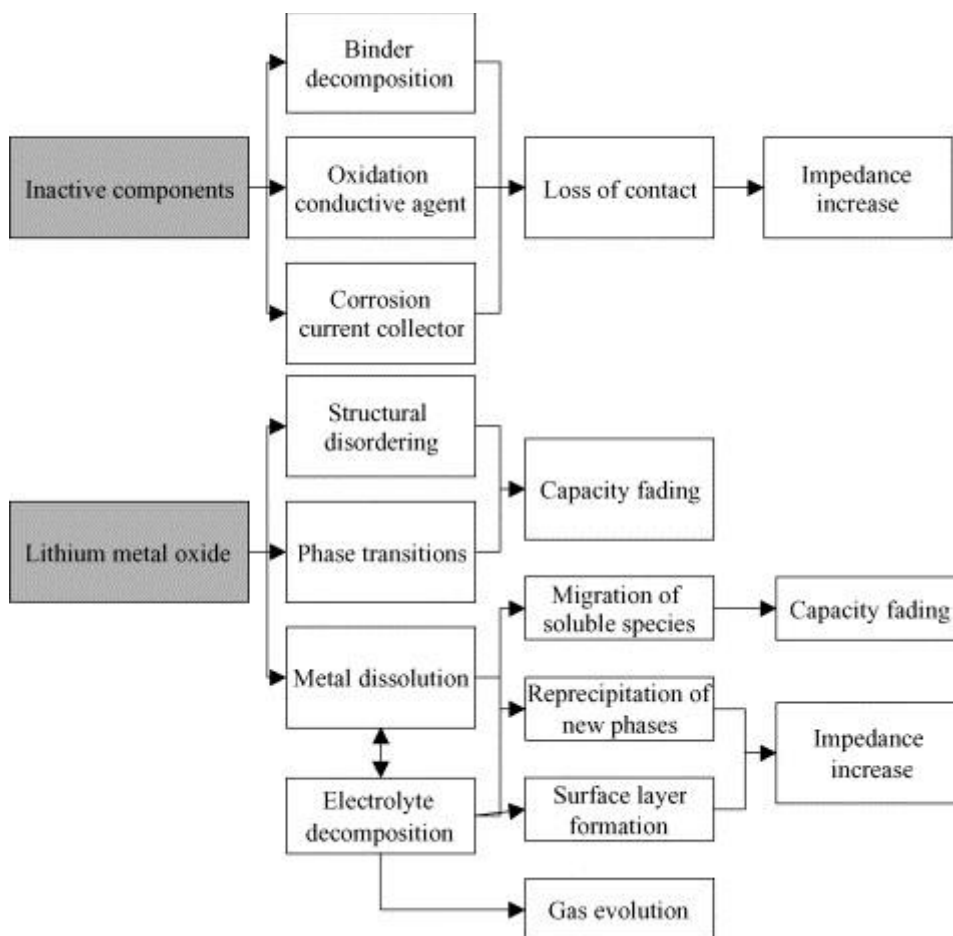


Figure 1.11 Cause and effect of degradation mechanisms in cathodes.<sup>58</sup>

For NMC-622, Ruan *et al.* have systematically studied the degradation mechanisms for cut-off voltages of 4.2, 4.5 and 4.8 V.<sup>59</sup> While practically zero capacity fade was observed for cells charged up to 4.2 V after 100 cycles, those charged to higher values showed gradual capacity fade with cells charged to 4.8 V showing more rapid capacity fade and larger impedances after 100 cycles. Cation mixing between Li<sup>+</sup> and Ni<sup>2+</sup> was observed to increase upon higher voltage charging, thus facilitating the formation of spinel and rock-salt type surface phases as previously mentioned. Examination of the electrode morphology highlights the presence of micro-pores, micro-cracks and obvious intra-granular cracks for materials charged up to 4.2, 4.5 and 4.8 V respectively, with a 4-5 nm amorphous CEI observed *via* TEM imaging for the latter. Initial discharge capacities of 161, 197 and 237 mAh g<sup>-1</sup> were achieved, with retentions of 98, 90 and 65 % for cut-off voltages of 4.2, 4.5 and 4.8 V respectively. Despite severe performance loss when highly charged (4.8 V), the discharge capacities and retention for moderately charged (4.5 V) NMC-622 are promising.

The drive for increasing the nickel content in order to realise higher specific capacities is not the only focus when designing new cathode technologies. The minimisation of cobalt content is another hugely important factor due to cost, toxicity, but perhaps most importantly the ethical issues surrounding the cobalt supply chain. The Democratic Republic of Congo (DRC) accounts for  $\approx$  50 % of the world's cobalt mining, where it is mined from copper-cobalt ores.<sup>60</sup> Cobalt availability is therefore greatly affected by the geopolitical stability of the DRC, where instabilities can lead to significant price fluctuations, price volatility and widespread supply disruptions of cobalt.<sup>61</sup> Economics aside, and more importantly, there is also a human cost to cobalt mining. Oppressed women, men and children as young as six years old toil away, doing backbreaking work to obtain cobalt ore for as little as £0.50 per bag (relating to approximately one day's work). Conditions are terrible, with no protection against airborne mineral dust or contaminated water supplies.<sup>62</sup> Cobalt refining is also geographically concentrated, with most mined cobalt being sent to China for refinement, further placing risks on supply volatility.<sup>61</sup>

NMC-811 has gained considerable attention for its advantages over lower nickel content cathodes. With deliverable capacities of  $\approx$  200 mAh g<sup>-1</sup> and an average voltage of  $\approx$  3.8 V vs. Li/Li<sup>+</sup>, NMC-811 is approximately 25 % more energy dense than LiCoO<sub>2</sub>.<sup>63</sup> Like with LiNiO<sub>2</sub>, the synthesis of NMC-811 is not trivial, with minimisation of cation mixing between Li<sup>+</sup> and Ni<sup>2+</sup> a difficult task and the formation of extra Li containing compounds such as Li<sub>2</sub>CO<sub>3</sub> and LiOH during synthesis can have a negative impact on cell

performance.<sup>64,65</sup> Furthermore, as has been mentioned before, a higher nickel content leads to poor thermal and structural stabilities, especially at high states of charge, with capacity fade observed over many cycles. Although good discharge capacity was generally observed for NMC-532 and NMC-622 when an upper cut-off potential of 4.2 to 4.5 V was implemented, NMC-811 synthesised by a co-precipitation method by Noh *et al.* showed a discharge capacity retention of 70 % after 100 cycles when charged to 4.3 V, indicating that degradation processes in NMC-811 occur in a much more facile manner.<sup>63</sup> These degradation processes are widely acknowledged to be initiated at higher states of charge due to the rapid performance fade at voltages greater than 4.2 V vs. Li/Li<sup>+</sup>.<sup>66</sup> Figure 1.12 shows the relationships between Ni content, thermal stabilities and initial discharge capacities for a range of LiNi<sub>x</sub>Mn<sub>y</sub>Co<sub>1-x-y</sub>O<sub>2</sub> compositions, highlighting the poor thermal stabilities associated with very nickel rich compositions which yields poor safety characteristics also.

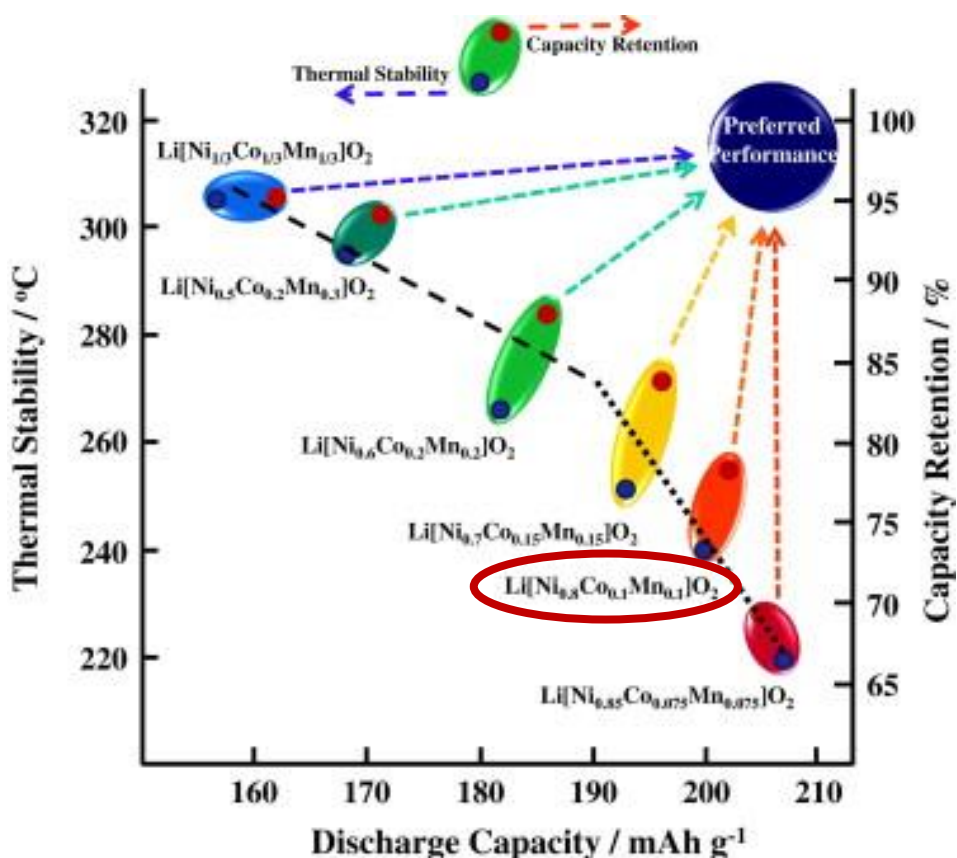


**Figure 1.12** Comparison of thermal stabilities and discharge capacities achieved for a range of LiNi<sub>x</sub>Mn<sub>y</sub>Co<sub>1-x-y</sub>O<sub>2</sub> materials. NMC-811 is circled.<sup>63</sup>

The thermal stability and structural changes of various layered oxides (NMC-433, NMC-532, NMC-622 and NMC-811) in the charged state (4.3 V) has been studied by Bak *et al.* using *in-situ* time resolved X-ray diffraction and mass spectrometry.<sup>67</sup> The onset

temperatures corresponding to the formation of spinel and rock-salt phases was recorded, alongside mass spectroscopy profiles for oxygen release. Upon heating the charged cathode materials up to 600 °C, it was observed that NMC-811 exhibited the lowest onset temperature of thermal decomposition of 135 °C (corresponding to the rhombohedral to spinel phase transition) with a gradual transition from spinel to rock-salt observed between 155 to 365 °C. NMC-622 showed slightly higher onset temperatures for the same transitions, whereas NMC-532 and NMC-433 showed much higher onset temperatures. For NMC-532, the spinel phase was observed to form between 235 to 315 °C and the rock-salt phase was not observed even at 600 °C. Mass spectrometry revealed oxygen release peaks at temperatures that coincided well with the phase transitions. Whereas the oxygen profiles for NMC-433 and NMC-532 suggest the release of small amounts of O<sub>2</sub> gas spread over a wide temperature range, for NMC-622 and NMC-811 significant peaks were observed. NMC-811 displayed the most intense peak, occurring between 130 to 150 °C, corresponding to a substantial release of oxygen which could cause serious safety problems for a real battery system - the reaction of released oxygen with a highly reactive electrolyte could cause fires and thermal runaway as previously discussed for LiCoO<sub>2</sub>.

It is suggested for NMC-811 that structural changes may not provide a major contribution to the fast capacity fade that is often observed. Li *et al.* probed the changes in structure on charging to 4.4 V vs. Li/Li<sup>+</sup> using XRD and found no significant changes to the atomic structure on recovered electrodes after 200 cycles, despite a large c-axis contraction at high potentials during charge.<sup>68</sup> This is inconsistent with degradation mechanisms occurring in LiNiO<sub>2</sub> associated with high states of charge where a H2 to H3 phase transition is observed and generates lattice strains within particles which lead to cracking.<sup>69,70</sup> It is suggested that other processes, such as parasitic reactions between the electrolyte and the delithiated cathode may play a more crucial role in poor electrochemical performances. The absence of an O3 to O1 phase change has been corroborated in 2019 by Märker *et al.* at Cambridge in a study to examine changes in structure and Li<sup>+</sup> diffusion under electrochemical cycling.<sup>71</sup> Using synchrotron XRD, the c parameter of NMC-811 also showed the same behaviour as was shown by Li *et al.* - a gradual expansion until 4.2 V vs. Li/Li<sup>+</sup> followed by a sudden contraction on further charge to 4.4 V. In order to probe the Li<sup>+</sup> diffusion at different states of charge, <sup>7</sup>Li solid-state NMR was utilised which allows one to observe local diffusional behaviours as opposed to bulk diffusion. It was found that fast Li<sup>+</sup> ion hopping commenced at ≈ 20 % state of charge (SOC) and reached a maximum hopping rate between 40 to 50 % SOC with a sharp decrease in ionic mobility observed between 70 to 75 % SOC. This corresponds to the contraction of the c axis

aforementioned, where a collapsing Li layer impedes the Li mobility. From the studies of degradation of NMC-811 it is obvious that to sustain good cell performance, electrochemical cycling should be limited to an upper cut-off voltage of  $\approx 4.2$  V to avoid the onset of severe layer contraction and further degradation processes that hinder good performance. However, employing this relatively low cut-off potential reduces the amount of deliverable discharge capacities, which, it can be argued, negates the purpose of these nickel rich compositions. Therefore, it is logical to investigate modifications that can be made to prevent the onset of degradation.

### 1.4.3 Mitigating Degradation in nickel rich layered oxides

On the one hand it is clear that the development of high capacity nickel rich layered oxide cathodes is severely hindered by the onset of debilitating degradation processes which occur under operation at higher voltages, but on the other hand, it is these higher voltages that are crucial in delivering high discharge capacities of  $> 200$  mAh g<sup>-1</sup> such as for NMC-811. The massive commercial success of LiCoO<sub>2</sub> and NMC-111 truly shows the benefits these layered oxides offer and therefore, in order to fully realise the high capacities posed by nickel rich layered oxides, these degrading processes must be mitigated or prevented entirely. Several strategies have been investigated for these purposes and will be discussed here.

One strategy involves introducing electrochemically inactive cations into the transition metal layers in order to suppress instabilities. This doping mechanism is hoped to favourably influence the cation mixing arrangement and suppress unwanted phase transitions. Aluminium doped LiNiO<sub>2</sub> have been widely studied by Rougier, Ozhuku, Zhong and Wang who used solid state synthetic methods to obtain the final material.<sup>72,73,74,75</sup> Further research has employed the use of sol-gel methods and co-precipitation techniques to incorporate Al<sup>3+</sup> ions into the LiNiO<sub>2</sub> structure.<sup>76,77</sup> This research has yielded common results of improved cycle life and reduced capacity fade which is attributed to an increase in thermal stability imparted by ability of Al<sup>3+</sup> to migrate into tetrahedral sites which disrupts the cationic migration responsible for phase changes at elevated temperatures.<sup>78</sup> Owing to favourable characteristics already imparted by the presence of Co<sup>3+</sup> in LiNi<sub>1-x</sub>Co<sub>x</sub>O<sub>2</sub> system, similar systems of LiNi<sub>1-x-y</sub>Co<sub>x</sub>Al<sub>y</sub>O<sub>2</sub> (with  $0 \leq x, y \leq 1$ ) have been extensively researched and can be referred to as NCA-type materials. When introducing electrochemically inactive dopants into the structure at the expense of active cations such as Ni and Co as is the case with NCA materials, it is imperative to keep the dopant concentrations as low as possible in order to keep reversible capacity losses to a minimum and also to mitigate impurity formation. Therefore, many studied systems focus on Al<sup>3+</sup>

contents of 5 to 15 %. For example, Madhavi *et al.* studied Al doping in  $\text{LiNi}_{0.7}\text{Co}_{0.3-x}\text{Al}_x\text{O}_2$  for  $0 \leq x \leq 0.15$  systems and found improved capacity retention for samples with  $x = 0.05$ , 0.1 compared to the undoped sample. However, it is clear from their results that capacity fading still occurs, with the best performing sample where  $x = 0.05$  showing a discharge capacity retention of only 70 % after 50 cycles.<sup>79</sup> Guilmard *et al.* synthesised  $\text{LiNi}_{0.7}\text{Co}_{0.15}\text{Al}_{0.15}\text{O}_2$  using a co-precipitation technique that delivered average discharge capacities of 150 mAh g<sup>-1</sup> at a C/20 rate with lower polarisation as has been observed in similar  $\text{LiNi}_{1-y}\text{Al}_y\text{O}_2$  materials studied by the same researchers.<sup>80</sup> For battery cycling, the current rate is often expressed with notation of C/h where C is the charge drawn from the cell during total reduction/oxidation of the electrode and h is the time in hours in which this charge will be passed. For example, a cell cycled at a rate of C/10 is expected to fully discharge in 10 hours and fully charge in 10 hours if the theoretical capacity can be achieved. Following from these advances, in 2002 the company SAFT commercialised  $\text{LiNi}_{0.8}\text{Co}_{0.15}\text{Al}_{0.05}\text{O}_2$ , with their technology showing significant improvements in electrochemical performance and cell safety. With this composition, NCA materials have been shown to achieve specific discharge capacities close to 200 mAh g<sup>-1</sup> when cycled between 2.75 to 4.3 V vs. Li/Li<sup>+</sup> at a rate of C/5 and capacity retentions of up to 94.2 % over 60 cycles.<sup>81</sup> The material commercialised by SAFT has shown energy densities of 120 to 130 Wh kg<sup>-1</sup> over 1000 cycles at 80 % depth of charge.<sup>82</sup> This material's composition is considered optimal for  $\text{LiNi}_{1-x-y}\text{Co}_x\text{Al}_y\text{O}_2$  materials and is currently one of the materials used in Tesla electric vehicles.<sup>83</sup> However, although commercialised, much like  $\text{LiCoO}_2$ , NCA has its share of concerns, including poor thermal stabilities which arise from the Ni<sup>4+</sup> rich delithiated state, resulting in oxygen evolution which can jeopardise the safety of the battery.<sup>84</sup>

Doping of layered oxides has also been achieved with other cations such as Ga, Mg and Ti. For example, doping small quantities of Ga<sup>3+</sup> cations into  $\text{LiCoO}_2$  to form compositions  $\text{LiCo}_{1-x}\text{Ga}_x\text{O}_2$  ( $x = 0.025, 0.05$ ) has been shown to yield a prominent improvement of discharge capacity retentions at higher cut-off potentials up to 4.5 V vs. Li/Li<sup>+</sup> compared to pristine  $\text{LiCoO}_2$ . Furthermore, this doping also suppresses large changes in the lattice c parameter during cycling which improves reversibility. It has furthermore been shown that improved thermal stability and ionic conductivity arise in doped  $\text{LiCoO}_2$  from the presence of small amounts of Ga<sup>3+</sup>.<sup>85,86</sup> Gallium doping has also shown enhanced cycling performance and stabilities when doped compositions  $\text{LiNi}_{1-x}\text{Ga}_x\text{O}_2$ ,  $\text{LiGa}_x\text{Mg}_y\text{Ni}_{1-x-y}\text{O}_2$  and  $\text{LiCo}_{0.25}\text{Ga}_{0.05}\text{Ni}_{0.7}\text{O}_2$ .<sup>87-89</sup> Magnesium doping has also shown to impart cycling performance improvements. For a series of Mg<sup>2+</sup> doped  $\text{LiNiO}_2$  with compositions  $\text{LiNi}_{1-y}\text{Mg}_y\text{O}_2$ , improved cycling stabilities were observed which were attributed to the presence of

electrochemically inactive  $\text{Mg}^{2+}$  residing in the lithium layer and preventing local collapse of the inter-slab space during the deintercalation process. Low doping amounts of  $y < 0.1$  resulted in  $\text{Mg}^{2+}$  residing wholly in the lithium layer, while larger doping amounts resulted in some  $\text{Mg}^{2+}$  occupying spaces in the Ni layer, leading to the production of charge compensating  $\text{Ni}^{4+}$  species, although after charging it was found that all  $\text{Mg}^{2+}$  migrated into the lithium layer. Because of the inactive electrochemical character of the doped  $\text{Mg}^{2+}$ , specific capacities are reduced upon increased doping and Mg contents of 5 % or less are optimal.<sup>90-92</sup> Small quantities of magnesium doping in NMC-622 ( $\text{LiNi}_{0.6-x}\text{Mn}_{0.2}\text{Co}_{0.2}\text{Mg}_x\text{O}_2$  with  $x = 0.01, 0.03$  and  $0.05$ ) has also been shown to be beneficial in improving capacity retention, rate capabilities and the degree of Li/Ni cation mixing, with the best improvements seen for the  $x = 0.01$  sample.<sup>93</sup> The incorporation of titanium on the transition metal sites of high nickel content layered oxides has also proven to improve the electrochemical performance of the material through increased structural stabilities. The samples of Ti- substituted NMC-811 show superior cycling stability when cycled to 4.5 V, compared to a pristine sample of NMC-811 with only a slight compromise of achieved capacities and rate capabilities with an optimum dopant amount of 2 %. Post mortem SEM and XRD analysis of cycled material has also highlighted the suppression of particle cracking in the doped samples and further suppression of cell volume changes during, indicating superior mechanical stability imparted by the presence of  $\text{Ti}^{4+}$  cations within the structure.<sup>94</sup>

Evidently, doping with aliovalent and electrochemically inactive cations has been shown to be beneficial in enhancing electrochemical and thermal stabilities in a variety of high nickel content layered cathode materials. The range of dopants that can be incorporated is clearly much broader than what has been presented above and thus a rich playground for optimisation and tailoring of material properties is available. Many further dopants such as Mo, Na, W, Zr, have been investigated and presented in the literature.<sup>6,95-99</sup>

Alongside doping, techniques involving the coating of primary or secondary particles with a stable material, and thus forming a passivating layer have also been shown improve the electrochemical properties and stabilities of cathode materials. This is especially effective in high nickel content cathodes at high states of charge where the surface becomes highly reactive and parasitic electrode-electrolyte reactions lead to severe material degradation including  $\text{O}_2$  release and the formation of a CEI. By coating these highly reactive surfaces with an unreactive material, direct contact between the active material and the electrolyte solution is prevented which in turn suppresses the parasitic side reactions and heat generation. Coating with metal oxides such as  $\text{MgO}$ ,  $\text{Al}_2\text{O}_3$ ,  $\text{SiO}_2$ ,

TiO<sub>2</sub>, ZnO, SnO<sub>2</sub>, and ZrO<sub>2</sub> have been shown to markedly improve electrochemical performances of many electrode materials including improved reversible capacities, increased coulombic efficiencies (most importantly in the first cycle), rate capabilities and an enhanced overcharge tolerance.<sup>100</sup> For example, a ZrO<sub>2</sub> coating applied to NMC-111 has been shown to greatly improve capacity retention across 45 cycles under cycling with an upper potential cut-off of 4.5 V, where coated materials retained capacities of at least 160 mAh g<sup>-1</sup> (≈ 89 % retention) for slower cycling rates, compared to ≈ 76 % retention for the uncoated sample. Improved rate capabilities were also seen, where for cycling rates between 0.1 to 0.5C the ZrO<sub>2</sub> coated sample exhibited identical discharge capacities, alongside suppression of impedance growth also improving the cycling properties of the NMC-111.<sup>101</sup> A 100 nm thick sulfated ZrO<sub>2</sub> coating applied to spherical NMC-811 particles exhibited extremely high capacity retentions of 98.8 % after 50 cycles at room temperature, compared with 91.1 % exhibited by the pristine NMC-811 electrode. Capacity retention at 60 °C was also greatly improved from 64.9 % for a pristine electrode to 79.2 % and 88.9 % for ZrO<sub>2</sub> and sulphated-ZrO<sub>2</sub> coated samples. This has been rationalised by the ZrO<sub>2</sub> layer physically suppressing metal dissolution by protecting the active material from HF attack alongside suppressing deleterious electrode-electrolyte side reactions, with the sulphur component of the coating acting chemically to modify and stabilise the CEI formed.<sup>102</sup> Alumina (Al<sub>2</sub>O<sub>3</sub>) coatings have also been investigated and are desirable due to the low cost and non-toxic nature of Al<sub>2</sub>O<sub>3</sub>. Coatings deposited by atomic layer deposition (ALD) on NMC-111 particles were shown to have beneficial effects on the cycling performance including high deliverable capacities of 166 mAh g<sup>-1</sup> between 3.0 to 4.5 V at 1C, a 96 % capacity retention over 110 cycles and an excellent rate capability of 137 mAh g<sup>-1</sup> at 4 C was also achieved. Cycling at elevated temperatures (55 °C) showed an outstanding improvement in capacity retention from only 14 % for a pristine sample of NMC-111 to 92 % with the coating applied.<sup>103</sup> A 2 nm thick Al<sub>2</sub>O<sub>3</sub> coating applied by ALD to NMC-811 particles also manifested improvements in initial discharge capacities, initial coulombic efficiencies and the capacity retention over 100 cycles. A higher initial discharge capacity of 213 mAh g<sup>-1</sup> with a first cycle efficiency of 84 % could be attained for the coated sample compared to 198 mAh g<sup>-1</sup> and 76 % achieved respectively for pristine NMC-811 when cycled up to a high upper cut off potential of 4.6 V. Suppression of side reactions and phase transitions brought about by the protective Al<sub>2</sub>O<sub>3</sub> coating is proposed to be responsible for these improvements.<sup>104</sup> Further cycling studies in 2 Ah pouch cells of Al<sub>2</sub>O<sub>3</sub> ALD coated NMC-811 showed an improvement of 40 % in the cycling performances and TEM/SAED structural characterisation showed that the Al<sub>2</sub>O<sub>3</sub> coating prevented layered-to-spinel phase

transitions at the surface. These results were confirmed with electron energy loss spectroscopy (EELS), showing transition metals in a reduced oxidation state at the surface, consistent with oxygen loss and the associated layered to spinel phase change, whereas no change in the bulk structure was observed using neutron powder diffraction.<sup>105,106</sup>

#### 1.4.4 Polyanionic Frameworks

Although the layered transition metal oxide cathodes such as LCO, NMC and NCA are abundant in commercial applications and possess favourable features for commercialisation, their lack of structural and thermal stability, alongside the presence of harmful and expensive elements such as Co are unfavourable both economically and socially. Considering these limitations, polyanionic materials have become of great interest for alternative cathode technologies where non-toxicity, abundance and low cost of constituent elements, alongside improved safety play vital roles. Such compounds consist of three-dimensional frameworks built on transition metals whereupon the redox reaction occurs and a moiety  $(XO_4)^{n-}$  or the derivative  $(X_mO_{3m+1})^{n-}$  where  $X = P, S, Si, B$ . Due to the rigid covalent  $X-O$  bonds, these form very stable frameworks providing long term structural stability essential to long cycle life and good safety.<sup>107</sup> The nature of these  $X-O$  bonds also acts to increase the working voltage of such materials compared to their oxide counterparts through what is known as the “inductive effect”.<sup>108</sup> In this, the covalency of the  $X-O$  bond increases the ionic character of the  $M-O$  bond which in turn lowers the position of the  $M^{2+/3+}$  redox couple relative to  $Li/Li^+$ , resulting in a greater difference between the two couples and leads to a higher cell voltage. The greater the covalent character of the  $X-O$  bond, the greater the ionic character of the  $M-O$  bond and the greater redox potential relative to lithium. The lowering of the  $M^{2+/3+}$  couple due to increasing ionic character of the  $M-O$  bond occurs due to the lowering of the  $t_{2g}$  antibonding orbital relative to lithium which is brought on by a lessening of the quantum mechanical repulsions between bonding and antibonding orbitals present for increasingly covalent character bonding. A visualisation of the energy level changes due to the induction effect is shown in Figure 1.13

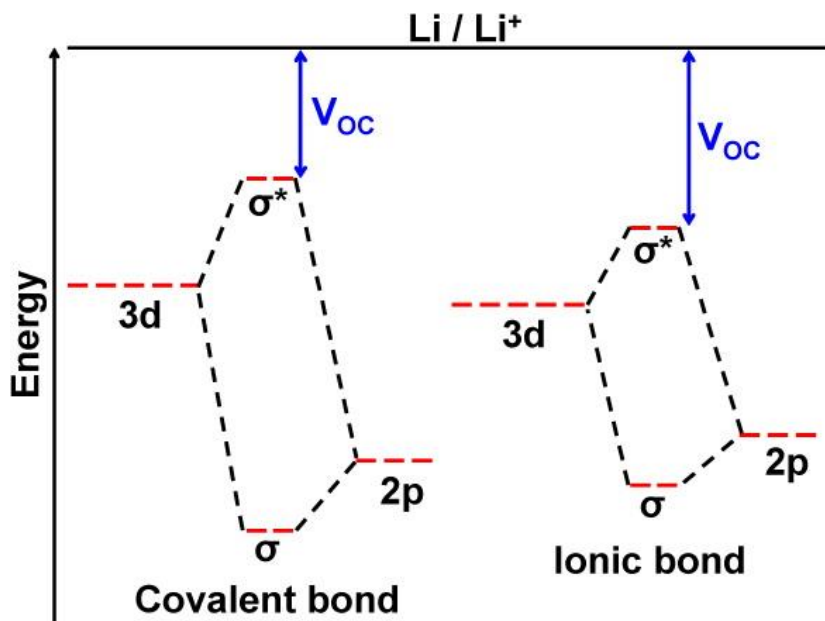


**Figure 1.13** Energy level diagrams depicting the difference in energy levels between the  $\sigma$  bonding and anti-bonding orbitals (formed between 3d orbitals on transition metals  $M^{n+}$  and oxygen 2p orbitals). The effect of the nature of the M-O bond *i.e.* covalent or ionic, on the open circuit voltage,  $V_{OC}$ , is evident.

#### 1.4.4.1 LiFePO<sub>4</sub>

Perhaps the most well known and most researched polyanionic cathode material is the phospho-olivine LiFePO<sub>4</sub> (LFP), with reversible Li<sup>+</sup> extraction first reported by Padhi and Goodenough in 1997.<sup>109</sup> The material benefits from excellent thermal and structural stability due to the strong P-O bonds present. Moreover, it has a relatively high theoretical capacity of 170 mAh g<sup>-1</sup>, a flat voltage plateau at a relatively high voltage of 3.45 V and as the only transition metal present is Fe which presents a safer, cheaper and less toxic option compared with layered oxide type materials (which are hindered in these aspects by the presence of cobalt in the structure). Excellent cycling stability is also observed for LiFePO<sub>4</sub> due to the minimal volume change to the crystal structure upon insertion and extraction of Li<sup>+</sup> cations.

Olivine type LiFePO<sub>4</sub> adopts an orthorhombic unit cell symmetry described by the *Pnma* space group. The framework is built upon a distorted oxygen hexagonal packing arrangement where Li<sup>+</sup> and Fe<sup>2+</sup> occupy a half of the octahedral sites, generating FeO<sub>6</sub> and LiO<sub>6</sub> octahedra respectively, and P occupies 1/8 of the tetrahedral sites, generating PO<sub>4</sub> tetrahedra. This can also be understood as layers of distorted corner sharing FeO<sub>6</sub> octahedra within the *bc* plane of the crystal, with adjacent planes bridged by PO<sub>4</sub> tetrahedra. As the FeO<sub>6</sub> octahedra are only corner sharing, this leads to poor electronic delocalisation and hence poor electronic conductivity. Furthermore, as a result of the

connectivity of octahedra throughout the structure,  $\text{Li}^+$  cation movement is restricted to channels along the  $b$  plane, making  $\text{LiFePO}_4$  a poor ionic conductor owing to this 1D diffusion mechanism. The structure of  $\text{LiFePO}_4$  is shown in Figure 1.14. The poor intrinsic electronic and ionic conductivities of  $\text{LiFePO}_4$  make electrochemical utilisation of the pristine material impractical. However, by implementing strategies such as carbon coating and morphology control of  $\text{LiFePO}_4$  materials, both of these obstacles can be overcome respectively. The carbon coating process generally involves mixing  $\text{LiFePO}_4$  powders with a carbon source, followed by a high temperature heat treatment. Carbon sources can be organic (*e.g.* glucose, sucrose, citric acid and lactose) which are excellent at forming homogenous coatings and allowing good control of layer structure and thickness, or inorganic (*e.g.* carbon nanotubes, graphite or acetylene black) which can provide higher quality carbon (*e.g.* more conductive) but coating parameters are difficult to control.<sup>110</sup> Morphological control to enhance ionic diffusion is an equally important factor, where careful control of particle size and shape can aid to shorten  $\text{Li}^+$  diffusion path lengths. For example, since the 1D diffusion pathway in  $\text{LiFePO}_4$  occurs along the [010] direction, synthesis of nanostructures with large [010] surface areas should enhance the electrochemical performance. This has been demonstrated in nanosheets, nanowires, nanoparticles and core-shell structures to yield materials with excellent rate performances and long cycle lives.<sup>111-113</sup> As a result of these modifications,  $\text{LiFePO}_4$  has advanced to show good performance electrochemically with very stable cycling characteristics and very little degradation seen over its lifetime.

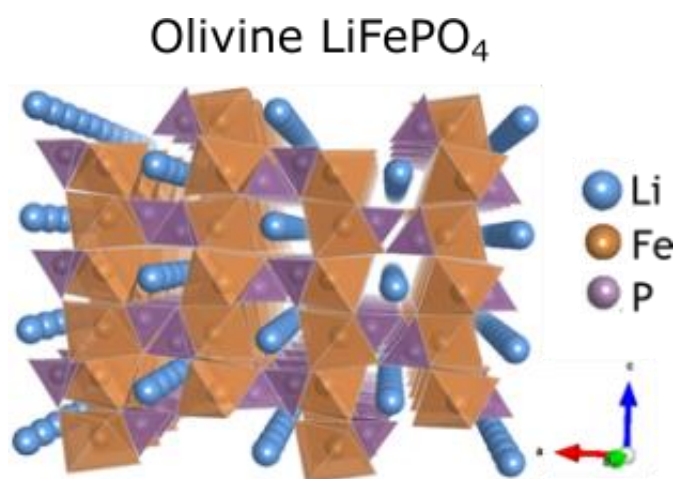


**Figure 1.14** Crystal structure of the olivine phase of  $\text{LiFePO}_4$ , showing the channels of lithium along [010].

#### 1.4.4.2 $\text{LiFeSO}_4\text{F}$ fluorosulfate materials

The success of  $\text{LiFePO}_4$  has led researchers to further investigate polyanionic materials for LIB cathodes. In order to obtain similar materials but possessing higher energy

densities, the induction effect can again be implemented. Building on the  $\text{LiFePO}_4$  framework, replacement of the  $(\text{PO}_4)^{3-}$  group with the more electronegative  $(\text{SO}_4)^{2-}$  group will serve to push down the  $\text{Fe}^{2+/3+}$  redox couple even further, thus increasing the overall cell potential. This has been shown in isostructural NASICON frameworks  $\text{Li}_2\text{Fe}_3(\text{PO}_4)_3$  and  $\text{Fe}_2(\text{SO}_4)_3$ , where an open circuit voltage increase of 0.8 eV was observed upon substitution of the  $(\text{PO}_4)^{3-}$  units with  $(\text{SO}_4)^{2-}$  groups.<sup>114</sup> However, it is evident that with the different charges on the  $(\text{PO}_4)^{3-}$  and the  $(\text{SO}_4)^{2-}$  groups, that in order to preserve charge neutrality, a monovalent anion must also be incorporated into the material, with the highly electronegative  $\text{F}^-$  being a sensible choice. While this anion is an essential addition, it also serves to further enhance material properties due to its high electronegativity acting to further decrease the voltage of the  $\text{Fe}^{2+/3+}$  redox couple.<sup>115</sup> Owing to the dual effect of having both an electron withdrawing sulphate group and a highly electronegative fluoride anion in the structure, the fluorosulphate material  $\text{LiFeSO}_4\text{F}$  presents a promising higher voltage Fe-containing cathode material. Compared to the olivine structure of  $\text{LiFePO}_4$ , which exhibits an average voltage of 3.45 V vs.  $\text{Li}/\text{Li}^+$  operating on the  $\text{Fe}^{2+/3+}$  redox couple, the tavorite and triplite phases of  $\text{LiFeSO}_4\text{F}$  display redox voltages of 3.6 and 3.9 V respectively, acting on the same redox couple. The origin of this voltage difference between polymorphs is believed to lie in the difference of anionic networks of the two phases, more specifically related to the differing arrangements of F anions around the transition metal, which will be discussed in the following section.<sup>116</sup> The increased voltages offered by these two polymorphs, alongside the inherent safety, stability and low cost, makes these materials highly desirable as a consideration for advanced cathode technologies.

#### 1.4.4.3 Structures of $\text{LiFeSO}_4\text{F}$ and possible diffusion pathways

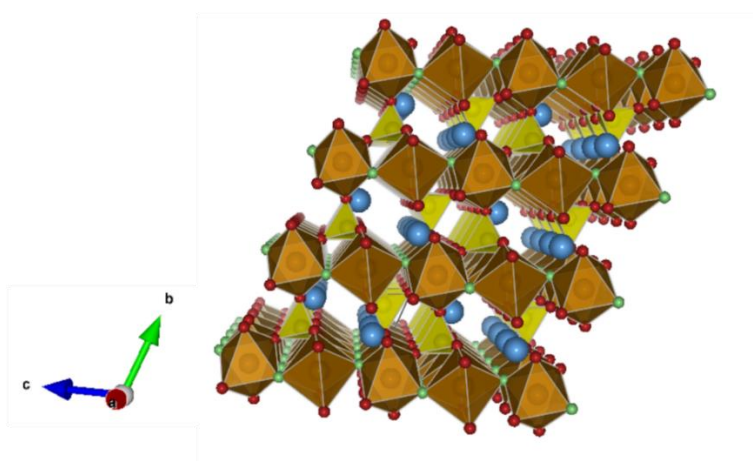
The lower voltage phase of  $\text{LiFeSO}_4\text{F}$  is isostructural with the mineral tavorite,  $\text{LiFePO}_4\text{OH}$ , and crystallises in the triclinic  $P\bar{1}$  space group, hence the nomenclature of referring to this phase of  $\text{LiFeSO}_4\text{F}$  as the tavorite phase. The structure of  $\text{LiFeSO}_4\text{F}$  consists of chains of corner sharing  $\text{FeO}_4\text{F}_2$  octahedra along the  $c$  axis, which are connected by fluorine containing corners where the fluoride ions are located on opposite vertices within each octahedron. This corner-sharing, mediated through oppositely located fluoride ions, gives rise to alternate orientation of the  $\text{FeO}_4\text{F}_2$  octahedra along the chain. The structure is cross-linked by Fe-O-S-O-Fe chains, formed by the connectivity of each oxygen in octahedra to a sulphur atom, forming  $\text{SO}_4$  tetrahedra. Corner sharing  $\text{SO}_4$  units act to induce a physical separation between the  $\text{FeO}_4\text{F}_2$  chains, resulting in three primary open tunnels within the structure along the  $[100]$ ,  $[010]$  and  $[101]$  directions.  $\text{Li}^+$  ions are located within these tunnels.<sup>117</sup> The higher voltage triplite phase of  $\text{LiFeSO}_4\text{F}$

crystallises in the monoclinic  $C2/c$  space group, with a structure that can be regarded as a disordered analogue of tavorite, where the Fe and Li do not sit on distinct crystallographic sites and are instead randomly distributed across two sites. Further differences include edge sharing connectivity between adjacent  $\text{FeO}_4\text{F}_2$  octahedra which results in two crystallographically unique chains along the  $[010]$  and  $[101]$  directions, alongside a *cis* orientation of F atoms in each octahedra instead of the *trans* orientation as seen in tavorite.<sup>118</sup> It is these differing orientations that give rise to the voltage disparity observed between the two phases. Visualisations of the crystallographic structures of both tavorite and triplite phases of  $\text{LiFeSO}_4\text{F}$  are displayed in Figure 1.15, where the complicated nature of the triplite phase compared to tavorite is clearly shown.

Using atomistic simulation techniques alongside a conventional hopping model, Tripathi *et al.* have determined that long-range Li diffusion in tavorite  $\text{LiFeSO}_4\text{F}$  occurs in zig-zag jumps down the  $[100]$ ,  $[010]$  and  $[111]$  directions conduction channels, with the  $[111]$  conduction exhibiting the lowest energy path for diffusion. A series of four unique diagonal hops shared between all of these channels lead to continuous interconnecting paths within the structure and effectively allow 3D transport of  $\text{Li}^+$  ions throughout. The open nature of these transport pathways, alongside the low activation energies calculated for each hop ( $E_a = 0.36$  eV for transport along the  $[111]$  direction and  $E_a \approx 0.45$  eV for other hops) and calculated Li diffusion coefficients on the same order of magnitude as is calculated for  $\text{LiCoO}_2$  (in the range  $10^{-10}$  to  $10^{-8}$   $\text{cm}^2 \text{ s}^{-1}$ ) indicates that tavorite  $\text{LiFeSO}_4\text{F}$  could show fast and facile Li transport properties, thereby improving the charge and discharge capabilities when utilised in a LIB.<sup>117</sup> While Tripathi *et al.* have claimed facile Li transport along three directions, Mueller *et al.*, using density functional theory (DFT) methods have calculated fast ionic conduction occurs only along the  $[111]$  direction with an activation energy of 208 meV, with activation energies increasing to 700 and 976 meV for 2D and 3D conduction respectively, arguing that DFT methods provides a more accurate model than the potentials based methods used by Tripathi *et al.*<sup>119</sup> This 1D diffusional nature is corroborated by Adams and Rao who have predicted fast diffusion along  $[111]$  using molecular dynamics simulations and bond valence analysis with an activation energy of 0.1 eV.<sup>120</sup> For the triplite phase, the random ordering of Li and transition metal cations would presumably preclude any Li diffusion through lack of a coherent transport pathway. This was assumed due to the electrochemical inactivity exhibited by triplite  $\text{LiMnSO}_4\text{F}$ , however, triplite  $\text{LiFeSO}_4\text{F}$  has been shown to be electrochemically active.<sup>118,121-124</sup> Atomistic modelling by Lee and Park has suggested that the edge-sharing nature of octahedra connectivity in triplite aggravates the restriction of  $\text{Li}^+$  ion mobility, and only a channel along  $[010]$  is available for ion transport.<sup>125</sup>

Both tavorite and triplite phases of  $\text{LiFeSO}_4\text{F}$  clearly present an attractive option for future polyanionic cathode materials due to improved energy densities compared to  $\text{LiFePO}_4$  and improved safety characteristics and cost compared to conventional layered oxide materials. Indeed, the 3.9 V vs.  $\text{Li}/\text{Li}^+$  exhibited by the triplite phase is the highest reported voltage for an Fe-containing cathode and the proposed 3D nature of Li diffusion in tavorite  $\text{LiFeSO}_4\text{F}$  could yield improved rate capabilities over well-known materials such as  $\text{LiFePO}_4$ .

### (a) Tavorite



### (b) Triplite

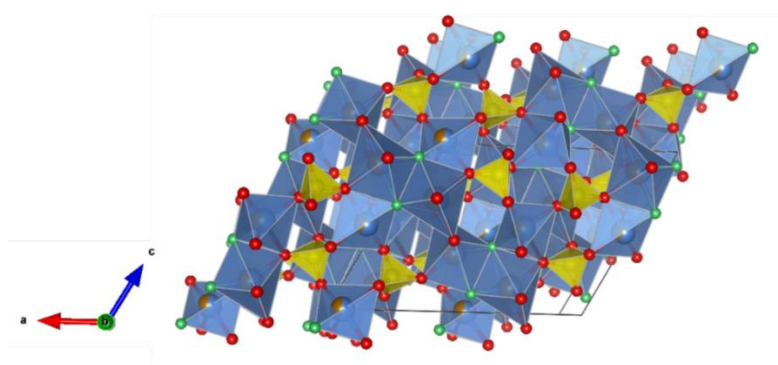


**Figure 1.15** Crystal structures for (a) tavorite phase  $\text{LiFeSO}_4\text{F}$  looking along the  $a$  direction and (b) triplite phase  $\text{LiFeSO}_4\text{F}$  looking along the  $b$  direction. In tavorite, Li (blue) and Fe (brown) sit on distinctly separate sites whereas in triplite they are evenly distributed over two crystallographic sites M1 and M2. Oxygen (red), fluorine (green) and  $(\text{SO}_4)^{2-}$  groups (yellow tetrahedra) are shown also.

## 1.5 Anode materials for lithium ion batteries

### 1.5.1 Lithium metal

The most elementary anode is metallic lithium itself, boasting a large theoretical specific capacity of  $3860 \text{ mAh g}^{-1}$ , alongside the lowest potential ( $-3.05 \text{ V}$  vs. the standard hydrogen electrode) and the lightest mass ( $6.94 \text{ g mol}^{-1}$ ) amongst metals, the utilisation of a purely metallic Li anode clearly presents a seemingly logical route to higher energy density lithium ion batteries. However, repeated Li electrodeposition on the anode can cause the continuous growth of Li dendrites during cycling, which are thin, needle-shaped crystals. These dendrites, while depleting the amount of electrochemically active lithium in the anode, can also propagate across the cell from anode to cathode during cycling, puncturing the separator and causing a short circuit which has the potential to start fires.<sup>126</sup> These dendrite related issues present the main roadblock in Li metal utilisation in anodes for secondary batteries.

### 1.5.2 Carbon based anodes

The process of  $\text{Li}^+$  ion intercalation into host structures in cathode technologies can also be applied for practical anodes resulting in the elimination of the Li plating process and the conditions for dendritic growth. This has been demonstrated by the reversible intercalation of Li into graphite to form  $\text{Li}_x\text{C}_6$  species ( $0 \leq x \leq 1$ ). The complete reversible intercalation of 1 Li per 6 carbon atoms results in a theoretical specific capacity of  $372 \text{ mAh g}^{-1}$  for these types of lithiated carbon. For graphite and related graphitised carbons,  $\text{Li}^+$  ions are able to move into and out of layers within the structures, akin to layered  $\text{LiMO}_2$  cathodes. Akira Yoshino (co-recipient of the 2019 Nobel Prize in Chemistry) and co-workers at Asahi Kasei Corporation published a patent in 1986 describing the first prototype of a LIB operating with a modified  $\text{LiCoO}_2$  electrode coupled with a graphitised carbon anode made from coke fired at temperatures between  $80$  to  $1400^\circ\text{C}$ .<sup>127</sup> Dahn's group also demonstrated more reversible intercalation in graphite and similar petroleum coke materials.<sup>128</sup> The first-generation commercialised LIB pioneered by Sony in 1991 consisted of a coke anode, elaborately heat treated under optimum conditions to yield relatively low energy densities of  $200 \text{ Wh l}^{-1}$  and  $80 \text{ Wh kg}^{-1}$ . The second generation LIB by Sony used a type of non-graphitisable carbon known as hard carbon, with larger layer spacings able to incorporate more Li cations than the previous generation, evidenced by the improved energy densities of  $295 \text{ Wh l}^{-1}$  and  $120 \text{ Wh kg}^{-1}$ . Finally, for their third generation battery, Sony developed a graphite anode where elaborate preparation of the graphite and electrolyte yielded energy densities of  $> 400 \text{ Wh l}^{-1}$  and  $155 \text{ Wh kg}^{-1}$ .<sup>129</sup>

## 1.6 Sodium ion batteries

The success of lithium ion batteries has in no doubt revolutionised the portable electronics market and is set to impart the same effect on the electric vehicle market in the near future. This growing adoption of lithium ion technology brings into question whether the global availability and cost of lithium resources will be capable of sustaining the demands placed by our growing dependency on lithium ion systems. The long lifetimes of lithium ion batteries, and the difficulties encountered during recycling spent cells further exacerbates these concerns. It is clear that parallel development of alternative and complementary energy storage systems necessary to combat possible lithium shortages. Sodium ion batteries (NIBs) present one such option, owing to its many similarities to LIBs and the vast abundance of cheap global sodium sources for example, saltwater in the oceans.<sup>130</sup> Although adoption of NIBs would alleviate cost and availability concerns, they exhibit lower energy densities compared to LIBs due to the nature of the  $\text{Na}^+$  cation. It is both larger and heavier than  $\text{Li}^+$  while also displaying a  $\text{Na}/\text{Na}^+$  redox potential of  $-2.71$  V vs. the standard hydrogen electrode ( $0.3$  V smaller than that of  $\text{Li}/\text{Li}^+$ ), and therefore lower energy densities are inherent when comparing NIBs and LIBs.<sup>131</sup> Nevertheless, sodium secondary batteries are a promising complementary technology, best suited to applications where size and weight are of little concern, for example stationary grid storage applications. Indeed, development of sodium based secondary batteries is not new and initial research was carried out during the early research stages of the LIB. However, the superior energy densities provided by lithium resulted in efforts being focussed on this route instead.

Analogous to lithium layered oxide  $\text{LiCoO}_2$ , sodium cobalt oxides with the general formula  $\text{Na}_x\text{CoO}_2$  have been shown to reversibly intercalate  $\text{Na}^+$  ions electrochemically. In the composition range  $0.5 < x < 1$ , four different phases of material have been identified with  $\text{Na}^+$  occupying octahedral or trigonal prismatic coordination environments, noted as O and P type respectively in the literature. Phases O3, O'3, P3 and P2 have been identified within this sodium range where the number represents the number of distinguishable sodium containing layers.<sup>132,133</sup> These four phases have all been shown to react reversibly vs. sodium under galvanostatic cycling with the occurring reversible phase evolution  $\text{O3} \rightarrow \text{O'3} \rightarrow \text{P3}$  regardless of the initial phase for O3, O'3 and P3 phases. The P2 phase material with stoichiometry  $\text{Na}_{0.67}\text{CoO}_2$  has been shown to keep a consistent phase during cycling and shows a higher level of reversibility and improved cycle life and efficiencies.<sup>134</sup> The material  $\text{NaFePO}_4$  has also been investigated for use in NIBs. The olivine polymorph of  $\text{NaFePO}_4$  is expected to behave like  $\text{LiFePO}_4$ , with 1-dimensional conduction channels for  $\text{Na}^+$  diffusion. However, the stable polymorph of  $\text{NaFePO}_4$  is the

maricite phase, where the  $\text{Na}^+$  and  $\text{Fe}^{2+}$  cations essentially swap sites, presenting one-dimensional channels of  $\text{FeO}_6$  octahedra and no channels for  $\text{Na}^+$  cationic diffusion. Instead, both chemical and electrochemical delithiation methods can be applied to olivine  $\text{LiFePO}_4$  to yield  $\text{FePO}_4$  which can then be cycled vs. sodium to give olivine  $\text{NaFePO}_4$ .<sup>135,136</sup> Galvanostatic cycling of the material produced from the electrochemical Li-Na exchange method yielded discharge capacities close to  $120 \text{ mAh g}^{-1}$  with excellent retention over 50 cycles at a rate of  $C/20$ . Unexpectedly, however electrochemical activity in maricite  $\text{NaFePO}_4$  has recently been demonstrated by Kim *et al.* where a nanosized sample delivered an initial discharge capacity of  $142 \text{ mAh g}^{-1}$  with a capacity retention of 95 % over across 200 cycles.<sup>137</sup>

Sodium fluorophosphates including  $\text{NaVPO}_4\text{F}$ ,  $\text{Na}_3\text{V}_2(\text{PO}_4)_2\text{F}_3$ ,  $\text{Na}_{1.5}\text{VOPO}_4\text{F}_{0.5}$  and  $\text{Na}_2\text{FePO}_4\text{F}$  have shown in recent works to be promising candidates for sodium based cathode materials also, with  $\text{Na}_2\text{FePO}_4\text{F}$  delivering an initial discharge capacity of  $120 \text{ mAh g}^{-1}$  and dropping slightly over 10 cycles to  $\approx 105 \text{ mAh g}^{-1}$  at a rate of  $C/15$ .<sup>138</sup> Built on a network of bioctahedral  $\text{Fe}_2\text{O}_7\text{F}_2$  units consisting of  $\text{FeO}_4\text{F}_2$  octahedra, connected by bridging F atoms to form chains and joined by  $\text{PO}_4$  tetrahedra to form infinite layers of the  $[\text{FePO}_4\text{F}]$  moiety with the spaces between these layers providing a 2-dimensional diffusion path for  $\text{Na}^+$  cations.<sup>130,139</sup>

## 1.7 Synthesis of electrode materials

The resultant properties of functional materials such as battery electrodes rely immensely on the synthetic methodologies employed when preparing such materials. Electrochemical performance parameters such as deliverable specific capacities and rate capabilities are determined by the constituent materials' properties, for example crystal structure and particle sizes and morphologies, all of which are strongly dependent on the preparation methods. Employing the right synthesis methods where appropriate is therefore crucial for intelligent materials design and investigation into newer, more novel techniques could offer fundamental advances for future technologies.<sup>140</sup>

One of the most common synthetic methods for production of battery materials is solid state synthesis, in which powder precursors are intimately mixed (typically with a mortar and pestle) and heated in furnaces at high temperatures for long times so as to overcome mass transport limitations. Solid state synthesis is the most direct route to materials production and its simplicity allows the process to be easily scaled up for industrial materials production. These high temperatures and long reaction times present an energy expensive means of production and the solid-state mixing of precursors can lead to impurity phases easily forming. Procedures may also require repeated grinding and

calcinations, thus making the process even more lengthy. Attention is instead focussed on alternative procedures designed to yield purer materials with much greater control over structure and morphology coupled with decreased processing times and temperatures. Wet chemical methods such as sol-gel and co-precipitation are advantageous regarding these issues.

### **1.7.1 Sol-gel synthesis**

The sol-gel method is a wet chemical and low temperature approach often used in the preparation of metal oxides that has several advantages over conventional solid-state synthesis methods, originating from the production of a chemically homogenous precursor. This precursor can ensure atomic level mixing of reagents allowing for the synthesis of complex inorganic systems such as ternary and quaternary oxides at lower processing temperatures and shorter reaction times with less chance of impurity products forming from side reactions. Greater control of particle morphology and size is also enabled by sol-gel methodologies.<sup>141</sup>

In a traditional sol-gel reaction, metal alkoxide precursors are hydrolysed to form a colloidal suspension, referred to as the sol, which is then transformed into a gel, that can be described generally as a non-fluid 3D network that extends through a fluid phase. This gel is highly homogenous on the atomic level and can be further treated in order to remove the solvent fluid phase to yield a dry solid precursor, depending on the desired final application.<sup>142</sup> The sol-gel process, showing different processing routes, is shown in Figure 1.16.<sup>143</sup>

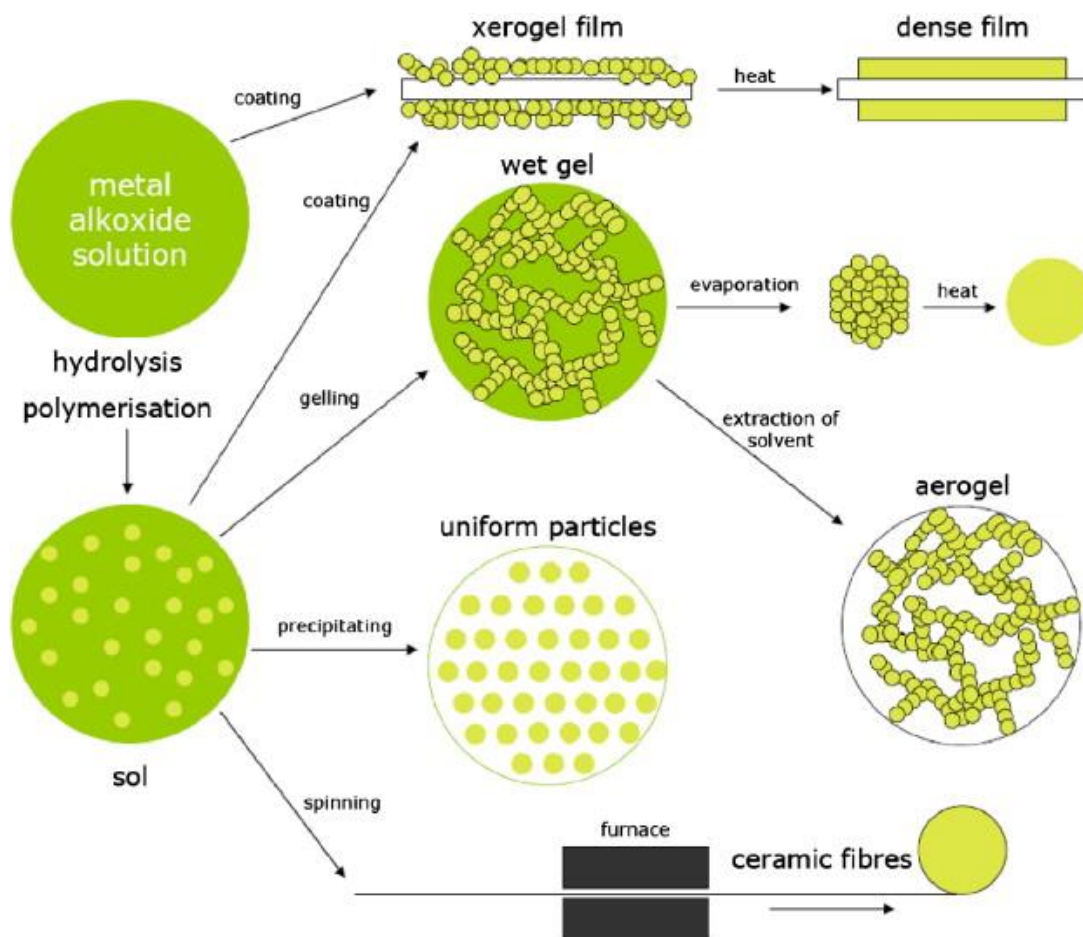


**Figure 1.16** Schematic of the sol-gel process for materials synthesis. The flexibility of both the sol and the gel is highlighted by the different possible processing techniques that can be applied in order to yield desired material properties.<sup>143</sup>

Several types of gels have been classified by Kakihana in 1996 including colloidal, metal-oxane polymer, metal complex and polymer complex types.<sup>144</sup> Of these, the metal complex type is widely used in metal oxide synthesis although whether these metal complexes can actually be classed as true gels is debatable since they usually form viscous solutions or glassy solids. However, these complexes do achieve the fundamental goal of forming a homogenous metal-containing precursor and are often cited in the literature and generalised as the ‘citrate sol-gel method’.<sup>141</sup>

The citrate sol-gel method is a popular technique in the synthesis of metal oxides, where the addition of a chelating agent solution to the sol promotes the formation of the metal complexes. This method is useful in sols containing metal precursors that can easily precipitate where the addition of a suitable chelating agent promotes the formation of metal complexes in solution and preventing any precipitation. Citric acid is a common choice, where its three carboxylic acid groups can dissociate and chelate the metal ions in the sol, forming the desired metal complexes. Citric acid is also cheap and readily

available alongside being an effective chelating agent. Common water-soluble metal precursors used in these synthetic methods include hydroxides, acetates and nitrates.

The sol-gel method has been widely applied in the synthesis of cathode materials for lithium ion batteries, for example  $\text{LiCoO}_2$ ,  $\text{LiNiO}_2$ ,  $\text{LiMn}_2\text{O}_4$  and several doped variants incorporating cations such as  $\text{Al}^{3+}$ ,  $\text{Cr}^{3+}$ ,  $\text{Ti}^{4+}$ , and  $\text{V}^{n+}$  have all been achieved *via* sol-gel methods to yield powders with good reported electrochemical performances attributed to the homogeneity at the atomic or molecular level and milder synthesis conditions leading to improved crystallinity, uniform particle distribution and smaller particle size.<sup>145</sup> There are also multiple reports on the preparation of NMC-111 by sol-gel type methods exhibiting favourable electrochemical characteristics. Julien *et al.*, using table sugar as a chelating agent, synthesised NMC-111 showing particle sizes in the range of 300 to 500 nm showing improved capacity retention compared to commercially available NMC-111.<sup>146</sup>

The sol-gel method is thus proposed to be a promising way of synthesising mixed metal electrodes, *e.g.* NMCs due to the homogeneity of the precursor promoting an even distribution of transition metal cations in the final material. This uniformity will lead to homogeneity across particle volumes during charge and discharge and could decrease the likelihood of particle degradation on cycling.

### 1.7.2 Microwave-assisted synthesis methods

In the field of materials manufacturing, factors such as energy efficiency and sustainability are key in the future of materials synthesis and processing. Conventional solid-state synthesis techniques which are commercially common, often require long reaction times at high temperatures and have an associated large energy cost and therefore present a rather inefficient means to materials production. Microwave assisted technologies, on the other hand, offer potential solutions to these issues though the realisation of rapid synthesis and processing at lower temperatures, vastly improving the energy efficiency of processes and additionally allowing for improvements in properties of functional materials and also the discovery of new materials with interesting properties.<sup>147</sup> Microwaves form part of the electromagnetic spectrum, with wavelengths between 1 m and 1 mm corresponding to frequencies ranging from 300 MHz to 300 GHz, although commercially available microwave generators operate at 2.45 GHz.

The application of microwaves to enable rapid heating has been widely implemented across many areas of both solution and solid-state chemistry. For example, in solution based methods, microwaves have been utilised widely across organic synthesis and

hydrothermal/solvothermal processing where fast reactions can be afforded due to the rapid temperature increases caused due to selective heating of a solvent by microwave radiation.<sup>148,149</sup> In solid-state synthesis, microwave heating has been implemented in ceramics processing including annealing and sintering steps showing improvements in homogeneity and densification respectively.<sup>150</sup> The ability of microwave assisted methods in yielding these interesting results lies in the coupling of microwave radiation with a specific component in the sample environment causing uniform heating throughout materials.

#### 1.7.2.1 Solution phase microwave heating

The solvothermal synthesis process involves the heating of reactants in a high temperature liquid medium (the technique is often called hydrothermal when the solvent is water). Conventionally, energy is transferred from a traditional heat source, for example an oven, to the liquid solvent through conduction, convection and radiation processes. Traditional solvothermal reactions often require long reaction times (up to a few days) and the use of high-power equipment which inevitably induces a large energy cost. Conversely, microwave-assisted solvothermal methods have the ability to yield product with very rapid reaction times and the required equipment generally operates on lower power (typically a few hundred Watts). This rapid heating, enabled by the microwave dielectric heating effect, occurs due to interactions between the solvent and the incident microwave radiation which causes the generation of heat by the solvent itself in its bulk. The heat is generated over the entire volume of solvent and results in uniform heating allowing for rapid reaction times alongside the suppression of side reactions. The temperature gradient of a reaction vessel showing uniform heating of a solvent facilitated by microwave radiation is shown in Figure 1.17, alongside the corresponding set up heated *via* conventional methods. Other benefits to microwave-assisted synthetic methodologies include excellent reproducibility due to improved control over reaction parameters which is beneficial to both product quality and general safety of the process and the possibility of automation and high throughput synthesis.<sup>151</sup>

The microwave dielectric heating effect arises from the interactions between microwave radiation and dipoles or charges within a reaction medium. For many microwave solvothermal reactions, the heating arises from the interaction of a dipolar solvent with microwaves. Upon the application of electromagnetic radiation to a dipolar solvent, the dipole will align itself with the electromagnetic field. When the field polarisation is reversed, the solvent molecules will re-orient themselves in order for the dipole to re-align with the new field polarisation. A continually alternating electromagnetic field will

therefore cause continuous re-orientation of the molecules as they try to align the dipole with the ever-changing field. This continuous rotation results in heat generation through frictional losses. The effectiveness of solvents for microwave synthesis is evaluated by considering two factors, (i) the dielectric constant,  $\epsilon'$  which is a measure of the ability of a material to store electromagnetic energy through polarisation and (ii) the dielectric loss factor,  $\epsilon''$  which describes how efficiently the material can convert stored electromagnetic energy into heat. Most commonly these values are combined in order to describe the loss tangent

$$\tan\delta = \frac{\epsilon''}{\epsilon'} \quad (1.3)$$

where higher values of loss tangent correspond to solvents that will give more rapid heat generation when penetrated by microwave radiation.<sup>148</sup>

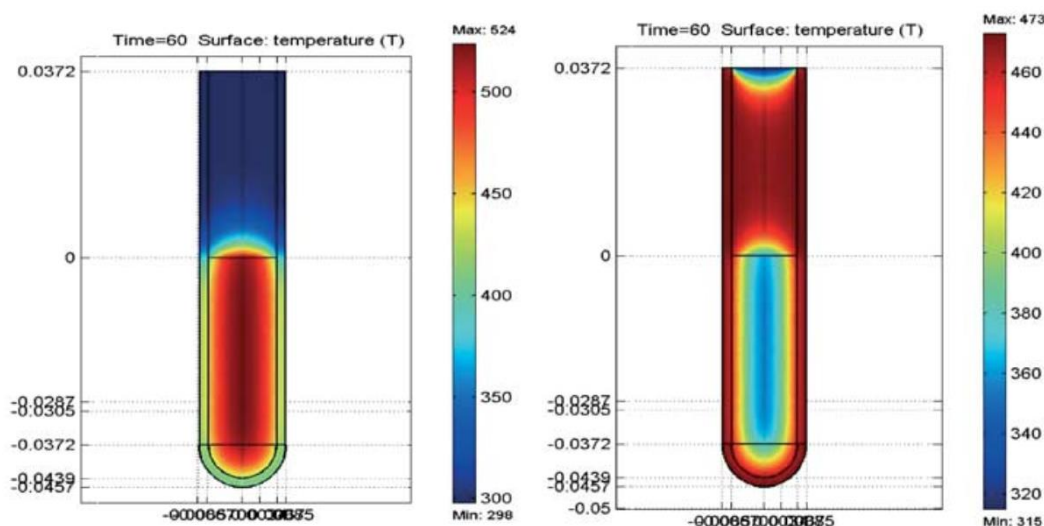


**Figure 1.17** Temperature profiles of a liquid reaction medium after 60 s facilitated by microwave irradiation (left) and conventional heating in an oil bath (right) highlighting the entire volume undergoes uniform and rapid heating, whereas the medium is heated from the outside inwards in the conventional heating. The vertical scale zero corresponds to the meniscus.<sup>151</sup>

Microwave solvothermal synthesis methods have been widely used to make cathode materials for LIBs. The high level of precision in controlling reaction parameters has proved useful in the synthesis of  $\text{LiFePO}_4$ , where the need for nanostructured forms of  $\text{LiFePO}_4$  is essential to realise effective ionic diffusion rates. For example, crystalline  $\text{LiFePO}_4$  has been synthesised using a microwave assisted method in benzyl alcohol and irradiation with microwaves at  $180^\circ\text{C}$  for only 3 minutes. The synthesised product displays small particle morphologies and high discharge capacities of  $160\text{ mAh g}^{-1}$  with little fading

over extended cycling.<sup>152</sup> The ability to access metastable phases and polymorphs has also been demonstrated by Assat and Manthiram, who obtained the high pressure *Cmcm* phase of  $\text{LiMPO}_4$  ( $M = \text{Mn, Fe, Co and Ni}$ ) by a microwave solvothermal method in tetraethylene glycol with reaction temperatures between 275 to 300 °C and reaction times between 10 to 40 minutes depending on the identity of the transition metal cation.<sup>153</sup> The literature on microwave-assisted solvothermal synthesis for battery materials is dominated by reports on phospho-olivines such as  $\text{LiFePO}_4$ , however, the method has also been used to synthesise  $\text{Li}_2\text{MSiO}_4$  ( $M = \text{Fe, Mn}$ ) cathodes at 300 °C for 25 minutes and fluorosulphate cathode material  $\text{LiFeSO}_4\text{F}$  with reaction parameters of 230 °C for 10 minutes, again highlighting a viable low temperature and rapid route to battery material fabrication.<sup>122,154</sup>

#### 1.7.2.2 Solid-state microwave heating

Microwaves can also be applied in the area of inorganic solid-state synthesis, where microwave assisted furnaces often work on a hybrid method, combining both microwave and conventional heating mechanisms. Whereas the main heating mechanism in solution based microwave synthesis is through the rotation of solvent molecules in response to an alternating electromagnetic field, the mechanism in inorganic solids differs due to the static nature of atoms in a solid, disabling any kinds of friction arising from movement. Instead, the pure solid-state microwave heating mechanism is facilitated by a conduction mechanism whereby the alternating electromagnetic field gives rise to a current of mobile charge carriers in the reactants when they absorb the microwave energy. This current is travelling in phase with the field and causes resistive heating in the sample.<sup>150</sup> However, several problems are encountered when heating solid state materials purely by microwaves, firstly, most commercial microwave instruments operating at 2.45 GHz do not allow for efficient coupling of microwaves to many materials at room temperature and this makes initial heating difficult. Secondly, thermal runaway can occur with materials where the specimen drastically overheats and inherent temperature gradients can lead to severe temperature non-uniformities which can result in materials cracking and physical non-uniformity in final samples. Finally, poor microstructural characteristics of the surface are evident in microwave treated samples due to the inside-out direction of heating, with poor microstructural characteristics of the core seen for conventional heating. In order to overcome these issues, hybrid heating techniques have been developed which combine microwave heating with infrared heat sources.<sup>155</sup> Hybrid heating furnaces are lined with a high dielectric loss susceptor material, that is capable of efficient absorption of microwaves and the subsequent conversion to heat energy especially at low temperatures. The heat generated by the susceptor is then transferred

by the conventional techniques of conduction, convection and radiation to the sample. As the sample heats up by conventional means, it becomes more able to couple to the microwave radiation and a balance of both heating mechanisms ensures greater uniformity between the surface and the core. Common susceptors for such applications include silicon carbide, carbon and copper monoxide.

Previous work carried out in our group has included microwave assisted solid state synthesis of many oxide materials for ceramic electrolytes for example Zn-, Ga- and Al-doped LBLTO garnets, Al- and Ga-doped LLZO garnets, In- and Y-doped  $\text{Li}_6\text{Hf}_2\text{O}_7$  materials,  $\text{Li}_{1.5}\text{La}_{1.5}\text{MO}_6$  ( $M = \text{W}^{6+}, \text{Te}^{6+}$ ) Li-rich and  $\text{Na}_{1.5}\text{La}_{1.5}\text{TeO}_6$  Na-rich double perovskites.<sup>156-159</sup>

It is clear that microwave-assisted synthesis methods offer an attractive route to advanced materials synthesis and processing from both an economical and scientific perspective by offering much more rapid and energy efficient processes while also providing the opportunity to access different reaction pathways. This in turn can lead to metastable phases that are difficult to obtain using conventional synthetic routes and reaction products with structural and chemical differences imparting interesting and beneficial properties such as nanoparticulate samples to enhance ionic conductivities.

## 1.8 Aims

The research carried out during this PhD aims to investigate materials that provide high energy density cathodes for lithium ion battery applications. Gaining a thorough understanding of these materials and the structure-property relationships that underpin their functionality is essential in realising their use in future battery applications especially when pertaining to electric vehicle applications.

A focus has been placed on the development of synthetic routes to these materials based upon the use of microwave radiation that can offer softer synthesis conditions with reduced energy consumption. Materials that promise higher voltages *i.e.* fluorinated polyanionic and higher capacities *i.e.* nickel rich layered oxides are both under investigation here. The main focus of this work lies in the high nickel content layered oxide NMC-811 due to the large specific capacities that it can deliver which makes it an excellent candidate for use in electric vehicles. A microwave-assisted sol-gel synthetic route to NMC-811 has mainly been investigated here owing to the dual benefits afforded by both the sol-gel and microwave aspects of this route where the sol-gel process allows for a good level of homogeneity in transition metal distributions to be achieved. As these nickel rich cathodes often show degradation on cycling that act to ultimately limit the battery lifetime, understanding the causes of these processes and the effect they have

on the electrochemical cycling behaviour are of great importance. Implementing coating and doping methods in order to suppress such degradation processes with work carried out here aiming to implement such features to NMC-811 and analysing the effect that these modifications have on the properties of the NMC-811.

Using a wide range of different structural, morphological and electrochemical analysis techniques helps to build-up a more detailed picture of the complex nature of these materials and helps to elucidate the structure-property relationships present. Laboratory based techniques such as PXRD, SEM, EDX and electrochemical testing used in conjunction with central facility based methods such as XANES, EXAFS, NPD and PDF analysis to elucidate bulk and local structural arrangements and  $\mu^+$ -SR to investigate transport properties help to achieve this by providing information that spans a range of length-scales. Understanding such properties of these higher energy density materials will guide future synthetic roadmaps to new and improved materials for energy applications.

## 2 Materials and experimental methods

### 2.1 Materials

The following chemicals were purchased and used as supplied without any further purification:  $\text{FeSO}_4 \cdot 7\text{H}_2\text{O}$  (Sigma Aldrich), LiF (Sigma Aldrich), tetraethylene glycol (TEG) (Alfa Aesar), tetrahydrofuran (THF) (Fisher), acetone (VWR), ethanol (VWR),  $\text{NaCH}_3\text{COO}$  (Sigma Aldrich), NaF (Sigma Aldrich),  $\text{NH}_4\text{H}_2\text{PO}_4$  (Sigma Aldrich),  $\text{FeC}_2\text{O}_4 \cdot 2\text{H}_2\text{O}$  (Alfa Aesar),  $\text{Co}(\text{CH}_3\text{CO}_2)_2 \cdot 4\text{H}_2\text{O}$  (Alfa Aesar),  $\text{Ni}(\text{CH}_3\text{CO}_2)_2 \cdot 4\text{H}_2\text{O}$  (Alfa Aesar),  $\text{Mn}(\text{CH}_3\text{CO}_2)_2 \cdot 4\text{H}_2\text{O}$  (Alfa Aesar),  $\text{Li}(\text{CH}_3\text{CO}_2)$  (Sigma Aldrich), citric acid (Sigma Aldrich),  $\text{Al}(\text{NO}_3)_3 \cdot 9\text{H}_2\text{O}$  (Alfa Aesar),  $\text{Mg}(\text{CH}_3\text{CO}_2)_2 \cdot 4\text{H}_2\text{O}$  (Alfa Aesar),  $\text{NiSO}_4 \cdot 6\text{H}_2\text{O}$  (Sigma Aldrich),  $\text{MnSO}_4 \cdot \text{H}_2\text{O}$  (Sigma Aldrich),  $\text{CoSO}_4 \cdot 7\text{H}_2\text{O}$  (sigma Aldrich), NaOH (Alfa Aesar) and  $\text{LiOH} \cdot \text{H}_2\text{O}$  (Sigma Aldrich).

For battery fabrication the following were used: 1 M lithium hexafluorophosphate ( $\text{LiPF}_6$ ) in ethylene carbonate (EC) and dimethyl carbonate (DMC) 1:1 v/v (Solvionic), 1 M  $\text{LiPF}_6$  in EC and ethylmethyl carbonate (EMC) 3:7 w/w + 1 % VC (SoulBrain), Whatman glass microfibre filter as separators, carbon black KETJEN BLACK EC-600JD (AkzoNobel), polytetrafluoroethylene (PTFE) (Fisher), Li metal ribbon (Sigma Aldrich), polyvinylidene fluoride (PVDF) (Sigma Aldrich) and N-Methyl-2-pyrrolidone (NMP) (Sigma Aldrich).

### 2.2 Synthetic methodologies

#### 2.2.1 Dehydration of $\text{FeSO}_4 \cdot 7\text{H}_2\text{O}$ to $\text{FeSO}_4 \cdot \text{H}_2\text{O}$

Commercial blue coloured  $\text{FeSO}_4 \cdot 7\text{H}_2\text{O}$  (stored in an Ar filled glovebox with  $\text{H}_2\text{O}$  and  $\text{O}_2$  levels < 0.5 ppm) powder was transferred to a tube furnace equipped with flowing Ar gas and heated up to 100 °C with a heating rate of 5 °C per minute, with a dwell time at 100 °C of 3 hours. The obtained white, chalky textured  $\text{FeSO}_4 \cdot \text{H}_2\text{O}$  powder was thoroughly ground and was stored in an Ar filled glovebox for future use.

#### 2.2.2 Microwave assisted synthesis of tavorite $\text{LiFeSO}_4\text{F}$

$\text{FeSO}_4 \cdot 7\text{H}_2\text{O}$  (0.187 g 1.0 mmol) and LiF (0.0285 g 1.1 mmol) were weighed out and added to a 10 mL cylindrical stainless steel ball mill jar with a 12 mm diameter stainless steel ball. The jar was sealed under Ar in a glovebox and transferred to a Retsch MM200 Mixer Mill where the powders were milled for 1 hour at 20 Hz. Then, 0.0099 g (0.5 mmol) of the milled powder was then added to a 10 mL quartz vessel containing 5 mL of TEG and sealed under Ar. The reaction mixture was magnetically stirred for 10 minutes at room temperature before being transferred to a CEM Discover SP microwave synthesiser (operating at 2.45 GHz) for 1 hour at 230 °C with an additional pre-stirring step of two

minutes used to ensure complete mixing. After the synthesis, the obtained white powder was centrifugally washed with THF ( $3 \times 10$  mL for 10 minutes) and acetone ( $1 \times 10$  mL) and dried at  $\approx 80$  °C on a hot plate and ground before being stored in an Ar filled glovebox. Exposure to air was minimised to  $< 1$  hour in order to avoid oxidation of the  $\text{Fe}^{2+}$  within the sample. Oxidation could be evidenced by the off-white powder developing an orange hue. To obtain  $\approx 1$  g of powder suitable for muon measurements, the synthesis was repeated under identical conditions  $\approx 10$  times and the powders were combined.

### 2.2.3 Conversion of tavorite $\text{LiFeSO}_4\text{F}$ to triplite $\text{LiFeSO}_4\text{F}$

To facilitate the conversion of tavorite to triplite  $\text{LiFeSO}_4\text{F}$ , 0.15 g of the microwave synthesised tavorite powder described in the previous section was pressed into a 10 mm pellet under 2 tonnes of uniaxial pressure. The pellet was then transferred to a tube furnace equipped with flowing Ar gas and subject to a heat treatment at 350 °C for 4.5 hours with a heating rate of 5 °C per minute used. The obtained powder was dark brown/black in colour and was stored in a glovebox.

### 2.2.4 Solid state synthesis of $\text{Na}_2\text{FePO}_4\text{F}$

$\text{NaCH}_3\text{COO}$  (0.205 g, 2.5 mmol),  $\text{NaF}$  (0.105 g, 2.5 mmol),  $\text{NH}_2\text{H}_2\text{PO}_4$  (0.2875 g, 2.5 mmol) and  $\text{FeC}_2\text{O}_4 \cdot 2\text{H}_2\text{O}$  (0.3598 g, 2.0 mmol) were ball milled under Ar for 2 hours at 20 Hz in a Retsch MM200 Mixer Mill in a 1:1:1:0.8 molar ratio. The milled mixture was then transferred to a tube furnace equipped with Ar/ $\text{H}_2$  (5%) gas flowing and heated to 350 °C at a heating rate of 5 °C per minute with a dwell time of 5 hours in order to decompose the precursors. Once cool, the obtained powder was thoroughly ground using an agate mortar and pestle and transferred to the tube furnace for further heating at 600 °C for 5 hours under Ar/ $\text{H}_2$  (5%) flow. A brown powder was obtained.

### 2.2.5 Sol-gel synthesis of layered oxides $\text{LiNi}_x\text{Mn}_y\text{Co}_{1-x-y}\text{O}_2$

#### Synthesis of the $\text{LiNi}_x\text{Mn}_y\text{Co}_{1-x-y}\text{O}_2$ sol-gel precursor

Stoichiometric amounts of  $\text{Ni}(\text{CH}_3\text{CO}_2)_2 \cdot 4\text{H}_2\text{O}$ ,  $\text{Mn}(\text{CH}_3\text{CO}_2)_2 \cdot 4\text{H}_2\text{O}$ ,  $\text{Co}(\text{CH}_3\text{CO}_2)_2 \cdot 4\text{H}_2\text{O}$  and  $\text{Li}(\text{CH}_3\text{CO}_2)$  (5 to 10 % excess of Li) powders were weighed out and added to a 600 mL beaker rinsed with deionised  $\text{H}_2\text{O}$ . Specific quantities are listed in Table 2.1. Approximately 100 mL of deionised  $\text{H}_2\text{O}$  was further added and the solution was stirred magnetically until all of the powders had fully dissolved (adding more  $\text{H}_2\text{O}$  if necessary to facilitate solvation). To this, a solution of fully dissolved citric acid of approximately 50 mL was added and the resultant sol was stirred magnetically on a stirrer-hot plate at 150 °C in order to evaporate the solvent. This process took  $\approx 4$  hours with a viscous gel obtained at the end. The gel was then pre-dried at  $\approx 300$  °C in a heating

mantle in a fumehood to obtain a black coloured ash. The ash was transferred to an alumina crucible and heated in a Carbolite box-furnace at 450 °C for 14 hours to remove carbon species originating from the acetate groups and the citric acid. The obtained precursor was ground with a mortar and pestle and stored for later use.

**Table 2.1** Quantities of precursors used for the sol-gel microwave-assisted synthesis of  $\text{LiNi}_x\text{Mn}_y\text{Co}_{1-x-y}\text{O}_2$  materials.

Composition	$\text{Ni}(\text{Ac})_2 \cdot 4\text{H}_2\text{O}$	$\text{Mn}(\text{Ac})_2 \cdot 4\text{H}_2\text{O}$	$\text{Co}(\text{Ac})_2 \cdot 4\text{H}_2\text{O}$	$\text{Li}(\text{Ac})$	Citric acid
NMC-111	1.1210 g (4.5 mmol)	1.1198 g (4.5 mmol)	1.1030 g (4.5 mmol)	0.9355 g (14.175 mmol)	5.187 g (27 mmol)
NMC-622	2.2394 g (9 mmol)	0.7352 g (3 mmol)	0.7468 g (3 mmol)	1.1880 g (18 mmol)	5.76 g (30 mmol)
NMC-811	2.9861 g (12 mmol)	0.3676 g (1.5 mmol)	0.3734 g (1.5 mmol)	1.1880 g (18 mmol)	5.76 g (30 mmol)

### Heat treatment of the sol-gel precursor to form crystalline $\text{LiNi}_x\text{Mn}_y\text{Co}_{1-x-y}\text{O}_2$

Portions of the previously obtained precursor were transferred to an alumina crucible and heated in either a Carbolite conventional box furnace or a CEM Phoenix microwave furnace (2.45 GHz) and heated at temperatures between 650 °C to 900 °C for times between 1 to 12 hours which will be specified in the text. High nickel content samples were stored in an Ar filled glovebox after synthesis.

#### 2.2.6 Dispersion based $\text{Al}_2\text{O}_3$ coating of $\text{LiNi}_{0.8}\text{Mn}_{0.1}\text{Co}_{0.1}\text{O}_2$

First, a stock solution of  $\text{Al}(\text{NO}_3)_3 \cdot 9\text{H}_2\text{O}$  in ethanol with a concentration of  $1 \text{ mg ml}^{-1}$  was made up. From this stock solution an appropriate volume was then pipetted to a portion of microwave-synthesised NMC-811 of 100 mg in a vial to correspond to 0.2, 0.5 and 1.0 wt.% of  $\text{Al}_2\text{O}_3$  with respect to the initial NMC-811 mass. Quantities are listed in Table 2.2. Ethanol was then added to the vial to make up more volume to allow for adequate stirring. The solution/dispersion was then magnetically stirred for 10 minutes before undergoing sonication for 45 minutes at room temperature in an ultrasonic bath. The dispersion was then heated gently under magnetic stirring at  $\approx 60 \text{ }^\circ\text{C}$  to evaporate off the ethanol. Dried powder was then transferred to an alumina crucible and heated at 400 °C for 3 hours under air in a Carbolite box furnace. The obtained powder was then stored in an Ar filled glovebox.

**Table 2.2** Quantities of reactants used in the alumina coating of NMC-811.

Coating weight	Mass of NMC-811 (mg)	Mass of Al <sub>2</sub> O <sub>3</sub> (mg)	Mass of Al(NO <sub>3</sub> ) <sub>3</sub> ·9H <sub>2</sub> O (mg)	Volume of stock solution (ml)
0.2 wt.%	100	0.2	1.48	1.48
0.5 wt.%	100	0.5	3.68	3.68
1.0 wt.%	100	1.0	7.36	7.36

### 2.2.7 Microwave assisted co-precipitation synthesis of LiNi<sub>0.8</sub>Mn<sub>0.1</sub>Co<sub>0.1</sub>O<sub>2</sub>

Approximately 30 ml metal sulphate solutions of the correct concentration were made up (quantities of metal sulphate and deionised H<sub>2</sub>O are listed in Table 2.3) and were added dropwise to 65 ml of deionised H<sub>2</sub>O in 3 different 600 ml beakers under magnetic stirring. 10 ml of the nickel sulphate solution was added followed by 10 ml of the manganese solution and 10 ml of the cobalt solution. Each of these were added to the three beakers thus using 30 ml of the metal sulphate solutions overall. Then, 5 ml of a 6 M NaOH solution was added dropwise to each beaker and stirred for 10 minutes to facilitate the precipitation of a metal hydroxide precursor. The reaction was then left for 1 hour in order to allow the precipitate to settle and was then washed 6 times with deionised H<sub>2</sub>O. The precipitate was then dried and heated at 450 °C for 14 hours. This was then mixed with LiOH (3 % excess Li) using a mortar and pestle and the final mixture was heated at 850 °C for 1 hour in a CEM Phoenix microwave furnace (2.45 GHz) to form NMC-811. The synthesised NMC-811 was stored in an Ar filled glovebox until further use.

**Table 2.3** Quantities of metal sulphate reactants and deionised H<sub>2</sub>O used to make up solutions of the appropriate concentration for the co-precipitation synthesis of NMC-811.

Metal sulphate	Mass (g)	Volume H <sub>2</sub> O (ml)
NiSO <sub>4</sub> ·6H <sub>2</sub> O	6.5112	30.96
MnSO <sub>4</sub> ·H <sub>2</sub> O	0.5257	31.08
CoSO <sub>4</sub> ·7H <sub>2</sub> O	0.8557	30.44

### 2.2.8 Sol-gel microwave-assisted synthesis of Al<sup>3+</sup> and Mg<sup>2+</sup> doped LiNi<sub>0.8</sub>Mn<sub>0.1</sub>Co<sub>0.1</sub>O<sub>2</sub>

The synthesis of Al<sup>3+</sup> and Mg<sup>2+</sup> doped NMC-811 was carried out using the same procedure as that described in Section 2.2.5 for the sol-gel synthesis of pristine NMC-811 but with some precursor quantities altered in order to synthesise the targeted composition. Al(NO<sub>3</sub>)<sub>3</sub>·9H<sub>2</sub>O and Mg(CH<sub>3</sub>COO)<sub>2</sub>·4H<sub>2</sub>O were used as the Al<sup>3+</sup> and Mg<sup>2+</sup> sources

respectively with 0.3676 g (1.5 mmol)  $\text{Mn}(\text{CH}_3\text{COO})_2 \cdot 4\text{H}_2\text{O}$ , 0.3734 g (1.5 mmol)  $\text{Co}(\text{CH}_3\text{COO})_2 \cdot 4\text{H}_2\text{O}$  and 5.76 g and (30 mmol) citric acid. The quantities used of the other reactants are listed in Table 2.4. Reactions carried out in the microwave furnace to yield the doped NMC-811 compounds were carried out at 850 °C for 3 hours.

**Table 2.4** Quantities of  $\text{Ni}(\text{Ac})_2 \cdot 4\text{H}_2\text{O}$ ,  $\text{Al}(\text{NO}_3)_3 \cdot 9\text{H}_2\text{O}$   $\text{Mg}(\text{Ac})_2 \cdot 4\text{H}_2\text{O}$   $\text{Li}(\text{Ac})$  precursors used for the sol-gel microwave-assisted synthesis of  $\text{Al}^{3+}$  and  $\text{Mg}^{2+}$  doped NMC-811 materials.

Composition	$\text{Ni}(\text{Ac})_2 \cdot 4\text{H}_2\text{O}$	$\text{Al}(\text{NO}_3)_3 \cdot 9\text{H}_2\text{O}$	$\text{Mg}(\text{Ac})_2 \cdot 4\text{H}_2\text{O}$	$\text{Li}(\text{Ac})$
1 % Al	2.9488 g (11.85 mmol)	0.0563 g (0.15 mmol)	0	1.1880 g (18 mmol)
2 % Al	2.9111 g (11.7 mmol)	0.1126 g (0.3 mmol)	0	1.1880 g (18 mmol)
1 % Mg	2.9861 g (12 mmol)	0	0.0322 g (0.15 mmol)	1.1642 g (17.64 mmol)

## 2.3 Characterisation Techniques

### 2.3.1 Powder x-ray diffraction (PXRD)

The form of electromagnetic radiation known as X-rays were discovered by Wilhelm Roentgen in 1895 and, as part of the electromagnetic spectrum, exhibit wave particle duality evidenced by single slit diffraction (wave-like nature) and scattering of X-rays from electrons (the Compton Effect, particle-like nature). With typical wavelengths of the same order of magnitude as atomic dimensions (1 to 100 Å), X-rays are perfectly primed for studying a vast range of crystalline materials.<sup>160</sup> Powder X-ray diffraction (PXRD) is a powerful and widely used technique for elucidating structural properties of materials. It is one of the most useful techniques for general structural analysis due to fast data collection times, the fact that it is non-destructive to samples and the general ease of access to the equipment. In PXRD the sample takes the form of a finely ground, homogenised powder (as opposed to single crystal X-ray diffraction with utilises single crystals of a specific compound) and the bulk composition is studied. This is especially useful in compositional analysis of multiphase powders. The technique relies upon the scattering of incident X-rays from different atoms in the lattice. Ideally these X-rays are monochromatic but in reality they consist of several, similar wavelengths *i.e.*  $K_{\alpha 1}$ ,  $K_{\alpha 2}$  and sometimes  $K_{\beta}$  wavelengths are used during these experiments. Generation of X-rays generally occurs by heating up a filament in order to produce electrons which are accelerated in a vacuum chamber under potentials of 10 to 60 kV towards a metal target (often Cu, Mo or Cr) from which X-rays are generated when the electrons hit the target.

A spectrum of generated X-rays using this method shows two distinct regions. Firstly, a continuous region where white (polychromatic) X-rays are produced by deceleration of electrons. This is often called *bremstrahlung* (German for *braking radiation*) and the spectrum is smooth. On the other hand, the characteristic region is also observed and consists of discrete peaks. These peaks arise from the ejection of a core shell (1s) electron from an atom, with an electron from a higher energy level dropping down to take its place accompanied the release of X-rays equal in energy to the difference between these two energy levels. For example, the characteristic spectrum of copper consists of two distinct wavelengths of emitted X-rays, called  $K_{\alpha}$  and  $K_{\beta}$ , where  $K_{\alpha}$  radiation with a wavelength of 1.5406 Å, is most often selected using a monochromator for PXRD experiments.

Because X-rays are a type of electromagnetic radiation, they interact with the electron density (*i.e.* the electron cloud) associated with each atom, being first absorbed by the electron density which causes a movement in the electron cloud and resulting in re-radiation of X-rays of identical frequency - as if the incident radiation were being reflected. No energy loss between incident and outgoing radiation is observed and hence can be described as elastic scattering. The crystal lattice where diffraction occurs can be thought of as a three-dimensional, ordered array of atoms that repeats infinitely in space. Atoms can form planes and it is from these planes that diffraction occurs. Described by Bragg's law, elastic scattering results in a change of direction of incident radiation with constructive interference fulfilling the Bragg condition:

$$n\lambda = 2d\sin\theta \quad (2.1)$$

where  $n$  is the order of the diffracted beam (a positive integer),  $\lambda$  is the wavelength of the incident beam,  $d$  is the lattice spacing between neighbouring planes and  $\theta$  is the angle at which X-rays are incident on the sample.<sup>161</sup> This is shown graphically in Figure 2.1. The positions of atoms within the lattice and the number of electrons that each atom has bears large influence over the scattering intensities and positions respectively, with lighter atoms (generally consisting of smaller amounts of electrons) such as H and Li being essentially invisible to X-rays and heavy atoms (which generally have larger numbers of electrons) dominating diffraction patterns.

Many lab-based diffractometers utilise Bragg-Brentano geometry regarding the set-up of X-ray source, sample and detector. In this geometry, the X-ray source is fixed in position while the sample (mounted on a flat-plate holder) and the detector are allowed to rotate through  $\theta$  and  $2\theta$  respectively, allowing the angle between incident radiation and the

sample to be scanned through a range of values. The detector, therefore detects X-rays at specific angles of  $\theta$  ( $2\theta$  is instead used when reporting data), giving large counts at angles where constructive interference occurs. Diffractograms for PXRD data are often displayed as detected intensity vs. the  $2\theta$  angle and collected data can be compared against reference diffractograms (obtained from online databases such as the Inorganic Crystal Structure Database (ICSD)) to elucidate structural composition. Therefore, PXRD can be considered as a ‘fingerprinting’ technique for crystalline materials. This fingerprinting aspect is used to carry out phase analysis of synthesised materials, where the presence of any possible impurity phases in the prepared sample can be identified by additional peaks in the collected data compared to the reference patterns. Impurity phases can be confirmed by comparing these additional peaks to a variety of reference patterns for logical impurities in the sample (*i.e.* unreacted reagents, possible side products and decomposition products *etc.*). By careful analysis of PXRD data using refinement processes, properties such as lattice parameters, cell volume, atomic positions and site occupancies can be deduced.

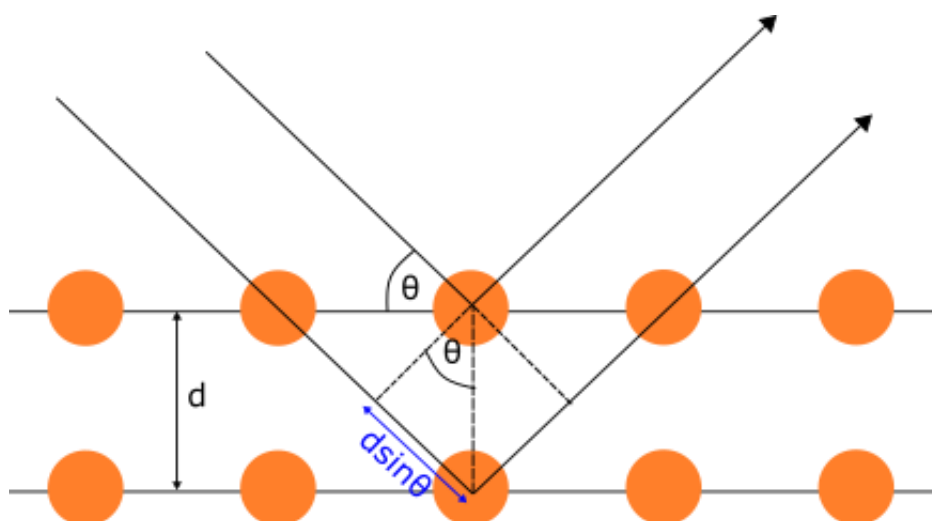


**Figure 2.1** Illustration of the geometry used for the derivation of the  $n\lambda = 2d\sin\theta$  form of Bragg's law. Adapted from Dinnebier and Billinge.<sup>161</sup>

PXRD characterisation presented in this thesis were carried out on two different diffractometers. The first was a PANalytical X'Pert powder diffractometer using  $\text{CuK}\alpha$  radiation operated at 40 kV and 40 mA. Data were collected in a  $2\theta$  range 10 to  $70^\circ$  in step sizes of  $0.02^\circ$ . The second diffractometer was a Rigaku MiniFlex benchtop powder diffractometer using  $\text{CuK}\alpha$  radiation operated at 40 kV and 15 mA. Data were collected between 10 to  $70^\circ$  with a step size of  $0.02^\circ$ . Phase analysis was carried out by comparing collected data to reference patterns collected from the ICSD, with the comparison being carried out in a general data plotting program.

### 2.3.2 Neutron Powder Diffraction (NPD)

As previously mentioned, one limitation to the PXRD technique is the sensitivity to atoms with low electron density resulting in light atoms such as Li being essentially invisible to X-rays. For materials containing Li, therefore, a complementary method is valuable for determining important parameters such as Li content and site occupancies. Neutron powder diffraction bears much the same properties as PXRD but with neutrons being used as the probe instead of X-rays. Commonly thought of as a particle (indeed one of the fundamental particles contained within atoms and responsible for all matter) neutrons display wave-like properties also and can be described by a wavelength. By carefully tuning the speed of neutrons, wavelengths with the same order of magnitude as the typical separation between atoms in a solid material ( $\approx 1 \text{ \AA}$ ), can be selected. The method of interaction between neutrons and atoms lies in the atomic nuclei rather than the electron densities and the scattering interaction is quantified by the scattering length  $b$ . The quantification of the scattering length is not well understood but depends on the makeup of the nucleus and the orientation of its spin relative to that of the neutron.<sup>162</sup> As a result of this, the coherent scattering lengths bear no discernible trend such as is seen between scattering factors and atomic number with X-ray scattering. This is hugely beneficial when studying materials containing light atoms such as lithium. Furthermore, as there is no relation between atomic number and scattering cross section with neutrons, atoms which sit next to each other in the periodic table (*e.g.* Mn, Fe, Ni and Co) often have different scattering cross sections allowing them to be distinguished from each other and isotopes can easily be distinguished also.<sup>163</sup> For example, the coherent scattering lengths of lithium isotopes are 2.00 fm (*fermi*,  $1 \text{ fm} = 10^{-13} \text{ cm}$ ) for  $^6\text{Li}$  (with 7.5 % abundance) and -2.22 fm for  $^7\text{Li}$  (92.5 % abundance) thus yielding a total scattering length of -1.9 fm for natural lithium.<sup>164</sup> Furthermore the coherent scattering lengths of Ni, Mn and Co are 10.30 fm, -3.73 fm and 2.49 fm respectively allowing for each of these to be easily distinguished.

The production of neutrons suitable for diffraction requires large scale facilities such as the Institut Laue Langevin (ILL) in Grenoble or ISIS Pulsed Neutron and Muon Source at the Rutherford Appleton Laboratory in Oxfordshire. Both of these facilities generate neutrons in different ways. The ILL is a reactor source where neutrons are produced as a result of nuclear fission and a continuous, monochromatic neutron beam is fired at the sample, working in much the same way as PXRD. Spallation sources, such as ISIS produce pulses of neutrons by colliding proton pulses into a tantalum target, and operate on a time of flight (TOF) method, where the neutron's wavelength can be determined from its velocity as per the De Broglie relationship. Neutrons with longer wavelengths have a lower

velocity and will take more time to traverse the distance from source to detector as opposed to shorter wavelength, faster neutrons. The De Broglie relationship is combined with the Bragg equation to determine neutron wavelength as:

$$\lambda = h/m_n v = ht/m_n L = 2d \sin \theta \quad (2.2)$$

where  $\lambda$  is the neutron wavelength,  $h$  is Planck's constant ( $h = 6.626 \times 10^{-34} \text{ m}^2 \text{ kg s}^{-1}$ ),  $m_n$  is the mass of the neutron ( $m_n = 1.675 \times 10^{-27} \text{ kg}$ ),  $t$  is the time taken to travel between source and detector and  $L$  is the distance between the source and the detector. In TOF measurements, a polychromatic neutron beam is employed, giving a direct determination of neutron wavelength and allowing for the use of fixed detectors arrays. The stationary detectors are commonly grouped into different banks that are distributed around the solid angle of the sample as shown in Figure 2.2 for the Polaris instrument at ISIS.<sup>165</sup>

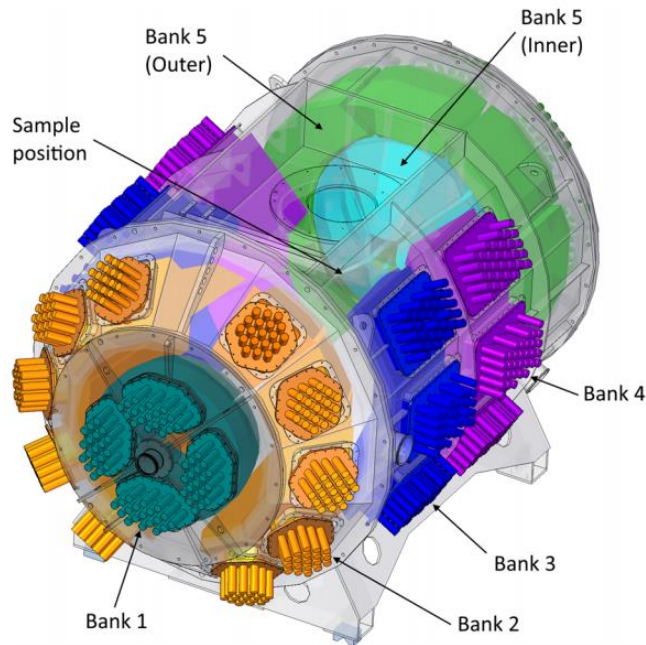


**Figure 2.2** The Polaris diffractometer at ISIS. Detectors are grouped into different banks, differentiated here by colour. The neutron beam enters in the top right hand corner and exits in the middle section of Bank 1.<sup>165</sup>

The NPD data presented in this thesis were collected on the Polaris instrument at the ISIS Pulsed Neutron and Muon Source, at the Rutherford Appleton Laboratory in the UK. Polaris is high intensity, medium resolution powder diffractometer optimised for the rapid characterisation of structures. Resolutions ( $\Delta d/d$ ) on Polaris range from 0.3 % to 2.7 % from Bank 5 (back scattering detector bank) to Bank 1 (very low angle detector bank) respectively.<sup>165</sup> Approximately 3 g of sample were loaded into 6 mm diameter vanadium cans which were loaded into an auto-changer (for room temperature

measurements) or a cryostat for low temperature measurements at 60 K. Vanadium cans are chosen due to the very small scattering length of vanadium. Measurements were performed at room temperature and at 60 K for each sample with a run time of approximately 8 hours per sample per temperature.

### 2.3.3 Rietveld Method

In the case of PXRD and NPD data, Rietveld refinements are carried out to obtain structural parameters such as cell dimensions, atomic positions and site occupancies. Such refinements basically compare the collected data with data simulated for a model structure. The Rietveld approach to refinement utilises a least squares approach in order to iteratively refine a theoretical structural model until a fit is achieved that best matches the observed data. The best fit is determined by a minimisation in the difference function between the observed data and the calculated fit. The Rietveld algorithm determines the difference function as the sum of the weighted squared differences between the observed and calculated intensities:

$$M = \sum_i W_i \left[ y_i(obs) - \frac{1}{c} y_i(calc) \right]^2 \quad (2.3)$$

where  $M$  is the difference function, the index  $i$  refers to the  $i^{\text{th}}$  atom,  $W_i$  is a statistical weight determined from an uncertainty estimate for the observed data,  $y(obs)$  and  $y(calc)$  are the observed and theoretical profiles respectively and  $c$  is the overall scale factor between the two profiles such that:

$$y(calc) = c \cdot y(obs) \quad (2.4)$$

Refinements are performed on several structural and instrumental parameters, with each one being refined iteratively until a minimisation is reached.<sup>166</sup> Once fully refined, the structural model should be considered as a good representation of the real structure and parameter values obtained during the refinement, such as cell parameters, cell volume, atomic positions and site occupancies for the structure are obtained. To determine the goodness of the refinement and the level of agreement between the observed and calculated profiles, statistical values are employed. There are three important statistical values calculated - the weighted profile R-factor ( $R_{wp}$ ), the expected R-factor ( $R_{exp}$ ) and the goodness of fit value ( $\chi^2$ ). The weighted R-factor is calculated as:

$$R_{wp}^2 = \frac{M^2}{\sum_i W_i (y_i(obs))^2} \quad (2.5)$$

Where it can be seen that  $R_{wp}$  is the square root of the minimised function scaled by the weighted intensities. The  $R_{exp}$  factor is calculated as:

$$R_{exp}^2 = \frac{(N - P)}{\sum_i W_i (y_i(obs))^2} \quad (2.6)$$

Where  $N$  is the number of data points and  $P$  is the number of parameters. Generally,  $N$  is a lot larger than  $P$  and tends to dominate the numerator. This factor indicates the theoretical minimum R-factor that can be obtained taking account of the number of data points. Logically therefore, for good profile matching  $R_{wp}$  should be close in value to  $R_{exp}$ . This can be determined by the ratio of both of these numbers to yield a general goodness of fit value,  $\chi^2$  (“chi squared”) which is calculated as:

$$\chi^2 = \left[ \frac{R_{wp}}{R_{exp}} \right]^2 \quad (2.7)$$

For good profile matching, and hence a good refinement, the R-factors (often reported as percentages) should be as small as possible and  $\chi^2$  should be as close to unity as possible.<sup>167</sup>

In this thesis, Rietveld refinements conducted on data obtained by PXRD and NPD were carried out using the GSAS-II program. For PXRD refinements the refinement was carried out in the general following order: (i) background polynomial, (ii) scale factor, (iii) cell parameters, (iv) zero point and sample displacement, (v) profile parameters, (vi) atomic positions where appropriate and (vii) site occupancies where appropriate. For refinements of NMC layered oxides, the atomic positions were not refined, with the 3a sites positioned at (0,0,0) and the 3b sites positioned at (0,0,0.5) and 6c (oxygen) sites at (0,0,0.24).  $U_{iso}$  were also not refined and were kept at the same value as reported in the downloaded CIF file. Site occupancies were refined as reported in the results chapters.

Structural analysis was carried out on the NPD data for each sample by Rietveld refinements using the GSAS-II program.<sup>168</sup> Data collected from detector bank 5 on the Polaris diffractometer were used in order to fit a model of  $R\bar{3}m$  NMC-811. Structural and profile parameters were refined in the following order: (i) scale factor, (ii) a 6-coefficient Chebyshev background function, (iii) cell parameters, (iv) absorption, (v) profile parameters (vi) atomic positions where necessary and (vii) fractional occupancies of atoms where appropriate constraints were applied. Constraints applied to the fractional occupancies were added to keep the total lithium content equal to 1, the total nickel content equal to 0.8 and the total of the Co and Mn contents equal to 0.2. An equivalence between Li on the 3b site and Ni on the 3a site was also introduced.

### 2.3.4 Neutron Pair Distribution Function analysis (PDF)

Whereas conventional diffraction methods with Bragg analysis act to probe the bulk structure of crystalline materials, total scattering methods can be used to elucidate information pertaining to the local structure which is of great interest in nanomaterials and more complex materials which exhibit varying degrees of disorder at this local level. This is useful in examples such as materials with long range order but possessing aperiodic modifications to the average structure, materials with limited long range order *e.g.* nanocrystals, gels and turbostratic materials and even materials with no long range order for example glasses, other amorphous solids and liquids. Total scattering techniques utilise both Bragg and diffuse scattering which yield information on the average and periodic structure and local deviations from perfectly regular units respectively with the diffuse scattering contribution dominating at higher scattering angles. Total scattering experiments can be performed using neutrons or X-rays and require short wavelength, high energy particles, often requiring the use of national synchrotron facilities and neutron sources (although laboratory based X-ray diffractometers allowing for the collection of total scattering data are becoming more common). Pair distribution function (PDF) analysis can be used with the total scattering data collected for a specific material and is a powerful tool for the study of non-periodic materials or crystalline materials that display some level of aperiodicity at a local level.<sup>169</sup> The PDF analysis involves the Fourier transform of the total scattering data, generating the probability of finding any two atoms at a given interatomic distance. This can be easier visualised as a histogram of interatomic spacings weighted by both the quantity and scattering length of different atoms within a specific sample. This can be described mathematically by equation 2.8:

$$G(r) = 4\pi[\rho(r) - \rho_0] \quad (2.8)$$

where  $G(r)$  is the atomic PDF,  $\rho_0$  is the average atomic number density  $\rho(r)$  is the atomic pair density where the variable  $r$  is some radial distance. Thus, this function yields information on the number of atoms at a distance  $r$  from a reference atom with the PDF producing a peak at radial distances corresponding to characteristic distances between atomic pairs. To calculate the function  $G(r)$ , the Fourier transform of the total scattering function  $S(Q)$  is taken as shown in equation 2.9

$$G(r) = \frac{2}{\pi} \int_0^{\infty} Q[S(Q) - 1] \sin(Qr) dQ \quad (2.9)$$

where  $Q$  is the magnitude of the momentum transfer vector  $\mathbf{Q} = \mathbf{k}_i - \mathbf{k}_f$  and  $Q = 4\pi\sin(\theta)/\lambda$ . The structure function  $S(Q)$  is obtained from scattering experiments and contains the

measured intensities from a sample. For good quality PDF data, it is important to measure diffraction data over a wide  $Q$  range to ensure adequate real-space resolution. The data collected from the neutron diffraction experiments outlined in Section 2.3.2 was also used to generate PDFs. The data were collected at 60 K and room temperature using run times of at least 8 hours per sample, which were then processed using the GudrunN program in order to obtain the PDF radial distribution function  $G(r)$ .<sup>170</sup> Data processing involved correcting for background, empty containers, attenuation and multiple scatterings to yield  $S(Q)$  where a high  $Q_{\max}$  value of  $52 \text{ \AA}^{-1}$  used during the Fourier transform. Fitting of an average crystallographic structural model to the experimental data was carried out using a least squares refinement procedure in PDFgui using an  $r$ -range of 1 to 30  $\text{\AA}$ .<sup>171</sup> The scale factor, lattice parameters, quadratic dynamic correlation factors ( $\delta_1$  and  $\delta_2$ ),  $Q_{\text{damp}}$  and  $Q_{\text{broad}}$  were refined.  $Q_{\text{damp}}$  and  $Q_{\text{broad}}$  model the intensity dampening and the PDF peak broadening respectively. Site occupancies and anisotropic lattice displacements were not refined. Similarly to Rietveld refinements, a reliability factor  $R_w$  is calculated from

$$R_w = \left( \frac{\sum w_i (G_i^{\text{exp}} - G_i^{\text{calc}})^2}{\sum w_i (G_i^{\text{exp}})^2} \right)^{1/2} \quad (2.10)$$

where  $w_i$  is a weighting factor and  $G_i^{\text{exp}}$  and  $G_i^{\text{calc}}$  are the experimental and calculated PDFs respectively.

### 2.3.5 X-ray Absorption Spectroscopy (XANES and EXAFS)

X-ray absorption spectroscopy (XAS) is a powerful and versatile tool that can be used to provide information on the local geometric and electronic structure of materials. The technique utilises the absorption of high energy X-ray radiation (0.1 to 100 keV) by core electrons within atoms. When the energy of the incident X-ray radiation is equal to or greater than the binding energy of the core electron, the electron is excited and will be ejected from the core state into higher energy unoccupied orbitals or into the continuum. Different elements have different core electron binding energies and therefore, by tuning the energy of the incident X-ray radiation specific elements can be selected for measurements. During a typical measurement, the X-ray absorption ( $\mu$ ) is analysed as a function of the energy of the incident beam. In transmission mode set-up, this energy dependent absorption,  $\mu(E)$  can be measured with respect to the initial and transmitted X-ray intensities,  $I_0$  and  $I_t$  respectively as

$$\mu(E) = \ln (I_0/I_t) \quad (2.11)$$

During a typical experiment, the X-ray energy is scanned from a lower to higher value while the absorption is measured. When the incident X-ray energy matches the core electron binding energy a sharp rise in absorption is measured and this is referred to as the “edge”. Depending on the energy level of the core electron to be ejected, different edges can be selected, where the edge is denoted by typical X-ray energy level nomenclature. For example, the K edge refers to excitation of the  $1s$  electron level, L edges refer to the  $2s$  and  $2p$  levels and M edges refer to  $3s, p, d$  levels.

Depending on the material properties under investigation, two different energy regions can be explored. The XANES region, located on either side of the absorption edge which can determine oxidation state and local geometry of the absorber atom and the EXAFS region, located at higher energies that sheds insight into the local structure surrounding the absorber atom. Figure 2.3 highlights the XANES and EXAFS regions with respect to the absorption edge.

#### **X-ray absorption near edge structure (XANES)**

XANES, which can also be referred to as Near Edge X-ray Absorption Fine Structure (NEXAFS) concerns the region of the XAS spectrum encompassing the absorption edge and *ca.* 50 to 100 eV either side of the edge. Analysis of the XANES region provides information on electronic structural properties of the absorber atom such as oxidation state and local coordination geometries. Atoms in higher oxidation states will have more tightly bound core electrons and thus higher binding energies, shifting the rising edge and the edge maxima to slightly higher energies.<sup>172</sup> Spectral features occurring before the absorption edge within the XANES region, referred to as pre-edge features, can also offer valuable information. Pre-edge features arise due to quadrupole-allowed dipole-forbidden  $1s \rightarrow 3d$  excitation where  $\Delta l = \pm 2$  and are therefore weak in intensity in comparison to the dipole allowed  $\Delta l = \pm 1$  edge. Deviations from centrosymmetry and the occurrence of  $3d$ - $4p$  orbital mixing on the metal atom act to relax the dipole selection rule and allow pre-edge features to be observed in the spectrum with intensities of the pre-edge features determined by the extent of deviation and orbital mixing. The pattern contained within the pre-edge feature contains information on spin-state, oxidation-state, ligand field splitting and multiplet effects present. Comparison of measured data with data obtained from standards of known oxidation state and coordination geometries allows for the determination of these properties in the material under investigation.

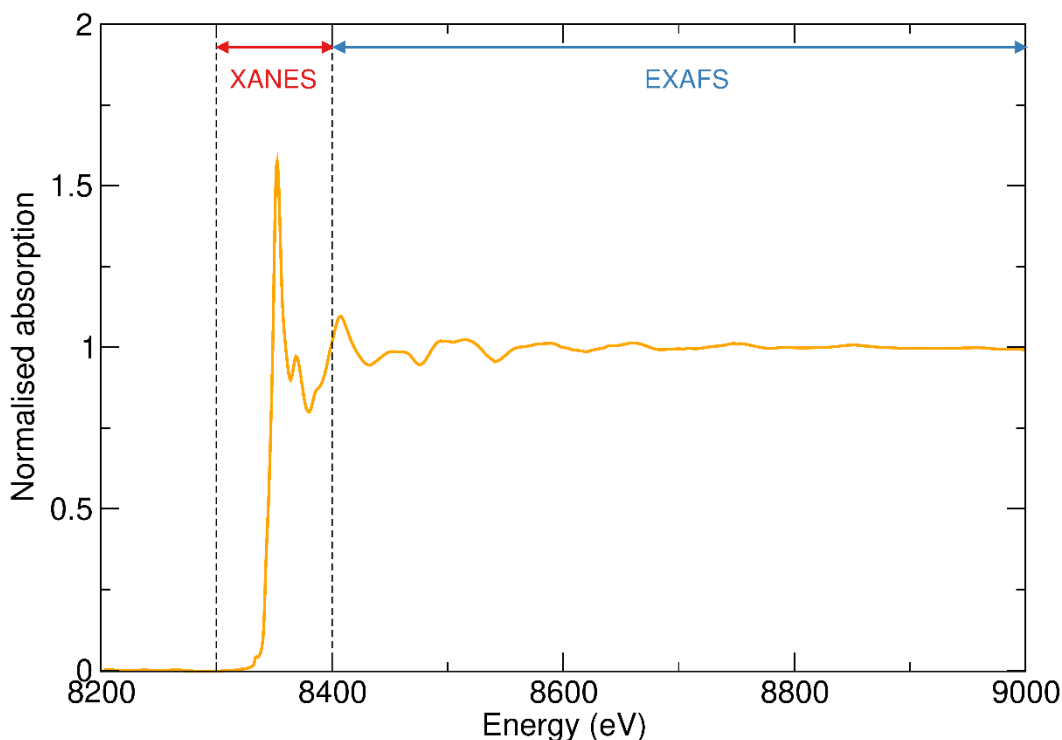


**Figure 2.3** XAS data highlighting the XANES and EXAFS regions with respect to the absorption edge. Data shown here was collected at the Ni K-edge for NMC-811.

### Extended X-ray absorption fine structure (EXAFS)

The EXAFS region in a typical XAS spectrum is located at energies above the XANES region and can be described as an oscillatory modulation in the X-ray absorption coefficient in this high energy region. EXAFS can yield information pertaining to the numbers and types of atoms in the immediate environment of the absorbing atom alongside accurate absorber-neighbour distances. At energies larger than the binding energy, the core shell electron is ejected into the continuum and can interact with electrons in neighbouring, non-excited atoms. Wave-particle duality allows one to consider this photoelectron to possess wave-like properties, and if the neighbouring atoms are considered to be point scatterers, the backscattered electron waves can interfere with forward-propagating waves once the photoelectron wave returns to the absorber atom, modifying the final-state wavefunction at the absorber. This modified transmitted wave shows up as a modulation in the absorption coefficient.

The XAS data reported in this thesis were collected on the I20-scanning beamline at the Diamond Light Source synchrotron in the UK. Samples were prepared by casting cathode slurries into carbon-coated aluminium foil and punching electrode disks. AMPIX cells were then assembled in an Ar filled glovebox using a glass microfibre separator, lithium foil as a counter electrode and 1 M LiPF<sub>6</sub> in EC:EMC 3:7 w/w + 1 % VC as the electrolyte. AMPIX

cells<sup>173</sup> were assembled with this process described in more detail in Section 2.3.9. The samples were exposed to the synchrotron X-ray radiation and data were collected in transmission mode. During the *operando* measurements, cells were connected to a BioLogic potentiostat and cycled at a rate of C/5 between 3.0 to 4.5 V vs. Li/Li<sup>+</sup> with full XANES and EXAFS measurements taken every 0.1 V. The data were processed and normalised using the Athena software package.<sup>174</sup>

### 2.3.6 Scanning Electron Microscopy (SEM)

Scanning electron microscopy is a powerful tool in the visualisation of materials on the small scale, shedding insight into particle size, particle morphology and the homogeneity of these two properties throughout a sample. In a standard optical microscope, light is used alongside a system of lenses in order to magnify images of small objects. However, the size of object to be magnified is limited by the wavelength of visible light. Electron microscopes utilise a beam of short wavelength electrons, focused by magnets in order to image specimens down to the nanometre scale. A beam of thermionically emitted electrons is first generated from an electron gun fitted with a tungsten filament. The beam then passes through several magnetic lenses to focus the beam and reduce its spot diameter to the appropriate size. This focused beam is allowed to scan across the surface of the sample, producing various different signals that provide information on sample topography and composition, as highlighted in Table 2.5.

**Table 2.5** Signal types produced during scanning electron microscopy and the information provided.

Signal type	Information provided
Secondary electrons	Topographical
Back-scattered electrons	Atomic numbers and topographical
X-ray	Composition
Cathodoluminescence	Electrical
Auger electrons	Surface sensitive composition

For general surface imaging applications, back scattered electrons (BSEs) and secondary electrons (SEs) are commonly used. Back scattered electrons are caused when an incident electron scatters elastically from an atom within the sample and can provide information on regions deep within the sample. The production of back scattered electrons is dependent on the mass of the scattering element, with heavy elements scattering more strongly and thus appearing brighter in an SEM image. BSEs thus, can be particularly

useful for identification of regions of chemical heterogeneity and possible impurities in the sample. On the other hand, secondary electrons are ejected from atoms in the sample during inelastic scattering processes between incident electrons and the sample. The number of SEs produced depends on the angle at which the incident beam strikes the sample surface, with steeper surfaces and edges yielding more SEs compared to flat surfaces. Therefore, the intensities of SEs as a function of position directly generates a topographical image of the sample surface.

SEM images were obtained from a Carl Zeiss Sigma variable pressure analytical SEM with operating voltages between 5 and 15 kV and an FEI Inspect F50 SEM at an operating voltage of 10 kV. Sample preparation was carried out by adhering the powder samples onto an adhesive conductive carbon tab which was then attached to an aluminium stub. Coating of the NMC samples was not required as they are electronically conductive.

### **2.3.7 Energy Dispersive X-ray spectroscopy (EDX)**

Energy dispersive X-ray spectroscopy is a technique used to determine the elemental composition of a sample. When a beam of high energy electrons is incident on a sample, stimulation of X-ray emission can occur when an incident electron ejects an inner-shell electron, producing an electron hole which can be filled by an outer-shell electron dropping down. The difference in energy between the outer shell and the inner shell manifests itself as an X-ray possessing that particular energy. Characteristic energies for different atoms can be referenced and compared to the X-rays emitted from the sample in order to determine its elemental composition. As an electron beam is required for EDX, it is often combined with common SEM equipment with the user selecting a different detector to examine the EDX data. All EDX data reported in this thesis were recorded using the same sample preparation and the same electron microscopes reported above with the Oxford microanalysis program utilised for data acquisition and analysis.

### **2.3.8 Muon spin relaxation spectroscopy ( $\mu^+$ -SR)**

The  $\mu^+$ -SR technique is used in battery materials to study local ionic diffusion of cations. Cationic diffusion is a hugely important property of battery materials as this strongly influences the performance of the cell, particularly the power delivery and the charge and discharge rate capabilities. Several macroscopic techniques are popular in studying ionic diffusion, the most widely used being electrochemical impedance spectroscopy (EIS). However, as a bulk technique, EIS is limited by large scale effects such as grain boundaries and interfaces between electrodes. Grain boundaries are highly dependent on material processing factors such as sintering time and conditions

implemented during pellet pressing (*i.e.* pressing under higher pressure and higher temperatures reduces grain boundaries) and so comparison across the literature proves unreliable. Local, or microscopic, techniques, conversely, do not rely upon such post-synthesis processing and can provide a good measure of inherent ionic conductivity which could prove a more reliable way of comparing materials. Quasi-elastic neutron scattering (QENS), nuclear magnetic resonance (NMR) and  $\mu^+$ -SR are all examples of microscopic analysis methods. However, QENS suffers from long measurement times and limited detection time-scale of  $10^{-9}$  to  $10^{-12}$  s with some ionic species diffusion timescales falling outside of this range. NMR offers a wide timescale and has been widely used in analysing microscopic lithium diffusion in several materials. The NMR technique, however, can be hindered by the presence of highly paramagnetic ions which can interfere with the spin-lattice relaxation rate ( $1/T_1$ ) and can serve to complicate the diffusional analysis. The  $\mu^+$ -SR technique presents advantages over QENS and NMR including the ability to study materials containing paramagnetic ions due to the fact that electronic and nuclear contributions to the muon spin depolarisation can be separated. Furthermore, operating on a time scale of  $10^{-5}$  -  $10^{-8}$  s,  $\mu^+$ -SR is perfectly primed to probe long-range and consecutive short range jumps between interstitial sites in a lattice.<sup>175,176</sup>

The muon itself can be described as a fundamental particle and is a generation II lepton. Considered as a heavier form of the electron, muons are spin-1/2 particles with a mass of 105.7 MeV, a mean lifetime of 2.2  $\mu$ s, and come in negatively and positively charged forms. Negatively charged muons implant close to atomic nuclei and are much less sensitive to condensed matter phenomena. On the other hand, the positive muon implants in regions of high electron density and close to the regions of interest, therefore it is the positive muon,  $\mu^+$ , that is selected for  $\mu^+$ -SR experiments.<sup>177</sup>

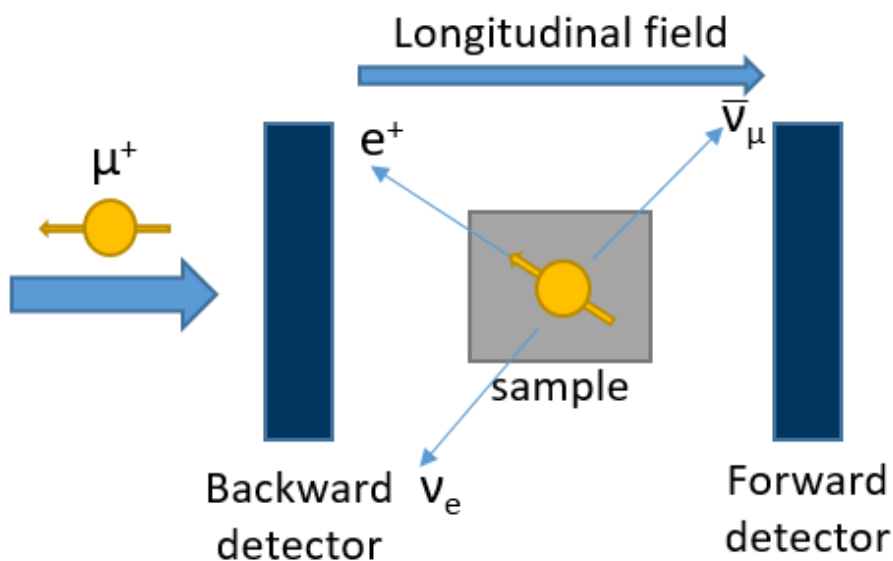


**Figure 2.4** Schematic of a typical  $\mu^+$ -SR experiment where decay positrons are detected in the forwards and backwards detectors. Adapted from S. J. Blundell.<sup>177</sup>

The muon fluxes required for  $\mu^+$ -SR experiments can only be generated by high energy particle accelerators, and so  $\mu^+$ -SR can only be performed at national facilities such as ISIS, PSI in Switzerland, TRIUMF in Canada and J-PARC in Japan. A high energy proton beam (800 MeV at ISIS) is fired at a target to produce positive pions,  $\pi^+$ , via collisions with protons in the target (a graphite target is used at ISIS). These pions decay with a mean lifetime of 26 ns into a positive muon and a muon neutrino. Because of parity violation due to the pion decay being mediated by the weak interaction, the resultant beam of muons is essentially 100 % spin polarised. When the muon beam strikes the sample, muons are implanted at interstitial sites within the structure close to areas with high electronegativity (*i.e.* close to  $O^{2-}$  anions for oxides). While implanted, the muon's spin experiences a local field distribution ( $\Delta$ ) which is caused by the surrounding static local nuclear magnetic environment and a fluctuation rate ( $\nu$ ) induced by the motion of surrounding nuclei. In the case of cation conductors for batteries,  $\nu$  is largely affected by  $Li^+$  or  $Na^+$  diffusion. Such effects serve to perturb the muon spins with a resultant depolarisation of the spin ensemble over time.

With a mean lifetime of 2.2  $\mu s$ , the muons decay via a three-body decay to yield a positron and two neutrinos. Of most use is the positron which is preferentially emitted in the same direction as the direction which the muon spin was pointing in at the instant of decay. This allows one to be able to follow the time evolution of the muon spin polarisation by monitoring the time evolution of the decay positron asymmetry,  $A(t)$ , in two sets of detectors placed behind and in front of the sample:

$$A(t) = A(0)G_z(t) = \frac{N_F(t) - \alpha N_B(t)}{N_F(t) + \alpha N_B(t)} \quad (2.12)$$

where  $A(0)$  is the initial positron asymmetry,  $G_z(t)$  is the depolarisation function,  $N_F$  and  $N_B$  are the positron counts in the forwards and backwards detectors respectively and  $\alpha$  is an instrument and sample dependent calibration constant. By fitting the data to a suitable depolarisation function, important parameters such as  $\Delta$  and  $\nu$  mentioned above can be obtained that give valuable insight into lithium diffusion dynamics.

$\mu^+$ -SR experiments were carried out on the EMU instrument at ISIS Pulsed Neutron and Muon Source and the data was analysed using the WiMDA program.<sup>178</sup> The EMU spectrometer is a 96 detector instrument optimised for zero field (ZF) and longitudinal field (LF) measurements. Powder samples of  $\approx 1$  g were loaded into titanium sample holders with up to 2 titanium backing discs to ensure tight packing of the powder and sealed with a 25  $\mu\text{m}$  thick titanium window. Titanium is chosen as it depolarises muons very weakly. Muons with an energy of 3.2 MeV were implanted into the samples. The temperature was controlled from 100 K to a maximum of 500 K in 20 K steps using the available closed cycle refrigerator set-up. The temperature range was chosen to encompass the thermally activated region. Data were collected at ZF and an extra two LFs (ranging from 5 to 15 G) for each temperature and the calibration constant  $\alpha$  was estimated from a transverse field calibration measurement at 100 G. The application of LFs parallel to the muon beam decouples interactions between the muon spins and the nuclear contributions from surrounding atoms. Furthermore, by simultaneously fitting multiple magnetic field measurements, more reliable fits can be obtained.

### 2.3.9 Galvanostatic cycling

When assessing potential materials for use in lithium ion batteries such as electrodes and electrolytes, it is of vital importance to ascertain how they perform in action. Galvanostatic cycling with potential limitation (GCPL) is one widely used electrochemical testing method where a constant current is applied to the battery over time and the resulting change in potential is observed. As the name suggests, GCPL operates within a limited, defined potential window, with a positive current applied through the cell until the voltage reaches the upper limit after which the current changes polarisation to lower the voltage to the lower limit. For cathode materials, these actions correspond to the charge and discharge processes respectively. The main objective in galvanostatic cycling tests is to obtain how much energy the cell is able to store and release during charge and discharge respectively. This is obtained by measuring the capacity of the cell under analysis. The specific capacity of the active material is most

often expressed in units of mAh g<sup>-1</sup> where large capacities are desirable. This specific capacity is essentially a measure of the amount of mAh that can be drawn from the cell under specific charge and discharge conditions including voltage range, current applied and temperature. As mentioned in Chapter 1, each specific material has a theoretical capacity dependent upon the amount of Li<sup>+</sup> that can be extracted/intercalated and the molecular mass of the compound. Specific capacities delivered during cycling should be as close as possible to the theoretical capacity where lower specific capacities would indicate some problem with the sample being tested. The GCPL method can also be used to determine the rate capability of the cell *i.e.* how well the cell performs upon the application of higher currents.

Galvanostatic cycling experiments presented in this thesis were mainly conducted in Swagelok type cells on a BioLogic VSP potentiostat. Cells were fabricated in an Ar filled glovebox with a pellet of electrode material (with a composition of active material:carbon black:PTFE in a 60:30:10 wt.% ratio), a Whatman glass microfibre separator, a 1 M LiPF<sub>6</sub> in ethylene carbonate (EC) and dimethyl carbonate (DMC) 1:1 v/v solution as the electrolyte and a lithium metal disk as the counter electrode. For some cells a 1 M LiPF<sub>6</sub> in EC:EMC 3:7 w/w (+1 % VC) electrolyte was used where this will be specified in the text. Figure 2.5(a) shows a typical set-up of a Swagelok type cell. A small number of cells presented here were fabricated in a coin-cell set up, shown in Figure 2.5(b). For these, an electrode slurry was prepared from active material:carbon black:PVDF in a 90:5:5 wt.% ratio and organic solvent N-Methyl-2-pyrrolidone (NMP). The slurries were mixed using a Thinky mixer and were cast onto carbon-coated aluminium sheets using a doctor blade to form 15 µm thick coatings. The sheets were dried at 80 °C for 1 hour to remove the NMP and were transferred to a vacuum oven overnight at 80 °C before coin-cell assembly. Electrode disks were then punched from the sheet. CR2032 coin cells were assembled in an Ar filled glovebox in a similar manner to the Swagelok cells but with the cathode pellet replaced by the dried cathode disks. In-operando XAS measurements were carried out in the AMPIX cell developed at Argonne National Laboratory shown in Figure 2.5(c).<sup>173</sup> Cathode sheets for the AMPIX cells were fabricated as described above for coin cells and Kapton windows were used in order to allow X-rays to be transmitted through the cell. It will be specified in the text throughout this thesis which cell set-up was used.

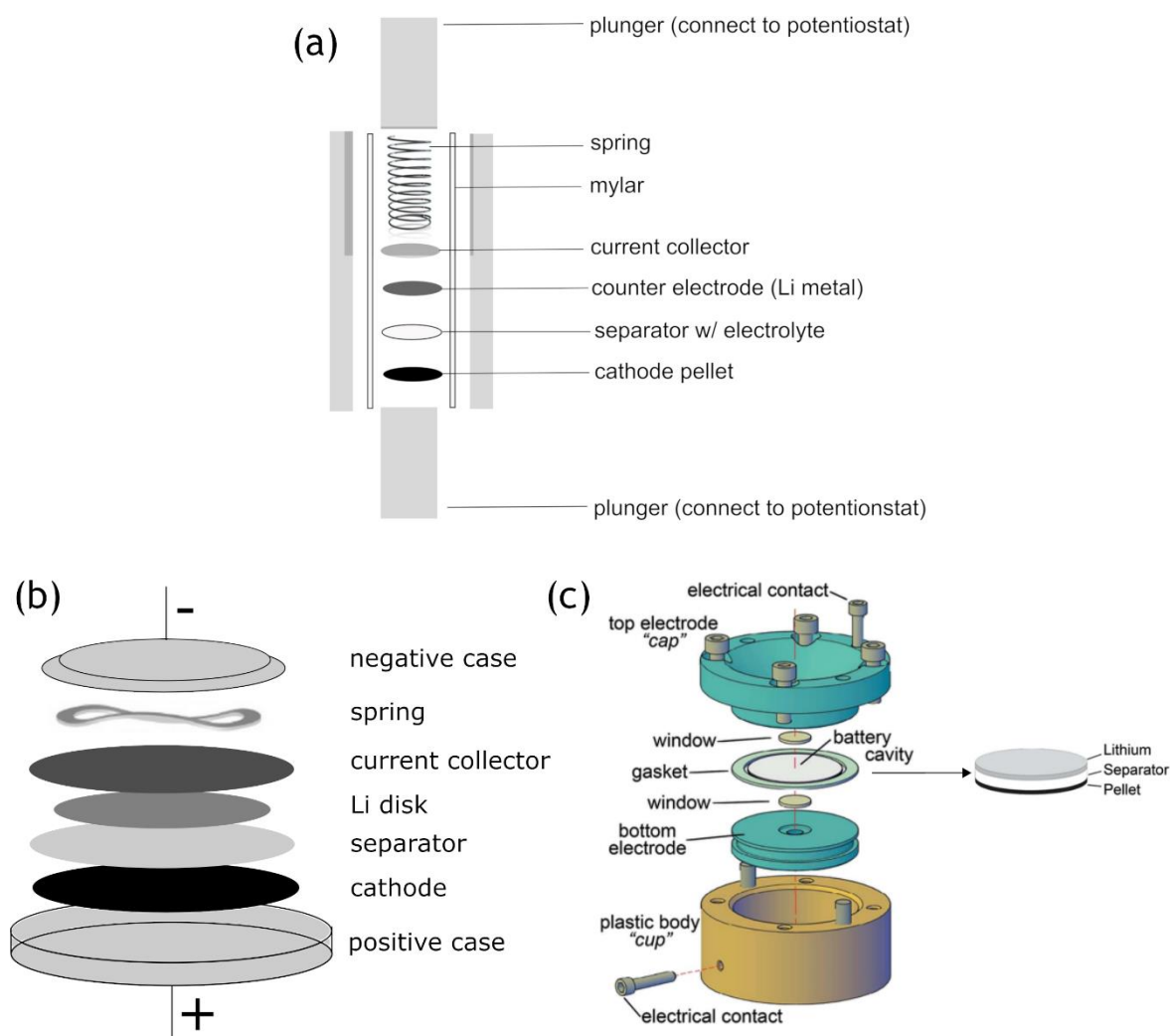


**Figure 2.5** Set-ups of the three different types of battery cells used in this thesis showing (a) Swagelok type cells, (b) CR2032 coin cells and (c) the AMPIX cell. The AMPIX cell diagram reproduced from Borkiewicz *et al.*<sup>173</sup>

## 3 Muon spin relaxation studies of polyanionic cathodes

### 3.1 Introduction

Olivine structured  $\text{LiFePO}_4$  has seen commercial success in high power applications such as replacements for lead acid batteries in boats, e-bikes and e-scooters. However, poor intrinsic electronic and ionic conductivities necessitate additional processing steps such as carbon coating and nano-sizing in order to realise good electrochemical performances and alternative and improved polyanionic materials constitute a major research area for next generation cathodes.

Despite its limitations,  $\text{LiFePO}_4$  has positioned itself as a highly esteemed cathode material and the opportunity to tailor this more, by replacing the phosphate with the more electronegative sulphate group, for example, would be undoubtedly desirable in increasing working voltages through the inductive effect, with an additional negatively charged  $\text{F}^-$  anion to preserve charge balance as explained previously in Chapter 1.  $\text{LiFeSO}_4\text{F}$  presents a promising higher voltage Fe-containing cathode material with the tavorite and triplite phases displaying working voltages of 3.6 and 3.9 V vs.  $\text{Li}/\text{Li}^+$  respectively, corresponding to the  $\text{Fe}^{2+/3+}$  redox couple, which is higher than that observed in  $\text{LiFePO}_4$  at 3.45 V vs.  $\text{Li}/\text{Li}^+$ . Thus, the connectivity of the polyanion structures has a huge influence on the redox potentials observed. A critical analysis of the ionic diffusion in these increasingly important fluoride-containing cathodes is, however currently missing and is important as ion diffusion within such materials underpins their (dis)charge behaviour. Computational analysis suggests a low activation energy ( $\approx 0.4$  eV) for  $\text{Li}^+$  mobility and AC and DC conductivity measurements indicate higher  $\text{Li}^+$  diffusion coefficients for  $\text{LiFeSO}_4\text{F}$  compared to  $\text{LiFePO}_4$ .<sup>115,117</sup> The impressive performances achieved by these fluoride containing electrodes positions such materials favourably for potential applications in high energy density demanding technologies, and unravelling their ionic diffusional mechanisms will guide future synthetic roadmaps to new and improved electrode materials.

As previously mentioned,  $\mu^+$ -SR offers a variety advantages over techniques such as EIS, NMR and QENS for studying ionic motion. Muon spin relaxation spectroscopy has been previously used in order to successfully probe the local ionic diffusion in a range of cathodes and electrolytes for Li and Na ion batteries including microwave synthesised  $\text{LiFe}_{1-x}\text{Mn}_x\text{PO}_4$ ,  $\text{LiCoO}_2$ ,  $\text{LiNi}_{1/3}\text{Mn}_{1/3}\text{Co}_{1/3}\text{O}_2$ ,  $\text{Li}_{6.5}\text{Al}_{0.25}\text{La}_{2.92}\text{Zr}_2\text{O}_{12}$ ,  $\text{NaFePO}_4$ ,  $\text{NaCoO}_2$ ,  $\text{NaMn}_2\text{O}_4$  and  $\text{Na}_{1.5}\text{La}_{1.5}\text{TeO}_6$ .<sup>156,179-185</sup> In these cases, the spin-polarised muon is embedded within the sample locating close to electronegative species such as oxide ions. In the case of fluoride containing electrodes, one question that remains open is the effect of the

fluoride ion on the diffusion properties. Up to now, the  $\mu^+$ -SR technique has not been applied to battery materials containing ions of greater electronegativity such as the fluoride ion. Spin polarised positive muons can bind strongly to fluoride ions to form a number of possible species such as F- $\mu$ -F and F- $\mu$ .<sup>186,187</sup> On one hand, since the most likely stopping site for the muon is close to the electronegative fluoride ion there remains the question of whether strong binding between these will preclude observation of any effects by diffusing Li-ions near that stopping site. On the other hand, this binding interaction could place the muon in a prime location to effectively “see” the nearby diffusing Li ions.

In this chapter, the  $\mu^+$ -SR technique has been used as a local scale probe in order to investigate microscopic Li- and Na-diffusion across a range of interesting polyanionic materials as potential cathodes for higher energy density polyanionic technologies which include LiFeSO<sub>4</sub>F, Na<sub>2</sub>FePO<sub>4</sub>F and the maricite phase of NaFePO<sub>4</sub>. From modelling the  $\mu^+$ -SR experimental data to a model incorporating ionic diffusion, the temperature dependence of field fluctuation rates and local field distribution widths were extracted, allowing for the calculation of thermal activation energies and diffusion coefficients for ionic motion. The measurements involving LiFeSO<sub>4</sub>F and Na<sub>2</sub>FePO<sub>4</sub>F furthermore give insight into the ability to carry out  $\mu^+$ -SR experiments on fluorine containing species, where the highly electronegative fluorine anion could preclude cationic diffusion induced muon spin perturbation. By showing that muons can be applied to the study of microscopic ionic diffusion in materials containing highly electronegative polyanions, a new and rich area of materials research could be established regarding the use of muons as a local probe for establishing the microscopic ionic diffusion mechanisms in high performance, high voltage electrodes.

### **3.2 Local Li<sup>+</sup> diffusion in fluorosulphate LiFeSO<sub>4</sub>F measured using $\mu^+$ -SR**

The iron containing tavorite polymorph, named after the mineral with composition LiFePO<sub>4</sub>(OH), was first reported in 2009.<sup>115</sup> The material was synthesised *via* an ionothermal method by reacting FeSO<sub>4</sub>·H<sub>2</sub>O with a slight excess of LiF in the ionic liquid EMI-TFSI in a PTFE lined steel bomb at 300 °C for 5 hours. Such low temperatures are required due to the thermal decomposition of LiFeSO<sub>4</sub>F which occurs at around 400 °C, inhibiting the use of conventional solid-state synthesis methods which typically require higher temperatures to overcome diffusional requirements of reactants. Aqueous routes are also precluded due to the high solubility of sulphates in water.<sup>115</sup> While the aforementioned research utilised ionic liquids to achieve tavorite LiFeSO<sub>4</sub>F, the high cost of these exotic reaction media (*ca.* \$500 per gram) raises questions about the scalability

of such methods. Researchers from Nazar's group have demonstrated a scalable solvothermal method for tavorite  $\text{LiFeSO}_4\text{F}$  synthesis using tetraethylene glycol (TEG) as the solvent at  $220\text{ }^\circ\text{C}$  for 60 hours.<sup>188</sup> The monohydrate precursor,  $\text{FeSO}_4\cdot\text{H}_2\text{O}$  is structurally similar to  $\text{LiFeSO}_4\text{F}$  and when these phases are projected along the [110] and [100] respectively the same sequence of octahedra and tetrahedra is observed, where the oxygen site corresponding to the water of crystallisation is the fluorine site in the  $\text{LiFeSO}_4\text{F}$  structure. These structural similarities imply that the reaction between  $\text{FeSO}_4\cdot\text{H}_2\text{O}$  (*i.e.*,  $\text{HFeSO}_4\text{OH}$ ) and  $\text{LiF}$  occurs *via* a topotactic route, with  $\text{F}^-$  essentially replacing the  $\text{O}^{2-}$  from the  $\text{H}_2\text{O}$  molecule and a  $\text{Li}^+$  required to preserve charge compensation to form the tavorite phase  $\text{LiFeSO}_4\text{F}$ .<sup>115</sup>

### 3.2.1 Microwave-assisted synthesis of tavorite phase $\text{LiFeSO}_4\text{F}$

In an effort to synthesise tavorite  $\text{LiFeSO}_4\text{F}$  for  $\mu^+$ -SR measurements, a similar approach to the microwave-assisted technique reported by Tripathi *et al.* was used.<sup>122</sup> Initially, the  $\text{FeSO}_4\cdot 7\text{H}_2\text{O}$  precursor was subjected to a short heat treatment at  $60\text{ }^\circ\text{C}$  for 45 minutes in a vacuum oven to yield the desired monohydrate precursor. After ball milling for 2 hours with a slight excess of  $\text{LiF}$  (1:1.1 molar ratio) the mixture was transferred to a 35 mL quartz vessel containing 20 mL TEG for reaction in a CEM Discover SP microwave synthesiser. In order to replicate the heating conditions outlined in the reference paper, a temperature of  $230\text{ }^\circ\text{C}$  was programmed. However, due to the power limits of the microwave synthesizer (300 W) the reaction mixture could not be heated past a temperature of  $220\text{ }^\circ\text{C}$  without causing a build-up of heat in the equipment's heat sink, causing the program to terminate for safety reasons. Because of the lower reaction temperature of  $220\text{ }^\circ\text{C}$  it was decided to prolong the reaction time from 10 minutes to 30 minutes in order to facilitate a greater extent of reaction. The PXRD pattern measured for the obtained material after washing is shown in Figure 3.1.

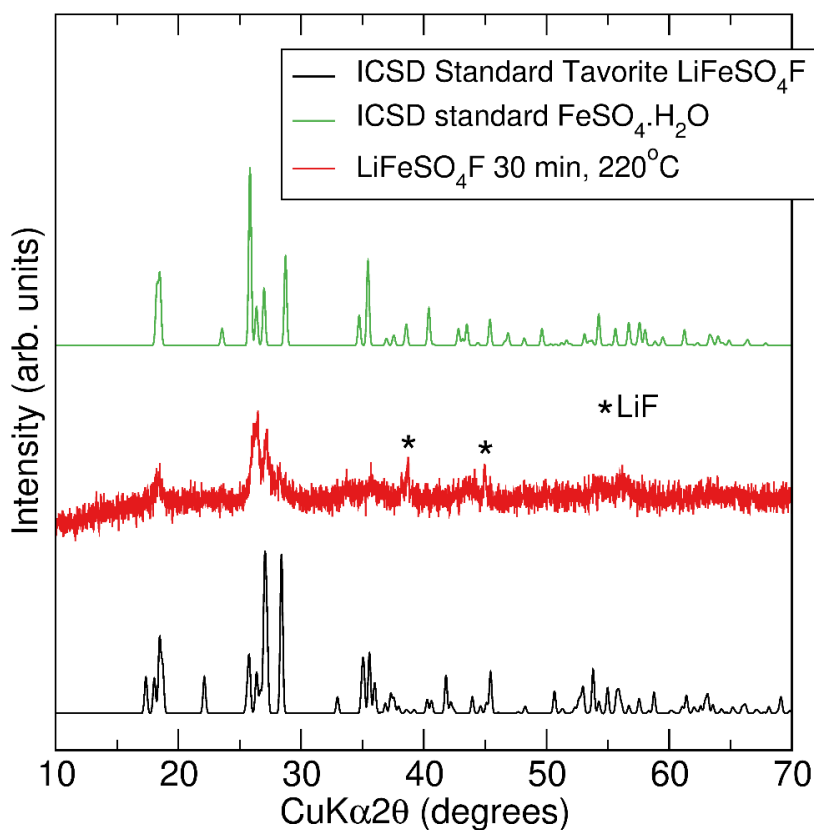


**Figure 3.1** PXR D pattern of the product formed during microwave solvothermal heating of  $\text{FeSO}_4 \cdot \text{H}_2\text{O}$  and  $\text{LiF}$  precursors for 30 minutes at  $220^\circ\text{C}$  in a TEG medium (red), alongside reference patterns for tavorite phase  $\text{LiFeSO}_4\text{F}$  (black) and  $\text{FeSO}_4 \cdot \text{H}_2\text{O}$  (green) obtained from the ICSD (collection code 182944).<sup>189</sup> Peaks indicating the presence of  $\text{LiF}$  are also annotated (\*).

It can be clearly seen that the pattern obtained suffers from a high background with poorly defined peaks, making elucidation of the resulting phase difficult. Owing to the similarity in structure between tavorite phase  $\text{LiFeSO}_4\text{F}$  and starting material  $\text{FeSO}_4 \cdot \text{H}_2\text{O}$ , their PXR D patterns are also alike. The low-resolution pattern for the synthesised product makes it extremely difficult to search for peaks which would be able to resolve the difference, such as the peaks at  $2\theta$  values of  $\approx 22^\circ$  and  $33^\circ$  for tavorite  $\text{LiFeSO}_4\text{F}$ . However, by closer inspection of the relative intensities of the cluster of peaks between  $25$  to  $30^\circ$  it appears that these match more closely with the ICSD reference pattern for  $\text{FeSO}_4 \cdot \text{H}_2\text{O}$  rather than for the ICSD reference pattern for  $\text{LiFeSO}_4\text{F}$ . Furthermore, the presence of  $\text{LiF}$  in the collected PXR D data, located by asterisks in Figure 3.1 further corroborate evidence of a lack of reaction between the two precursors. The obtained PXR D data would be unsuitable for Rietveld analysis owing to the quality of the data. Despite this, the obtained powder was subjected to a further 3.5 hour solid state heat treatment at  $350^\circ\text{C}$  under an inert atmosphere to try and facilitate the transformation to the triplite phase  $\text{LiFeSO}_4\text{F}$ . Temperatures for this reaction must be kept below  $400^\circ\text{C}$

so as not to cause thermal decomposition of the fluorosulphate species. The product obtained after this short solid-state heat treatment was characterised using PXRD, with the resultant pattern shown in Figure 3.2.

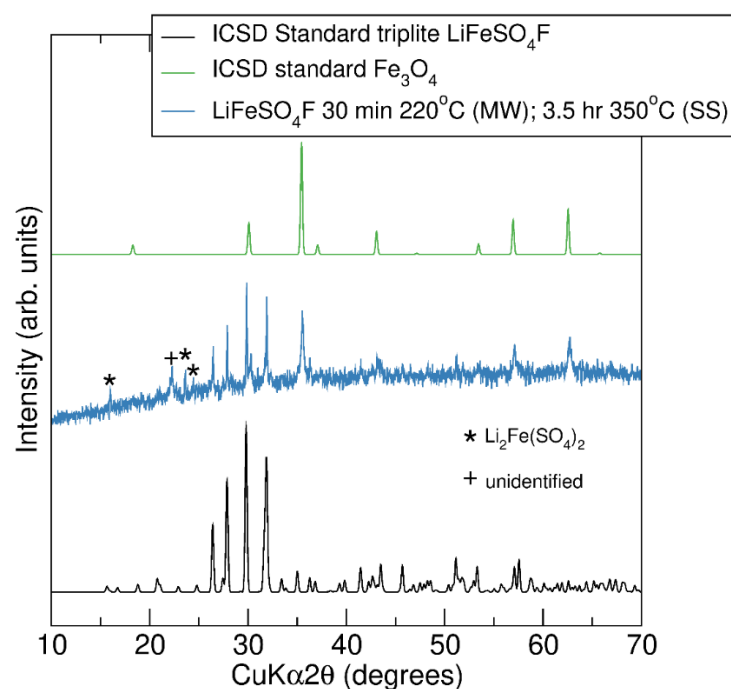


**Figure 3.2** PXRD pattern of the product formed during the short, solid state heat treatment of the tavorite-like precursor at 350 °C for 3.5 hours under Ar (blue), alongside reference patterns for triplite phase LiFeSO<sub>4</sub>F (black) and Fe<sub>3</sub>O<sub>4</sub> (green) obtained from the ICSD (collection codes 187799 and 26410). Also annotated are small amounts of Li<sub>2</sub>Fe(SO<sub>4</sub>)<sub>2</sub> impurity (\*) and an unidentified phase (+).

The PXRD pattern reveals that triplite LiFeSO<sub>4</sub>F has been formed alongside various other phases. The main impurity phase is shown to be the ferrimagnetic iron oxide, Fe<sub>3</sub>O<sub>4</sub> (also known as magnetite), where Fe<sup>2+</sup> and Fe<sup>3+</sup> are distributed over different crystallographic sites. The presence of Fe<sup>3+</sup> indicates that some quantity of Fe<sup>2+</sup> has been oxidised in the reaction, despite carrying the reaction out under inert conditions, with this oxidation leading to the onset of Fe<sub>3</sub>O<sub>4</sub> formation. Furthermore, the presence of small amounts of Li<sub>2</sub>Fe(SO<sub>4</sub>)<sub>2</sub> phase in the PXRD pattern could be indicative of the onset of thermal decomposition of triplite LiFeSO<sub>4</sub>F despite the reaction being carried out below the reported decomposition temperature for the compound. Thermal decomposition of the sulphate group could be the contributor of oxygen for the oxidation of Fe<sup>2+</sup> to Fe<sup>3+</sup>. These results indicated the initial difficulties faced in trying to synthesise both phases of LiFeSO<sub>4</sub>F. To understand how synthesis parameters affected the quality of the produced samples, it was then decided to investigate several different steps in the process.

The first step in the synthetic process is the dehydration of the initial  $\text{FeSO}_4 \cdot 7\text{H}_2\text{O}$  precursor. This step is required at the beginning as  $\text{FeSO}_4 \cdot \text{H}_2\text{O}$  cannot be bought commercially and thus must be produced from  $\text{FeSO}_4 \cdot 7\text{H}_2\text{O}$ . The initial experiment relied on the dehydration step taking place at  $60^\circ\text{C}$  for 45 minutes in a vacuum environment which was reported to have worked in previous work done in the group. To examine whether this step does actually produce the monohydrate, a PXRD measurement was performed on the sample after this short heat treatment. However, it was observed that the tetrahydrate was actually formed instead of the monohydrate. To form the monohydrate, it was decided to follow the dehydration procedure described by Nazar's group, heating  $\text{FeSO}_4 \cdot \text{H}_2\text{O}$  in a tube furnace at  $100^\circ\text{C}$  for 3 hours under a constant flow of  $\text{Ar}/\text{H}_2$  (5 %) gas. Figure 3.3 shows the PXRD patterns obtained for both dehydration strategies, alongside ICSD reference patterns for the monohydrate and the tetrahydrate (collection codes 71345 and 23912 respectively). Clearly, from the figure, it is seen that  $\text{FeSO}_4 \cdot \text{H}_2\text{O}$  is successfully synthesised during the technique at  $100^\circ\text{C}$  for 3 hours under  $\text{Ar}/\text{H}_2$  (5%). Therefore, subsequent reactions utilise this method during the initial dehydration step.

After the careful optimisation of several further reaction parameters, including atmosphere used during the dehydration step, ball milling time, reaction time and mass of reactants used in the reaction (PXRD patterns for synthesised species during optimisation of several parameters are shown in Figures 7.1 to 7.6 in the appendix),  $\text{LiFeSO}_4\text{F}$  was successfully synthesised. The optimised reaction conditions involved a 1 hour ball milling time between  $\text{FeSO}_4 \cdot \text{H}_2\text{O}$  and  $\text{LiF}$  (1:1.1 molar ratio) reactants before the microwave solvothermal heating step which was performed at  $230^\circ\text{C}$  for 1 hour (described in detail in Section 2.2.2).

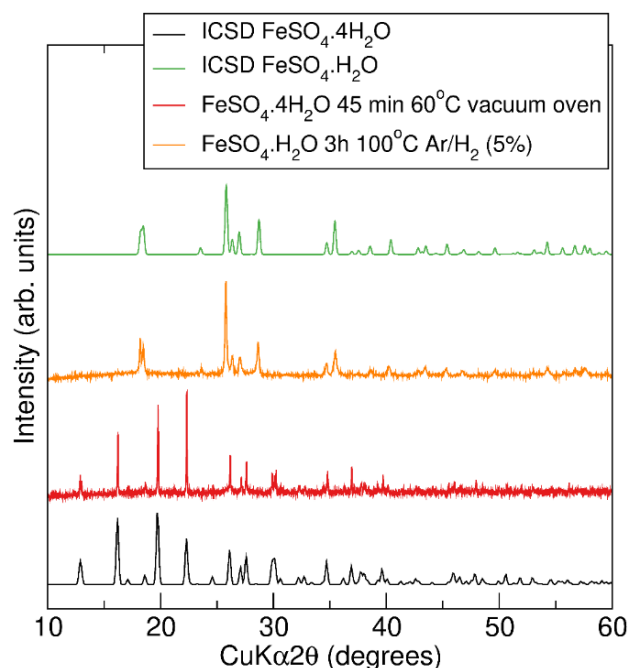


**Figure 3.3** PXRD patterns for two different dehydration strategies applied to  $\text{FeSO}_4 \cdot 7\text{H}_2\text{O}$ . The product after heating in a vacuum oven for 45 minutes at  $60^\circ\text{C}$  (red) is clearly the tetrahydrate form whereas the monohydrate can be formed in a tube furnace reaction at  $100^\circ\text{C}$  under a flow of  $\text{Ar}/\text{H}_2$  (5 %) for 3 hours (orange). Reference ICSD diffraction patterns are also displayed for  $\text{FeSO}_4 \cdot 4\text{H}_2\text{O}$  (black) and  $\text{FeSO}_4 \cdot \text{H}_2\text{O}$  (green).

Figure 3.4 shows the Rietveld analysis on the PXRD data obtained for the synthesised  $\text{LiFeSO}_4\text{F}$  powder. The analysis was performed using the GSAS-II program using a starting model of  $P\bar{1}$   $\text{LiFeSO}_4\text{F}$  obtained from the ICSD (collection code 182944) with an additional phase of  $Fm\bar{3}m$   $\text{LiF}$  (collection code 18012) as small quantities of remaining  $\text{LiF}$  reactant have been reported.<sup>168,189</sup> The refinement was prepared for 19 variables, including scale factor, zero point, sample displacement, 6 background coefficients (fitted with a Chebyshev function), lattice parameters, microstrain and size parameters and Fe isotropic displacement parameters. All other atomic positions, displacements parameters and site fractions were not refined. Good agreement with the experimental data and the calculated model can be seen with  $R_{wp}$  and  $\chi^2$  values of 2.26 % and 1.18 obtained respectively. The phase and weight fractions of  $\text{LiF}$  were calculated as 0.25 % and 0.1 % respectively, indicating an insubstantial quantity of  $\text{LiF}$  present in the product. The refined unit cell parameters, alongside statistical agreement factors  $R_{wp}$  and  $\chi^2$  are shown in Table 3.1. Calculated lattice parameters show good agreement with comparable data in the literature and the fit and model of  $\text{LiFeSO}_4\text{F}$  obtained here can be considered a good indicator of the formation of tavorite  $\text{LiFeSO}_4\text{F}$  phase. Successive microwave

reactions were performed under identical conditions to produce *ca.* 1 g of LiFeSO<sub>4</sub>F powder to be utilised in the following  $\mu^+$ -SR experiments.

With the synthesis of good quality tavorite LiFeSO<sub>4</sub>F, it could be converted to the triplite phase by a solid-state heat treatment. It was found that heating a 0.15 g pellet of the tavorite LiFeSO<sub>4</sub>F in a tube furnace at 350 °C for 4.5 hours under a flow of Ar resulted in good quality triplite phase with no discernible impurity phases. Figure 3.5 shows the Rietveld refinement carried out on PXRD data obtained for triplite, showing a good fit to the data could be achieved using a *C2/c* model obtained from the ICSD (collection code 187799), with Table 3.2 detailing the calculated lattice parameters and statistical agreement factors. The refinement was prepared for 15 variables, including scale factor, zero point, sample displacement, 6 background coefficients (fitted with a Chebyshev function), lattice parameters, microstrain and size parameters. All other atomic positions, displacements parameters and site fractions were not refined. Impurities found in previous attempts at triplite synthesis could therefore be most likely attributed to the poor quality starting material. However, the triplite LiFeSO<sub>4</sub>F was not used in  $\mu^+$ -SR experiments, as its synthesis was refined after the muon experiments took place.

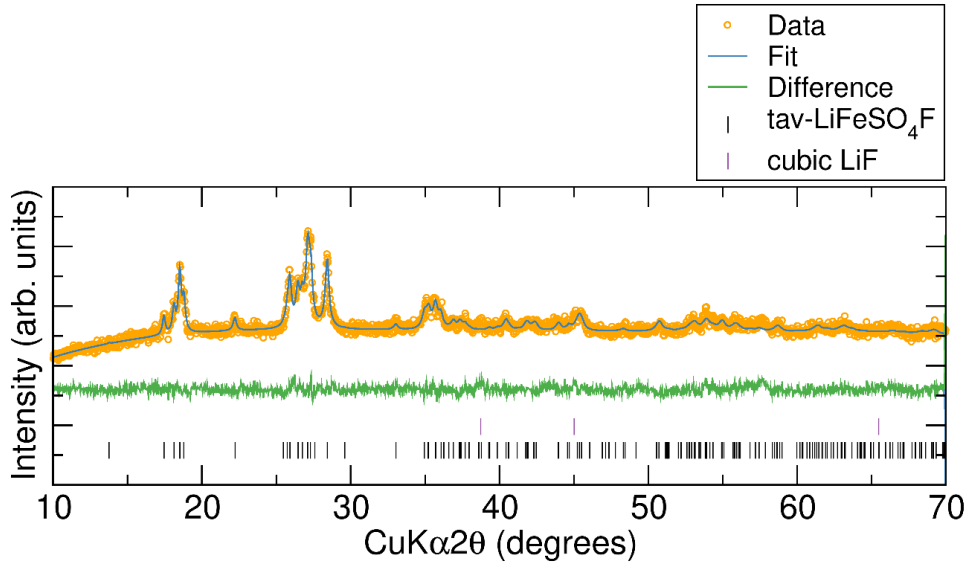


**Figure 3.4** Rietveld refinement for the microwave synthesised tavorite LiFeSO<sub>4</sub>F PXRD data using a model consisting of two phases, *P* $\bar{1}$  LiFeSO<sub>4</sub>F and *Fm* $\bar{3}$ *m* LiF, with  $R_{wp} = 2.26\%$  and  $\chi^2 = 1.18$ .

**Table 3.1** Calculated lattice parameters for microwave synthesised tavorite  $\text{LiFeSO}_4\text{F}$  and atomic parameters obtained from the Rietveld refinement using a model containing  $P\bar{1}$   $\text{LiFeSO}_4\text{F}$  and  $Fm\bar{3}m$   $\text{LiF}$  crystalline phases.

Tavorite $\text{LiFeSO}_4\text{F}$		$R_{wp} = 2.26 \%$	$\chi^2 = 1.18$	$V = 178(1) \text{ \AA}^3$		
$P\bar{1}$		$a = 5.14(4) \text{ \AA}$	$b = 5.44(4) \text{ \AA}$	$c = 7.16(8) \text{ \AA}$		
		$\alpha = 106.62(7)^\circ$	$\beta = 107.16(8)^\circ$	$\gamma = 97.74(5)^\circ$		
Atom	Site	x	y	z	Uiso ( $\text{\AA}^2$ )	Frac.
Li1	2i	0.2700	0.6340	0.7570	0.00524	1.0
Fe1	1b	0.0000	0.0000	0.5000	0.02(4)	1.0
Fe2	1a	0.0000	0.0000	0.0000	0.04(5)	1.0
S1	2i	0.3244	0.6381	0.2495	0.00823	1.0
O1	2i	0.5976	0.7469	0.4119	0.01494	1.0
O2	2i	0.1063	0.6407	0.3448	0.01494	1.0
O3	2i	0.3198	0.3564	0.1458	0.01494	1.0
O4	2i	0.2790	0.7708	0.1016	0.01494	1.0
F1	2i	0.1259	0.9144	0.7552	0.01494	1.0

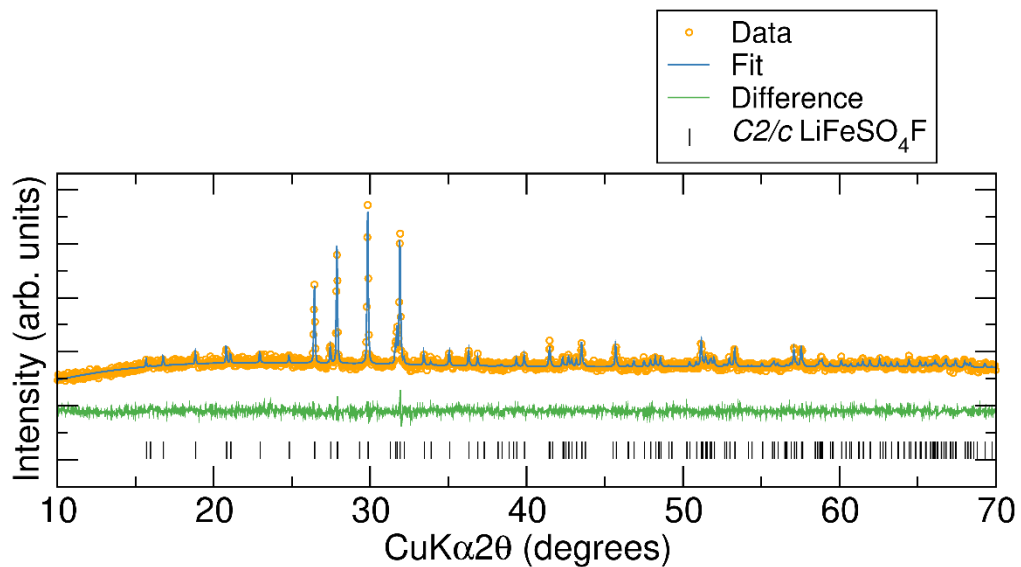


**Figure 3.5** Rietveld refinement for the PXRd data collected for triplite  $\text{LiFeSO}_4\text{F}$  synthesised by heating 0.15 g of the microwave assisted tavorite  $\text{LiFeSO}_4\text{F}$  for 4.5 hours at  $350^\circ \text{C}$  under Ar. Fit using a model of  $C2/c$  phase  $\text{LiFeSO}_4\text{F}$  with  $R_{wp} = 3.05 \%$  and  $\chi^2 = 1.18$

**Table 3.2** Calculated lattice parameters for triplite LiFeSO<sub>4</sub>F and atomic parameters obtained from the Rietveld refinement using a model containing the C2/c LiFeSO<sub>4</sub>F phase.

Triplite LiFeSO <sub>4</sub> F		$R_{wp} = 3.05\%$		$\chi^2 = 1.18$	$V = 712.05 (3) \text{ \AA}^3$	
C2/c		$a = 13.034(3) \text{ \AA}$	$b = 6.3941(2) \text{ \AA}$		$c = 9.840(1) \text{ \AA}$	
		$\alpha = 90^\circ$	$\beta = 119.753(4)^\circ$		$\gamma = 90^\circ$	
Atom	Site	x	y	z	Uiso ( $\text{\AA}^2$ )	Frac.
Li1	8f	0.6469	0.8947	0.8475	0.0215	0.426
Li2	8f	0.9473	0.2482	0.0007	0.027	0.574
Fe1	8f	0.6469	0.8947	0.8475	0.0215	0.574
Fe2	8f	0.9473	0.2482	0.0007	0.027	0.426
S1	8f	0.3279	0.5923	0.1967	0.0271	1.0
O1	8f	0.5976	0.7469	0.4119	0.0239	1.0
O2	8f	0.1063	0.6407	0.3448	0.0236	1.0
O3	8f	0.3198	0.3564	0.1458	0.0234	1.0
O4	8f	0.2790	0.7708	0.1016	0.0209	1.0
F1	8f	0.9867	0.4037	0.6091	0.043	1.0

### 3.2.2 Muon spin spectroscopy measurements on tavorite LiFeSO<sub>4</sub>F

One of the key determinants in effective lithium ion battery performance is the fast and facile motion of the Li<sup>+</sup> cations in the electrodes and electrolyte during cycling, enabling higher charging and discharging rates. Faster ionic diffusion being attainable at lower temperatures is furthermore highly valuable for batteries, especially for applications in electric vehicles where seasonal and regional low temperatures place limits on battery performance. Thus, determining the dynamics and kinetics of ionic diffusion in electrode materials is a key measurement in materials analysis. As previously mentioned in Section 2.3.8, methods that measure the bulk diffusional properties, such as EIS, are limited by resistive effects such as those arising from grain boundaries and here, local probes can offer us valuable and additional information. Here, the  $\mu^+$ -SR has been used to investigate the microscopic diffusion of Li<sup>+</sup> in tavorite phase LiFeSO<sub>4</sub>F prepared by a microwave solvothermal method. Aside from diffusional studies, this work was also attempted as a proof of concept in order to determine if the presence of highly electronegative fluoride anions would preclude the muon from the detection of Li<sup>+</sup> ion diffusion *via* strong  $\mu^+$ -F interactions. Although these types of interactions most likely only apply at low temperatures (< 100 K), proving that F<sup>-</sup> in the structure does not preclude measurement will be a useful step in widening the variety of structures that can be studied using  $\mu^+$ -SR.

Spin polarised positive muons were implanted into a powder sample of  $\text{LiFeSO}_4\text{F}$  contained within a titanium metal holder using the EMU instrument at the ISIS Pulsed Neutron and Muon Source. Measurements were taken in the temperature range 100 to 400 K at zero field (ZF) and applied longitudinal fields (LF) of 10 and 20 G. The raw data obtained for these measurements at 100 K and 300 K are shown in Figure 3.6 and represent the time evolution of the decay positron asymmetry. The decay positron asymmetry initially undergoes a rapid relaxation followed by a slower relaxation. The initial relaxation is broadly independent of the applied magnetic field and represents the interactions between the muon spin ensemble and the magnetic moments arising from the  $d$ -electrons of the  $\text{Fe}^{2+}$  cations ( $H_{int}^{3d}$ ). The latter slower relaxation is caused by interactions between the muon spin ensemble and the surrounding nuclear magnetic moments ( $H_{int}^N$ ) possessed by atomic isotopes with a non-zero spin in the structure *e.g.*  ${}^6\text{Li}$ ,  ${}^7\text{Li}$ ,  ${}^{57}\text{Fe}$  and  ${}^{19}\text{F}$ . It is observed that the application of higher longitudinal fields reduces this slower relaxation rate through the process of decoupling the muon's spin from the nuclear magnetic moments.

The raw data at each temperature were used to obtain fits using the WiMDA program by utilising equation 3.1 whose terms include **(a)**, an exponentially relaxing term to account for the interactions with  $3d$  magnetic moments alongside **(b)**, an exponentially relaxing dynamic Kubo-Toyabe function in order to extract information on the temperature dependence of  $\text{Li}^+$  diffusive behaviour, including the field fluctuation rate,  $\nu$ , and the local field distribution at the muon stopping site,  $\Delta$  and **(c)**, a constant background component.

$$A_0 P_{LF}(t) = \underbrace{A_F e^{-\lambda_F t}}_{\text{(a)}} + \underbrace{A_{KT} e^{-\lambda_{KT} t} \times G^{DGKT}(\Delta, \nu, t, H_{LF})}_{\text{(b)}} + \underbrace{A_{BG}}_{\text{(c)}} \quad (3.1)$$

The temperature dependence of the  $\nu$  and  $\Delta$  parameters, over the applied temperature range, are shown in Figure 3.7. The field fluctuation rate is perhaps the most important parameter here, as it provides information on the  $\text{Li}^+$  hopping rates and thus best describes the  $\text{Li}^+$  diffusion. From the values obtained from the data fitting, it can be seen that the  $\nu$  values remain relatively steady until a sharp increase is observed in the 200 to 260 K region which represents the onset of thermally activated  $\text{Li}^+$  diffusion and the escalating diffusivity as the sample temperature is increased. The thermally activated region is followed by a sharp drop after 260 K, a trend that is often observed in  $\mu^+$ -SR

studies of ionic conduction in cathode materials, and is thought to represent the point where  $\text{Li}^+$  diffusion becomes too fast to be detected by the  $\mu^+$ -SR technique.

The plot of the temperature dependence of the  $\Delta$  values shows a relatively stable region between 100 to 180 K before decreasing over the thermally activated region by  $\approx 0.06$  MHz which could be explained by changes in the local magnetic environment precipitated by increasing  $\text{Li}^+$  diffusion relating to faster  $\text{Li}^+$  hopping between sites. This is then followed by a region of increase by  $\approx 0.03$  MHz as the field fluctuation rate begins to rapidly drop off. For ionic diffusion in several electrode and electrolyte materials studied using  $\mu^+$ -SR, however,  $\Delta$  gradually decreases over the entire temperature ramp. This increase could arise from the fact that the muons are most likely distributed across two stopping sites close to both  $\text{O}^{2-}$  and  $\text{F}^-$  anions, with the  $\text{F}^-$  anion playing a role in the deviation from commonly observed trends. It could also be explained by small structural rearrangements *e.g.* oxygen or fluorine displacements near the muon stopping sites. However, similar trends have also been observed in  $\mu^+$ -SR carried out by Vidal Laveda *et al.* for cathode materials  $\text{LiFe}_{0.5}\text{Mn}_{0.5}\text{PO}_4$  and  $\text{LiFe}_{0.25}\text{Mn}_{0.75}\text{PO}_4$ , where  $\Delta$  increases by 0.2 to 0.3 MHz towards higher temperatures.<sup>180</sup>

The  $\mu^+$ -SR data collected clearly show behaviour that is characteristic to thermally activated  $\text{Li}^+$  diffusion within cathode frameworks. Therefore, it is evident that the presence of  $\text{F}^-$  within the structure does not preclude the measurement of local-scale  $\text{Li}^+$  diffusion using the  $\mu^+$ -SR technique.

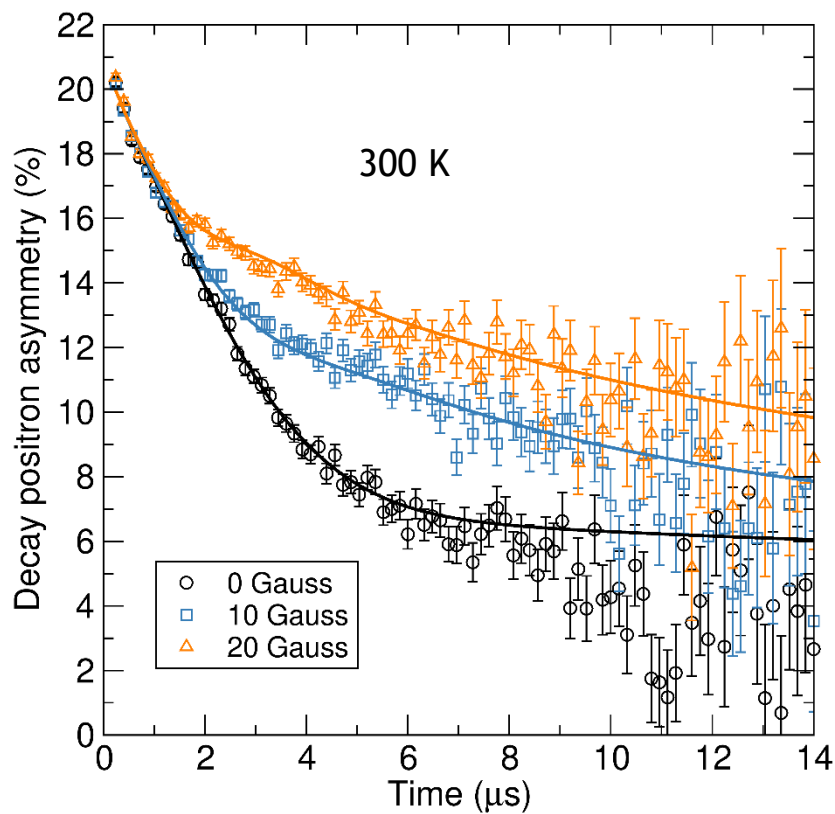
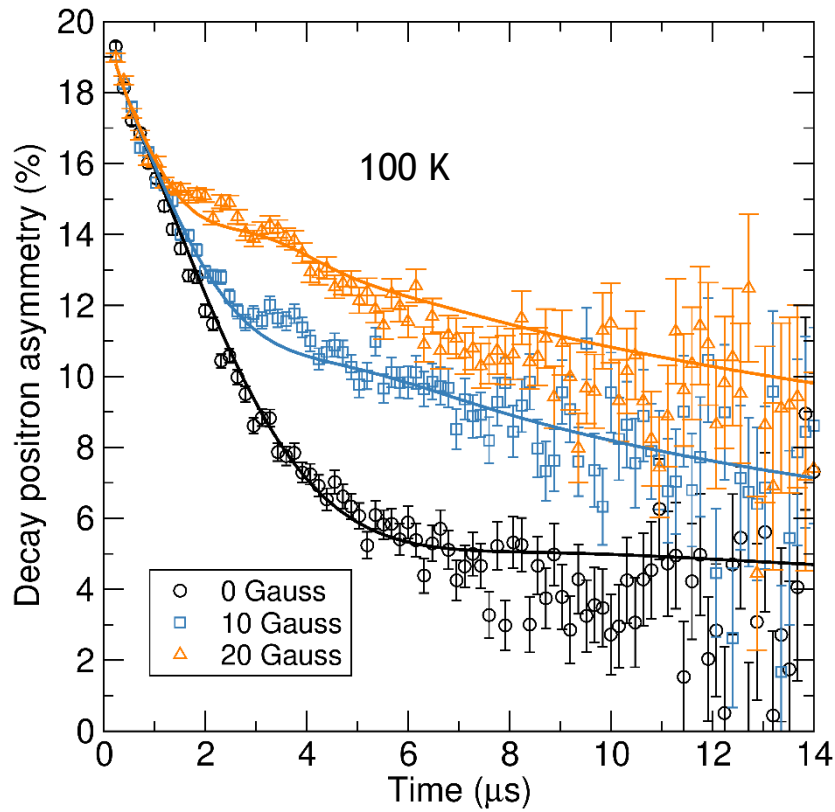


**Figure 3.6** Raw  $\mu^+$ -SR data obtained for tavorite phase  $\text{LiFeSO}_4\text{F}$  at 100 K (upper plot) and 300 K (lower plot) at zero field (black circles) and applied longitudinal fields of 10 G (blue squares) and 20 G (orange triangles) alongside the fit to the data using a dynamic Kubo-Toyabe function (solid lines).

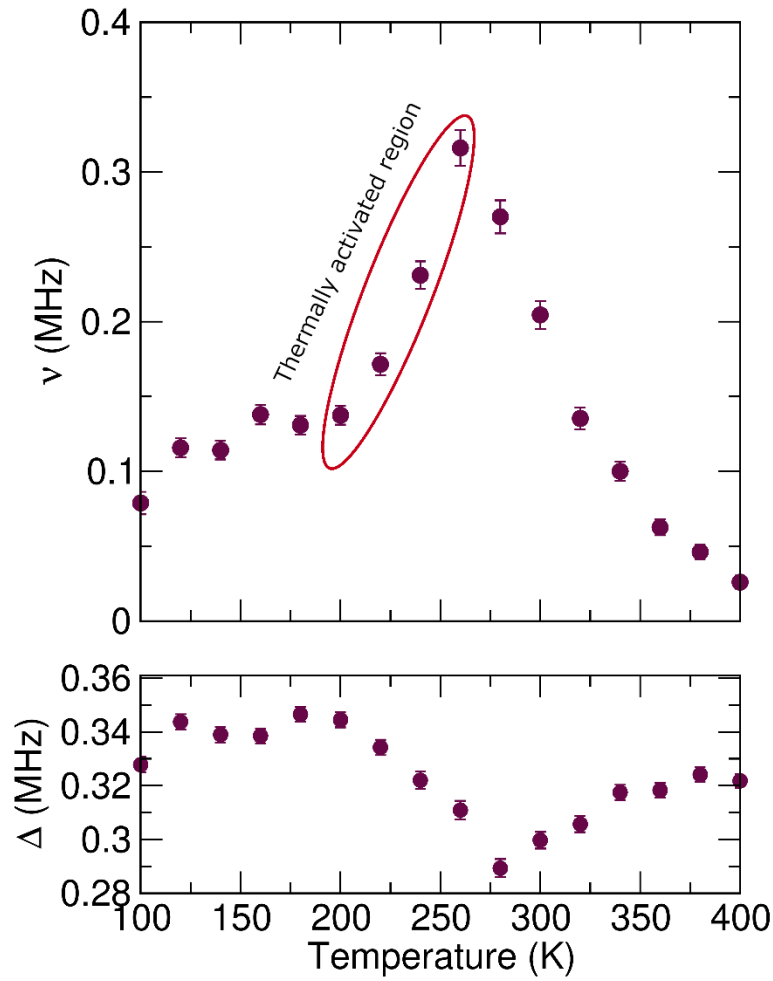


**Figure 3.7** Temperature dependence of the field fluctuation rate ( $\nu$ ) and the field distribution width at the muon stopping site ( $\Delta$ ) for  $\mu^+$ -SR data obtained for tavorite phase  $\text{LiFeSO}_4\text{F}$  between 100 - 400 K at ZF and LFs of 10, 20 G, fit using an exponentially relaxing Kubo-Toyabe function.

The activation energy,  $E_a$  for thermally activated  $\text{Li}^+$  hopping can be calculated from an Arrhenius plot over the identified thermally activated region, considering the Arrhenius equation:

$$\ln(\nu) = \frac{-E_a}{K_B T} + \ln(A) \quad (3.2)$$

where  $\nu$  is the field fluctuation rate calculated at temperature  $T$ ,  $K_b$  is the Boltzmann constant ( $1.3806488 \times 10^{-23} \text{ J K}^{-1}$ ) and  $A$  is a pre-exponential factor. Thus the activation energy can be calculated from the gradient of the straight line fit on the  $\ln(\nu)$  against  $1/T$  plot. The plot over the thermally activated region for the data obtained from  $\mu^+$ -SR measurements on tavorite  $\text{LiFeSO}_4\text{F}$  is shown in Figure 3.8 and from this analysis of the  $\mu^+$ -SR data, an activation energy of  $48 \pm 4 \text{ meV}$  was estimated for tavorite phase  $\text{LiFeSO}_4\text{F}$ . This value is very close to the activation energies estimated for microwave synthesised

LiFePO<sub>4</sub> by Ashton *et al.* and LiFe<sub>1-x</sub>Mn<sub>x</sub>PO<sub>4</sub> by Vidal Laveda *et al.*, which were calculated to be in the range of 46 to 122 meV.<sup>179,180</sup> These similarities are encouraging and indicate that a successful  $\mu^+$ -SR experiment was carried out, without any detrimental effects caused by the presence of highly electronegative F<sup>-</sup> anions within the structure. However, activation energy values of 0.99 eV have been obtained for tavorite phase LiFeSO<sub>4</sub>F from EIS measurements, highlighting the large discrepancies often observed between  $\mu^+$ -SR measurements and bulk measurements.<sup>115</sup> This is thought to be because the muon is not as sensitive to bulk phenomena that can cause extra impedances to ionic motion such as grain boundaries and surface effects that contribute to the long-range lithium diffusion; instead the muon probes the intra-grain diffusion of cations. It should also be noted that due to the low decomposition temperature of the fluorosulphate materials, sintering and/or hot pressing of pellets to improve particle-particle contact and reduce grain boundaries is precluded which could act to further increase activation energies in macroscopic methods such as EIS.

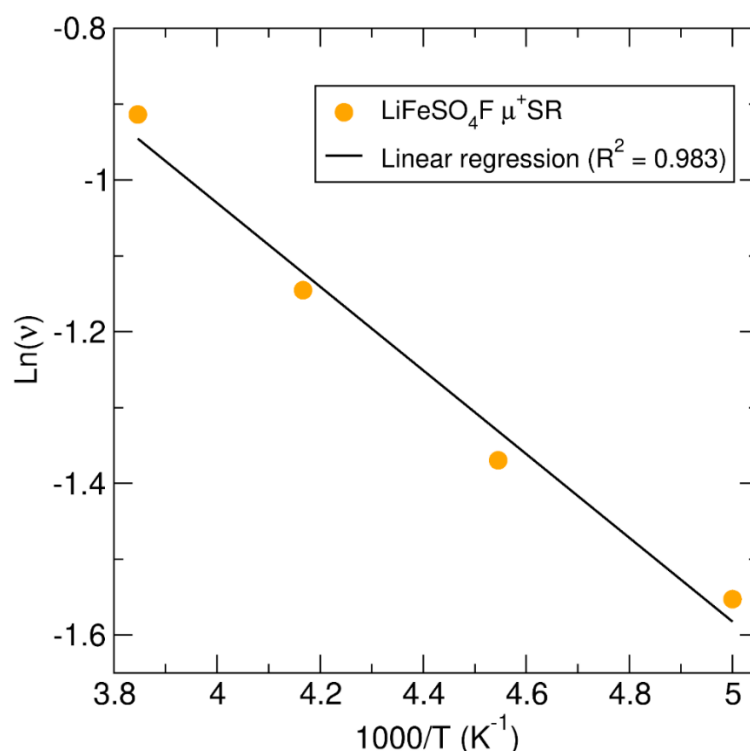


**Figure 3.8** Arrhenius plot of the field fluctuation rate over the thermally activated region calculated from  $\mu^+$ -SR measurements for tavorite phase LiFeSO<sub>4</sub>F. The calculated activation energy,  $E_a = 48$  meV.

To determine the lithium diffusion coefficient, it is essential to have an understanding of the pathways for ionic transport throughout the structure. Lithium ion transport is calculated to occur in a 3D fashion throughout various lithium containing channels in the

structure, but the main hopping paths can be understood by looking at the specific channels along [100] and [010], shown in Figure 3.9. Along the [100] channel there are two distinct hops for the lithium ions, labelled as P1 (5.07 Å) and P2 (3.91 Å) which propagate along the channel to form a zig-zag transport pathway. The same is seen for transport along the [010] direction where the unique hops are labelled as P3 (4.22 Å) and P4 (4.08 Å). While these channels indicate 1D diffusion, by combining different pairs of P1, P2, P3 and P4, a 3D network of ionic diffusion becomes apparent. These pathways have been calculated and described by Tripathi *et al.* and are summarised in Table 3.3.<sup>117</sup>

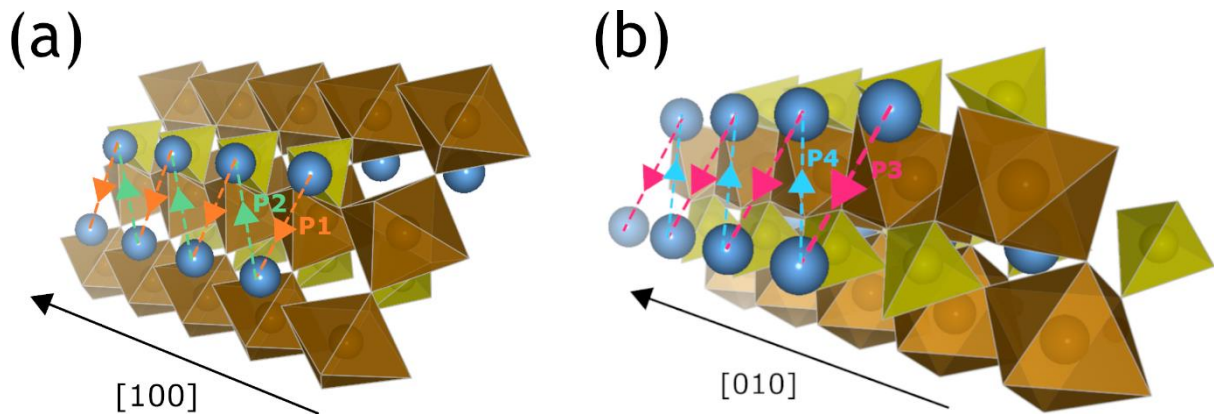


**Figure 3.9** Visualisation of the lithium diffusion pathway along the (a) [100] and (b) directions in tavorite phase  $\text{LiFeSO}_4\text{F}$ . Each pathways consists of two distinct hops, each with unique activation energies, designated coloured arrows, which build-up the zig-zag hopping pattern along the diffusion channel.

**Table 3.3** Diffusion directions for lithium ion transport in tavorite  $\text{LiFeSO}_4\text{F}$  and the distinct hops that describe the ionic diffusion. Adapted from Tripathi *et al.*<sup>117</sup>

Diffusion direction	Hops involved
[100]	P1 + P2
[010]	P3 + P4
[001]	P1 + P4
[101]	P2 + P4
[011]	P1 + P3
[111]	P2 + P3

Equation 3.3 is applied to calculate the lithium diffusion coefficient,  $D_{\text{Li}}$ , from  $\mu^+$ -SR where  $N_i$  represents the number of accessible Li sites in the  $i^{\text{th}}$  path,  $Z_{c,i}$  is the vacancy fraction of the destination site,  $s_i$  is the jump distance and  $\nu$  is the field fluctuation rate obtained from data fitting.

$$D_{Li} = \sum_{i=1}^n \frac{1}{N_i} Z_{v,i} s_i^2 \nu \quad (3.3)$$

It is calculated that the [111] pathway is the lowest energy migration path for ionic diffusion, and indeed even argued that it is the only viable path for diffusion as explained in Section 1.4.4. Therefore, only the [111] pathway will be considered for the calculation of the lithium diffusion coefficient in the microwave prepared LiFeSO<sub>4</sub>F. As a microscopic technique where the muon probe is directly positioned to “see” the lithium diffusion, it is believed that the spin perturbation will be affected by the lowest energy pathway, thus the choice of [111] pathway for diffusional analysis makes sense. If the [111] direction is considered as two hops of lengths 3.91 Å and 4.22 Å, and the Arrhenius line of best fit is extrapolated to gain  $\nu$  for 300 K, then the room temperature diffusion coefficient can be estimated as  $1.71 \times 10^{-9} \text{ cm}^2 \text{ s}^{-1}$ . This matches well with the diffusion coefficients predicted by atomistic modelling that are estimated to be within the range of  $10^{-10}$  to  $10^{-8} \text{ cm}^2 \text{ s}^{-1}$ .<sup>117</sup> The series of microwave synthesised LiFe<sub>1-x</sub>Mn<sub>x</sub>PO<sub>4</sub> ( $x = 0, 0.25, 0.5$  and  $0.75$ ) materials were estimated to have room temperature diffusion coefficients in the range  $2.0 \times 10^{-10}$  to  $6.25 \times 10^{-10} \text{ cm}^2 \text{ s}^{-1}$  which are comparable to that obtained for LiFeSO<sub>4</sub>F albeit lightly lower, highlighting the more favourable diffusion kinetics exhibited by LiFeSO<sub>4</sub>F.<sup>179,180</sup>

These results are furthermore comparable with diffusion coefficients estimated from  $\mu^+$ -SR experiments of LiCoO<sub>2</sub> ( $D_{Li}(300\text{K}) = 7 \times 10^{-10} \text{ cm}^2 \text{ s}^{-1}$ ).<sup>181</sup> As this research represents the first experimental study into local Li<sup>+</sup> diffusion in LiFeSO<sub>4</sub>F, comparisons of obtained diffusion coefficients for this material across other microscopic studies is unavailable. Bulk EIS (a.c.) and d.c. polarization methods have been used to measure conductivities on LiFeSO<sub>4</sub>F pellets by Recham *et al.* yielding electronic conductivities comparable to those obtained for LiFePO<sub>4</sub> and an ionic conductivity of  $4 \times 10^{-6} \text{ S cm}^{-1}$  at 147 °C, although no room temperature conductivity values are presented.<sup>115</sup> Thus, from these  $\mu^+$ -SR experiments it is suggested that tavorite LiFeSO<sub>4</sub>F presents a future cathode technology with improved microscale ionic diffusion kinetics.

### 3.3 Local Na<sup>+</sup> diffusion in Na<sub>2</sub>FePO<sub>4</sub>F measured using $\mu$ <sup>+</sup>-SR

Analogous to intercalation-based LIB technologies, the intercalation and diffusion of Na<sup>+</sup> cations throughout some crystalline structure is the basis of sodium ion battery technology. As previously discussed in Chapter 1, although sodium ion battery energy densities are lower than those obtained for analogous lithium ion batteries (due to the larger size and mass of the Na<sup>+</sup> cation and the decreased working potentials of *ca.* 0.3 V), sodium ion batteries present a promising complementary energy storage option where they are suited to larger scale applications such as stationary storage (*i.e.* grid applications) where size and weight are of less concern. As such, research into advanced sodium ion battery electrodes is ongoing, where the inductive effect can be implemented in designing cathodes that display polyanionic and fluorinated structures in an effort to increase working potentials.

Parallel to the lithium ion case, various phosphate based polyanionic structures are the most explored family of insertion hosts for advanced sodium ion batteries owing to the ease of synthesis/handling, high redox voltage, chemical/thermal stabilities and safe operation.<sup>190</sup> Various compositions have been investigated including NASICON (*e.g.* Na<sub>3</sub>V<sub>2</sub>(PO<sub>4</sub>)<sub>3</sub>), olivine (*e.g.* NaFePO<sub>4</sub>), pyrophosphate (*e.g.* Na<sub>2</sub>FeP<sub>2</sub>O<sub>7</sub>, Na<sub>1.66</sub>Fe<sub>1.17</sub>P<sub>2</sub>O<sub>7</sub>), mixed phosphate (*e.g.* Na<sub>4</sub>Fe<sub>3</sub>(PO<sub>4</sub>)<sub>2</sub>P<sub>2</sub>O<sub>7</sub>) and fluorophosphates (*e.g.* Na<sub>1.5</sub>VPO<sub>4</sub>F<sub>1.5</sub>, Na<sub>2</sub>FePO<sub>4</sub>F) which show deliverable specific capacities close to the theoretical specific capacities and working voltages ranging from 2.8 to 4 V vs. Na/Na<sup>+</sup> highlighting both good electrochemical performances obtained and the flexibility of cathode composition, allowing bespoke tailoring of properties to suit differing applications.<sup>138,191-196</sup> The fluorophosphate Na<sub>2</sub>FePO<sub>4</sub>F, which displays an average operating potential of 3 V vs. Na/Na<sup>+</sup>, is interesting because it invokes the induction effect with further addition of the F<sup>-</sup> anion to enhance the working potential, as has been studied in LiFeSO<sub>4</sub>F cathodes.<sup>197</sup>

Figure 3.10 shows the crystallographic structure of Na<sub>2</sub>FePO<sub>4</sub>F, which consists of a polyhedral framework of face-sharing FeO<sub>4</sub>F<sub>2</sub> building blocks that form Fe<sub>2</sub>O<sub>7</sub>F<sub>2</sub> bioctahedral units which are arranged in parallel chains along the a-axis by connecting F<sup>-</sup> anions. These chains are bridged along the c-axis by the PO<sub>4</sub> groups which form infinite slabs of FePO<sub>4</sub>F in the [101] plane, in between which the Na<sup>+</sup> ions reside.<sup>198</sup> This produces ionic transport pathways along the [100] and the [001] directions, yielding 2D ionic diffusion characteristics. Two unique interlayer sodium sites are apparent, Na1 that lies close to the middle of the layer and Na2 that is nestled close to the FePO<sub>4</sub>F sheets. During cycling, only one Na equivalent is extracted/inserted from/into the structure with the remaining Na<sup>+</sup> cations acting as pillars to stabilise the structure, resulting in observed

volume changes of only 3.7 %.  $\text{Na}_2\text{FePO}_4\text{F}$  can also be cycled vs. Li to yield  $\text{LiNaFePO}_4\text{F}$  upon the first cycle and then is able to operate as a lithium ion battery. Overall,  $\text{Na}_2\text{FePO}_4\text{F}$  is a very interesting polyanionic material for sodium ion batteries, with one of these reasons being the 2D pathways for Na-ion diffusion which could promote favourable charge/discharge behaviour.

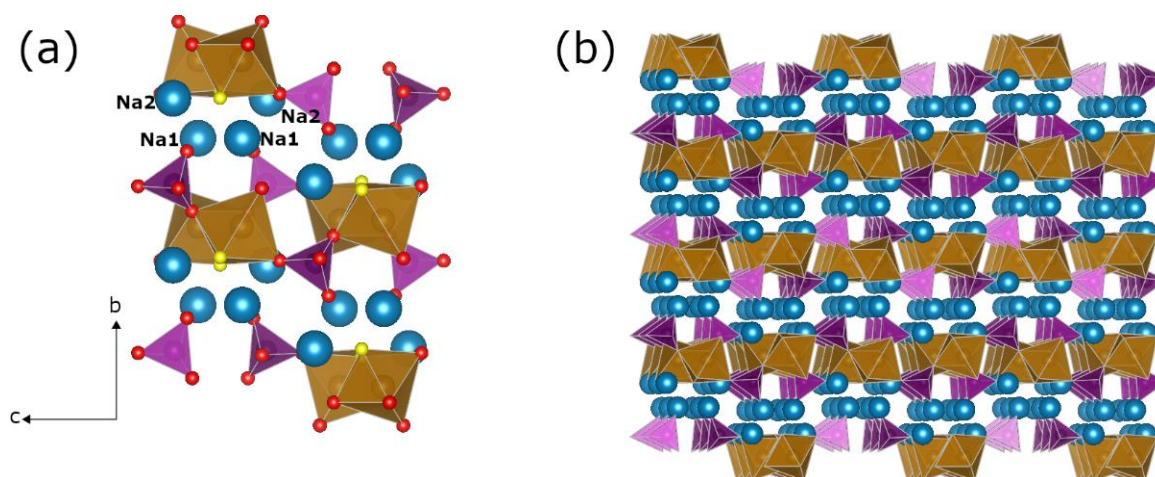


**Figure 3.10** Visualisation of the crystallographic structure of *Pbcn*  $\text{Na}_2\text{FePO}_4\text{F}$  showing (a) the unit cell and the positions of the two unique sodium sites and (b) expansion of the structure to highlight its layered nature allowing for  $\text{Na}^+$  diffusion along the [100] and [001] directions.

Sodium ions are presented by blue spheres and  $(\text{PO}_4)^{3-}$  and  $\text{FeO}_4\text{F}_2$  units are represented by purple and brown polyhedral respectively. Oxygen and fluorine ions are represented by red and yellow spheres respectively.

The results presented in the previous section show that the microscopic lithium diffusion in fluorine containing polyanionic cathode material  $\text{LiFeSO}_4\text{F}$  can be measured using  $\mu^+$ -SR, with no preclusion of the lithium diffusion measurement occurring despite the presence of highly electronegative  $\text{F}^-$  anions which could bind too strongly to the muon spin ensemble. Thus, similar diffusional studies should be able to be carried out on  $\text{Na}_2\text{FePO}_4\text{F}$  in order to assess the microscopic diffusion kinetics of the  $\text{Na}^+$  ions. Already drawing many parallels with lithium ion battery research, the  $\mu^+$ -SR technique has been applied to study the diffusion properties of  $\text{Na}^+$  cations in several compounds. For example, cathode materials  $\text{NaCoO}_2$ ,  $\text{NaFePO}_4$ ,  $\text{NaMn}_2\text{O}_4$ ,  $\text{NaV}_2\text{O}_4$  and solid state electrolyte candidate  $\text{Na}_{1.5}\text{La}_{1.5}\text{TeO}_6$ .<sup>158,175,183,199,200</sup>

### 3.3.1 Synthesis and structural characterisation of $\text{Na}_2\text{FePO}_4\text{F}$

The  $\text{Na}_2\text{FePO}_4\text{F}$  powder was synthesised using a conventional solid state method as described in Section 2.2.4. Figure 3.11 shows the PXR pattern obtained for the synthesised powder against a reference pattern for *Pbcn*  $\text{Na}_2\text{FePO}_4\text{F}$  obtained from the

ICSD (collection code 167044).<sup>201</sup> The formation of majority  $\text{Na}_2\text{FePO}_4\text{F}$  phase is evidenced from the sharp peaks in the measured data matching the  $\text{Na}_2\text{FePO}_4\text{F}$  reference pattern peaks. However, a small amount of impurity phase(s) is evident from a cluster of peaks between  $2\theta$  values of approximately 30 to 40 °. One phase that could be attributed to two of these impurity peaks is  $\text{Fe}_2\text{O}_3$ ; however, the synthesised powder showed no response when a magnet was placed in close proximity with the powder, where an attraction/repulsion response would be expected for  $\text{Fe}_2\text{O}_3$ . If the impurity cannot conduct  $\text{Na}^+$  cations, then its contribution (if any) to the muon spin perturbation will be decoupled upon application of longitudinal fields and so can be negated.

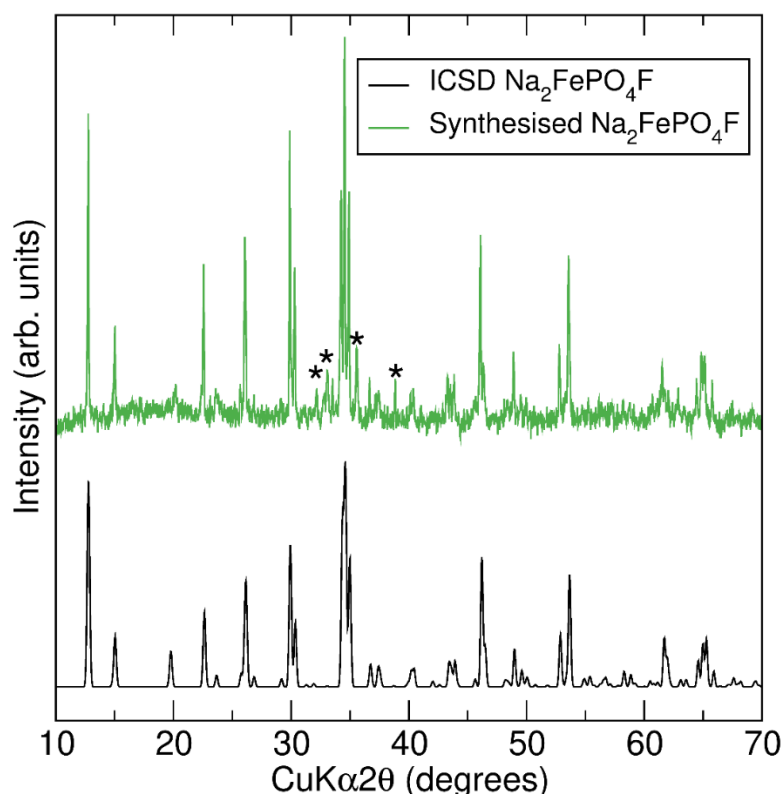


**Figure 3.11** PXR D data obtained for  $\text{Na}_2\text{FePO}_4\text{F}$  synthesised by a solid state method. The reference pattern was obtained from the ICSD (collection code 167044). The presence of an unidentified impurity phase is highlighted by asterisks.

Figure 3.12 shows the results obtained from a Rietveld refinement performed using a *Pbcn*  $\text{Na}_2\text{FePO}_4\text{F}$  model fit to the PXR D data. The refinement was prepared for 19 variables, including scale factor, zero point, sample displacement, 6 background coefficients (fitted with a Chebyshev function), lattice parameters, atomic position and site occupancy of Fe and P atoms, microstrain and size parameters. All other atomic positions, displacements parameters and site fractions were not refined. The region containing the majority of the small peaks between 30 to 40 ° attributed to impurity

phases is highlighted. The fit obtained is shown to be a good fit despite these impurities, with the difference function consisting of mainly background signal from the measured data. All of the major, most intense peaks can be indexed to the orthorhombic *Pbcn* space group. Table 3.4 details the calculated lattice parameters and goodness of fit parameters  $R_{wp}$  and  $\chi^2$  obtained from the fit. The calculated lattice parameters and the cell volume show good agreement with previously reported literature values including both experimentally obtained values and those calculated using computational methods. For example, a difference of  $< 1\%$  is calculated for the sample presented here and for experimental and calculated parameters presented by Tripathi *et al.*<sup>139</sup>

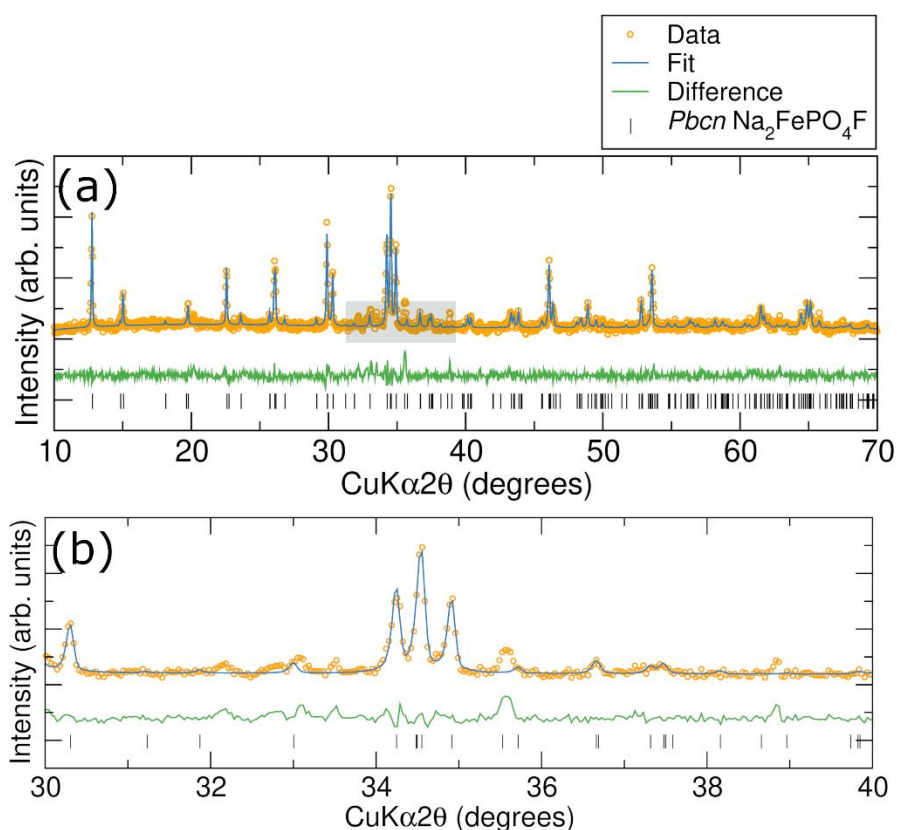


**Figure 3.12** Rietveld refinement between (a) 10 to 70 degrees for the solid-state synthesised tavorite  $\text{Na}_2\text{FePO}_4\text{F}$  PXRD data using a model consisting of *Pbcn*  $\text{Na}_2\text{FePO}_4\text{F}$ , with  $R_{wp} = 3.97\%$  and  $\chi^2 = 1.42$ . Impurities mainly in the region between 30 to 40 degrees are shown shaded in blue and magnified for clarity in (b).

**Table 3.4** Calculated lattice parameters, atomic parameters and goodness of fit parameters  $R_{wp}$  and  $\chi^2$ , for  $\text{Na}_2\text{FePO}_4\text{F}$  obtained from the Rietveld refinement using a model containing  $Pbcn$   $\text{Na}_2\text{FePO}_4\text{F}$ .

$\text{Na}_2\text{FePO}_4\text{F}$		$R_{wp} = 3.97\%$		$\chi^2 = 1.42$	$V = 859.1(8) \text{ \AA}^3$	
$Pbcn$		$a = 5.241(2) \text{ \AA}$		$b = 13.881(4) \text{ \AA}$	$c = 11.807(4) \text{ \AA}$	
		$\alpha = 90^\circ$		$\beta = 90^\circ$	$\gamma = 90^\circ$	
Atom	Site	x	y	z	Uiso ( $\text{ \AA}^2$ )	Frac.
Na1	8d	0.2633	0.2446	0.3281	0.01	1.0
Na2	8d	0.2395	0.1249	0.0836	0.01	1.0
Fe1	8d	0.229(3)	0.0067(9)	0.3301(7)	0.01	1.021(19)
P1	8d	0.1857(35)	0.3776(11)	0.875(14)	0.01	1.003(29)
O1	8d	0.2663	0.3882	-0.0396	0.01	1.0
O2	8d	0.2846	0.2837	0.1330	0.01	1.0
O3	8d	-0.0905	0.3948	0.1027	0.01	1.0
O4	8d	0.3398	0.4636	0.1515	0.01	1.0
F1	4c	0.0000	0.1238	0.2500	0.01	1.0
F2	4c	0.5000	0.1009	0.2500	0.01	1.0

### 3.3.2 Muon spin spectroscopy measurements on $\text{Na}_2\text{FePO}_4\text{F}$

The  $\mu^+$ -SR technique was used here in order to prove the microscopic diffusion of  $\text{Na}^+$  cations within the  $\text{Na}_2\text{FePO}_4\text{F}$  structure. Measurements were carried out using the EMU instrument at the ISIS Pulsed Neutron and Muon Source, whereby a beam of spin polarised positive muons was fired at the powder sample (*ca.* 1 g in a titanium holder) where they become implanted and stop at sites close to electronegative species, before decaying with a mean lifetime of 2.2  $\mu\text{s}$ . In the case of  $\text{Na}_2\text{FePO}_4\text{F}$ , muons are likely to be implanted in interstitial sites close to  $\text{F}^-$  or  $\text{O}^{2-}$  sites. This places the muons in excellent positions to effectively “see” the diffusing  $\text{Na}^+$  cations as shown in Figure 3.13.

During the experiment, measurements were taken in a temperature range of 200 to 600 K with an interval of 20 K between subsequent temperatures. At each temperature, measurements were taken at zero field and longitudinal fields of 10 and 20 G. Raw data obtained from measurements at 300 K is shown in Figure 3.14, where the time evolution of the muon spin ensemble asymmetry is presented. An initial fast and field independent relaxation is observed up to approximately 1.5  $\mu\text{s}$ , corresponding to the interactions between the muon spin ensemble and the magnetic moments belonging to the 3d electrons on  $\text{Fe}^{2+}$ . After 1.5  $\mu\text{s}$ , the relaxations are slower and show a dependence on the

applied field strength. These relaxations are caused by interactions between the muon spin ensemble and the local nuclear magnetic moments e.g.  $^{23}\text{Na}$ ,  $^{57}\text{Fe}$ ,  $^{31}\text{P}$  and  $^{19}\text{F}$ . It is observed that the relaxation is slower at higher magnitudes of applied longitudinal fields, corresponding to the greater extent of decoupling between muon spin ensemble and the local nuclear magnetic moments.

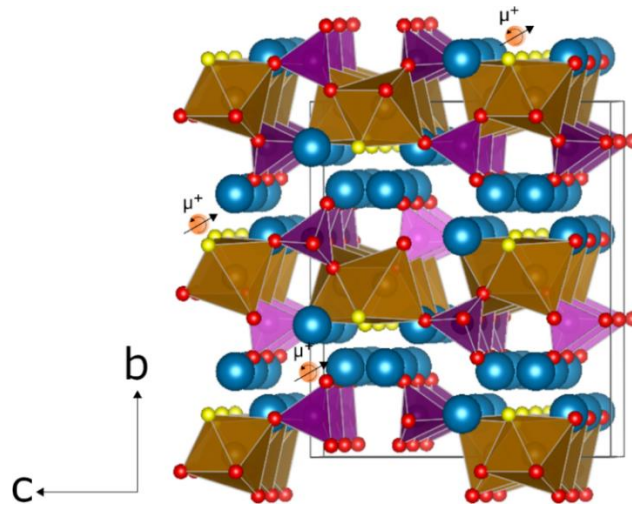


**Figure 3.13** Visualisation of some possible stopping sites for muons implanted into Na<sub>2</sub>FePO<sub>4</sub>F powder. Muons (orange spheres) implanted close to electronegative sites such as O<sup>2-</sup> (red spheres) and F<sup>-</sup> (yellow spheres) are in good positions to “see” the Na<sup>+</sup> (blue spheres) diffusion.

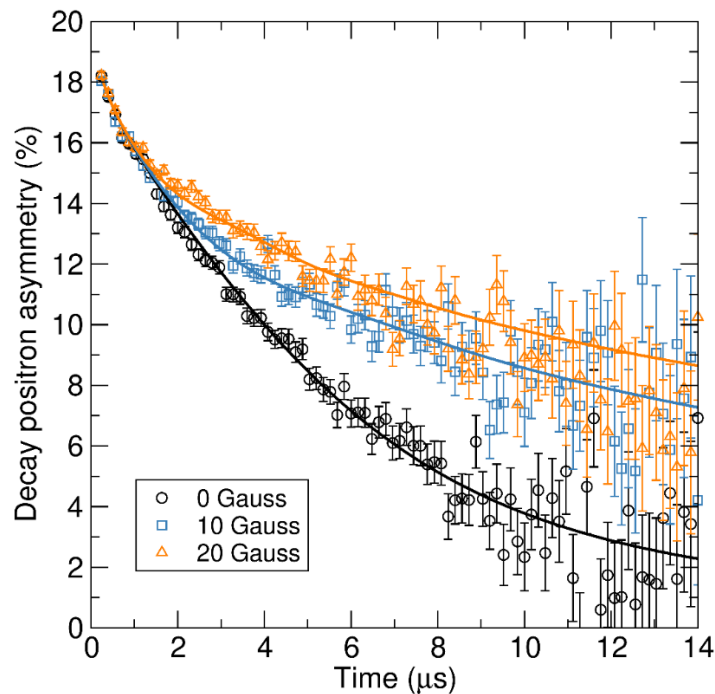


**Figure 3.14** Raw  $\mu^+$ -SR data obtained for Na<sub>2</sub>FePO<sub>4</sub>F measured at 300 K at zero field (black circles) and applied longitudinal fields of 10 G (blue squares) and 20 G (orange triangles) alongside the fit to the data using a dynamic Kubo-Toyabe function (solid lines).

At each temperature, an equation comprising of a dynamic Kubo-Toyabe function alongside an exponentially relaxing term to account for interactions with  $3d$  magnetic moments and a constant background component (presented earlier in equation 3.1) was fit to the obtained raw data from the  $\mu^+$ -SR measurements using the WiMDA program, in order to extract values for the field fluctuation rate ( $\nu$ ) which corresponds to the kinetics of the  $\text{Na}^+$  diffusion and the local field distribution width ( $\Delta$ ).

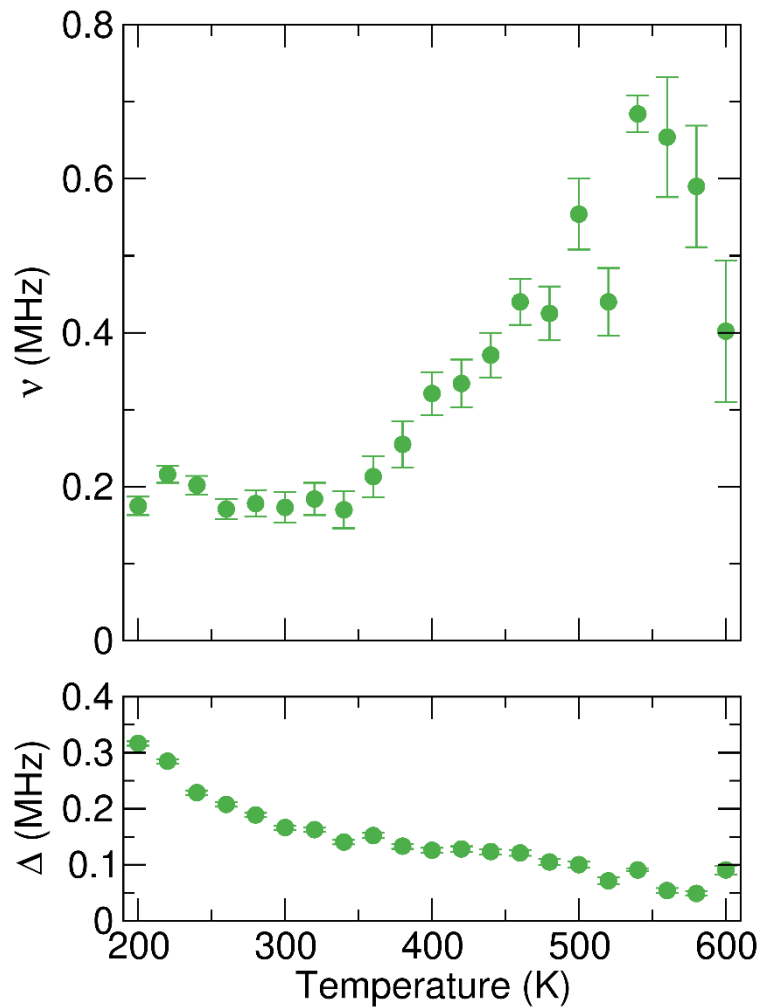


**Figure 3.15** Temperature dependence of the field fluctuation rate ( $\nu$ ) and the field distribution width at the muon stopping site ( $\Delta$ ) for  $\mu^+$ -SR data obtained for tavorite phase  $\text{Na}_2\text{FePO}_4\text{F}$  between 200 - 600 K at ZF and LFs of 10 and 20 G, fit using an exponentially relaxing Kubo-Toyabe function.

The temperature dependence of the  $\nu$  and  $\Delta$  parameters, over the applied temperature range are shown in Figure 3.15. The field fluctuation rate provides information on the  $\text{Na}^+$  hopping rates and thus best describes the  $\text{Na}^+$  diffusion. From the values obtained from the data fitting it can be seen that the  $\nu$  values begin to steadily increase from  $\approx 360$  K to 540 K which is most likely precipitated by fast  $\text{Na}^+$  diffusion throughout the

structure. At temperatures higher than 540 K, the field fluctuation rates begin to decrease again, indicating that the  $\text{Na}^+$  diffusion has become too fast for the  $\mu^+$ -SR technique to detect. The temperature dependence of the local field distribution width,  $\Delta$  shows a general trend of a steady decrease as the temperature is increased, with reasonably steady values between 0.15 to 0.10 MHz over the thermally activated region of 360 K to 540 K which is often observed in these types of experiments. To calculate the activation energy,  $E_a$ , for ionic diffusion, the region between 360 K to 540 K was analysed. The Arrhenius analysis is shown in Figure 3.16 where an activation energy of  $E_a = 102$  meV can be estimated from the gradient. In comparison to other sodium containing materials studied using  $\mu^+$ -SR, the activation energy is smaller, but of similar magnitude to those reported in the literature, for example, activation energies for thermally activated in  $\text{Na}^+$  diffusion  $\text{Na}_{1.5}\text{La}_{1.5}\text{TeO}_6$ ,  $\text{NaMn}_2\text{O}_4$  and  $\text{NaV}_2\text{O}_4$  were estimated to be 163, 180 and 225 meV respectively while  $\text{Na}_{0.7}\text{CoO}_2$  was calculated to have a higher activation energy of 478 meV.<sup>175,185,199,200</sup> It is also evident that the activation energies calculated for  $\text{Na}^+$  diffusion are larger than those values commonly obtained for lithium containing cathode materials *e.g.*  $E_a = 48$  meV for  $\text{LiFeSO}_4\text{F}$ , indicating more sluggish diffusion kinetics for  $\text{Na}^+$  diffusion which is most likely attributed to the larger mass of the  $\text{Na}^+$  ion ( $22.9898 \text{ g mol}^{-1}$ ) compared to  $\text{Li}^+$  ( $6.941 \text{ g mol}^{-1}$ ).

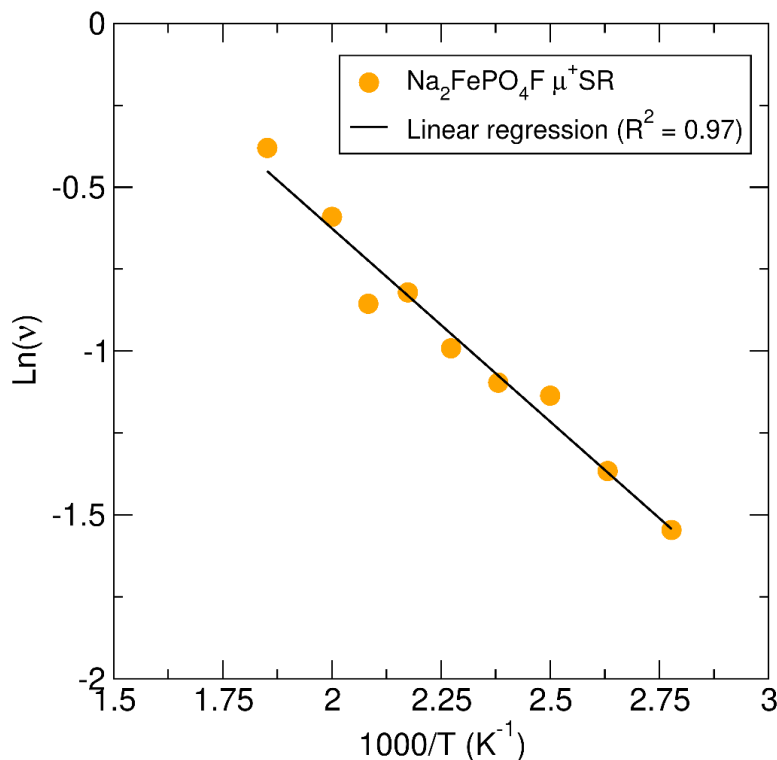


**Figure 3.16** Arrhenius plot of the field fluctuation rate over the thermally activated region calculated from  $\mu^+$ -SR measurements for  $\text{Na}_2\text{FePO}_4\text{F}$ . The calculated activation energy,  $E_a$ , is calculated as 102 meV.

Considering that Na<sup>+</sup> diffusion is expected to occur through channels along the [100] and [001] directions within the Na<sub>2</sub>FePO<sub>4</sub>F structure, the diffusion coefficient can be calculated from equation 3.3 as  $D_{\text{Na}[100]} = a^2 \nu / 8$  and  $D_{\text{Na}[001]} = c^2 \nu / 8$  where  $a$  and  $c$  are the lattice parameters derived from Rietveld refinements,  $N_{[100]} = 2$ ,  $S_{[100]} = a/2$ ,  $N_{[001]} = 2$ ,  $S_{[001]} = c/2$  and  $\nu$  is the field fluctuation rate obtained from the  $\mu^+$ -SR fits. This models the Na<sup>+</sup> ions hopping to interstitial sites along each channel. Therefore, the diffusion coefficients can be estimated at 300 K as  $D_{\text{Na}[100]} = 5.94 \times 10^{-11} \text{ cm}^2 \text{ s}^{-1}$  and  $D_{\text{Na}[001]} = 3.01 \times 10^{-10} \text{ cm}^2 \text{ s}^{-1}$  with a combined diffusion coefficient calculated as  $D_{\text{Na}} = 3.60 \times 10^{-10} \text{ cm}^2 \text{ s}^{-1}$ . Table 3.5 details the diffusion coefficients obtained at 300 K and an elevated temperature of 400 K where diffusion occurs at faster rates. The values presented here compare favourably with other values presented in the literature, for example room temperature coefficients of  $3.99 \times 10^{-11} \text{ cm}^2 \text{ s}^{-1}$  and  $1.1 \times 10^{-11} \text{ cm}^2 \text{ s}^{-1}$  were calculated for Na<sub>0.7</sub>CoO<sub>2</sub> and NaMn<sub>2</sub>O<sub>4</sub> using  $\mu^+$ -SR, placing Na<sub>2</sub>FePO<sub>4</sub>F as a good contender for future cathode development.

**Table 3.5** Calculated  $D_{\text{Na}}$  values for Na<sub>2</sub>FePO<sub>4</sub>F at 300 K and 400 K, showing individual [100] and [001] diffusion coefficients and the combined diffusion coefficient obtained from the sum of the two pathways according to equation 3.3.

Temp (K)	$D_{\text{Na}[100]} (\text{cm}^2 \text{ s}^{-1})$	$D_{\text{Na}[001]} (\text{cm}^2 \text{ s}^{-1})$	$D_{\text{Na}} \text{ combined} (\text{cm}^2 \text{ s}^{-1})$
300	$5.94 \times 10^{-11}$	$3.01 \times 10^{-10}$	$3.60 \times 10^{-10}$
400	$1.10 \times 10^{-10}$	$5.59 \times 10^{-10}$	$6.69 \times 10^{-10}$

### 3.4 Local Na<sup>+</sup> diffusion in maricite NaFePO<sub>4</sub> measured using $\mu^+$ -SR

The olivine phase of NaFePO<sub>4</sub> is the direct sodium analogue of olivine LiFePO<sub>4</sub>, both exhibiting 1D Li<sup>+</sup> and Na<sup>+</sup> diffusion along the [010] direction. However, olivine NaFePO<sub>4</sub> is not the most thermodynamically stable configuration and thus synthesis via conventional techniques is precluded. The thermodynamically stable phase is named the maricite phase and its framework bears strong resemblance to that of the olivine phase but with the Fe<sup>2+</sup> and Na<sup>+</sup> cations essentially swapping crystallographic sites, most likely caused by the larger ionic radius of Na<sup>+</sup> compared to Li<sup>+</sup>.<sup>202</sup> Consequently, 1D chains of edge-sharing FeO<sub>6</sub> octahedra are formed along the [010] direction with no cationic diffusion channels (Figure 3.17) formed thus hindering Na<sup>+</sup> diffusion throughout the structure. As a result, maricite NaFePO<sub>4</sub> has been believed to be electrochemically inactive, but recent reports have shown that this is not the case with amorphous samples and unexpectedly with crystalline samples at elevated temperatures.<sup>137,203-205</sup>

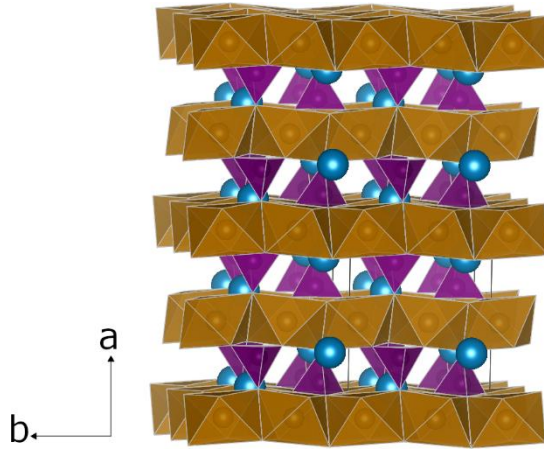


**Figure 3.17** Structure of the maricite phase of  $\text{NaFePO}_4$  where  $\text{Fe}^{2+}$  and  $\text{Na}^+$  essentially swap crystallographic sites compared to the olivine phase, forming chains of  $\text{FeO}_6$  (brown octahedra) along the  $[010]$  direction and immobile  $\text{Na}^+$  cations (blue spheres). Purple octahedra represent  $\text{PO}_4$  groups.

In order to investigate whether any microscopic  $\text{Na}^+$  diffusion occurs in maricite  $\text{NaFePO}_4$ ,  $\mu^+$ -SR measurements were carried out on a *ca.* 1 g powder sample synthesised by a microwave-assisted solvothermal method from heterometallic alkoxide precursors as detailed by J. Vidal Laveda. The sample used here has been characterised using PXRD to confirm its phase purity in the PhD thesis of J. Vidal Laveda.<sup>206</sup> The powder sample was packed inside a titanium holder and placed in the EMU instrument (at ISIS Neutron and Muon Source) for measurements.

Measurements were performed within a temperature range of 200 to 600 K with an interval of  $\approx 20$  K between subsequent temperature set-points. At each temperature, measurements were taken at zero field and applied longitudinal fields of 10 and 20 G to decouple the interactions between the muon spin ensemble and the local nuclear magnetic fields. Figure 3.18 presents the raw data collected at 300 K alongside fits to the data calculated using the Keren function. The Keren function is an analytical expression of the Abragam function and describes the time evolution of the decay positron asymmetry,  $P_z(t)$  with respect to the field fluctuation rate,  $\nu$  and the local field distribution width,  $\Delta$  and is comparable to the dynamic Kubo-Toyabe function.<sup>207</sup> The Keren function is shown in equation 3.4 where  $P_z(t)$ ,  $\nu$  and  $\Delta$  are as previously described,  $\omega$  is the Larmor precession frequency in the applied longitudinal field and  $\lambda$  accounts for the temperature independent relaxation associated with the electronic moments (*e.g.* arising from  $3d$  electrons on  $\text{Fe}^{2+}$ ).

$$P_z(t) = \exp[-\Gamma(\Delta, \nu, \omega, t)t] \exp(-\lambda t) \quad (3.4)$$

The time evolution of the decay positron asymmetry exhibits the same features as previously presented in this chapter for  $\text{LiFeSO}_4\text{F}$  and  $\text{Na}_2\text{FePO}_4\text{F}$ : a fast, initial temperature independent relaxation accounted for *via* the interactions between the muon spin ensemble and the electronic magnetic moments arising from  $3d$  electrons on  $\text{Fe}^{2+}$ , and a slower more temperature dependent relaxation attributed to interactions between the muon spin ensemble and local nuclear moments for,  $^{23}\text{Na}$ ,  $^{57}\text{Fe}$  and  $^{31}\text{P}$ , including interactions caused by diffusing ionic species. From fitting the Keren function to the data, the  $\nu$  and  $\Delta$  parameters could be extracted and their temperature dependence is shown in Figure 3.19.

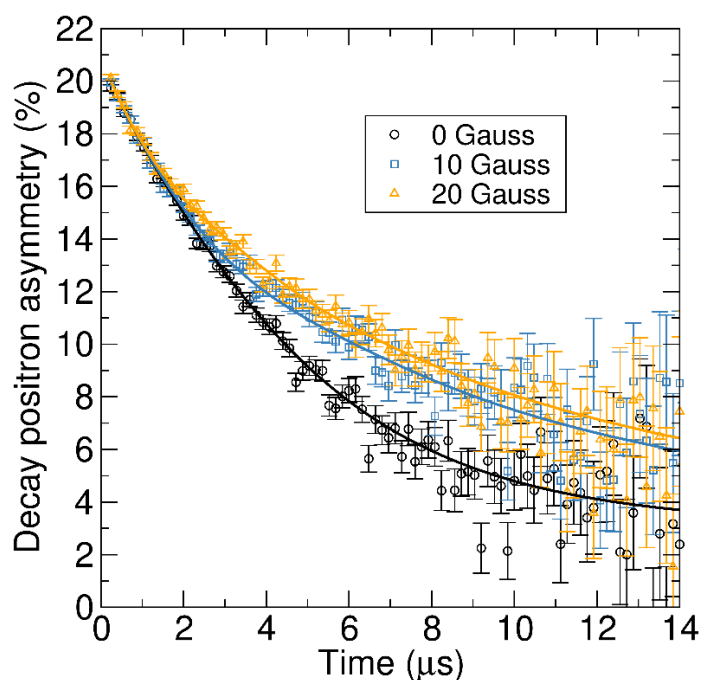


**Figure 3.18** Raw  $\mu^+$ -SR data obtained for maricite phase  $\text{NaFePO}_4$  measured at 300 K at zero field (black circles) and applied longitudinal fields of 10 G (blue squares) and 20 G (orange triangles) alongside the fit to the data using the Keren function (solid lines).

Unlike the field fluctuation rates presented earlier in this chapter (and those present in the literature for similar measurements) there is a distinct lack of a thermally activated region for maricite  $\text{NaFePO}_4$ . The field fluctuation rates remain consistently below 0.1 MHz across the entire temperature range, even at high temperatures of 600 K. This strongly suggests that there is no occurrence of  $\text{Na}^+$  ionic diffusion throughout the structure as it is highly unlikely that, should there be  $\text{Na}^+$  diffusion, it is too fast for the  $\mu^+$ -SR technique to detect. The local field distribution width,  $\Delta$  shows a steady decreasing trend from  $\approx 0.2$  MHz to 0.1 MHz over the temperature range which could possibly be attributed to immobile ions increasingly rattling in voids as the temperature is increased. From our observations on the  $\mu^+$ -SR results collected for maricite  $\text{NaFePO}_4$ , it can be

strongly inferred that thermally activated  $\text{Na}^+$  diffusion is precluded even at temperatures up to 600 K, supporting the narrative of electrochemical activity induced by the formation of amorphous  $\text{FePO}_4$  upon initial desodiation as suggested by Kim *et al*, and suggests that the parent  $\text{NaFePO}_4$  material is required to undergo some further treatment *e.g.* ball milling or initial desodiation to promote electrochemical activity.<sup>137</sup>

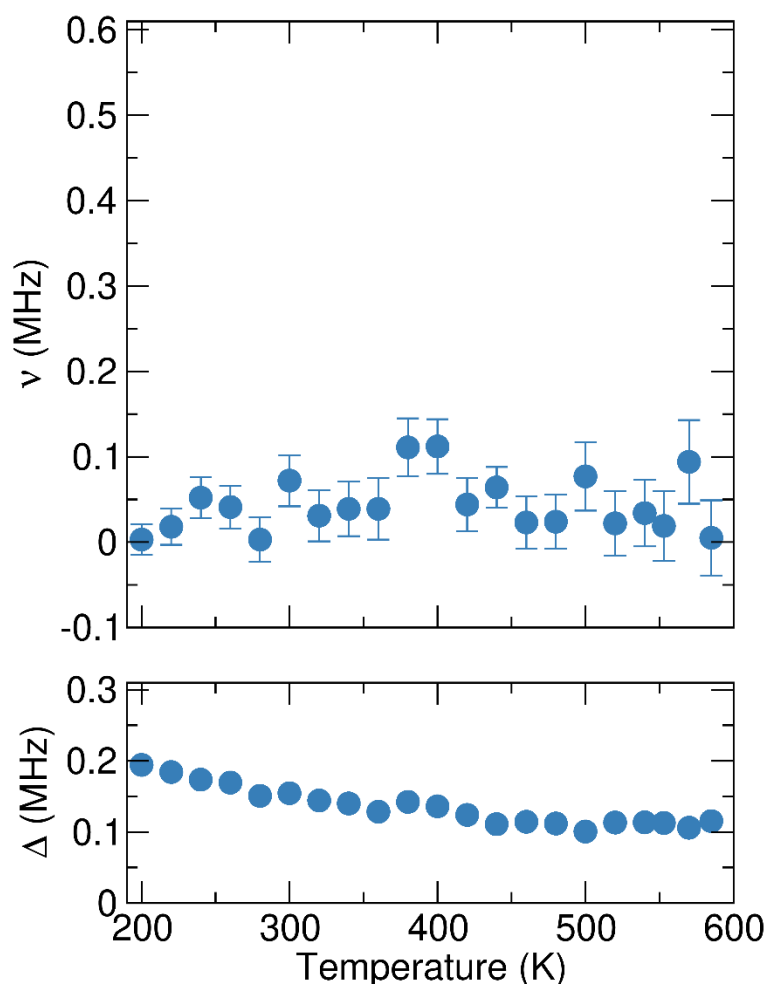


**Figure 3.19** Temperature dependence of the field fluctuation rate ( $\nu$ ) and the field distribution width at the muon stopping site ( $\Delta$ ) for  $\mu^+$ -SR data obtained for maricite phase  $\text{NaFePO}_4$  between 200 - 600 K at ZF and LFs of 10 and 20 G, fit using the Keren function.

### 3.5 Conclusions

In this chapter, muon spin spectroscopy has been utilised to investigate microscopic ionic diffusion in polyanionic cathode materials tavorite phase  $\text{LiFeSO}_4\text{F}$ ,  $\text{Na}_2\text{FePO}_4\text{F}$  and maricite phase  $\text{NaFePO}_4$ . The  $\text{LiFeSO}_4\text{F}$ , which was synthesised by a low temperature microwave-assisted solvothermal method, exhibits an onset of  $\text{Li}^+$  diffusion at  $\approx 200$  K and a low activation energy of 48 meV which suggests that the thermally activated  $\text{Li}^+$  diffusion process is facile even at temperatures below room temperature. A diffusion coefficient of  $D_{\text{Li}} = 1.71 \times 10^{-9} \text{ cm}^2 \text{ s}^{-1}$  was calculated from the  $\mu^+$ -SR data which compares

well with other cathode materials measured with  $\mu^+$ -SR and with expected diffusion coefficients, suggesting good intra-grain transport of  $\text{Li}^+$  ions. The thermally activated sodium diffusion in a sample of solid-state synthesised  $\text{Na}_2\text{FePO}_4\text{F}$  was calculated, using  $\mu^+$ -SR data, as 102 meV with higher diffusion onset temperatures (*ca.* 360 K) compared to Li-containing cathodes and lower diffusion coefficients of  $3.60 \times 10^{-10} \text{ cm}^2 \text{ s}^{-1}$  (300 K) and  $6.69 \times 10^{-10} \text{ cm}^2 \text{ s}^{-1}$  (400 K) were calculated for  $\text{Na}_2\text{FePO}_4\text{F}$  highlighting the more sluggish kinetics of the heavier  $\text{Na}^+$  ion. The diffusion kinetics of  $\text{Na}_2\text{FePO}_4\text{F}$  however, are enhanced compared to other sodium containing cathodes studied by  $\mu^+$ -SR, indicating that it could be an attractive option for advanced sodium ion battery cathodes.

The fluorine containing nature of both  $\text{LiFeSO}_4\text{F}$  and  $\text{Na}_2\text{FePO}_4\text{F}$  and their ability to be studied using  $\mu^+$ -SR to ascertain the microscopic ionic diffusion characteristics have also proven that strong  $\mu^+$ - $\text{F}^-$  binding does not preclude the measurement of local diffusion for the first time. The  $\mu^+$ -SR technique allows for the microscale diffusion to be directly probed, yielding valuable insight into the intrinsic, atomic scale diffusion, with results indicating much more favourable kinetics compared to bulk scale methods, suggesting that advanced engineering of cathodes could unlock increasingly facile and fast diffusion of cations.

The  $\mu^+$ -SR collected and analysed for the maricite phase of  $\text{NaFePO}_4$  showed no evidence of  $\text{Na}^+$  diffusion even at elevated temperatures up to 600 K, which supports the general evidence pertaining to the immobility of the  $\text{Na}^+$  ions within the structure. This serves to further verify that the application of the  $\mu^+$ -SR technique to study ionic diffusion yields meaningful results.

Regarding future work,  $\mu^+$ -SR measurements of local  $\text{Li}^+$  diffusion in the triplite phase of  $\text{LiFeSO}_4\text{F}$  should be undertaken to investigate any differences in microscopic cation motion in both of these candidate electrode materials. Considering the proposed disorder between Li/Fe in the triplite structure, carrying out local-scale structural analysis on both phases using *e.g.* neutron total scattering and PDF analysis, could reveal the true nature of the Li/Fe ordering in these samples, would also help to provide a greater insight into the differences and the structure-property relationships between these two highly interesting  $\text{LiFeSO}_4\text{F}$  polymorphs.

Furthermore, carrying out  $\mu^+$ -SR measurements to study the  $\text{Li}^+$  diffusion properties in the lithium containing analogue of  $\text{Na}_2\text{FePO}_4\text{F}$ ,  $\text{Li}_2\text{FePO}_4\text{F}$  would allow some interesting comparisons between both the  $\text{Na}_2\text{FePO}_4\text{F}$  studied here and  $\text{LiFePO}_4$  that has been studied elsewhere.

The work presented here is limited to the thermally activated microscopic ionic diffusion, with  $\mu^+$ -SR measurements carried out on pristine powder samples. Recent work in our group with collaborators at ISIS has developed a cell that is suitable for *in-situ* muon measurements where the electrochemically induced ionic diffusion can be studied. Carrying on this work to investigate the *in-situ* behaviour of the local-scale  $\text{Li}^+$  and  $\text{Na}^+$  diffusion in both  $\text{LiFeSO}_4\text{F}$  and  $\text{Na}_2\text{FePO}_4\text{F}$  would also be a logical next step for taking forward the work presented in this chapter.

## 4 Microwave assisted sol-gel synthesis of layered $\text{LiNi}_x\text{Mn}_y\text{Co}_{1-x-y}\text{O}_2$ cathodes

### 4.1 Introduction

The transition metal layered oxides present a promising option for lithium ion battery cathodes which is clearly evidenced by the commercialisation and success of materials such as  $\text{LiCoO}_2$  and  $\text{LiNi}_{1/3}\text{Mn}_{1/3}\text{Co}_{1/3}\text{O}_2$  (NMC-111). However, the ever-increasing necessity of higher energy density batteries coupled with the problematic safety and procurement issues regarding cobalt has led researchers to consider new layered oxides containing limited quantities of cobalt within the structure.

High nickel content NMCs present a highly attractive option due to the higher specific capacities (potentially greater than  $200 \text{ mAh g}^{-1}$ ) unlocked by the increased nickel content *via* the  $\text{Ni}^{2+}/\text{Ni}^{3+}/\text{Ni}^{4+}$  redox-active couples that provide the majority of the reversible capacity in these cathodes.<sup>208</sup> It is difficult to oxidise beyond  $\text{Co}^{3.6+}$  without oxidising  $\text{O}^{2-}$  and the  $\text{Mn}^{4+}$  present is electrochemically inactive thus the increased capacities rely heavily on nickel content.<sup>209</sup> The presence of  $\text{Mn}^{4+}$  and  $\text{Co}^{3+}$  within these structures is still required to facilitate improved stabilities and cyclability, improved rate capabilities and reduced degrees of Li/Ni site mixing.<sup>210</sup> Thus the layered oxides with compositions  $\text{LiNi}_x\text{Mn}_y\text{Co}_{1-x-y}\text{O}_2$  where  $x \geq 0.5$  are a focus. Compositions such as  $\text{LiNi}_{0.6}\text{Mn}_{0.2}\text{Co}_{0.2}\text{O}_2$  (NMC-622) and  $\text{LiNi}_{0.8}\text{Mn}_{0.1}\text{Co}_{0.1}\text{O}_2$  (NMC-811) have garnered much attention for commercialisation in EVs due to the high energy densities afforded by their increased nickel contents compared to NMC-111. For example, many reports of NMC-811 presented in the literature have been shown to achieve discharge capacities of  $\approx 200 \text{ mAh g}^{-1}$  which presents a great improvement over the  $\approx 160 \text{ mAh g}^{-1}$  delivered by NMC-111.<sup>211-214</sup>

Many synthetic routes to these layered oxides in the literature proceed through a co-precipitation method, however a sol-gel route has been the focus in the work presented here due to several advantages over conventional methods including excellent mixing on the atomic level facilitated by this process alongside lower synthesis temperatures, shorter heating times and smaller particle sizes at the nanometre level.<sup>7-12</sup> Furthermore, the addition of a microwave-assisted heating step has been utilised here owing to the advantages presented by microwave-assisted sintering including rapid and uniform heat generation which could facilitate shorter reaction times and the production of nanometre scale particles alongside more uniform particle distributions.<sup>150,155</sup>

This chapter details work carried out on the microwave-assisted sol-gel synthesis of NMC-111, NMC-622 and NMC-811, including structural, morphological and electrochemical characterisation, alongside muon spin spectroscopy in order to investigate the local Li<sup>+</sup> diffusion across both microwave-synthesised and commercial samples. Work involving the optimisation of microwave-assisted synthesis conditions for NMC-811 is also presented within this chapter, focussing on the structural and electrochemical optimisation *i.e.* minimising site mixing and achieving higher capacity cycling and improved cycling stabilities of synthesised materials.

## 4.2 Results and Discussion

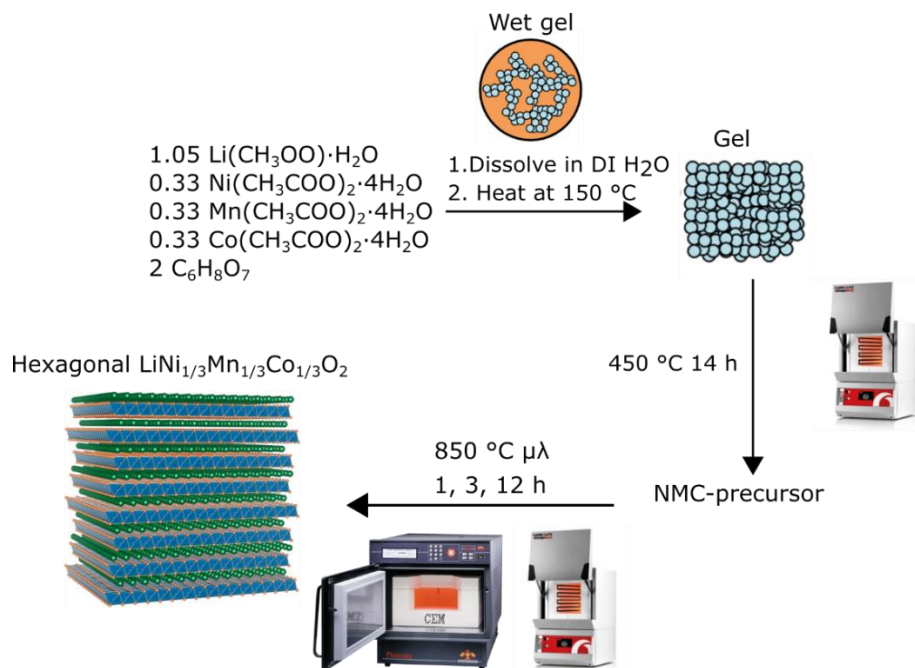
### 4.2.1 Synthesis and structural characterisation of LiNi<sub>1/3</sub>Mn<sub>1/3</sub>Co<sub>1/3</sub>O<sub>2</sub> prepared from a microwave assisted sol-gel process

The preparations of LiNi<sub>1/3</sub>Mn<sub>1/3</sub>Co<sub>1/3</sub>O<sub>2</sub> were carried out as described in section 2.2.5. The reaction involved the dissolution of metal acetate precursors in deionised water followed by the addition of a solution of citric acid under magnetic stirring. This led to the formation of a complex with a homogenous distribution of metal cations on the atomic level. The water was evaporated from the sol at  $\approx 150$  °C on a stirrer-hot plate to form a viscous gel which was then dried and transferred to a conventional box furnace to be heated at 450 °C for 14 hours to allow the carbon from the precursors to be burnt and removed from the sample. The dried powder precursor was then subject to a final heat treatment at 850 °C to form well crystallised NMC-111. This is shown in Schematic 4.1. This final heat treatment was conducted using both a conventional furnace (12 hours, designated 12C here) and a CEM Phoenix microwave-assisted furnace (1 or 3 hours, designated 1MW and 3MW here) which uses microwave radiation (2.45 GHz) to quickly heat up a liner made from susceptor material, which then allows for the transfer of heat to the sample through conventional means. As higher temperatures are reached, the reactants themselves can also couple to microwaves directly resulting in direct heating of the reactants.<sup>219</sup> Chapter 1 discusses microwave assisted heating mechanisms in more detail.

The PXRD patterns collected for the three synthesised samples is shown in Figure 4.1. From the PXRD patterns for samples obtained from all of these reaction conditions, it can be seen that a 1 hour reaction time is adequate in forming the correct phase, with no impurity peaks observed for any of the samples. Rietveld refinements were carried out on the data collected for NMC-111 samples and are shown here in Figure 4.2 The refinements were carried out using the GSAS-II program and using a starting model of  $R\bar{3}m$  LiNi<sub>1/3</sub>Mn<sub>1/3</sub>Co<sub>1/3</sub>O<sub>2</sub> obtained from the ICSD (collection code 171750) which was fit to

the collected data within the  $2\theta$  range of  $10^\circ$  to  $60^\circ$ .<sup>168,220</sup> The refinement was prepared for 15 variables, including scale factor, zero point, sample displacement, 6 background coefficients (fitted with a Chebyshev function), lattice parameters, microstrain and size parameters and Ni site occupancies. All other atomic positions, displacement parameters and site fractions were not refined. As can be visually observed in the fitting plots, there is a good agreement between the fitted model and the collected PXRD data for all three samples indicating that materials with a high degree of phase purity have been synthesised.

All three samples show similar lattice parameters and calculated cell volumes (Table 4.1) agree well with values for NMC-111 reported in the literature.<sup>221</sup> The sample synthesised by conventional methods has a calculated weighted profile R-factor value of  $R_{wp} = 2.3\%$  which are lower than those obtained for the microwave 3h sample ( $R_{wp} = 4.4\%$ ) and the microwave 1 h sample ( $R_{wp} = 3.9\%$ ) which could be attributed to the higher backgrounds observed in the PXRD data collected for the microwave synthesised samples likely caused by the smaller particle sizes produced evidenced by SEM and explained in the following section. However, observation of the  $\chi^2$  values reveals smaller values for the microwave synthesised samples of 1.07 and 1.20 for the 3MW and 1MW samples respectively, whereas the sample produced using a conventional heating step reveals a value of  $\chi^2$  of 1.33. Nevertheless, the fits obtained show a good visual agreement with the data. From applying suitable constraints during the refinement process, the nickel content in the 3a (lithium layer) and 3b (transition metal layer) sites can be estimated and the extent of Li/Ni disorder evaluated. The content of  $Mn^{4+}$  and  $Co^{3+}$  were fixed at 0.3333 each, since it has been confirmed by neutron powder diffraction that only  $Ni^{2+}$  migrates to the lithium layers for similar compound  $LiNi_{0.4}Mn_{0.4}Co_{0.2}O_2$  and the refinement of Ni, Mn and Co simultaneously from PXRD data presents problems due to the similar scattering characteristics of the Ni, Mn and Co.<sup>222</sup> The similar ionic radii of  $Li^+$  and  $Ni^{2+}$  can result in cation exchange between the two separate layers where the presence of  $Ni^{2+}$  in the lithium layers can hinder lithium diffusion in the lattice and cause poor electrochemical performances. Strong Ni-O bonds can also act to hold neighbouring  $MO_2$  sheets together during cycling and thus hindering the  $Li^+$  mobility further.<sup>223</sup> Site mixing percentages of 1.95 %, 3.96 % and 10.08 % were estimated for samples 12C, 3MW and 1MW respectively, indicating that site disorder increases for the samples synthesised using shorter reaction times facilitated by microwave-assisted heating. It should be noted that site-mixing percentages were calculated from the percentage of Li that has been replaced by Ni in the lithium layer (rather than the percentage of Ni that has migrated to the Li layer).



**Schematic 4.1** Reaction scheme utilised for the microwave-assisted sol-gel synthesis of NMC-111.

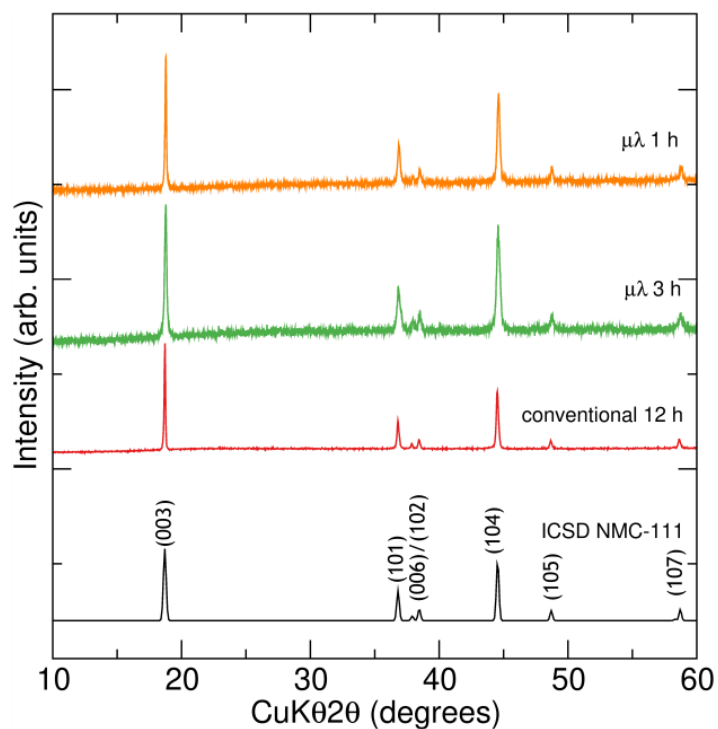


**Figure 4.1** PXRD patterns obtained from NMC-111 synthesised by a sol-gel method utilising both conventional and microwave-assisted heating alongside a standard PXRD pattern for NMC-111 obtained from the ICSD (collection code 171750).

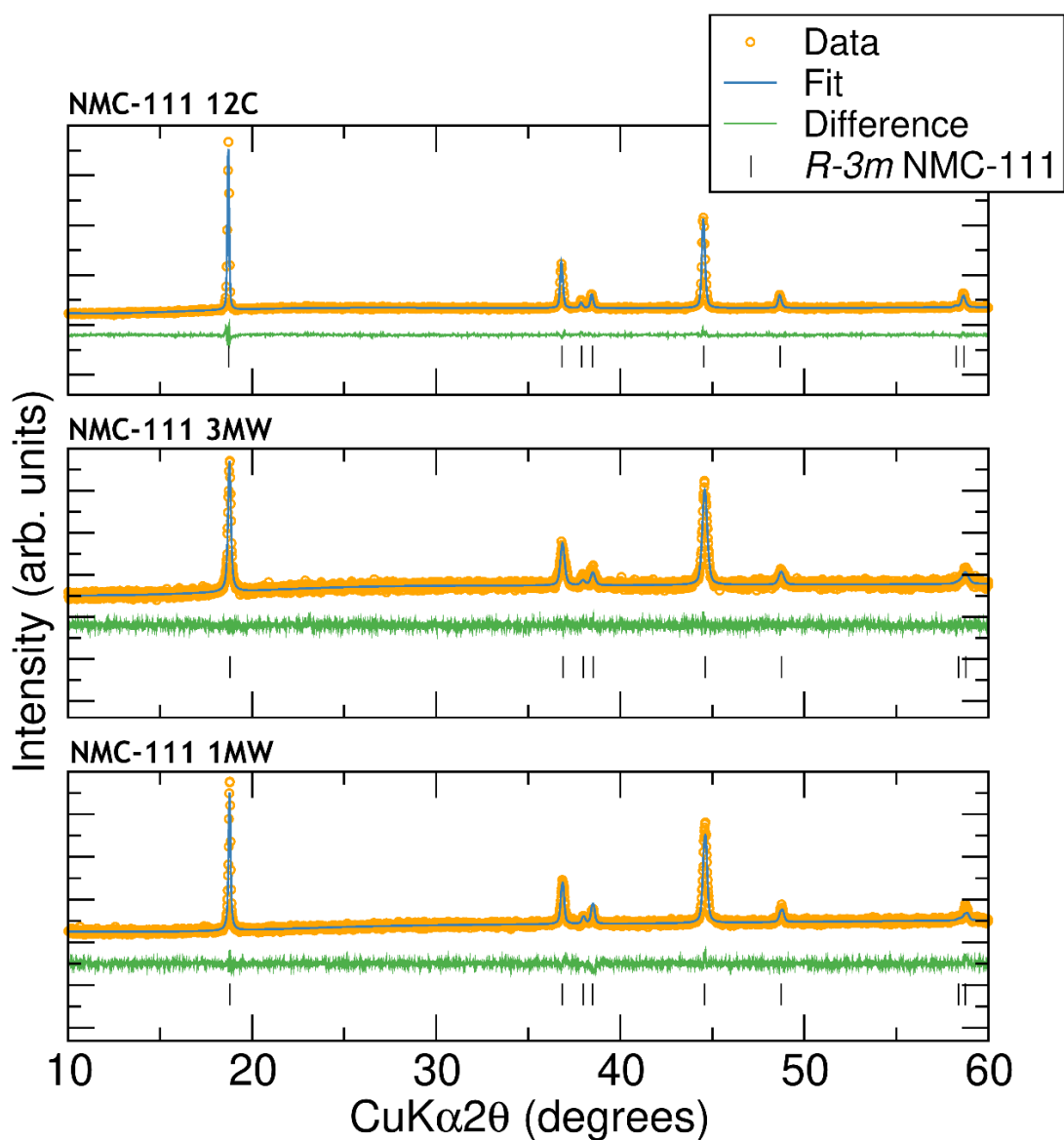


**Figure 4.2** Rietveld refinements on PXRD data obtained from three samples of NMC-111 synthesised by a sol-gel method using a conventional heating step for 8 hours and microwave-assisted heating steps of 3 hours and 1 hour. A model consisting of  $R\bar{3}m$  phase  $\text{LiNi}_{1/3}\text{Mn}_{1/3}\text{Co}_{1/3}\text{O}_2$  was fit to the collected PXRD data.

**Table 4.1** Calculated lattice parameters and Ni site occupancies for three samples of NMC-111 synthesised by a sol-gel method using a conventional heating step for 8 hours and microwave-assisted ( $\mu\lambda$ ) heating steps of 3 hours and 1 hour.

Sample	NMC-111 12C	NMC-111 3MW	NMC-111 1MW
Space group	$R\bar{3}m$	$R\bar{3}m$	$R\bar{3}m$
a (Å)	2.8607(3)	2.8610(8)	2.8649(4)
c (Å)	14.244(1)	14.226(3)	14.2507(17)
V (Å <sup>3</sup> )	100.96(2)	100.85(5)	101.30(3)
Ni1 occupancy	0.3138(2)	0.2937(40)	0.2325(20)
Ni2 occupancy	0.0195(20)	0.0396(40)	0.1008(20)
Li/Ni mixing	1.95 %	3.96 %	10.08 %
$R_{wp}$	2.303 %	4.417 %	3.858 %
$\chi^2$	1.33	1.07	1.20

#### 4.2.2 Scanning electron microscopy of $\text{LiNi}_{1/3}\text{Mn}_{1/3}\text{Co}_{1/3}\text{O}_2$ prepared using a microwave assisted sol-gel synthesis

To ascertain any morphological changes brought about from the application of the microwave assisted method, scanning electron microscopy (SEM) was used in order to investigate the particle size, morphology and homogeneity of the prepared NMC-111 particles. Figure 4.3 shows images obtained for NMC-111 prepared using (a,b) a conventional sol-gel method and a microwave assisted method comprising final heating steps of (c-e) 3 hours and (f-h) 1 hour. Particle size distribution histograms for each sample are shown in Figure 7.7 in the appendix.

For the NMC-111 prepared using a conventional heating step, particle sizes are observed to range from smaller particles sizes of  $\approx 150$  nm to larger particles exhibiting sizes closer to 700 nm, with an average particle size of 369 nm, highlighting the large degree of heterogeneity in particle size distribution. Conversely, those samples prepared using the microwave assisted method both show a greater degree of particle size uniformity and smaller particle sizes obtained with the SEM images shown in Figure 4.3 (c-h) highlighting that both microwave synthesised samples show approximate particle sizes in the range of 100 - 200 nm, with average particle sizes calculated as  $\approx 130$  nm for both microwave-synthesised samples. The results highlight the smaller particle sizes attained when a microwave assisted heating step is introduced. This can most likely be attributed to the shorter reaction times afforded which results in less time allowed for the particles to increase in size.

In the case of electrode materials for batteries, smaller particle sizes are often presented as being advantageous due to the decreased dimensions allowing shorter pathlengths for  $\text{Li}^+$  ions to diffuse which may result in better rate performance. The increased surface area produced from decreasing particle sizes also allows for a greater extent of electrode-electrolyte interactions which can improve wetting in materials that are unreactive when in contact with electrolyte, but in systems such as NMCs where surface reactivity increases upon higher states of charge and parasitic electrode-electrolyte reactions can cause degradation to the material. Wang *et al.* investigated the effect of surface area on cycling stability of nanostructured NMC-111 and found that while high surface areas exhibited initial high charge capacities, cycling stability was compromised when compared with lower surface area samples.<sup>224</sup> Whether these parasitic reactions occur and affect the cycling performance of the materials can be ascertained by examining the cycling performances of the cathode materials.

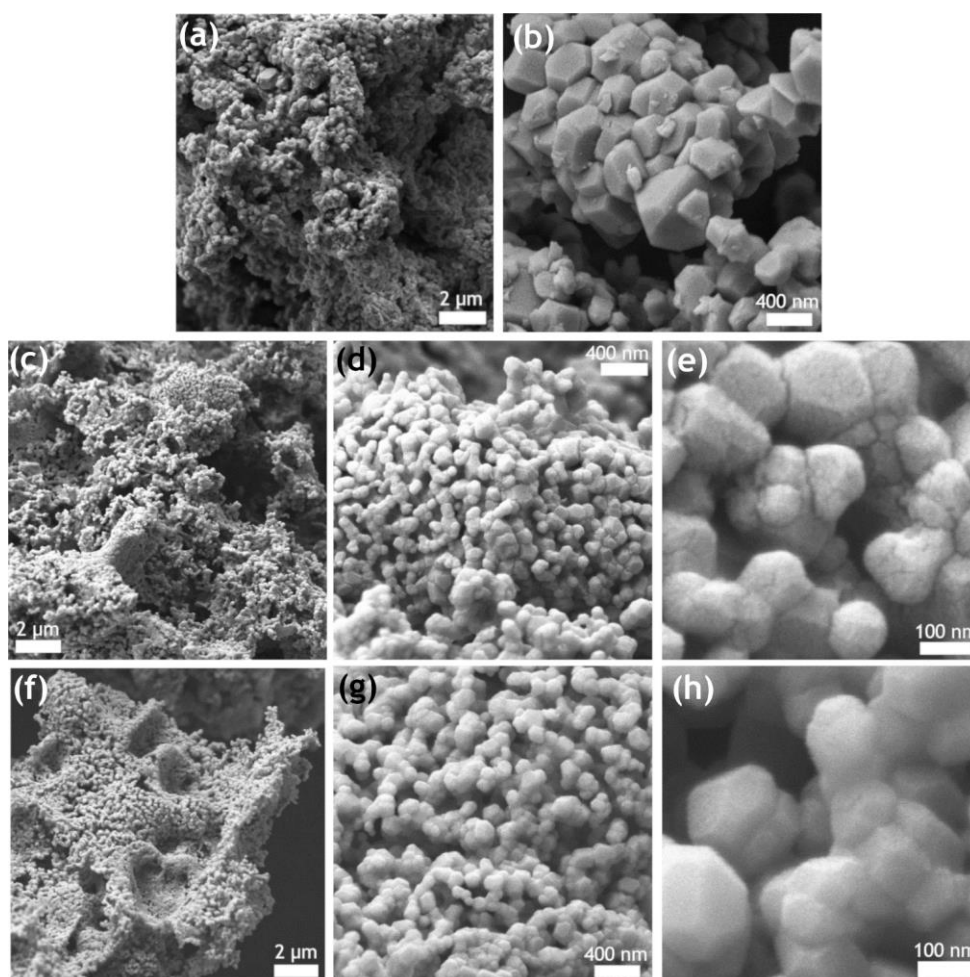


**Figure 4.3** SEM images of NMC-111 prepared using (a,b) a conventional sol-gel method and microwave-assisted sol-gel methods with a final heating step of (c-e) 3 hours and (f-h) 1 hour.

### 4.2.3 Electrochemical performances of $\text{LiNi}_{1/3}\text{Mn}_{1/3}\text{Co}_{1/3}\text{O}_2$ prepared using a microwave assisted sol-gel synthesis

Galvanostatic cycling with potential limitation (GCPL) was carried out on the three NMC-111 cathode materials outlined above. Swagelok type cells containing pellets of the cathode material mixed with conductive carbon black and PTFE (60:30:10 % wt. ratio) and a Li metal counter electrode were fabricated and measurements were performed on a BioLogic VSP potentiostat. A constant current of  $C/10$  was applied and the cells were cycled between 2.5 - 4.6 V vs.  $\text{Li}/\text{Li}^+$ . As the synthesised NMC-111 powders were all prepared in the discharged state (*i.e.* containing lithium) the first step involved the application of a positive current to charge the cell and remove lithium from the cathode material. During the charge process, lithium is removed from  $\text{LiNi}_{1/3}\text{Mn}_{1/3}\text{Co}_{1/3}\text{O}_2$  to form delithiated  $\text{Li}_{1-x}\text{Ni}_{1/3}\text{Mn}_{1/3}\text{Co}_{1/3}\text{O}_2$  with an accompanying  $\text{Ni}^{2+}$  to  $\text{Ni}^{4+}$  oxidation process and  $\text{Co}^{3+}/\text{Co}^{4+}$  oxidation occurring at voltages greater than 4.5 V evidenced by *in-situ* X-ray absorption spectroscopy.<sup>225</sup> As this is a solid solution process rather than a two phase one, a flat plateau is not observed in the cycling profiles unlike that observed for  $\text{LiFePO}_4$ . Figures 4.4, 4.5 and 4.6 present the voltage-capacity profiles, voltage-composition plots, cycling stability, coulombic efficiencies achieved and differential capacity ( $dQ/dV$ ) plots for the three different samples of NMC-111 prepared by this conventional and microwave-assisted sol-gel methodology.

For the NMC-111 12C sample, prepared using a final conventional heating step at 850 °C, Figure 4.4(a) shows that a large initial charge capacity of 200  $\text{mAh g}^{-1}$  is obtained, corresponding to an initial removal of  $\approx 0.73 \text{ Li}^+$  from the structure ascertained from the voltage composition plot shown in Figure 4.4(b). An initial discharge capacity of 164  $\text{mAh g}^{-1}$  is achieved which corresponds to the re-insertion of 0.6  $\text{Li}^+$  into the layered structure. Therefore, a first cycle coulombic efficiency of only  $\approx 82 \%$  is calculated and shown in Figure 4.4(c). Such poor first cycle coulombic efficiencies are common in nickel containing layered oxides when charged up to high voltages such as 4.6 V and can be explained by the formation of a CEI on particle surfaces, precipitated by the increased reactivity of the cathode surface at high states of charge.<sup>226</sup> The CEI formed can act to consume both the electrolyte and the active cathode material resulting in an overall loss of capacity. If the CEI is more insulating than the cathode, then re-insertion of  $\text{Li}^+$  into the cathode is furthermore hindered due to an increased charge transfer resistance and this can also lead to lower discharge capacities achieved after this initial charge process. Although a low coulombic efficiency is calculated for the 1<sup>st</sup> cycle, this improves upon subsequent cycles as shown in Figure 4.4(b) with efficiencies of between 96 - 99 % achieved after the 3<sup>rd</sup> cycle. The delivered discharge capacity after 10 cycles was

154 mAh g<sup>-1</sup> with a discharge capacity retention of 94 % achieved, indicating stable cycling over 10 cycles.

Inspection of the differential capacity plot for cycles 1, 2 and 10 (Figure 4.4(d)) reveals an intense oxidation peak at 3.78 V which is part of a broader feature between 3.6 to 4.2 V during the first charge, which is typical of the Ni<sup>2+/4+</sup> redox process.<sup>45</sup> A broad reduction feature between 3.8 to 3.2 V is observed for the first cycle also. The intense oxidation peak is observed to shift to slightly higher values of 3.9 V for the 2<sup>nd</sup> and 10<sup>th</sup> cycle although the intensity of the 2<sup>nd</sup> and 10<sup>th</sup> cycle oxidation peak is greatly reduced. The reduction feature broadly stays in the same region for the 2<sup>nd</sup> cycle albeit with a lower intensity, and shifts to slightly higher voltages for the 10<sup>th</sup> cycle. Thus there is a decrease in the polarization between the 2<sup>nd</sup> and 10<sup>th</sup> cycles indicating enhanced reversibility. The oxidation feature observed only in the 2<sup>nd</sup> cycle at  $\approx$  4.4 V could correspond to some degree of Co<sup>3+/4+</sup> oxidation, although this is not observed during the 10<sup>th</sup> cycle.

The charge-discharge profiles for the NMC-111 3MW sample is shown in Figure 4.5(a). Similar to the previous material, a large initial charge capacity of 260 mAh g<sup>-1</sup> is obtained with the subsequent discharge capacity reducing to 156 mAh g<sup>-1</sup> which is a larger drop than what is observed for the previous NMC-111 12C sample. From the voltage-composition plot shown in Figure 4.5(b) it can be seen that 0.95 Li<sup>+</sup> are extracted in the first cycle and 0.55 Li<sup>+</sup> re-inserted during the first discharge process corresponding to a large amount of irreversible Li<sup>+</sup> extraction. The open circuit voltage (V<sub>oc</sub>) observed for NMC-111 3MW is 1.59 V (shown for clarity in Figure 7.8(a) in the appendix) compared to 3.05 V observed for the NMC-111 12C sample and therefore, some extra capacity could arise from the additional 1.46 V afforded to the NMC-111 3MW sample. The lower open circuit voltage observed could arise from initial inadequate wetting of the electrode which could improve over time during the first cycle. Cells were fabricated and immediately cycled, leaving little time for the electrolyte to fully wet the electrode. It was observed in later studies that the open circuit voltage of similar electrodes increased to values  $\approx$  3 V when left for a period of time before cycling. However, whereas the NMC-111 12C cathode exhibits stable charge and discharge capacities across the 10 cycles, the NMC-111 3MW cathode shows capacities that gradually decrease upon subsequent cycles, with the discharge capacity decreasing from 156 mAh g<sup>-1</sup> to 112 mAh g<sup>-1</sup> of capacity delivered on the 10<sup>th</sup> cycle, representing a discharge capacity retention of 72 %. Furthermore, the charge and discharge capacities observed for the 9<sup>th</sup> and 10<sup>th</sup> cycle show very similar values and their voltage-capacity profiles have a large

degree of overlap, possibly suggesting that the capacities might begin to level off at this point and little more decrease will be observed.

Similar to the trend observed for the NMC-111 12C sample, a poor first cycle coulombic efficiency of only 60 % was calculated, increasing to between 84 - 89 % on continued cycling as shown in Figure 4.5(c). These values are lower than those for the NMC-111 12C sample, indicating that on each cycle the amount of lithium removed from the cathode is higher than what is subsequently re-inserted upon discharge, which leads to the gradual observed decrease in capacities upon cycling. Although there is an increased extent of Li/Ni mixing for the NMC-111 3MW sample compared to the 12C sample, a value of  $\approx 4\%$  compares well with other reported samples of similar composition. For example, samples of  $\text{LiNi}_{0.45}\text{Mn}_{0.45}\text{Co}_{0.1}\text{O}_2$  with cation mixing amounts of 6 % were found to have excellent cycling performances.<sup>227</sup> The gradual decrease of capacity over 10 cycles could be attributed to increased charge transfer resistance upon repeat cycling, enabled possibly by a growing CEI layer.

The differential capacity plot showing data for the 1<sup>st</sup>, 2<sup>nd</sup> and 10<sup>th</sup> cycle (Figure 4.5(d)) shows an oxidation peak at 3.76 V assigned to the  $\text{Ni}^{2+/4+}$  oxidation, which shifts to higher voltages of 3.87 V and 3.98 V upon increased cycling. A corresponding small shift in the reduction feature to lower voltages is also observed from 3.70 V during the first discharge to 3.68 V and 3.64 V for the 2<sup>nd</sup> and 10<sup>th</sup> cycles respectively. This indicates an increase in the polarization of the redox processes and suggests an increase in irreversibility occurs, which could help to explain the gradual capacity fading on repeated cycling. A noisy and irreversible oxidation feature is also observed for this sample at a high voltage of 4.4 V up to the cut-off potential at 4.6 V which could indicate  $\text{Co}^{3+/4+}$  oxidation, a high voltage phase transition such as O3 to O1, or could be evidence of the irreversible CEI formation occurring during each cycle, perpetuated by continual exposure of new surface areas during cycling.

The charge-discharge profiles, cycling stability plot and calculated coulombic efficiencies for NMC-111 1MW are shown in Figures 4.6(a) and (c). Similar to the results collected for the two previous samples, a large initial charge capacity of 213  $\text{mAh g}^{-1}$  was delivered, followed by a much decreased discharge capacity of 130  $\text{mAh g}^{-1}$  corresponding to a first charge coulombic efficiency of only 61 %. The capacities further decrease at a faster rate than was observed for the NMC-111 3MW, with NMC-111 1MW delivering a discharge capacity of only 71  $\text{mAh g}^{-1}$  after 10 cycles, giving a discharge capacity retention of only 55 % which is a much poorer result than that obtained from the previous two samples of NMC-111.

From the voltage-composition plot in Figure 4.6(b), it is observed that approximately 0.77 Li<sup>+</sup> are initially extracted during the first charge from a low open circuit voltage of 1.62 V to 4.6 V vs. Li/Li<sup>+</sup> which is close to the behaviour of the first charge of the conventional synthesis NMC-111 presented previously. A further 0.47 Li<sup>+</sup> are subsequently re-inserted into the structure upon the first discharge. This first cycle behaviour is not vastly dissimilar to that shown by the conventionally heated NMC-111, however the performance of the NMC-111 1MW drastically worsens upon continued cycling, evidenced by the poor discharge capacity retention observed over the 10 cycles. The good initial charge capacity coupled with severe capacity fading over only 10 cycles indicates that the NMC-111 1MW suffers from poor stability which could arise from structural and/or surface degradation that is brought on after the initial charging process. The large degree of cation mixing (10.08 %) calculated for this sample no doubt has a detrimental effect on the cycling performance, as large amounts of Ni<sup>2+</sup> in the lithium layer leads to inferior kinetics and poor cycling performances.<sup>228</sup> For example, layered oxide LiNi<sub>0.5</sub>Mn<sub>0.5</sub>O<sub>2</sub> where Li/Ni site mixing was calculated as 10.85 % (close in value to the 10.08 % calculated for our NMC-111 1MW sample), the discharge capacity was observed to rapidly decrease from 160 mAh g<sup>-1</sup> to 90 mAh g<sup>-1</sup> over approximately 20 cycles when charged to 4.4 V vs. Li/Li<sup>+</sup> with compositions possessing smaller degrees of cation disorder showing more stability in the discharge capacity under the same cycling conditions.<sup>229</sup>

Another contributing factor to the poor cycling performances exhibited by this sample could arise from increased reactivity upon charging which is further accelerated by the high surface areas afforded by the decreased particle sizes. From the SEM analysis presented previously, both the 3MW and the 1MW NMC-111 samples exhibit similar particle sizes and size homogeneity which could explain the gradual capacity fading observed in these two samples compared to the sample synthesised using a conventional heating step which showed excellent discharge capacity retention over 10 cycles. The larger surface areas allow a greater extent of parasitic electrode-electrolyte surface interactions resulting in a greater loss of active material and the perpetual formation of resistive CEI layers upon cycling. Particle cracking which can be facilitated by structural rearrangements upon cycling (e.g. the O3 to O1 phase change associated with high states of charge) can also introduce new and exposed surface areas which are then susceptible to further electrolyte reactions leading to further loss of active material on cycling.

The differential capacity plots for the 1<sup>st</sup>, 2<sup>nd</sup> and 10<sup>th</sup> cycles (Figure 4.6(d)) show similar properties to the NMC-111 3MW sample. An initial oxidation peak at 3.8 V assigned to Ni<sup>2+/4+</sup> oxidation is observed which is followed by shifting to higher voltages of 3.9 V and

4.0 V during the 2<sup>nd</sup> and 10<sup>th</sup> cycle with reduced intensities and broadening of the feature occurring during cycling. The corresponding reduction features remain at approximately the same voltage during the 1<sup>st</sup>, 2<sup>nd</sup> and 10<sup>th</sup> cycles but with decreasing intensity and broadening observed. The shift of the oxidation peaks coupled with the static nature of the reduction peaks relate to an increase in polarization of the cathode as before. An irreversible feature between 4.4 V - 4.5 V is also observed which could also suggest the perpetual formation of an insulating CEI layer as explained for the 3MW sample prior.

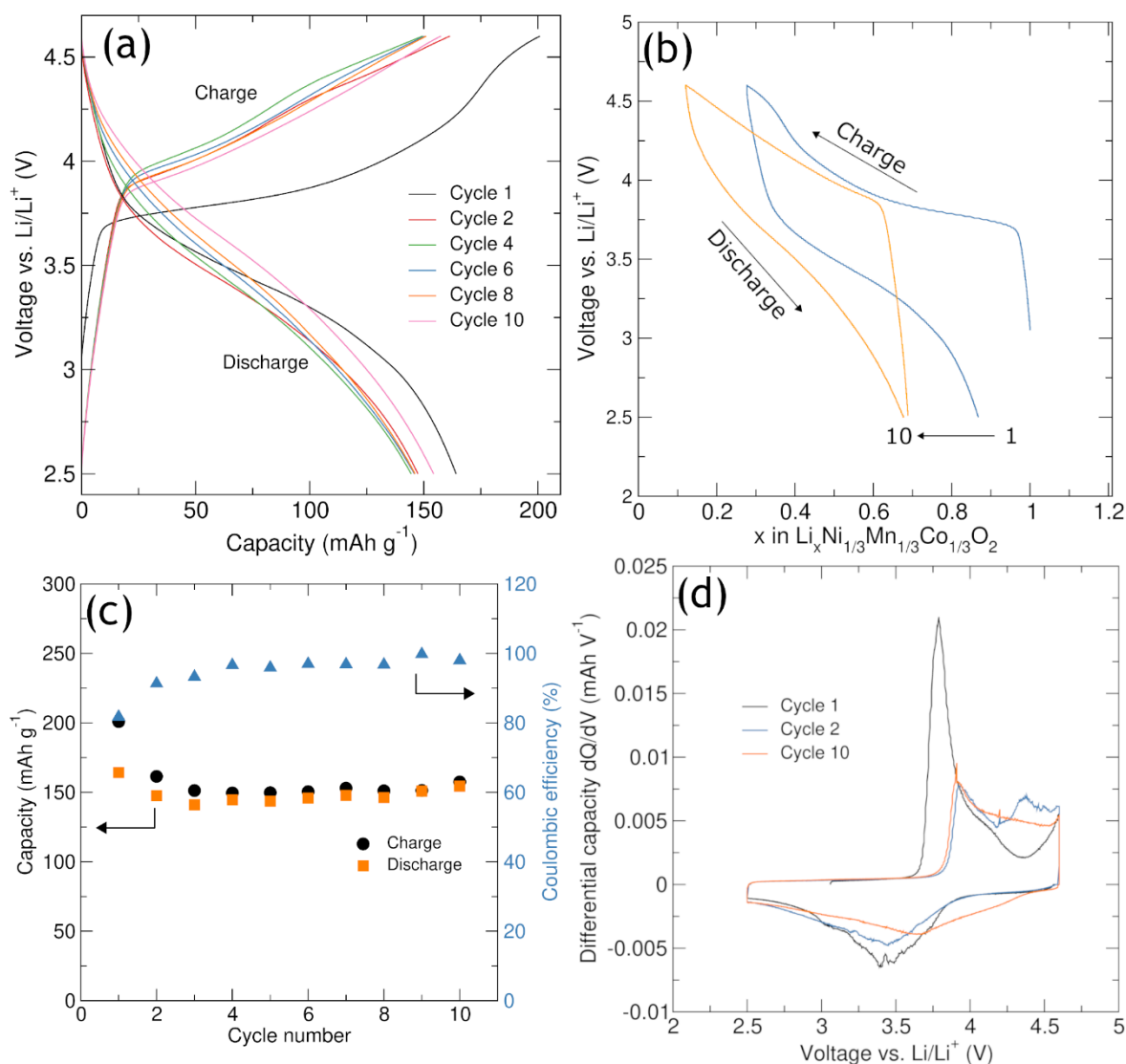


**Figure 4.4** Electrochemical data obtained for NMC-111 synthesised *via* a conventional sol-gel method at 850 °C for 12 hours and cycled between 2.5 - 4.6 V vs. Li/Li<sup>+</sup> at a rate of C/10 in a Swagelok type cell. Including (a) charge-discharge profiles, (b) voltage-composition plot for cycles 1 and 10, (c) charge and discharge capacity stability and coulombic efficiencies over 10 cycles and (d) differential capacity dQ/dV plots for cycles 1, 2 and 10.

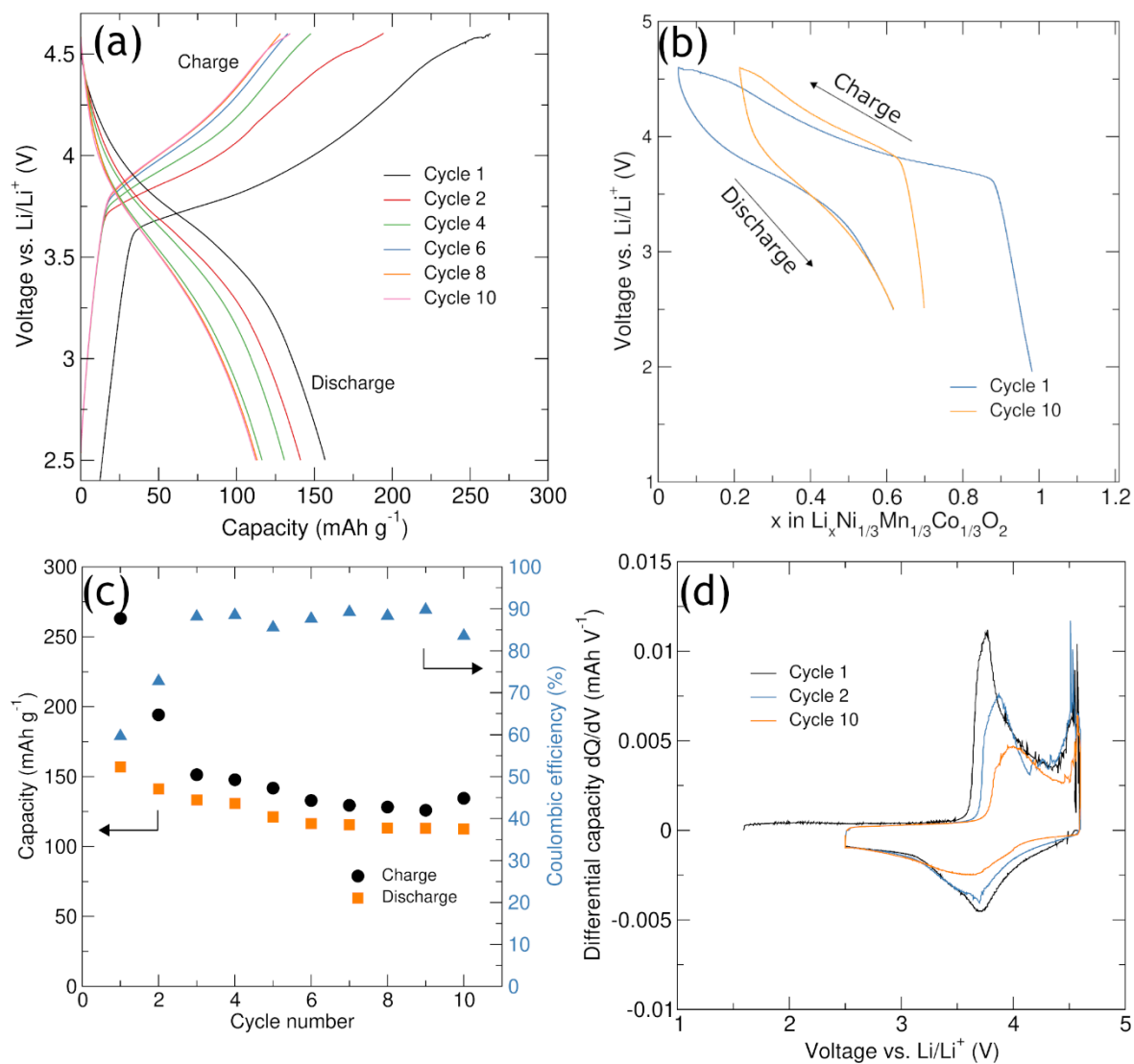


**Figure 4.5** Electrochemical data obtained for NMC-111 synthesised via a microwave-assisted sol-gel method at 850 °C for 3 hours and cycled between 2.5 - 4.6 V vs.  $\text{Li/Li}^+$  at a rate of C/10 in a Swagelok type cell. Including (a) charge-discharge profiles, (b) voltage-composition plot for cycles 1 and 10, (c) charge and discharge capacity stability and coulombic efficiencies over 10 cycles and (d) differential capacity  $dQ/dV$  plots for cycles 1, 2 and 10.

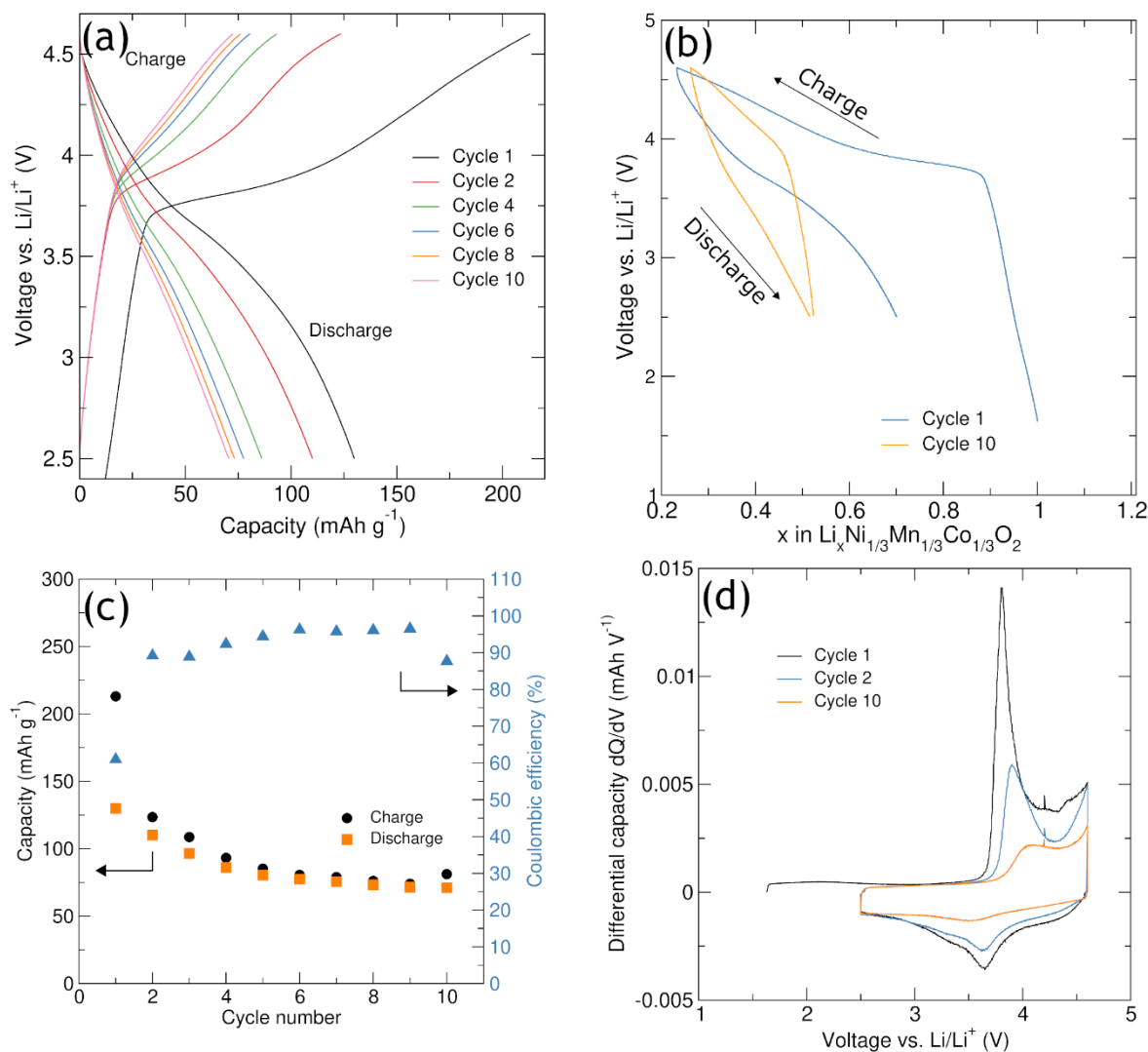


**Figure 4.6** Electrochemical data obtained for NMC-111 synthesised via a microwave-assisted sol-gel method at 850 °C for 1 hour and cycled between 2.5 - 4.6 V vs. Li/Li<sup>+</sup> at a rate of C/10 in a Swagelok type cell. Including (a) charge-discharge profiles, (b) voltage-composition plot for cycles 1 and 10, (c) charge and discharge capacity stability and coulombic efficiencies over 10 cycles and (d) differential capacity dQ/dV plots for cycles 1, 2 and 10.

#### 4.2.4 Post-cycling structural and morphological analysis of LiNi<sub>1/3</sub>Mn<sub>1/3</sub>Co<sub>1/3</sub>O<sub>2</sub>

In order to investigate any changes to the structure of the NMC-111 samples brought on by the charge and discharge processes, post-cycling PXRD and SEM were performed on the samples. The cycled cells were disassembled in an Ar-filled glovebox and the NMC-111 cathode pellets were collected and washed with THF in order to remove any remaining electrolyte species, before being dried and stored in a glovebox. Each material analysed was in the discharged state. PXRD data, shown in Figure 4.7, was collected for each sample to ascertain whether any significant structural changes had occurred during cycling. As can be seen, each sample has retained the rhombohedral  $R\bar{3}m$  structure

related to the layered oxides, indicating that no significant irreversible structural transformations observable by PXRD have occurred over the 10 cycles and therefore a good degree of structural stability was exhibited by the NMC-111 materials. There is no evidence in the PXRD patterns collected of the O1 phase which would manifest itself with notable additional and intense reflections at  $2\theta \approx 19.5^\circ$ ,  $42^\circ$  and  $55^\circ$ .<sup>220</sup> An additional peak at  $2\theta \approx 18^\circ$  is observed and can be assigned to PTFE within the sample which originates from the PTFE binder used when fabricating the cathode pellets. This is not removed during the washing step and so remains in the cathode powder. While there are no unexpected additional peaks in the NMC-111 12C and 3MW samples, a small peak at  $2\theta \approx 43^\circ$  is observed in the data collected on the 1MW sample which could be attributed to a small amount of NiO phase present. The formation of NiO is usually observed on the surface of high nickel content  $\text{LiNi}_x\text{Mn}_y\text{Co}_{1-x-y}\text{O}_2$  ( $x > 0.5$ ) materials as a result of the high reactivity of  $\text{Ni}^{4+}$  on the surface, suggesting that the NMC-111 1MW sample exhibits an unusually high surface reactivity for a low nickel content material, which, as previously discussed, leads to poor electrochemical performances upon repeated cycling.

The retaining of the  $R\bar{3}m$  structure is also confirmed by Rietveld refinements carried out using the PXRD data alongside a model of phase  $R\bar{3}m$ . The refinement was prepared for 15 variables, including scale factor, zero point, sample displacement, 6 background coefficients (fitted with a Chebyshev function), lattice parameters, microstrain and size parameters and Ni site occupancies. All other atomic positions, displacement parameters and site fractions were not refined. Good fits to the data could be calculated for all three samples as evidenced in Figure 4.8 and Table 4.2 which shows that good values of  $\chi^2$  (1.15, 1.12 and 1.59 for NMC-111 12C, 3MW and 1MW respectively) were obtained for each fit. From inspection of the lattice parameters calculated from the refinements and comparison to those obtained for the pre-cycled material (Table 4.1), it is observed that there is little change to the lattice parameters after undergoing 10 charge-discharge cycles, except for the  $c$  parameter in NMC-111 1MW which increases from  $14.25 \text{ \AA}$  to  $14.32 \text{ \AA}$  (which is not within the standard errors) indicating an expansion of the layers which could be associated with a delithiated end-product. This could occur when the presence of surface layers (from deleterious electrode-electrolyte reactions for example) increases the charge-transfer resistance and prevent  $\text{Li}^+$  cations from re-intercalating into the structure on discharge. The Li/Ni site mixing was also estimated from Rietveld refinements using the same procedure from the pre-cycled samples. Site disorders of 3.34 % and 5.51 % were obtained for NMC-111 12C and 3MW respectively, indicating an increase in cation mixing upon cycling which could be explained by the movement of  $\text{Ni}^{2+}$  into empty lithium sites during the initial, irreversible capacity loss where the lost  $\text{Li}^+$

cannot reinsert into the structure. This process could also happen during subsequent charge cycles upon extraction of  $\text{Li}^+$  and the production of empty  $\text{Li}^+$  sites. A good fit could not be obtained from refinements for the NMC-111 1MW sample using a model with Li/Ni site mixing (when Ni site occupancies were refined, a negative value for Ni2 was always calculated), and the best fit was found for a model containing no anti-site mixing at all.

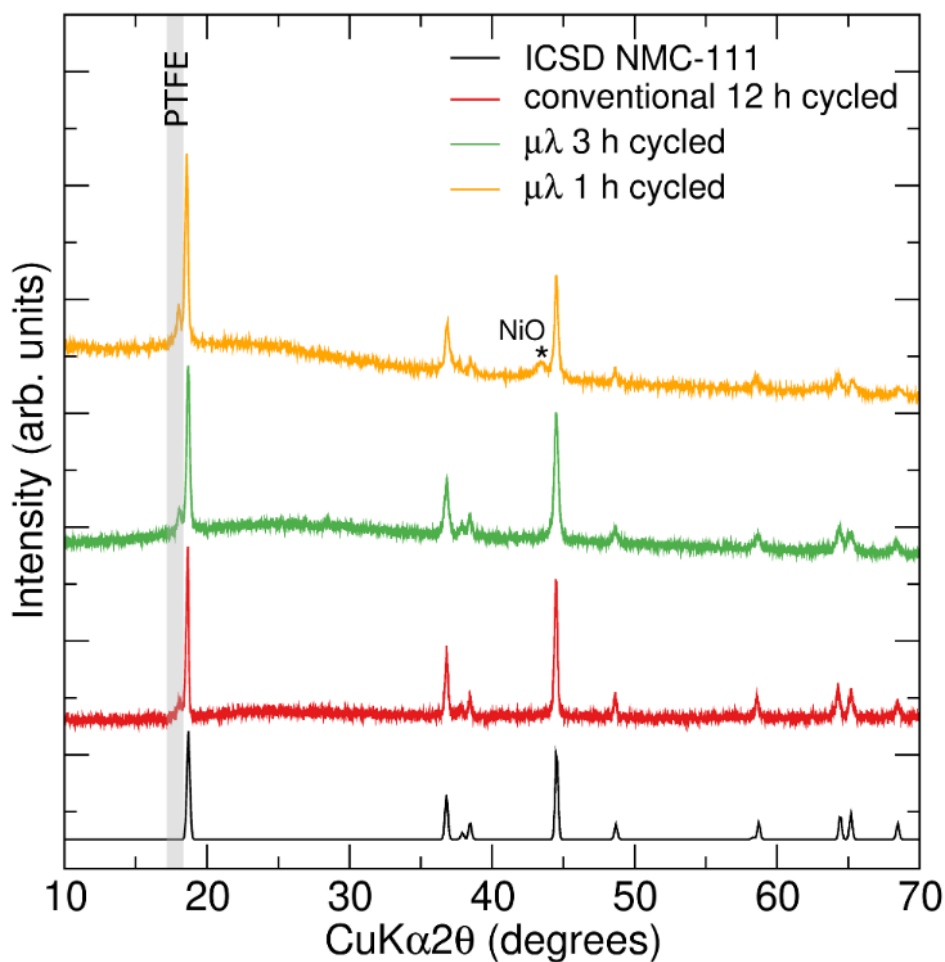


**Figure 4.7** PXR D patterns collected after cycling for the three NMC-111 materials. A peak corresponding to PTFE (from the cathode mix) at  $2\theta \approx 18^\circ$  is highlighted in a grey box and a possible NiO impurity in the 1 h sample is labelled by (\*).

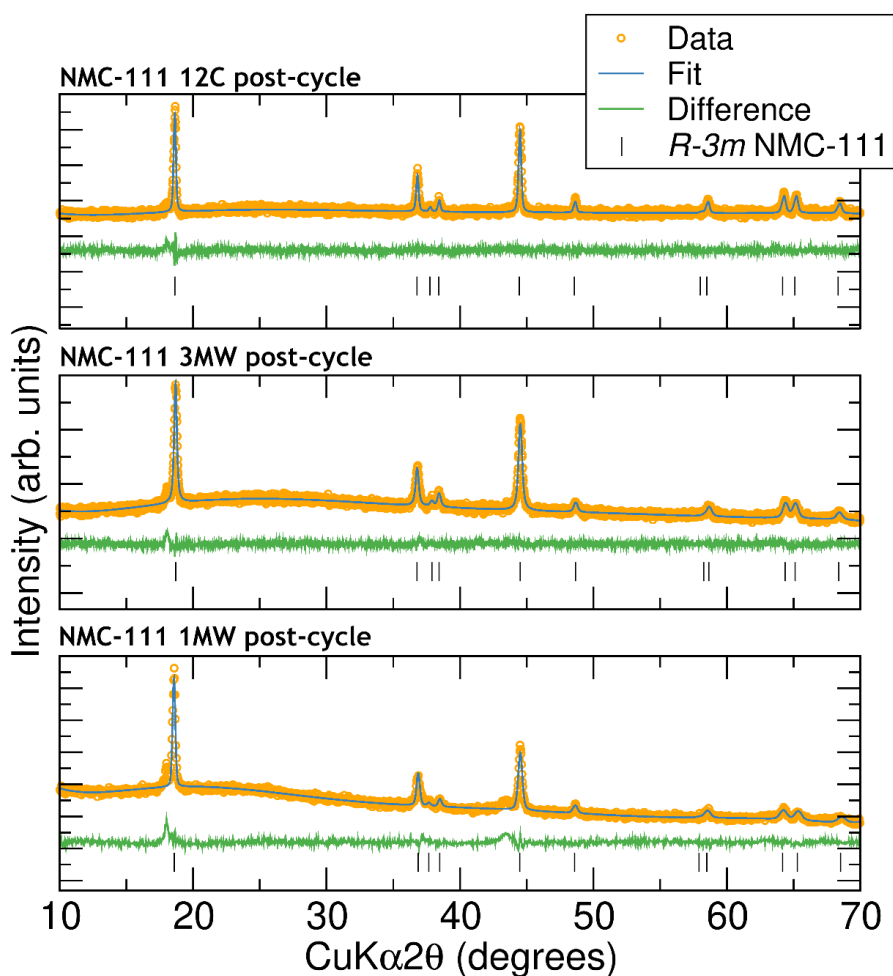


**Figure 4.8** Rietveld refinements on PXRD data collected from three samples of NMC-111 after cycling in a Swagelok cell between 2.5 - 4.6 V vs. Li/Li<sup>+</sup> at a rate of C/10 for 10 cycles. A model consisting of  $R\bar{3}m$  phase  $\text{LiNi}_{1/3}\text{Mn}_{1/3}\text{Co}_{1/3}\text{O}_2$  was fit to the collected PXRD data.

**Table 4.2** Calculated lattice parameters and Ni site occupancies for three samples of cycled NMC-111.

Sample	NMC-111 12h PC	NMC-111 3h $\mu\lambda$ PC	NMC-111 1h $\mu\lambda$ PC
Space group	$R\bar{3}m$	$R\bar{3}m$	$R\bar{3}m$
a (Å)	2.8615(6)	2.86094(24)	2.855(18)
c (Å)	14.2890(23)	14.23355(84)	14.3199(73)
V (Å <sup>3</sup> )	101.324(37)	100.893(9)	101.123(122)
Ni1 occupancy	0.2999(10)	0.2782(10)	n/a
Ni2 occupancy	0.0334(10)	0.0551(10)	n/a
Li/Ni mixing	3.34 %	5.51 %	n/a
$R_{wp}$	4.847 %	3.403 %	3.734 %
$\chi^2$	1.15	1.12	1.59

The SEM analysis of the NMC-111 materials after cycling is shown in Figure 4.9 (with size distribution histograms shown in Figure 7.9 in the appendix) and suggests very little morphological changes are apparent. The NMC-111 12C sample shows negligible change in average particle size indicating that significant particle cracking has not occurred. The images obtained for NMC-111 3MW also do not highlight any significant change in particle morphology or size distributions, with an average particle size of  $\approx 130$  nm calculated (which was reported for the pre-cycled samples also). It should be noted that the presence of clusters of very small particles appearing in the SEM image obtained for NMC-111 3MW most likely represent the presence of the carbon black that was mixed in with the NMC-111 during pellet fabrication. The SEM imaging of NMC-111 1MW (Figure 4.9(b)) reveals that some morphological changes might have occurred during cycling. It is observed that the particle size homogeneity post-cycling is different than that obtained for the pre-cycled materials (Figure 4.3(f-h)) with some smaller particles amongst larger particles, which could indicate some degree of particle cracking and breakage, although this is hard to ascertain from these images alone. The average particle size for this sample was calculated to be  $\approx 130$  nm which mirrors the average particle size calculated for the pre-cycled sample.

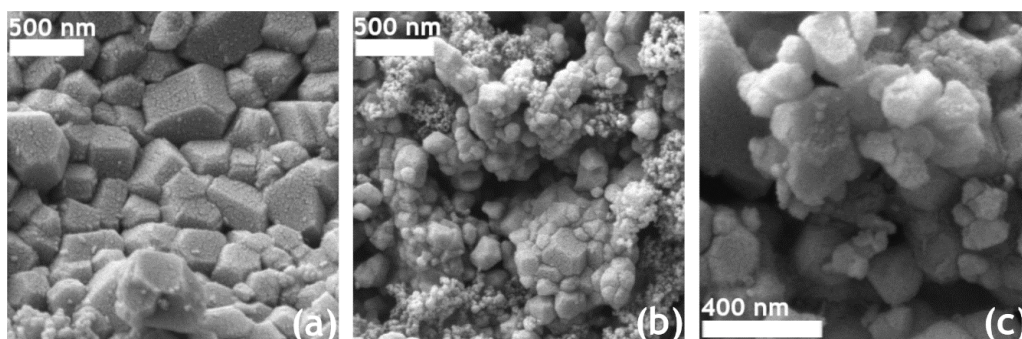
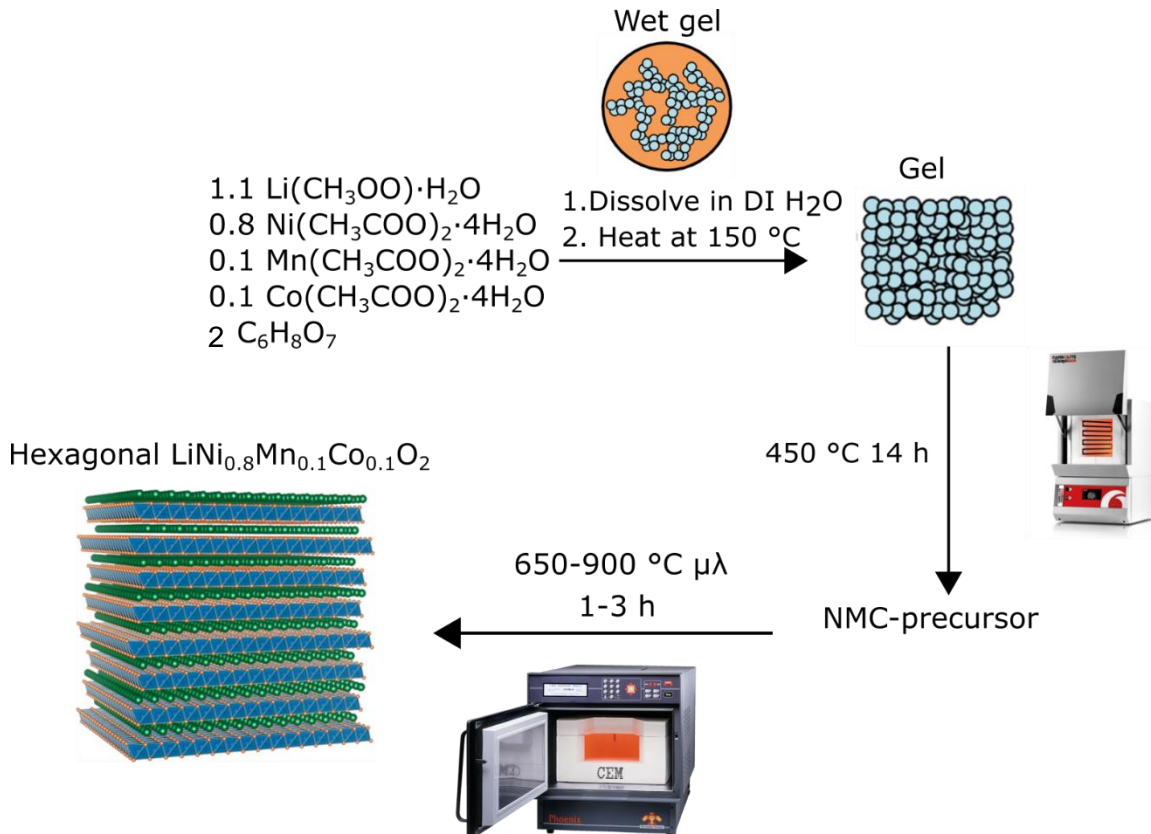


**Figure 4.9** SEM images obtained for NMC-111 (a) 12C, (b) 3MW and (c) 1MW samples after cycling. Very small observed particles are most likely carbon black particles.

#### 4.2.5 Structural and Electrochemical characterisation of $\text{LiNi}_{0.8}\text{Mn}_{0.1}\text{Co}_{0.1}\text{O}_2$ and $\text{LiNi}_{0.6}\text{Mn}_{0.2}\text{Co}_{0.2}\text{O}_2$ synthesised by a microwave-assisted sol-gel method

A similar microwave-assisted sol-gel approach was adopted for the synthesis of NMC-811 and NMC-622 where the reaction methodology used in this section is displayed in Schematic 4.2.



**Schematic 4.2** Reaction schematic for the microwave-assisted sol-gel synthesis of rhombohedral, layered oxide  $\text{LiNi}_{0.8}\text{Mn}_{0.1}\text{Co}_{0.1}\text{O}_2$ , where the final heating step was carried out in a CEM Phoenix microwave furnace between  $650\text{ }^\circ\text{C}$  -  $900\text{ }^\circ\text{C}$  for with reaction times between 1 - 3 hours to yield NMC-811 product. Stoichiometries of starting materials are adapted to prepare NMC-622.

Similar to NMC-811, the high nickel content layered oxide  $\text{LiNi}_{0.6}\text{Mn}_{0.2}\text{Co}_{0.2}\text{O}_2$  (NMC-622) is also of interest for high energy density cathodes for use in e.g. electric vehicles. Although containing a smaller proportion of nickel compared to NMC-811, NMC-622 provides enhanced stabilities with only a small loss in deliverable capacities. This section will briefly cover some work carried out on the microwave-assisted sol-gel synthesis of NMC-811 and NMC-622 which were prepared in order to undertake muon-spin spectroscopy measurements detailed in the following section. The NMC-811 and NMC-622

was synthesised by a microwave-assisted sol-gel method as described previously, utilising a final heating step at 850 °C for 2 hours.

To ascertain the phase purity of the sample and extract the lattice parameters, PXRD combined with Rietveld analysis was performed where the obtained refinement plots and calculated parameters are shown in Figure 4.10 and Table 4.3. The model used was based on the structure of NMC-111 obtained from the ICSD (collection code 171750) where the CIF file was modified to change the transition metal content accordingly. The refinement was prepared for 15 variables, including scale factor, zero point, sample displacement, 6 background coefficients (fitted with a Chebyshev function), lattice parameters, microstrain and size parameters and Ni site occupancies. All other atomic positions, displacement parameters and site fractions were not refined. The model assumed that Li primarily resided on the 3a sites, transition metals on the 3b sites and oxygen on the 6c sites. The site mixing between Li and Ni on the 3a and 3b sites was allowed with appropriate constraints such that the  $\text{LiNi}_{0.8}\text{Mn}_{0.1}\text{Co}_{0.1}\text{O}_2$  and  $\text{LiNi}_{0.6}\text{Mn}_{0.2}\text{Co}_{0.2}\text{O}_2$  stoichiometries were retained (*i.e.* the occupancies of the Ni1 and Ni2 sites totalled to 0.8 and 0.6 respectively for NMC-811 and NMC-622). The refinement results show good visual fits to the data was obtained with no obvious evidence pertaining to the presence of impurity phases. The lattice parameters are also consistent with those reported in the literature for NMC-811 and NMC-622.<sup>71,230</sup> Additionally, low  $R_{wp}$  and  $\chi^2$  values were gained from the refinements further consolidating the good fits achieved.

The degree of cation ordering observed in the system can be estimated by analysing the intensity ratio of the (003) and (104) peaks. As the 003 reflection is a supercell reflection whose intensity is dependent on cation order and the 104 reflection is a subcell reflection whose intensity should be independent of cation order, the ratio  $I_{(003)}/I_{(104)}$  should be a direct indicator of interlayer cation order, with values of  $I_{(003)}/I_{(104)} < 1.2$  indicating that undesirable cation mixing is present in the sample.<sup>211,231</sup> Importantly, however, it should be noted that this method of characterising the anti-site mixing is subjective, owing to the fact that peak intensities at different scattering angles can be modified by experimental parameters such as peak broadening, peak asymmetry, preferred orientation *etc.* Nevertheless, while not a quantitative method, it can provide some qualitative indication of any large differences in anti-site mixing between different samples provided they are of similar composition and have been prepared (both synthetically and for PXRD data collection) in a similar fashion. Results from Rietveld refinements of PXRD and NPD data are able to yield more quantitative answers. From the PXRD data for NMC-811 and NMC-622 the  $I_{(003)}/I_{(104)}$  ratios were calculated as 1.23 and 1.82

respectively, indicating a lower level of Li/Ni mixing is expected for the NMC-622 sample compared to the NMC-811 sample. From the Rietveld analysis the percentage of Li/Ni mixing could be quantified as 7.32 % and 3.49 % for NMC-811 and NMC-622 respectively. Whereas the mixing in NMC-622 is relatively low and suggests that small presence of Ni on the 3a sites should not hinder the Li<sup>+</sup> diffusion during cycling, the mixing present in NMC-811 is much higher and could result in cycling issues. High degrees of Li/Ni mixing are commonly observed in higher nickel content materials such as NMC-811 due to the similar ionic radii of Ni<sup>2+</sup> (0.76 Å) and Li<sup>+</sup> (0.69 Å) which makes the cationic mixing more facile.<sup>232</sup> For example, high amounts of Li/Ni mixing of between 8.1 % - 22 % in NMC-811 have been reported in the literature.<sup>231,233</sup>

To investigate the resultant particle morphology from the short, microwave-assisted heating step, the samples were also examined using SEM. The analysis presented here was conducted using an Inspect F50 SEM. Images obtained from this analysis are shown in Figure 4.11 (with size distribution histograms shown in Figure 7.10). Both samples exhibit non-uniform size and shape distributions, with particle sizes approximately ranging from 400 nm to 1.4 μm for NMC-811 and 200 nm to 1 μm for NMC-622, with average particle sizes of ≈ 800 nm and 400 nm calculated for NMC-811 and NMC-622 respectively. This shows that, under identical reaction conditions, NMC-811 is generally composed of larger particle sizes than NMC-622. These are also larger than the NMC-111 particles obtained under similar synthesis conditions (Figure 4.3) suggesting that the microwave-assisted sol-gel method used here produces larger particles for higher nickel content compositions. Furthermore, the observed particle morphologies also show heterogeneous behaviour with no obvious preferred shapes or facets exhibited.

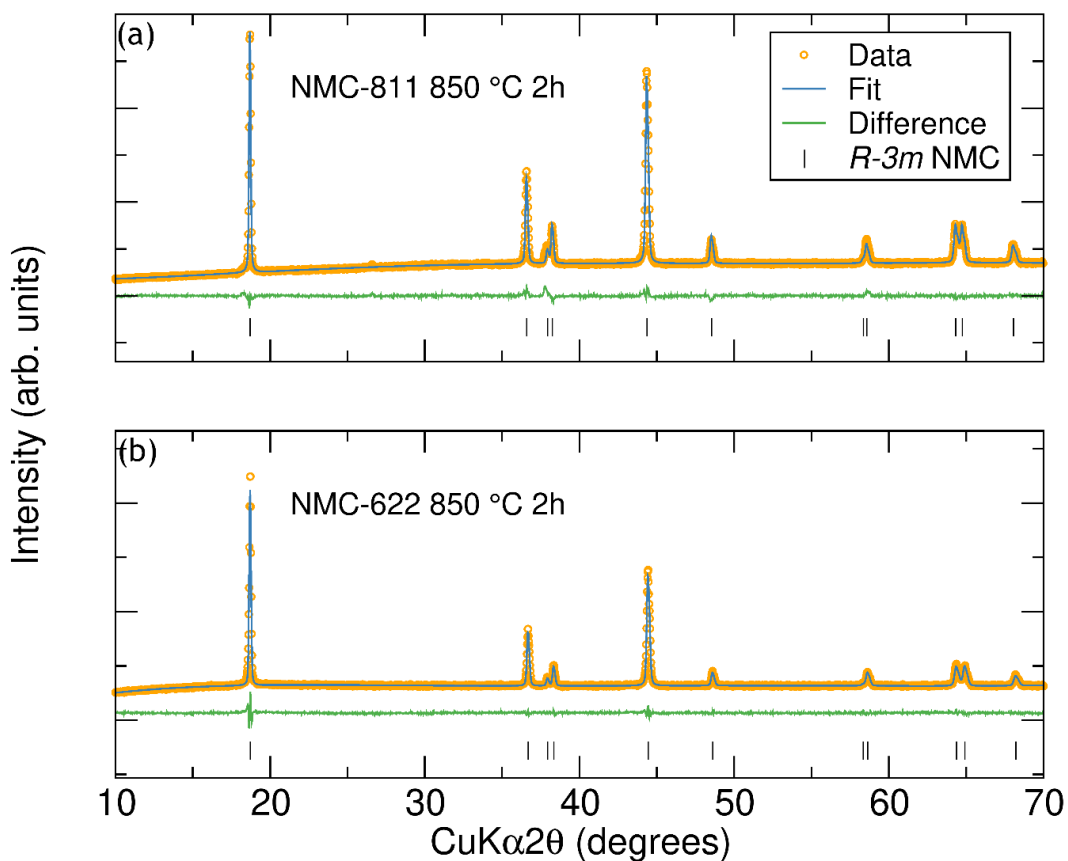


**Figure 4.10** Rietveld refinements on PXRD data obtained from (a) NMC-811 and (b) NMC-622 synthesised by a microwave-assisted sol-gel method with a reaction time of 2 hours at 850 °C. A model of  $R\bar{3}m$  phase  $\text{LiNi}_{0.8}\text{Mn}_{0.1}\text{Co}_{0.1}\text{O}_2$  or  $\text{LiNi}_{0.6}\text{Mn}_{0.2}\text{Co}_{0.2}\text{O}_2$  was fit to the collected PXRD data respectively.

**Table 4.3** Calculated lattice parameter and Li/Ni mixing from Rietveld refinements and calculated  $I_{(003)}/I_{(104)}$  ratios obtained for NMC-811 and NMC-622 synthesised by a microwave-assisted sol-gel method with a reaction time of 2 hours at 850 °C.

Sample	NMC-811 $\mu\lambda$ 850 ° 2 h	NMC-622 $\mu\lambda$ 850 ° 2 h
Space group	$R\bar{3}m$	$R\bar{3}m$
a (Å)	2.87784(44)	2.86831(6)
c (Å)	14.22373(57)	14.21170(18)
V (Å <sup>3</sup> )	102.018(22)	101.258(2)
Ni1 occupancy	0.7268(10)	0.5651(10)
Ni2 occupancy	0.0732(10)	0.0349(10)
Li/Ni mixing	7.32 %	3.49 %
$I_{(003)}/I_{(104)}$	1.23	1.82
$R_{wp}$	2.664 %	2.301 %
$\chi^2$	1.57	1.45

In order to investigate the cycling performance of the synthesised NMC-811 and NMC-622, galvanostatic cycling was performed on a Maccor cyler between 3.0 and 4.2 V vs. Li/Li<sup>+</sup> with a constant current applied corresponding to charge and discharge rates of C/2. An NMC-622 containing cathode film was prepared by mixing pristine NMC-622 powder with carbon black and PVDF in a 90:5:5 wt. % ratio using a mixer type ball mill. The powder mixture was then mixed with NMP solvent to form a slurry which was then made into thin sheets of 15 µm thickness. This process is described more fully in Section 2.3.9. Cathode films were loaded into CR2032 coin cells with a lithium counter electrode, glass microfiber separator and a 1 M LiPF<sub>6</sub> in EC:DMC 1:1 v/v standard electrolyte. The charge and discharge profiles obtained over 20 cycles are shown in Figure 4.12. For the NMC-811 an initial charge capacity of 183 mAh g<sup>-1</sup> is delivered followed by a discharge capacity of 137 mAh g<sup>-1</sup> corresponding to a 25 % irreversible capacity loss upon the first cycle. For NMC-622 it can be seen that initial charge and discharge capacities of 169 mAh g<sup>-1</sup> and 149 mAh g<sup>-1</sup> are delivered respectively with a 12 % irreversible capacity loss upon this first cycle. These irreversible losses can be attributed to the oxidation of Ni<sup>2+</sup> in the lithium sites to Ni<sup>3+</sup> causing local shrinkage around the Ni<sup>3+</sup> ions and ultimately making the reinsertion of Li<sup>+</sup> more difficult upon discharge.<sup>234</sup>

Over 30 cycles the discharge capacities from NMC-811 decrease to 104 mAh g<sup>-1</sup> highlighting the poor cycling stabilities often observed for such high nickel content cathodes. Similar behaviour is observed by Bi *et al.* for a sample of NMC-811 synthesised in air at 850 °C.<sup>235</sup> For the NMC-622 cell, after the first cycle the discharge capacities are shown to decrease to ≈ 135 mAh g<sup>-1</sup> where they remain relatively stable over the following 19 cycles. This shows that a good degree of cycling stability is exhibited by the microwave synthesised NMC-622 material and the capacities achieved agree well with those obtained for NMC-622 synthesised by a sol-gel method at 850 °C in air by Lee *et al.* who reported first cycle charge and discharge capacities of approximately 175 mAh g<sup>-1</sup> and 145 mAh g<sup>-1</sup> between 2.75 - 4.3 V vs. Li/Li<sup>+</sup> at a cycling rate of C/10. However, whereas the microwave-synthesised NMC-622 sample showed stability over at least 20 cycles, their sample showed a gradual decrease in charge and discharge capacities over 100 cycles, with the discharge capacity after 20 cycles approximately 125 mAh g<sup>-1</sup>.<sup>236</sup>

The syntheses of NMC-811 and NMC-622 presented here represent the synthesis undertaken in order to produce powder samples for the µ<sup>+</sup>-SR experiments presented in the following section. Work involving the optimisation of the synthesis parameters for the microwave-assisted sol-gel production of NMC-811 is presented later in Section 4.2.7.

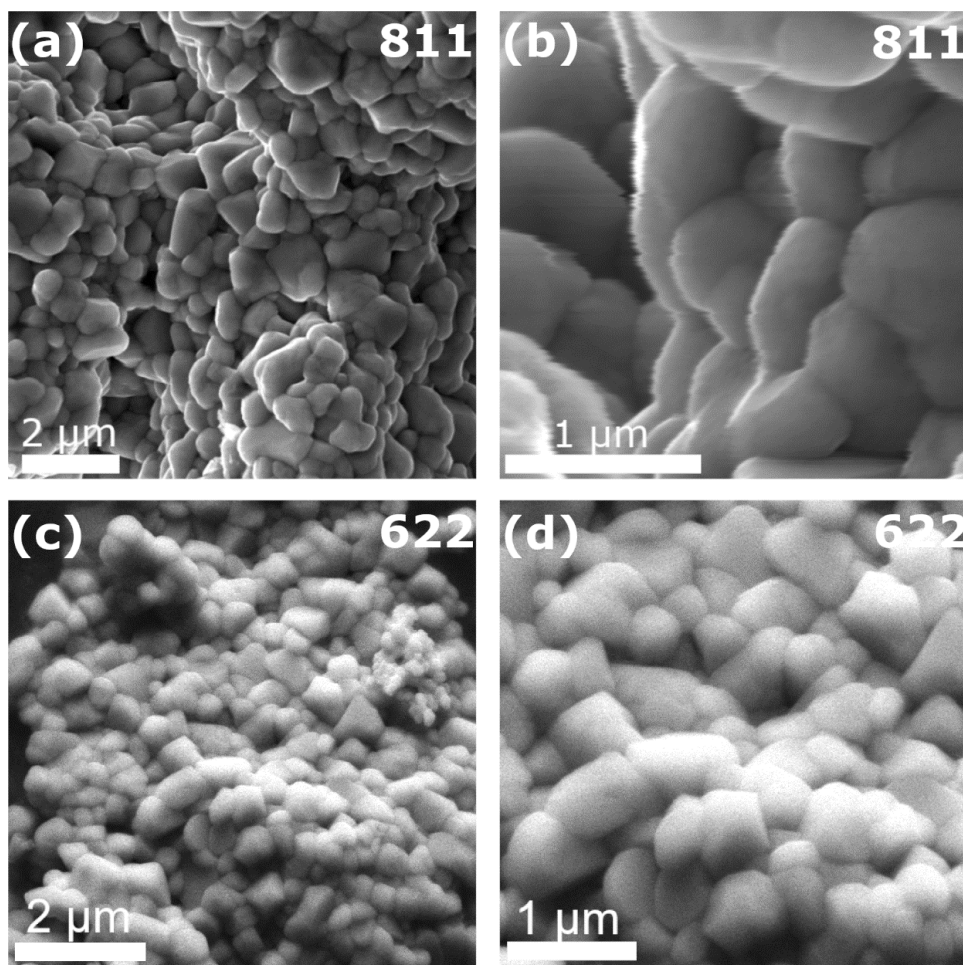


**Figure 4.11** SEM images at magnifications of (a,b) NMC-811 and (c,d) NMC-622 prepared by a microwave-assisted sol-gel method at 850 °C for 2 hours.

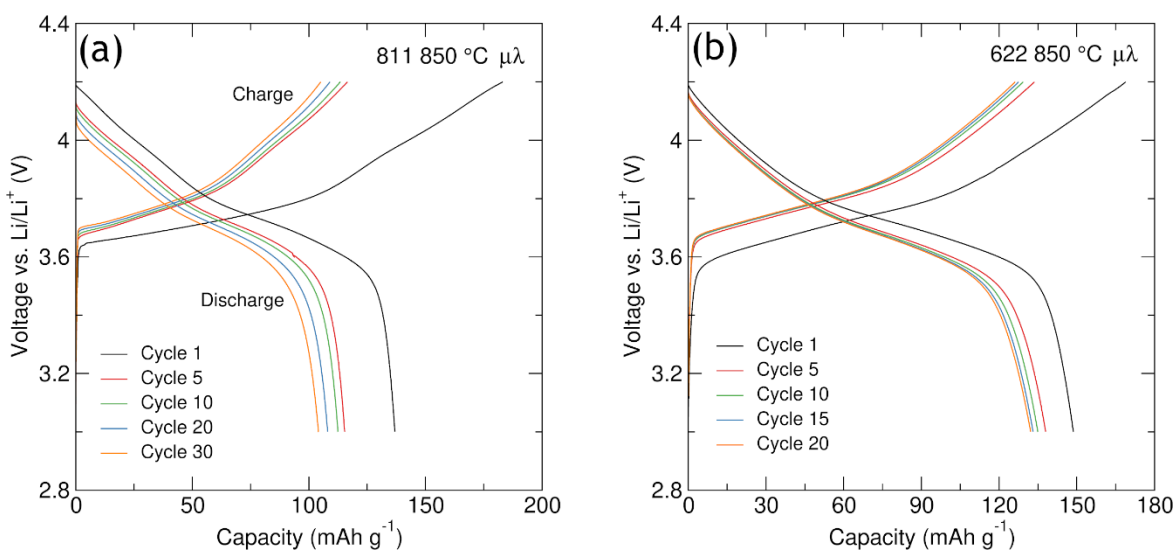


**Figure 4.12** Charge discharge profiles obtained from galvanostatic cycling at room temperature of (a) NMC-811 and (b) NMC-622 cathode pellets (NMC: carbon black: PVDF in a 90:5:5 wt% ratio) synthesised by a microwave-assisted sol-gel method with a reaction time of 2 hours at 850 °C. Coin cells were cycled between 3.0 - 4.2 V vs. Li/Li<sup>+</sup> at a rate of C/10.

#### 4.2.6 Muon spin spectroscopy measurements on high nickel content layered oxides $\text{LiNi}_{0.8}\text{Mn}_{0.1}\text{Co}_{0.1}\text{O}_2$ and $\text{LiNi}_{0.6}\text{Mn}_{0.2}\text{Co}_{0.2}\text{O}_2$

As presented in Chapter 3, muon spin spectroscopy ( $\mu^+$ -SR) is an interesting and useful technique that can be used for studying the local ionic diffusion properties of both electrode and electrolyte materials for lithium ion batteries. In this section, the  $\mu^+$ -SR technique was used in order to study microscopic  $\text{Li}^+$  diffusion characteristics in four different layered oxide samples - two samples NMC-811 and NMC-622 synthesised by a microwave assisted sol-gel method and two samples of both obtained from a commercial supplier.

Zero-field and longitudinal field measurements at different temperatures were carried out as described previously in this thesis for  $\text{LiFeSO}_4\text{F}$  and  $\text{Na}_2\text{FePO}_4\text{F}$  materials, where a ca. 1 g sample of NMC powder in a titanium holder was subject to muon implantation from a beam of spin polarised muons on the EMU instrument at ISIS. For layered oxide material  $\text{Li}_x\text{Ni}_{1/3}\text{Mn}_{1/3}\text{Co}_{1/3}\text{O}_2$  it has been determined by DFT calculations that the muon implantation site is close to  $\text{O}^{2-}$  anions, where the muons sit in interstitial sites with a typical bond length of  $d_{\mu-\text{O}} \approx 1.12 \text{ \AA}$  with all stopping sites roughly equivalent from an electrostatic viewpoint.<sup>237</sup>

The raw data obtained at 300 K and 400 K, which describes the time evolution of the positron decay asymmetry for each sample is shown in Figure 4.13 for NMC-811 and Figure 4.14 for NMC-622. Solid lines in the raw data plots show the fits obtained by applying an exponentially relaxing dynamic Kubo-Toyabe function simultaneously to the raw data collected at each applied field. Each material undergoes very similar behaviour in the decay positron asymmetry, characterised by an initial fast relaxation up to  $\approx 2 \mu\text{s}$  for all of the samples which are attributed to the interactions between the muon spin and the paramagnetic moments originating from unpaired  $3d$  electrons on transition metal ions. In layered oxides, the transition metal electron configurations are  $\text{Ni}^{2+}$  ( $d^8$ ,  $t_{2g}^6 e_g^2$ )  $\text{Ni}^{3+}$  ( $d^7$  low-spin,  $t_{2g}^6 e_g^1$ ),  $\text{Mn}^{4+}$  ( $d^3$ ,  $t_{2g}^3$ ) and  $\text{Co}^{3+}$  ( $d^6$ ,  $t_{2g}^6$ ) meaning that only the  $\text{Ni}^{2+}$ ,  $\text{Ni}^{3+}$  and  $\text{Mn}^{4+}$  ions will contribute to this paramagnetic relaxation as  $\text{Co}^{3+}$  is diamagnetic.<sup>225</sup> A slower relaxation is observed thereafter which can be attributed to the interactions between the muon spin and the surrounding nuclear magnetic fields from  $^6\text{Li}$  (7.6 % abundance),  $^7\text{Li}$  (92.4 % abundance),  $^{55}\text{Mn}$  (100 % abundance),  $^{59}\text{Co}$  (100 % abundance) and  $^{61}\text{Ni}$  (1.1 % abundance) which all possess a non-zero nuclear magnetic moment. At 300 K the ZF-spectra show evidence of a Kubo-Toyabe type relaxation with the relaxation rate decreasing upon an increase in temperature to 400 K indicating the dynamic behaviour of the  $\text{Li}^+$  ions. This observation is consistent with high temperature  $\mu^+$ -SR data presented

by Sugiyama *et al.* and Månsson *et al.* on several compositions of  $\text{Li}_x\text{Ni}_{1/3}\text{Mn}_{1/3}\text{Co}_{1/3}\text{O}_2$ .<sup>182,237</sup> It is observed that the NMC-622 sample exhibits a stronger Kubo-Toyabe type relaxation at 300 K than NMC-811 which could be explained by slower diffusion of  $\text{Li}^+$  in NMC-622 at this temperature compared to NMC-811. At longitudinal fields of 5 G and 10 G, the relaxation rate in each sample also decreases owing to the gradual decoupling of interactions between the muon spin and the local nuclear environment. The data for each sample were fit considering Equation 4.1 using an exponentially relaxing dynamic Gaussian Kubo-Toyabe function, such that:

$$A_0P(t) = A_{KT}G^{DGKT}(\Delta, \nu, t) \exp(-\lambda t) + A_{BG} \quad (4.1)$$

where  $A_0$  is the initial ( $t = 0$ ) asymmetry,  $P(t)$  is the muon spin depolarization function and  $A_{KT}G^{DGKT}$  is the dynamic Kubo-Toyabe function from which the field fluctuation rate,  $\nu$  and the static width of the local field distribution,  $\Delta$  can be extracted.  $A_{BG}$  is the background asymmetry and the exponential term describes the rapid paramagnetic fluctuations from the transition metal ions.

From the fittings, the temperature dependence of the field fluctuation rates and the static width of the local field distribution for each sample could be extracted and are shown in Figure 4.15. All of the studied samples show similar behaviour for both of these parameters, for example, the field fluctuation rates ( $\nu$ ) shown in Figures 4.15(a) and (b) follow a similar trend of initially exhibiting a reasonably flat plateau region before increasing as the temperature is raised due to the onset and gradual increase of thermally activated  $\text{Li}^+$  diffusion. For both of the NMC-811 samples, this increase in  $\nu$  is shown to occur at  $\approx 200$  K with the fluctuation rate sharply rising to between  $\approx 2.6$  MHz to 2.8 MHz for the sol-gel and commercial samples respectively at the end point. This behaviour is more subtle for the NMC-622 samples where a gradual increase in  $\nu$  can be observed starting at 200 K although this is much less sharp than the behaviour observed in the NMC-811 samples with the rising field fluctuation rate becoming more intense at higher temperatures. It is also noted that lower field fluctuation rates are observed at higher temperatures for NMC-622 compared to NMC-811 suggesting that  $\text{Li}^+$  diffusion is slower in NMC-622.

The extracted field fluctuation rates for both of the NMC-811 samples show very close overlap, indicating that the microscopic  $\text{Li}^+$  diffusion behaviour for both of these materials is expected to be very similar. It is noted that measurements performed on the commercial NMC-811 begin at 140 K rather than 100 K as for the other samples. This was due to limited time on the muon beamline and therefore the lower temperature measurements, where no changes in the field fluctuation rate are expected were not

carried out. Conversely, there is a difference between the extracted  $\nu$  parameters for the different NMC-622 samples. The sol-gel NMC-622 consistently exhibits lower values compared to the commercial sample, although the behaviour of the temperature dependence is very similar. This difference most likely arises due to slower  $\text{Li}^+$  diffusion in the sol-gel sample compared to the commercial sample. This could possibly be attributed to factors such as an apparent increased Li/Ni mixing calculated for the sol-gel sample ( $\approx 2.3\%$  and  $1.9\%$  for the sol-gel and commercial samples respectively) whereby more Ni residing in the Li layer could block the diffusion pathways.

All four samples show almost identical behaviour for the temperature dependence of the  $\Delta$  parameter characterised by a gradual decrease from  $\approx 0.35$  MHz to  $\approx 0.25$  MHz across the measured temperature range, which could be explained by the changing local magnetic fields as a result of the thermally activated lithium diffusion process.

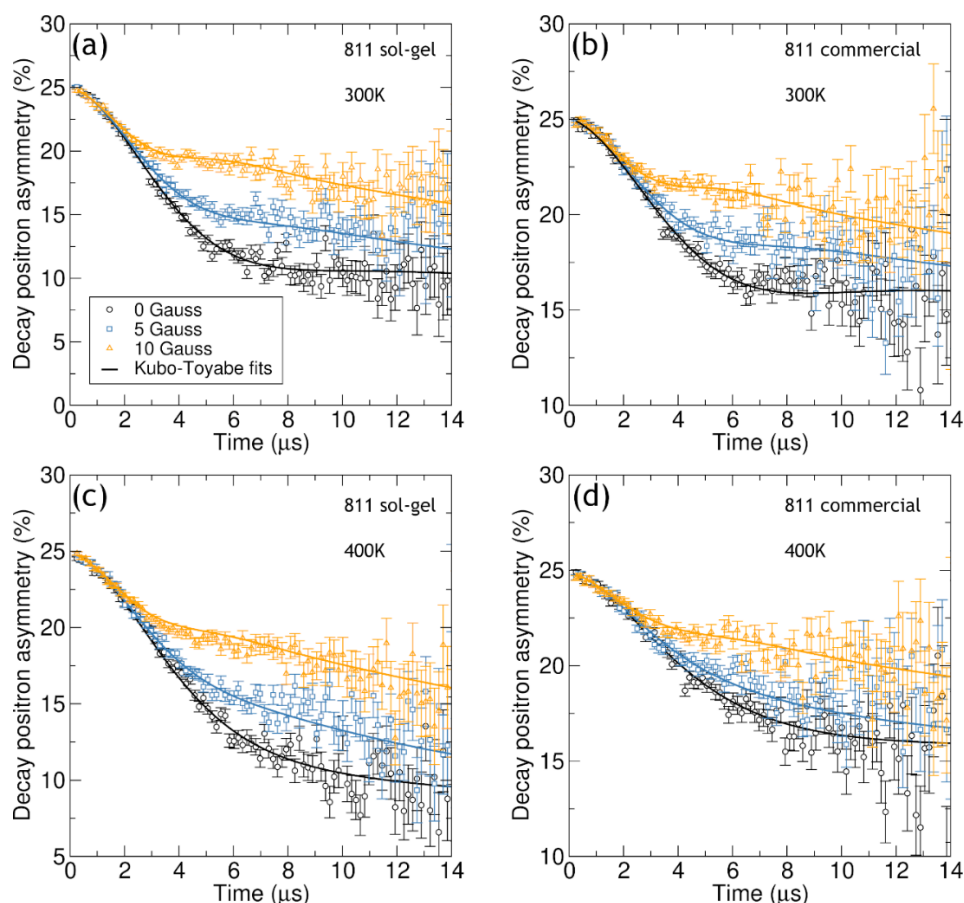


**Figure 4.13** Raw  $\mu^+$ -SR data collected at (a) 300 K for layered oxide NMC-811 synthesised by the microwave-assisted sol-gel method and (b) NMC-811 obtained from a commercial supplier and at (c) 400 K for layered oxide NMC-811 synthesised by the microwave-assisted sol-gel method and (d) NMC-811 obtained from a commercial supplier. Data at zero field (black circles) and applied longitudinal fields of 5 G (blue squares) and 10 G (orange triangles) is shown alongside the fit to the data using a dynamic Kubo-Toyabe function (solid lines).

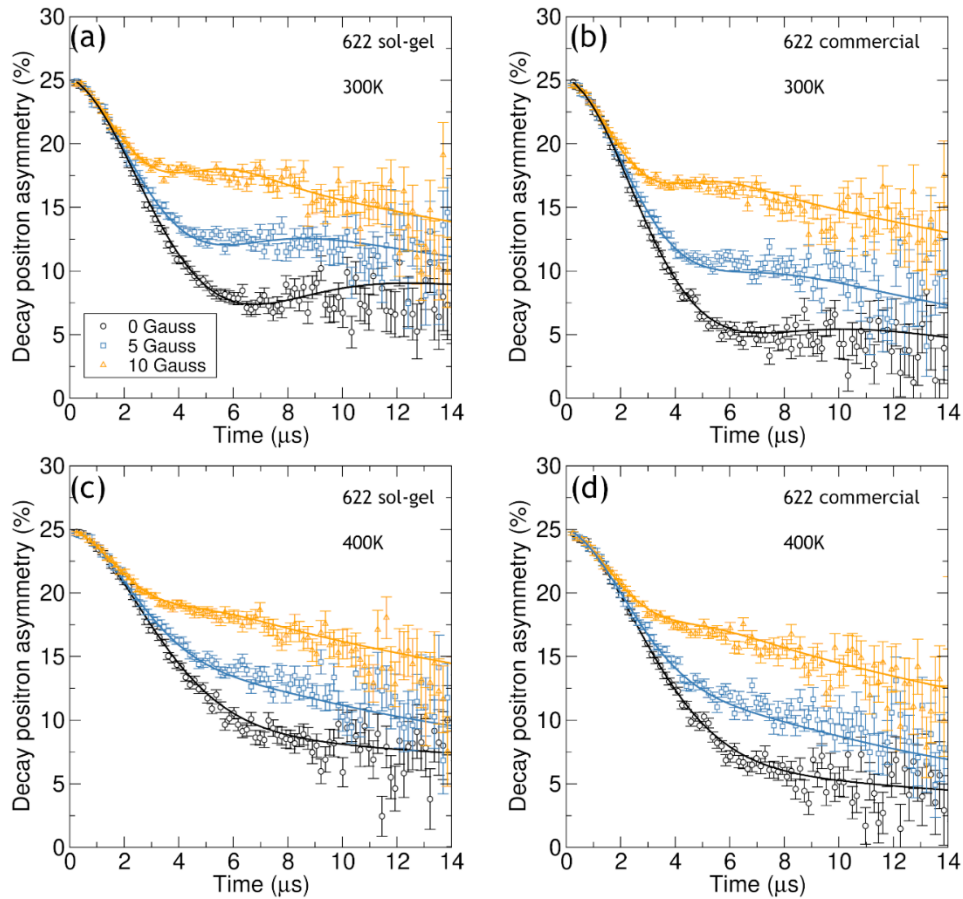


**Figure 4.14** Raw  $\mu^+$ -SR data collected at (a) 300 K for layered oxide NMC-622 synthesised by the microwave-assisted sol-gel method and (b) NMC-622 obtained from a commercial supplier and at (c) 400 K for layered oxide NMC-622 synthesised by the microwave-assisted sol-gel method and (d) NMC-622 obtained from a commercial supplier. Data at zero field (black circles) and applied longitudinal fields of 5 G (blue squares) and 10 G (orange triangles) is shown, alongside the fit to the data using a dynamic Kubo-Toyabe function (solid lines).

The activation energy,  $E_a$  for thermally activated  $\text{Li}^+$  hopping can be calculated from an Arrhenius plot over the identified thermally activated region, considering the Arrhenius equation:

$$\ln(\nu) = \frac{-E_a}{K_B T} + \ln(A) \quad (4.2)$$

where  $\nu$  is the field fluctuation rate calculated at temperature  $T$ ,  $K_B$  is the Boltzmann constant ( $1.3806488 \times 10^{-23} \text{ J K}^{-1}$ ) and  $A$  is a pre-exponential factor. Thus the activation energy can be calculated from the gradient of the straight line fit on the  $\ln(\nu)$  against  $1/T$  plot. The plot over the thermally activated region for the data obtained from  $\mu^+$ -SR measurements on all four NMC samples studied here is shown in Figure 4.16 with activation energies for the NMC811 sol-gel, NMC-811 commercial, NMC-622 sol-gel and

NMC-622 commercial estimated as 44 meV, 48 meV, 54 meV and 53 meV respectively, highlighting good agreement between the sol-gel and commercial samples for each composition. These values also compare well with results published by Sugiyama *et al.* who used the studied the  $\text{Li}^+$  diffusion in  $\text{Li}_x\text{Ni}_{1/3}\text{Mn}_{1/3}\text{Co}_{1/3}\text{O}_2$  materials with differing lithium contents and calculated activation energy values of 74 meV and 43 meV for highly lithiated compositions of  $x = 1$  and  $x = 0.93$  respectively.<sup>237</sup> Another  $\mu^+$ -SR study on  $\text{Li}_x\text{Ni}_{1/3}\text{Mn}_{1/3}\text{Co}_{1/3}\text{O}_2$  by Månsson *et al.* reported activation energies of  $\approx 100$  meV for compositions of  $x = 1$  and  $x = 0.3$  indicating that there are published discrepancies between samples of the same composition in the literature which is most likely sensitive to the data processing methodology used.<sup>182</sup>

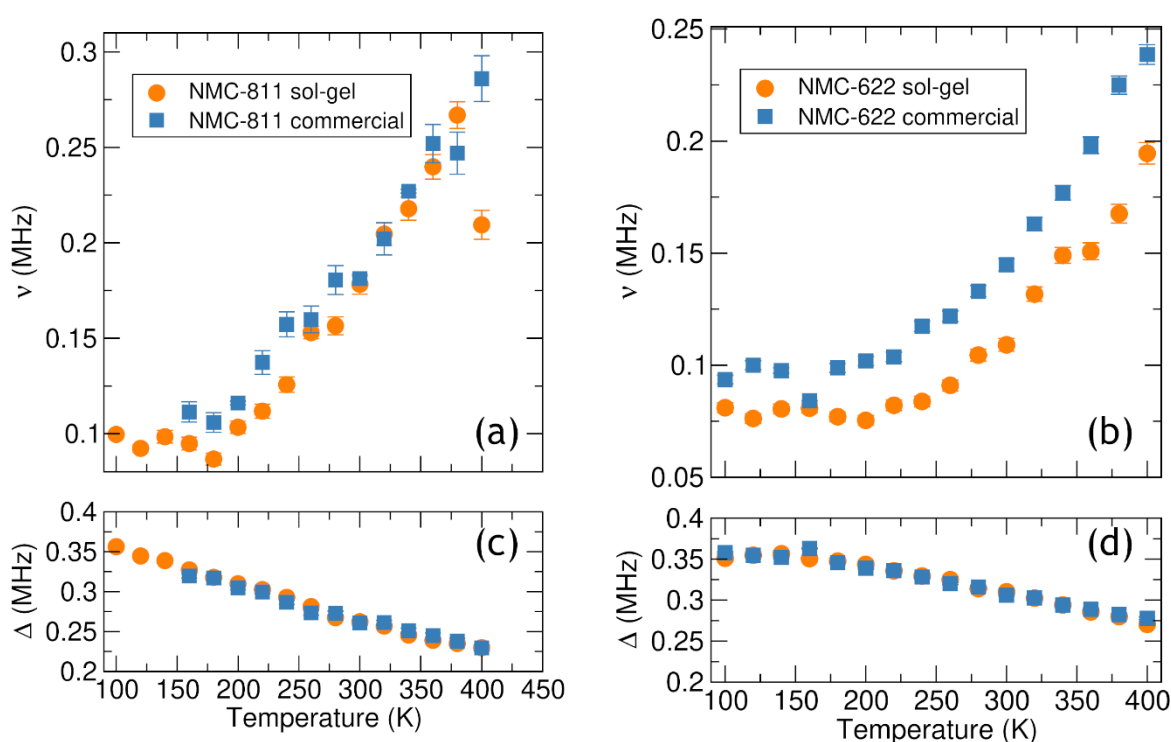


**Figure 4.15** Temperature dependence of the field fluctuation rate ( $\nu$ ) and the field distribution width at the muon stopping site ( $\Delta$ ) for  $\mu^+$ -SR data obtained for (a) and (c) NMC-811 sol-gel and commercial samples and (b) and (d) NMC-622 sol-gel and commercial between 100 K to 400 K at ZF and LFs of 5 and 10 G, fit using an exponentially relaxing Kubo-Toyabe function.

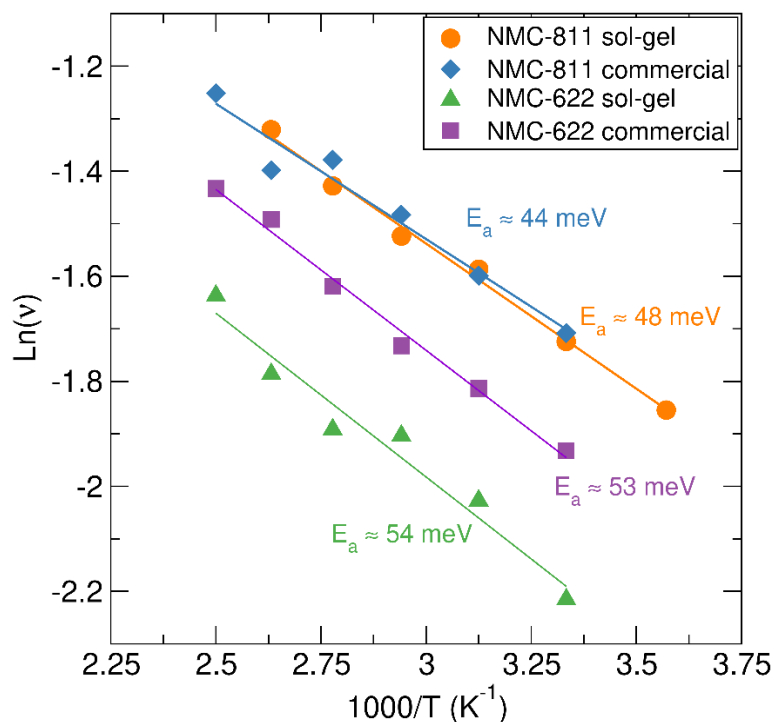


**Figure 4.16** Arrhenius plot of the field fluctuation rate over the thermally activated region calculated from  $\mu^+$ -SR measurements for NMC-811 sol-gel (circles), NMC811 commercial (diamonds), NMC-622 sol-gel (triangles) and NMC-622 commercial (squares). Activation energies were estimated as 44 meV, 48 meV, 54 meV and 53 meV respectively.

To calculate lithium diffusion coefficients for each sample, the available paths for  $\text{Li}^+$  transport must be considered. In layered transition metal oxides such as  $\text{LiNi}_x\text{Mn}_y\text{Co}_{1-x-y}\text{O}_2$  there are two possible jump-paths within the lithium containing layer (*i.e.* the *ab* plane) that enable lithium diffusion. The most obvious path involves the hopping from one lithium 3a site an adjacent 3a lithium site with a path-length equal to the *a* lattice parameter, whereas the other possible pathway involves a jump to interstitial sites with a path-length equal to  $a/\sqrt{3}$ . This is shown in Figure 4.17 where possible jumps for path 1 are shown by blue arrows and those for path 2 are highlighted by magenta arrows. To calculate the diffusion coefficient,  $D_{\text{Li}}$  therefore, the *a* lattice parameter obtained from previous Rietveld refinements is required and Equation 4.3 is used where  $N_i$  is the number of accessible  $\text{Li}^+$  sites in the available path,  $Z_{v,i}$  is the vacancy fraction of the destination sites and  $s_i$  is the jump distance between adjacent  $\text{Li}^+$  sites in the  $i^{\text{th}}$  path and  $\nu$  is the field fluctuation rate obtained from  $\mu^+$ -SR measurements. For layered oxides with general formula  $\text{Li}_n\text{Ni}_x\text{Mn}_y\text{Co}_{1-x-y}\text{O}_2$  path 1:  $N_1 = 6$ ,  $Z_{v,1} = 1-n$ ,  $s_1 = a$  and for path 2:  $N_2 = 3$ ,  $Z_{v,2} = 1$  and  $s_2 = a/\sqrt{3}$ . For the samples studied here it is assumed that the material is fully lithiated *i.e.*  $n = 1$  and thus only path 2 involving hops to interstitial sites will be considered in the calculations of the diffusion coefficients.

$$D_{Li} = \sum_{i=1}^n \frac{1}{N_i} Z_{v,i} s_i^2 v \quad (4.3)$$

To obtain the magnitude of the  $a$  lattice parameter, Rietveld refinements were carried out on PXRD collected for each commercial sample, using models with appropriate transition metal stoichiometry for the NMC-811 and NMC-622 compositions and also accounting for Li/Ni site mixing that may occur between the lithium  $3a$  site and the transition metal  $3b$  site. Appropriate constraints were applied during the refinement in order to preserve the correct stoichiometry of the compound. The refinement was prepared for 15 variables, including scale factor, zero point, sample displacement, 6 background coefficients (fitted with a Chebyshev function), lattice parameters, microstrain and size parameters and Ni site occupancies. All other atomic positions, displacement parameters and site fractions were not refined. The refinement results and extracted lattice parameters are shown in Figure 4.18 and Table 4.4. Good fits to the data were achieved evidenced by the low  $R_{wp}$  and  $\chi^2$  values obtained and  $a$ -axis lattice parameters of 2.872 Å and 2.871 Å were achieved for NMC-811 and NMC-622 respectively.

Diffusion coefficients at 300 K and activation energies estimated for the four samples studied are listed in Table 4.5. The diffusion coefficients at 300 K were calculated for the sol-gel and commercial samples of NMC-811 as  $1.64 \times 10^{-11} \text{ cm}^2 \text{ s}^{-1}$  and  $1.66 \times 10^{-11} \text{ cm}^2 \text{ s}^{-1}$  respectively which strongly suggests that the microscopic diffusion characteristics are very similar for both materials. For sol-gel and commercial samples of NMC-622, the diffusion coefficients at 300 K were calculated as  $9.97 \times 10^{-12} \text{ cm}^2 \text{ s}^{-1}$  and  $1.33 \times 10^{-11} \text{ cm}^2 \text{ s}^{-1}$  respectively. For comparison,  $D_{Li}$  at 300 K for NMC-111 was calculated as  $3.5 \times 10^{-12} \text{ cm}^2 \text{ s}^{-1}$  by Månsson *et al.* and it is thus observed that the diffusion coefficients increase with increasing nickel content.<sup>182</sup> This trend has also been observed for the chemical diffusion coefficient calculated for NMC-111, NMC-622 and NMC-811 using the GITT method.<sup>63</sup> Electrochemical impedance spectroscopy (EIS) studies have produced  $D_{Li}$  values of  $6.43 \times 10^{-12} \text{ cm}^2 \text{ s}^{-1}$  and  $2.18 \times 10^{-14} \text{ cm}^2 \text{ s}^{-1}$  for NMC-811 and NMC-622 respectively, indicating improved diffusion characteristics for nickel rich layered oxides between the micro and macro scales.<sup>238,239</sup>

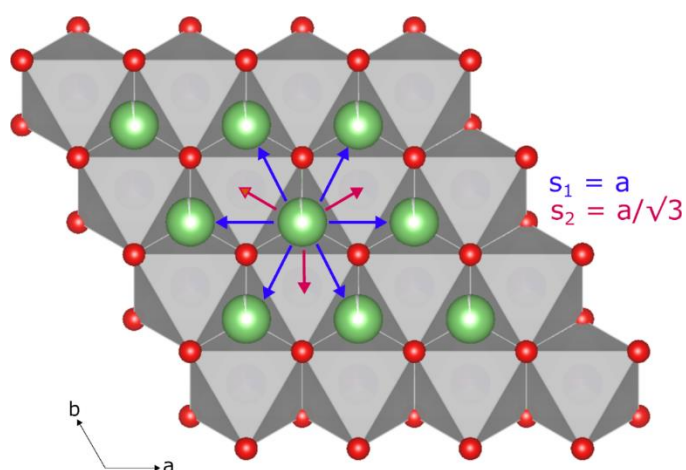


**Figure 4.17** Projection onto the lithium containing  $ab$  plane for  $R\bar{3}m$   $\text{LiMO}_2$  ( $M = \text{Ni}, \text{Mn}, \text{Co}$ ) showing the two different jump-paths available for  $\text{Li}^+$  diffusion. One path involves a jump to an adjacent Li site with a distance of  $a$  and the other path involves a jump to an interstitial site with distance  $a/\sqrt{3}$ .

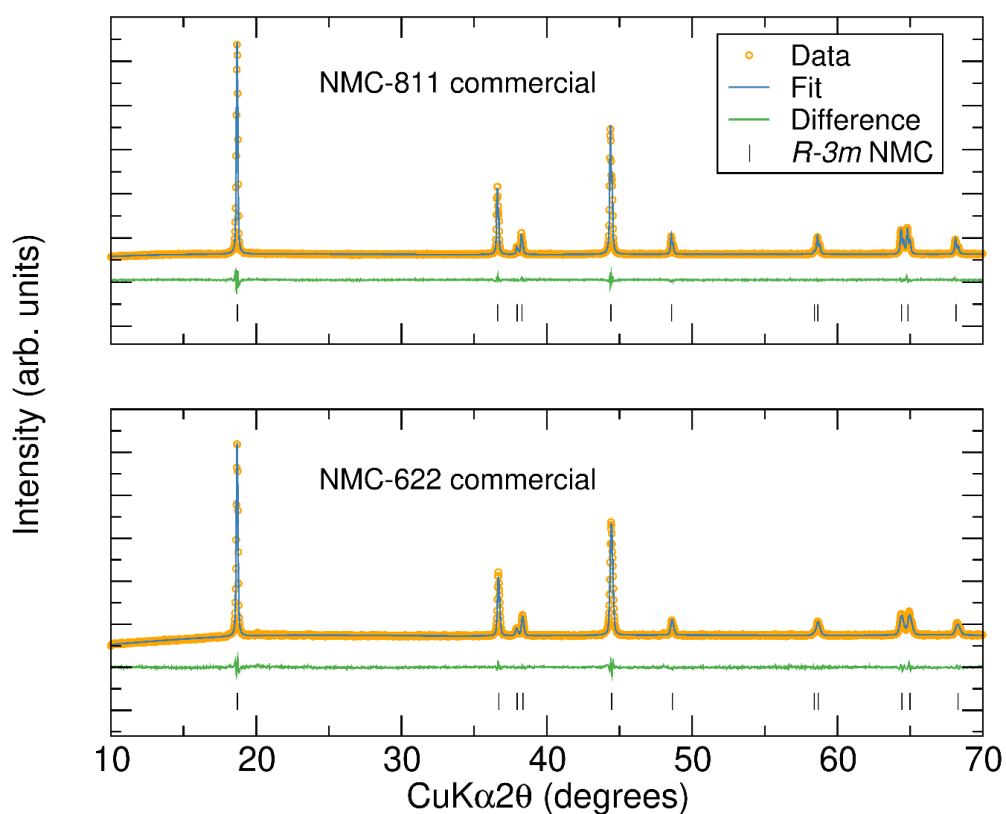


**Figure 4.18** Rietveld refinements on PXRD data obtained from NMC-811 and NMC-622 obtained from a commercial supplier. Models of  $R\bar{3}m$  phase  $\text{LiNi}_{0.8}\text{Mn}_{0.1}\text{Co}_{0.1}\text{O}_2$  and  $\text{LiNi}_{0.6}\text{Mn}_{0.2}\text{Co}_{0.2}\text{O}_2$  were fit to the corresponding collected PXRD data.

**Table 4.4** Calculated lattice parameter and Li/Ni mixing from Rietveld refinements and calculated  $I_{(003)}/I_{(104)}$  ratios obtained for samples of NMC-811 and NMC-622 obtained from a commercial supplier.

Sample	NMC-811 commercial	NMC-622 commercial
Space Group	$R\bar{3}m$	$R\bar{3}m$
a (Å)	2.87200(5)	2.87075(11)
c (Å)	14.19898(26)	14.22641(57)
V (Å <sup>3</sup> )	101.428(3)	101.535(8)
Ni1 occupancy	0.07869(10)	0.5736(10)
Ni2 occupancy	0.0131(10)	0.0264(10)
Li/Ni mixing	1.31 %	2.64 %
$I(003)/I(104)$	1.68	1.72
$R_{wp}$	2.460 %	1.954 %
$\chi^2$	1.59	1.21

**Table 4.5** Activation energies and room temperature (300 K) diffusion coefficients calculated from  $\mu^+$ -SR measurements for microwave synthesised sol-gel samples of NMC-811 and NMC-622 (850 °C, 2 h) and samples of both obtained from a commercial supplier.

Sample	Activation energy (meV)	Diffusion coefficient (cm <sup>2</sup> s <sup>-1</sup> )
NMC-811 sol-gel	48 (±1.8)	$1.64 \times 10^{-11}$
NMC-811 commercial	44 (±4.6)	$1.66 \times 10^{-11}$
NMC-622 sol-gel	54 (±5.5)	$9.97 \times 10^{-12}$
NMC-622 commercial	53 (±2.5)	$1.33 \times 10^{-11}$

#### 4.2.7 Optimisation of the microwave assisted sol-gel synthesis of $\text{LiNi}_{0.8}\text{Mn}_{0.1}\text{Co}_{0.1}\text{O}_2$

The temperature and time of the final microwave-assisted heating step was varied between 650 and 900 °C and 1 to 3 hours in order to investigate the minimum times and temperatures required to yield layered NMC-811 with good structural and electrochemical properties. The focus of this chapter has been the NMC-811 composition, due to the interest it has received from both academia and industry as the frontrunner for next generation LIB cathodes for automotive applications.

The PXRD patterns collected for a range of synthesised samples with a microwave reaction time of 1 hour and microwave reaction temperatures of 650 °C, 750 °C, 800 °C, 850 °C and 900 °C are shown in Figure 4.19. Figure 4.19(a) shows the complete PXRD patterns collected between  $2\theta$  angles of 10 to 70 ° alongside a reference pattern for NMC-811 obtained from the ICSD (collection code 171750). From inspection of the data, it is evident that all five materials show intense peaks at reflections corresponding to rhombohedral  $R\bar{3}m$  NMC-811 indicating that all samples possess a  $\alpha\text{-NaFeO}_2$  layered type structure. However, it can be seen from the PXRD pattern that the sample heated at 650 °C contains an impurity phase, evidenced by the presence of additional peaks between  $2\theta$  values of 20 to 35 °. This is shown in greater magnification in Figure 4.19(b) where the peaks within this region were found to correspond to  $\text{Li}_2\text{CO}_3$  phase. These peaks are also encountered in the 750 °C and 800 °C samples although to a much lesser extent and only become evident upon magnification of the 20 - 35 ° region, indicating that the quantity of  $\text{Li}_2\text{CO}_3$  phase is decreasing upon an increase in temperature. No obvious trace of  $\text{Li}_2\text{CO}_3$  is observed in the PXRD data collected for the 850 °C and 900 °C samples. The presence of  $\text{Li}_2\text{CO}_3$  in the samples heated at 650, 750 and 800 °C could be explained by the presence of excess lithium originating from the 20 % excess of lithium acetate precursor used during the reaction. Excess lithium of  $\approx 20\%$  are common in sol-gel reactions to compensate for lithium evaporation that can occur at high temperature heating. Thermal decomposition of  $\text{Li}_2\text{CO}_3$  (reported to occur between  $\approx 720$  to 1000 °C) will most likely not be a factor in the disappearance of  $\text{Li}_2\text{CO}_3$  from samples fired at higher temperatures because the decomposition product  $\text{LiO}_2$  will most likely recombine with atmospheric  $\text{CO}_2$  to form  $\text{Li}_2\text{CO}_3$  again, and so presence of  $\text{Li}_2\text{CO}_3$  would remain in the PXRD pattern.<sup>240</sup>  $\text{Li}_2\text{CO}_3$  phase could also be present as an impurity due to the heating conditions not being high enough to facilitate the successful incorporation of lithium into the layered structure.

The degree of cation ordering observed in the system can be understood by analysing the intensity ratio of the (003) and (104) peaks. The ratio  $I_{(003)}/I_{(104)}$  should be a direct indicator of interlayer cation order, with values of  $I_{(003)}/I_{(104)} < 1.2$  indicating that undesirable cation mixing is present in the sample.<sup>211,231</sup> The sample fired at 650 °C has a calculated  $I_{(003)}/I_{(104)}$  ratio of 0.58 which is clearly very much smaller than 1.2, thus suggesting a large degree of cation disorder which could be facilitated by the deficiency of lithium in the sample due to the low firing temperature. This then can allow Ni<sup>2+</sup> cations to distribute across the two layers, producing a sample with greater cation disorder. The calculated  $I_{(003)}/I_{(104)}$  ratios for the 780, 800 and 850 °C samples are 1.41, 1.32 and 1.26 respectively, indicating a good level of cation ordering in the structure, whereas the calculated ratio for the 900 °C sample was 1.04 suggesting that cation ordering begins to decrease again slightly upon heating to high temperatures. The amount of Li<sub>2</sub>CO<sub>3</sub> impurity in the 750 and 800 °C sample is minimal and most likely arises from unreacted lithium.

The peak splitting of the (108) and (110) doublet, shown for all samples in Figure 4.19(c) is also an indicator of good rhombohedral ordering in the structure.<sup>241</sup> From the data collected, it is evident that the sample fired at 650 °C shows no splitting of these reflections at all, again indicating a poor level of ordering whereas all of the other samples show a splitting of these reflections correlating to improved ordering at temperatures above 650 °C.

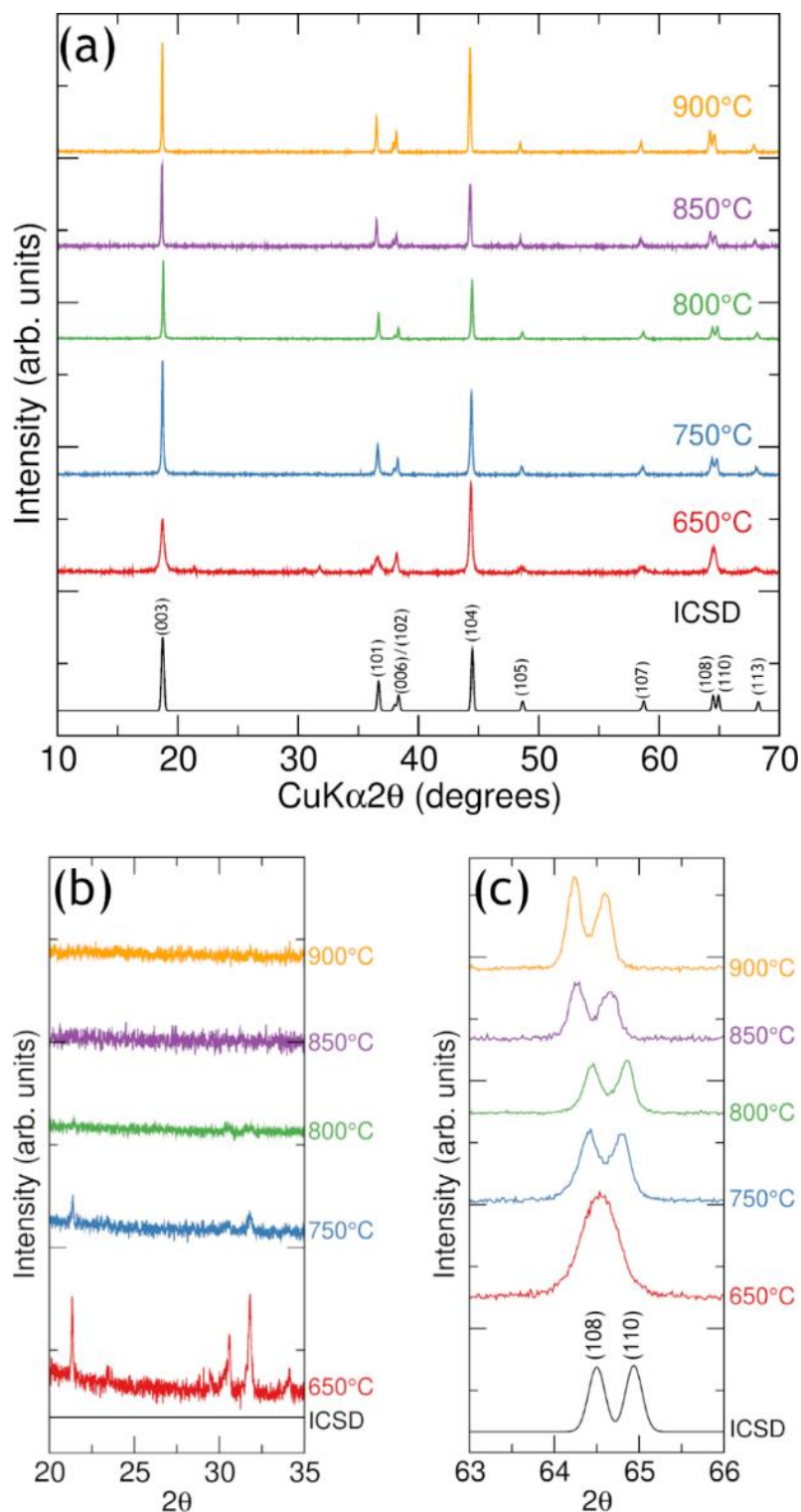


**Figure 4.19** PXRD patterns collected between  $2\theta$  angles of (a) 10 - 70 ° for NMC-811 synthesised by a microwave-assisted sol-gel method with a reaction time of 1 hour and reaction temperatures of 650 °C, 750 °C, 800 °C, 850 °C and 900 °C. A standard pattern for NMC-811 obtained from the ICSD is shown also. Portions of the data between (b) 20 - 25 ° and (c) 63 - 66 ° are also shown to highlight any present impurity phases and the peak splitting of the (108) and (110) reflections indicating the “layered-ness” of the structure.

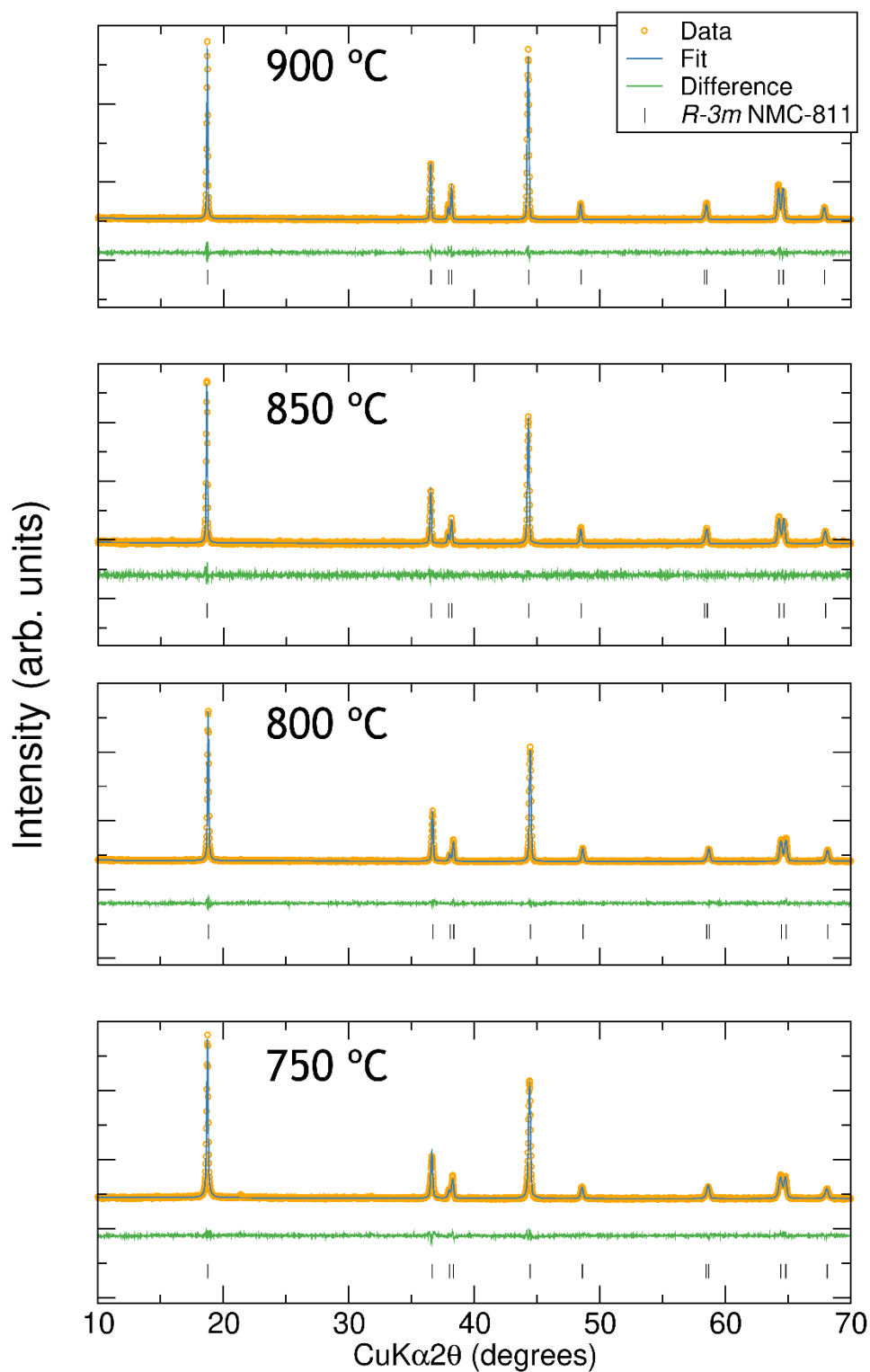


**Figure 4.20** Rietveld refinements on PXRD data obtained from NMC-811 samples synthesised by a microwave-assisted sol-gel method with a reaction time of 1 hour and reaction temperatures of 750 °C, 800 °C, 850 °C and 900 °C. A model consisting of  $R\bar{3}m$  phase  $\text{LiNi}_{0.8}\text{Mn}_{0.1}\text{Co}_{0.1}\text{O}_2$  was fit to the collected PXRD data.

**Table 4.6** Calculated lattice parameter and Li/Ni mixing from Rietveld refinements and calculated  $I_{(003)}/I_{(104)}$  ratios obtained for NMC-811 samples synthesised by a microwave-assisted sol-gel method with a reaction time of 1 hour and reaction temperatures of 750 °C, 800 °C, 850 °C and 900 °C.

Sample	900 °C	850 °C	800 °C	750 °C
Space group	$R\bar{3}m$	$R\bar{3}m$	$R\bar{3}m$	$R\bar{3}m$
a (Å)	2.88623(11)	2.87983(20)	2.87266(12)	2.87089(17)
c (Å)	14.24358(38)	14.22123(73)	14.19037(44)	14.17814(62)
V (Å <sup>3</sup> )	102.757(7)	102.141(12)	101.413(8)	101.201(11)
Ni1 occupancy	0.679(1)	0.0763(20)	0.7473(10)	0.7425(10)
Ni2 occupancy	0.121(1)	0.7237(20)	0.0527(10)	0.0575(10)
Li/Ni mixing	12 %	7.63 %	5.27 %	5.75 %
$I_{(003)}/I_{(104)}$	1.04	1.26	1.32	1.41
$R_{wp}$	4.801 %	8.630 %	4.795 %	5.1 %
$\chi^2$	1.30	1.12	1.25	1.48

Rietveld refinements were carried out on the samples fired at 750 °C, 800 °C, 850 °C and 900 °C in order to obtain lattice parameters and to quantitatively analyse the Li/Ni site mixing. Refinements were carried out using the GSAS-II program by fitting a model of  $R\bar{3}m$  NMC-811 obtained from the ICSD to the collected PXRD data, with refinements plots shown in Figure 4.20 and extracted parameters shown in Table 4.6. The refinement was prepared for 15 variables, including scale factor, zero point, sample displacement, 6 background coefficients (fitted with a Chebyshev function), lattice parameters, microstrain and size parameters and Ni site occupancies. All other atomic positions, displacement parameters and site fractions were not refined. The model assumed that Li primarily resided on the 3a sites, transition metals on the 3b sites and oxygen on the 6c sites. The site mixing between Li and Ni on the 3a and 3b sites was allowed with appropriate constraints such that the  $\text{LiNi}_{0.8}\text{Mn}_{0.1}\text{Co}_{0.1}\text{O}_2$  stoichiometry was retained (*i.e.* the occupancies of the Ni1 and Ni2 sites totalled to 0.8). Visually, Figure 4.20 shows that good fits have been obtained for each sample with little deviation from the background observed, with corresponding low  $R_{wp}$  and  $\chi^2$  factors, thus all materials can be described by an  $R\bar{3}m$  layered structure and can be considered to have a good level of phase purity. Extracted refinement parameter including lattice parameters, Li/Ni mixing percentages and goodness of fit factors are displayed in Table 4.6, alongside  $I_{(003)}/I_{(104)}$  ratios

calculated from PXRD data. It is observed that the  $a$  and  $c$  lattice parameters increase upon the application of higher firing temperatures which is accompanied by an increase in the unit cell volume. Previous studies on NMC-811 by Idris and West have observed similar behaviour in materials prepared between 800 to 900 °C under N<sub>2</sub> gas and attribute this increase in lattice parameters to the loss of oxygen from the structure at high firing temperatures.<sup>231</sup>

From the refinement of nickel occupancy over  $3a$  and  $3b$  sites (corresponding to nickel in the lithium layer and the transition metal layer respectively) with appropriate constraints to ensure the overall nickel content remained 0.8, the extent of Li/Ni mixing could be evaluated. The Mn<sup>4+</sup> and Co<sup>3+</sup> content was fixed at 0.1 and the resulting Li/Ni mixing were calculated as 12 %, 7.63 %, 5.27 % and 5.75 % for the samples fired at 900 °C, 850 °C, 800 °C and 750 °C respectively, highlighting that for the reaction conditions utilised here, the site mixing increases upon increasing reaction temperature.

While an impurity phase of Li<sub>2</sub>CO<sub>3</sub> was observed for the 650 °C and slight impurities of the same compound were observed for the 750 °C and 800 °C samples of NMC-811, it was decided to test out longer reaction times to evaluate whether this would facilitate the formation of impurity free NMC-811 at these lower temperatures. Samples of NMC-811 were produced by the microwave-assisted sol-gel method described previously, with an increase from 1 hour to 3 hours for the reaction time. The sol-gel precursor powder was loaded into an alumina crucible and fired at temperatures of 650 °C, 750 °C and 775 °C in air. Figure 4.21(a) shows the collected PXRD patterns for these samples in the  $2\theta$  range 10 to 70 ° where it can be seen that no improvement has occurred in the 650 °C sample compared to that shown in Figure 4.19(a) despite the longer reaction times, indicating that the temperature of 650 °C is simply too low to facilitate the full extent of reaction in order to produce phase pure NMC-811. This is corroborated by the portions of the data shown in Figure 4.21(b) and (c) which show the PXRD pattern in magnified  $2\theta$  ranges of 20 - 35 ° and 63 - 66 ° respectively. Figure 4.21(b) shows the characteristic peaks assigned to a Li<sub>2</sub>CO<sub>3</sub> impurity phase as observed for the sample fired for 1 hour previously discussed, and Figure 4.21(c) shows no splitting of the (108) and (110) reflections as was observed previously indicating that a poorly ordered rhombohedral structured material has been produced. Not surprisingly, the  $I_{(003)}/I_{(104)}$  ratio was calculated as 0.56 which shows no improvement over the material synthesised for 1 hour at 650 °C.

The sample fired at 750 °C for 3 hours shows much less impurity of Li<sub>2</sub>CO<sub>3</sub> than the sample fired for 1 hour. In this case, the peaks are very discrete and are barely noticeable above the background, indicating that longer reaction times in the microwave furnace have

successfully reduced the amount of  $\text{Li}_2\text{CO}_3$  impurity in the final product. However, from Figure 4.21(c) it is observed that there is only a slight splitting of the (108) and (110) reflections which would relate to structure with a decreased layered nature compared to previous samples. The sample fired at 775 °C for 3 hours shows no signs of impurity phase within the 20 to 35 ° range and a splitting of the (108) and (110) reflections indicating a good degree of “layered-ness” is exhibited by the structure, although the calculated  $I_{(003)}/I_{(104)}$  ratio was calculated as 1.15 which is slightly below 1.2 and could be an indication of slightly more cation mixing than is desired.

Rietveld refinements were carried out for the samples fired at 750 °C and 775 °C by fitting a model of  $R\bar{3}m$  NMC-811 obtained from the ICSD (collection code 171750) to the collected PXRD data, with refinements plots shown in Figure 4.22 and extracted parameters shown in Table 4.7. The refinements were prepared in the same way as previously described for the earlier NMC-811 samples. The refinement plots and extracted low  $R_{wp}$  and  $\chi^2$  values show that good fits to the data have been achieved during the refinement process and that both structures can be described by an  $R\bar{3}m$  phase. The lattice parameters obtained are similar for both samples, with slight differences observed in the  $a$  and  $c$  parameters but very similar cell volumes were calculated for both. From the refinement of nickel occupancy over  $3a$  and  $3b$  sites with appropriate constraints to ensure the overall nickel content remained 0.8, the extent of Li/Ni mixing could be evaluated. The  $\text{Mn}^{4+}$  and  $\text{Co}^{3+}$  content was fixed at 0.1 and the resulting Li/Ni mixing were calculated as 5.61 % and 9.49 % for the samples fired at 775 °C and 750 °C respectively. These results seem to suggest that the structure of NMC-811 for samples fired at 750 °C seems to become less ordered, with an increased level of site mixing observed for longer microwave heating times.

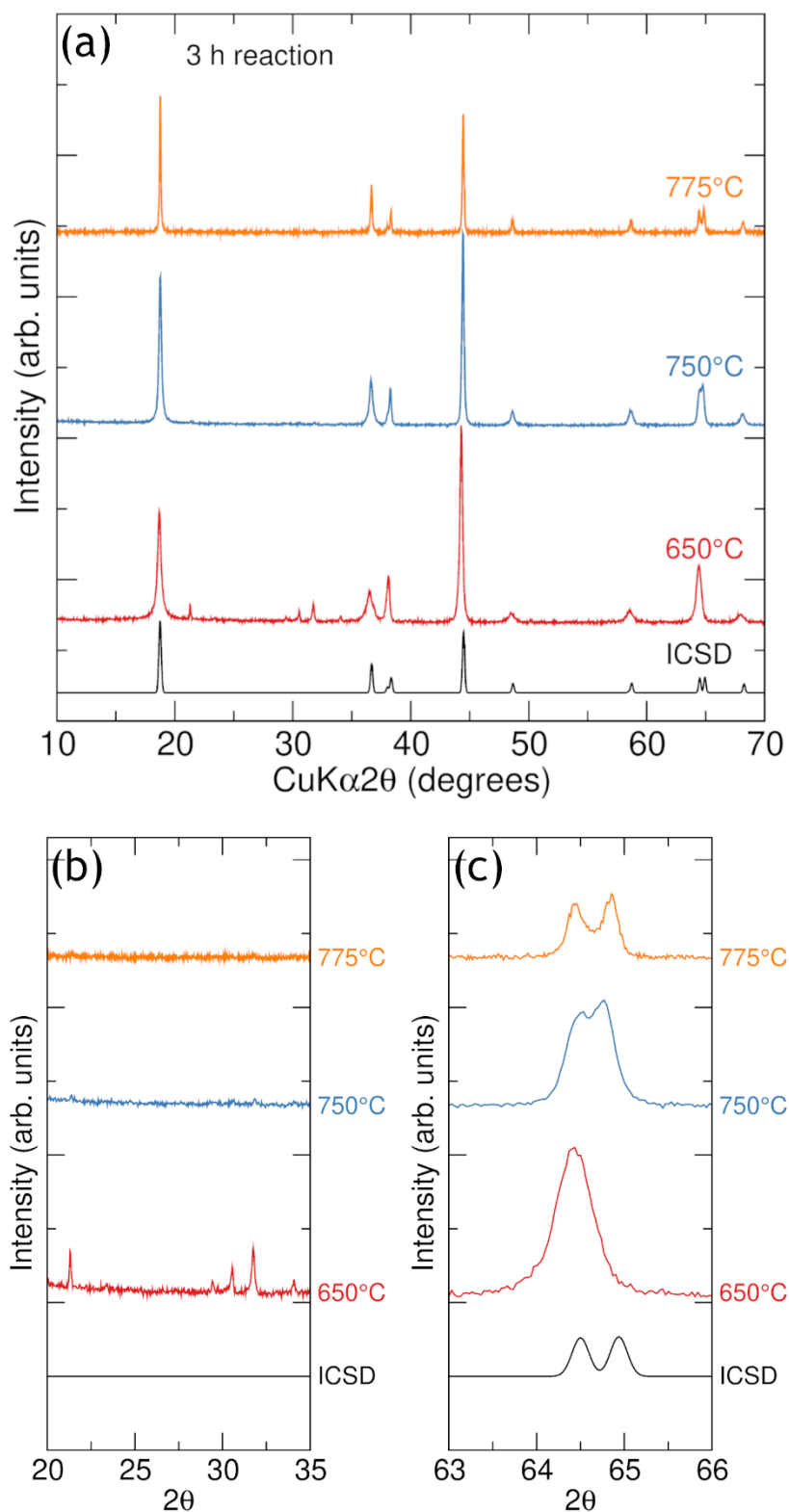


**Figure 4.21** PXRD patterns collected between  $2\theta$  angles of (a) 10 - 70 ° for NMC-811 synthesised by a microwave-assisted sol-gel method with a reaction time of 3 hours and reaction temperatures of 650 °C, 750 °C and 775 °C. A standard pattern for NMC-811 obtained from the ICSD is shown also. Portions of the data between (b) 20 - 25 ° and (c) 63 - 66 ° are also shown to highlight any present impurity phases and the peak splitting of the (108) and (110) reflections indicating the “layered-ness” of the structure.

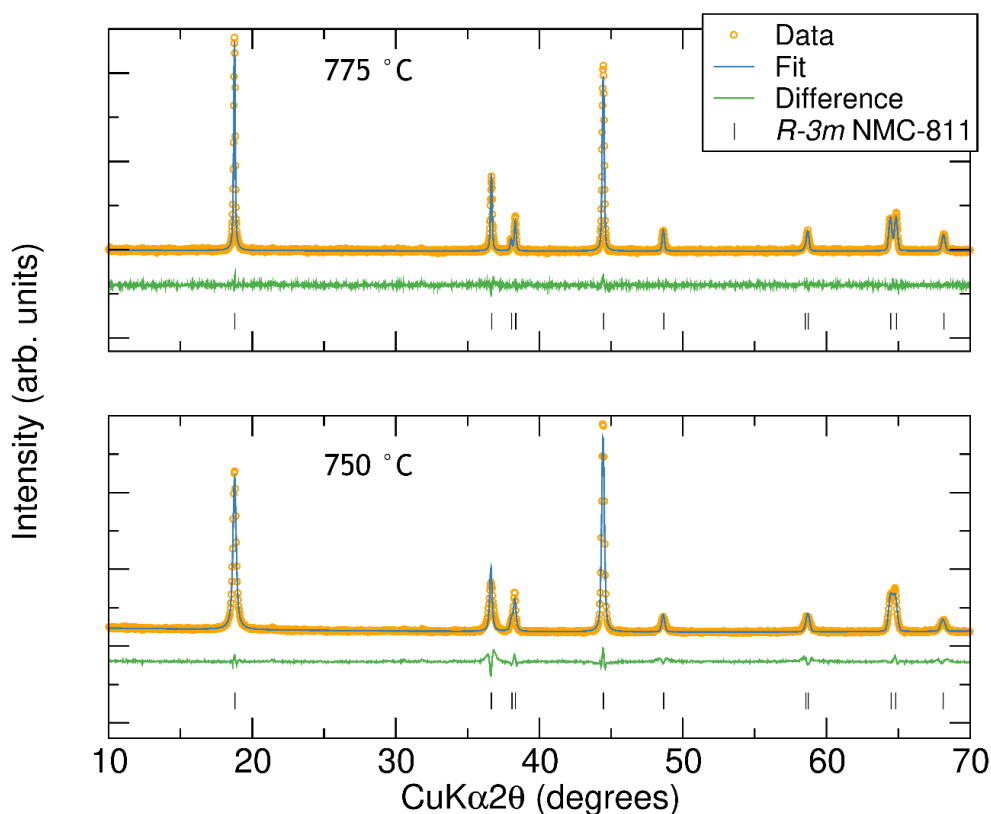


**Figure 4.22** Rietveld refinements on PXRD data obtained from NMC-811 samples synthesised by a microwave-assisted sol-gel method with a reaction time of 3 hours and reaction temperatures of 775 °C and 750 °C. A model consisting of  $R\bar{3}m$  phase  $\text{LiNi}_{0.8}\text{Mn}_{0.1}\text{Co}_{0.1}\text{O}_2$  was fit to the collected PXRD data.

**Table 4.7** Calculated lattice parameter and Li/Ni mixing from Rietveld refinements and calculated  $I_{(003)}/I_{(104)}$  ratios obtained for NMC-811 samples synthesised by a microwave-assisted sol-gel method with a reaction time of 3 hours and reaction temperatures of 750 °C and 775 °C.

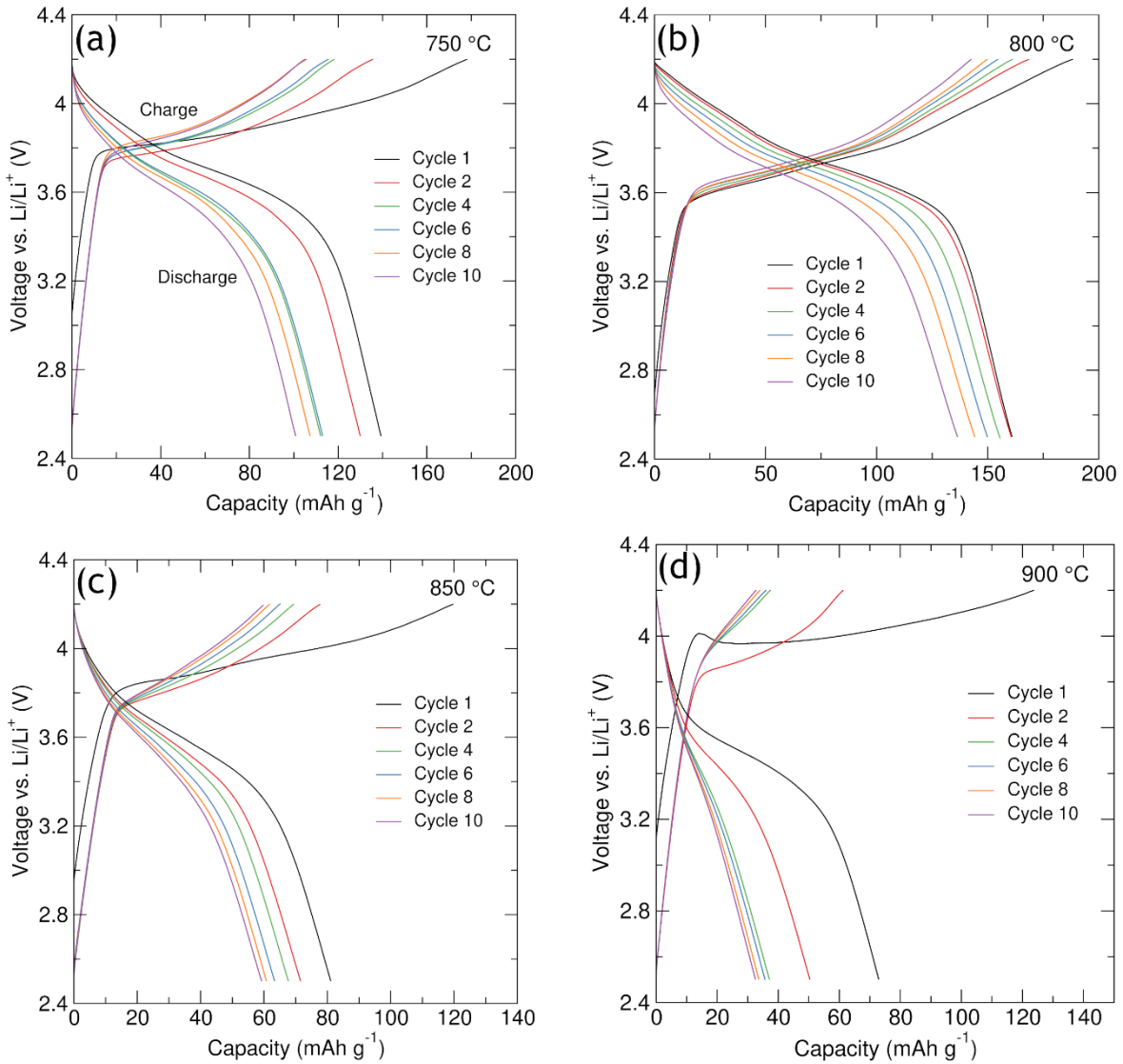
Sample	775 °C	750 °C
Space group	$R\bar{3}m$	$R\bar{3}m$
a (Å)	2.86835(16)	2.87046(20)
c (Å)	14.16765(58)	14.15595(92)
V (Å <sup>3</sup> )	100.947(10)	101.012(12)
Ni1 occupancy	0.7439(10)	0.7051(20)
Ni2 occupancy	0.0561(10)	0.0949(20)
Li/Ni mixing	5.61 %	9.49 %
$I_{(003)}/I_{(104)}$	1.15	0.77
$R_{wp}$	6.466 %	5.945 %
$\chi^2$	1.17	2.06

#### 4.2.8 Electrochemical performance of $\text{LiNi}_{0.8}\text{Mn}_{0.1}\text{Co}_{0.1}\text{O}_2$ synthesised by a microwave-assisted sol-gel method

Galvanostatic cycling of the prepared  $\text{LiNi}_{0.8}\text{Mn}_{0.1}\text{Co}_{0.1}\text{O}_2$  materials was carried out at room temperature on a BioLogic VSP potentiostat between 2.5 to 4.2 V vs. Li/Li<sup>+</sup> where a constant current corresponding to a rate of C/10 for each specific material was applied. The NMC-811 materials were mixed with conductive carbon black and a PTFE binder in a 60:30:10 % wt. ratio. An upper cut-off voltage of 4.2 V was applied to avoid severe degradation processes that may occur at higher voltages due to the presence of a large amount of unstable Ni<sup>4+</sup> cations in the charged state causing parasitic electrode-electrolyte reactions.<sup>242</sup> Figure 4.23 shows the charge-discharge capacity profiles obtained for the NMC-811 samples with a heating time of 1 hour and heating temperatures of 750 °C to 900 °C. Good initial charge capacities of 178 mAh g<sup>-1</sup> and 188 mAh g<sup>-1</sup> were achieved for the samples fired at 750 °C and 800 °C respectively, with corresponding initial discharge capacities of 140 mAh g<sup>-1</sup> and 161 mAh g<sup>-1</sup> resulting in irreversible capacity losses of 38 mAh g<sup>-1</sup> and 27 mAh g<sup>-1</sup> respectively (Figure 4.23(a),(b)). From inspection of cycling profiles of NMC-811 in the literature, an irreversible capacity loss is often observed. For example, several NMC-811 samples prepared by a fast co-precipitation method by Ling Jun Li *et al* suffered from irreversible capacity losses in the range of 50 to 60 mAh g<sup>-1</sup> between the first charge and discharge.<sup>214</sup> This is most likely attributed to the formation of a passivating layer upon the first charging process and local collapse of the lithium layer. However, from Figure 4.23(c) and (d) it can be seen that initial charge capacities of only  $\approx 120$  mAh g<sup>-1</sup> were achieved for the samples fired at 850 °C and 900 °C which could indicate a lithium deficient material or the blocking of Li<sup>+</sup> diffusion pathways facilitated by the increased amount of cation disorder present according to the Rietveld refinements presented previously. Furthermore, each material suffers from further irreversible capacity losses of approximately 40 mAh g<sup>-1</sup> and 50 mAh g<sup>-1</sup> for the 850 °C and 900 °C samples respectively between the first charge and discharge processes.

Each sample also suffers from capacity fading as evidenced by the charge and discharge capacity retention plots in Figure 4.24. The prepared NMC-811 samples fired at 750 °C, 800 °C, 850 °C and 900 °C show discharge capacity retentions of 72.4 %, 84.7 %, 73.1 % and 44.7 % respectively, highlighting that although the initial charge and discharge capacities for the 850 °C sample were low, its discharge capacity retention over 10 cycles compared reasonably well with the 750 °C and 800 °C samples suggesting that if the capacities could be improved, this material might show good cycling performances. The calculated coulombic efficiencies, also shown in Figure 4.24, show that each material

possesses good efficiencies close to 100 % after between 1 to 3 cycles with low initial efficiencies related to irreversible capacity loss and further electrode conditioning processes (*i.e.* electrode-electrolyte wetting) which commonly occur during the first few cycles.



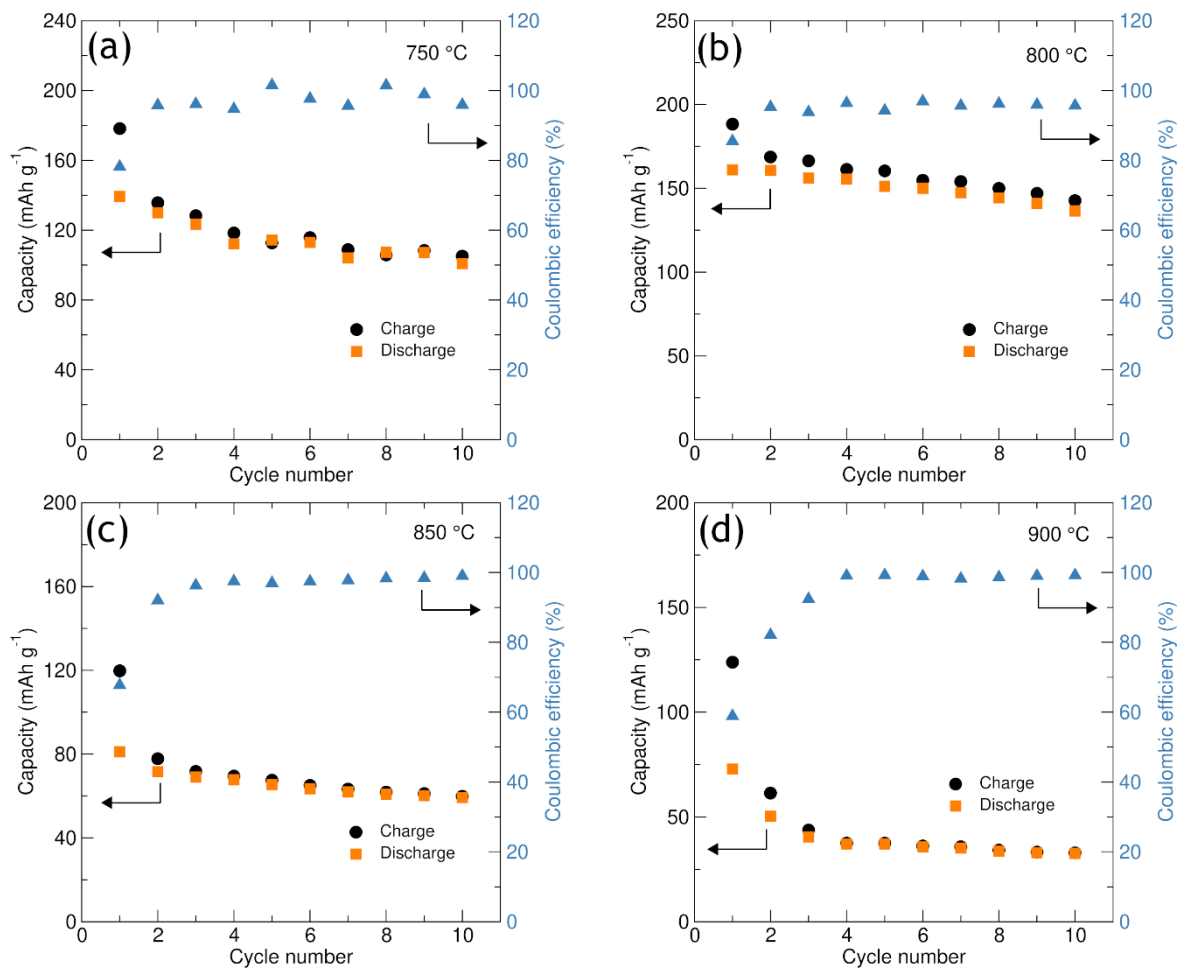
**Figure 4.23** Charge discharge profiles obtained from galvanostatic cycling at room temperature of  $\text{LiNi}_{0.8}\text{Mn}_{0.1}\text{Co}_{0.1}\text{O}_2$  cathode pellets (NMC-811: carbon black: PTFE in a 60:30:10 wt% ratio) synthesised by a microwave-assisted sol-gel method with a reaction time of 1 hour and reaction temperatures of (a) 750 °C, (b) 800 °C, (c) 850 °C and (d) 900 °C. Swagelok type cells were cycled between 2.5 - 4.2 V vs.  $\text{Li}/\text{Li}^+$  at a rate of  $C/10$ .

Figure 4.25 displays the differential capacity plots obtained from the galvanostatic cycling of the microwave-synthesised NMC-811 materials fired for 1 hour at 4.16(a) 750 °C, (b) 800 °C, (c) 850 °C and (d) 900 °C. The evolution of the differential capacity for the 750 °C sample during the first charge process shows an intense peak at  $\approx 3.82$  V followed by a less intense feature at  $\approx 4.0$  V and a final feature beginning at 4.2 V. Upon

cycling, these features reduce in intensity relating to the capacity fade observed. The potential at which the intense charging peak occurs at shifts to 3.77 V upon the 2<sup>nd</sup> cycle before gradually increasing to  $\approx$  3.84 V by the 10<sup>th</sup> cycle. During the discharge process from 4.2 V to 2.5 V a weak feature centred at  $\approx$  4.0 V followed by a more intense peak at 3.71 V is observed, with both features decreasing in intensity over the 10 cycles, and a gradual decrease in the voltage of the more intense peak upon cycling to 3.63 V. The positions of these charge and discharge features in the differential capacity plots are consistent with previous reports for  $\text{LiNi}_{0.8}\text{Mn}_{0.1}\text{Co}_{0.1}\text{O}_2$ .<sup>63,71,242</sup> The increase in voltage of the intense charge peak and the decrease in voltage of the discharge peak highlight an increase in polarization upon cycling, suggesting an increase in the charge transfer resistance of the cathode. Degradation of the cathode by loss of active material *via* parasitic electrode-electrolyte interactions can facilitate the formation of passivating surface layers which would explain an increase in electrode polarization.

The differential capacity plots for the samples fired at 800 °C and 850 °C show similar results to those obtained for the 750 °C sample, although it is noted that the 800 °C sample shows reduced polarization and improved overlap between profiles, indicating improved reversibility during cycling compared to the other samples which is also evidenced by the highest capacity retention achieved across the range of samples studied. Whereas the 750 °C, 800 °C and 850 °C samples all showed broadly similar behaviour in their differential capacity profiles, the 900 °C sample possesses significant differences. The data for the first cycle in Figure 4.25(d) has been omitted for greater clarity between subsequent cycles. The 1<sup>st</sup> and 2<sup>nd</sup> cycle data are presented in the appendix Figure 7.11 and shows a very intense peak at 3.97 V. On closer inspection of the profile, and by following the charge data along the x-axis, there is an initial peak at 4.0 V after which the voltage actually decreases followed by the intense peak at 3.97 V. This corresponds to the kink seen in the charge-discharge profile (Figure 4.23 (d)) and is unique to this specific sample, presenting unusual charging behaviour. After the first cycle one charge peak is observed shifting from 3.86 V in the 2<sup>nd</sup> cycle to 4.07 V in the 10<sup>th</sup> cycle which occurs at higher voltages here compared to the most intense peaks observed for the previous samples. One peak at 3.46 V is observed upon discharge which does not appear to change position upon cycling but appears at lower voltages than in the previous samples. However, the relatively high values of the charging peak coupled with the low discharging peak relate to a high polarization of the electrode both during the cycling process and in general compared to the samples prepared at lower temperatures which could help to explain the very poor cycling results obtained for the 900 °C sample. Such discrepancies observed for this material between the 1<sup>st</sup> and 2<sup>nd</sup>

cycle and the corresponding low capacities achieved thereafter could be an indication of some extensive structural change occurring upon the first cycle rather than the gradual effects consistent with surface degradation observed for the other samples.



**Figure 4.24** Charge discharge capacity retention and calculated coulombic efficiencies obtained from galvanostatic cycling at room temperature of  $\text{LiNi}_{0.8}\text{Mn}_{0.1}\text{Co}_{0.1}\text{O}_2$  cathode pellets (NMC-811: carbon black: PTFE in a 60:30:10 wt% ratio) synthesised by a microwave-assisted sol-gel method with a reaction time of 1 hour and reaction temperatures of (a) 750 °C, (b) 800 °C, (c) 850 °C and (d) 900 °C. Swagelok type cells were cycled between 2.5 - 4.2 V vs. Li/Li<sup>+</sup> at a rate of C/10.

The charge and discharge profiles and capacity retentions obtained from the galvanostatic cycling of NMC-811 samples from a 3 hour microwave-assisted heating step at temperatures of 750 °C and 775 °C are shown in Figures 4.26 and 4.27. Vast improvements in delivered capacities and cycling stabilities are clear. For example, the 750 °C sample exhibits an initial charge capacity of 189 mAh g<sup>-1</sup> followed by an initial discharge capacity of 161 mAh g<sup>-1</sup> resulting in a small irreversible capacity loss of 28 mAh g<sup>-1</sup>. Over 14 cycles, stable cycling behaviour is also observed with charge and discharge capacity retentions calculated as 81.5 % and 95.0 % respectively. Excellent

coulombic efficiencies of > 97 % are also achieved after the first cycle. The 775 °C NMC-811 sample also shows excellent electrochemical properties with charge and discharge capacities of 209.7 mAh g<sup>-1</sup> and 183.3 mAh g<sup>-1</sup> delivered during the first cycle, representing the highest discharge capacity achieved across all of the previous samples studied.

Alongside excellent initial capacities, charge and discharge retention was calculated as 87.2 % and 98.9 % respectively also representing the highest cycling stability even when only the first 5 cycles are compared for each sample (Table 7.1 in appendix). Only 5 cycles are presented here due to problems during cycling resulting after ≈ 5 cycles, possibly due to the cell short-circuiting. The extended cycling behaviour of the 775 °C sample is shown in Figure 7.12(a) in the appendix, showing various voltage drop spikes upon the 6<sup>th</sup> charge cycle followed by continuous charge up to ≈ 450 mAh g<sup>-1</sup> before displaying normal discharge behaviour. To determine whether the effect was a unique occurrence, a replica cell was cycled using fresh cathode material produced using the same reaction parameters and the same behaviour was observed as shown in Figure 7.12(b) in the appendix. Despite this behaviour, excellent coulombic efficiencies > 97.7 % were also calculated over the 5 cycles, demonstrating excellent consistency between the energy put into the cell vs. the energy delivered from the cell.

The excellent reversibility of both the 750 °C and 775 °C is also evidenced in the differential capacity (dQ/dV) plots shown in Figure 4.28. As before, charging peaks centred at approximately 3.75 V, 4.04 V alongside appearance of a feature at 4.2 V, followed by discharging features at ≈ 4.06 V and 3.70 V are all observed for both samples, which is consistent with that reported in the literature.<sup>63,71,242</sup> For the 750 °C sample the intensity of the features decreases very slightly during cycling with a more noticeable difference between the 1<sup>st</sup> and 2<sup>nd</sup> cycles. For the 775 °C sample, a slight decrease is observed between the 1<sup>st</sup> and 2<sup>nd</sup> cycles also but there is excellent overlap between the following cycles highlighting excellent reversibility for both samples. To understand more fully the cycling behaviour of these materials, and to assess variability across different samples, it would be imperative to carry out repeat cycling measurements for each sample in any future work conducted on the materials.

Rate capability testing was carried out on the NMC-811 sample prepared using a 3 hour microwave-synthesis step at 750 °C. It was decided to use this specific sample as it was able to deliver reasonably high and stable capacities over 14 cycles. The instability of the 775 °C sample after 5 cycles deemed this material unsuitable for rate capability testing which often requires > 40 cycles in order to explore a range of cycling rates. Rate

capability testing involves galvanostatic cycling between an upper and lower cut-off voltage performed at increasing current rates to investigate what capacities can be delivered upon increasing cycling rates. The testing presented here was carried out in Swagelok type half-cell configurations utilising an electrode pellet of NMC-811 mixed with conductive carbon black and a PTFE binder in a 60:30:10 % wt. ratio, a metallic lithium counter electrode and 1 M LiPF<sub>6</sub> in EC:DMC (1:1 v/v) electrolyte. Galvanostatic cycling was performed between 2.5 - 4.2 V vs. Li/Li<sup>+</sup> at currents corresponding to rates of C/10, C/5, C/2, 1 C, 2 C, 5 C, 10 C with a final rate of C/10 in order to identify if capacity losses can be recovered upon re-application of slower cycling rates. The rate capability results for the 3 hour 750 °C sample are shown in Figure 4.29. It is observed that the capacity drops as increasingly higher currents are applied which is caused by inadequate lithium diffusion at these high cycling rates *i.e.* smaller proportions of the Li<sup>+</sup> ions have enough time to successfully intercalate and de-intercalate as higher currents are applied. Although the capacity falls to very low values of  $\approx 7 \text{ mAh g}^{-1}$  at high rates of 10 C, upon re-application of a C/10 current rate, capacities of  $\approx 155 \text{ mAh g}^{-1}$  are recovered showing that cycling at high C rates has not degraded the material.

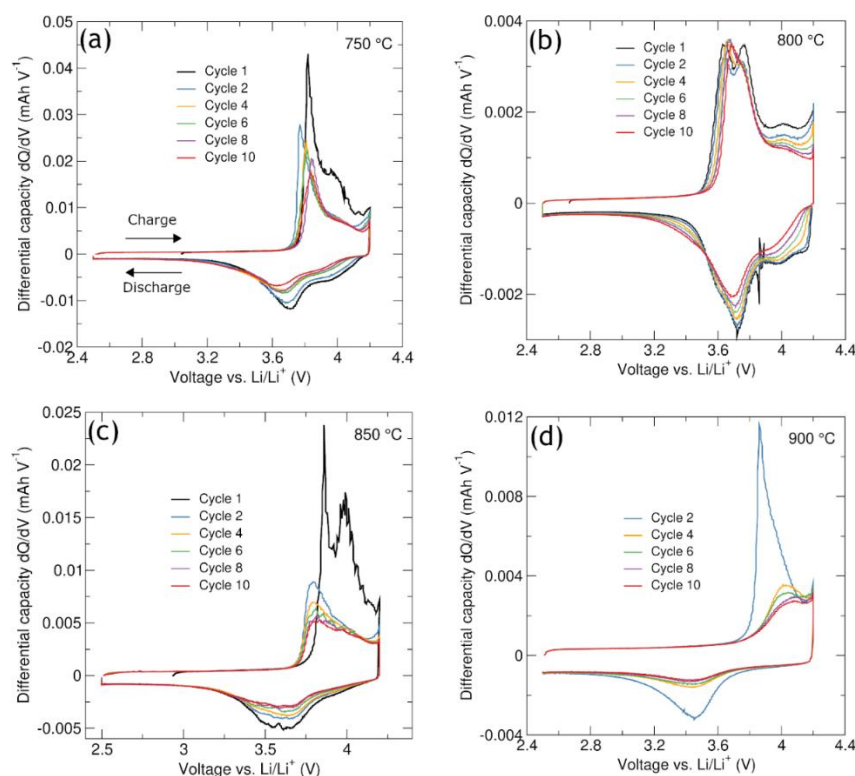


**Figure 4.25** Differential capacity ( $dQ/dV$ ) profiles obtained from galvanostatic cycling at room temperature of LiNi<sub>0.8</sub>Mn<sub>0.1</sub>Co<sub>0.1</sub>O<sub>2</sub> cathode pellets (NMC-811: carbon black: PTFE in a 60:30:10 wt% ratio) synthesised by a microwave-assisted sol-gel method with a reaction time of 1 hour and reaction temperatures of (a) 750 °C, (b) 800 °C, (c) 850 °C and (d) 900 °C. Swagelok type cells were cycled between 2.5 - 4.2 V vs. Li/Li<sup>+</sup> at a rate of C/10.

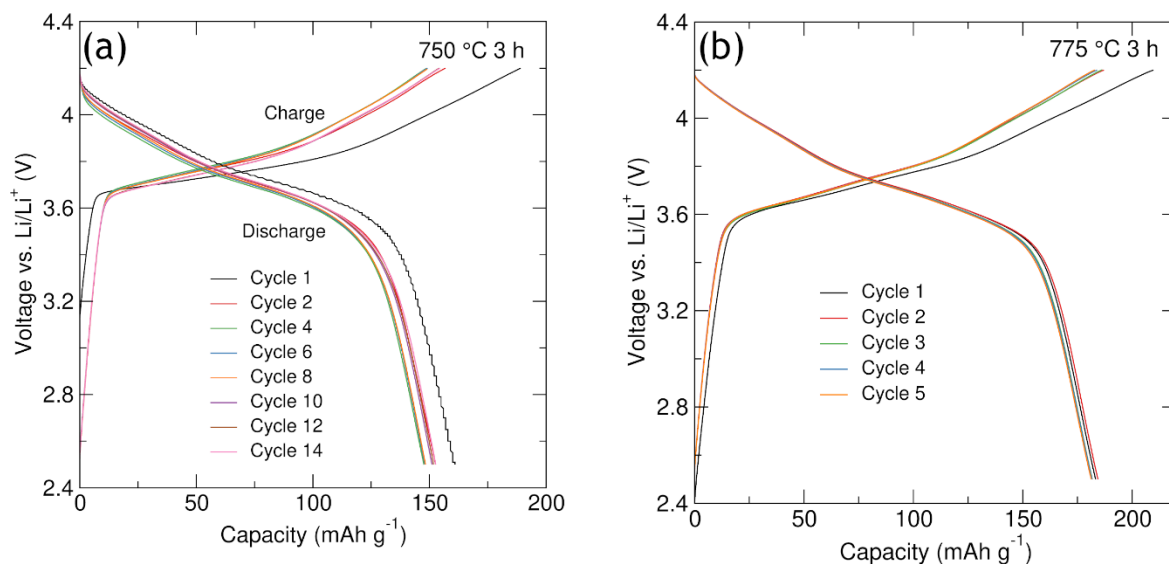


**Figure 4.26** Charge discharge profiles obtained from galvanostatic cycling at room temperature of  $\text{LiNi}_{0.8}\text{Mn}_{0.1}\text{Co}_{0.1}\text{O}_2$  cathode pellets (NMC-811: carbon black: PTFE in a 60:30:10 wt% ratio) synthesised by a microwave-assisted sol-gel method with a reaction time of 3 hours and reaction temperatures of (a) 750 °C and (b) 775 °C. Swagelok type cells were cycled between 2.5 - 4.2 V vs.  $\text{Li}/\text{Li}^+$  at a rate of C/10.

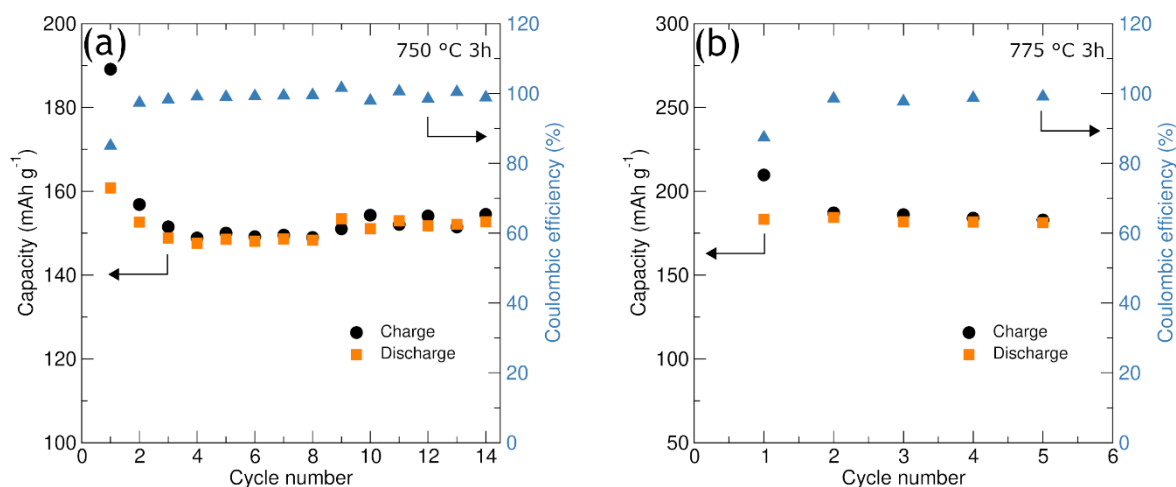


**Figure 4.27** Charge and discharge capacity retention and calculated coulombic efficiencies obtained from galvanostatic cycling at room temperature of  $\text{LiNi}_{0.8}\text{Mn}_{0.1}\text{Co}_{0.1}\text{O}_2$  cathodes synthesised by a microwave-assisted sol-gel method with a reaction time of 3 hours and reaction temperatures of (a) 750 °C and (b) 775 °C. Swagelok type cells were cycled between 2.5 - 4.2 V vs.  $\text{Li}/\text{Li}^+$  at a rate of C/10.

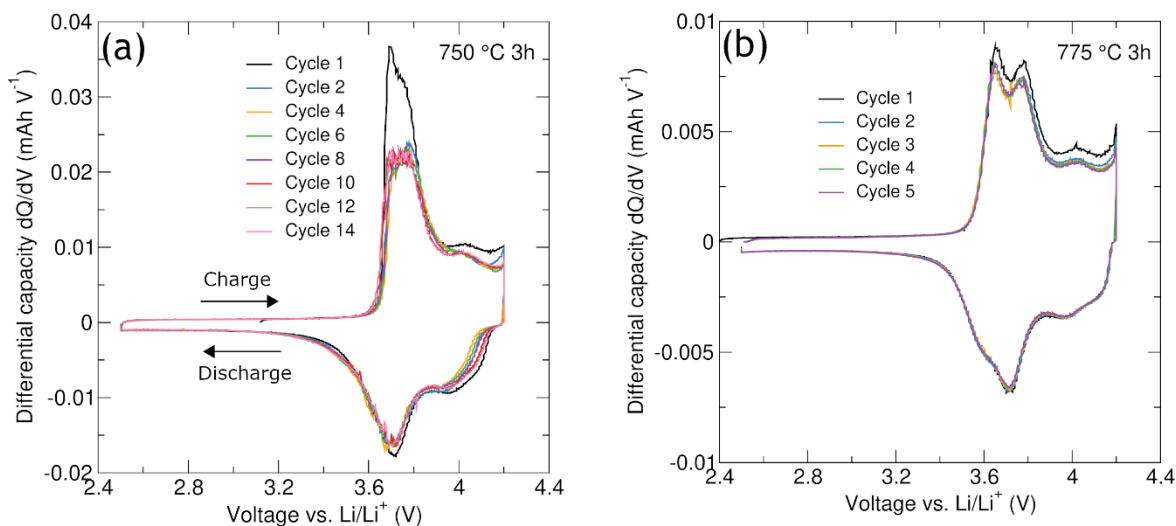


**Figure 4.28** Differential capacity ( $dQ/dV$ ) profiles obtained from galvanostatic cycling at room temperature of  $\text{LiNi}_{0.8}\text{Mn}_{0.1}\text{Co}_{0.1}\text{O}_2$  cathode pellets (NMC-811: carbon black: PTFE in a 60:30:10 wt% ratio) synthesised by a microwave-assisted sol-gel method with a reaction time of 3 hours and reaction temperatures of (a)  $750\text{ }^\circ\text{C}$  and (b)  $775\text{ }^\circ\text{C}$ . Swagelok type cells were cycled between 2.5 - 4.2 V vs.  $\text{Li/Li}^+$  at a rate of C/10.

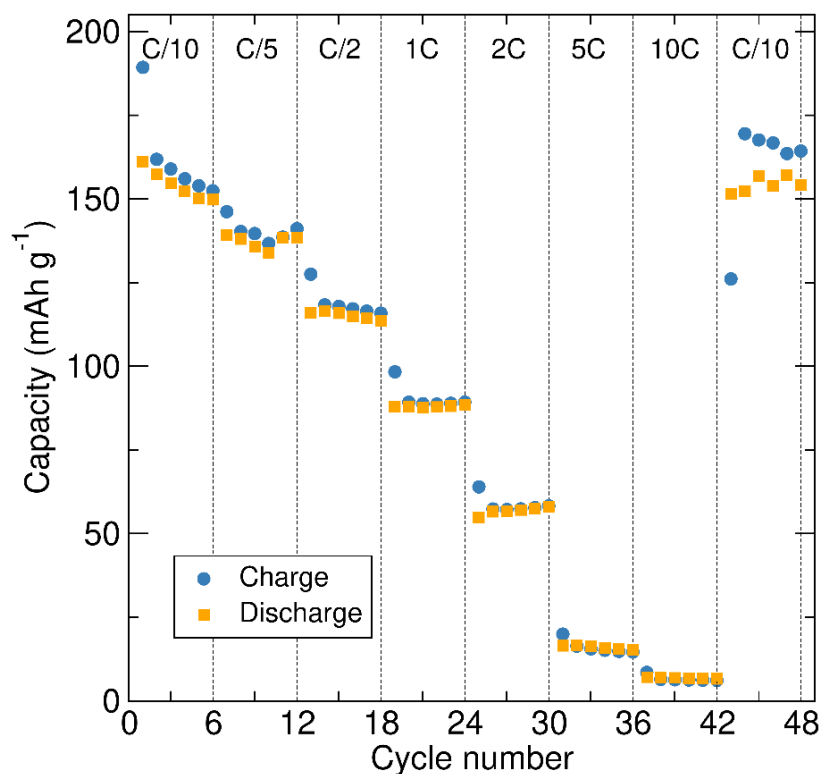


**Figure 4.29** Rate capabilities for the specific charge and discharge capacities obtained from galvanostatic cycling at room temperature of NMC-811  $750\text{ }^\circ\text{C}$  3h sample synthesised by a microwave-assisted sol-gel method. Swagelok type cells were cycled between 2.5 - 4.2 V vs.  $\text{Li/Li}^+$ .

#### 4.2.9 Scanning electron microscopy of $\text{LiNi}_{0.8}\text{Mn}_{0.1}\text{Co}_{0.1}\text{O}_2$ prepared using a microwave assisted sol-gel synthesis

SEM was used here to investigate the resultant particle sizes and morphologies obtained for NMC-811 materials synthesised using the microwave-assisted sol-gel method. High resolution SEM analysis was conducted here using a Carl Zeiss Sigma variable pressure analytics SEM equipped with Oxford Instruments microanalysis. Figure 4.30 shows the images collected from samples heated at  $750\text{ }^\circ\text{C}$  with reaction times of 1 hour and 3 hours, with particle size distributions for each sample shown in Figure 7.13 in the appendix. It can be seen that each sample shows a heterogeneous distribution of particle size and morphologies although it is observed that the particle morphologies seem to show defined edges rather than a more spherical type morphology. On increasing the reaction time, it is also observed that the particle size appears to increase, with particle sizes ranging from approximately 100 nm to 600 nm to 300 nm to  $1.5\text{ }\mu\text{m}$  for the 1 hour and 3 hour samples respectively. Average particle sizes for both samples were calculated as approximately 280 nm and 630 nm for the 1 h and 3 h samples respectively. Furthermore, by comparing the SEM analysis here obtained for NMC-811 to the SEM analysis previously presented for NMC-111 (Figure 4.3) it is observed that larger particle sizes are produced during the synthesis of NMC-811 alongside a more heterogeneous distribution of both particle size and morphology.

Alongside imaging, compositional microanalysis was also conducted using energy-dispersive X-ray spectroscopy (EDX) mapping on the sample synthesised at  $750\text{ }^\circ\text{C}$  for 3 hours. The mapping results obtained for the distributions of Ni, Mn and Co within the sample are shown in Figure 4.31 and highlight a homogenous distribution of transition metals within the portion of the imaged sample and most likely is representative of a homogenous distribution throughout the sample. This is evidence of the good transition metal cationic mixing that could be facilitated by the sol-gel technique.

As the best performing NMC-811 previously synthesised, the SEM results for sample synthesised at  $775\text{ }^\circ\text{C}$  for 3 hours are highlighted in Figure 4.32, with particle size distribution histograms shown in Figure 7.15 in the appendix. Again, a heterogeneous distribution of particle size and morphology is evident. The particle size range observed for the portions of the sample presented here is approximately 200 nm to  $1.5\text{ }\mu\text{m}$  with an average particle size of  $\approx 430\text{ nm}$  calculated. From the image displayed in Figure 4.32(b) it is evident that there exists a number of particles presenting more defined polyhedral faces which typically describe a particle with higher crystallinity. This effect can also be

observed in the 750 °C 3 hour sample, whereas the particles presented for the 750 °C 1 hour sample show edges and faces that are less defined and this could help to explain the enhanced cycling properties obtained for both of the 3 hour samples.

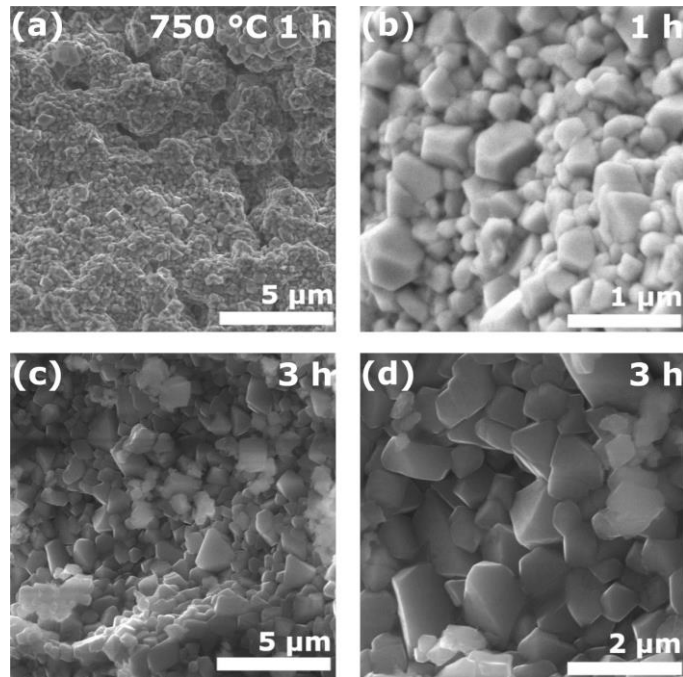


**Figure 4.30** SEM images of NMC-811 synthesised by a microwave-assisted sol-gel synthesis with a reaction temperature of 750 °C and reaction times of (a,b) 1 hour and (c,d) 3 hours.

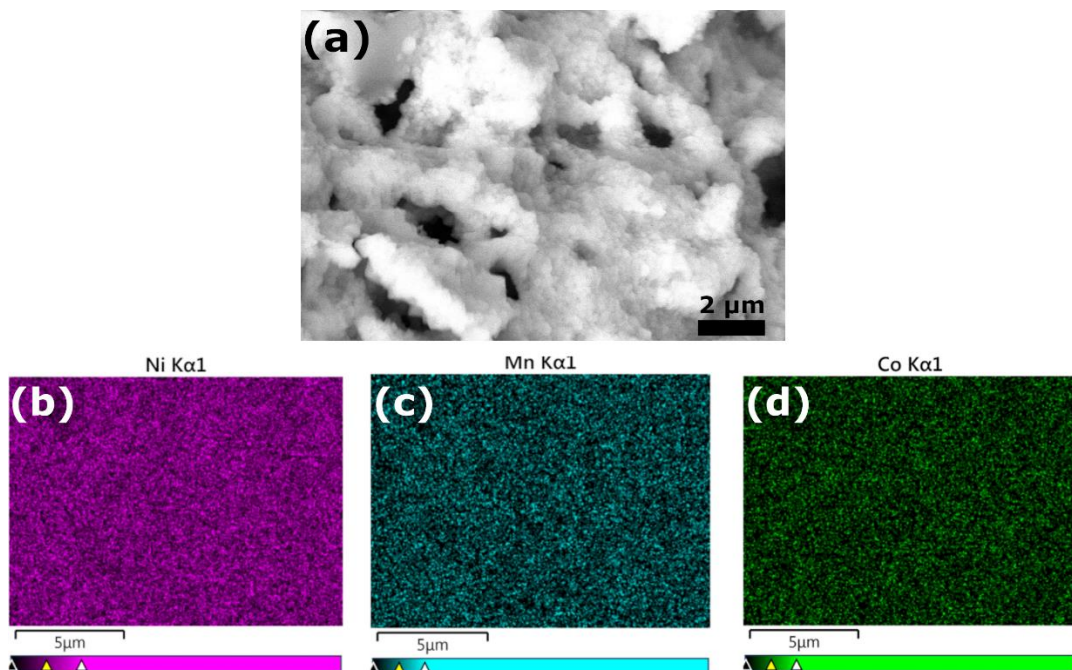


**Figure 4.31** (a) SEM image of NMC-811 and elemental mapping results obtained for (b) Ni, (c) Mn and (d) Co from SEM-EDX analysis of the NMC-811 sample synthesised at 750 °C for 3 hours using a microwave-assisted sol-gel method.

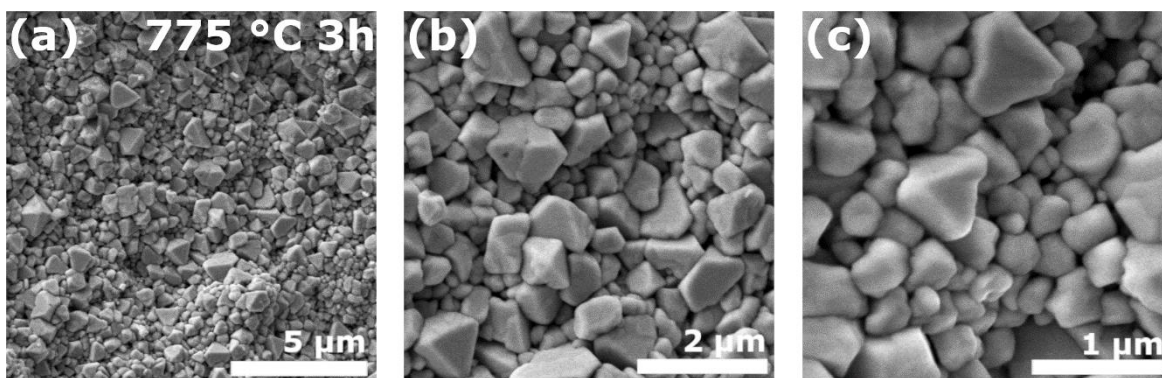


**Figure 4.32** SEM images of NMC-811 synthesised by a microwave-assisted sol-gel synthesis with a reaction temperature of 775 °C for 3 hours at different magnifications of (a)  $\times 10000$ , (b)  $\times 25000$  and (c)  $\times 50000$ .

### 4.3 Conclusions

In this chapter the microwave-assisted sol-gel synthesis of  $\text{LiNi}_{1/3}\text{Mn}_{1/3}\text{Co}_{1/3}\text{O}_2$  and nickel-rich  $\text{LiNi}_{0.6}\text{Mn}_{0.2}\text{Co}_{0.2}\text{O}_2$  and  $\text{LiNi}_{0.8}\text{Mn}_{0.1}\text{Co}_{0.1}\text{O}_2$  has been demonstrated. Structural and morphological characterisation has also been conducted using PXRD, SEM and EDX and electrochemical analysis has been performed using galvanostatic cycling techniques.

For NMC-111 the utilisation of a microwave-assisted heating step in the formation of the product allowed for shorter reaction times with the  $R\bar{3}m$  phase being formed with only a 1 hour reaction time at 850 °C with no evidence of impurity phases in the PXRD data. However, an increase in the Li/Ni cation mixing was observed from Rietveld analysis for the microwave prepared samples with a larger degrees of mixing calculated for sample heated for 1 hour. SEM analysis showed that shorter microwave-assisted reaction times of 1 and 3 hours facilitated the formation of smaller and more uniform particles compared to a sample of NMC-111 prepared *via* conventional heating. However, during cycling the microwave prepared samples showed enhanced capacity fade across 10 cycles compared to the conventional sample despite similar behaviour upon the first charging process which could most likely be attributed to the increased Li/Ni mixing precipitated by the shorter, microwave heating step and the increase in surface area due to the smaller particle sizes obtained which undergo parasitic electrode-electrolyte reactions upon high states of charge (in this case up to 4.6 V vs. Li/Li<sup>+</sup>).

Progressing to the higher nickel content layered oxides, NMC-811 and NMC-622 synthesised by the microwave-assisted sol-gel method have also been presented here. PXRD and Rietveld analysis highlight that  $R\bar{3}m$  phase can be successfully synthesised for both materials with no evidence of impurity phases although the Li/Ni cation mixing is observed to increase in NMC-811 compared to NMC-622 which is commonly reported.

Examination of the particle morphology using SEM has also revealed an increase in the particle size and a decrease in the particle shape and size uniformity upon increasing nickel content when the microwave-assisted sol-gel method is used.

Galvanostatic cycling of the NMC-622 and NMC-811 materials has also revealed good first cycle charge capacities of  $\approx 180 \text{ mAh g}^{-1}$ , with discharge capacities dropping to an approximately steady value of  $130 \text{ mAh g}^{-1}$  over 20 cycles for NMC-622 and a gradual discharge capacity fade from  $137 \text{ mAh g}^{-1}$  to  $104 \text{ mAh g}^{-1}$  observed for NMC-811 over 30 cycles, indicating the presence of processes contributing to cathode degradation.

The transport properties of microwave synthesised and commercially obtained NMC-811 and NMC-622 have also been examined here using muon spin spectroscopy measurements to investigate and compare the microscopic  $\text{Li}^+$  diffusion characteristics between the materials. Very little difference in activation energies and diffusion properties were observed between microwave synthesised and commercial NMC-811 where a room temperature lithium diffusion coefficient of  $\approx 1.65 \times 10^{-11} \text{ cm}^2 \text{ s}^{-1}$  was estimated for both. The NMC-622 samples showed higher activation energies and lower diffusion coefficients than NMC-811, indicating more sluggish Li-diffusion is expected, although all samples show much faster diffusion compared to NMC-111 studied by  $\mu^+$ -SR highlighting further benefits to these nickel rich cathodes alongside increased capacities.

Finally, the optimisation of the time and temperature parameters for the microwave-assisted sol-gel synthesis of NMC-811 was investigated where a sample heated at  $775 \text{ }^\circ\text{C}$  for 3 hours showed excellent discharge capacities of  $183 \text{ mAh g}^{-1}$  with no capacity loss observed over 5 cycles although cell instabilities occurred prohibiting testing after 5 cycles. Excellent cycling stabilities over at least 14 cycles with discharge capacities of  $\approx 150 \text{ mAh g}^{-1}$  were also observed for a sample of NMC-811 prepared with a  $750 \text{ }^\circ\text{C}$ . Examination of the morphologies of these samples using SEM also revealed the presence of a portion of particles with more defined edges, indicating the possibility of faceted particles and EDX microanalysis revealed a uniform distribution of transition metal cations throughout the sample owing to the atomic mixing afforded by the sol-gel synthesis.

In hindsight, although the smaller particles sizes afforded by the fast microwave-assisted reactions were desirable for their ability to possibly improve cycling performances through enhanced ionic conduction, the cycling results presented in this chapter show that the smaller particle sizes instead generally result in poor electrochemical performances. Most likely, the increased surface areas resulting from decreased particle size likely plays a role in accelerating any surface induced degradation (*i.e.* deleterious

electrode-electrolyte reactions) that can consume active material and lead to rapid capacity fade.

To further build upon the work presented here, the scope of future work relating to the microwave-assisted synthesis of NMCs would likely include a similar process of reaction time and temperature optimisation but ensuring that the reaction is carried out under an oxygen atmosphere. The role of oxygen is likely pivotal in mitigating oxygen loss from the lattice which can reduce the amount of Ni<sup>2+</sup> in the lattice (with more Ni<sup>3+</sup> present instead) and thus mitigate the extent of Li/Ni site mixing. Using these oxygen rich reaction environments is critical in the synthesis of Ni-rich layered oxides and “beyond” NMC-811 compositions (e.g. LiNiO<sub>2</sub>) which will be highly important for future cathode research. It will also be of importance to carry out cycling experiments using a number of repeat cells to confidently report the cycling behaviour of these materials and to be able to draw more reliable trends and conclusions.

To overcome problems relating to the enlarged surface area, alternative synthetic methodologies should be combined with the microwave-assisted heating step. For example, co-precipitation reactions carried out using a stirred tank reactor can yield large secondary particles (of  $\approx 10$  to  $20 \mu\text{m}$  diameter) made from smaller primary particles (of size  $< 200 \text{ nm}$ ). These dense secondary particles can inhibit electrolyte ingress and thus can mitigate the electrode-electrolyte reactions, while maintaining good ionic conductivities through the small sizes of the primary particles. Molten salt type reactions could also be implemented to form large, “single-crystal” type morphologies which have received much attention recently due to their excellent cycling stabilities that is afforded by the ability to retain structural integrity on cycling owing to the fact that intergranular fracture does not occur in such morphologies.<sup>230,243</sup> *Operando* or *in-situ* transmission electron microscopy (TEM) studies could also be carried out on these materials to elucidate any surface changes that occur on cycling in these samples. TEM can identify new surface phases (e.g. NiO, spinel or amorphous phases) and monitor how these evolve during cycling.

As mentioned in Chapter 3, performing *in-situ*  $\mu^+$ -SR studies on Ni-rich layered oxide cathodes would yield a unique perspective on electrochemically induced local scale Li<sup>+</sup> diffusion in such materials and may begin to reveal differences in the Li<sup>+</sup> diffusion during cycling between e.g. commercial and laboratory-prepared samples which was not evident in this body of work for NMC-811.

## 5 Degradation mitigation in nickel rich layered oxide $\text{LiNi}_{0.8}\text{Mn}_{0.1}\text{Co}_{0.1}\text{O}_2$ via coating and doping strategies

### 5.1 Introduction

While nickel-rich layered oxides present advantageous capacity increases, challenges remain in mitigating degradation processes which lead to pronounced capacity fading upon cycling which ultimately limits the practical use of such materials. Structural instabilities caused by unfavourable degrees of Li/Ni cation mixing, parasitic electrode-electrolyte surface reactions, oxygen release and active material depletion contribute to this degradation and involve effects such as bulk structural changes, micro-structural changes, changes to the Li-ion diffusion kinetics and increased charge transfer resistance upon cycling which all contribute to poor electrochemical performances upon cycling.<sup>66,68,244,245</sup> Several strategies may be implemented to mitigate these degradation processes including the application of a protective coating to the cathode material<sup>100,208,246-248</sup>, doping of particular crystallographic sites in the cathode's structure with foreign cations<sup>91,233,249-251</sup>, the synthesis of concentration gradient and core-shell structures<sup>252</sup> and electrolyte additives.<sup>253-255</sup>

In this chapter coating and doping strategies are presented for the NMC-811 composition. This composition was chosen due to the interest in NMC-811 as a next generation cathode in LIBs for automotive applications, and the interest from the Faraday Institution's Degradation project in investigating degradation mitigation strategies for NMC-811 specifically. Several coatings have been reported in the literature and broadly fall into three distinct categories - oxides (e.g.  $\text{Al}_2\text{O}_3$ ,  $\text{ZrO}_2$ ,  $\text{MgO}$ ,  $\text{La}_2\text{O}_3$  and  $\text{TiO}_2$ )<sup>246,248,256-260</sup>, phosphates (e.g.  $\text{AlPO}_4$ ,  $\text{Co}_3(\text{PO}_4)_2$  and  $\text{Ni}_3(\text{PO}_4)_2$ )<sup>261-263</sup> and fluorides (e.g.  $\text{AlF}_3$  and  $\text{CaF}_2$ )<sup>264-266</sup>. These coatings are designed to act as a barrier to prevent direct contact between the electrode and the electrolyte, especially at states of high charge where the highly oxidative  $\text{Ni}^{4+}$  cation is present, and thus mitigating potentially harmful side reactions that can lead to electrode degradation such as surface phase transformations (e.g. the formation of rock-salt and spinel phases) and attack from hydrofluoric acid (HF). Such coatings that are also stable in air could also make handling of NMC-811 and further high nickel content electrodes easier. For example, Ramasamy *et al.* reported improved performances for an NMC-811 cathode coated with  $\text{Al}_2\text{O}_3$  via atomic layer deposition (ALD) with a capacity retention of 76 % after 500 cycles at a rate of 5C compared to a 47 % retention observed for a pristine NMC-811 electrode under the same cycling conditions.<sup>248</sup> An *in-situ* hybrid  $\text{Li}_3\text{PO}_4$ - $\text{AlPO}_4$ - $\text{Al}(\text{PO}_3)_3$  coating applied to NMC-811 also showed improved capacity retention compared to pristine NMC-811, where an initial  $\text{Al}(\text{PO}_3)_3$  coating

precursor was used which reacts with residual lithium (*i.e.*  $\text{Li}_2\text{CO}_3$  and  $\text{LiOH}$ ) to form the multi-component coating.<sup>267</sup>

The addition of dopant ions into the layered structure is a commonly reported method to improve material properties.  $\text{LiNi}_x\text{Mn}_y\text{Co}_{1-x-y}\text{O}_2$  compositions can be regarded as solid solutions between  $\text{LiNiO}_2$ - $\text{LiCoO}_2$ - $\text{LiMnO}_2$  phases where the  $\text{Co}^{3+}$  decreases the Li/Ni cation mixing and improves the well-ordered layered properties and  $\text{Mn}^{4+}$  acts as a structural stabiliser presenting much improved electrochemical and thermal properties compared with pristine  $\text{LiNiO}_2$ .<sup>208</sup> However, cycling stabilities still suffer due to surface instabilities present especially in the nickel rich layered oxides, thus investigating different dopant cations for these NMC systems is of great interest. For example, cation substitution in both Li 3a and transition metal 3b sites have been reported in the literature including cations such as  $\text{Na}^+$ ,<sup>268</sup>  $\text{Mg}^{2+}$ ,<sup>269,270</sup>  $\text{Al}^{3+}$ ,<sup>75,269,271,272</sup> and  $\text{Ti}^{4+}$ .<sup>269,273</sup> In the cases of  $\text{Na}^+$  and  $\text{Mg}^{2+}$  where the dopant cations are expected to reside on the lithium sites, these electrochemically inactive dopants are thought to act as a stabilising “pillar” within the lithium layers, providing structural stability during cycling. Dopants that are targeted towards the transition metal sites such as  $\text{Al}^{3+}$  and  $\text{Ti}^{4+}$  are also expected to stabilise the layered structure and also increase the thermal stability of the cathode.<sup>92,269</sup> Weigel *et al.* have studied the structural and electrochemical aspects of NMC-811 doped with various cations including  $\text{Mg}^{2+}$ ,  $\text{Al}^{3+}$  and  $\text{Ti}^{4+}$  and observed improved capacity retentions compared with pristine NMC-811 when cycled at 45 °C at a C/3 rate. Lower polarization was also observed under these conditions for the  $\text{Al}^{3+}$  and  $\text{Mg}^{2+}$  doped samples alongside decreased charge transfer and surface film resistances compared to a pristine NMC-811 sample.<sup>269</sup>

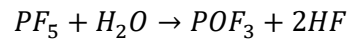
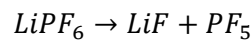
This chapter initially introduces a solution-based coating method utilised for applying a lightweight  $\text{Al}_2\text{O}_3$  coating to microwave-synthesised NMC-811 to try and improve its cycling performance. Samples with different coating thicknesses were synthesised with any changes to the bulk structure probed with PXRD measurements. Galvanostatic cycling measurements carried out show the effectiveness of a 0.2 wt.%  $\text{Al}_2\text{O}_3$  coating. *Operando* X-ray absorption spectroscopy on the Ni K-edge, utilising both XANES and EXAFS regions, has been carried out to examine whether any changes in the uncoated and coated material during cycling are observed. Neutron powder diffraction coupled with pair distribution function analysis on these materials is also presented to probe changes in both the bulk and local atomic structure. The sol-gel microwave-assisted synthesis of Al- and Mg-doped NMC-811 materials is also presented, followed by muon-spin spectroscopy

analysis on these doped materials in order to investigate the effects on microscopic ionic diffusion that may arise as a result of this foreign cationic doping.

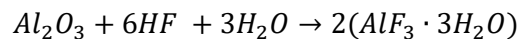
## 5.2 Results and discussion

### 5.2.1 Degradation mitigation in $\text{LiNi}_{0.8}\text{Mn}_{0.1}\text{Co}_{0.1}\text{O}_2$ via the application of an $\text{Al}_2\text{O}_3$ coating by a liquid phase dispersive technique

Protective surface coatings can be utilised to mitigate surface reactions which lead to gradual capacity loss in the nickel-rich layered oxides such as NMC-811. By applying chemically stable coatings which do not prohibit ionic and electronic conduction, the highly reactive  $\text{Ni}^{4+}$ -containing surface is protected from direct contact with the electrolyte at high states of charge, preventing the occurrence of parasitic electrode-electrolyte reactions that can be responsible for the formation of thick surface layers such as NiO and spinel phases that can inhibit ionic diffusion and deplete the amount of electrochemically-active material within the cathode. Alumina,  $\text{Al}_2\text{O}_3$ , has attracted attention as a coating due to its low cost, safety, abundance and its ability to act as both a passivating agent to prevent any undesirable side-reactions and as a scavenger for the trace amounts of HF that can be generated in the  $\text{LiPF}_6$ -based electrolyte. This is formed in the presence of water (often found in trace amounts within common electrolytes) according to the reactions:

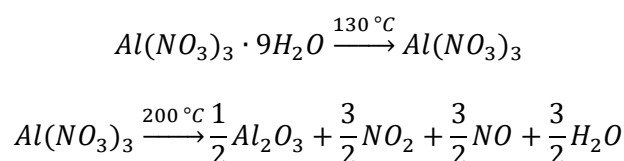


The  $\text{Al}_2\text{O}_3$  coating can act as a scavenger of both HF and water according to the reaction:

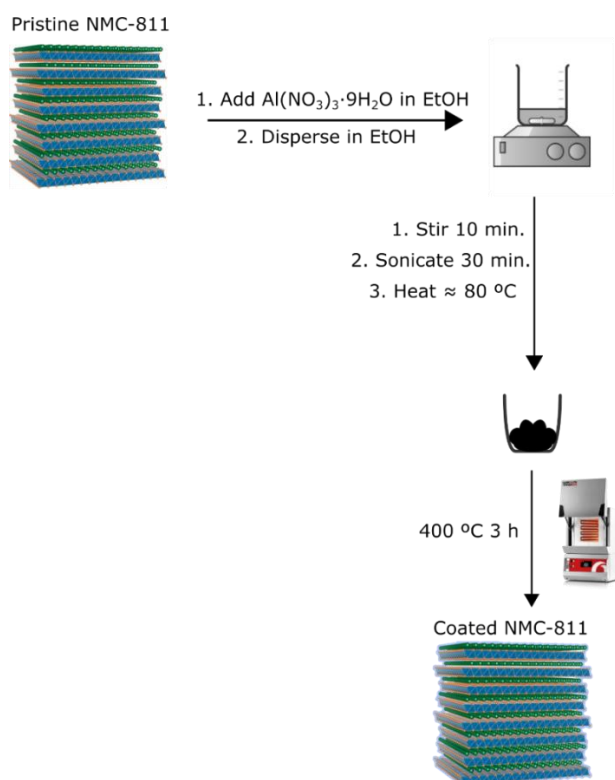


where the  $\text{AlF}_3 \cdot 3\text{H}_2\text{O}$  species formed continues to act as a passivating layer, albeit without the ability as a HF or  $\text{H}_2\text{O}$  scavenger, as reported by Oh *et al.*<sup>274</sup> The ability of  $\text{Al}_2\text{O}_3$  to also act as a water scavenger allows the suppression of further HF formation. It is noted, however that this offers a time-limited solution to parasitic reactions as no further protection is offered to any unprotected areas once the  $\text{Al}_2\text{O}_3$  is fully depleted. In this section, a solution-based dispersion method has been used to coat NMC-811 with  $\text{Al}_2\text{O}_3$ . More advanced methods such as ALD have been reported in the literature; however the method presented here offers a cheap and possibly scalable solution to coating. The NMC-811 sample chosen for coating was prepared by a microwave-assisted sol-gel method at 850 °C for 1 hour. This sample was introduced in Chapter 4 and was chosen to

investigate whether its poor electrochemical performance could be improved *via* this coating technique. The Al<sub>2</sub>O<sub>3</sub> coating, adapted from a method reported by Hildebrand *et al.* was applied by adding appropriate volumes of a 1 mg mL<sup>-1</sup> Al(NO<sub>3</sub>)<sub>3</sub>·9H<sub>2</sub>O ethanol stock solution to a portion of NMC-811 powder corresponding to a final Al<sub>2</sub>O<sub>3</sub> mass of 0.2, 0.5 and 1.0 wt.% compared to the mass of NMC-811.<sup>275</sup> Further ethanol was added to produce a dispersion of NMC-811 powder. The dispersion was stirred and sonicated before solvent evaporation (under stirring) and the obtained powder was heated at 400 °C for 3 hours to facilitate the removal of the bound H<sub>2</sub>O species and the decomposition of the nitrate species and form an amorphous Al<sub>2</sub>O<sub>3</sub> phase according to a two-step reaction<sup>276,277</sup>:



The coating methodology has been described in full detail in Chapter 2 and is shown in Schematic 5.1.



**Schematic 5.1** Reaction schematic for the Al<sub>2</sub>O<sub>3</sub> coating of LiNi<sub>0.8</sub>Mn<sub>0.1</sub>Co<sub>0.1</sub>O<sub>2</sub> *via* an ethanol based dispersion method, where an appropriate amount of Al(NO<sub>3</sub>)<sub>3</sub>·9H<sub>2</sub>O stock solution is added to NMC-811 which is then dispersed in ethanol, sonicated, heated at 80 °C to evaporate the solvent and heated at 400 °C for 3 hours to form an amorphous Al<sub>2</sub>O<sub>3</sub> coating.

### 5.2.1.1 Structural characterisation of $\text{Al}_2\text{O}_3$ coated $\text{LiNi}_{0.8}\text{Mn}_{0.1}\text{Co}_{0.1}\text{O}_2$

After the coating procedure outlined above was complete, samples were initially analysed using PXRD to investigate whether any structural changes had occurred during the coating. The  $\text{Al}_2\text{O}_3$  coating is designed to form an amorphous and thin coating layer around particles and therefore no structural changes should be visible in the powder diffraction data. PXRD data collected for pristine NMC-811 and samples coated with 0.2, 0.5 and 1.0 wt.%  $\text{Al}_2\text{O}_3$  (with respect to the original mass of NMC-811) are shown in Figure 5.1. Most likely due to poor choice of instrument optics (*i.e.* a divergence slit that is too large), the (003) peak is less intense than is expected. However, this is consistent across all of the samples measured here and it is observed that no crystalline impurity phases or crystalline  $\text{Al}_2\text{O}_3$  are observed in the diffraction patterns and all patterns display the characteristic peaks associated with  $R\bar{3}m$  layered oxides indicating that no major structural changes have occurred during the coating process. Therefore, it can be ascertained that the NMC-811 structure is retained during the coating procedure.

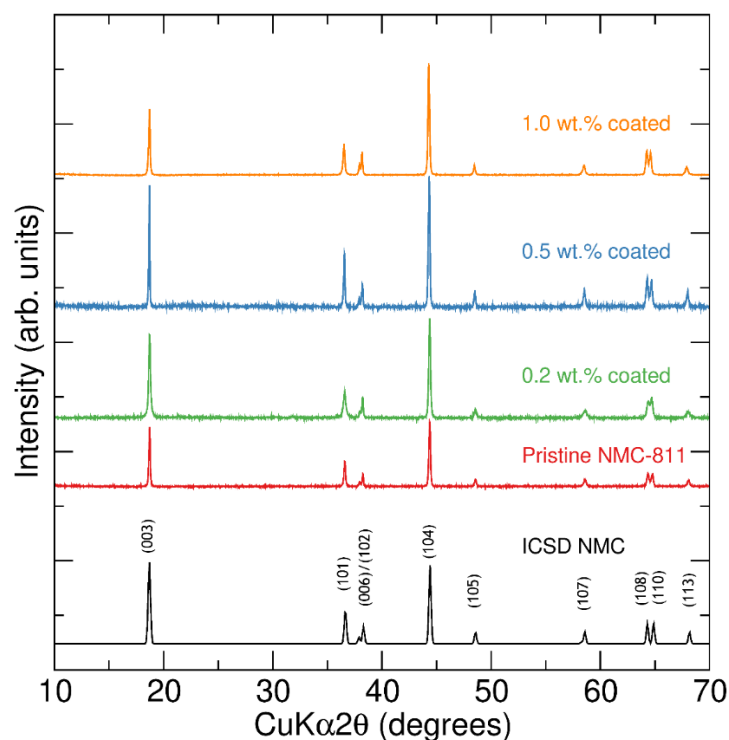


**Figure 5.1** PXRD data collected for microwave-synthesised pristine NMC-811 (850 °C, 1 hour) and NMC-811 samples coated with 0.2, 0.5 and 1.0 wt.%  $\text{Al}_2\text{O}_3$  using the dispersion method coating process. A standard pattern obtained from the ICSD for NMC is also shown.

### 5.2.1.2 Galvanostatic cycling of $\text{Al}_2\text{O}_3$ coated $\text{LiNi}_{0.8}\text{Mn}_{0.1}\text{Co}_{0.1}\text{O}_2$

Each of the coated materials was electrochemically tested using the galvanostatic (constant current) cycling method to investigate the effectiveness of the coatings. Half-

cells were fabricated using a pellet of cathode material consisting of coated NMC-811 active material, KETJEN carbon black and PTFE in a 60:30:30 wt.% ratio which were subject to ball milling for 10 minutes at 20 Hz in a Retsch MM200 mixer mill before being pressed into a pellet. Swagelok-type cells were then constructed using this cathode pellet, a lithium metal disk as the counter and reference electrode, a glass microfiber separator and 1 M LiPF<sub>6</sub> in EC:DMC (1:1 v/v) electrolyte. Cells were cycled using a BioLogic potentiostat between 2.5 V to 4.2 V vs. Li/Li<sup>+</sup> at a current density corresponding to a rate of C/10. As the NMC-811 cathode material is synthesised in the lithiated, discharged state, a charging step was initially performed, followed by a discharging process with this overall process repeated over at least 10 cycles. The charge and discharge plots obtained under these conditions for the 0.2, 0.5 and 1.0 wt.% coated NMC-811 materials are shown in Figure 5.2. The 0.2 wt.% coated samples show an initial charge capacity of 166 mAh g<sup>-1</sup> followed by a discharge capacity of 144 mAh g<sup>-1</sup> corresponding to a first cycle coulombic efficiency of 86.7 %. This first cycle shows a large improvement over the cycling results presented for pristine NMC-811 in Chapter 4 where initial charge and discharge capacities of approximately 120 mAh g<sup>-1</sup> and 80 mAh g<sup>-1</sup> were delivered respectively, with a first cycle coulombic efficiency of 66 %. The cycling stability of the 0.2 wt.% coated NMC-811 is also vastly superior to that for the pristine material. Although the discharge capacity is observed to drop slightly between the 1<sup>st</sup> and 2<sup>nd</sup> discharge, across the 10 cycles it remains stable at between 136 mAh g<sup>-1</sup> and 140 mAh g<sup>-1</sup> which marks a substantial improvement compared to the pristine material. It should be noted that only 10 cycles were performed here due to cell failure shown in Figure 7.16 in the appendix. This was also observed across a number of repeat cells, with the results here pertaining to the cell that managed to sustain the longest cycling duration.

Although excellent stabilities were observed for the 0.2 wt.% coated NMC-811, it is clear from the charge-discharge profiles in Figures 5.2(c,d) for the 0.5 wt.% and the 1.0 wt.% samples that increasing the coating mass (and thus most likely the coating thickness) has a detrimental effect on the cycling stabilities. Although a similar initial discharge capacity of 175 mAh g<sup>-1</sup> was observed for the 0.5 wt.% coated sample, a following initial discharge capacity of 126 mAh g<sup>-1</sup> was achieved, representing a smaller first cycle coulombic efficiency of 71.9 % compared to the 0.2 wt.% coated sample. Poor cycling stabilities are also observed across 18 cycles evidenced by the gradual decrease in capacities over cycling seen in the voltage-capacity plot, although this decrease becomes less pronounced beyond the 12<sup>th</sup> cycle where the discharge capacity falls from 89 mAh g<sup>-1</sup> to 82 mAh g<sup>-1</sup> between the 12<sup>th</sup> and 18<sup>th</sup> cycle.

Increasing the coating weight to 1.0 wt.% appears to exacerbate the poor cycling performances more. Similar to the 0.2 wt.% and 0.5 wt.% samples, an initial discharge capacity of 171 mAh g<sup>-1</sup> is delivered. However this is followed by an initial discharge capacity of 109 mAh g<sup>-1</sup> representing a larger loss of capacity compared to the previous samples. A more rapid capacity fade over 18 cycles is also observed in this sample with the discharge capacity reaching 40 mAh g<sup>-1</sup> during the final (18<sup>th</sup>) cycle. The cycling performance thus becomes worse with increased coating weights, which is most likely due to increased coating thicknesses impeding both the ionic and electronic conductivities.

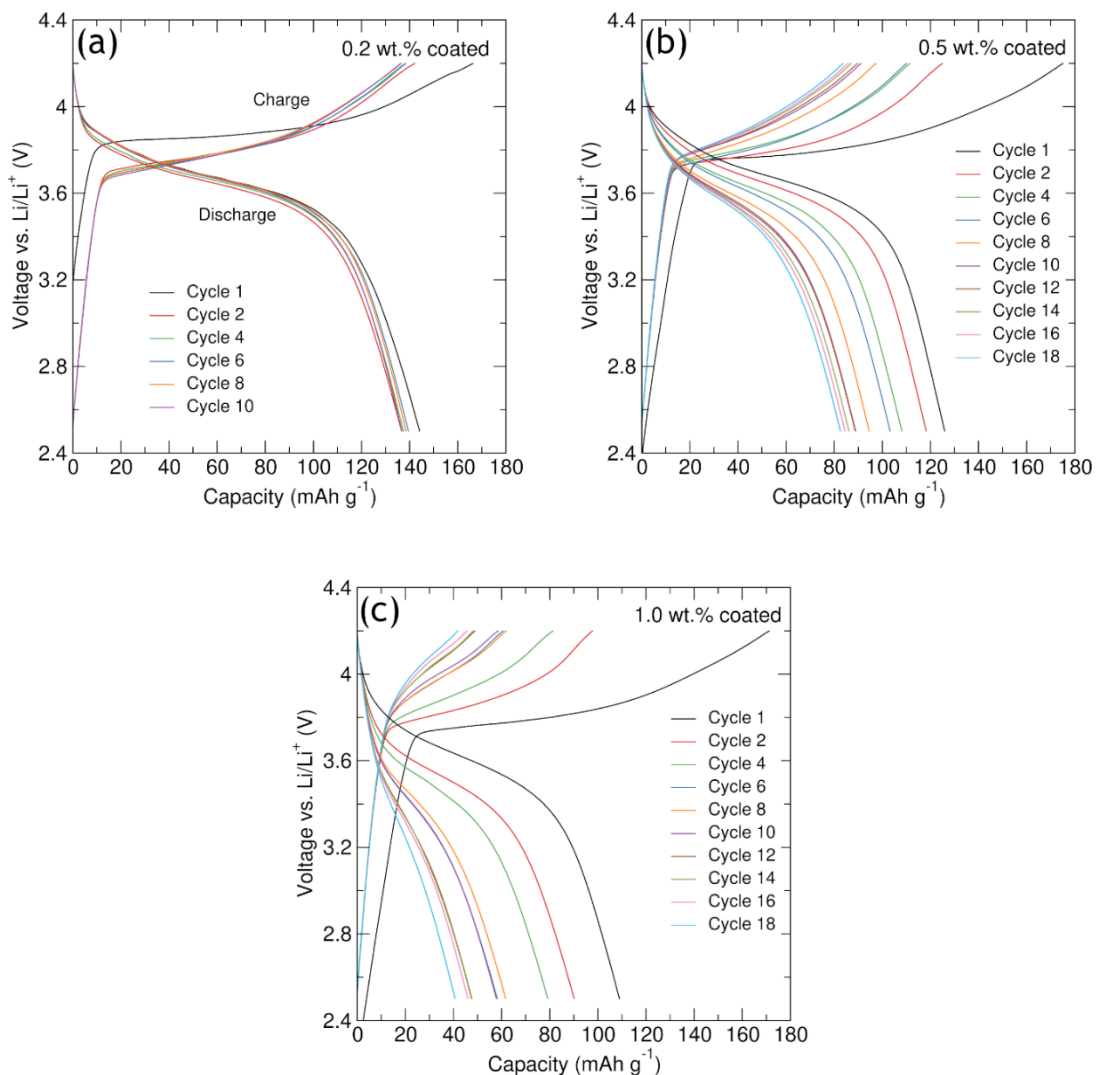


**Figure 5.2** Charge-discharge profiles obtained from galvanostatic cycling of coated NMC-811 materials with (a) 0.2 wt.%, (b) 0.5 wt.% and (c) 1.0 wt% Al<sub>2</sub>O<sub>3</sub> coatings cycled in Swagelok-type half-cells between 2.5 V - 4.2 V vs. Li/Li<sup>+</sup> at a rate of C/10.

Figure 5.3 displays the discharge capacities and calculated coulombic efficiencies up to cycle 10 to 18 for pristine NMC-811 and 0.2, 0.5 and 1.0 wt.% Al<sub>2</sub>O<sub>3</sub> coated NMC-811. The

0.2 wt.% coated NMC-811 sample displays much improved stabilities which is clearly evident even across 10 cycles. Discharge capacity retentions across the first 10 cycles can also be calculated for each sample as 73 %, 94 %, 71 % and 53 % for pristine NMC-811 and 0.2, 0.5 and 1.0 wt.% coated NMC-811 respectively, further highlighting the vast improvements in cycling stability facilitated by the 0.2 wt.% coating. Across 18 cycles the discharge capacity retention for the 0.5 and 1.0 wt.% coated materials were calculated as 66 % and 37 % respectively. The calculated Coulombic efficiencies are also shown in Figure 5.3 where values close to 100 % are observed for all samples after the 1<sup>st</sup> cycle. The improvement in the first cycle coulombic efficiency for the 0.2 wt.% sample (87 %) compared to the other samples (68 %, 71 % and 64 % for pristine NMC-811 and 0.5 and 1.0 wt.% coated NMC-811 respectively) is also clearly evident here.

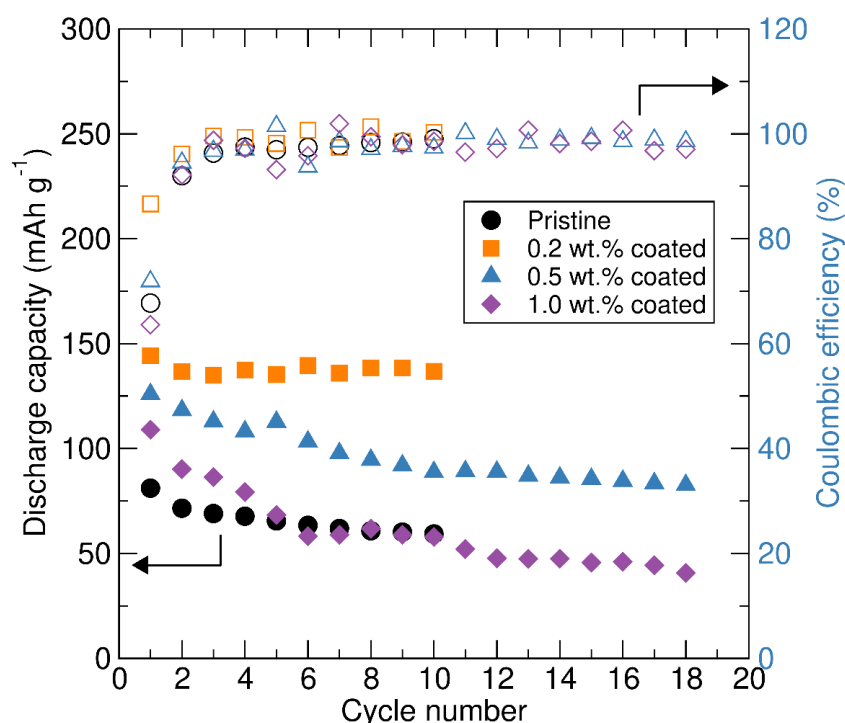


**Figure 5.3** Discharge capacity retentions and Coulombic efficiencies for pristine NMC-811 and the 0.2, 0.5 and 1.0 wt.% coated samples of NMC-811 across the first 10 - 18 cycles for materials cycled in Swagelok-type half-cells between 2.5 V - 4.2 V vs. Li/Li<sup>+</sup> at a rate of C/10.

Differential capacity profiles were also compiled from the galvanostatic cycling data and are shown for the three coated samples in Figure 5.4. The charging portions of the 1<sup>st</sup> cycle data were significantly more intense than in subsequent cycles and have thus been cropped to allow for greater clarity of the differential capacity behaviour beyond the 1<sup>st</sup> cycle. For the 0.2 wt.% coated sample, an initial charging peak is observed at  $\approx 3.85$  V corresponding to the Ni<sup>2+</sup>/Ni<sup>4+</sup> redox couples along with a feature at 4.16 V which could be related to the onset of the Co<sup>3+</sup>/Co<sup>4+</sup> redox couple and/or other structural changes

such as an H2 - H3 type transition. A weak discharge feature is observed at  $\approx 3.87$  V followed by a more intense peak at  $\approx 3.67$  V. This behaviour matches with that observed for uncoated NMC-811 samples presented in Chapter 4. The first charge peak shifts down to  $\approx 3.74$  V following the first cycle indicating a reduction in the polarization since the discharge features do not exhibit a voltage shift. Excellent overlap is then observed across the remaining 9 cycles indicating very stable cycling which is facilitated by the lightweight  $\text{Al}_2\text{O}_3$  coating. This stability most likely arises from the ability of the  $\text{Al}_2\text{O}_3$  coating to act as a barrier between NMC-811 and the electrolyte, thus protecting the cathode active material surface from deleterious electrode-electrolyte reactions, which can both consume active material and promote surface phases that can act to increase the charge transfer resistance. Both of these effects can contribute to capacity fade upon cycling in uncoated NMC-811 materials. For the 0.5 wt.% and the 1.0 wt.% coatings similar differential capacity behaviour is observed. An initial charging peak attributed to  $\text{Ni}^{2+}/\text{Ni}^{4+}$  redox couples appears at approximately 3.76 V which overall shifts to slightly higher voltages across cycling. This shift is more pronounced in the 1.0 wt.% coated sample where a shift to  $\approx 4.12$  V is observed compared to 3.80 V for the 0.5 wt.% coated sample. This is accompanied by a discharge peak that shifts to lower voltages upon cycling where the 0.5 wt.% sample peak shifts from  $\approx 3.68$  V to  $\approx 3.58$  V and the discharge peak of the 1.0 wt.% sample shifts from 3.63 V down to  $\approx 3.35$  V. This correlates to an increase in the polarization of both materials upon repeated cycling with the effect more pronounced in the 1.0 wt.% sample compared to the 0.5 wt.% coated sample. The thicker coating most likely attained with a heavier coating weight could contribute more to charge-transfer resistance, thus higher polarizations are observed. The profile features also become increasingly broader and less intense for both of these samples during cycling attributed to the reduction of the plateau-type region following severe capacity fading.

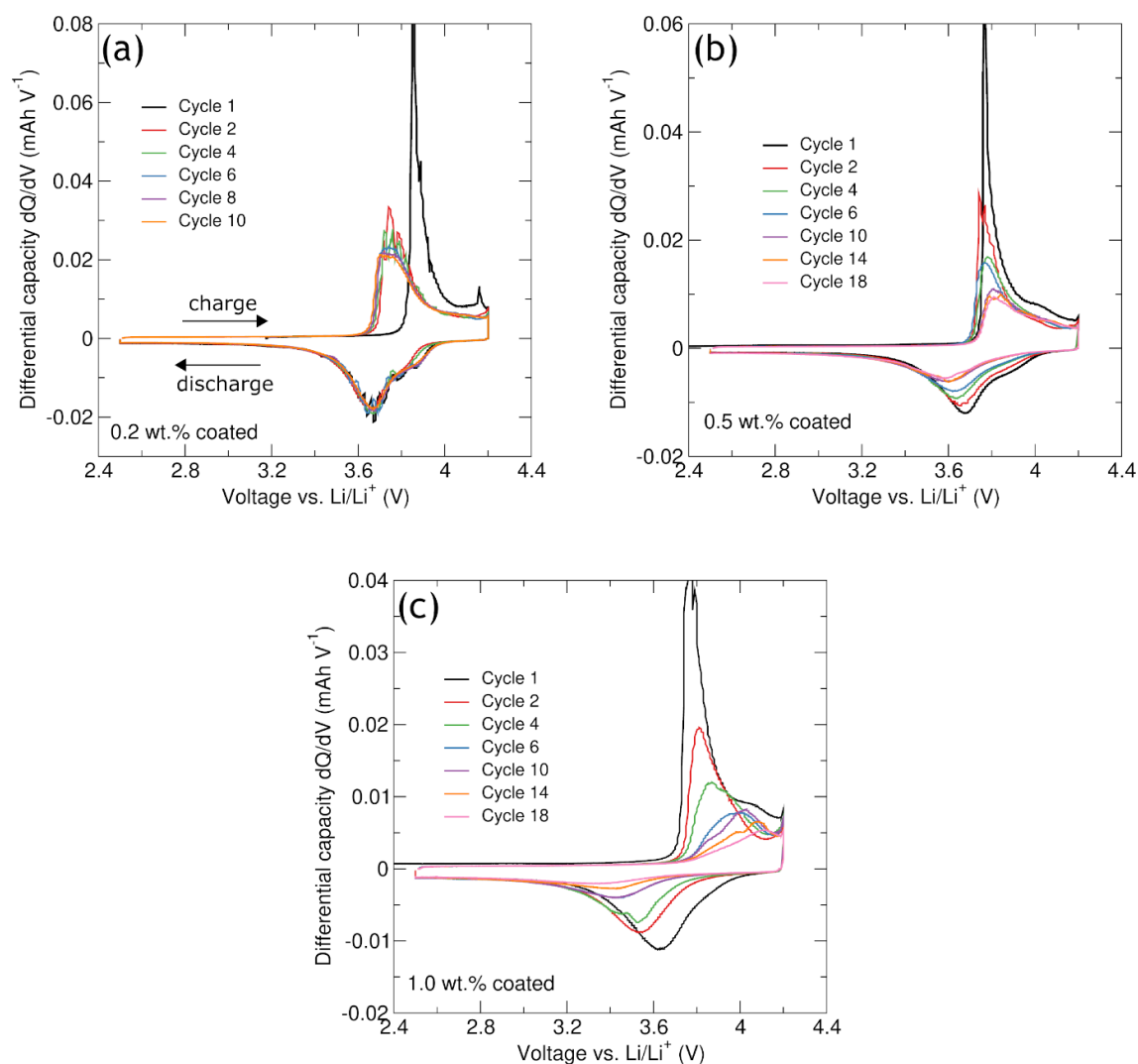


**Figure 5.4** Differential capacity ( $dQ/dV$ ) profiles obtained from galvanostatic cycling at room temperature of (a) 0.2 wt.%, (b) 0.5 wt.% and (c) 1.0 wt.%  $\text{Al}_2\text{O}_3$  coated NMC-811. Swagelok-type half-cells were cycled between 2.5 V - 4.2 V vs.  $\text{Li}/\text{Li}^+$  at a rate of C/10.

### 5.2.1.3 Post-cycling PXRD analysis of $\text{Al}_2\text{O}_3$ coated $\text{LiNi}_{0.8}\text{Mn}_{0.1}\text{Co}_{0.1}\text{O}_2$

To determine whether any structural changes occurred to the coated core NMC-811 during cycling, PXRD was carried out on the cycled materials from the previous galvanostatic cycling tests. Cells were disassembled in an Ar-filled glovebox and the cathode pellet was washed with THF to remove any residual electrolyte species before being dried and stored in a glovebox prior to analysis.

The collected PXRD data for each coated sample is shown in Figure 5.5. While the 0.5 wt.% and 1.0 wt.%  $\text{Al}_2\text{O}_3$  coated samples finished their assigned cycling protocols correctly and were thus obtained in the discharged state, the cell containing the 0.2 wt.% coated sample experienced a malfunction during its 11<sup>th</sup> cycle (shown in Figure 7.16 in the appendix) and so the material collected remained in the charged state. The PXRD

data collected for this sample therefore shows much broadened peaks compared to the discharged sample which has been observed by Yin *et al.* for delithiated NMC-111.<sup>220</sup> However, it is evident from the data presented in Figure 5.5 that for each sample the measured peaks can be ascribed to a layered  $\alpha$ -NaFeO<sub>2</sub>  $R\bar{3}m$  phase indicating that no significant structural transformations have occurred upon cycling. There is no evidence of any extra peaks except for an additional peak at  $2\theta \approx 18^\circ$  which results from the PTFE binder used to fabricate the cathode pellets. There may also be some small quantity of Li<sub>2</sub>CO<sub>3</sub> present in the 0.2 wt.% sample evidenced by small peaks between  $20^\circ$  to  $35^\circ 2\theta$ . There is also no evidence in the PXRD patterns collected of the presence of the O1 phase, even in the charged sample, which would be evidenced by additional peaks at  $2\theta \approx 19.5^\circ$ ,  $42^\circ$  and  $55^\circ 2\theta$ . This matches with other reports of NMC-811 where no O3  $\rightarrow$  O1 phase change has been detected.<sup>71,278</sup> This phase has been observed in layered oxides such as LiNi<sub>1/3</sub>Mn<sub>1/3</sub>Co<sub>1/3</sub>O<sub>2</sub> and LiNiO<sub>2</sub> at highly charged states and is thought to facilitate particle cracking during cycling.<sup>69,220</sup>

#### 5.2.1.4 Scanning electron microscopy analysis of 0.2 wt.% Al<sub>2</sub>O<sub>3</sub> coated LiNi<sub>0.8</sub>Mn<sub>0.1</sub>Co<sub>0.1</sub>O<sub>2</sub>

SEM analysis of the 0.2 wt.% Al<sub>2</sub>O<sub>3</sub> coated NMC-811 powder was conducted to investigate whether the coating process had any effect on the resultant particle size and morphology. This sample was chosen due to it being the only coated sample that showed excellent electrochemical stability when cycled under a constant current. The SEM analysis for this material was conducted on a Carl Zeiss Sigma variable pressure analytics SEM with images collected at magnifications of 5000, 26000 and 54000 (left to right) shown in Figure 5.6. The particle size distribution for this sample is also shown in Figure 7.17 in the appendix. The obtained images show little deviation from those collected for pristine NMC-811 samples in Chapter 4, characterised by non-uniform particle size and shape distributions. Particle sizes ranging between approximately 150 nm to 600 nm are observed and are of a similar magnitude to those reported previously in Chapter 4 synthesised for 1 hour at 750 °C highlighting that the short microwave reaction time is essential for obtaining these small particles. An average particle size of approximately 300 nm was calculated for this sample, which is similar to that calculated for the 750 °C 1 h sample (282 nm). Interestingly, the particles in Figure 5.6 display faceted features characterised by defined particle edges and visible faces. This is also observed in SEM images obtained from pristine NMC-811 samples presented previously. Therefore, the fact that no observable changes in the particle size and shape and the uniformity of these parameters occurs upon undergoing the coating method highlights that the original particle morphology is preserved during this procedure. It is unlikely that the Al<sub>2</sub>O<sub>3</sub>

coating cannot be observed in these secondary electron SEM images presented here as this very light coating most likely does not have an effect on the topography of the particles.

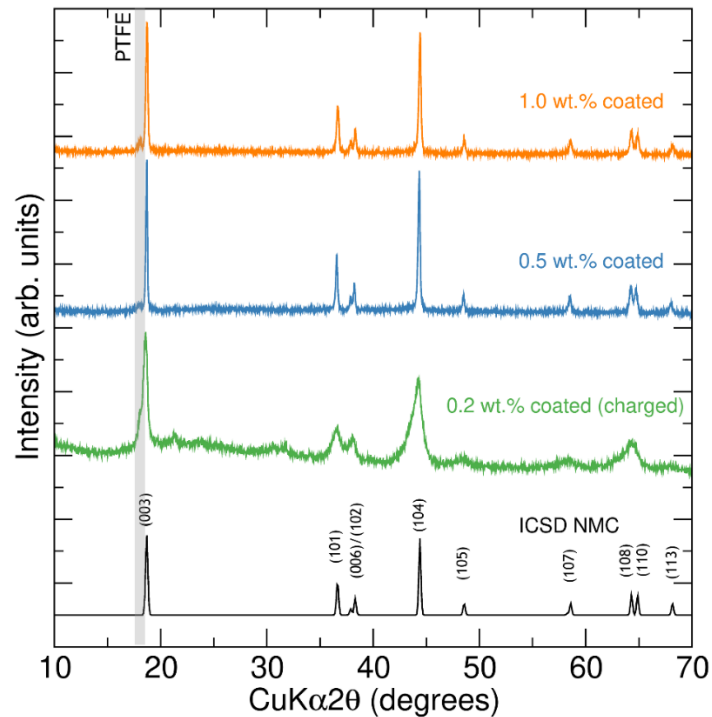


**Figure 5.5** PXRD patterns collected after cycling for the 0.2 wt.%, 0.5 wt.% and the 1.0 wt.%  $\text{Al}_2\text{O}_3$  coated NMC-811 for cathodes cycled in Swagelok-type half-cells between 2.5 V - 4.2 V vs.

$\text{Li}/\text{Li}^+$  at a rate of C/10. A peak corresponding to PTFE (from the binder) at  $2\theta \approx 18^\circ$  is highlighted in a grey box. Due to cell failure the pattern collected for the 0.2 wt.% coated sample corresponds to the material obtained in charged state whereas the data were collected for the 0.5 wt.% and 1.0 wt.% samples in the discharged state.

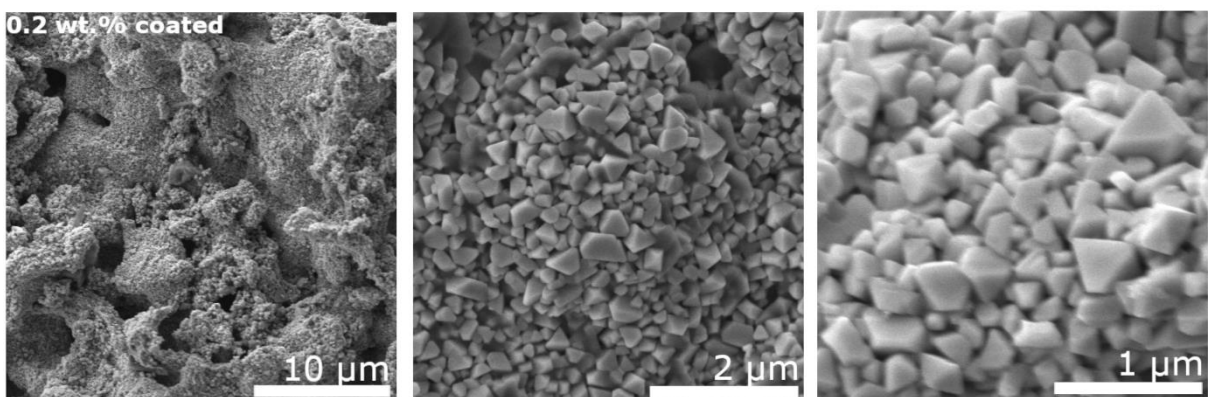


**Figure 5.6** SEM images of 0.2 wt.%  $\text{Al}_2\text{O}_3$  coated NMC-811 at increasing levels of magnification.

### 5.2.1.5 Extended galvanostatic cycling studies of 0.2 wt.% Al<sub>2</sub>O<sub>3</sub> coated LiNi<sub>0.8</sub>Mn<sub>0.1</sub>Co<sub>0.1</sub>O<sub>2</sub>

To assess the long term cycling properties of the 0.2 wt.% Al<sub>2</sub>O<sub>3</sub> coated NMC-811, extended cycling tests were conducted on this material and on pristine NMC-811 synthesised by the microwave-assisted solvothermal method with a reaction time of 1 hour at 850 °C. The tests conducted followed the galvanostatic cycling protocol using the application of a constant current corresponding to a rate of C/20 for the first two cycles and then applying a higher current corresponding to a rate of C/2 for up to 500 cycles with a potential window between 3.0 V and 4.2 V vs. Li/Li<sup>+</sup>. For extended cycling tests, low currents (slower rates) are not practical due to time constraints (*e.g.* cycling for 500 cycles at C/10 would take  $\approx$  400 days). Swagelok-type cells were fabricated using a pellet of cathode material mixed with KETJEN carbon black and PTFE in a 60:30:10 wt.% ratio, a lithium metal disk as the counter and reference electrode, a glass microfiber separator soaked in 1 M LiPF<sub>6</sub> in EC:DMC (1:1 v/v) electrolyte. Cells were connected to a BioLogic VSP potentiostat and cycled according to the protocol described above.

Figure 5.7 shows the voltage-capacity plots obtained from the extended cycling tests of (a) pristine NMC-811 and (b) 0.2 wt.% coated NMC-811. The uncoated (pristine) sample delivers an initial charge capacity of 189 mAh g<sup>-1</sup> which is close to the theoretical capacity of NMC-811 of 200 mAh g<sup>-1</sup> when charged to 4.2 V. However, upon initial discharge a loss of 54 mAh g<sup>-1</sup> occurs resulting in a delivered discharge capacity of 135 mAh g<sup>-1</sup>. This discharge capacity further falls to 126 mAh g<sup>-1</sup> upon the 2<sup>nd</sup> discharge within the C/20 cycling rate portion of the cycling test, indicating that degradation processes are occurring here. When the current density is increased to a rate of C/2 a large drop in capacity is observed to approximately 32 mAh g<sup>-1</sup> clearly showing the poor rate capability of this material. The discharge capacities remain at low values, dropping to  $\approx$  25 mAh g<sup>-1</sup> during the 50<sup>th</sup> cycle, before showing slightly increased values upon cycle 250 and 500 as shown in charge-discharge plots. The 0.2 wt.% coated sample (Figure 5.7(b)) shows similar behaviour upon the first cycle with initial charge and discharge capacities of 185 mAh g<sup>-1</sup> and 139 mAh g<sup>-1</sup> measured respectively. However, whereas the uncoated sample showed a capacity loss between the 1<sup>st</sup> and 2<sup>nd</sup> cycles, the coated sample shows excellent overlap between the 1<sup>st</sup> and 2<sup>nd</sup> discharge curves with a capacity of 138 mAh g<sup>-1</sup> achieved after the 2<sup>nd</sup> discharge showing excellent stability compared to the uncoated sample within the C/20 portion of the cycling. Upon the application of a higher current corresponding to a rate of C/2, a drop in capacities are observed, although this is less severe than that observed for the uncoated sample. The 5<sup>th</sup> cycle discharge yields a capacity of 82 mAh g<sup>-1</sup> which falls to approximately 73 mAh g<sup>-1</sup> upon the 10<sup>th</sup>

cycle. However, the discharge profiles show that this remains stable around this figure for the 50<sup>th</sup> and 100<sup>th</sup> cycles, with a slight increase upon the 250<sup>th</sup> cycle, indicating some degree of improved stability compared to the uncoated sample, albeit with a poor rate capability at C/2. However, upon the 500<sup>th</sup> cycle a mere 9.8 mAh g<sup>-1</sup> discharge capacity has been achieved suggesting a severe and late onset of cell degradation or failure occurring.

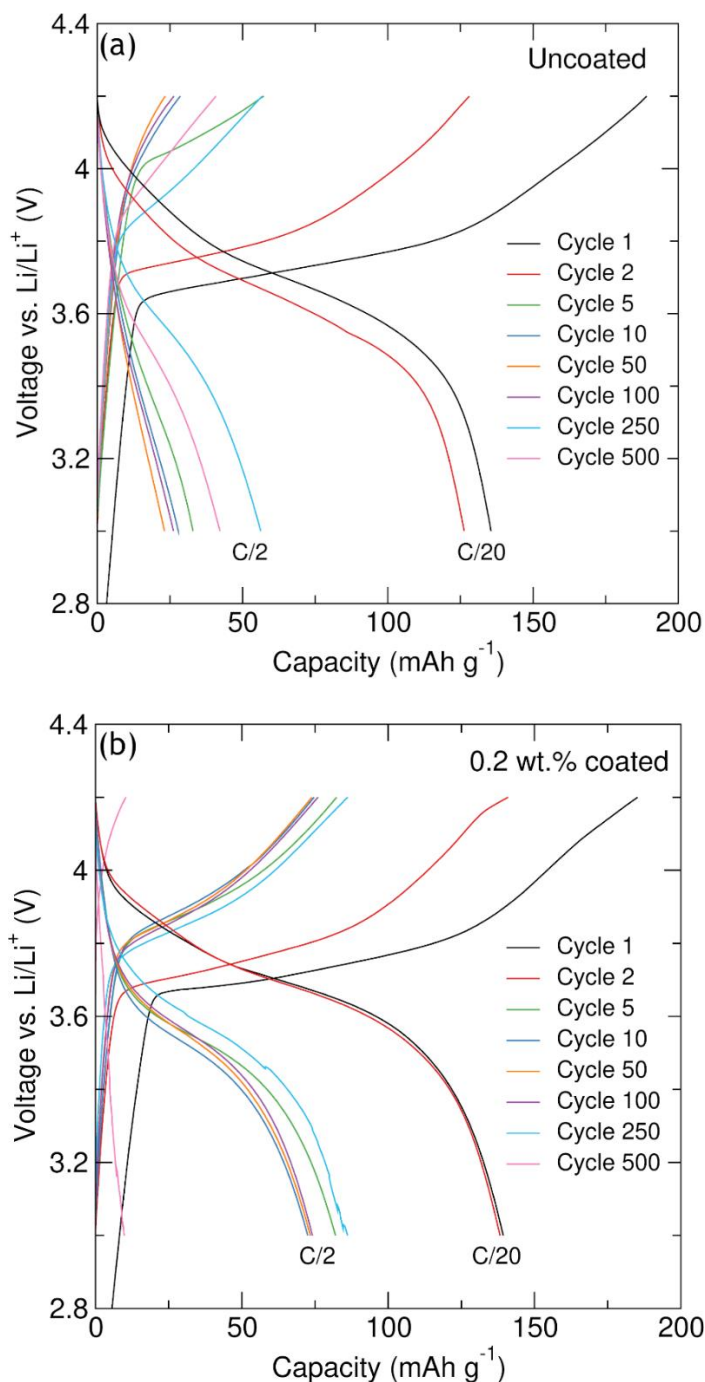


**Figure 5.7** Charge-discharge profiles obtained from galvanostatic cycling of (a) uncoated NMC-811 and (b) NMC-811 coated with 0.2 wt.% Al<sub>2</sub>O<sub>3</sub> cycled in Swagelok-type half-cells between 3.0 V - 4.2 V vs. Li/Li<sup>+</sup> at a rate of C/20 for 2 cycles and then C/2 up to 500 cycles.

For greater clarity into the discharge capacity behaviour over 500 cycles, the lower portion of Figure 5.8 displays the discharge capacity vs. cycle number for the 1<sup>st</sup>, 2<sup>nd</sup>, 5<sup>th</sup> and then every further 5<sup>th</sup> cycle up to cycle number 500 for the pristine NMC-811 (black circles) and the 0.2 wt.% coated NMC-811 (orange squares) for the cycling protocol detailed above. Coulombic efficiencies are also shown in the upper portion of the plot, using unfilled symbols of the same shape and colour. The plot clearly shows that higher discharge capacities are achieved for the coated sample compared to the uncoated sample. It is also clear to see that the coated sample suffers from a rapid capacity fade near the 380<sup>th</sup> cycle, where the discharge capacity values obtained actually fall below those obtained for the uncoated sample. Furthermore, the discharge capacities achieved across cycles are shown to be relatively unstable for both samples as they both show large fluctuations. For example, the discharge capacities achieved for the coated sample seem to fluctuate between values of  $\approx 65 \text{ mAh g}^{-1}$  to  $\approx 95 \text{ mAh g}^{-1}$  and those for the uncoated sample appear to fluctuate between  $\approx 17 \text{ mAh g}^{-1}$  and  $\approx 65 \text{ mAh g}^{-1}$ . Whether this is due to an inherent fluctuation within the samples or changes in capacity due to minor temperature fluctuations comes into question. The cells were cycled outside of a temperature controlled chamber and therefore are subject to changes in local temperature according to, for example, time of day or the day-to-day temperature fluctuations common in the UK.

For the coated sample the Coulombic efficiencies shown in the upper portion of Figure 5.8 have an average value of 98 % (excluding the 1<sup>st</sup> cycle efficiency) although a large fluctuation between 75 % and 113 % which could be attributed to temperature fluctuations. The uncoated sample shows an average efficiency of 98.5 % with within a range of 91 % - 105 %. These cells were not cycled concurrently and it is a possibility that the uncoated cell was not subject to the same temperature changes as the coated cell.

Alongside the charge-discharge profiles and the capacity retention, the differential capacity behaviour of the uncoated and 0.2 wt.% coated NMC-811 samples obtained from the long-term galvanostatic cycling data was analysed and plotted in Figure 5.9. The uncoated sample of NMC-811 (Figure 5.9(a)) exhibits a wide initial charging peak centred at  $\approx 3.71 \text{ V}$  ascribed to the  $\text{Ni}^{2+}/\text{Ni}^{4+}$  oxidation process and a corresponding discharge peak at  $\approx 3.70 \text{ V}$  for the reduction process. These peak positions describe a low initial polarization of the material with only a 0.01 V difference between processes. Upon the 2<sup>nd</sup> cycle, the oxidation and reduction peaks shift to higher and lower values of 3.75 V and 3.68 V respectively yielding a difference of 0.07 V which is evidence of an increase in the polarization. During the C/2 portion of the cycling (cycle 3 onwards) it is evident

in the differential capacity plot that the peak intensities severely decrease and become broader with the data obtained for cycle 100 barely showing any distinct features. Compared to the C/20 cycles, the charge and discharge peak positions shift to higher and lower values respectively indicating a large degree of polarization with a difference of 0.38 V calculated for the 500<sup>th</sup> cycle. This increase in polarization likely plays a role in the poor capacities achieved for the sample. Figure 5.9(b) shows the differential capacity data for the 0.2 wt.% coated sample of NMC-811 obtained from the long-term galvanostatic cycling. Upon initial charging, a peak at  $\approx 3.68$  V is observed originating from the Ni<sup>2+</sup>/Ni<sup>4+</sup> oxidation with a corresponding reduction peak at  $\approx 3.70$  V correlating to a small degree of polarization as was previously observed with the first cycle analysis of the uncoated material. Upon the 2<sup>nd</sup> cycle at C/20 there is a slight shift in both of the peaks to 3.71 V and 3.69 V which still results in a small degree of polarization. This is expected due to the similarities observed between the 1<sup>st</sup> and 2<sup>nd</sup> cycles in the capacity-voltage plot in Figure 5.7(b). An average polarization of 0.29 V is observed for cycles 5, 100 and 250 which is reduced compared to the 500<sup>th</sup> cycle polarization calculated for the uncoated sample. The differential capacity profile for the 500<sup>th</sup> cycle of the 0.2 wt.% coated sample is featureless owing to the low capacities originating from the steep rise and drop of the capacity as a function of voltage exhibiting no resemblance of a plateau-like region. Nevertheless, despite poor rate capabilities with an applied current of C/2, the long-term cycling of the uncoated and 0.2 wt.% coated NMC-811 highlight that higher capacities are enabled by the Al<sub>2</sub>O<sub>3</sub> coating across hundreds of cycles.

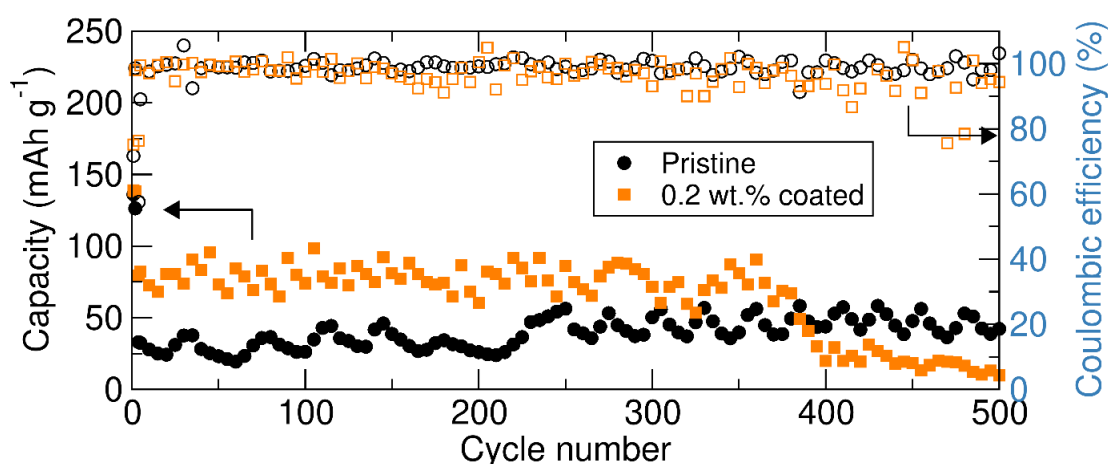


**Figure 5.8** Discharge capacity retentions obtained (filled symbols) and Coulombic efficiencies (unfilled symbols) calculated from galvanostatic cycling of uncoated NMC-811 (black circles) and NMC-811 (orange squares) coated with 0.2 wt.% Al<sub>2</sub>O<sub>3</sub> cycled in Swagelok-type half-cells between 3.0 V - 4.2 V vs. Li/Li<sup>+</sup> at a rate of C/20 for 2 cycles and then C/2 up to 500 cycles.

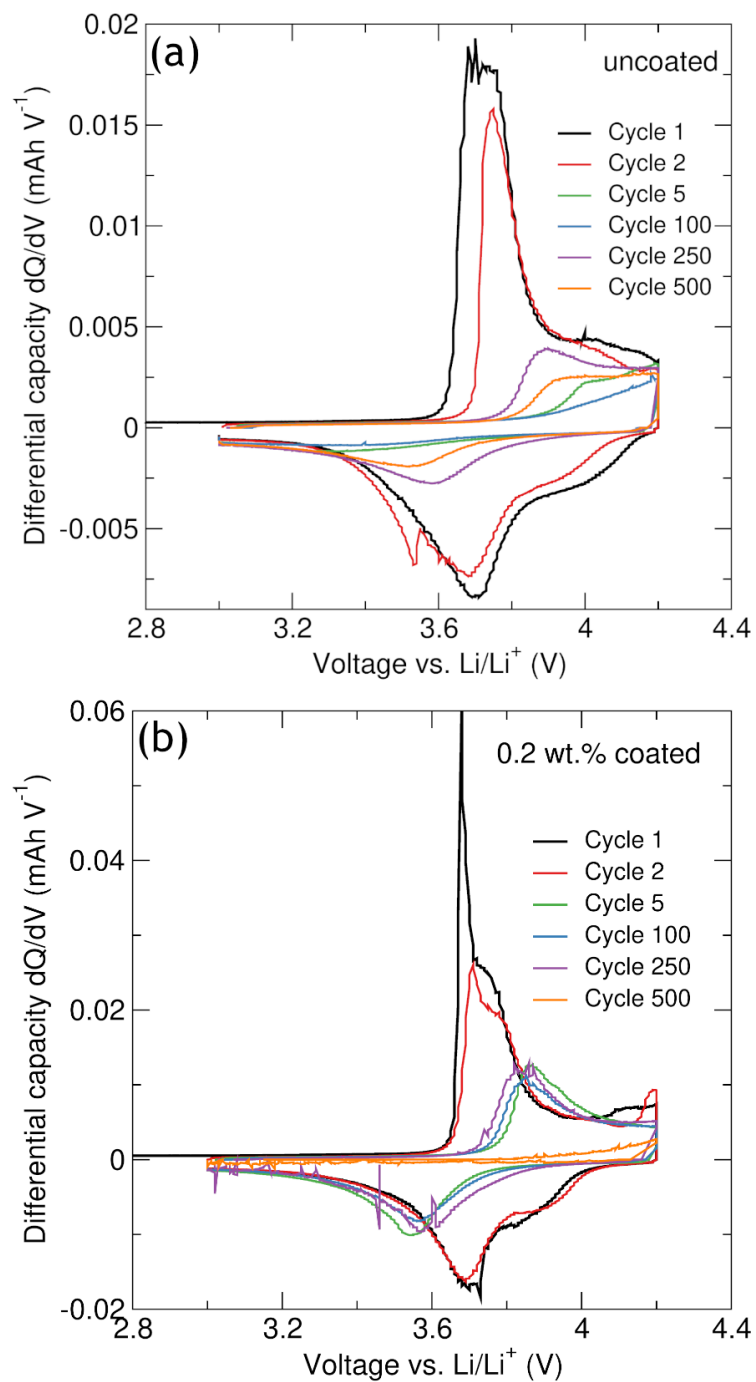


**Figure 5.9** Differential capacity ( $dQ/dV$ ) profiles obtained from galvanostatic cycling of (a) uncoated NMC-811 and (b) NMC-811 coated with 0.2 wt.%  $Al_2O_3$  cycled in Swagelok-type half-cells between 3.0 V - 4.2 V vs. Li/Li<sup>+</sup> at a rate of C/20 for 2 cycles and then C/2 up to 500 cycles.

### 5.2.2 *Operando* X-ray absorption spectroscopy analysis of Al<sub>2</sub>O<sub>3</sub> coated LiNi<sub>0.8</sub>Mn<sub>0.1</sub>Co<sub>0.1</sub>O<sub>2</sub>

As it is the nickel cations that directly influence both the high specific capacities achievable in high nickel content cathodes and the degradation processes occurring during cycling, element specific analyses techniques such as X-ray absorption spectroscopy (XAS) allow for a deeper understanding of these processes. It is of particular interest to study the transition metal redox reactions occurring in the cathode during cycling and thus *in-situ* analysis offers a route for gaining such insight. By studying the XAS data, the oxidation states and the local nearest-neighbour coordination environments can be monitored during cycling.

Samples of NMC-811 obtained from a commercial supplier, and uncoated and 0.2 wt.% Al<sub>2</sub>O<sub>3</sub> coated NMC-811 samples synthesised by the microwave-assisted solvothermal method were studied here. XAS measurements on the Ni K-edge were performed at the I20 beamline at the Diamond Light Source synchrotron in the UK. Cathode samples were loaded into AMPIX cells with a metallic lithium counter electrode, a glass microfibre separator and 1 M LiPF<sub>6</sub> in EC:EMC (3:7 wt.%) with 1 % VC electrolyte and connected to a BioLogic VSP potentiostat for electrochemical cycling. Cycling was performed between 3.0 to 4.5 V vs. Li/Li<sup>+</sup> at a current rate of C/5 (assuming a theoretical specific capacity of 200 mAh g<sup>-1</sup>) with each XAS measurement performed at approximately 0.1 V intervals. Measurements were taken between 8203 eV and 9040 eV to encompass both the XANES and EXAFS regions.

Figure 5.10 shows the data collected in the XANES region for fresh samples of the studied materials including Figure 5.10(a) the full XANES region and (b) the pre-edge region. Also included are the reference data for NiO and commercial NMC-111 where Ni<sup>2+</sup> exists in octahedrally coordinated environments. The commercially-obtained NMC-811 was used as a reference for the in-house prepared samples of NMC-811. The rising-edge and edge feature is assigned to the excitation of a core electron (from the 1s shell in the case of the K-edge) to the 4p orbitals. By looking at the rising-edge and edge-step portions of the data, the commercial sample of NMC-811 shows the same shape as those obtained for NiO and NMC-111 indicating that the Ni cations exist in similar coordination environments but with a shift to slightly higher edge energies for NMC-811 that corresponds to a shift to a higher oxidation state. It is known that NMC-111 contains Ni<sup>2+</sup> cations whereas the unequal stoichiometries between Ni, Co and Mn in NMC-811 result in a distribution of Ni<sup>2+</sup> and Ni<sup>3+</sup> cations leading to an increase in the average nickel oxidation state. This increase is manifested in the shifted position of the Ni K-edge observed. All

of the NMC-811 samples measured here show similar profiles for the edge region with an intense peak at energies of  $\approx 8352.4$  eV indicating that all three samples contain  $\text{Ni}^{2/3+}$  cations with similar average oxidation states. The pre-edge region, highlighted in Figure 5.10(b) is present when a normally dipole forbidden transition from a  $1s$  core electron to the  $3d$  orbitals is allowed due to orbital mixing between  $p$ - and  $d$ -orbitals which can occur when deviations from centrosymmetry in the coordination environment occur. A shift to slightly higher energies is observed in this region for NMC-811 compared to NiO and NMC-111 which is a further indication of the increased average oxidation state of the nickel cations.

The XANES data collected during the electrochemical cycling are shown in Figure 5.11 for the (a,b) commercial, (c,d) uncoated and (e,f) 0.2 wt.%  $\text{Al}_2\text{O}_3$  coated samples of NMC-811 where the data collected during the charging and discharging steps are shown in the left and right hand plots respectively. All of the profiles displayed show similar shapes characterised by the pre-edge, rising edge and edge features as observed for the pristine samples of NMC and reference samples presented above, showing that there is not a drastic change in the nickel environment and the consequent structure of the cathode during cycling. From the charging data, a difference in the edge energy is observed during the charging process for all three samples that is characterised by a shift to higher energies ascribed to the oxidation of the  $\text{Ni}^{2+}/\text{Ni}^{3+}$  cations to  $\text{Ni}^{4+}$  as  $\text{Li}^+$  cations are removed from the cathode material. Upon discharging, shown in the right-hand plots for all three samples, it is clear that any effects on the absorption behaviour of the cathodes is less pronounced compared to the behaviour upon charging for all three samples.

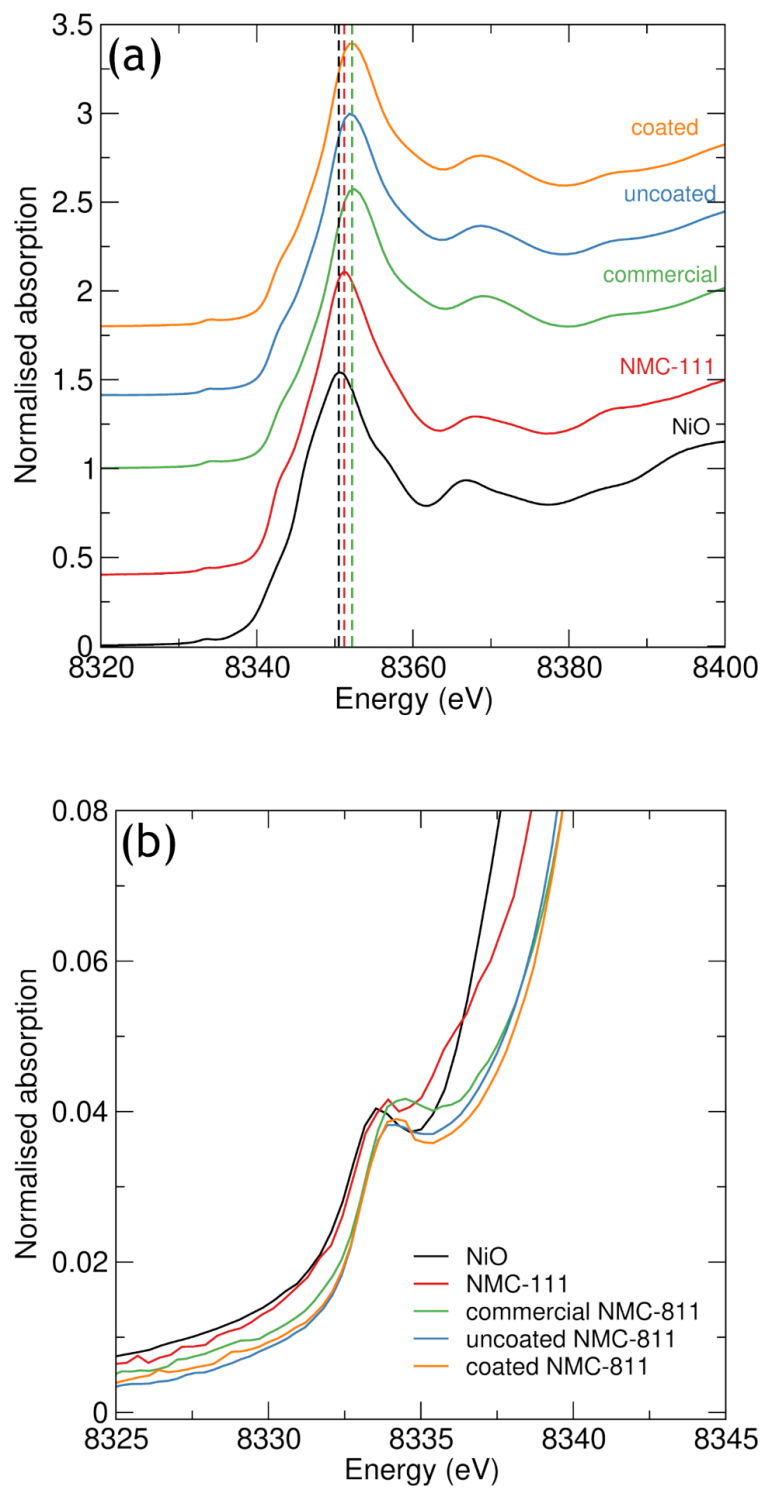


**Figure 5.10** (a) XANES region and (b) the pre-edge region from the XAS data collected on the Ni K-edge for commercial NMC-811, uncoated NMC-811 and 0.2 wt.%  $\text{Al}_2\text{O}_3$  coated NMC-811 synthesised by a microwave assisted sol-gel method. Standard for NiO and  $\text{LiNi}_{1/3}\text{Mn}_{1/3}\text{Co}_{1/3}\text{O}_2$  are also included.

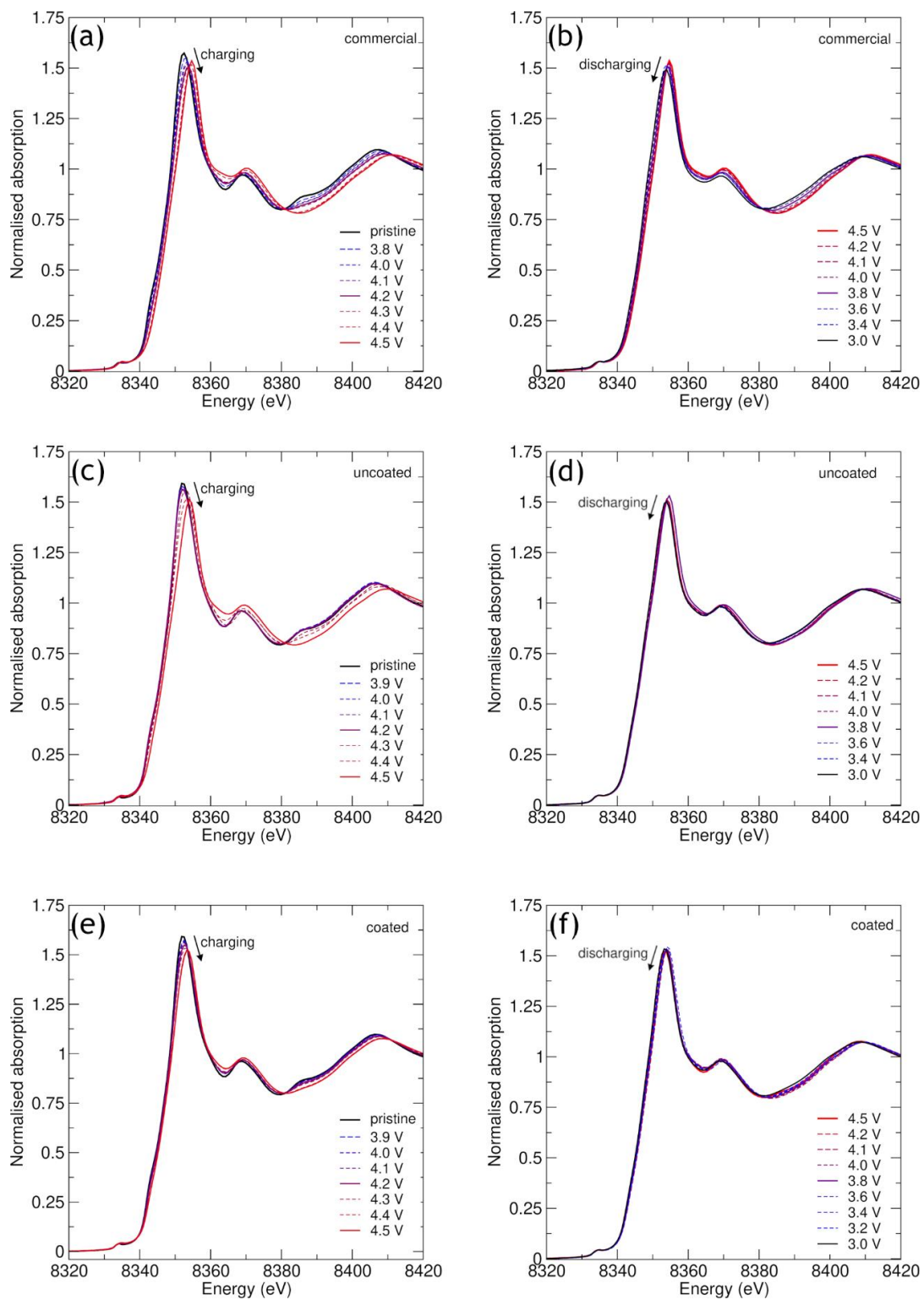


**Figure 5.11** XANES region for the *in-situ* XAS data collected on the Ni K-edge for AMPIX cells containing (a,b) NMC-811 obtained from a commercial supplier, (c,d) uncoated and (e,f) 0.2 wt.% coated NMC-811 synthesised by a microwave-assisted sol-gel method. AMPIX cells were cycled between 3.0 V - 4.5 V vs. Li/Li<sup>+</sup> at a rate of C/5. Left and right panels show charging and discharging data respectively.

Figure 5.12 shows the edge transition region in greater detail for each sample, accompanied by a y-offset for each data set upon charge and discharge allowing for greater clarity between states of charge. For the commercial sample, shown in Figures 5.12(a,b) for the charging and discharging processes respectively, there is a clear shift in the position of the absorption edge and the top of the absorption peak during charging to 4.5 V with a gradual increase in the edge transition observed during intermediate states of charge measured at approximate intervals of 0.1 V. A upper cut off voltage of 4.5 V was chosen in order to study the degradation processes to a greater extent, as voltages > 4.2 V significantly contribute to these processes.

When a positive current was applied to the cell to start the charging process, the operating voltage immediately rose to  $\approx 3.8$  V vs. Li/Li<sup>+</sup> hence why the 2<sup>nd</sup> point of measurement was collected at this point. This gradual shift to higher energies of the absorption edge corresponds to the gradual oxidation of the Ni<sup>2+</sup> and Ni<sup>3+</sup> cations present in the NMC-811 to Ni<sup>4+</sup> resulting in a greater binding energy of core shell electrons due to the increased positive charge on the cation.

During discharge from 4.5 V to 3.0 V shown in Figure 5.12(b), a gradual decrease in the energy of the absorption edge is observed corresponding to the reduction of Ni<sup>4+</sup> cations back to Ni<sup>2+</sup> and Ni<sup>3+</sup> during the intercalation of Li<sup>+</sup> cations into the layered NMC-811 structure. It is observed, however, that upon discharge down to 3.0 V the position of the absorption edge does not fully revert to the initial energy observed before cycling, indicating that the average oxidation state of nickel irreversibly increases after one full electrochemical cycle. This could be due to some migration of nickel into the lithium layers during the first charging step which would preclude the full re-insertion of lithium upon subsequent discharge. A smaller amount of intercalated lithium corresponds to a reduction in the extent of transition metal reductions due to charge conservation. Furthermore, the formation of spinel-type surface phases can sometimes occur in high nickel content electrodes (especially when cycled to reasonably high voltages such as 4.5 V vs. Li/Li<sup>+</sup>) where the nickel resides in the +3 oxidation state upon lithiation. If this occurred, it would serve to increase the overall average oxidation state of the Ni cations within the electrode material.

While the commercial sample of NMC-811 showed a gradual increase of the absorption edge energy during charging, the uncoated sample of NMC-811 synthesised by the microwave-assisted sol-gel method shows no change in the edge energy up to 4.2 V vs. Li/Li<sup>+</sup> characterised by a good overlap of the edge profiles. At voltages greater than 4.2 V, the edge region experiences a gradual shift to higher energies ascribed to oxidation of

the  $\text{Ni}^{2+}$  and  $\text{Ni}^{3+}$  to  $\text{Ni}^{4+}$ . These results indicate that the onset of delithiation occurs at higher voltages compared to the commercial sample which suggests that some additional resistive feature is present in the material that could be a structural or a surface feature. Upon discharge it is observed that there is a much less pronounced change between the profiles compared to both the charging profiles for this sample and the discharging profiles for the commercial sample. Upon close inspection of the profiles it can be seen however, that there is an overall decrease in the edge energy between the fully charged and fully discharged state. The profiles for the initial discharging down to  $\approx 3.8$  V show good overlap within the edge region which is indicative of little change in the Ni oxidation state occurring, similar as that observed during the charging step, again suggesting some form of overpotential required to start the reduction of the Ni.

As was observed in the commercial sample, the position of the absorption edge at the end of discharge remains at a higher energy than that observed for the fresh uncycled material. This would suggest that the fully discharged material contains a distribution of nickel cations with an overall higher oxidation state than what is observed in the uncycled sample. As before, this could be rationalised by migration of nickel ions into the lithium layer thus preventing the re-insertion of a corresponding amount of lithium and possibly the formation of  $\text{Ni}^{3+}$  containing spinel-like phases on the surface forming from the highly reactive charged surface. In this case, the results arising from such effects are likely to be more severe than in the commercial sample, possibly due to the short reaction times utilised in the microwave reaction (which has been shown to increase the Li/Ni mixing) and the increased surface areas present in these microwave-synthesised samples.

Similar behaviour is also observed during the charging and discharging of the coated sample shown in Figure 5.12(e,f) respectively where an increase in the energy of the absorption edge during charging occurs. This is much less pronounced than that observed for the commercial sample and shows a gradual increase (similar to the commercial sample) rather than the sudden onset of an edge shift as observed in the uncoated, microwave-synthesised sample. Upon discharge of the cell containing the coated NMC-811 material, between 4.2 V and 3.0 V a decrease in the edge position can be seen although, as observed before, the profile obtained for the fully discharged material does not revert back to the same as that obtained for the uncycled material. Furthermore, there is an increase in the edge energy from 4.5 V to 4.2 V suggesting an oxidation of the Ni cations which is strange and warrants further, future investigation. One suggestion could arise from possible relaxation of the material once the current was switched off during measurements.

Furthermore, analysis of only the K-edge spectra might not be sufficient to gain complete insight into the oxidation states as reported by Kubobuchi *et al.* who also utilised L-edge XANES coupled with first principles calculations to better understand the valence states and redox behaviour of Ni, Mn and Co cations in NMC-111 and found that more complex effects such as lattice distortions could change the shapes and positions of the absorption profiles.<sup>279</sup> The behaviour of the Ni cations in NMC-811 is likely to be complex and thus warrants such further analysis.

Analysis of the pre-edge region can also provide information on the nickel environments during electrochemical cycling. Observation of the full XANES region (Figure 5.11) reveals the existence of a weak pre-edge region at energies of approximately 8335 eV. The pre-edge feature originates from the electric-dipole-forbidden but quadrupole-allowed 1s to 3d transition and the occurrence of this peak can be used as a probe for geometry, as any deviations from centrosymmetric coordination of the metal absorbers are manifested in increased intensity of this feature, and as a probe into the metal oxidation state which is related to the energy at which the pre-edge feature appears.

Pre-edge features measured on the Ni K-edge in NMC type compounds are reported to be weak in intensity owing to the highly symmetrical environments often found for NiO<sub>6</sub> octahedra. Figure 5.13 shows the pre-edge regions during charge and discharge, obtained from the XANES spectra for the three samples of NMC-811 studied. As expected from the data obtained at the absorption edge, a shift in the energy of the pre-edge peak to higher energies is observed upon the charging of the material related to the oxidation of the Ni<sup>2+</sup> and Ni<sup>3+</sup> to Ni<sup>4+</sup> during delithiation. These shifts match the behaviour exhibited by the edge transitions, involving gradual transitions for the commercial and coated samples and a shift above 4.2 V for the uncoated sample. Alongside these shifts, there is also an increase in the intensity of the pre-edge peak during charge, indicating geometrical deviations from centrosymmetry for the Ni cation environments. This is very noticeable for all samples between the uncycled and charged states where the intensity appears to increase the most in the case of the uncoated, microwave-synthesised sample. One possible reason for the deviation from symmetry could be due to oxygen oxidation that can occur upon high states of charge that could result in changes to the Ni-O bonds and lead to a more distorted environment creating structural instabilities. The fact that this increase in intensity is damped for the coated sample suggests that the Al<sub>2</sub>O<sub>3</sub> coating can aid to protect the Ni cations from these distorted environments which could help to aid in the overall stability of the structure. This also suggests that these geometric distortions could be the result of surface degradation of the material e.g. reaction with the

electrolyte, since the main role of the coating is to protect the active material from surface degradation. Similar to the XANES data collected during discharge previously presented on the three samples, very little change is observed in the pre-edge region during discharging.

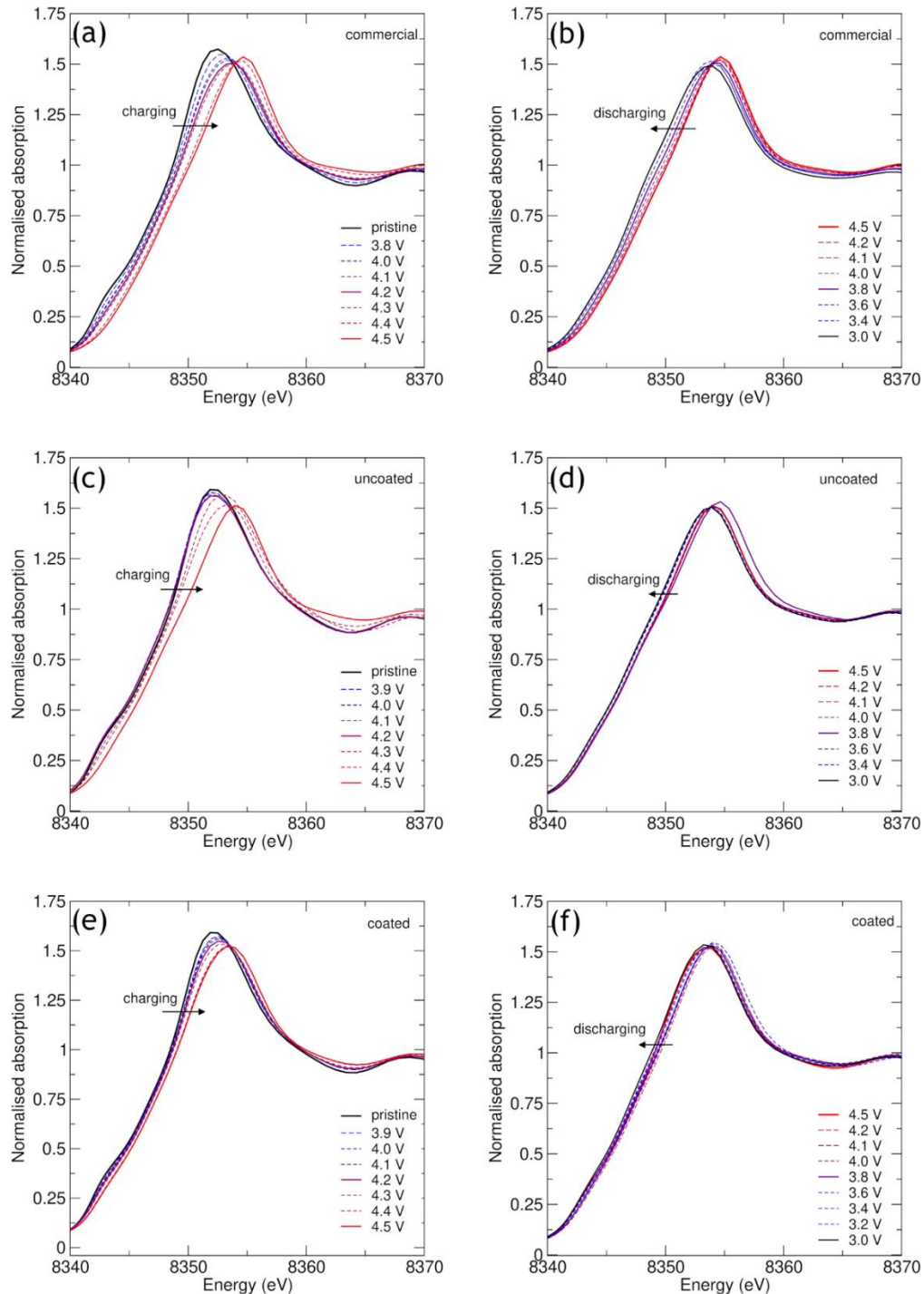


**Figure 5.12** The edge region of the XANES data collected on the Ni K-edge for the *in-situ* XAS measurements for AMPIX cells containing (a,b) NMC-811 obtained from a commercial supplier, (c,d) uncoated and (e,f) 0.2 wt.% coated NMC-811 synthesised by a microwave-assisted sol-gel method. Left and right panels show charging and discharging data respectively.

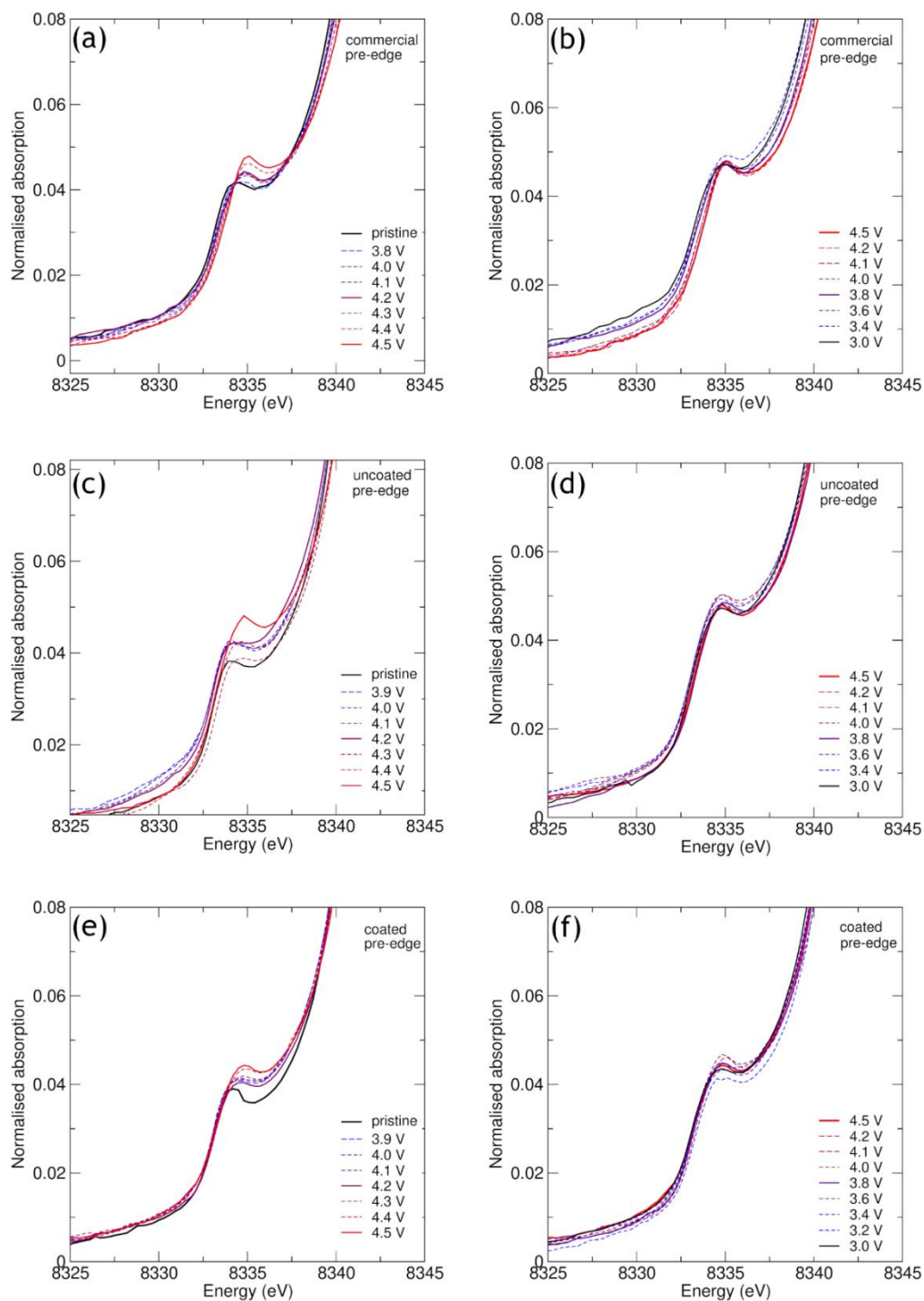


**Figure 5.13** Pre-edge XANES region for the *in-situ* XAS data collected on the Ni K-edge for AMPIX cells containing (a,b) NMC-811 obtained from a commercial supplier, (c,d) uncoated and (e,f) 0.2 wt.% coated NMC-811 synthesised by a microwave-assisted sol-gel method. Left and right panels show charging and discharging data respectively.

While the XANES region of the XAS spectra sheds insight into the coordination environment of the metal absorber atom, the EXAFS region can provide information on structure and bonding. EXAFS analysis was performed for each sample during electrochemical cycling alongside the XANES analysis in order to correlate the state of

charge with changes to the intensities of the Ni-O and Ni-M first and second shell peaks. Figure 5.14 shows the magnitude of the Fourier transformed EXAFS spectra for each of the samples during charge (right hand plots) and discharge (left hand plots). Each of the spectra show two distinct peaks corresponding to the first shell Ni-O distances at approximately 1.4 Å and the Ni-M distances at approximately 2.5 Å. These spectra have not been phase corrected for the photoelectron phase shifts thus distances between the Ni absorber atom and the backscattering atoms are  $\approx 4$  Å shorter than the actual distances. It is noted that, if phase corrected, the positions of the Ni-M peak would lie at  $\approx 2.9$  Å which is consistent with the  $a$  lattice parameter for this structure.

For all samples, the  $r$  value of both Ni-O and Ni-M peaks shifts to lower values upon charging indicating a contraction of the Ni-O and Ni-M interatomic distances that occur as a result of the oxidation of the Ni cations. Upon discharge there is not a noticeable change in the  $r$  value of these peaks suggesting some form of structural irreversibility. It is difficult to compare this behaviour to that reported for similar samples across the literature as most studies report only the first charge process. The intensity of the Ni-O peak is shown to increase during charging while the shape of the peak changes also. In the pristine sample, the Ni-O peak appears to consist of two features which merge during charging. This can be attributed to the presence of some Jahn-Teller Ni<sup>3+</sup> cations in the pristine NMC-811 (as expected) which produces a distorted octahedral environment for the Ni cations consisting of two different Ni-O bond lengths. The oxidation to Ni<sup>4+</sup> results in a diminution of the Jahn-Teller effect and results in an increase in the intensity of the Ni-O peak. Similar behaviour has been reported for LiNi<sub>0.85</sub>Co<sub>0.15</sub>O<sub>2</sub> system under charge studied by Balasubramanian *et al.*<sup>280</sup> This effect is more pronounced in the commercial sample, indicating that an incomplete conversion to Ni<sup>4+</sup> is not achieved for the microwave-synthesised samples.

Upon discharge, the distinctive two feature Ni-O peak is not observed. Partial loss of oxygen from the structure at high states of charge could facilitate this effect where the oxidation state of Ni in the lithiated material would have to be lower to compensate for loss of oxygen. Furthermore, the Li/Ni anti-site mixing could be at play here also: the replacement of a Li<sup>+</sup> by Ni<sup>2+</sup> would lead to the conversion of an equivalent amount of Ni<sup>3+</sup> to Ni<sup>2+</sup> in the lattice. Close observation of the data obtained for the samples at the end of discharge appear to show that this effect is more pronounced in the uncoated sample compared to the commercial and coated samples which both show a small indication of Ni<sup>3+</sup> at 3.0 V, thus suggesting that the Al<sub>2</sub>O<sub>3</sub> coating suppresses oxygen loss. XAS performed on the O K-edge might be a future complementary technique that could aid in further

understanding of the behaviour reported here. The 2<sup>nd</sup> observed peak at approximately 2.5 Å corresponds to the interaction between the nickel absorber atoms and neighbouring metal atoms e.g. Ni, Mn, Co and Li. As the backscattering from lithium is expected to be very weak, and the proportion of Ni is much larger than that of Mn and Co the Ni-Ni distances are likely to be the dominant contribution to this peak. As previously mentioned, the position of the Ni-M peak shifts to lower  $r$  values upon charging which is consistent with the model of the contracting  $a$  lattice parameter that has been reported.<sup>71</sup>

These XAS results, from both the XANES and EXAFS regions present an interesting insight into the *operando* behaviour of the nickel cations in high nickel content cathode NMC-811 during both charge and discharge, while also providing some insight into the differences achieved via the application of a protective Al<sub>2</sub>O<sub>3</sub> coating.

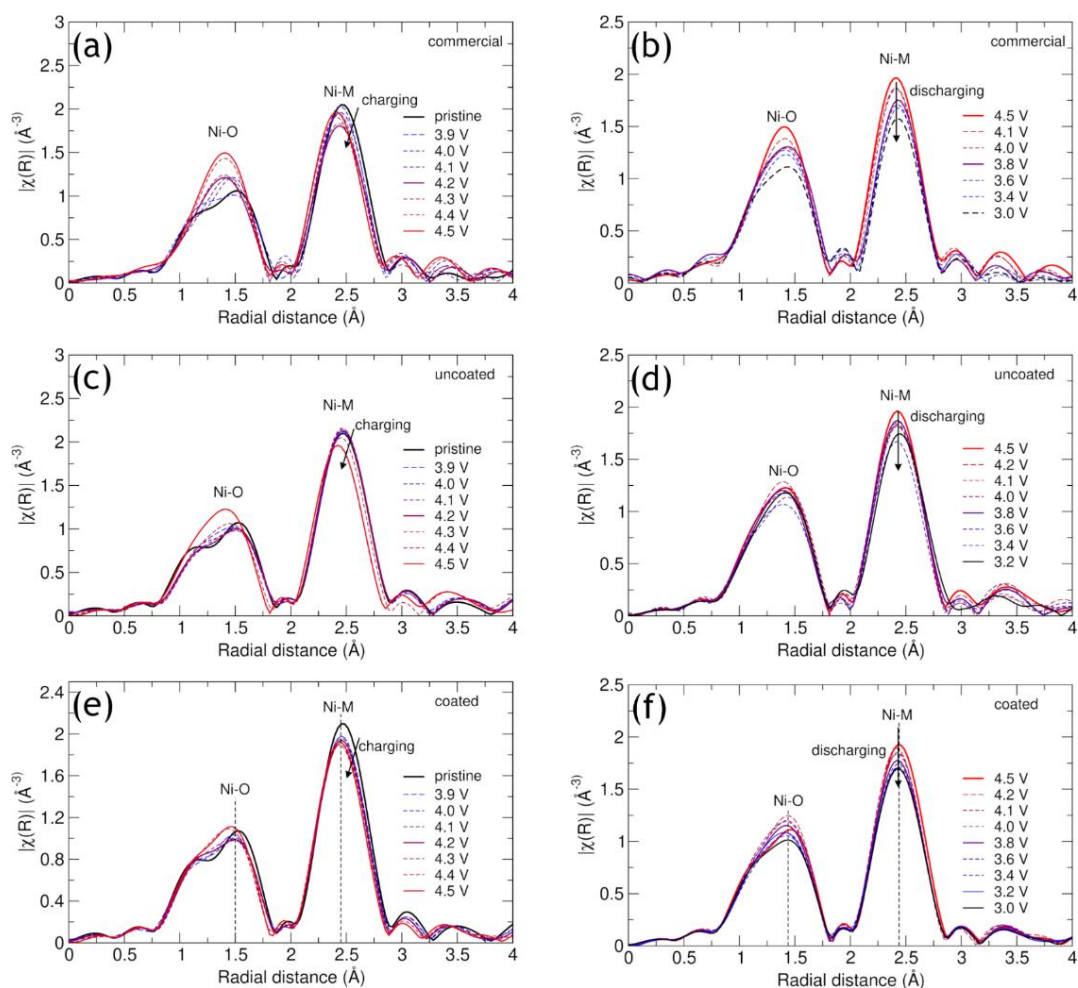


**Figure 5.14** Magnitude of the Fourier transformed EXAFS spectra for the *in-situ* XAS data collected on the Ni K-edge for (a,b) NMC-811 obtained from a commercial supplier, (c,d) uncoated and (e,f) 0.2 wt.% coated NMC-811 synthesised by a microwave-assisted sol-gel method. Left and right panels show charging and discharging data respectively.

## 5.2.3 Neutron powder diffraction and total scattering studies of Al<sub>2</sub>O<sub>3</sub> coated LiNi<sub>0.8</sub>Mn<sub>0.1</sub>Co<sub>0.1</sub>O<sub>2</sub>

### 5.2.3.1 Neutron powder diffraction of commercial, uncoated and 0.2 wt.% coated microwave-synthesised LiNi<sub>0.8</sub>Mn<sub>0.1</sub>Co<sub>0.1</sub>O<sub>2</sub>

NMC-811 powders were analysed using neutron powder diffraction (NPD) at the Polaris beamline at the ISIS Pulsed Neutron and Muon source in the UK. Using a microwave-assisted co-precipitation method, samples of pristine and 0.2 wt.% coated NMC-811 were analysed alongside NMC-811 obtained from a commercial supplier for comparison. The co-precipitation method was used here instead of the sol-gel method due to a combination of large sample sizes required for NPD (*ca.* 3 g), time restraints and the malfunction of the microwave furnace, ultimately precluding the sol-gel method due to the small batch sizes (*ca.* 100 to 200 mg batch sizes) required for good quality sample. In the co-precipitation method, solutions of transition metal sulphates were mixed together in stoichiometric amounts followed by the addition of concentrated NaOH in order to form a transition metal hydroxide precipitate. Lithium hydroxide could then be added to the powder precursor and heated in a microwave-assisted furnace for 1 hour at 850 °C to yield NMC-811. This is described in full detail in Chapter 2. It was found that the NMC-811 phase could be successfully synthesised using batch sizes of up to 1 g for this method. The coating technique was conducted in exactly the same manner as reported previously. The samples were not synthesised using an enriched <sup>7</sup>Li precursor to allow better comparison with the commercial sample (which is presumably synthesised using natural lithium precursors).

Figure 5.15 shows the laboratory PXRD data collected both the uncoated and 0.2 wt.% Al<sub>2</sub>O<sub>3</sub> coated NMC-811 prepared via this method. No impurity phases are observable in the data for both samples and the coating procedure does not have any discernible effect on the bulk structure. It is noted that the intensities obtained for the (003) reflection are lower than expected due to the nature of the sample holder used affecting the intensities at low angles, thus the ratio of the (003)/(104) peaks cannot be reliably used to obtain information on the Li/Ni mixing. The fits from the NPD data obtained for all samples at 60 K and at room temperature are shown in Figures 5.16 and 5.17 respectively. Excellent fits were obtained for all three samples at both temperatures. All neutron refinements were prepared for 18 (or 20) variables, including scale factor, absorption correction, 6 background coefficients (fitted with a Chebyshev function), lattice parameters, microstrain and size parameters and Ni, Li and O site occupancies and the O z-position. All other atomic positions, displacement parameters (set at 0.01) and site fractions were not refined. The model assumed that Li primarily resided on the 3a sites, transition

metals on the 3*b* sites and oxygen on the 6*c* sites. The site mixing between Li and Ni on the 3*a* and 3*b* sites was allowed with appropriate constraints such that the LiNi<sub>0.8</sub>Mn<sub>0.1</sub>Co<sub>0.1</sub>O<sub>2</sub> stoichiometries was retained: the occupancies of the Ni1 and Ni2 sites totalled to 0.8 and Li1 and Li2 occupancies totalled 1.0. For the data obtained at 60 K, the Mn and Co occupancies were also refined, with the constraint applied that their total occupancy must be equal to 0.2 (these refined occupancies were then kept constant for the room temperature refinements). The structural parameters calculated from the Rietveld refinements are shown in Tables 5.1, 5.2 and 5.3 for the data obtained at 60 K and in Tables 5.4, 5.5 and 5.6 for the room temperature measurements. The lattice parameters for all three samples calculated from the refinements for the data collected at a temperature of 60 K show slightly lower lattice parameters than those calculated for the room temperature data which is expected due to the effect of temperature on lattice expansion and contraction. The commercially supplied sample also shows a much lower percentage of anti-site Li/Ni mixing of approximately 1.7 % compared to 9.3 % and 9.0 % calculated for the microwave-synthesised uncoated and Al<sub>2</sub>O<sub>3</sub> coated samples respectively. These high degrees of Li/Ni mixing observed in the microwave-synthesised co-precipitation samples compare well with those obtained for the microwave-synthesised sol-gel samples presented in the previous chapter, suggesting that the short microwave-assisted step is the primary factor in promoting unfavourable Li/Ni mixing.

For the room temperature neutron diffraction data collected on all three samples, the lattice parameters increase slightly as mentioned previously. There are small differences observed in the behaviour of the anti-site mixing compared to that at 60 K for the commercial sample: the Li/Ni mixing slightly increases from 1.7 % to 3.0 % whereas the mixing in uncoated and coated microwave-synthesised samples appears to be unchanged by the change in temperature (within error).

The room temperature lattice parameters and the Li/Ni mixing obtained for both microwave-synthesised samples are also very similar, indicating that the Al<sub>2</sub>O<sub>3</sub> coating process does not significantly alter the bulk crystallographic properties of the NMC-811. This is expected because as the coating is assumed to be very lightweight and the coating procedure does not utilise temperatures higher than 400 °C which should not alter the structural properties. At room temperature the lattice parameters for the commercial sample are slightly lower than those calculated for the microwave-synthesised samples with the change in the *c* parameter greater than that observed in the *a* parameter. The increase in the *c* parameter for the microwave-synthesised samples could be due to the increased interlayer mixing for these samples. A similar increase in atomic parameters

with increased Li/Ni mixing has also been reported by Idris and West for NMC-811.<sup>231</sup> The lattice parameters obtained from room temperature NPD experiments also compare well with those obtained from laboratory PXRD Rietveld refinements shown in Figure 5.18 and Table 5.7 for the microwave synthesised samples and Figure 4.18 and Table 4.4 for the commercially obtained sample of NMC-811. These refinements were carried out as previously described for NMC-811 samples in Chapter 4.

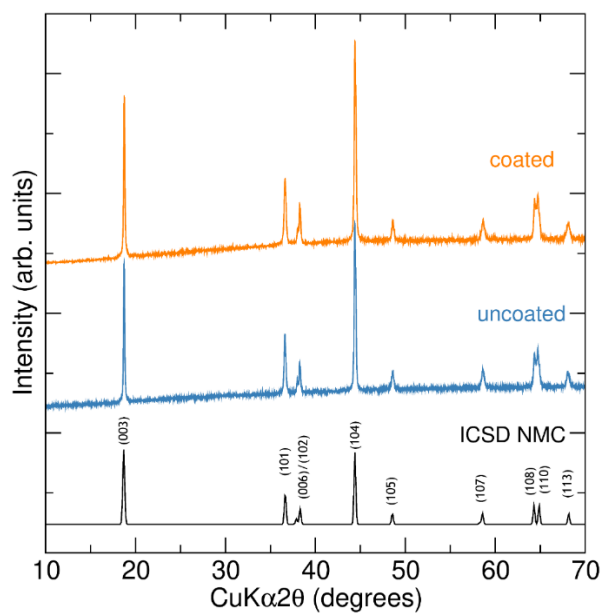


**Figure 5.15** Laboratory PXRD data collected for uncoated and 0.2 wt.%  $\text{Al}_2\text{O}_3$  coated NMC-811 synthesised by a microwave-assisted co-precipitation method at 850 °C for 1 hour. A reference pattern of NMC obtained from the ICSD is also included with the reflections labelled.

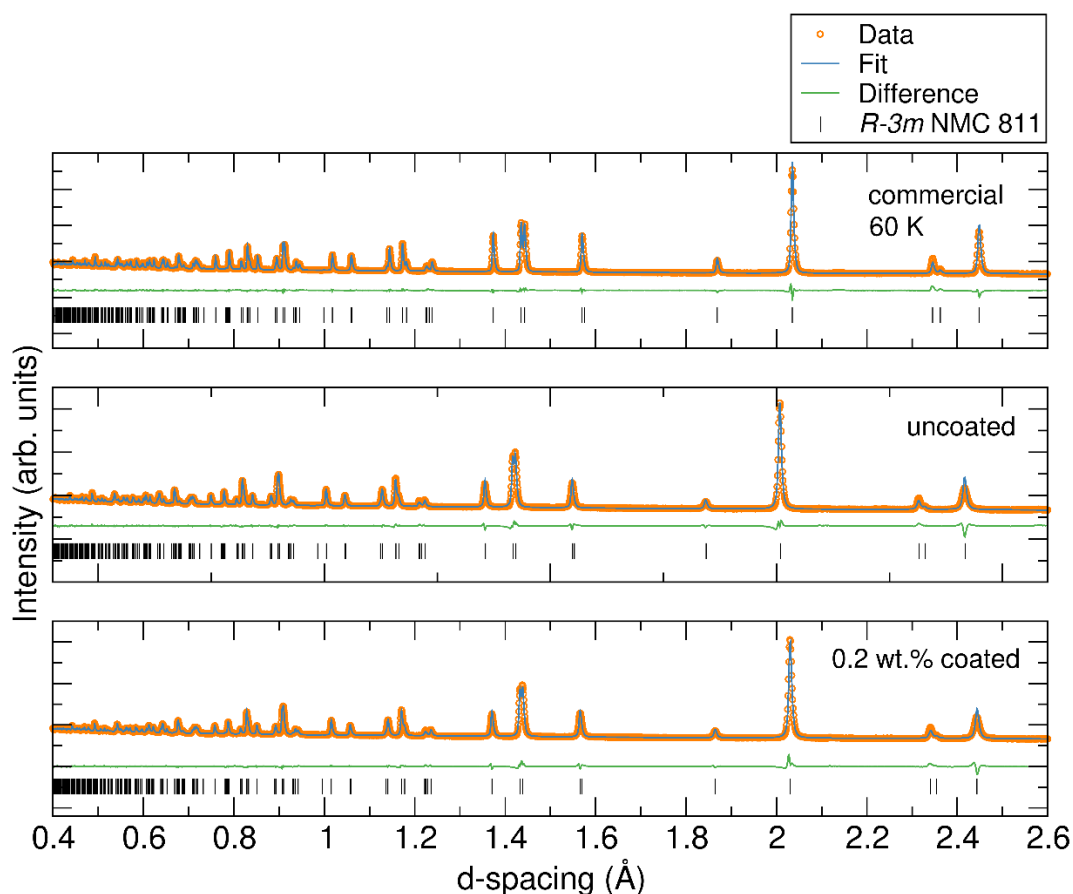


**Figure 5.16** Rietveld refinements of neutron powder diffraction data collected on Polaris at ISIS (detector bank 5) at 60 K for commercial NMC-811, uncoated microwave co-precipitation synthesised NMC-811 and 0.2 wt.%  $\text{Al}_2\text{O}_3$  coated microwave co-precipitation NMC-811.

**Table 5.1** Structural parameters of the commercial NMC-811 sample from Rietveld analysis of NPD data at 60 K.

NMC-811 comm.		$R_{wp} = 2.01 \%$		$\chi^2 = 6.27$	$d = 4.7113 \text{ g cm}^{-3}$	
60K		$a = 2.86877(4) \text{ \AA}$		$c = 14.16740(14) \text{ \AA}$	$V = 100.974(1) \text{ \AA}^3$	
$R\bar{3}m$						
Atom	Site	x	y	z	Uiso ( $\text{\AA}^2$ )	Frac.
Li1	3a	0.0000	0.0000	0.0000	0.01	0.983(1)
Li2	3b	0.0000	0.0000	0.5000	0.01	0.017(1)
Co1	3b	0.0000	0.0000	0.5000	0.01	0.119(1)
Ni1	3b	0.0000	0.0000	0.5000	0.01	0.783(1)
Ni2	3a	0.0000	0.0000	0.0000	0.01	0.017(1)
Mn1	3b	0.0000	0.0000	0.5000	0.01	0.081(1)
O1	6c	0.0000	0.0000	0.24140(4)	0.01	0.942(4)

**Table 5.2** Structural parameters of the uncoated microwave-synthesised NMC-811 sample from Rietveld analysis of NPD data at 60 K.

<b>NMC-811 uncoated 60K</b>		$R_{wp} = 2.11 \%$		$\chi^2 = 8.40$		$d = 4.7935 \text{ g cm}^{-3}$	
$R\bar{3}m$		$a = 2.83108(6) \text{ \AA}$		$c = 13.9587(2) \text{ \AA}$		$V = 96.891(2) \text{ \AA}^3$	
Atom	Site	x	y	z	Uiso ( $\text{\AA}^2$ )	Frac.	
Li1	3a	0.0000	0.0000	0.0000	0.01	0.907(3)	
Li2	3b	0.0000	0.0000	0.5000	0.01	0.093(3)	
Co1	3b	0.0000	0.0000	0.5000	0.01	0.096(1)	
Ni1	3b	0.0000	0.0000	0.5000	0.01	0.707(3)	
Ni2	3a	0.0000	0.0000	0.0000	0.01	0.093(3)	
Mn1	3b	0.0000	0.0000	0.5000	0.01	0.104(1)	
O1	6c	0.0000	0.0000	0.24171(5)	0.01	0.874(8)	

**Table 5.3** Structural parameters of the microwave-synthesised, 0.2 wt%  $\text{Al}_2\text{O}_3$  coated NMC-811 sample from Rietveld analysis of NPD data at 60 K.

<b>NMC-811 coated 60K</b>		$R_{wp} = 2.12 \%$		$\chi^2 = 8.36$		$d = 4.633 \text{ g cm}^{-3}$	
$R\bar{3}m$		$a = 2.86339(6) \text{ \AA}$		$c = 14.1178(23) \text{ \AA}$		$V = 100.244(2) \text{ \AA}^3$	
Atom	Site	x	y	z	Uiso ( $\text{\AA}^2$ )	Frac.	
Li1	3a	0.0000	0.0000	0.0000	0.01	0.910(3)	
Li2	3b	0.0000	0.0000	0.5000	0.01	0.090(3)	
Co1	3b	0.0000	0.0000	0.5000	0.01	0.096(1)	
Ni1	3b	0.0000	0.0000	0.5000	0.01	0.710(3)	
Ni2	3a	0.0000	0.0000	0.0000	0.01	0.090(3)	
Mn1	3b	0.0000	0.0000	0.5000	0.01	0.104(1)	
O1	6c	0.0000	0.0000	0.24187(5)	0.01	0.874(8)	

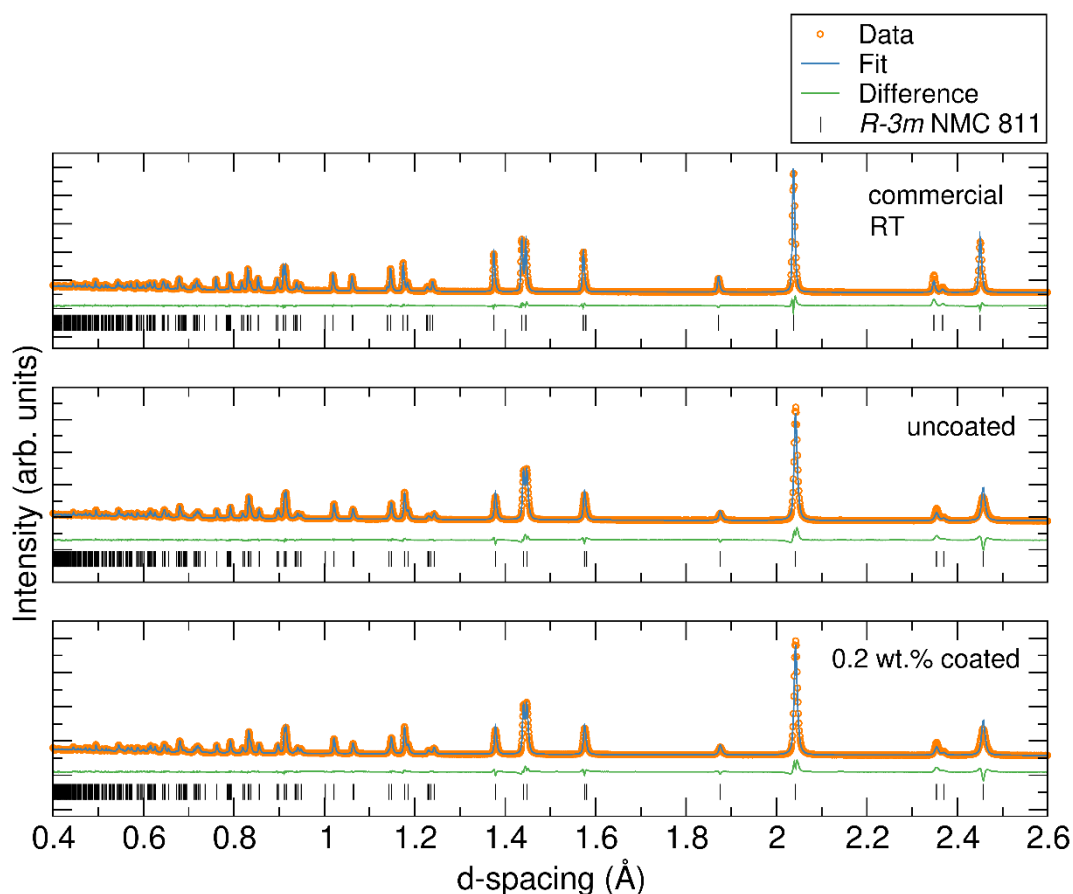


**Figure 5.17** Rietveld refinements of neutron powder diffraction data collected on Polaris at ISIS (detector bank 5) at room temperature for commercial NMC-811, uncoated microwave co-precipitation synthesised NMC-811 and 0.2 wt.%  $\text{Al}_2\text{O}_3$  coated microwave co-precipitation NMC-811.

**Table 5.4** Structural parameters of the commercial NMC-811 sample from Rietveld analysis of NPD data at room temperature.

NMC-811 comm. RT		$R_{wp} = 3.09\%$	$\chi^2 = 8.47$	$d = 4.642 \text{ g cm}^{-3}$		
$R\bar{3}m$		$a = 2.87145(4) \text{ \AA}$	$c = 14.19782(13) \text{ \AA}$	$V = 101.381(1) \text{ \AA}^3$		
Atom	Site	x	y	z	Uiso ( $\text{\AA}^2$ )	Frac.
Li1	3a	0.0000	0.0000	0.0000	0.01	0.970(3)
Li2	3b	0.0000	0.0000	0.5000	0.01	0.030(3)
Co1	3b	0.0000	0.0000	0.5000	0.01	0.119
Ni1	3b	0.0000	0.0000	0.5000	0.01	0.770(3)
Ni2	3a	0.0000	0.0000	0.0000	0.01	0.030(3)
Mn1	3b	0.0000	0.0000	0.5000	0.01	0.081
O1	6c	0.0000	0.0000	0.24127(3)	0.01	0.910(7)

**Table 5.5** Structural parameters of the uncoated microwave-synthesised NMC-811 sample from Rietveld analysis of NPD data at room temperature.

<b>NMC-811 uncoated RT</b>		$R_{wp} = 3.29 \%$	$\chi^2 = 8.93$	$d = 4.513 \text{ g cm}^{-3}$		
$R\bar{3}m$		$a = 2.87904(6) \text{ \AA}$	$c = 14.2121(2) \text{ \AA}$	$V = 102.019(2) \text{ \AA}^3$		
Atom	Site	x	y	z	Uiso ( $\text{\AA}^2$ )	Frac.
Li1	3a	0.0000	0.0000	0.0000	0.01	0.904(3)
Li2	3b	0.0000	0.0000	0.5000	0.01	0.096(3)
Co1	3b	0.0000	0.0000	0.5000	0.01	0.096
Ni1	3b	0.0000	0.0000	0.5000	0.01	0.704(3)
Ni2	3a	0.0000	0.0000	0.0000	0.01	0.096(3)
Mn1	3b	0.0000	0.0000	0.5000	0.01	0.104
O1	6c	0.0000	0.0000	0.24174(4)	0.01	0.849(7)

**Table 5.6** Structural parameters of the microwave-synthesised, 0.2 wt%  $\text{Al}_2\text{O}_3$  coated NMC-811 sample from Rietveld analysis of NPD data at room temperature.

<b>NMC-811 coated RT</b>		$R_{wp} = 3.38 \%$	$\chi^2 = 8.85$	$d = 4.522 \text{ mg cm}^{-3}$		
$R\bar{3}m$		$a = 2.87913(6) \text{ \AA}$	$c = 14.21295(22) \text{ \AA}$	$V = 102.032(2) \text{ \AA}^3$		
Atom	Site	x	y	z	Uiso ( $\text{\AA}^2$ )	Frac.
Li1	3a	0.0000	0.0000	0.0000	0.01	0.909(3)
Li2	3b	0.0000	0.0000	0.5000	0.01	0.091(3)
Co1	3b	0.0000	0.0000	0.5000	0.01	0.096
Ni1	3b	0.0000	0.0000	0.5000	0.01	0.709(3)
Ni2	3a	0.0000	0.0000	0.0000	0.01	0.091(3)
Mn1	3b	0.0000	0.0000	0.5000	0.01	0.104
O1	6c	0.0000	0.0000	0.24186(4)	0.01	0.854(7)

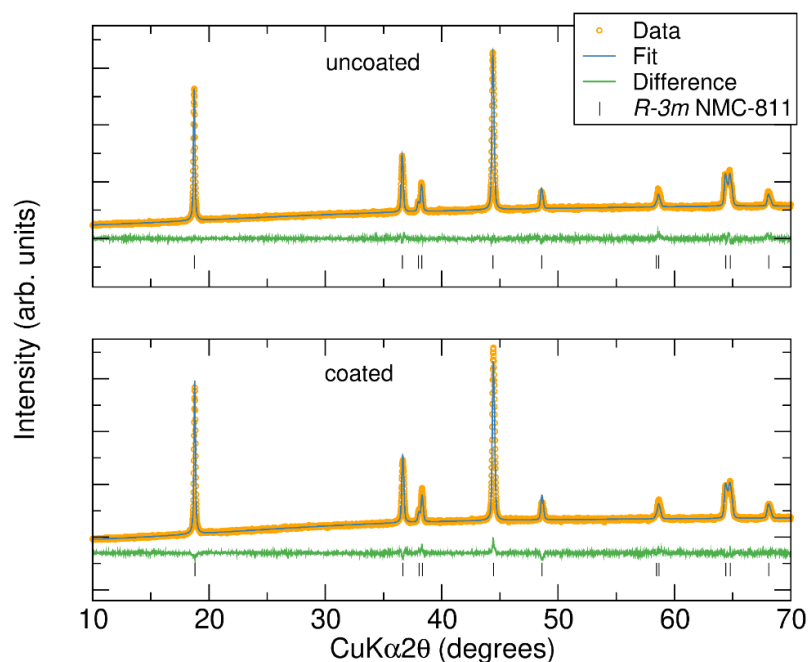


**Figure 5.18** Rietveld refinements of laboratory PXRD data collected at room temperature for, uncoated microwave co-precipitation synthesised NMC-811 and 0.2 wt.% Al<sub>2</sub>O<sub>3</sub> coated microwave co-precipitation NMC-811.

**Table 5.7** Lattice parameters obtained from the Rietveld refinements of PXRD data at room temperature.

Sample	Uncoated	Coated
a (Å)	2.87636(4)	2.86929(10)
c (Å)	14.20556(37)	14.16806(39)
V (Å <sup>3</sup> )	101.783(4)	101.016(6)
Ni1 occupancy	0.695(1)	0.722(1)
Ni2 occupancy	0.105(1)	0.078(1)
$R_{wp}$	2.879 %	2.783 %
$\chi^2$	0.91	0.95

### 5.2.3.2 Neutron Pair Distribution Function (PDF) of uncoated and 0.2 wt.% Al<sub>2</sub>O<sub>3</sub> coated LiNi<sub>0.8</sub>Mn<sub>0.1</sub>Co<sub>0.1</sub>O<sub>2</sub>

The diffraction results presented in the previous section provide an insight into the long-range average crystallographic structure. However, this average structure may not be fully representative of the whole material where deviations from periodicity may be important *e.g.* local scale distortions. The local atomic structure can be probed using total scattering methods coupled with pair distribution function (PDF) analysis which gives information on atom-atom distances. This technique has been described in detail in Chapter 2.

Here, time of flight powder neutron diffraction at 60 K and room temperature was used to calculate PDFs of the commercial NMC-811 and the uncoated and 0.2 wt.% Al<sub>2</sub>O<sub>3</sub> coated microwave-synthesised NMC-811. The time of flight NPD data collected are the same as those presented in the previous chapter but treated appropriately to calculate the PDFs. The data from all 5 detector banks on Polaris was processed using the Gudrun program<sup>170</sup> in order to obtain the Fourier transform of the total scattering function  $S(Q)$  using  $Q_{\text{max}} = 52 \text{ \AA}^{-1}$  to yield the radial distribution function  $G(r)$ . This has been described more fully in Chapter 2.

The raw neutron PDF data generated for all three samples at 60 K and room temperature in the range from 1 Å - 100 Å are shown in Figures 5.19 and 5.20 respectively. There are two important peaks that appear in the raw data - the peak at approximately 1.9 Å which corresponds to the metal-oxygen distances and a peak at approximately 2.9 Å ascribed to the metal-metal distances. This is comparable to the radial functions obtained from EXAFS measurements presented earlier in this chapter considering the phase corrections required for the EXAFS data which would increase the peak positions by  $\approx 0.4 \text{ \AA}$ . The intensity of the metal-O peak is positive in this case because the contributions from the positive scatterers (Ni and Co) are larger than those with negative scattering length (Li and Mn). The PDFs of isostructural materials with higher manganese contents *e.g.* NMC-111 and LiNi<sub>0.5</sub>Mn<sub>0.5</sub>O<sub>2</sub> have been reported in the literature where the intensity of this peak lower relative to the average intensity of the PDF in NMC-111 and a negative peak is observed at slightly lower  $r$  values corresponding to Mn-O bonds in LiNi<sub>0.5</sub>Mn<sub>0.5</sub>O<sub>2</sub>.<sup>47,281</sup>

As the raw data tends to higher  $r$  values, a dampening effect is observed which indicates a decrease in the long-range order typically associated with crystalline materials. This dampening can give some qualitative information on expected ranges of particle size *e.g.* a larger dampening effect can suggest the presence of particles within the nano range.

There is no discernible difference in the degree of damping across all of the studied samples, indicating that each sample possesses similar ranges of long-range crystallinity. The peaks at  $r$  values greater than 3 Å are a superposition of numerous environments and are thus difficult to assign.

Figure 5.21 shows the comparisons between the 60 K and the room temperature PDFs calculated for all three samples. It is observed across all samples that the PDFs at 60 K display more features than the room temperature data which is most noticeable in the peaks corresponding to O-O and M-M distances. This suggests that more environments exist for atoms at a temperature of 60 K compared to room temperature. Higher temperatures result in increased thermal motion of atoms which serves to broaden out these different environments. It should be noted that peaks below 1.9 Å are termination ripples that originate during the data processing step due to the Fourier transform being applied at a finite  $Q$  and they do not correspond to any real structural correlations.

In order to better compare the three samples, Figure 5.22 shows the superimposed data for the sample at (a) 60 K and (b) room temperature, where similar behaviour is observed across all samples with the microwave-synthesised samples showing more similar behaviour compared to the commercial sample. At 60 K, the peak at approximately 1.9 Å is split for all samples which could indicate distortions in the  $MO_6$  octahedra resulting in different M-O distances. This effect could arise from the presence of Jahn-Teller  $Ni^{3+}$  cations in the structure which causes elongation of the axial Ni-O bonds and thus a resulting distorted  $MO_6$  octahedron. This effect is also still observed in the room temperature data although to a lesser degree. The feature centred at  $\approx 2.9$  Å is shown to comprise of at least three peaks which describe the O-O, Li-metal and metal-metal distances with similar behaviour in the profile shapes observed across all three samples at this temperature suggesting a host of different atom-atom distances. At room temperature these features appear to significantly coalesce to yield a feature that is centred around a prominent peak with small shoulders observable on either side. As for the 60 K data there are no significant deviations across the three samples with the microwave-synthesised samples exhibiting more similar behaviour compared to the commercial sample.

It is very unlikely that the presence of the  $Al_2O_3$  coating is observed in the PDF data here owing to the fact that the particle sizes of the NMC-811 ( $> 100$  nm) are much larger than the length scale probed by the neutron total scattering data ( $< 100$  Å).

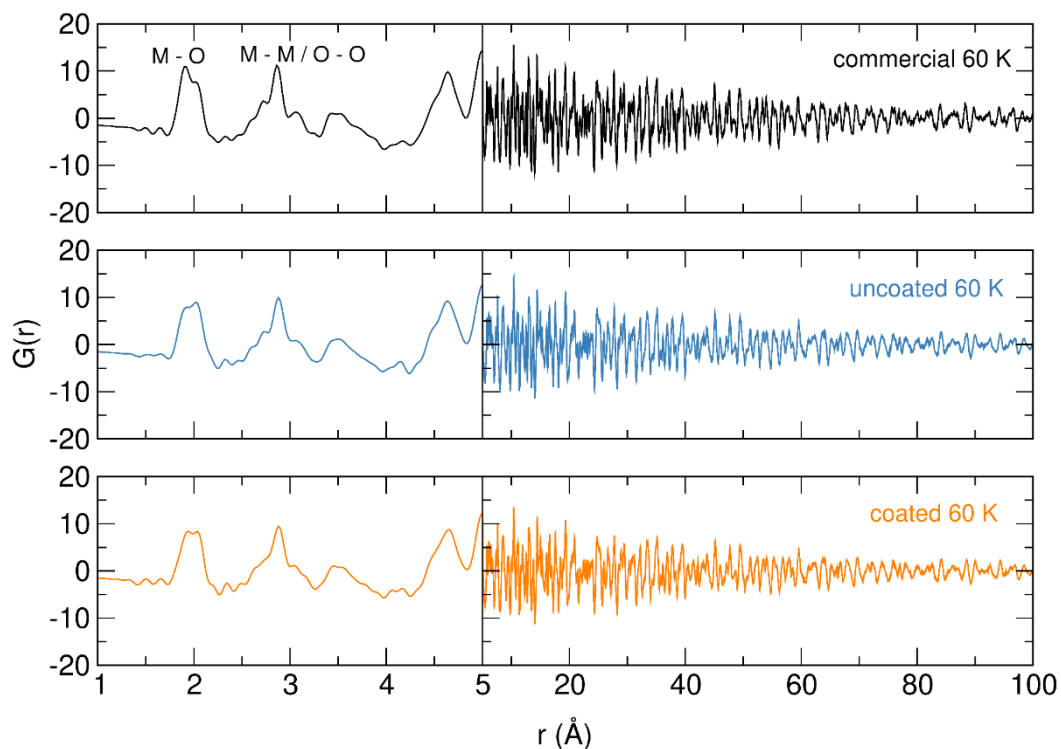


**Figure 5.19** Raw neutron PDF data obtained at 60 K for commercial NMC-811, microwave synthesised uncoated NMC-811 and 0.2 wt.% coated NMC-811 in the range from 1 Å - 100 Å. The scattering data was terminated at  $Q_{\max} = 52 \text{ \AA}^{-1}$ .

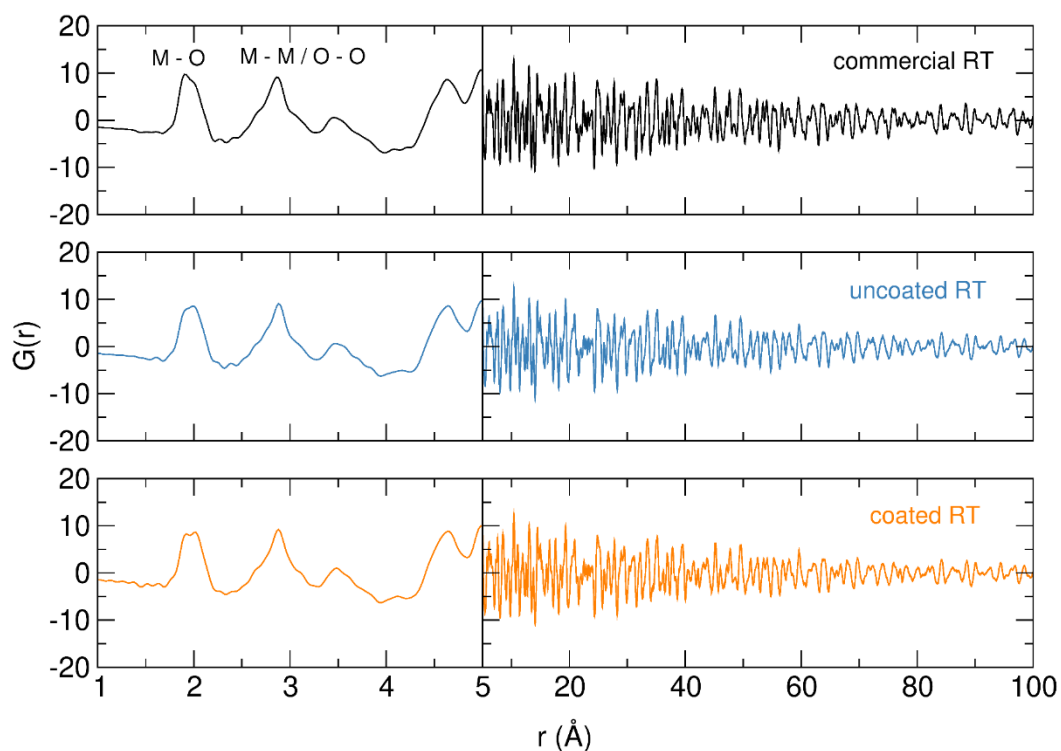


**Figure 5.20** Raw neutron PDF data obtained at room temperature for commercial NMC-811, microwave synthesised uncoated NMC-811 and 0.2 wt.% coated NMC-811 in the range from 1 Å - 100 Å. The scattering data was terminated at  $Q_{\max} = 52 \text{ \AA}^{-1}$ .

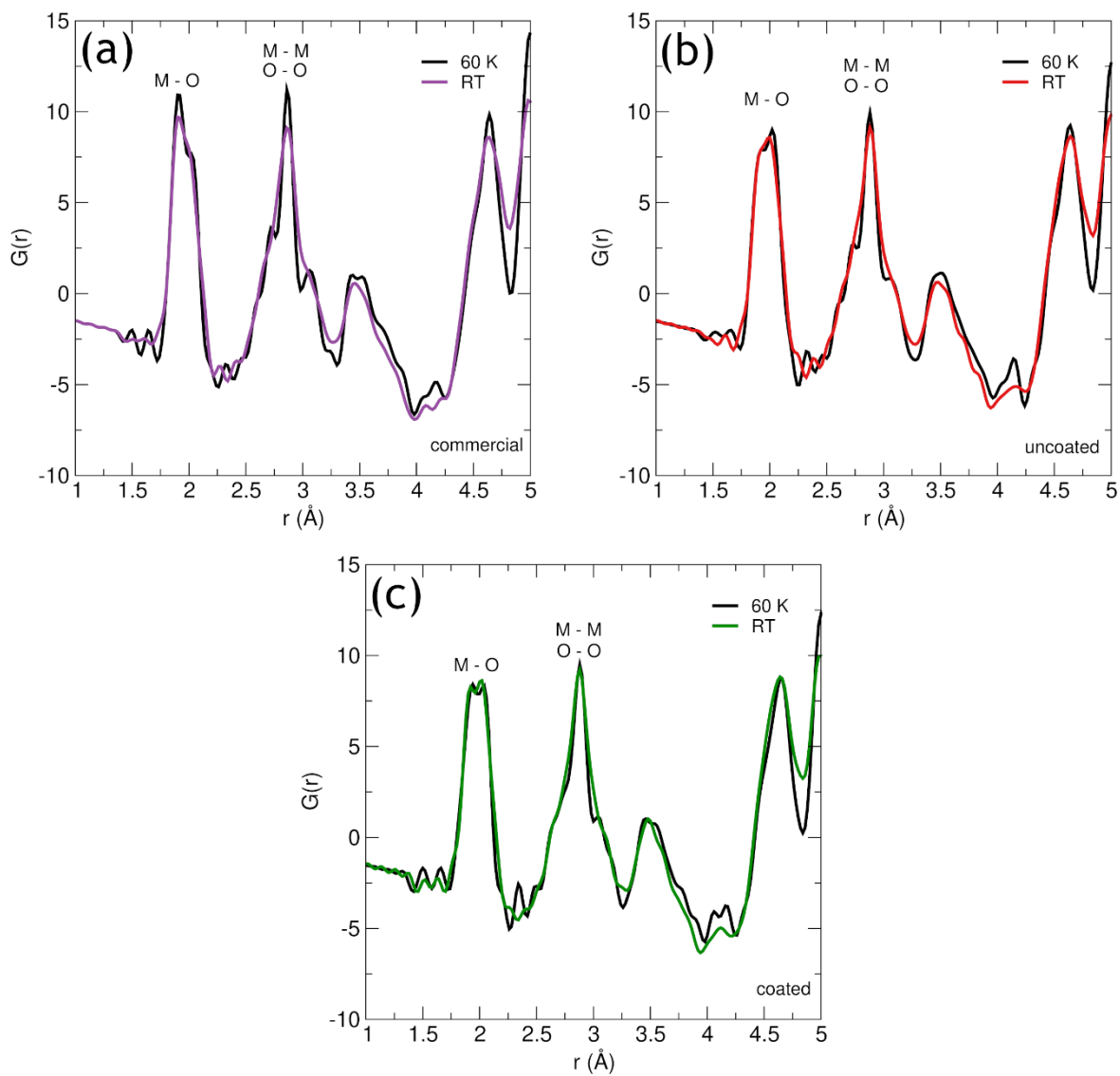


**Figure 5.21** Superimposed raw neutron PDF data 1 Å - 5 Å for (a) commercial, (b) uncoated and (c) coated samples of NMC-811 obtained at 60 K and room temperature.

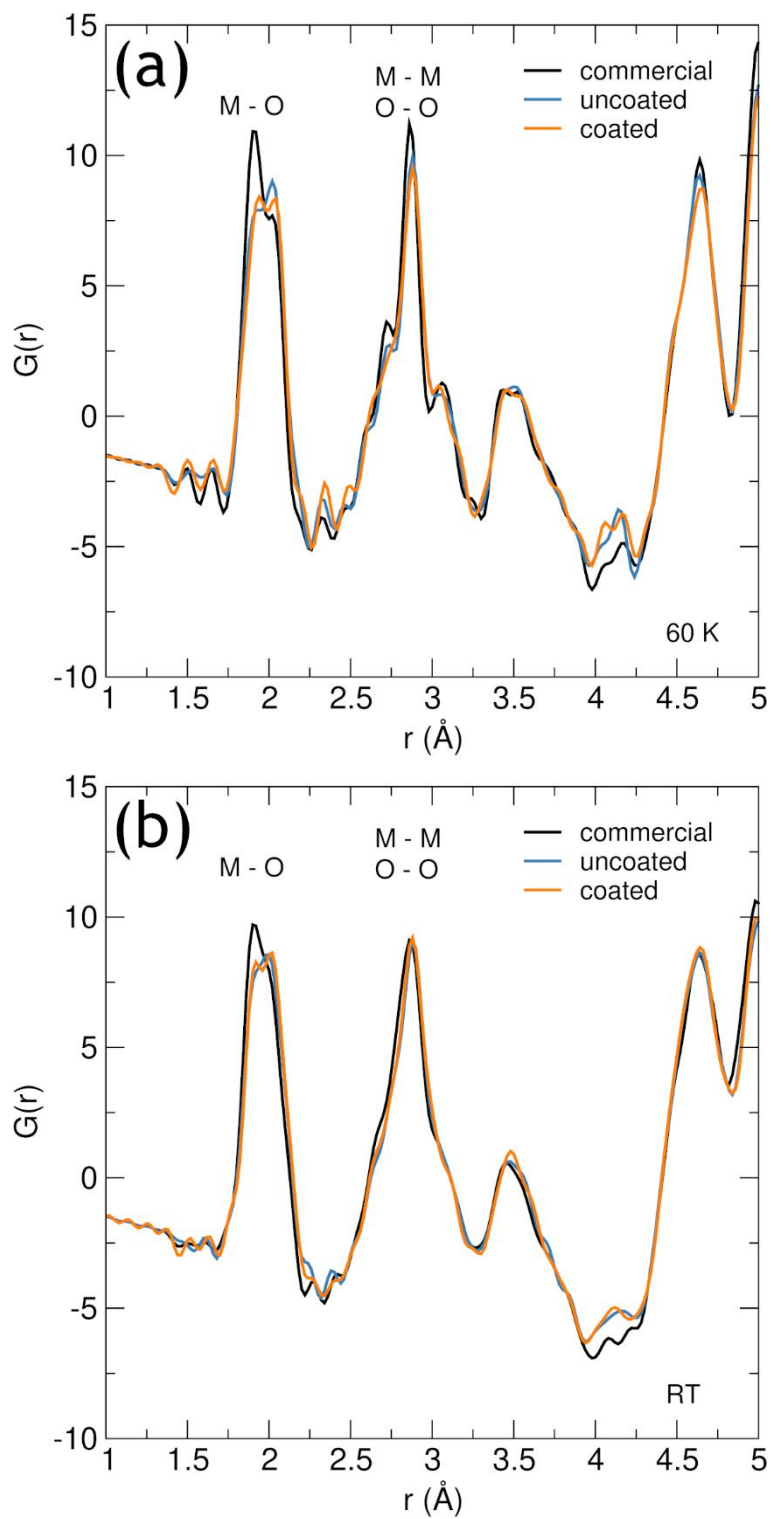


**Figure 5.22** Superimposed raw neutron PDF data between 1 Å - 5 Å for commercial, uncoated and coated samples of NMC-811 obtained at (a) 60 K and (b) room temperature.

The neutron PDF data collected for the commercial NMC-811 and the microwave-synthesised uncoated and 0.2 wt.% Al<sub>2</sub>O<sub>3</sub> coated NMC-811 were modelled by a least-squares refinement process to an average crystallographic structure using the PDFgui program.<sup>171</sup> The model used for the refinement of each sample at each temperature was taken from the results obtained from the NPD Rietveld refinements for that specific sample and temperature. Each of the models were based on the layered  $R\bar{3}m$   $\alpha$ -NaFeO<sub>2</sub> structure with the Li/Ni mixing calculated from refinements of the NPD data taken into consideration. The model also assumes a homogenous distribution of metals in each layer. The data for each sample were fit in the  $r$ -range between 1 Å - 30 Å.

The refinement data for the three NMC-811 PDFs at 60 K are shown in Figure 5.23. At larger values of  $r$ , a good fit to the data is achieved suggesting that the average crystallographic model is a good match for the experimental PDFs. Upon observation of the 1 Å to 5 Å region it is observed that the model does not adequately describe the data for all three samples with the model unable to describe the split nature of the  $M$ -O peak observed most likely caused from local MO<sub>6</sub> octahedra distortions. A poor fit to the feature describing the O-O and  $M$ - $M$  distances is also observed indicating that the model is unable to account for local-scale disorder in the atomic environments. The calculated lattice parameters and the  $R_w$  values obtained for the fits at 60 K are shown in Table 5.8. The  $R_w$  value obtained for the commercial NMC-811 is lower than that of those obtained for the microwave-synthesised samples suggesting that the microwave-synthesised samples might possess a greater degree of local disorder that is more difficult to model using the average crystallographic structure.

The lattice parameters calculated for the uncoated and coated samples are very similar and are larger than those calculated for the commercial sample. This is opposite to what was observed in lattice parameters calculated from NPD refinements at 60 K but matches the trend observed in the room temperature parameters. The fit to the room temperature PDF data between 1 Å and 30 Å is shown in Figure 5.24 with the calculated lattice parameters and  $R_w$  values presented in Table 5.9. Better fits are obtained for the microwave-synthesised samples evidenced by the lower  $R_w$  values between 0.12 - 0.14 obtained. However, the model calculated for the commercial sample shows a slightly higher  $R_w$  value of 0.17 compared to 0.14 obtained while fitting the 60 K data. From visual inspection of the refinement profiles, it appears that improved fits have been achieved at room temperature, especially in the  $r$ -range greater than 5 Å, most likely owing to the coalescing of distinct atomic environments due to increased thermal displacements at higher temperatures which serves to remove the peaks that were not well-modelled in

the 60 K data. However, the 1 Å - 5 Å region still shows some areas where the model does not adequately fit the data and thus describe the local-structure.

Nevertheless, the PDF data here can tell us about the similarity in local structure apparent for both the uncoated and the coated microwave-synthesised NMC-811 samples indicating that the coating and the coating process does not alter the structure significantly. Slight differences are observed between the commercial sample and the microwave-synthesised samples which does suggest that the synthesis method can alter the local structure. Similar fitting problems have been reported for NMC-111 and  $\text{LiNi}_{0.5}\text{Mn}_{0.5}\text{O}_2$  where using a model based on the average crystallographic structure assuming a random distribution of metals within their respective layers, yielded poor fits to the PDF data.<sup>47,281</sup> To obtain improved fits, Reverse Monte Carlo (RMC) modelling was employed to explore possible ordering of cations and local distortions arising from different M-O distances. For both materials, a model involving a non-random distribution of Ni and Mn cations in the transition metal layers were found to fit the data excellently. These results suggest that RMC modelling is essential in building a model that successfully describes the local structure of such layered oxides and work on this for the samples presented here is forthcoming.

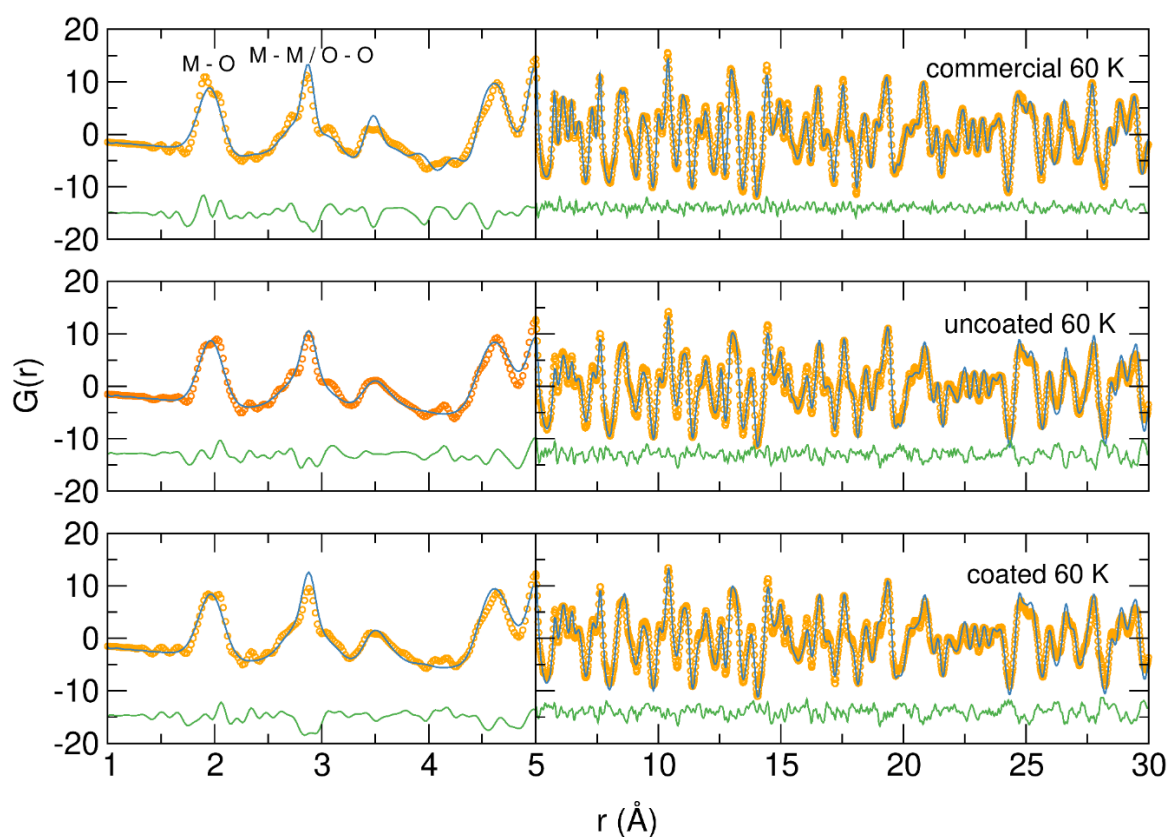


**Figure 5.23** Fits of the neutron PDF data for commercial NMC-811 and uncoated and 0.2 wt.%  $\text{Al}_2\text{O}_3$  coated microwave-synthesised NMC-811 between 1 Å - 30 Å at 60 K.

**Table 5.8** Lattice parameters and  $R_w$  values obtained from neutron PDF fits of commercial, uncoated and coated NMC-811 between 1 Å - 30 Å at 60 K.

60 K

Sample	Commercial NMC-811	Uncoated NMC-811	Coated NMC-811
a	2.87635	2.88209(18)	2.88268(24)
c	14.2012	14.241(2)	14.241(2)
$R_w$	0.143659	0.21333	0.237533

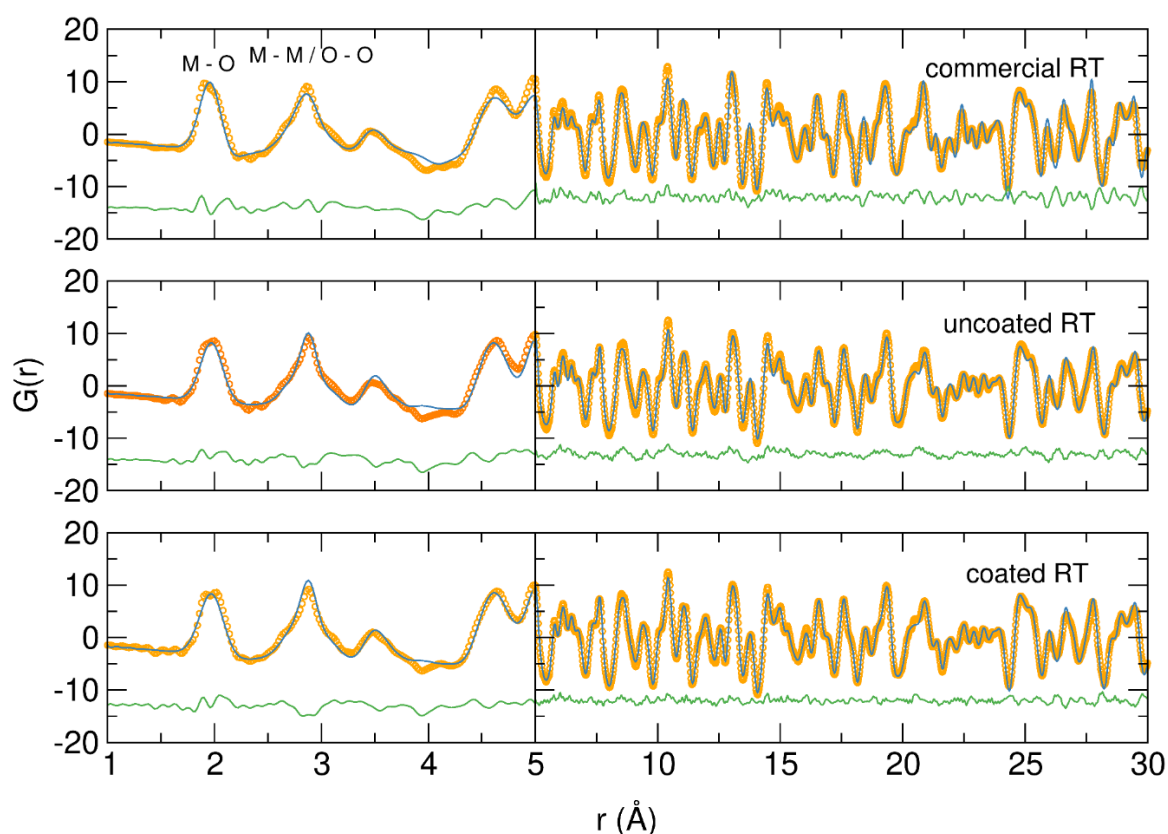


**Figure 5.24** Fits of the neutron PDF data for commercial NMC-811 and uncoated and 0.2 wt.%  $Al_2O_3$  coated microwave-synthesised NMC-811 between 1 Å - 30 Å at room temperature.

**Table 5.9** Lattice parameters and  $R_w$  values obtained from neutron PDF fits of commercial, uncoated and coated NMC-811 between 1 Å - 30 Å at room temperature.

Room temperature

Sample	Commercial NMC-811	Uncoated NMC-811	Coated NMC-811
$a$ (Å)	2.87601(22)	2.88382 (29)	2.88377(29)
$c$ (Å)	14.239(2)	14.257 (3)	14.260(3)
$R_w$	0.165	0.143625	0.117343

## 5.2.4 Local-scale diffusional studies on Al<sup>3+</sup> and Mg<sup>2+</sup> doped LiNi<sub>0.8</sub>Mn<sub>0.1</sub>Co<sub>0.1</sub>O<sub>2</sub>

### 5.2.4.1 Synthesis and structural characterisation of Al<sup>3+</sup> and Mg<sup>2+</sup> doped LiNi<sub>0.8</sub>Mn<sub>0.1</sub>Co<sub>0.1</sub>O<sub>2</sub>

The process of incorporating electrochemically-inactive dopant cations into the layered NMC type structures e.g. NMC-111, NMC-622 and NMC-811, NCA and LiNiO<sub>2</sub> has also been shown to improve cycling performances. Two well studied dopants are the Al<sup>3+</sup> and Mg<sup>2+</sup> cations mentioned previously in this chapter which are suspected to impart increased structural stabilities. Here, Al-doped and Mg-doped NMC-811 was synthesised using the same microwave-assisted sol-gel procedure used throughout this thesis, using Al(NO<sub>3</sub>)<sub>3</sub>·9H<sub>2</sub>O and Mg(CH<sub>3</sub>COO)<sub>2</sub>·4H<sub>2</sub>O as the dopant precursors respectively. Stoichiometric quantities of these were added to the metal acetate sol at the beginning of the reaction. The rest of the reaction was carried out as previously described with an extended reaction time of 3 hours at 850 °C was found to reproducibly form NMC-811 with no visible impurity phases in the PXRD data. The synthesised materials were targeted to have compositions LiNi<sub>1-x</sub>Al<sub>x</sub>Mn<sub>0.1</sub>Co<sub>0.1</sub>O<sub>2</sub> for x = 0.1, 0.2 for the Al-doped materials and Li<sub>1-2x</sub>Mg<sub>x</sub>Ni<sub>0.8</sub>Mn<sub>0.1</sub>Co<sub>0.1</sub>O<sub>2</sub> with x = 0.1 for the Mg-doped compound thus with Al<sup>3+</sup> cations residing within the transition metal layer and Mg<sup>2+</sup> cations sitting in the lithium layer. For dopant levels of < 2 %, Mg<sup>2+</sup> is predicted to enter the lithium layer due to the similar sizes of the Li<sup>+</sup> (0.76 Å) and Mg<sup>2+</sup> (0.72 Å) cations. Al<sup>3+</sup> cations are calculated to favour occupation in the Ni sites.<sup>270,282</sup>

The Rietveld refinements carried out on the PXRD data for the doped samples is shown in Figure 5.25. A structure based on the layered  $R\bar{3}m$  NMC type structure was used with added dopant atoms accordingly. The refinements were prepared in exactly the same manner as those reported for NMC-811 in chapter 4, as dopant atom positions and occupancies were not refined. Excellent fits to the data were achieved from a visual inspection of the refinement profiles. Table 5.10 lists the calculated lattice parameters and  $\chi^2$  values obtained from the fits and those calculated for pristine NMC-811 from the previous chapter. Both the *a* and *c* lattice parameters are observed to decrease with increasing Al<sup>3+</sup> content and increase with the addition of Mg<sup>2+</sup> into the lattice. Contraction of the *a* parameter with Al-doping is consistent with that reported in the literature however the *c* parameter contraction does not match with the very small increases reported.<sup>75,269</sup>

The refinement data here also show that the Li/Ni mixing is reduced from 7.32 % in the pristine sample to 5.38 % and 5.21 % for the 1 % and 2 % Al-doped samples respectively. This decrease in the anti-site mixing could bring about a reduction in the *c* parameter as

has been reported from the NPD data refinements presented previously in this chapter commercial NMC-811 (low mixing, smaller  $c$  parameter) and microwave synthesised NMC-811 (higher Li/Ni mixing, larger  $c$  parameter). The expansion of the lattice parameters calculated for the  $\text{Mg}^{2+}$  doped sample is consistent with the trend reported by Xie *et al.* for Mg-doped  $\text{LiNi}_{0.94}\text{Co}_{0.06}\text{O}_2$ .<sup>270</sup>

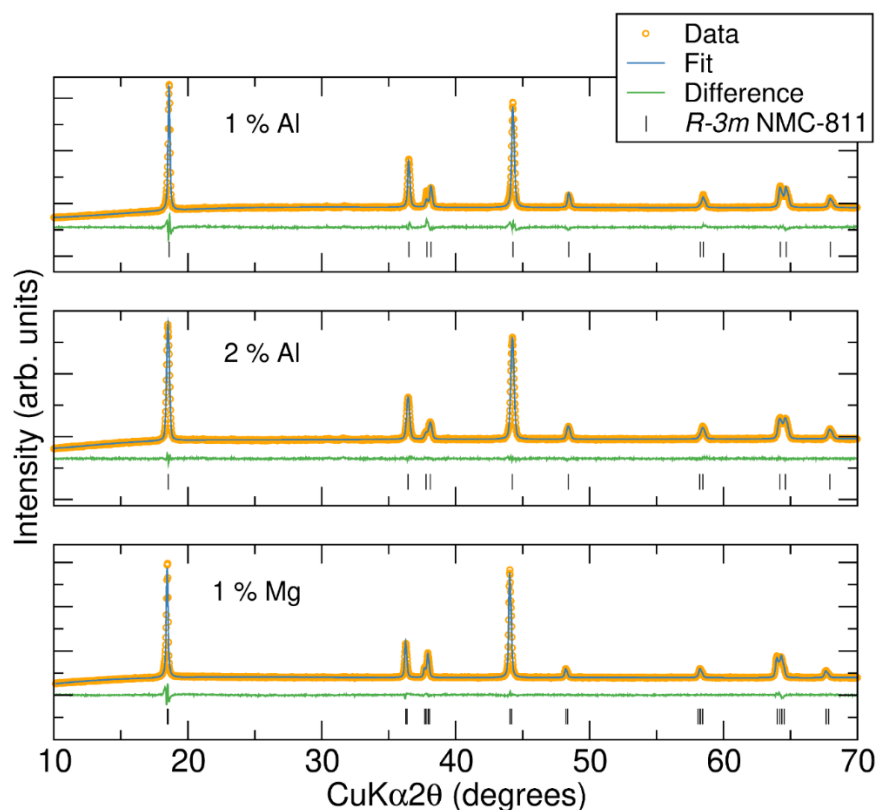


**Figure 5.25** Rietveld refinements of laboratory PXRD data collected at room temperature for NMC-811 synthesised by a microwave-assisted sol-gel method with 1 %, 2 %  $\text{Al}^{3+}$ -doping on the Ni site and 1 %  $\text{Mg}^{2+}$ -doping on the Li site.

**Table 5.10** Lattice parameters and  $\chi^2$  values calculated from the Rietveld refinements on 1 % and 2 %  $\text{Al}^{3+}$ -doped NMC-811 and 1 %  $\text{Mg}^{2+}$ -doped NMC-811.

Sample	Pristine	1 % $\text{Al}^{3+}$	2 % $\text{Al}^{3+}$	1 % $\text{Mg}^{2+}$
$a$ (Å)	2.87784(44)	2.87474(22)	2.86706(14)	2.88007(8)
$c$ (Å)	14.22373(57)	14.21257(79)	14.17239(50)	14.21195(31)
$V$ (Å <sup>3</sup> )	102.018(22)	101.718(14)	100.890(9)	102.130(3)
Ni1 occupancy	0.7268(10)	0.736(1)	0.728(1)	0.738(1)
Ni2 occupancy	0.0732(10)	0.054(1)	0.052(1)	0.048(1)
$R_{wp}$	2.65 %	3.32 %	1.80 %	3.46 %
$\chi^2$	1.57	2.08	1.11	2.27

#### 5.2.4.2 Muon spin spectroscopy of microwave synthesised $\text{LiNi}_{0.79}\text{Al}_{0.01}\text{Mn}_{0.1}\text{Co}_{0.1}\text{O}_2$ and $\text{Li}_{0.98}\text{Mg}_{0.01}\text{Ni}_{0.8}\text{Mn}_{0.1}\text{Co}_{0.1}\text{O}_2$

The muon-spin relaxation ( $\mu^+$ -SR) technique has been presented in Chapter 3 and Chapter 4 in order to study the local ionic diffusion in polyanionic materials and pristine NMC-811 and NMC-622. In this section, the  $\mu^+$ -SR technique has been used in order to investigate whether any changes in the microscopic Li-diffusion of NMC-811 are introduced as a result of  $\text{Al}^{3+}$  and  $\text{Mg}^{2+}$  doping within the layered structure.

Zero-field and longitudinal field measurements at different temperatures were carried out as described previously in this thesis where a *ca.* 1 g sample of doped NMC-811 powder in a titanium holder was subject to muon implantation from a beam of spin polarised muons on the EMU instrument at ISIS. As explained in Chapter 4, the implanted muons reside in interstitial sites close to  $\text{O}^{2-}$  anions with a typical bond length of  $d_{\mu-\text{O}} \approx 1.12 \text{ \AA}$ .<sup>237</sup>

The raw data obtained at 300 K and 400 K, which describes the time evolution of the positron decay asymmetry for each sample is shown in Figure 5.26 for 1 % Al-doped NMC-811 and Figure 5.27 for 1 % Mg-doped NMC-811. Solid lines in the raw data plots show the fits obtained by applying an exponentially relaxing dynamic Kubo-Toyabe function simultaneously to the raw data collected at each applied field. Each material undergoes very similar behaviour in the decay positron asymmetry, characterised by an initial fast relaxation up to  $\approx 2 \mu\text{s}$  for all of the samples attributed to the interactions between the muon spin and the paramagnetic moments originating from unpaired  $3d$  electrons on the  $\text{Ni}^{2+}$ ,  $\text{Ni}^{3+}$  and  $\text{Mn}^{4+}$  transition metal cations. This relaxation is independent of the field applied. A slower, field dependent relaxation is then observed for each sample which can be attributed to the interactions between the muon spin and the surrounding nuclear magnetic fields from  ${}^6\text{Li}$ ,  ${}^7\text{Li}$ ,  ${}^{55}\text{Mn}$ ,  ${}^{59}\text{Co}$ ,  ${}^{61}\text{Ni}$ ,  ${}^{27}\text{Al}$  (100 % abundance) and  ${}^{25}\text{Mg}$  (10 % abundance).

At 300 K, the ZF-spectra of both doped NMC-811 materials show evidence of a Kubo-Toyabe type relaxation with the relaxation rate increasing upon an increase in temperature to 400 K indicating the dynamic behaviour of the  $\text{Li}^+$  ions. This observation is consistent with that presented previously for pristine NMC-811 and NMC-622 in Chapter 4. Both samples show similar relaxation behaviour at both temperatures suggesting that  $\text{Li}^+$  diffusion dynamics might be very similar for both materials. At longitudinal fields of 5 G and 10 G, the relaxation rate in each sample also decreases owing to the gradual decoupling of interactions between the muon spin and the local nuclear environment. The data for each sample were fit considering Equation 5.1 using an exponentially relaxing dynamic Gaussian Kubo-Toyabe function, such that:

$$A_0 P(t) = A_{KT} G^{DGKT}(\Delta, \nu, t) \exp(-\lambda t) + A_{BG} \quad (5.1)$$

where  $A_0$  is the initial ( $t = 0$ ) asymmetry,  $P(t)$  is the muon spin depolarization function and  $A_{KT} G^{DGKT}$  is the dynamic Kubo-Toyabe function from which the field fluctuation rate,  $\nu$  and the static width of the local field distribution,  $\Delta$  can be extracted.  $A_{BG}$  is the background asymmetry and the exponential term describes the rapid paramagnetic fluctuations from the transition metal ions.

From the fittings, the temperature dependence of the field fluctuation rates and the static width of the local field distribution for each sample could be extracted and are shown in Figure 5.28. The results obtained previously for sol-gel, microwave-synthesised NMC-811 are also included for ease of comparison. It can be seen that at low temperatures the 1 % Al-doped sample exhibits a reasonably flat region up to approximately 200 K, with low fluctuation rates. The 1 % Mg-doped sample decreases in fluctuation rate slightly between 100 K and 140 K before settling at values close to those obtained for the Al-doped sample. At temperatures greater than 200 K the field fluctuation rate gradually increases, although it is clear that this is a slower process than that observed for the pristine NMC-811 as the field fluctuation rate values extracted for both Al- and Mg-doped sample are consistently lower than those obtained during the fitting of the pristine NMC-811  $\mu^+$ -SR data, suggesting that the dopant cations play a role in hindering the  $\text{Li}^+$  ionic diffusion. The rise in field fluctuation rate observed here is due to the onset and increasing rate of thermally activated  $\text{Li}^+$  ion diffusion and reach values of  $\approx 0.23$  MHz and  $\approx 0.19$  MHz at 400 K for the Al- and Mg-doped samples respectively.

The data extracted from the Kubo-Toyabe fits of the temperature dependence of the static width of the local field distribution,  $\Delta$ , is shown in the lower portion of Figure 5.28. At higher temperatures of *e.g.* 200 K - 400 K there is a good degree of similarity in this parameter across the pristine NMC-811 and the 1 % Al-doped and 1 % Mg-doped NMC-811 where the  $\Delta$  value is observed to gradually decrease upon increasing temperature from  $\approx 0.3$  MHz to  $\approx 0.2$  MHz which is commonly reported for these types of  $\mu^+$ -SR studies on electrode materials and could be explained by changes in the local magnetic field distribution caused by the thermally activated lithium diffusion process. At the lower end of the applied temperature range there is some deviation observed across the three samples. While the  $\Delta$  values for NMC-811 begin at  $\approx 0.35$  MHz at 100 K, the values obtained at this temperature for the Al- and Mg-doped samples were approximately 0.49 MHz and 0.46 MHz respectively and are thus noticeably higher than for the pristine sample. All of the pristine samples of NMC-811 and NMC-622 studied by  $\mu^+$ -SR in Chapter

4 exhibited near identical  $\Delta$  behaviour across the entire temperature range, suggesting that the introduction of the  $\text{Al}^{3+}$  and  $\text{Mg}^{2+}$  dopants into the structure also introduces some interesting lower temperature magnetic behaviour and warrants future further investigation using low-temperature magnetism techniques.

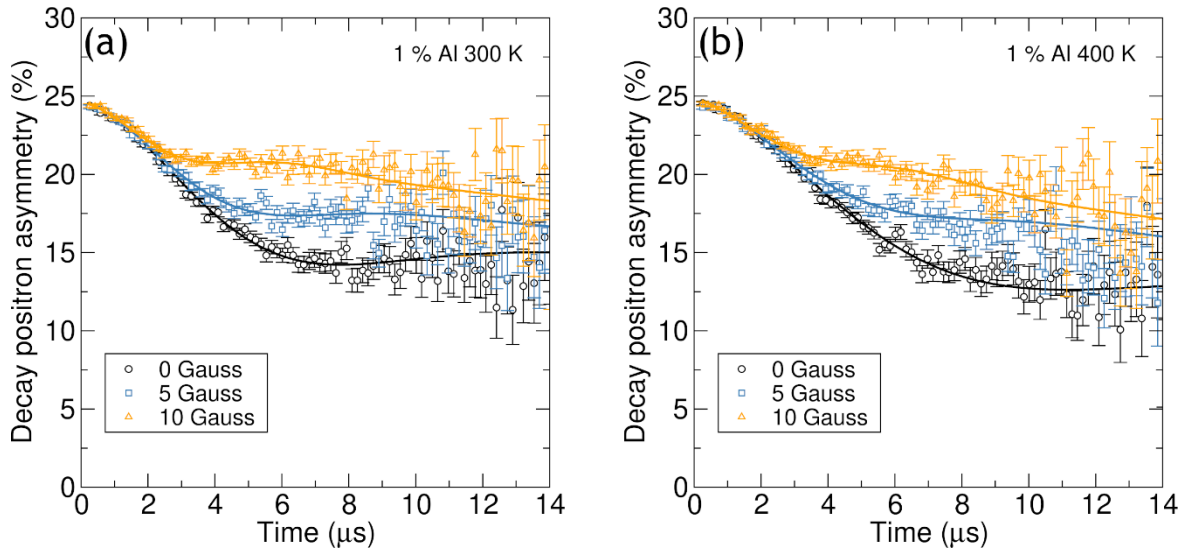


**Figure 5.26** Raw  $\mu^+$ -SR data collected at (a) 300 K for 1 % Al-doped NMC-811 synthesised by the microwave-assisted sol-gel method and (b) 400 K 1 % Al-doped NMC-811 prepared by a microwave assisted sol-gel method. Data at zero field (black circles) and applied longitudinal fields of 5 G (blue squares) and 10 G (orange triangles) is shown alongside the fit to the data using a dynamic Kubo-Toyabe function (solid lines).

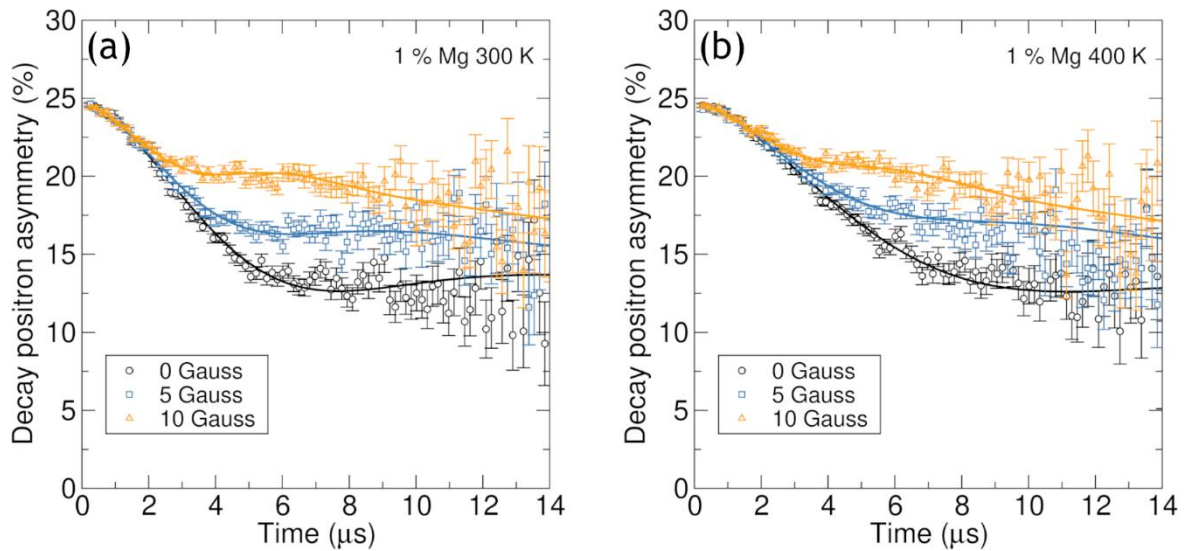


**Figure 5.27** Raw  $\mu^+$ -SR data collected at (a) 300 K for 1 % Mg-doped NMC-811 synthesised by the microwave-assisted sol-gel method and (b) 400 K 1 % Mg-doped NMC-811 prepared by a microwave assisted sol-gel method. Data at zero field (black circles) and applied longitudinal fields of 5 G (blue squares) and 10 G (orange triangles) is shown alongside the fit to the data using a dynamic Kubo-Toyabe function (solid lines).

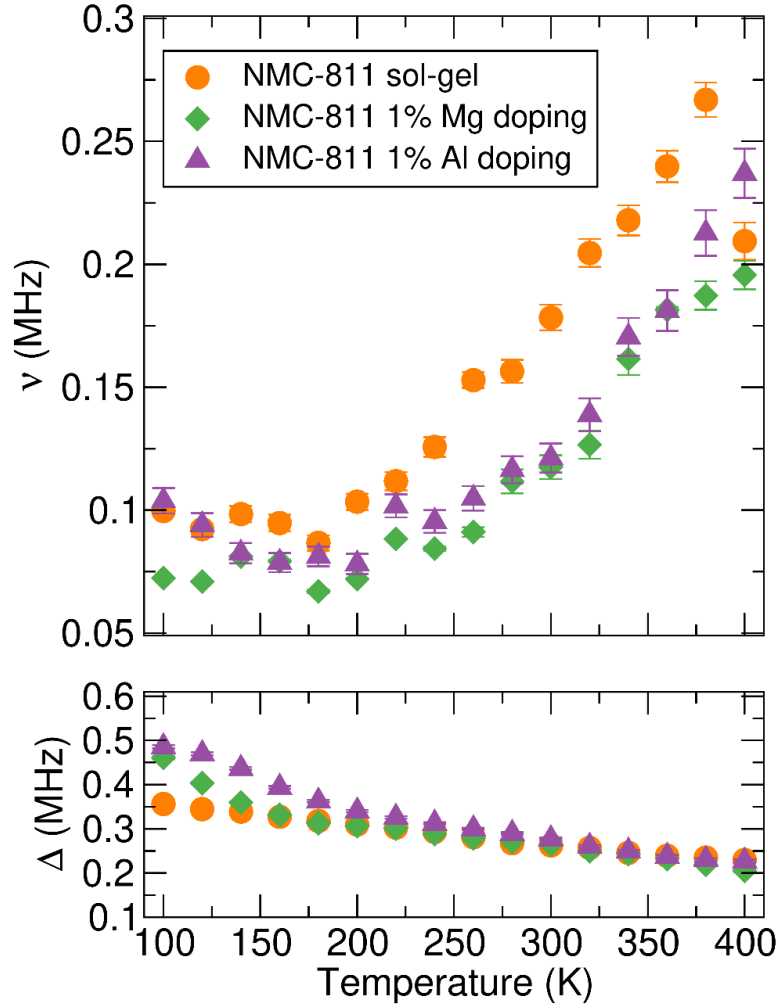


**Figure 5.28** Temperature dependence of the field fluctuation rate ( $\nu$ ) and the field distribution width at the muon stopping site ( $\Delta$ ) for  $\mu^+$ -SR data obtained for sol-gel and microwave-synthesised pristine NMC-811 (circles), 1 % Mg-doped NMC-811 (diamonds) and 1 % Al-doped NMC-811 (triangles) between 100 K to 400 K at ZF and LFs of 5 and 10 G, fit using an exponentially relaxing Kubo-Toyabe function.

The activation energy,  $E_a$  for thermally activated  $\text{Li}^+$  hopping can be calculated from an Arrhenius plot over the identified thermally activated region, considering the Arrhenius equation:

$$\ln(\nu) = \frac{-E_a}{K_B T} + \ln(A) \quad (5.2)$$

where  $\nu$  is the field fluctuation rate calculated at temperature  $T$ ,  $K_B$  is the Boltzmann constant ( $1.3806488 \times 10^{-23} \text{ J K}^{-1}$ ) and  $A$  is a pre-exponential factor. Thus the activation energy can be calculated from the gradient of the straight line fit on the  $\ln(\nu)$  against  $1/T$  plot. The plot over the thermally activated region for the data obtained from  $\mu^+$ -SR measurements on the 1 % Al-doped and 1 % Mg-doped NMC-811 samples studied here is

shown in Figure 5.29 alongside that obtained for the sol-gel NMC-811 sample presented in Chapter 4. The activation energies for the 1 % Al-doped and 1 % Mg-doped NMC-811 samples were estimated as 70 meV and 64 meV respectively. These activation energies are higher than that calculated for the pristine sample of NMC-811 prepared under the same synthesis conditions and thus further indicates that the dopant cations play a role in hindering the Li<sup>+</sup> ion diffusion by introducing a higher energy barrier in order to enable thermal diffusion. At the time of writing, this work constitutes the only work on diffusional analysis of doped NMC to the author's knowledge, however Muto *et al.* reported that Mg<sup>2+</sup> doped LiNi<sub>0.8</sub>Co<sub>0.15</sub>Al<sub>0.05</sub>O<sub>2</sub> (NCA) exhibited higher activation energies than pristine NCA (of ≈ 10 %) through EIS experiments.<sup>283</sup>

To calculate the diffusion coefficients, the possible lithium diffusion pathways need to be determined. As described in Chapter 4, for layered oxides there exists two pathways for lithium diffusion, involving the hopping from one lithium 3a site an adjacent 3a lithium site with a path-length equal to the *a* lattice parameter, and the other possible pathway involving a jump to interstitial sites with a path-length equal to *a*/√3. This is shown in Figure 4.17 where possible jumps for path 1 are shown by yellow arrows and those for path 2 are highlighted by blue arrows. To calculate the diffusion coefficient,  $D_{Li}$  therefore, the *a* lattice parameter obtained from previous Rietveld refinements is required and Equation 5.3 is used where  $N_i$  is the number of accessible Li<sup>+</sup> sites in the available path,  $Z_{v,i}$  is the vacancy fraction of the destination sites and  $s_i$  is the jump distance between adjacent Li<sup>+</sup> sites in the *i*<sup>th</sup> path and  $\nu$  is the field fluctuation rate obtained from  $\mu^+$ -SR measurements. For layered oxides with general formula Li<sub>*n*</sub>Ni<sub>*x*</sub>Mn<sub>*y*</sub>Co<sub>1-*x-y*</sub>O<sub>2</sub> path 1:  $N_1 = 6$ ,  $Z_{v,1} = 1-n$ ,  $s_1 = a$  and for path 2:  $N_2 = 3$ ,  $Z_{v,2} = 1$  and  $s_2 = a/\sqrt{3}$ .

$$D_{Li} = \sum_{i=1}^n \frac{1}{N_i} Z_{v,i} s_i^2 \nu \quad (5.3)$$

For 1 % Al-doped and 1 % Mg-doped NMC-811 the *a* lattice parameters were calculated as 2.875 Å and 2.884 Å respectively from Rietveld refinements. For the Al-doped sample, only pathway 2 is considered due to an assumed full occupancy of the lithium layers. For the Mg-doped sample, there is a lithium vacancy fraction of 0.02 due to charge compensation required for Mg<sup>2+</sup> doping on the Li<sup>+</sup> site and therefore both pathways will be considered. Diffusion coefficients at 300 K were calculated as  $1.11 \times 10^{-11} \text{ cm}^2 \text{ s}^{-1}$  and  $1.10 \times 10^{-11} \text{ cm}^2 \text{ s}^{-1}$  for the Al-doped and Mg-doped NMC-811 samples respectively. These are lower than that calculated for pristine NMC-811 ( $1.64 \times 10^{-11} \text{ cm}^2 \text{ s}^{-1}$ ) which was expected due to the lower fluctuation rates obtained for both of the doped samples.

Little change in the lattice parameters is observed for small doping quantities therefore the field fluctuation rate will have the greater effect on the magnitude of the diffusion coefficient.

Table 5.11 lists the calculated activation energies and diffusion coefficients at 300 K for the Al- and Mg-doped NMC-811 samples alongside those calculated previously for pristine NMC-811 for comparison. Although in this work the targeted composition of the Mg-doped NMC was  $\text{Li}_{0.98}\text{Mg}_{0.01}\text{Ni}_{0.8}\text{Mn}_{0.1}\text{Co}_{0.1}\text{O}_2$ , there remains some debate surrounding whether the  $\text{Mg}^{2+}$  dopant resides in lithium sites or in transition metal sites. If the  $\text{Mg}^{2+}$  sits in the lithium layer it presents a hindrance to the mobile  $\text{Li}^+$  ions and could act to block  $\text{Li}^+$  diffusion in some pathways. However, if the  $\text{Mg}^{2+}$  in this case sits on a nickel site it could allow  $\text{Ni}^{2+}$  cations to sit on the lithium site again which again would present a blockage in the diffusional pathways. Either way, the increased activation energies and decreased diffusion coefficients for Mg-doped NMC-811 are logical. The contraction in the  $c$  parameter observed for the Al-doped sample compared to the pristine sample could lower the  $\text{Li}^+$  diffusion through shrinkage of the layer spacing and thus the diffusion pathways.

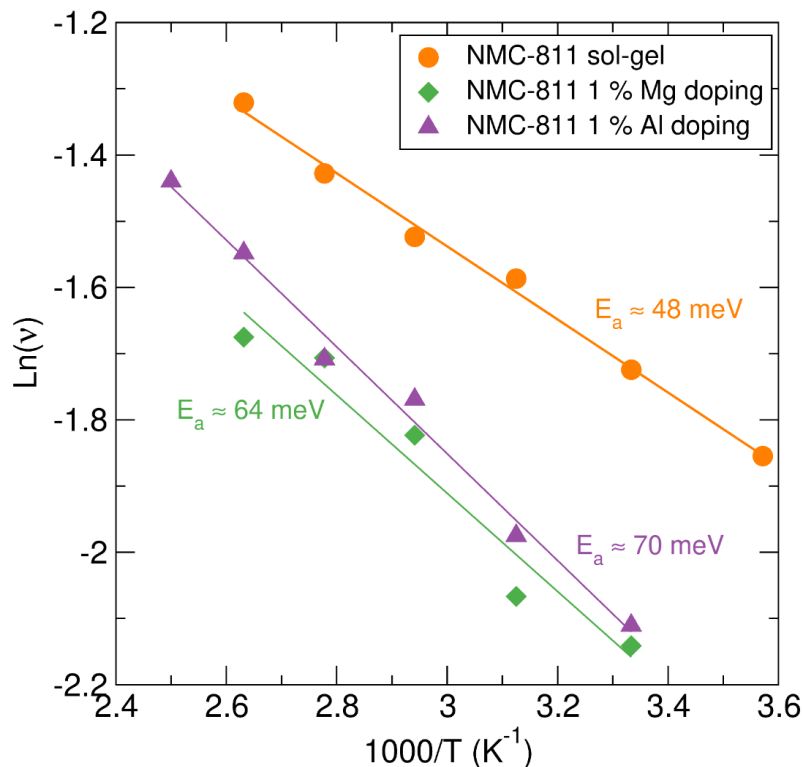


**Figure 5.29** Arrhenius plot of the field fluctuation rate over the thermally activated region calculated from  $\mu^+$ -SR measurements for NMC-811 sol-gel (circles), 1 % Mg-doped NMC-811 (diamonds) and 1 % Al-doped NMC-811 (triangles). Activation energies were estimated as 48, 64, and 70 meV respectively.

**Table 5.11** Activation energies and room temperature (300 K) diffusion coefficients calculated from  $\mu^+$ -SR measurements for microwave synthesised sol-gel samples of NMC-811, 1 % Al-doped NMC-811 and 1 % Mg-doped NMC-811.

Sample	Activation energy (meV)	Diffusion coefficient ( $\text{cm}^2 \text{s}^{-1}$ )
NMC-811 pristine	48 ( $\pm 1.8$ )	$1.64 \times 10^{-11}$
1 % Mg doped NMC-811	64.0 ( $\pm 3.5$ )	$1.10 \times 10^{-11}$
1 % Al doped NMC-811	69.6 ( $\pm 8.6$ )	$1.11 \times 10^{-11}$

### 5.3 Conclusions

In this chapter,  $\text{Al}_2\text{O}_3$  coated and  $\text{Al}^{3+}$  and  $\text{Mg}^{2+}$  doped samples of NMC-811 have been investigated. A simple and inexpensive ethanol-based dispersion coating process has been utilised in order to apply an  $\text{Al}_2\text{O}_3$  coating to NMC-811 materials synthesised by the sol-gel microwave assisted which show poor electrochemical properties in their pristine state. It was found that a lightweight coating corresponding to 0.2 wt.% significantly enhanced the cycling properties of this microwave-synthesised NMC-811. A discharge capacity of  $140 \text{ mAh g}^{-1}$  was initially achieved, which although is not optimum, is higher than that obtained without the coating. An excellent discharge capacity retention of 94 % was maintained across 10 cycles compared to 74 % observed for the uncoated sample and improved first cycle coulombic efficiencies were observed in the coated sample indicating that the coating could be helping to mitigate the deleterious side reactions that are a major contributor to cathode degradation. Heavier coating weights of 0.5 wt.% and 1.0 wt.% were found to be less effective with the performance becoming worse as the coating weight increased.

Owing to the significant improvements in cycling imparted by the 0.2 wt.% coated material, *operando* XAS experiments were performed on commercial, uncoated and coated materials to monitor the changes in the Ni oxidation state and local atomic environment during cycling by analysis of the XANES and EXFAS spectra respectively. Oxidation of the Ni cations was confirmed during the cycling by monitoring the change in energy of the Ni K-edge as a function of voltage. The shifts observed for the commercial sample were greater than those observed for the microwave-synthesised samples suggesting a greater extent of oxidation to  $\text{Ni}^{4+}$  is experienced by the commercial sample and could help to explain the low capacities observed for the microwave-synthesised samples. The differences observed in the pre-edge region in the XANES spectra indicate that a greater deviation from centrosymmetry is observed during the first charge for the uncoated sample compared to the coated sample suggesting the occurrence of some

instabilities that could result in rapid degradation which seem to be suppressed more in the coated sample. Analysis of the EXAFS region confirms the presence of the Jahn-Teller Ni<sup>3+</sup> cation in the pristine state and a contraction of Ni-Ni and Ni-M bonds upon charging is observed.

Neutron powder diffraction coupled with PDF analysis was then used in order to examine the bulk and local structure of commercial, uncoated and coated NMC-811 samples. Increased Li/Ni mixing was confirmed for the microwave-synthesised samples compared to the commercial sample, most likely owing to the short reaction times of 1 hour used for these materials. Little change was observed between the uncoated and coated samples, confirming that no difference to the bulk crystallographic structure. The local structure examined from the PDFs again confirm the similarity of the uncoated and coated samples showing that the coating and the coating process have little impact upon the NMC-811 structure itself. Reasonably good fits to the PDFs were obtained at room temperature using an average crystallographic  $R\bar{3}m$  layered structure with the microwave-synthesised samples achieving better fits compared to the commercial sample indicating good levels of crystallinity with less disorder and/or structural distortions. However, RMC modelling considering cation clusters could still be employed in the future to obtain improved fits.

The muon spin relaxation measurements performed on 1 % Al<sup>3+</sup> and Mg<sup>2+</sup> doped samples of sol-gel microwave-synthesised NMC-811 reveal increased activation energies for thermally activated Li<sup>+</sup> diffusion and lower diffusion coefficients compared to a pristine sample synthesised under the same conditions. This indicates that while these dopants may provide enhanced cycling and structural stabilities, their rate capabilities may be compromised.

To expand the body of work presented in this chapter, future work focussing on the characterisation of the Al<sub>2</sub>O<sub>3</sub> layer applied to NMC-811 in this chapter would provide valuable insight into how the coating thickness directly influences the effectiveness of the coating. Owing to the fact that the coating technique was adapted from the literature, experiments confirming the presence and the thickness of the coating layers were not carried out. Infrared spectroscopy measurements could be carried out to confirm the presence of Al<sub>2</sub>O<sub>3</sub> on the surface of the NMC particles. TEM experiments could be used in the future to investigate the thickness of the layers deposited by the dispersion-based method used here, and how the weight percentage of Al<sub>2</sub>O<sub>3</sub> correlates to this layer thicknesses. *Operando* TEM studies on these Al<sub>2</sub>O<sub>3</sub> coated cathodes could

also reveal how these coating layers evolve during cycling and identify any effects such as layer cracking that could limit their lifetimes.

Whereas the XAS measurements carried out here were done on the Ni K-edge, to understand how the surface of the material evolves during cycling, Ni L-edge soft XAS measurements could be carried out in the future, opening up the opportunity to relate the surface XAS behaviour to the bulk XAS behaviour during cycling. Ni L-edge XAS is a surface sensitive technique that can identify the surface Ni oxidation state and thus reveal the presence of reconstruction layers such as rock salt and spinel-type phases.<sup>284</sup>

Although only Al<sup>3+</sup> and Mg<sup>2+</sup> dopants have been presented here, there exists a rich playground of potential dopants, with the option to incorporate more than one dopant into these layered oxide structures too. However, due to the low atomic percentages of dopants typically used for doping cathode structures (ideally < 5%) there exists the question of where the dopants reside - whether they truly “dope” the structure uniformly or whether they can segregate to the particle surfaces or to the grain boundaries, as has been observed with W<sup>6+</sup> dopants in similar layered oxide cathodes.<sup>99</sup> To examine the distribution of dopant cations, future work could implement TEM measurements with elemental mapping to identify where these low quantities of Al<sup>3+</sup> and Mg<sup>2+</sup> dopants presented in this chapter locate within the NMC particles. Optimisation of Al<sup>3+</sup> and Mg<sup>2+</sup> dopant concentrations on the resultant cycling stability could also be identified through galvanostatic cycling measurements on NMC-811 for dopant quantities of between 1 % to 5%. Carrying out *in-situ* muon measurements on these doped NMC-811 samples would provide insight into how the Al<sup>3+</sup> and Mg<sup>2+</sup> dopants affect the Li<sup>+</sup> diffusion during cycling and could reveal interesting behaviour that cannot be ascertained from muon measurements carried out on the powder samples.

## 6 Overall conclusions and future work

### 6.1 Overall conclusions

In this thesis, a selection of high energy density cathode materials for lithium ion batteries have been synthesised and examined using a variety of both laboratory and central facility based techniques involving diffraction, microscopy, spectroscopy and electrochemical experiments. Such high energy density materials studied include fluorine containing polyanionic materials such as  $\text{LiFeSO}_4\text{F}$  which provide increased working potentials and high nickel-content layered oxide NMCs that can deliver higher capacities owing to the increased nickel content. Microwave-assisted synthesis methods have been focussed on here owing to the reduced processing times and resulting reduced energy consumptions that can be afforded by such processes.

The microscopic ionic diffusion in the tavorite phase of  $\text{LiFeSO}_4\text{F}$ , which has been studied using the muon-spin relaxation spectroscopy technique has been presented here. The  $\mu^+$ -SR technique is rapidly gaining popularity in electrochemical energy storage research due to its ability to act as a probe of the local-scale ionic diffusion occurring in electrode and solid-electrolyte materials, shedding insight into the intrinsic diffusional behaviours of transport ions such as  $\text{Li}^+$  and  $\text{Na}^+$  within frameworks without being masked by impeding bulk effects such as contributions from grain boundaries. A previously reported method for the microwave-assisted solvothermal synthesis of  $\text{LiFeSO}_4\text{F}$  has been adapted here to successfully obtain the tavorite phase of the material for the  $\mu^+$ -SR studies. The data collected from such experiments can describe the behaviour of the thermally activated cationic motion and have revealed an activation energy of 48 meV and a room temperature diffusion coefficient of  $1.71 \times 10^{-9} \text{ cm}^2 \text{ s}^{-1}$  which indicate an improved performance compared to similarly synthesised olivines  $\text{LiFe}_{1-x}\text{Mn}_x\text{PO}_4$  showing that such fluorosulphate materials offer a viable new cathode technology.

The versatility of the  $\mu^+$ -SR technique in probing different charge carriers is also represented here through the study of  $\text{Na}^+$  ion diffusion in fluorophosphate material  $\text{Na}_2\text{FePO}_4\text{F}$ . Compared to typical values obtained for  $\text{Li}^+$  diffusion, higher activation energies (102 meV) and lower diffusion coefficients ( $3.6 \times 10^{-9} \text{ cm}^2 \text{ s}^{-1}$ ) are calculated here for  $\text{Na}^+$  diffusion as expected for the larger and heavier  $\text{Na}^+$  ions thus providing evidence for the reliability of the  $\mu^+$ -SR technique. This reliability has also been shown *via* measurements performed on the maricite phase of  $\text{NaFePO}_4$  which is an ionic insulator, where the muon measurements show no evidence of  $\text{Na}^+$  diffusion. The results obtained for both fluorinated samples also serve to evidence that the presence of highly electronegative F<sup>-</sup> anions does not preclude the measurement of the  $\text{Li}^+$  motion as has

been previously anticipated, opening up the  $\mu^+$ -SR method for the analysis of a wider range of materials in the future.

Although polyanionic cathode materials generally exhibit excellent stabilities and higher voltages, it is the layered oxides that have found most commercial use with high nickel content NMCs poised to lead the electric vehicle revolution. This thesis places a large focus on the microwave-assisted synthesis of NMC-811 where PXRD, scanning electron microscopy and galvanostatic cycling studies have all been used to investigate the structural, morphological and electrochemical properties of NMC-811 samples synthesised at a range of times and temperatures. A sol-gel microwave-assisted method has been introduced where the sol-gel procedure promotes a good level of mixing between transition metal cations. It has been shown that successful synthesis of the layered  $R\bar{3}m$  phase with negligible impurities has been demonstrated at temperatures of 750 °C with a reaction time as little as 1 hour. However, through Rietveld refinements on the PXRD data large degrees of undesirable Li/Ni anti-site mixing has been revealed for these microwave synthesised samples which is more prominent in samples synthesised at increasing temperatures. This anti-site mixing is also a lot higher than in commercially supplied NMC-811 suggesting that the microwave-assisted sintering step at such short times could play a pivotal role in promoting the Li/Ni mixing. This is also mirrored in the poor galvanostatic cycling behaviour observed that is mainly characterised by large capacity losses after the 1<sup>st</sup> cycle and rapid capacity fading upon subsequent cycles. However, excellent results have been observed for a sample of NMC-811 prepared at 775 °C for 3 hours suggesting that optimisation of such synthetic methods is essential and that even small changes in reaction parameters can prove detrimental to the material properties.

Scanning electron microscopy revealed that small particle sizes can be obtained that can be attributed to the short reaction times applied. The average particle size is seen to increase, and the particle size homogeneity decreases upon increasing the nickel content in the material.

Local-scale diffusional studies using  $\mu^+$ -SR have also revealed very similar diffusional behaviour between microwave-synthesised samples and commercially obtained samples with lower activation energies and higher diffusion coefficients calculated for materials with higher nickel contents.

A significant improvement in the cycling stability of microwave-synthesised NMC-811 has been demonstrated here *via* the application of an amorphous  $Al_2O_3$  protective coating applied using a simple and potentially scalable dispersion method. The results obtained

also suggest that lightweight coatings of at most 0.2 wt.% are effective, with heavier coatings failing to improve the poor electrochemical performances.

Advanced central facility-based analysis techniques including XAS, NPD and PDF analysis have been used here to study this coated material in greater detail. *Operando* XANES studies have revealed that the Al<sub>2</sub>O<sub>3</sub> coating may be able to suppress geometric distortions at high voltages up to 4.5 V during cycling compared to the uncoated NMC-811. Neutron powder diffraction measurements on NMC-811 samples have confirmed the greater extent of Li/Ni mixing present in microwave-synthesised samples compared to commercially supplied samples and further confirm that no significant bulk structural changes are generated by the Al<sub>2</sub>O<sub>3</sub> coating and the coating process. Total scattering NPD measurements coupled with PDF analysis have also been used to investigate the local-structure related to atom-atom distances. The reasonably good fitting obtained from results indicate that highly crystalline NMC-811 is produced using the microwave-assisted method and no significant differences are observed between the coated and uncoated samples.

The successful incorporation of small amounts of dopant Al<sup>3+</sup> and Mg<sup>2+</sup> cations into the NMC-811 structure has also been demonstrated using a microwave-assisted sol-gel method with  $\mu^+$ -SR studies revealing that the Li<sup>+</sup> cation mobility in these materials is compromised compared to un-doped NMC-811 even at as little as 1 mol.% doping.

Overall, the analysis of the high energy density materials presented in this thesis aims to provide further insights into the structure-property relationships in such materials that ultimately underpin their resultant functionality. Good functionality is paramount for these to be realised in future, electric-vehicle and other high energy density applications. A new, microwave-assisted method for the synthesis of high energy density cathode materials has also been presented here, with results suggesting that the optimisation of reaction parameters can yield good electrochemical performances and could represent a quick and lower energy means of producing the next-generation of lithium ion battery cathodes.

## 6.2 Future work

Each piece of research presented throughout this thesis undoubtedly opens up new avenues for further future investigations, with some of these presented in this section.

Regarding the polyanionic cathodes studied in Chapter 3, although  $\mu^+$ -SR studies revealed good microscopic cationic diffusional behaviour in tavorite phase LiFeSO<sub>4</sub>F, it would be interesting to perform the same measurements on the higher voltage triplite phase which

exhibits electrochemical activity despite the absence of obvious diffusion pathways throughout the framework. Understanding this complex diffusion on a microscopic length would provide greater insight into the fundamental properties governing performance in these important class of cathode materials.

While the microwave-assisted sol-gel synthetic route to nickel rich NMCs has been shown to produce crystalline materials in as little as 1 hour, it is clear that the electrochemical performances of such materials are severely compromised owing to large degrees of Li/Ni mixing present. Recent work done in our group has revealed that improved cycling stabilities can be achieved by heating the materials under an oxygen atmosphere. The development of microwave-assisted heating under an oxygen atmosphere should therefore be undertaken in the future to ascertain the properties of nickel-rich materials synthesised at short reaction times under O<sub>2</sub>.

Although the Al<sub>2</sub>O<sub>3</sub> coating method that was introduced here showed significant cycling improvements, the application of coatings using more sophisticated methods such as atomic layer deposition would allow for precise tailoring of coatings and allow for control over the coating thickness and coverage.

The optimisation of doping quantities and investigation of different dopants for microwave-synthesised NMC-811 would be an interesting future avenue of research, where the possibility of co-doping with several dopants to possibly provide synergistic improvements in cycling performances could be investigated.

The study of *operando* PXRD measurements on all samples also provides a route for further exploration in order to understand how the lattice parameters change during cycling and whether certain synthetic routes are able to suppress irreversible changes during cycling. *Operando* NPD studies would also be highly informative in order to understand how the Li/Ni mixing changes during cycling *e.g.* observing whether more Ni<sup>2+</sup> can be confirmed to migrate into the lithium layer during the first cycle.

There is also an interest in transitioning to low or zero-content Co cathodes through the development of “beyond” NMC-811 cathodes employing higher nickel contents *e.g.* LiNi<sub>0.9</sub>Mn<sub>0.05</sub>Co<sub>0.05</sub>O<sub>2</sub> or LiNiO<sub>2</sub>. Further doping on the Co site with stability enhancing cations would also serve to further decrease the Co quantity. Such high nickel content materials are expected to have stability issues but are capable of providing excellent theoretical capacities of > 200 mAh g<sup>-1</sup>. The development of controlled concentration gradients in such nickel-rich particles could present one route to the stabilisation of such materials, where the overall capacity is determined by the nickel-rich core and surface

stabilisations and enhanced rate capabilities can be implemented by the application of lower nickel content outer shells e.g. NMC-622.

While many of these proposed routes to further research involve the study of improved inorganic materials for lithium ion battery applications, the possibility of utilising redox-active organic based cathodes should also be highlighted. Such cathodes present a more sustainable option with the option to finely tune the molecular structure to tailor the specific capacities and the redox potentials.<sup>285,286</sup> One organic-based system that shows good promise for organic electrodes are the redox-active flavins which have many uses in biological applications.

In preliminary work carried out here, benzo-dipteridine derivatives (synthesised by collaborators at The University of Glasgow) have been tested in lithium ion half-cells set-ups.<sup>287</sup> These molecules have poor solubility in organic solvents and are capable of multiple reversible 1-electron reductions because of the 1,4-diazabuta-1,3-diene groups that can accommodate two electrons each.<sup>288</sup> The bis-flavin synthesised here is shown in Figure 6.1 where two 1,4-diazabuta-1,3-diene groups, shaded in red are observed, therefore giving the molecule the functionality to accommodate a total of four Li<sup>+</sup> cations. Synthesised bis-flavin powders were pressed into pellets with conductive carbon black and PTFE as a binder in a 40:40:20 wt.% ratio and cycled within a voltage window of 1.2 V - 4.0 V vs. a Li<sup>+</sup> metal counter electrode in Swagelok type cells. Cells were cycled at a rate of C/10 assuming that all 4 Li<sup>+</sup> are able to be added and removed during discharge and charge respectively. Figure 6.2(a) shows the cycling profiles obtained. It is observed that high specific capacities of approximately 250 mAh g<sup>-1</sup> are initially achieved which shows a gradual fading to  $\approx$  150 mAh g<sup>-1</sup> after the 50<sup>th</sup> cycle. This fading could arise from some solubility of the molecule in the organic based electrolyte which could be aggravated at high voltages. The same material was then cycled between a smaller voltage window of 1.5 - 3.2 V under the same cycling conditions, where a cycling rate of C/10 assuming only 2 Li<sup>+</sup> can be accommodated due to the lower potential window applied. The cycling profiles obtained using these conditions are shown in Figure 6.2(b). The delivered specific capacities are observed to be approximately half of what was achieved using the wider potential window which compares well with the idea that only half of the theoretical Li<sup>+</sup> are accommodated. However, across 50 cycles an excellent degree of stability is observed suggesting that stability can be gained at the expense of capacity. A comparison of the discharge capacity retentions and calculated Coulombic efficiencies for this molecule cycled between the two different potential ranges is shown in Figure 6.2(c). Furthermore, the cationic binding of such materials is not limited to

lithium. A cyclic voltammogram for the molecule vs. a sodium metal anode is shown in Figure 6.2(d). As the voltage is swept from the open circuit voltage to 1.0 V a reduction peak is observed at 2.5 V vs. Na/Na<sup>+</sup> corresponding to the binding of a Na<sup>+</sup> cation. As the voltage is then swept from 1.0 V to 4.2 V clear oxidation peaks are observed at 3.3 V.

Future work on such systems could include determining their applicability in flow batteries for large-scale storage, or even as cathode materials for newer systems such as Mg-ion batteries.

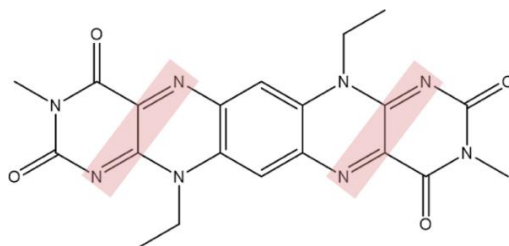


**Figure 6.1** Structure of the bis-flavin BF-Me2 with the 1,4-diazabutane-1,3-diene groups shaded in red.

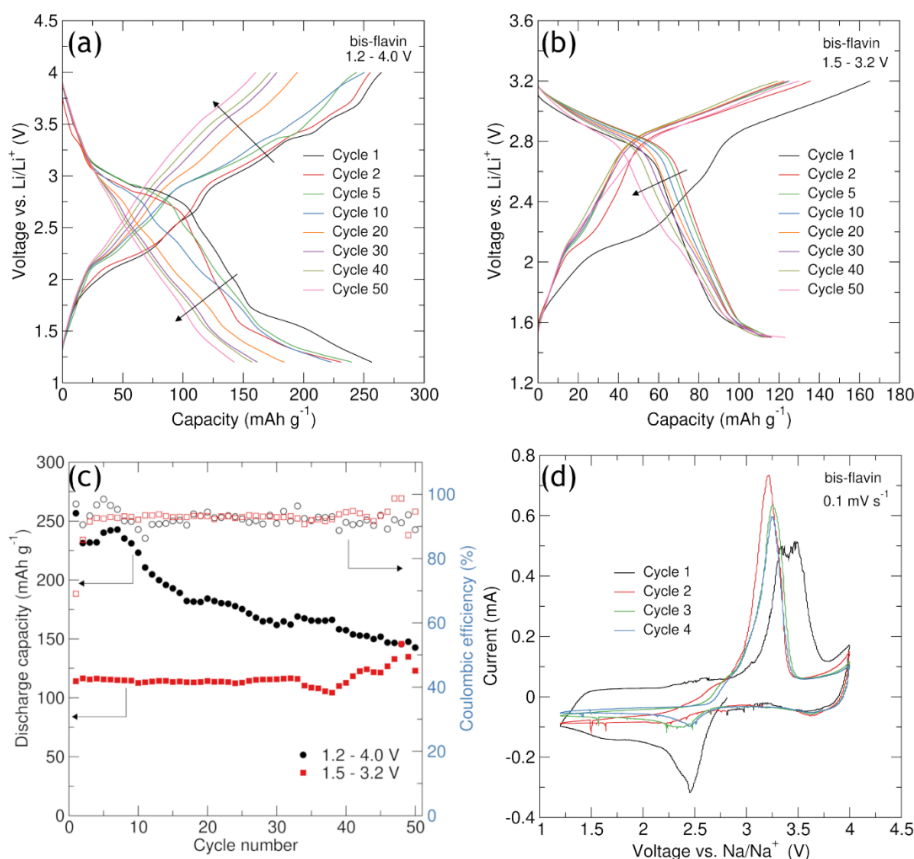


**Figure 6.2** Results obtained from galvanostatic cycling of the bis-flavin molecule in a Swagelok type cell between (a) 1.2 V - 4.0 V and (b) 1.5 V - 3.2 V vs. Li/Li<sup>+</sup> and (c) discharge capacity retentions and Coulombic efficiencies. The cyclic voltammogram obtained when the material was cycled vs. a sodium metal anode is shown in (d).

## References

- 1 M. S. Whittingham, *Science*, 1976, **192**, 1126-1127.
- 2 K. Mizushima, P. C. Jones, P. J. Wiseman and J. B. Goodenough, *Solid State Ionics*, 1981, **3-4**, 171-174.
- 3 J.-M. Tarascon and M. Armand, *Nature*, 2001, **414**, 359-367.
- 4 J. Rogelj, D. Huppmann, V. Krey, K. Riahi, L. Clarke, M. Gidden, Z. Nicholls and M. Meinshausen, *Nature*, 2019, **573**, 357-363.
- 5 Y. Ding, Z. P. Cano, A. Yu, J. Lu and Z. Chen, *Electrochem. Energy Rev.*, 2019, **2**, 1-28.
- 6 C. Liu, Z. G. Neale and G. Cao, *Mater. Today*, 2016, **19**, 109-123.
- 7 J. B. Goodenough and Y. Kim, *Chem. Mater.*, 2010, **22**, 587-603.
- 8 Q. Wang, L. Jiang, Y. Yu and J. Sun, *Nano Energy*, 2019, **55**, 93-114.
- 9 L. Hu, Z. Zhang and K. Amine, *Electrochem. commun.*, 2013, **35**, 76-79.
- 10 Z. Zhang, L. Hu, H. Wu, W. Weng, M. Koh, P. C. Redfern, L. A. Curtiss and K. Amine, *Energy Environ. Sci.*, 2013, **6**, 1806-1810.
- 11 A. Manthiram, X. Yu and S. Wang, *Nat. Rev. Mater.*, 2017, **2**, 16103.
- 12 F. Zheng, M. Kotobuki, S. Song, M. O. Lai and L. Lu, *J. Power Sources*, 2018, **389**, 198-213.
- 13 M. Pasta, D. Armstrong, Z. L. Brown, J. Bu, M. R. Castell, P. Chen, A. Cocks, S. A. Corr, E. J. Cussen, E. Darnbrough, V. Deshpande, C. Doerrer, M. S. Dyer, H. El-Shinawi, N. Fleck, P. Grant, G. L. Gregory, C. Grovenor, L. J. Hardwick, J. T. S. Irvine, H. J. Lee, G. Li, E. Liberti, I. McClelland, C. Monroe, P. D. Nellist, P. R. Shearing, E. Shoko, W. Song, D. S. Jolly, C. I. Thomas, S. J. Turrell, M. Vestli, C. K. Williams, Y. Zhou and P. G. Bruce, *J. Phys. Energy*, 2020, **2**, 32008.
- 14 S. Goriparti, E. Miele, F. De Angelis, E. Di Fabrizio, R. Proietti Zaccaria and C. Capiglia, *J. Power Sources*, 2014, **257**, 421-443.
- 15 W.-J. Zhang, *J. Power Sources*, 2011, **196**, 13-24.
- 16 Y. Sun, X. Hu, W. Luo, F. Xia and Y. Huang, *Adv. Funct. Mater.*, 2013, **23**, 2436-2444.

- 17 C. Delmas, H. Cognac-Auradou, J. M. Cocciantelli, M. Ménétrier and J. P. Doumerc, *Solid State Ionics*, 1994, **69**, 257-264.
- 18 K. West, B. Zachau-Christiansen, S. Skaarup, Y. Saidi, J. Barker, I. I. Olsen, R. Pynenburg and R. Koksang, *J. Electrochem. Soc.*, 1996, **143**, 820.
- 19 Z. Gao, H. Sun, L. Fu, F. Ye, Y. Zhang, W. Luo and Y. Huang, *Adv. Mater.*, 2018, **30**, 1705702.
- 20 V. Thangadurai, S. Narayanan and D. Pinzaru, *Chem. Soc. Rev.*, 2014, **43**, 4714-4727.
- 21 J. F. M. Oudenhoven, L. Baggetto and P. H. L. Notten, *Adv. Energy Mater.*, 2011, **1**, 10-33.
- 22 G. Zubi, R. Dufo-López, M. Carvalho and G. Pasaoglu, *Renew. Sustain. Energy Rev.*, 2018, **89**, 292-308.
- 23 A. Manthiram, *Nat. Commun.*, 2020, **11**, 1550.
- 24 H. J. Orman, P. J. Wiseman and IUCr, *Acta Crystallogr. Sect. C Cryst. Struct. Commun.*, 1984, **40**, 12-14.
- 25 G. G. Amatucci, J. M. Tarascon and L. C. Klein, *J. Electrochem. Soc.*, 1996, **143**, 1114.
- 26 T. Ohzuku and A. Ueda, *J. Electrochem. Soc.*, 1994, **141**, 2972.
- 27 C. Julien, A. Mauger, K. Zaghbi and H. Groult, *Inorganics*, 2014, **2**, 132-154.
- 28 T. Ohsaki, T. Kishi, T. Kuboki, N. Takami, N. Shimura, Y. Sato, M. Sekino and A. Satoh, *Journal of Power Sources*, 2005, **146**, 97-100.
- 29 A. Manthiram, A. Vadivel Murugan, A. Sarkar and T. Muraliganth, *Energy Environ. Sci.*, 2008, **1**, 621.
- 30 G. Dutta, A. Manthiram, J. B. Goodenough and J.-C. Grenier, *J. Solid State Chem.*, 1992, **96**, 123-131.
- 31 A. Hirano, R. Kanno, Y. Kawamoto, Y. Takeda, K. Yamaura, M. Takano, K. Ohyama, M. Ohashi and Y. Yamaguchi, *Solid State Ionics*, 1995, **78**, 123-131.
- 32 H. Arai, S. Okada, Y. Sakurai and J. Yamaki, *Solid State Ionics*, 1998, **109**, 295-302.
- 33 H. Arai, M. Tsuda, K. Saito, M. Hayashi and Y. Sakurai, *J. Electrochem. Soc.*, 2002,

149, A401.

- 34 S. Choi and A. Manthiram, *J. Electrochem. Soc.*, 2002, **149**, A1157.
- 35 B. Hwang, R. Santhanam and C. Chen, *J. Power Sources*, 2003, **114**, 244-252.
- 36 C. Julien, C. Letranchant, M. Lemal, S. Ziolkiewicz and S. Castro-Garcia, *J. Mater. Sci.*, 2002, **37**, 2367-2375.
- 37 W. Li and J. C. Currie, *J. Electrochem. Soc.*, 1997, **144**, 2773.
- 38 R. V. Chebiam, F. Prado and A. Manthiram, *J. Solid State Chem.*, 2002, **163**, 5-9.
- 39 P. He, H. Yu, D. Li and H. Zhou, *J. Mater. Chem.*, 2012, **22**, 3680.
- 40 T. Ohzuku and Y. Makimura, *Chem. Lett.*, 2001, **30**, 642-643.
- 41 N. Yabuuchi and T. Ohzuku, *J. Power Sources*, 2003, **119-121**, 171-174.
- 42 B. J. Hwang, Y. W. Tsai, D. Carlier and G. Ceder, *Chem. Mater.*, 2003, **15**, 3676-3682.
- 43 C.-H. Chen, C.-J. Wang and B.-J. Hwang, *J. Power Sources*, 2005, **146**, 626-629.
- 44 Z. Liu, A. Yu and J. Y. Lee, *J. Power Sources*, 1999, **81-82**, 416-419.
- 45 K. Shaju, G. Subba Rao and B. V. Chowdari, *Electrochim. Acta*, 2002, **48**, 145-151.
- 46 Y. Koyama, N. Yabuuchi, I. Tanaka, H. Adachi and T. Ohzuku, *J. Electrochem. Soc.*, 2004, **151**, A1545.
- 47 D. Zeng, J. Cabana, J. Bréger, W.-S. Yoon and C. P. Grey, *Chem. Mater.*, 2007, **19**, 6277-6289.
- 48 D. Li, Y. Sasaki, M. Kageyama, K. Kobayakawa and Y. Sato, *J. Power Sources*, 2005, **148**, 85-89.
- 49 D. Li, Y. Sasaki, K. Kobayakawa and Y. Sato, *Electrochim. Acta*, 2006, **51**, 3809-3813.
- 50 S. Yang, X. Wang, X. Yang, Y. Bai, Z. Liu, H. Shu and Q. Wei, *Electrochim. Acta*, 2012, **66**, 88-93.
- 51 S.-K. Jung, H. Gwon, J. Hong, K.-Y. Park, D.-H. Seo, H. Kim, J. Hyun, W. Yang and K. Kang, *Adv. Energy Mater.*, 2014, **4**, 1300787.
- 52 R. Qiao, J. Liu, K. Kourtakis, M. G. Roelofs, D. L. Peterson, J. P. Duff, D. T. Deibler,

- L. A. Wray and W. Yang, *J. Power Sources*, 2017, **360**, 294-300.
- 53 N. Y. Kim, T. Yim, J. H. Song, J.-S. Yu and Z. Lee, *J. Power Sources*, 2016, **307**, 641-648.
- 54 H. Rong, M. Xu, L. Xing and W. Li, *J. Power Sources*, 2014, **261**, 148-155.
- 55 H. Rong, M. Xu, Y. Zhu, B. Xie, H. Lin, Y. Liao, L. Xing and W. Li, *J. Power Sources*, 2016, **332**, 312-321.
- 56 M. Börner, F. Horsthemke, F. Kollmer, S. Haseloff, A. Friesen, P. Niehoff, S. Nowak, M. Winter and F. M. Schappacher, *J. Power Sources*, 2016, **335**, 45-55.
- 57 J. Vetter, P. Novák, M. R. Wagner, C. Veit, K.-C. Möller, J. O. Besenhard, M. Winter, M. Wohlfahrt-Mehrens, C. Vogler and A. Hammouche, *J. Power Sources*, 2005, **147**, 269-281.
- 58 M. Wohlfahrt-Mehrens, C. Vogler and J. Garche, *J. Power Sources*, 2004, **127**, 58-64.
- 59 Y. Ruan, X. Song, Y. Fu, C. Song and V. Battaglia, *J. Power Sources*, 2018, **400**, 539-548.
- 60 Geological Survey, *Minerals Yearbook 2008 Area Reports, International, Africa and the Middle East.*, United States Govt. Printing Office, 2010.
- 61 E. A. Olivetti, G. Ceder, G. G. Gaustad and X. Fu, *Joule*, 2017, **1**, 229-243.
- 62 S. Kara, I saw the unbearable grief inflicted on families by cobalt mining. I pray for change. The *Guardian* [Internet]. 2019 Dec 16 [cited 2020 August]. Available from  
<https://www.theguardian.com/global-development/commentisfree/2019/dec/16/i-saw-the-unbearable-grief-inflicted-on-families-by-cobalt-mining-i-pray-for-change>
- 63 H.-J. Noh, S. Youn, C. S. Yoon and Y.-K. Sun, *J. Power Sources*, 2013, **233**, 121-130.
- 64 J. Li, J. Camardese, S. Glazier and J. R. Dahn, *Chem. Mater.*, 2014, **26**, 7059-7066.
- 65 D.-H. Cho, C.-H. Jo, W. Cho, Y.-J. Kim, H. Yashiro, Y.-K. Sun and S.-T. Myung, *J. Electrochem. Soc.*, 2014, **161**, A920-A926.
- 66 R. Jung, M. Metzger, F. Maglia, C. Stinner and H. A. Gasteiger, *J. Electrochem. Soc.*, 2017, **164**, A1361-A1377.

- 67 S.-M. Bak, E. Hu, Y. Zhou, X. Yu, S. D. Senanayake, S.-J. Cho, K.-B. Kim, K. Y. Chung, X.-Q. Yang and K.-W. Nam, *ACS Appl. Mater. Interfaces*, 2014, **6**, 22594-22601.
- 68 J. Li, L. E. Downie, L. Ma, W. Qiu and J. R. Dahn, *J. Electrochem. Soc.*, 2015, **162**, A1401-A1408.
- 69 W. Li, J. N. Reimers and J. R. Dahn, *Solid State Ionics*, 1993, **67**, 123-130.
- 70 H. Li, N. Zhang, J. Li and J. R. Dahn, *J. Electrochem. Soc.*, 2018, **165**, A2985-A2993.
- 71 K. Märker, P. J. Reeves, C. Xu, K. J. Griffith and C. P. Grey, *Chem. Mater.*, 2019, **31**, 2545-2554.
- 72 A. Rougier, PhD Thesis, Bordeaux 1, 1995.
- 73 T. Ohzuku, A. Ueda and M. Kouguchi, *J. Electrochem. Soc.*, 1995, **142**, 4033.
- 74 Q. Zhong and U. von Sacken, *J. Power Sources*, 1995, **54**, 221-223.
- 75 G. Wang, S. Zhong, D. Bradhurst, S. Dou and H. Liu, *Solid State Ionics*, 1999, **116**, 271-277.
- 76 S. H. Park, K. S. Park, Y. K. Sun, K. S. Nahm, Y. S. Lee and M. Yoshio, *Electrochim. Acta*, 2001, **46**, 1215-1222.
- 77 M. Guilmard, A. Rougier, M. Grüne, L. Croguennec and C. Delmas, *J. Power Sources*, 2003, **115**, 305-314.
- 78 M. Guilmard, L. Croguennec, D. Denux and C. Delmas, *Chem. Mater.*, 2003, **15**, 4476-4483.
- 79 S. Madhavi, G. Subba Rao, B. V. Chowdari and S. F. Li, *J. Power Sources*, 2001, **93**, 156-162.
- 80 M. Guilmard, C. Poullerie, L. Croguennec and C. Delmas, *Solid State Ionics*, 2003, **160**, 39-50.
- 81 Z. Qiu, Y. Zhang, P. Dong, S. Xia and Y. Yao, *Solid State Ionics*, 2017, **307**, 73-78.
- 82 M. S. Whittingham, *Chem. Rev.*, 2004, **104**, 4271-4302.
- 83 J. Xu, F. Lin, M. M. Doeff and W. Tong, *J. Mater. Chem. A*, 2017, **5**, 874-901.
- 84 T.-H. Kim, J.-S. Park, S. K. Chang, S. Choi, J. H. Ryu and H.-K. Song, *Adv. Energy*

- Mater.*, 2012, **2**, 860-872.
- 85 D.-G. Tong, Y.-Y. Luo, Y. He, X.-Y. Ji, J.-L. Cao, L.-X. Tang, A.-D. Tang, K.-L. Huang and Q.-Y. Lai, *Mater. Sci. Eng. B*, 2006, **128**, 220-228.
- 86 S. M. Lala, L. A. Montoro, V. Lemos, M. Abbate and J. M. Rosolen, *Electrochim. Acta*, 2005, **51**, 7-13.
- 87 Y. Nishida, K. Nakane and T. Satoh, *J. Power Sources*, 1997, **68**, 561-564.
- 88 A. Yu, G. Subba Rao and B. V. Chowdari, *Solid State Ionics*, 2000, **135**, 131-135.
- 89 D. Tong, J. Cao, Q. Lai, A. Tang, K. Huang, Y. He and X. Ji, *Mater. Chem. Phys.*, 2006, **100**, 217-223.
- 90 C. Pouillier, L. Croguennec, P. Biensan, P. Willmann and C. Delmas, *J. Electrochem. Soc.*, 2000, **147**, 2061-2069.
- 91 C. Pouillier, L. Croguennec and C. Delmas, *Solid State Ionics*, 2000, **132**, 15-29.
- 92 M. Bianchini, M. Roca-Ayats, P. Hartmann, T. Brezesinski and J. Janek, *Angew. Chemie Int. Ed.*, 2019, **58**, 10434-10458.
- 93 Z. Huang, Z. Wang, X. Zheng, H. Guo, X. Li, Q. Jing and Z. Yang, *Electrochim. Acta*, 2015, **182**, 795-802.
- 94 R. Du, Y. Bi, W. Yang, Z. Peng, M. Liu, Y. Liu, B. Wu, B. Yang, F. Ding and D. Wang, *Ceram. Int.*, 2015, **41**, 7133-7139.
- 95 Y. Li, Q. Su, Q. Han, P. Li, L. Li, C. Xu, X. Cao and G. Cao, *Ceram. Int.*, 2017, **43**, 3483-3488.
- 96 S. A. Needham, G. X. Wang, H. K. Liu, V. A. Drozd and R. S. Liu, *J. Power Sources*, 2007, **174**, 828-831.
- 97 M. N. Ates, Q. Jia, A. Shah, A. Busnaina, S. Mukerjee and K. M. Abraham, *J. Electrochem. Soc.*, 2014, **161**, A290-A301.
- 98 S. Liu, Z. Dang, D. Liu, C. Zhang, T. Huang and A. Yu, *J. Power Sources*, 2018, **396**, 288-296.
- 99 U. H. Kim, D. W. Jun, K. J. Park, Q. Zhang, P. Kaghazchi, D. Aurbach, D. T. Major, G. Goobes, M. Dixit, N. Leifer, C. M. Wang, P. Yan, D. Ahn, K. H. Kim, C. S. Yoon and Y. K. Sun, *Energy Environ. Sci.*, 2018, **11**, 1271-1279.
- 100 C. Li, H. P. Zhang, L. J. Fu, H. Liu, Y. P. Wu, E. Rahm, R. Holze and H. Q. Wu,

- Electrochim. Acta*, 2006, 51, 3872-3883.
- 101 S. K. Hu, G. H. Cheng, M. Y. Cheng, B. J. Hwang and R. Santhanam, *J. Power Sources*, 2009, **188**, 564-569.
- 102 S. G. Woo, J. H. Han, K. J. Kim, J. H. Kim, J. S. Yu and Y. J. Kim, *Electrochim. Acta*, 2015, **153**, 115-121.
- 103 J. W. Kim, J. J. Travis, E. Hu, K. W. Nam, S. C. Kim, C. S. Kang, J. H. Woo, X. Q. Yang, S. M. George, K. H. Oh, S. J. Cho and S. H. Lee, *J. Power Sources*, 2014, **254**, 190-197.
- 104 W. Zhu, X. Huang, T. Liu, Z. Xie, Y. Wang, K. Tian, L. Bu, H. Wang, L. Gao and J. Zhao, *Coatings*, 2019, **9**, 92.
- 105 D. Mohanty, K. Dahlberg, D. M. King, L. A. David, A. S. Sefat, D. L. Wood, C. Daniel, S. Dhar, V. Mahajan, M. Lee and F. Albano, *Sci. Rep.*, 2016, **6**, 26532.
- 106 L. David, K. Dahlberg, D. Mohanty, R. E. Ruther, A. Huq, M. Chi, S. J. An, C. Mao, D. M. King, L. Stevenson and D. L. Wood, *ACS Appl. Energy Mater.*, 2019, **2**, 1308-1313.
- 107 Z. Gong and Y. Yang, *Energy Environ. Sci.*, 2011, **4**, 3223.
- 108 A. Manthiram and J. B. Goodenough, *J. Power Sources*, 1989, **26**, 403-408.
- 109 A. K. Padhi, K. S. Nanjundaswamy and J. B. Goodenough, *J. Electrochem. Soc.*, 1997, **144**, 1188.
- 110 J. Wang and X. Sun, *Energy Environ. Sci.*, 2015, **8**, 1110-1138.
- 111 Y. Zhao, L. Peng, B. Liu and G. Yu, *Nano Lett.*, 2014, **14**, 2849-2853.
- 112 J. Yang, J. Wang, Y. Tang, D. Wang, B. Xiao, X. Li, R. Li, G. Liang, T.-K. Sham and X. Sun, *J. Mater. Chem. A*, 2013, **1**, 7306.
- 113 Y. Wang, Y. Wang, E. Hosono, K. Wang and H. Zhou, *Angew. Chemie Int. Ed.*, 2008, **47**, 7461-7465.
- 114 A. K. Padhi, V. Manivannan and J. B. Goodenough, *J. Electrochem. Soc.*, 1998, **145**, 1518.
- 115 N. Recham, J.-N. Chotard, L. Dupont, C. Delacourt, W. Walker, M. Armand and J.-M. Tarascon, *Nat. Mater.*, 2010, **9**, 68-74.
- 116 M. Ben Yahia, F. Lemoigno, G. Rouse, F. Boucher, J. M. Tarascon and M. L.

- Doublet, *Energy Environ. Sci.*, 2012, **5**, 9584-9594.
- 117 R. Tripathi, G. R. Gardiner, M. S. Islam and L. F. Nazar, *Chem. Mater.*, 2011, **23**, 2278-2284.
- 118 P. Barpanda, M. Ati, B. C. Melot, G. Rousse, J. N. Chotard, M. L. Doublet, M. T. Sougrati, S. A. Corr, J. C. Jumas and J. M. Tarascon, *Nat. Mater.*, 2011, **10**, 772-779.
- 119 T. Mueller, G. Hautier, A. Jain and G. Ceder, *Chem. Mater.*, 2011, **23**, 3854-3862.
- 120 S. Adams and R. Prasada Rao, *Solid State Ionics*, 2011, **184**, 57-61.
- 121 J. Dong, X. Yu, Y. Sun, L. Liu, X. Yang and X. Huang, *J. Power Sources*, 2013, **244**, 716-720.
- 122 R. Tripathi, G. Popov, X. Sun, D. H. Ryan and L. F. Nazar, *J. Mater. Chem. A*, 2013, **1**, 2990.
- 123 M. Ati, M. Sathiya, S. Boulineau, M. Reynaud, A. Abakumov, G. Rousse, B. Melot, G. Van Tendeloo and J.-M. Tarascon, *J. Am. Chem. Soc.*, 2012, **134**, 18380-18387.
- 124 M. Ati, B. C. Melot, J.-N. Chotard, G. Rousse, M. Reynaud and J.-M. Tarascon, *Electrochem. commun.*, 2011, **13**, 1280-1283.
- 125 S. Lee and S. S. Park, *J. Phys. Chem. C*, 2014, **118**, 12642-12648.
- 126 M. D. Tikekar, S. Choudhury, Z. Tu and L. A. Archer, *Nat. Energy*, 2016, **1**, 16114.
- 127 A. Yoshino, K. Sanechika, T. Nakajima. Secondary battery, US Patent 4668595A, May 9, 1986.
- 128 R. Fong, U. von Sacken and J. R. Dahn, *J. Electrochem. Soc.*, 1990, **137**, 2009.
- 129 Y. Nishi, *Chem. Rec.*, 2001, **1**, 406-413.
- 130 V. Palomares, P. Serras, I. Villaluenga, K. B. Hueso, J. Carretero-González and T. Rojo, *Energy Environ. Sci.*, 2012, **5**, 5884.
- 131 N. Yabuuchi, K. Kubota, M. Dahbi and S. Komaba, *Chem. Rev.*, 2014, **114**, 11636-11682.
- 132 J.-J. Braconnier, C. Delmas, C. Fouassier and P. Hagenmuller, *Mater. Res. Bull.*, 1980, **15**, 1797-1804.
- 133 C. Delmas, J.-J. Braconnier, C. Fouassier and P. Hagenmuller, *Solid State Ionics*,

- 1981, 3-4, 165-169.
- 134 L. W. Shacklette, T. R. Jow and L. Townsend, *J. Electrochem. Soc.*, 1988, **135**, 2669.
- 135 S.-M. Oh, S.-T. Myung, J. Hassoun, B. Scrosati and Y.-K. Sun, *Electrochem. commun.*, 2012, **22**, 149-152.
- 136 Y. Zhu, Y. Xu, Y. Liu, C. Luo and C. Wang, *Nanoscale*, 2013, **5**, 780-787.
- 137 J. Kim, D.-H. Seo, H. Kim, I. Park, J.-K. Yoo, S.-K. Jung, Y.-U. Park, W. A. Goddard III and K. Kang, *Energy Environ. Sci.*, 2015, **8**, 540-545.
- 138 N. Recham, J. N. Chotard, L. Dupont, K. Djellab, M. Armand and J. M. Tarascon, *J. Electrochem. Soc.*, 2009, **156**, A993
- 139 R. Tripathi, S. M. Wood, M. S. Islam and L. F. Nazar, *Energy Environ. Sci.*, 2013, **6**, 2257-2264.
- 140 A. S. Aricò, P. Bruce, B. Scrosati, J.-M. Tarascon and W. van Schalkwijk, *Nat. Mater.*, 2005, **4**, 366-377.
- 141 A. E. Danks, S. R. Hall and Z. Schnepp, *Mater. Horizons*, 2016, **3**, 91-112.
- 142 C. J. Brinker and G. W. Scherer, *Sol-gel science : the physics and chemistry of sol-gel processing*, Academic Press, 1990.
- 143 A. Cannavale, F. Fiorito, M. Manca, G. Tortorici, R. Cingolani and G. Gigli, *Build. Environ.*, 2010, **45**, 1233-1243.
- 144 M. Kakihana, *J. Sol-Gel Sci. Technol.*, 1996, **6**, 7-55.
- 145 H. Liu, Y. P. Wu, E. Rahm, R. Holze and H. Q. Wu, *J. Solid State Electrochem.*, 2004, **8**, 450-466.
- 146 N. Kızıldağ-Yavuz, M. Herklotz, A. M. Hashem, H. M. Abuzeid, B. Schwarz, H. Ehrenberg, A. Mauger and C. M. Julien, *Electrochim. Acta*, 2013, **113**, 313-321.
- 147 D. E. Clark, D. C. Folz and J. K. West, *Mater. Sci. Eng. A*, 2000, **287**, 153-158.
- 148 D. M. P. Mingos and D. R. Baghurst, *Chem. Soc. Rev.*, 1991, **20**, 1.
- 149 B. I., O. V. and U. Ortiz, in *The Development and Application of Microwave Heating*, InTech, 2012.
- 150 H. J. Kitchen, S. R. Vallance, J. L. Kennedy, N. Tapia-Ruiz, L. Carassiti, A.

- Harrison, A. G. Whittaker, T. D. Drysdale, S. W. Kingman and D. H. Gregory, *Chem. Rev.*, 2014, **114**, 1170-1206.
- 151 J.-S. Schanche, *Mol. Divers.*, 2003, **7**, 291-298.
- 152 I. Bilecka, A. Hintennach, I. Djerdj, P. Novák and M. Niederberger, *J. Mater. Chem.*, 2009, **19**, 5125.
- 153 G. Assat and A. Manthiram, *Inorg. Chem.*, 2015, **54**, 10015-10022.
- 154 T. Muraliganth, K. R. Stroukoff and A. Manthiram, *Chem. Mater.*, 2010, **22**, 5754-5761.
- 155 M. Oghbaei and O. Mirzaee, *J. Alloys Compd.*, 2010, **494**, 175-189.
- 156 M. Amores, T. E. Ashton, P. J. Baker, E. J. Cussen and S. A. Corr, *J. Mater. Chem. A*, 2016, **4**, 1729-1736.
- 157 M. Amores, S. A. Corr and E. J. Cussen, *J. Electrochem. Soc.*, 2017, **164**, A6395-A6400.
- 158 M. Amores, P. J. Baker, E. J. Cussen and S. A. Corr, *Chem. Commun.*, 2018, **54**, 10040-10043.
- 159 M. Amores, PhD Thesis, The University of Glasgow, 2018.
- 160 V. K. Pecharsky and P. Y. Zavalij, *Fundamentals of powder diffraction and structural characterization of materials*, Springer US, 2005.
- 161 R. E. Dinnebier and S. J. L. Billinge, in *Powder Diffraction*, Royal Society of Chemistry, Cambridge, 2008, 1-19.
- 162 D. S. Sivia, *Elementary scattering theory: for X-ray and neutron users*, Oxford University Press, 2011.
- 163 A. M. Balagurov, I. A. Bobrikov, N. Y. Samoylova, O. A. Drozhzhin and E. V Antipov, *Russ. Chem. Rev.*, 2014, **83**, 1120-1134.
- 164 V. F. Sears, *Neutron News*, 1992, **3**, 26-37.
- 165 R. I. Smith, S. Hull, M. G. Tucker, H. Y. Playford, D. J. McPhail, S. P. Waller and S. T. Norberg, *Rev. Sci. Instrum.*, 2019, **90**, 115101.
- 166 H. M. Rietveld and IUCr, *J. Appl. Crystallogr.*, 1969, **2**, 65-71.
- 167 B. H. Toby, *Powder Diffr.*, 2006, **21**, 67-70.

- 168 B. H. Toby, R. B. Von Dreele and IUCr, *J. Appl. Crystallogr.*, 2013, **46**, 544-549.
- 169 A. K. Cheetham and A. L. Goodwin, *Nat. Mater.*, 2014, **13**, 760-762.
- 170 A. K. Soper, Rutherford Appleton Laboratory Technical Report RAL-TR-2011-013.
- 171 C. L. Farrow, P. Juhas, J. W. Liu, D. Bryndin, E. S. Božin, J. Bloch, T. Proffen and S. J. L. Billinge, *J. Phys. Condens. Matter*, 2007, **19**, 335219.
- 172 J. Yano and V. K. Yachandra, *Photosynth. Res.*, 2009, **102**, 241-254.
- 173 O. J. Borkiewicz, B. Shyam, K. M. Wiaderek, C. Kurtz, P. J. Chupas and K. W. Chapman, *J. Appl. Crystallogr.*, 2012, **45**, 1261-1269.
- 174 B. Ravel and M. Newville, in *Journal of Synchrotron Radiation*, International Union of Crystallography, 2005, **12**, 537-541.
- 175 M. Månsson and J. Sugiyama, *Phys. Scr.*, 2013, **88**, 068509.
- 176 I. McClelland, B. Johnston, P. J. Baker, M. Amores, E. J. Cussen and S. A. Corr, *Annu. Rev. Mater. Res.*, 2020, **50**, 371-393.
- 177 S. J. Blundell, *Contemp. Phys.*, 1999, **40**, 175-192.
- 178 F. Pratt, *Phys. B Condens. Matter*, 2000, **289-290**, 710-714.
- 179 T. E. Ashton, J. V. Laveda, D. A. MacLaren, P. J. Baker, A. Porch, M. O. Jones and S. A. Corr, *J. Mater. Chem. A*, 2014, **2**, 6238-6245.
- 180 J. V. Laveda, B. Johnston, G. W. Paterson, P. J. Baker, M. G. Tucker, H. Y. Playford, K. M. Ø. Jensen, S. J. L. Billinge and S. A. Corr, *J. Mater. Chem. A*, 2018, **6**, 127-137.
- 181 J. Sugiyama, K. Mukai, Y. Ikedo, H. Nozaki, M. Månsson and I. Watanabe, *Phys. Rev. Lett.*, 2009, **103**, 147601.
- 182 M. Månsson, H. Nozaki, J. M. Wikberg, K. Pra, Y. Sassa, M. Dahbi, K. Kamazawa, K. Sedlak, I. Watanabe and J. Sugiyama, *J. Phys. Conf. Ser.*, 2014, **551**, 012037.
- 183 J. Sugiyama, H. Nozaki, I. Umegaki, M. Harada, Y. Higuchi, E. J. Ansaldo, J. H. Brewer, Y. Miyake, G. Kobayashi and R. Kanno, *J. Phys. Conf. Ser.*, 2014, **551**, 012012.
- 184 I. Umegaki, H. Nozaki, M. Harada, M. Månsson, H. Sakurai, I. Kawasaki, I. Watanabe and J. Sugiyama, *Proc. 14th Int. Conf. on Muon Spin Rotation, Relaxation and Resonance ( $\mu$ SR2017)*, *JPS Conf. Proc.*, 2018, **21**, 011018.

- 185 M. Amores, P. J. Baker, E. J. Cussen and S. A. Corr, *Chem. Commun.*, 2018, **54**, 10040-10043.
- 186 J. S. Möller, P. Bonfà, D. Ceresoli, F. Bernardini, S. J. Blundell, T. Lancaster, R. De Renzi, N. Marzari, I. Watanabe, S. Sulaiman and M. I. Mohamed-Ibrahim, *Phys. Scr.*, 2013, **88**, 068510.
- 187 J. S. Möller, D. Ceresoli, T. Lancaster, N. Marzari and S. J. Blundell, *Phys. Rev. B - Condens. Matter Mater. Phys.*, 2013, **87**, 121108.
- 188 R. Tripathi, T. N. Ramesh, B. L. Ellis and L. F. Nazar, *Angew. Chemie Int. Ed.*, 2010, **49**, 8738-8742.
- 189 B. C. Melot, G. Rouse, J.-N. Chotard, M. Ati, J. Rodríguez-Carvajal, M. C. Kemei and J.-M. Tarascon, *Chem. Mater.*, 2011, **23**, 2922-2930.
- 190 P. Barpanda, L. Lander, S. Nishimura and A. Yamada, *Adv. Energy Mater.*, 2018, **8**, 1703055.
- 191 P. Moreau, D. Guyomard, J. Gaubicher and F. Boucher, *Chem. Mater.*, 2010, **22**, 4126-4128.
- 192 T. Honma, T. Togashi, N. Ito and T. Komatsu, *J. Ceram. Soc. Japan*, 2012, **120**, 344-346.
- 193 K.-H. Ha, S. H. Woo, D. Mok, N.-S. Choi, Y. Park, S. M. Oh, Y. Kim, J. Kim, J. Lee, L. F. Nazar and K. T. Lee, *Adv. Energy Mater.*, 2013, **3**, 770-776.
- 194 H. Kim, I. Park, D.-H. Seo, S. Lee, S.-W. Kim, W. J. Kwon, Y.-U. Park, C. S. Kim, S. Jeon and K. Kang, *J. Am. Chem. Soc.*, 2012, **134**, 10369-10372.
- 195 R. A. Shakoor, D. H. Seo, H. Kim, Y. U. Park, J. Kim, S. W. Kim, H. Gwon, S. Lee and K. Kang, *J. Mater. Chem.*, 2012, **22**, 20535-20541.
- 196 K. Chihara, A. Kitajou, I. D. Gocheva, S. Okada and J. I. Yamaki, *J. Power Sources*, 2013, **227**, 80-85.
- 197 Y. Kawabe, N. Yabuuchi, M. Kajiyama, N. Fukuhara, T. Inamasu, R. Okuyama, I. Nakai and S. Komaba, *Electrochem. commun.*, 2011, **13**, 1225-1228.
- 198 L. Sharma, P. K. Nayak, E. de la Llave, H. Chen, S. Adams, D. Aurbach and P. Barpanda, *ACS Appl. Mater. Interfaces*, 2017, **9**, 34961-34969.
- 199 X. Liu, X. Wang, A. Iyo, H. Yu, D. Li and H. Zhou, *J. Mater. Chem. A*, 2014, **2**,

14822-14826.

- 200 M. Månsson, I. Umegaki, H. Nozaki, Y. Higuchi, I. Kawasaki, I. Watanabe, H. Sakurai and J. Sugiyama, *J. Phys. Conf. Ser.*, 2014, **551**, 012035.
- 201 B. L. Ellis, W. R. Michael Makahnouk, W. N. Rowan-Weetaluktuk, D. H. Ryan and L. F. Nazar, *Chem. Mater.*, 2010, **22**, 1059-1070.
- 202 C. M. Burba and R. Frech, *Spectrochim. Acta - Part A Mol. Biomol. Spectrosc.*, 2006, **65**, 44-50.
- 203 Y. Liu, N. Zhang, F. Wang, X. Liu, L. Jiao and L.-Z. Fan, *Adv. Funct. Mater.*, 2018, **28**, 1801917.
- 204 J. Hwang, K. Matsumoto, T. Nohira and R. Hagiwara, *Electrochemistry*, 2017, **85**, 675-679.
- 205 J. Hwang, K. Matsumoto, Y. Orikasa, M. Katayama, Y. Inada, T. Nohira and R. Hagiwara, *J. Power Sources*, 2018, **377**, 80-86.
- 206 J. Vidal Laveda, PhD Thesis, The University of Glasgow, 2017.
- 207 A. Keren, *Phys. Rev. B*, 1994, **50**, 10039-10042.
- 208 P. Hou, J. Yin, M. Ding, J. Huang and X. Xu, *Small*, 2017, **13**, 1701802.
- 209 A. Manthiram, J. C. Knight, S. T. Myung, S. M. Oh and Y. K. Sun, *Adv. Energy Mater.*, 2016, **6**, 1501010.
- 210 K.-S. Lee, S.-T. Myung, K. Amine, H. Yashiro and Y.-K. Sun, *J. Electrochem. Soc.*, 2007, **154**, A971.
- 211 B. Huang, M. Wang, Z. Zhao, L. Chen and Y. Gu, *J. Alloys Compd.*, 2019, **810**, 151800.
- 212 S. W. Woo, S. T. Myung, H. Bang, D. W. Kim and Y. K. Sun, *Electrochim. Acta*, 2009, **54**, 3851-3856.
- 213 F. Wu, J. Tian, Y. Su, J. Wang, C. Zhang, L. Bao, T. He, J. Li and S. Chen, *ACS Appl. Mater. Interfaces*, 2015, **7**, 7702-7708.
- 214 L. J. Li, X. H. Li, Z. X. Wang, H. J. Guo, P. Yue, W. Chen and L. Wu, *Powder Technol.*, 2011, **206**, 353-357.
- 215 L. J. Li, X. H. Li, Z. X. Wang, L. Wu, J. C. Zheng and J. H. Li, *Trans. Nonferrous Met. Soc. China (English Ed.)*, 2010, **20**, s279-s282.

- 216 X. Zheng, X. Li, B. Zhang, Z. Wang, H. Guo, Z. Huang, G. Yan, D. Wang and Y. Xu, *Ceram. Int.*, 2016, **42**, 644-649.
- 217 K. Heo, J.-S. Lee, H.-S. Kim, M.-Y. Kim, H. Jeong, J. Kim and J. Lim, *J. Electrochem. Soc.*, 2018, **165**, A2955-A2960.
- 218 Y. Huang, Z. X. Wang, X. H. Li, H. J. Guo and J. X. Wang, *Trans. Nonferrous Met. Soc. China (English Ed.)*, 2015, **25**, 2253-2259.
- 219 E. E. Levin, J. H. Grebenkemper, T. M. Pollock and R. Seshadri, *Chem. Mater.*, 2019, **31**, 7151-7159.
- 220 S. C. Yin, Y. H. Rho, I. Swainson and L. F. Nazar, *Chem. Mater.*, 2006, **18**, 1901-1910.
- 221 K. M. Shaju, G. V. Subba Rao and B. V. R. Chowdari, *Electrochim. Acta*, 2002, **48**, 145-151.
- 222 M. Ma, N. A. Chernova, B. H. Toby, P. Y. Zavalij and M. S. Whittingham, *J. Power Sources*, 2007, **165**, 517-534.
- 223 S. B. Schougaard, J. Bréger, M. Jiang, C. P. Grey and J. B. Goodenough, *Adv. Mater.*, 2006, **18**, 905-909.
- 224 Y. Wang, J. Roller and R. Maric, *ACS Omega*, 2018, **3**, 3966-3973.
- 225 Y. W. Tsai, B. J. Hwang, G. Ceder, H. S. Sheu, D. G. Liu and J. F. Lee, *Chem. Mater.*, 2005, **17**, 3191-3199.
- 226 Y. Qian, P. Niehoff, M. Börner, M. Grütze, X. Mönnighoff, P. Behrends, S. Nowak, M. Winter and F. M. Schappacher, *J. Power Sources*, 2016, **329**, 31-40.
- 227 J. Xiao, N. A. Chernova and M. S. Whittingham, *Chem. Mater.*, 2008, **20**, 7454-7464.
- 228 E. Zhao, L. Fang, M. Chen, D. Chen, Q. Huang, Z. Hu, Q. B. Yan, M. Wu and X. Xiao, *J. Mater. Chem. A*, 2017, **5**, 1679-1686.
- 229 Z. Li, N. A. Chernova, M. Roppolo, S. Upreti, C. Petersburg, F. M. Alamgir and M. S. Whittingham, *J. Electrochem. Soc.*, 2011, **158**, A516.
- 230 H. Li, J. Li, X. Ma and J. R. Dahn, *J. Electrochem. Soc.*, 2018, **165**, A1038-A1045.
- 231 M. S. Idris and A. R. West, *J. Electrochem. Soc.*, 2012, **159**, A396-A401.
- 232 S. B. Schougaard, J. Bréger, M. Jiang, C. P. Grey and J. B. Goodenough, *Adv.*

- Mater.*, 2006, **18**, 905-909.
- 233 M. Chen, E. Zhao, D. Chen, M. Wu, S. Han, Q. Huang, L. Yang, X. Xiao and Z. Hu, *Inorg. Chem.*, 2017, **56**, 8355-8362.
- 234 L. Wang, J. Li, X. He, W. Pu, C. Wan and C. Jiang, *J. Solid State Electrochem.*, 2009, **13**, 1157-1164.
- 235 Y. Bi, W. Yang, R. Du, J. Zhou, M. Liu, Y. Liu and D. Wang, *J. Power Sources*, 2015, **283**, 211-218.
- 236 S. W. Lee, H. Kim, M. S. Kim, H. C. Youn, K. Kang, B. W. Cho, K. C. Roh and K. B. Kim, *J. Power Sources*, 2016, **315**, 261-268.
- 237 J. Sugiyama, K. Mukai, M. Harada, H. Nozaki, K. Miwa, T. Shiotsuki, Y. Shindo, S. R. Giblin and J. S. Lord, *Phys. Chem. Chem. Phys.*, 2013, **15**, 10402-10412.
- 238 Y. Li, F. Lai, X. Zhang, H. Wang, Z. Chen, X. He and Q. Li, *J. Taiwan Inst. Chem. Eng.*, 2019, **102**, 225-232.
- 239 W. Ahn, S. N. Lim, K. N. Jung, S. H. Yeon, K. B. Kim, H. S. Song and K. H. Shin, *J. Alloys Compd.*, 2014, **609**, 143-149.
- 240 J. W. Kim and H. G. Lee, *Metall. Mater. Trans. B Process Metall. Mater. Process. Sci.*, 2001, **32**, 17-24.
- 241 X. Zhang, A. Mauger, Q. Lu, H. Groult, L. Perrigaud, F. Gendron and C. M. Julien, *Electrochim. Acta*, 2010, **55**, 6440-6449.
- 242 J. Li, L. E. Downie, L. Ma, W. Qiu and J. R. Dahn, *J. Electrochem. Soc.*, 2015, **162**, A1401-A1408.
- 243 J. Li, A. R. Cameron, H. Li, S. Glazier, D. Xiong, M. Chatzidakis, J. Allen, G. A. Botton and J. R. Dahn, *J. Electrochem. Soc.*, 2017, **164**, A1534-A1544.
- 244 W. Liu, P. Oh, X. Liu, M. J. Lee, W. Cho, S. Chae, Y. Kim and J. Cho, *Angew. Chemie - Int. Ed.*, 2015, **54**, 4440-4457.
- 245 T. Li, X.-Z. Yuan, L. Zhang, D. Song, K. Shi and C. Bock, *Electrochem. Energy Rev.*, 2020, **3**, 43-80.
- 246 S. T. Myung, K. Izumi, S. Komaba, Y. K. Sun, H. Yashiro and N. Kumagai, *Chem. Mater.*, 2005, **17**, 3695-3704.
- 247 Y. Su, S. Cui, Z. Zhuo, W. Yang, X. Wang and F. Pan, *ACS Appl. Mater. Interfaces*,

2015, **7**, 25105-25112.

- 248 H. V. Ramasamy, S. Sinha, J. Park, M. Gong, V. Aravindan, J. Heo and Y. S. Lee, *J. Electrochem. Sci. Technol.*, 2019, **10**, 196-205.
- 249 Y. Il Jang, B. Huang, H. Wang, G. R. Maskaly, G. Ceder, D. R. Sadoway, Y. M. Chiang, H. Liu and H. Tamura, *J. Power Sources*, 1999, **81-82**, 589-593.
- 250 L. Croguennec, E. Suard, P. Willmann and C. Delmas, *Chem. Mater.*, 2002, **14**, 2149-2157.
- 251 C. Poullierie, L. Croguennec, P. Biensan, P. Willmann and C. Delmas, *J. Electrochem. Soc.*, 2000, **147**, 2061.
- 252 P. Hou, H. Zhang, Z. Zi, L. Zhang and X. Xu, *J. Mater. Chem. A*, 2017, **5**, 4254-4279.
- 253 D. Y. Wang, J. Xia, L. Ma, K. J. Nelson, J. E. Harlow, D. Xiong, L. E. Downie, R. Petibon, J. C. Burns, A. Xiao, W. M. Lamanna and J. R. Dahn, *J. Electrochem. Soc.*, 2014, **161**, A1818-A1827.
- 254 C. Täubert, M. Fleischhammer, M. Wohlfahrt-Mehrens, U. Wietelmann and T. Buhrmester, *J. Electrochem. Soc.*, 2010, **157**, A721.
- 255 X. Zuo, C. Fan, J. Liu, X. Xiao, J. Wu and J. Nan, *J. Electrochem. Soc.*, 2013, **160**, A1199-A1204.
- 256 J. Y. Liao and A. Manthiram, *J. Power Sources*, 2015, **282**, 429-436.
- 257 S. M. Lee, S. H. Oh, J. P. Ahn, W. Il Cho and H. Jang, *J. Power Sources*, 2006, **159**, 1334-1339.
- 258 E. Zhecheva, R. Stoyanova, G. Tyuliev, K. Tenchev, M. Mladenov and S. Vassilev, *Solid State Sci.*, 2003, **5**, 711-720.
- 259 G. T. K. Fey, P. Muralidharan, C. Z. Lu and Y. Da Cho, *Solid State Ionics*, 2005, **176**, 2759-2767.
- 260 B. V. R. Chowdari, G. V. Subba Rao and S. Y. Chow, *J. Solid State Electrochem.*, 2002, **6**, 565-567.
- 261 K. S. Tan, M. V. Reddy, G. V. S. Rao and B. V. R. Chowdari, *J. Power Sources*, 2005, **141**, 129-142.
- 262 Y. Kim and J. Cho, *J. Electrochem. Soc.*, 2007, **154**, A495.

- 263 D. J. Lee, B. Scrosati and Y. K. Sun, *J. Power Sources*, 2011, **196**, 7742-7746.
- 264 H. B. Kim, B. C. Park, S. T. Myung, K. Amine, J. Prakash and Y. K. Sun, *J. Power Sources*, 2008, **179**, 347-350.
- 265 Y.-K. Sun, S.-T. Myung, B.-C. Park and H. Yashiro, *J. Electrochem. Soc.*, 2008, **155**, A705.
- 266 S. J. Shi, J. P. Tu, Y. J. Mai, Y. Q. Zhang, Y. Y. Tang and X. L. Wang, *Electrochim. Acta*, 2012, **83**, 105-112.
- 267 Z. Feng, R. Rajagopalan, D. Sun, Y. Tang and H. Wang, *Chem. Eng. J.*, 2020, **382**, 122959.
- 268 H. Xie, K. Du, G. Hu, Z. Peng and Y. Cao, *J. Phys. Chem. C*, 2016, **120**, 3235-3241.
- 269 T. Weigel, F. Schipper, E. M. Erickson, F. A. Susai, B. Markovsky and D. Aurbach, *ACS Energy Lett.*, 2019, **4**, 508-516.
- 270 Q. Xie, W. Li and A. Manthiram, *Chem. Mater.*, 2019, **31**, 938-946.
- 271 S. H. Park, K. S. Park, Y. Sun Kook, K. S. Nahm, Y. S. Lee and M. Yoshio, *Electrochim. Acta*, 2001, **46**, 1215-1222.
- 272 C. H. Chen, J. Liu, M. E. Stoll, G. Henriksen, D. R. Vissers and K. Amine, *J. Power Sources*, 2004, **128**, 278-285.
- 273 K. C. Kam and M. M. Doeff, *J. Mater. Chem.*, 2011, **21**, 9991-9993.
- 274 Y. Oh, D. Ahn, S. Nam and B. Park, *J. Solid State Electrochem.*, 2010, **14**, 1235-1240.
- 275 S. Hildebrand, C. Vollmer, M. Winter and F. M. Schappacher, *J. Electrochem. Soc.*, 2017, **164**, A2190-A2198.
- 276 E. El-Shereafy, M. M. Abousekkina, A. Mashaly and M. El-Ashry, *J. Radioanal. Nucl. Chem.*, 1998, **237**, 183-186.
- 277 B. Pacewska and M. Keshr, *Thermochim. Acta*, 2002, **385**, 73-80.
- 278 H. H. Ryu, K. J. Park, C. S. Yoon and Y. K. Sun, *Chem. Mater.*, 2018, **30**, 1155-1163.
- 279 K. Kubobuchi, M. Mogi, M. Matsumoto, T. Baba, C. Yogi, C. Sato, T. Yamamoto, T. Mizoguchi and H. Imai, *J. Appl. Phys.*, 2016, **120**, 142125.

- 280 M. Balasubramanian, X. Sun, X. Q. Yang and J. McBreen, *J. Electrochem. Soc.*, 2000, **147**, 2903.
- 281 J. Bréger, N. Dupré, P. J. Chupas, P. L. Lee, T. Proffen, J. B. Parise and C. P. Grey, *J. Am. Chem. Soc.*, 2005, **127**, 7529-7537.
- 282 K. Min, S. W. Seo, Y. Y. Song, H. S. Lee and E. Cho, *Phys. Chem. Chem. Phys.*, 2017, **19**, 1762-1769.
- 283 S. Muto, K. Tatsumi, Y. Kojima, H. Oka, H. Kondo, K. Horibuchi and Y. Ukyo, *J. Power Sources*, 2012, **205**, 449-455.
- 284 L. Mu, Z. Yang, L. Tao, C. K. Waters, Z. Xu, L. Li, S. Sainio, Y. Du, H. L. Xin, D. Nordlund and F. Lin, *J. Mater. Chem. A*, 2020, **8**, 17487-17497.
- 285 W. Xu, A. Read, P. K. Koech, D. Hu, C. Wang, J. Xiao, A. B. Padmaperuma, G. L. Graff, J. Liu and J. G. Zhang, *J. Mater. Chem.*, 2012, **22**, 4032-4039.
- 286 J.-M. Tarascon, *ChemSusChem*, 2008, **1**, 777-779.
- 287 M. Cariello, B. Johnston, M. Bhosale, M. Amores, E. Wilson, L. J. McCarron, C. Wilson, S. A. Corr and G. Cooke, *ACS Appl. Energy Mater.*, 2020, **3**, 8302-8308.
- 288 H. Ohshiro, K. Mitsui, N. Ando, Y. Ohsawa, W. Koinuma, H. Takahashi, S. I. Kondo, T. Nabeshima and Y. Yano, *J. Am. Chem. Soc.*, 2001, **123**, 2478-2486.

## 7 Appendix

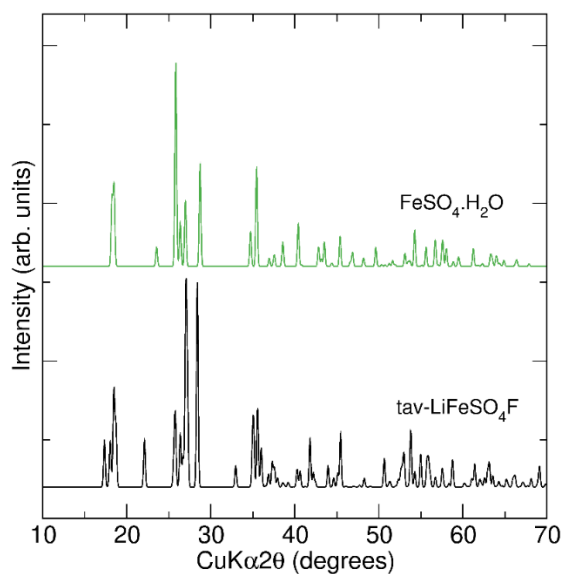


**Figure 7.1** ICSD reference patterns for tavorite LiFeSO<sub>4</sub>F (collection code 182944) and FeSO<sub>4</sub>·H<sub>2</sub>O (collection code 71345) showing the similarities between both patterns that can be attributed to the similar structures exhibited by both materials.

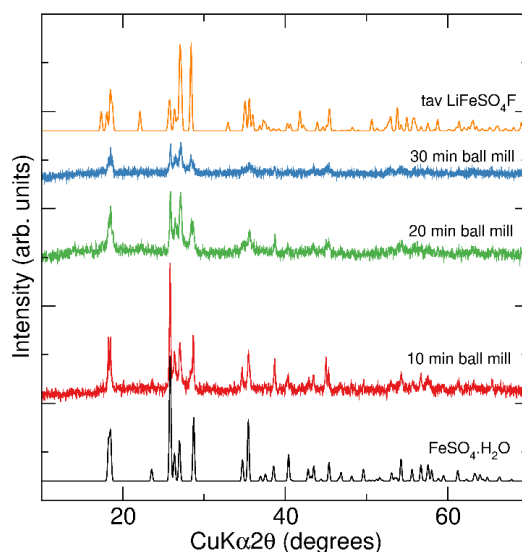


**Figure 7.2** PXR patterns collected for the product formed following the microwave assisted solvothermal synthesis of FeSO<sub>4</sub>·H<sub>2</sub>O and LiF (1:1.1 molar ratio) for 10 mins at 230 °C showing how ball milling time of the precursors affects the phase of the final product. Reactions were carried out in 5 mL of TEG in a 10 mL quartz vessel. Longer ball milling times of 30 minutes seem to form a product more like tavorite LiFeSO<sub>4</sub>F but with a much weaker intensity (PXR data was collected on samples of similar mass and set-up) indicating a degree of amorphous product as a result of the ball milling procedure.

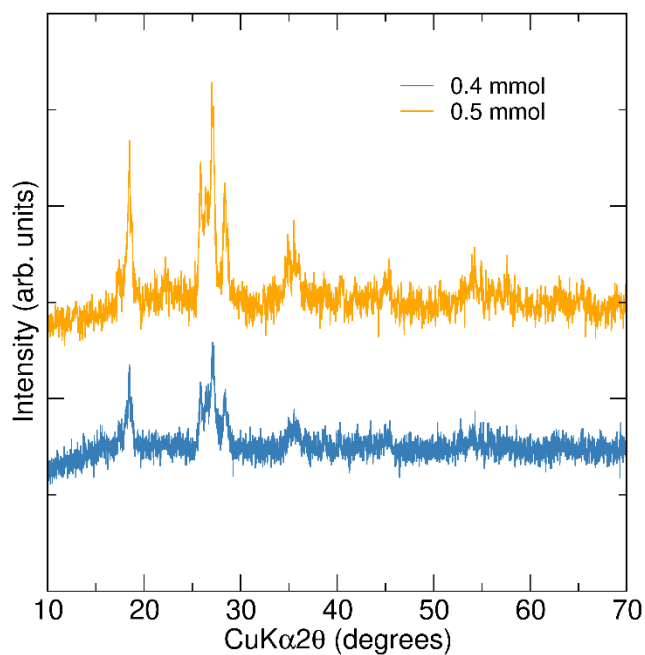


**Figure 7.3** PXR D patterns obtained for tavorite  $\text{LiFeSO}_4\text{F}$  obtained from a 10 minute,  $230\text{ }^\circ\text{C}$  microwave reactant with 0.4 mmol and 0.5 mmol of precursors used in the ball milling step and the final reaction. Larger amounts of reactants in the ball mill failed to mix together and would result in no reaction taking place under microwave heating. The ability to scale a successful reaction to 0.5 mmol helped with the preparation of 1 g for muon measurements.

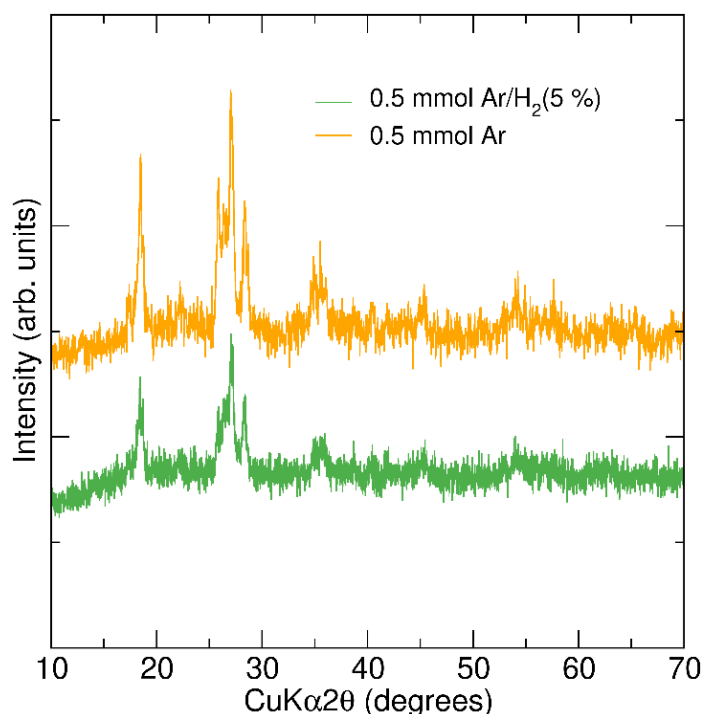


**Figure 7.4** PXR D patterns obtained from tavorite  $\text{LiFeSO}_4\text{F}$  obtained from a 10 minute,  $230\text{ }^\circ\text{C}$  microwave reactant with 0.5 mmol of precursors but different atmospheres during the dehydration step of  $\text{FeSO}_4\cdot 7\text{H}_2\text{O}$ . Similar masses of powder were used in the PXR D data collection and so peak intensities correlate to the crystallinity of the final material.

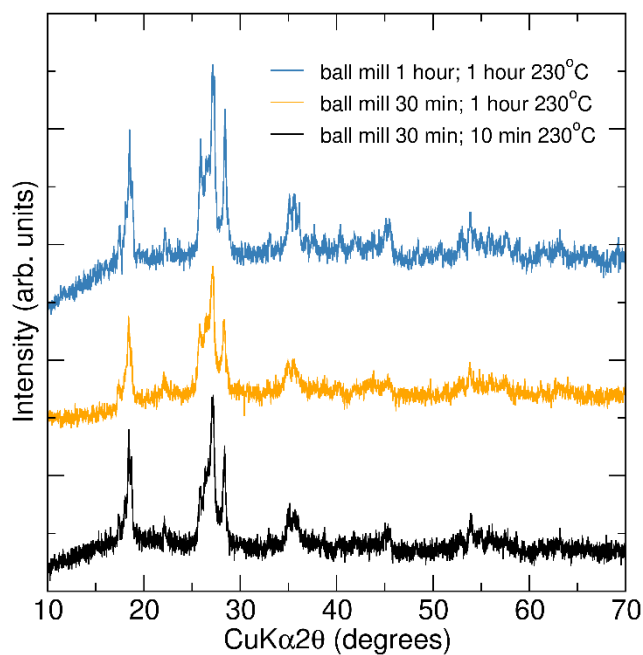


**Figure 7.5** PXR D patterns obtained for microwave synthesised tavorite  $\text{LiFeSO}_4\text{F}$  showing that an improved product can be formed with ball milling times of 30 mins and a reaction time of 1 hour at  $230^\circ\text{C}$ .

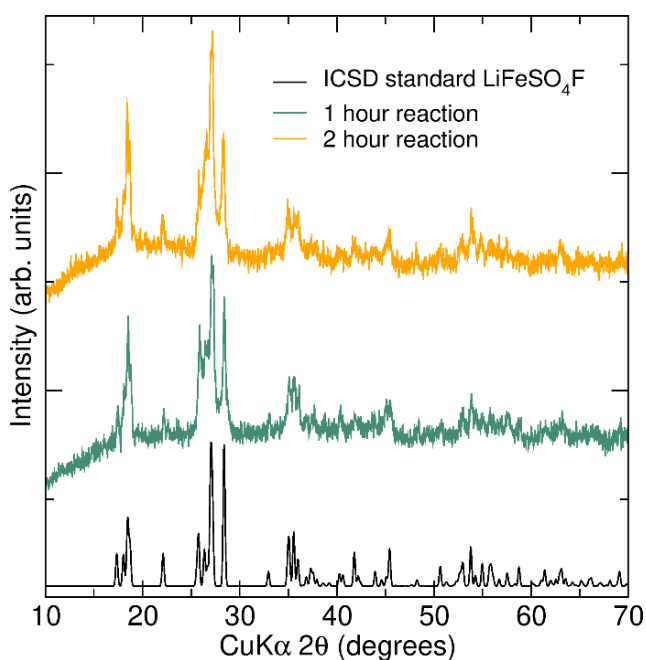


**Figure 7.6** PXR D patterns for tavorite phase  $\text{LiFePO}_4\text{F}$  using Ar in the initial dehydration of  $\text{FeSO}_4 \cdot 7\text{H}_2\text{O}$ , 0.5 mmol of reactants ball milled for 1 hour and then subject to microwave solvothermal heating in 5 ml of TEG in a 10 ml quartz vessel for reaction times of 1 hour and 2 hours. The peak intensities for  $2\theta$  values between  $25 - 30^\circ$  match better with those of the reference pattern for the sample reacted for 1 hour. Therefore, the 1-hour sample was carried forward for batch synthesis for muon measurements.

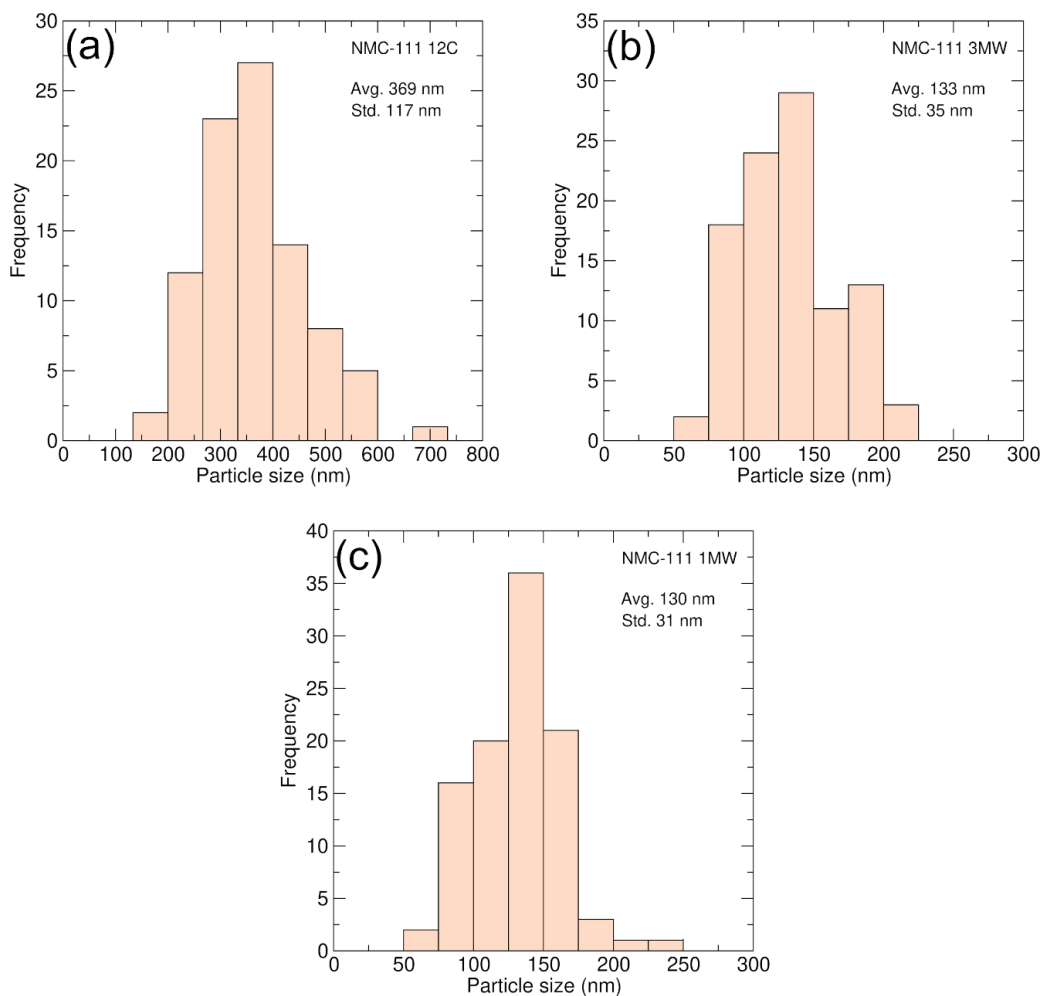


**Figure 7.7** Particle size distributions of NMC-111 prepared by (a) a conventional heating method (12 hours at 850 °C) and a microwave assisted method at 850 °C for (b) 3 hours and (c) 1 hour. Particle sizes were calculated for 100 particles.

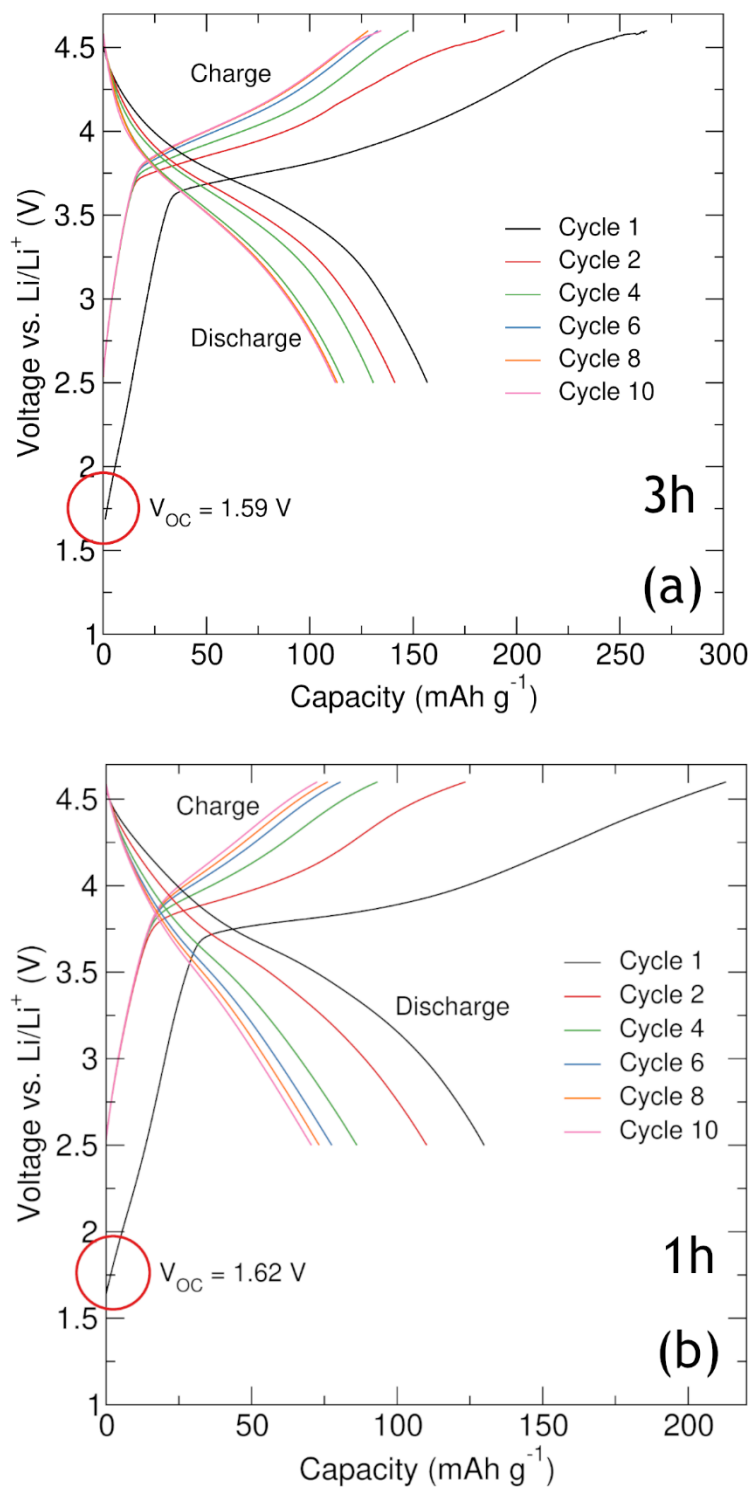


**Figure 7.8** Expanded plot of the charge and discharge profiles for NMC-111 synthesised by microwave-assisted method with reaction times of (a) 3 hours and (b) 1 hour showing the low open circuit voltages of 1.59 V and 1.62 V respectively obtained when the cell was initially connected to the potentiostat.

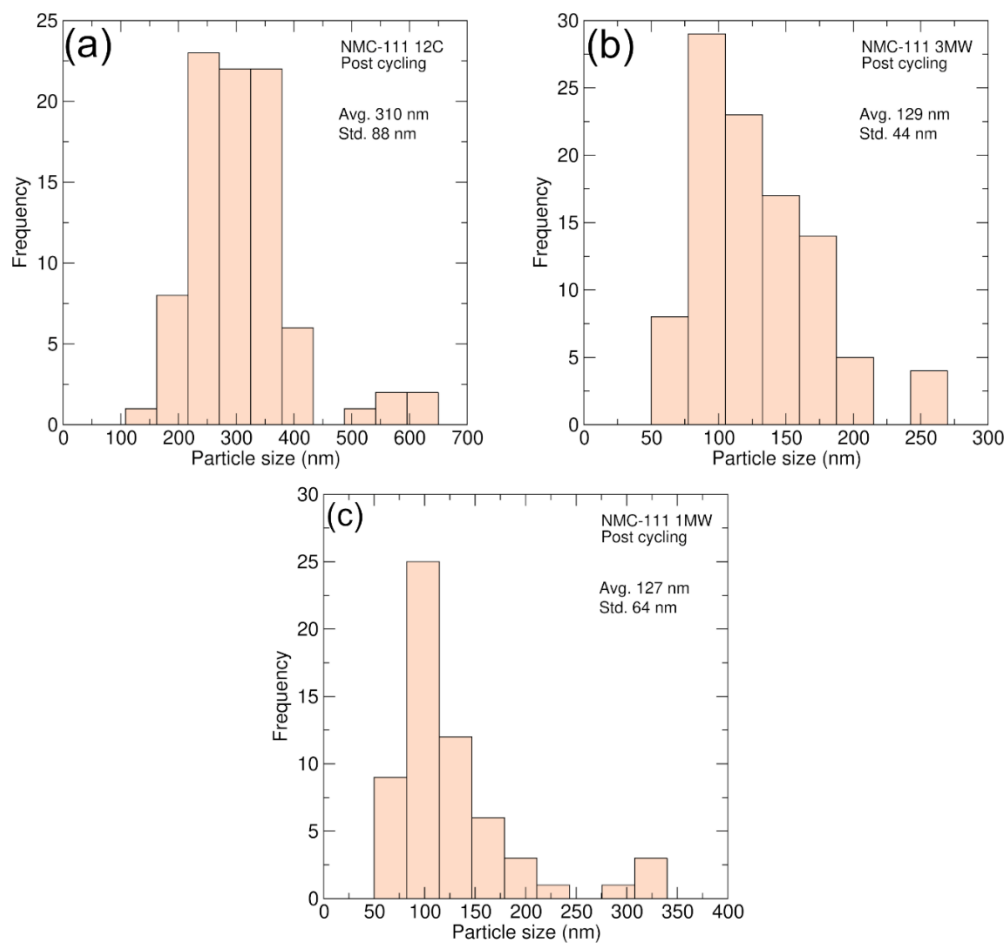


**Figure 7.9** Particle size distributions of NMC-111 after cycling, prepared by (a) a conventional heating method (12 hours at 850 °C) and a microwave assisted method at 850 °C for (b) 3 hours and (c) 1 hour. Particle sizes were calculated for 100 particles.

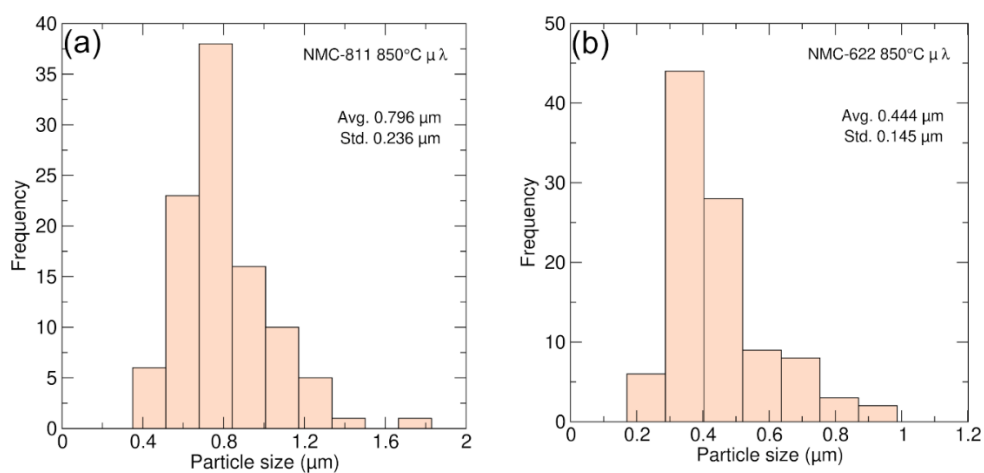


**Figure 7.10** Particle size distributions of (a) NMC-811 and (b) NMC-622 prepared by a microwave-assisted sol-gel method at 850 °C for 2 hours. Particle sizes were calculated for 100 particles.

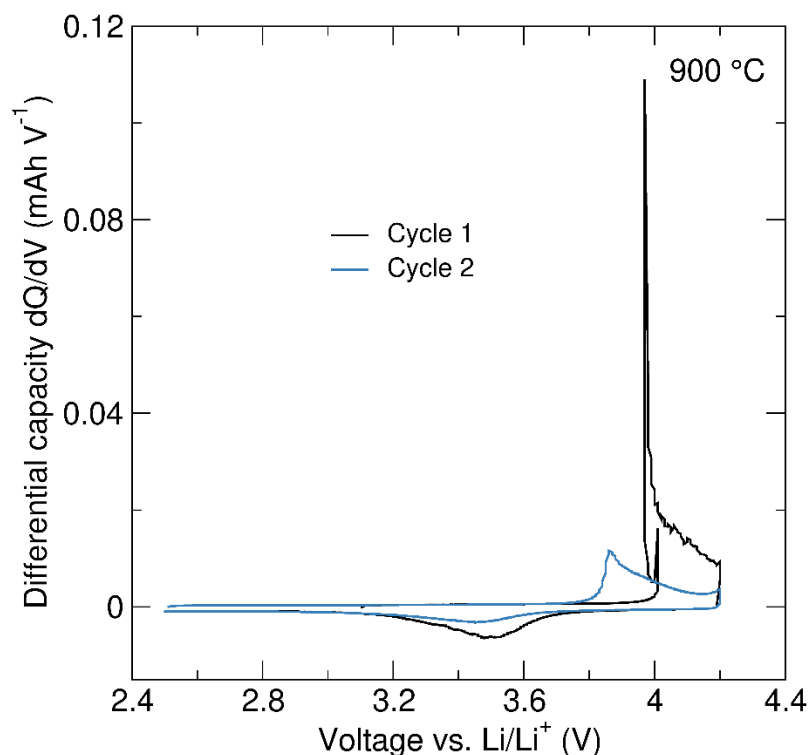


**Figure 7.11** Differential capacity ( $dQ/dV$ ) profiles for microwave synthesised NMC-811 at 900 °C over the first two cycles showing the intense charging peak obtained during the first cycle.

**Table 7.1** The discharge capacity retentions after the first 5 cycles calculated for microwave-synthesised NMC-811, showing that the best retention was exhibited by the 775 °C 3 hour sample.

Sample name	Discharge capacity retention after 5 cycles
NMC-811 1h 900 °C	51.0 %
NMC-811 1h 850 °C	80.8 %
NMC-811 1h 800 °C	93.9 %
NMC-811 1h 750 °C	82.1 %
NMC-811 3h 750 °C	92.4 %
NMC-811 3h 775 °C	98.9 %

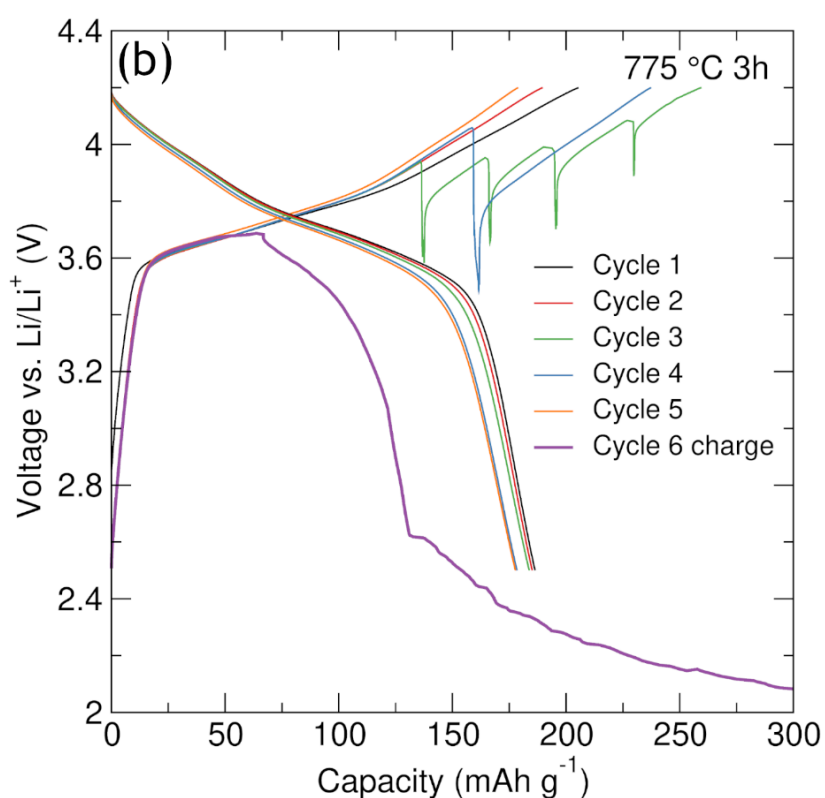
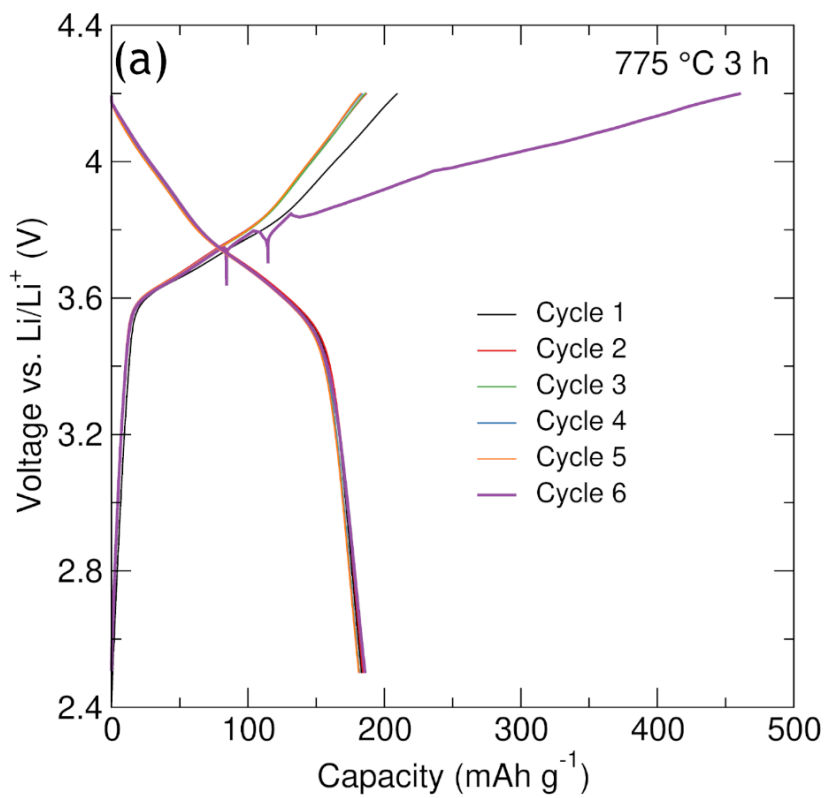


**Figure 7.12** Charge and discharge profiles obtained for the galvanostatic cycling of NMC-811 synthesised by a microwave-assisted sol-gel method at 775 °C for 3 hours. Excellent capacity retention is achieved over  $\approx$  5 cycles for repeat cells, however, evidence of cell failure is observed after this.

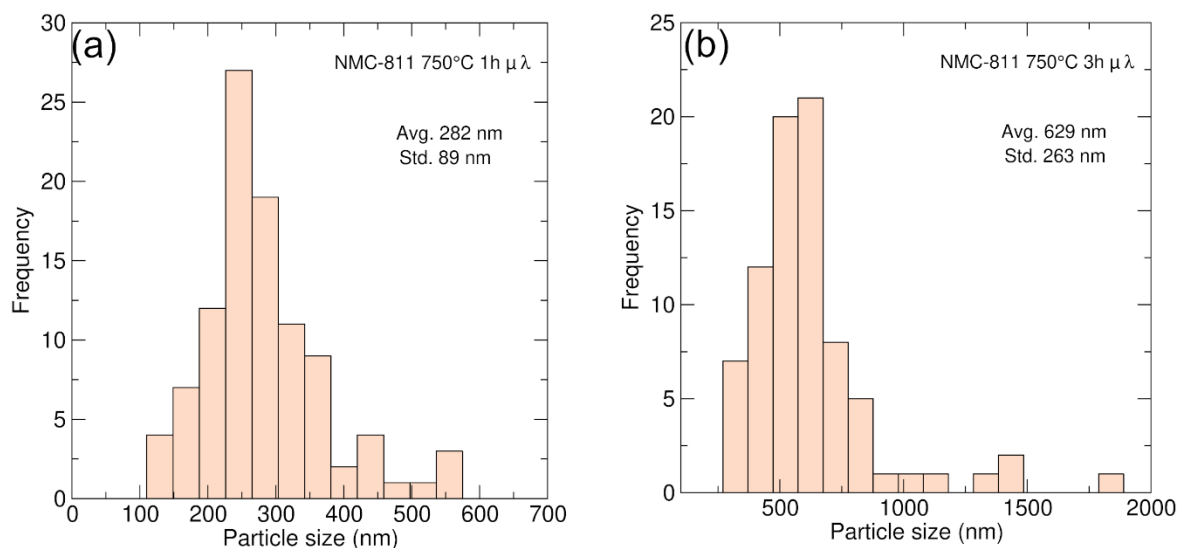


**Figure 7.13** Particle size distributions of NMC-811 prepared by a microwave-assisted sol-gel method at 750 °C for (a) 1 and (b) 3 hours. Particle sizes were calculated for 100 particles.

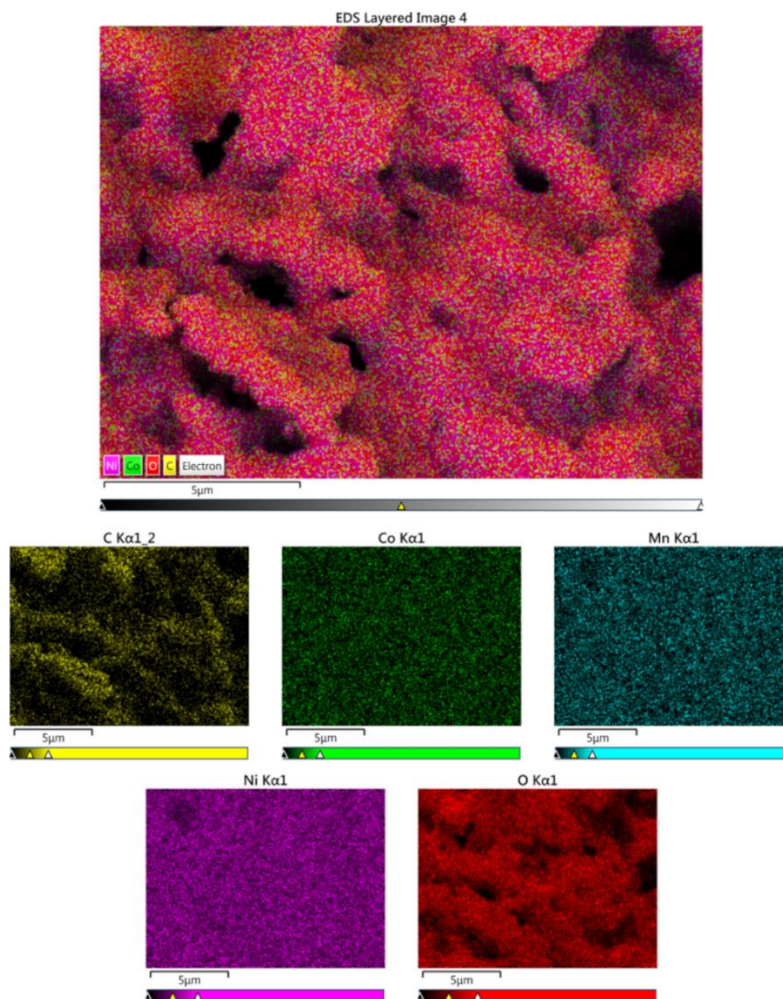


**Figure 7.14** Full elemental mapping data obtained from EDX analysis of the NMC-811 750 °C 3 h sample showing the EDS layered image of the analysed region alongside separate elemental maps for oxygen, cobalt, manganese, nickel and oxygen.

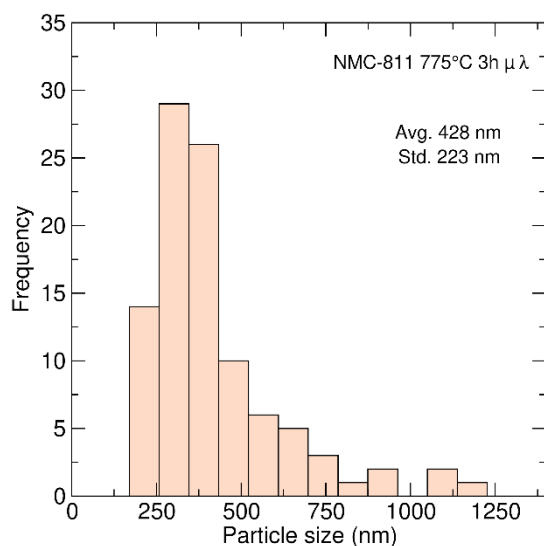


**Figure 7.15** Particle size distribution of NMC-811 prepared by a microwave-assisted sol-gel method at 775 °C for 3 hours. Particle sizes were calculated for 100 particles.

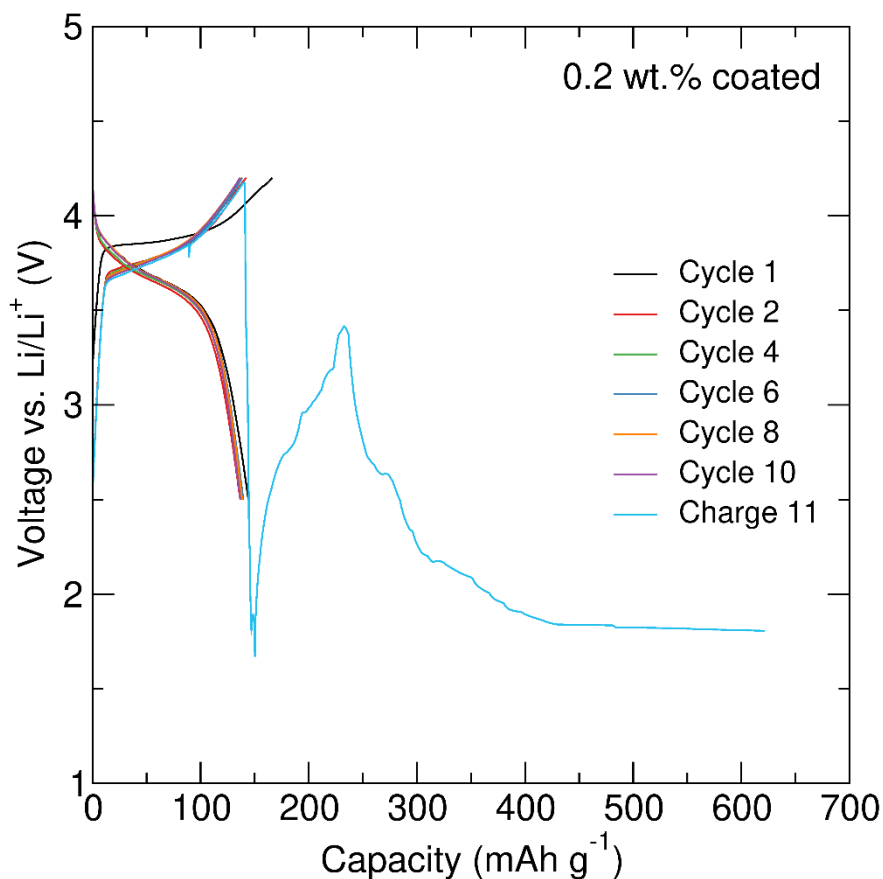


**Figure 7.16** Charge and discharge profiles of the 0.2 wt.%  $\text{Al}_2\text{O}_3$  coated NMC-811 showing the behaviour beyond the 10<sup>th</sup> cycle. Upon the end of the 11<sup>th</sup> charge process some malfunction happens rendering the cell inoperable.

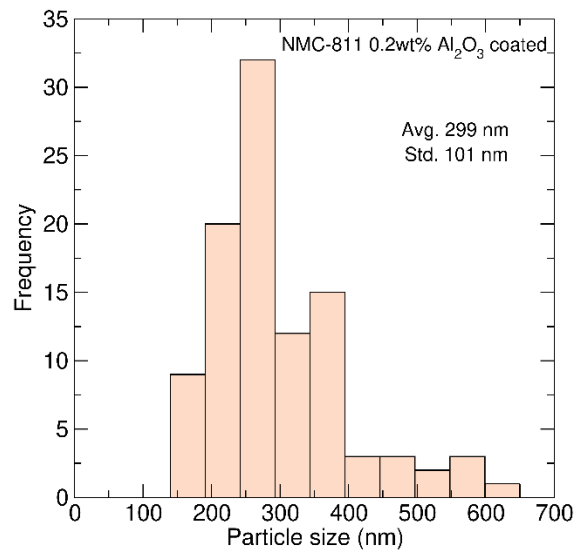


**Figure 7.17** Particle size distribution of 0.2 wt% Al<sub>2</sub>O<sub>3</sub> coated NMC-811. Particle sizes were calculated for 100 particles.